Acoustical Imaging 30

Michael P. André
Joie P. Jones
Hua Lee *Editors*

Acoustical Imaging

Springer

Acoustical Imaging

Volume 30

For further volumes:
http://www.springer.com/series/6903

Michael P. André · Joie P. Jones · Hua Lee
Editors

Acoustical Imaging

Volume 30

Springer

Editors
Prof. Michael P. André
Department of Radiology
Physics & Engineering Division
University of California
San Diego
CA 92093-9114
USA

and

San Diego VA Healthcare System
San Diego
CA 92161
USA
mandre@ucsd.edu

Prof. Hua Lee
Department of Electrical and Computer Engineering
University of California
Santa Barbara College of Engineering
Santa Barbara
CA 93106
USA
hualee@ece.ucsb.edu

Prof. Joie P. Jones
Department of Radiological Sciences
Irvine Medical Center
University of California
Orange
CA 92868
USA
jpjones@uci.edu

ISSN 0270-5117
ISBN 978-90-481-3254-6 e-ISBN 978-90-481-3255-3
DOI 10.1007/978-90-481-3255-3
Springer Dordrecht Heidelberg London New York

Library of Congress Control Number: 2008931481

International Advisory Board

Preface

The International Acoustical Imaging Symposium has been held continuously since 1968 as a unique forum for advanced research across the broad spectrum of topics in acoustical imaging. The interdisciplinary nature of the Symposium and the wide international participation are two of its main strengths. Scientists from around the world present papers in all fields of acoustical imaging in an informal environment conducive to lively discussion and cross-fertilization.

Acoustical Imaging remains a unique Symposium that promotes the sharing of technology, developments, methods and theory among all areas of acoustics. The fact that a loyal community of scientists has supported this Series for so many decades is evidence of its impact on the field. The Symposium series continues to thrive in a busy calendar of scientific meetings without the infrastructure of a professional society. It does so because those who attend and those who rely on the Proceedings as a well-known reference work acknowledge its value.

It is gratifying to see growth in the number of young scientists and students who attend the Symposium and who appear as authors in these Proceedings. This development is a testament to the efforts of the International Advisory Board and it bodes well for the future of the Symposium.

The 30th International Acoustical Imaging Symposium was held in Monterey, California USA during March 1–4, 2009. Volume 30 of the Proceedings marks a significant landmark in the series and accordingly contains an excellent comprehensive collection of papers presented in five major categories:

- Biomedical Imaging
- Acoustic Microscopy
- Non-Destructive Evaluation
- Systems Analysis
- Signal Analysis and Image Processing

As it has for more than 40 years, this volume of *Acoustical Imaging* offers both a broad perspective on the state of the art in the field as well as an in-depth look at its leading edge research. It is our privilege to be able to offer this collection and we express our sincere thanks to the contributing authors for making this series a continuing success.

This volume marks the passing of a colleague, friend and pioneer in the earliest days of *Acoustical Imaging*, Professor Glen Wade of the University of California, Santa Barbara. A modest biography of Dr. Wade appears in the Epilogue.

The 31st International Acoustical Imaging Symposium will be held April 10-13, 2011 in Warsaw, Poland.

San Diego, CA — Michael P. André
Orange, CA — Joie P. Jones
Santa Barbara, CA — Hua Lee

Acknowledgments

It is a given that any list of acknowledgements will be incomplete and so it is with our work on *Acoustical Imaging 30*. Nonetheless, it is very important that we express our sincere gratitude to all who attend, support and contribute their work to *Acoustical Imaging*. The following wonderful people, deserving of special recognition, have offered for many years wise counsel, good friendship and selfless assistance for several Symposia; without their help *Acoustical Imaging 30* would not have been possible: Piero Tortoli, Ph.D., Iwaki Akiyama, Ph.D., Becky Jones, and Janice André.

Contents

Contributors

P. Acevedo Universidad Nacional Autónoma de México, DISCA-IIMAS, México

I. Akiyama Department of Electrical and Electronic Engineering, Shonan Institute of Technology, Fujisawa, Japan

G. Akopyan University of California, Los Angeles, CA, USA

M. Alessandrini ARCES-DEIS, University of Bologna, Bologna, Italy

A. Ando Graduate School of Biomedical Engineering, Tohoku University, Japan

M.P. André Department of Radiology, University of California, San Diego, CA, USA; San Diego VA Healthcare System, San Diego, CA, USA

E.Yu. Bakulin Institute for Diagnostic Imaging Research, University of Windsor, Windsor, ON, Canada

L. Bassi Microelectronic Systems Design Laboratory, Electronics & Telecommunications Department, University of Florence, Firenze, Italy

D.B. Bennett Department of Electrical Engineering, Center for Advanced Surgical and Interventional Technology (CASIT), University of California, Los Angeles, CA, USA

M. Bernal Ultrasound Research Laboratory, Department of Physiology and Biomedical Engineering, Mayo Clinic College of Medicine, Rochester, MN, USA

A. Berry Department of Radiology, University of California, California, CA, USA

E. Boni Microelectronic Systems Design Laboratory, Electronics and Telecommunications Department, Università degli Studi di Firenze, Firenze, Italy

D. Borup Techniscan Medical Systems, Inc., Salt Lake City, UT, USA

E.R. Brown Department of Electrical and Computer Engineering, Center for Advanced Surgical and Interventional Technology (CASIT), University of California, Santa Barbara, CA, USA

V.A. Burov Department of Acoustics, Faculty of Physics, Moscow State University, Moscow, Russia

G. Busse Department for Non-Destructive Testing (IKT-ZfP), Institute for Polymer Technology, Universität Stuttgart, Stuttgart, Germany

K. Callahan Techniscan Medical Systems, Inc., Salt Lake City, UT, USA

S. Caporale University of Bologna DEIS, Bologna, Italy

A. Cellai Microelectronic Systems Design Laboratory, Electronics & Telecommunications Department, University of Florence, Firenze, Italy

L. Chen Department of Engineering, University of Cambridge, Cambridge, UK

C. Comstock Department of Radiology, University of California, California, CA, USA

A. Coron University of Hawaii, Honolulu, HI, USA

B.P. Cox Department of Bioengineering, Center for Advanced Surgical and Interventional Technology (CASIT), University of California, Los Angeles, CA, USA

M.O. Culjat Departments of Bioengineering and Surgery, Center for Advanced Surgical and Interventional Technology (CASIT), University of California, Los Angeles, CA, USA

A. Dallai Microelectronic Systems Design Laboratory, Electronics and Telecommunications Department, Università degli Studi di Firenze, Firenze, Italy

J. Dech The Institute for Diagnostic Imaging Research, University of Windsor, Windsor, ON, Canada

L. De Marchi ARCES-DEIS, University of Bologna, Bologna, Italy

A. Dentinger General Electric Corporate Research & Development, Albany, New York, USA

A. DiCarlo The Institute for Diagnostic Imaging Research, University of Windsor, Windsor, ON, Canada

J.-F. Dord Department of Mechanical Engineering, Department of Aeronautics and Astronautics, Stanford University, Stanford, CA, USA

D. Döring Department for Non-Destructive Testing (IKT-ZfP), Institute for Polymer Technology, Universität Stuttgart, Stuttgart, Germany

A. Durán Universidad Nacional Autónoma de México, DISCA-IIMAS, México

T. Eura Faculty of Engineering, Doshisha University, Kyoto, Japan

C. Farhat Department of Mechanical Engineering, Department of Aeronautics and Astronautics, Stanford University, Stanford, CA, USA

E.J. Feleppa Riverside Research Institute, New York, NY, USA

L. Francalanci Microelectronic Systems Design Laboratory, Electronics and Telecommunications Department, Università degli Studi di Firenze, Firenze, Italy

M. Fujiwara Faculty of System Design, Tokyo Metropolitan University, Tokyo, Japan

M. Fukuda Department of Electrical and Electronic Engineering, Faculty of Engineering and Resource Science, Akita University, Akita, Japan

M. Galperin Department of Radiology, University of California, California, CA, USA; Almen Laboratories, Inc., Vista, CA, USA

W.S. Gan Acoustical Technologies Singapore Pte Ltd, Singapore

D. Gavrilov Institute for Diagnostic Imaging Research, University of Windsor, Windsor, ON, Canada

A.H. Gee Department of Engineering, University of Cambridge, Cambridge, UK

G. Ghodsi Institute for Diagnostic Imaging Research, University of Windsor, Windsor, ON, Canada

H. Gomersall Department of Engineering, University of Cambridge, Cambridge, UK

J.F. Greenleaf Ultrasound Research Laboratory, Department of Physiology and Biomedical Engineering, Mayo Clinic College of Medicine, Rochester, MN, USA

W. Grill Institute of Experimental Physics II, University of Leipzig, Leipzig, Germany

W.S. Grundfest Department of Bioengineering, Center for Advanced Surgical and Interventional Technology (CASIT), University of California, Los Angeles, CA, USA

F. Guidi Microelectronic Systems Design Laboratory, Electronics & Telecommunications Department, University of Florence, Firenze, Italy

M. Hata University of Hawaii, Honolulu, HI, USA

Y. Hagiwara Department of Orthopaedic Surgery, Tohoku University School of Medicine, Japan

K. Hatori Tohoku University Graduate School of Dentistry, Sendai, Japan

K. Hillmann SAP Deutschland AG & Co. KG, Bensheim, Germany

N. Hozumi Aichi Institute of Technology, Toyota, Japan

U.Z. Ijaz Department of Engineering, University of Cambridge, Cambridge, UK

K. Imano Department of Electrical and Electronic Engineering, Faculty of Engineering and Resource Science, Akita University, Akita, Japan

E. Itoi Tohoku University Graduate School of Dentistry, Sendai, Japan

J.S. Jaffe Department of Electrical and Computer Engineering, University of California San Diego, San Diego, CA, USA

S. Johnson Techniscan Medical Systems, Inc., Salt Lake City, UT, USA

J.P. Jones Department of Radiological Sciences, Irvine Medical Center, University of California, Orange, CA, USA

A. Kamanyi Institute of Experimental Physics II, University of Leipzig, Leipzig, Germany

P.T. Khuri-Yakub Stanford University, Stanford, CA, USA

N. Kingsbury Department of Engineering, University of Cambridge, Cambridge, UK

Z. Klimonda Institute of Fundamental Technological Research, Polish Academy of Sciences, Warsaw, Poland

K. Kobayashi Honda Electronics Co. Ltd, Toyohashi, Japan

M. Kölsch Naval Postgraduate School, Monterey, CA, USA

M. Konno Faculty of System Design, Tokyo Metropolitan University, Tokyo, Japan

T. Kujawska Institute of Fundamental Technological Research Polish Academy of Sciences, Warsaw, Poland

P. Laugier Université Pierre et Marie Curie, Paris, France; CNRS, Paris, France

M. Ledgerwood Department of Radiology, University of California, California, CA, USA

D. Lee Hanmmersmith Hospital, London, UK

H. Lee Department of Electrical and Computer Engineering, Center for Advanced Surgical and Interventional Technology (CASIT), University of California, Santa Barbara, CA, USA

M. Lee Department of Bioengineering, Center for Advanced Surgical and Interventional Technology (CASIT), University of California, Los Angeles, CA, USA

S. Leeman Hanmmersmith Hospital, London, UK

V. Leshchynsky The Institute for Diagnostic Imaging Research, University of Windsor, Windsor, ON, Canada

D.-S. Lin Stanford University, Stanford, CA, USA

J. Litniewski Institute of Fundamental Technological Research, Polish Academy of Sciences, Warsaw, Poland

M. Lubrick The Institute for Diagnostic Imaging Research, University of Windsor, Windsor, ON, Canada

J. Machi University of Hawaii, Honolulu, HI, USA

R.Gr. Maev Chrysler/NSERC Industrial Research Chair in Applied Solid State Physics and Material Characterization, The Institute for Diagnostic Imaging Research, University of Windsor, Windsor, ON, Canada

A. Maeva Institute for Diagnostic Imaging Research, University of Windsor, Windsor, ON, Canada

E.Y. Maeva The Institute for Diagnostic Imaging Research, University of Windsor, Windsor, ON, Canada

S. Maggio ARCES-DEIS, University of Bologna, Bologna, Italy

A. Mahajan University of California, Los Angeles, CA, USA

E. Malyarenko Tessonics Corporation, Birmingham, MI, USA

J. Mamou Riverside Research Institute, New York, NY, USA

A. Marzani University of Bologna DEIS, Bologna, Italy

T. Masek Naval Postgraduate School, Monterey, CA, USA

C. Miyasaka The Pennsylvania State University, University Park, PA, USA

E.A. Mohamed Institute of Experimental Physics II, University of Leipzig, Leipzig, Germany

K. Nakamura Department of Electrical and Electronic Engineering, Tokyo Institute of Technology, Tokyo, Japan

S. Natarjan Department of Bioengineering, Center for Advanced Surgical and Interventional Technology (CASIT), University of California, Los Angeles, CA, USA

I. Nenadich Ultrasound Research Laboratory, Department of Physiology and Biomedical Engineering, Mayo Clinic College of Medicine, Rochester, MN, USA

W. Ngwa Department of Physics, University of Central Florida, Orlando, FL, USA

A. Nikoozadeh Stanford University, Stanford, CA, USA

E. Nolan Hanmmersmith Hospital, London, UK

A. Nowicki Polish Academy of Sciences, Institute of Fundamental Technological Research, Warsaw, Poland

M. O'Boyle Department of Radiology, University of California, San Diego, CA, USA

M. O'Donnell University of Washington, Seattle, WA, USA

H. Ojeda-Fournier Department of Radiology, University of California, California, CA, USA

K. Okubo Faculty of System Design, Tokyo Metropolitan University, Tokyo, Japan

L. Olson Department of Radiology, University of California, California, CA, USA

Ö. Oralkan Stanford University, Stanford, CA, USA

A. Palladini ARCES-DEIS, University of Bologna, Bologna, Italy

Y. Parisky Mammoth Hospital Medical Imaging Center, Mammoth Lakes, CA, USA

R.W. Prager Department of Engineering, University of Cambridge, Cambridge, UK

A. Ramalli Microelectronic Systems Design Laboratory, Electronics & Telecommunications Department, University of Florence, Firenze, Italy

S. Ricci Microelectronic Systems Design Laboratory, Electronics & Telecommunications Department, University of Florence, Firenze, Italy

P.L.D. Roberts Department of Electrical and Computer Engineering, University of California, San Diego, CA, USA

E. Rubio Universidad Nacional Autónoma de México, DISCA-IIMAS, México

O.D. Rumyantseva Department of Acoustics, Faculty of Physics, Moscow State University, Moscow, Russia

J. Sadler The Institute for Diagnostic Imaging Research, University of Windsor, Windsor, ON, Canada

Y. Saijo Graduate School of Biomedical Engineering, Tohoku University, Sendai, Japan

D. Sahn Oregon Health and Science University, Portland, OR, USA

S. Sakai Kanebo Cosmetics Inc., Kotobukimachi, Japan

M. Scebran ARCES-DEIS, University of Bologna, Bologna, Italy

F. Severin The Institute for Diagnostic Imaging Research, University of Windsor, Windsor, ON, Canada

I. Severina The Institute for Diagnostic Imaging Research, University of Windsor, Windsor, ON, Canada

K. Shapoori Tessonics Corporation, Birmingham, MI, USA

H.-C. Shin Department of Engineering, University of Cambridge, Cambridge, UK

K. Shivkumar University of California, Los Angeles, CA, USA

A.A. Shmelev Department of Acoustics, Faculty of Physics, Moscow State University, Moscow, Russia

R.S. Singh Department of Electrical and Computer Engineering, University of California, Santa Barbara, CA, USA

J. Smith Techniscan Medical Systems, Inc., Salt Lake City, UT, USA

I. Solodov Department for Non-Destructive Testing (IKT-ZfP), Institute for Polymer Technology, Universität Stuttgart, Stuttgart, Germany

N. Speciale ARCES-DEIS, University of Bologna, Bologna, Italy

D.N. Stephens University of California, Davis, CA, USA

N. Tagawa Faculty of System Design, Tokyo Metropolitan University, Tokyo, Japan

T. Takayasu Department of Electrical and Electronic Engineering, Tokyo Institute of Technology, Tokyo, Japan

A. Tanaka Faculty of Symbiotic Systems Science, Fukushima University, Fukushima, Japan

A. Taylor Department of Radiology, University of California, California, CA, USA

K. Thomenius General Electric Corporate Research & Development, Albany, NY, USA

S. Titov The Institute for Diagnostic Imaging Research, University of Windsor, Windsor, ON, Canada

B.R. Tittmann The Pennsylvania State University, University Park, PA, USA

P. Tortoli Microelectronic Systems Design Laboratory, Electronics & Telecommunications Department, University of Florence, Firenze, Italy

G.M. Treece Department of Engineering, University of Cambridge, Cambridge, UK

T. Tsuchiya Department of Information System Design, Doshisha University, Kyoto, Japan

M. von Buttlar Institute of Experimental Physics II, University of Leipzig, Leipzig, Germany

R. Wannemacher Institute of Experimental Physics II, University of Leipzig, Leipzig, Germany

Y. Watanabe Faculty of Life and Medical Sciences, Doshisha University, Kyoto, Japan

D. Wildes General Electric Corporate Research & Development, Albany, NY, USA

J. Wiskin Techniscan Medical Systems, Inc., Salt Lake City, UT, USA; Department of Bioengineering, University of Utah, Salt Lake City, UT, USA

J. Wójcik Institute of Fundamental Technological Research, Polish Academy of Sciences, Warsaw, Poland

I.O. Wygant Stanford University, Stanford, CA, USA

E. Yanagihara University of Hawaii, Honolulu, HI, USA

K. Yoshida Faculty of Life and Medical Sciences, Doshisha University, Kyoto, Japan

Part I
Biomedical Imaging

Performance of a Method to Standardize Breast Ultrasound Interpretation Using Image Processing and Case-Based Reasoning

M.P. André, M. Galperin, A. Berry, H. Ojeda-Fournier, M. O'Boyle, L. Olson, C. Comstock, A. Taylor, and M. Ledgerwood

Abstract Our computer-aided diagnostic (CADx) tool uses advanced image processing and artificial intelligence to analyze findings on breast sonography images. The goal is to standardize reporting of such findings using well-defined descriptors and to improve accuracy and reproducibility of interpretation of breast ultrasound by radiologists. This study examined several factors that may impact accuracy and reproducibility of the CADx software, which proved to be highly accurate and stabile over several operating conditions.

Keywords Breast cancer · Sonography · Computer-aided diagnosis · Image processing · Relative similarity · ROC analysis · Segmentation · Case-based reasoning

1 Introduction

Ultrasound is widely regarded as the adjunct procedure of choice to mammography screening, especially for distinguishing cystic from solid masses for which accuracy is 96–100% [1]. Ordinarily, if a lesion appears solid or indeterminate, biopsy is frequently recommended, although current estimates of the False Negative (FN) rate and Positive Predictive Value (PPV) for breast ultrasound are not definitive. Furthermore, even with combined information from mammography and ultrasound it is apparent that each radiologist may apply a different decision threshold to recommend biopsy of a suspicious mass. In addition, operator variability and image quality are often identified as important issues in medical breast ultrasound (US), perhaps one of the more difficult medical imaging procedures to perform [2].

Over several years, Almen Laboratories and the University of California, San Diego (UCSD) developed a sophisticated computer-aided diagnostic system for analyzing findings on breast sonography, Breast Companion® (BC) [3–5]. Although

M.P. André (✉)
Department of Radiology, University of California, San Diego, CA, USA; San Diego VA Healthcare System, San Diego, CA 92161, USA
e-mail: mandre@ucsd.edu

M.P. André et al. (eds.), *Acoustical Imaging*, Acoustical Imaging 30,
DOI 10.1007/978-90-481-3255-3_1,

BC began as a research tool, its clinical utility and ease of use have evolved considerably. A new user interface was developed for BC that incorporates a structured electronic medical reporting system in conformance with the American College of Radiology Breast Imaging Reporting and Data System (ACR BI-RADS®) sonography protocol and lexicon in an integrated workstation environment [6]. This portion of BC has been approved for clinical use by the USA Food and Drug Administration. The 332 cases in the Reference Library have known findings confirmed by biopsy, aspiration or 2-year benign follow-up and include a detailed BI-RADS report with descriptions and impressions provided by consensus of expert radiologists. BC CADx includes an integrated tutorial designed to train the use of CADx but also is now available for the general use of training the implementation of the BI-RADS® protocol and lexicon (BI-RADS Tutor®). It incorporates extensive "how-to" aids with demonstration videos that guide both experienced and novice practitioners through the definitions, lexicon and procedures of the ACR BI-RADS® ultrasound protocol using programmed learning and on-board coaching from three expert radiologists. BC may also be used to create individual teaching files of interesting cases.

The BC CADx is the first computer-aided *diagnostic* system as compared to a computer-aided *detection* tool that is traditionally designed for independently identifying suspicious areas on a screening examination. In the CADx domain, some level of suspicion may already exist from prior imaging results or physical exams (palpation, for example), which are the most common indications for breast sonography. BC is tailored as an aid to the radiologist for interpretation of the diagnostic breast ultrasound examination but the underlying technology is applicable to other medical imaging procedures including breast MRI, mammography, computed tomography of the lung, carotid artery flow analysis, etc., especially where the diseased areas(s) can be identified with visible borders and structured interpretation schemes are extant.

The purpose of this study was to examine specific factors that may impact the accuracy and reproducibility of results from the developed CADx software in future clinical use and to summarize its overall performance. The overall goals are to help standardize interpretation and reporting, to increase confidence in benign findings, to assist review of a large number of images such as produced by whole-breast ultrasound screening, to potentially reduce well-known inter-radiologist variability and to reduce the number of breast biopsies, approximately 80% of which are benign.

2 Materials and Methods

2.1 Database of Clinical Breast Sonograms

Under UCSD Institutional Review Board approval a database of 596 breast sonogram cases was assembled chronologically from the medical center Picture Archiving and Computer System (PACS) and computerized medical records system. When a suitable case was found by the Lead Radiologist where truth was confirmed

(2-year benign follow up or biopsy), all ultrasound images in the study were examined to ensure they were free of graphic overlays or markers, had at least two views of each mass, had minimal artifacts, had conclusive pathology results for biopsies, had a corresponding mammogram available, etc., in accordance with our acceptance and validation criteria. All images in the series for each selected case were de-identified following USA HIPAA rules and were added to the Research PACS archive.

The mix of case findings in the database was: simple cysts (165, 27.7%), complicated cysts (58, 9.7%), benign solid masses (242, 40.7%), malignant masses (133, 22.3%). The age range was 21–90 years old. The case mix of findings and age distribution of patients match very closely (<2% differences) to the 5-year average population of cases in the UCSD Moores Cancer Center Breast Imaging Service. It is a highly representative sample for the local institution plus it corresponds closely to reported national averages in the U.S., reported as 36% cysts, 7% complex cysts, 34% fibroadenomas and 22% malignant [7]. Based on our earlier research in reader performance and variability, [3] 580 cases provide sufficient sample size to detect differences of 0.02 in the area under the Receiver Operator Characteristic (ROC) curve for individual radiologists with 80% statistical power and alpha = 0.05 [8, 9].

Two subsets of the breast sonogram database were also assembled for testing reproducibility of BC. The first was comprised of 55 cases with confirmed findings in which the suspicious mass is visualized on at least two images, radial and antiradial. There were 10 simple cysts, 10 complicated cysts, 10 solid benign masses and 25 malignant masses in the subset. These images were acquired during the same imaging exam with the same ultrasound instrument and transducer for which agreement was determined by the two-tailed t-test and ROC area under the curve (A_Z). The second subset was comprised of 28 cases (40% malignant) where two ultrasound exams of the same mass were performed on two different occasions within a maximum of 3 weeks. One exam was acquired on a GE Logiq 9 scanner and the other on a Siemens Acuson. BC was used to calculate CLA for each image pair and agreement was measured by comparing A_Z and the kappa statistic.

2.2 Computer-Aided Diagnostic System

The CADx system provides extensive tools to define and segment breast masses, computes numeric features of the mass, compares the mass to images in a database of masses with known findings and outcomes (Reference Library, "RL"), then using Relative Similarity identifies, retrieves and displays almost instantaneously a cluster of the most similar cases. BC uses case-based reasoning analysis derived from known findings of the most similar cases in the retrieved cluster, which are determined based on measurement of parameters in the following categories: margins, shape, echogenicity, echo texture, orientation, and posterior acoustic attenuation pattern. BC provides numerical data on the mass in comparison to the most similar cases from the Reference Library and computes a Computerized Lesion Assessment (CLA) score, similar to the assessment category of the BI-RADS that ranges from 1 through 5 with 5 representing "definitely malignant." The BI-RADS scale is

not linear in correspondence with the ACR Guidance suggestion on probability of malignancy, but in practice a BI-RADS category of 4 or 5 is recommended for biopsy. BC requires no classifier training unlike artificial neural networks commonly used in computer-aided detection systems for screening examinations. The BC protocol functions with the "physician in the loop" at each step whereby the suspicious region on the image to be analyzed is selected by the radiologist who may choose more than one image if he/she so wishes.

CLA CADx score is computed (Equation 1) from the Relative Similarity (**R**) classifier derived from a N-dimensional vector **P**. Relative Similarity is calculated for a particular lesion $\mathbf{P}_{it}$ (the index of this "template" object) compared to the other lesions, $\mathbf{P}_k$ (k = 1, . . .L), where L is the number of masses it is compared to from the Reference Library and N is the number of features (L = 332 and N = 9 in the current BC CADx). Weighting factors, ω, may be applied to these results to enhance the classification; they are established by multi-factorial regression analysis of cases with known findings. Processing is nearly instantaneous.

$$\overline{R} = \left(\sum_{k=1}^{L} \left(p_k^t - P_k^t \right)^s \cdot \omega_k \right)^{1/s} \tag{1}$$

Figure 1 shows a screen image of BC for a complex cyst compared to other images in the RL. The mass is dark, with some internal echoes and posterior

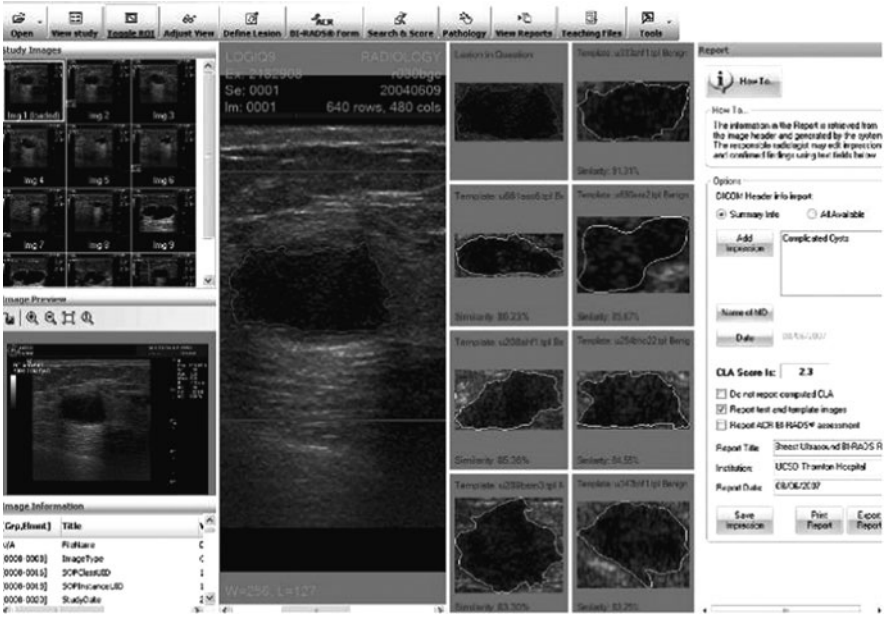

Fig. 1 Selected view of a complex cyst (*lower left*) from the sonogram series (*upper left*) is analyzed (*center panel*) and compared to other images from the Reference Library (*right center*). The CLA score 2.3 is displayed on the report template

enhancement consistent with a cyst but with irregular, less distinct margins possibly consistent with a solid mass. The margin of the mass is segmented from the surrounding tissue and depicted by the isocontour. Seven cases are automatically retrieved and displayed with contours on the right listed in rank order of Relative Similarity to the unknown mass. In this case, all seven of the "similar" masses were benign and a low CLA score of 2.3 was calculated (lower probability of malignancy).

Subsequent pages in BC provide the radiologist with forms to select BI-RADS descriptors and add recommendations and impressions for the final report that may be exported to PACS or the hospital information system.

3 Results

Four sub-specialty breast imaging radiologists independently assessed the 596 US exams in the database following the standard BI-RADS protocol and using a hard-copy ACR report form that includes final assessment category, descriptors and recommendations for follow-up interval or biopsy. ROC areas under the curve (A_Z) using the Metz fitting technique varied from 0.88 – 0.90 ± 0.02SE, the empirical ROC A_z was 0.83 – 0.85 ± 0.02SE and neither were significantly different between radiologists [10]. These results are very similar to those achieved in our prior studies and to those reported elsewhere for breast sonography. The results of the radiologist reader study, both ROC performance and inter-reader variability, offer a relevant benchmark for tests of BC CADx performance.

BC was tested in "standalone mode" whereby a senior radiologist provided careful segmentation of each mass to test the accuracy of the CLA computational output for the 596 confirmed cases. In this laboratory, not clinical, setting A_Z for BC (0.98 ± 0.02SE), was significantly higher than A_Z for the radiologists with statistical power of 93% and $p < 0.001$. All of the radiologists had very high Sensitivity (94–99%) for cancer and very high Negative Predictive Value (98–99%) as did BC (99% and 97%, respectively). As might be expected, the radiologists show lower Specificity (42–54%) and Positive Predictive Value (33–40%) since they likely apply lower decision thresholds to ensure they do not miss cancer.

Reproducibility of CADx performance was examined by comparing two views of the same mass, radial and anti-radial, acquired during the same examination for 55 masses. An example of such an image pair is shown in Fig. 2 for a benign fibroadenoma. These images show differences in shape and orientation more than in echo pattern, boundary, posterior shadowing or margins. Greater variability might be found in malignancies and solid benign masses with perhaps less variability in complicated cysts and simple cysts. The measured CLA values for the image pairs are listed in Table 1 by type of mass. No significant differences were found as indicated by the asterisk. The areas under the ROC curves for the two views were likewise not significantly different: 0.94 ± 0.03 for radial and 0.94 ± 0.03 for anti-radial.

Comparison of the two images acquired in different imaging sessions on two different scanners shows CADx performance was not statistically significantly different. ROC A_Z for CLA values was 0.96 ± 0.03 for the GE Logiq 9 scanner

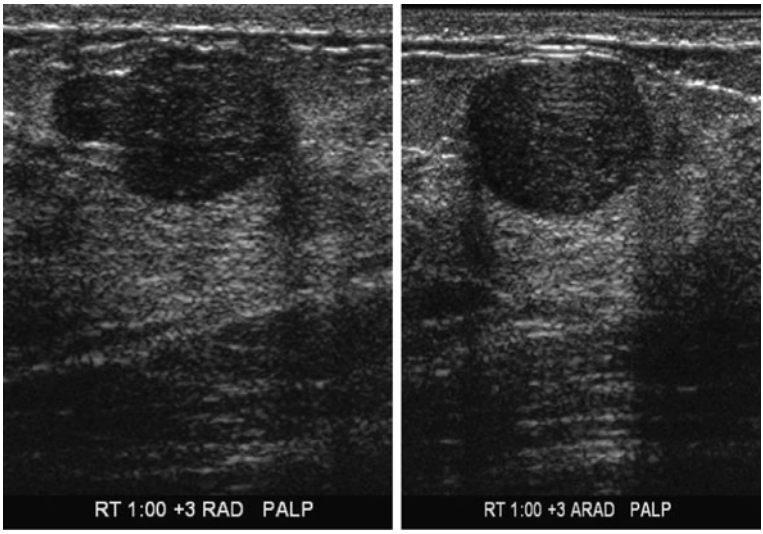

Fig. 2 Radial (*left*) and anti-radial (*right*) views of the same mass (fibroadenoma)

Table 1 CLA Values for two views of same mass (55 cases, 40% malignant)

Lesion Type	Radial Mean±SD	Anti-Radial Mean±SD	2-tailed p value
Simple cyst	2.00±0.00	2.00±0.00	1.000*
Complicated cyst	2.31±0.30	2.18±0.98	0.427*
Solid benign	2.93±1.21	2.95±1.23	0.936*
Malignant	4.40±0.81	4.56±0.73	0.482*

*No significant difference.

and 0.94 ± 0.05 for the Siemens Acuson. Agreement between the image pairs as measured by the kappa statistic was 0.72, which indicates substantial agreement.

4 Conclusions

Inter- and intra-reader variability are comparable for four radiologists reading the same set of 596 breast sonograms (2% of the ROC A_Z). Standalone ROC performance of the BC CLA ($A_Z = 0.98$) was found to be significantly higher than the four radiologists whose average $A_Z = 0.89$ for the fitted ROC curve and $A_Z = 0.84$ for the empirical one.

No significant difference was found when radial and anti-radial images of the same mass were compared or when images of the same mass were compared from two different examinations on two different scanners. These results suggest that the BC CADx is reproducible and independent of scanner or operator factors, although this issue warrants additional study.

We appreciate that the radiologist is faced with a decision-making task during interpretation of breast ultrasound that is influenced by many factors, not all of which were included in this study. Nonetheless, the improved results represent a very high performance. They also suggest that the BC CADx approach may be successful in the aims of aiding radiologists to reduce biopsies on benign masses and to achieve higher Specificity with minimal impact on Sensitivity. Investigation of the BC CADx in a clinical investigational setting is under way where a group of experienced radiologists are reading the database of 596 cases twice: first in the normal clinical manner following the ACR BI-RADS protocol, and second while using the electronic reporting system of the BC CADx including consideration of the CLA score prior to making their final recommendation. An interval of approximately 6 months will occur between imaging review sessions. This new study examines how the use of BC may impact accuracy of reading performance of the radiologists and it will document any changes in reader variability. The Multi-Reader Multi-Case study design applies the methods of Dorfman, Berbaum and Metz to detect a 3% change in A_Z as well as a 5% change in Specificity with 95% power [8].

Acknowledgements This work was supported in part by grant 2R44CA112858 from the National Institutes of Health, National Cancer Institute, USA and by the Gustavus and Louise Pfeiffer Research Foundation, Denville, NJ, USA.

We gratefully acknowledge the support of Julie Phan, B.S., Paul Feigin, Ph.D., Paul Clopton, M.S. and Janice J. André, M.S. during discussions of the details of this work.

References

1. Stavros, A.T., Thickman, D., Rapp, C.L., Dennis, M.A., Parker, S.H., Sisney, G.A.: Solid breast nodules: Use of sonography to distinguish between benign and malignant lesions. Radiology **196**, 123–134 (1995)
2. Lee, H.J., Kim, E.K., Kim, M.J., Youk, J.H., et al.: Observer variability of breast imaging reporting and data system (BI-RADS) for breast ultrasound. Eur. J. Radiol. **65**, 293–298 (2008)
3. André, M.P., Galperin, M., Contro, G., Omid, N., Olson, L., Comstock, C., Richman, K., O'Boyle, M.: Diagnostic performance of a computer-aided image analysis system for breast ultrasound. Acoustical Imaging **28**, 267–277 (2007)
4. Galperin, M., André, M.P., Contro, G., Omid, N.: Optimization of a breast mass classifier for computer-aided ultrasound analysis. Acoustical Imaging **28**, 341–348 (2007)
5. Galperin, M., André, M.P., Barker, C., Mantrawadi, L., Olson, L., O'Boyle, M.: Reproducibility of image analysis for breast ultrasound computer-aided diagnosis. Acoustical Imaging **29**, 397–402 (2008)
6. American College of Radiology: ACR Standards 2000–2001. Reston, VA: American College of Radiology (2000)
7. Imaginis Women's Health Resource (http://imaginis.com/breasthealth/diagnosis.asp) and American College of Radiology (http://www.acr.org/)
8. Dorfman, D.D., Berbaum, K.S., Metz, C.E.: Receiver operating characteristic rating analysis: Generalization to the population of readers and patients with the jackknife method. Invest. Radiol. **27**, 723–731 (1992)
9. Metz, C.E.: ROC methodology in radiographic imaging. Invest. Radiol. **21**, 720–733 (1986)
10. Lazarus E., Mainiero M.B., Schepps B., et al.: BI-RADS lexicon for US and mammography: Inter-observer variability and positive predictive value. Radiology **239**(2), 385–391 (2006)

High Resolution Ultrasonic Method for 3D Fingerprint Recognizable Characteristics in Biometrics Identification

R.Gr. Maev, E.Yu. Bakulin, A. Maeva, and F. Severin

Abstract Biometrics is a rapidly evolving scientific and applied discipline that studies possible ways of personal identification by means of unique biological characteristics. Such identification is important in various situations requiring restricted access to certain areas, information and personal data and for cases of medical emergencies. A number of automated biometric techniques have been developed, including fingerprint, hand shape, eye and facial recognition, thermographic imaging, etc. All these techniques differ in the recognizable parameters, usability, accuracy and cost. Among these, fingerprint recognition stands alone since a very large database of fingerprints has already been acquired. Also, fingerprints are key evidence left at a crime scene and can be used to indentify suspects. Therefore, of all automated biometric techniques, especially in the field of law enforcement, fingerprint identification seems to be the most promising. We introduce a newer development of the ultrasonic fingerprint imaging. The proposed method obtains a scan only once and then varies the C-scan gate position and width to visualize acoustic reflections from any appropriate depth inside the skin. Also, B-scans and A-scans can be recreated from any position using such data array, which gives the control over the visualization options. By setting the C-scan gate deeper inside the skin, distribution of the sweat pores (which are located along the ridges) can be easily visualized. This distribution should be unique for each individual so this provides a means of personal identification, which is not affected by any changes (accidental or intentional) of the fingers' surface conditions. This paper discusses different setups, acoustic parameters of the system, signal and image processing options and possible ways of 3-dimentional visualization that could be used as a recognizable characteristic in biometric identification.

Keywords Identification · Fingerprints · Skin · Acoustic microscopy · Biometrics

R.Gr. Maev (✉)
Chrysler/NSERC Industrial Research Chair in Applied Solid State Physics and Material Characterization, The Institute for Diagnostic Imaging Research, University of Windsor, Windsor, ON N9B 3P4, Canada
e-mail: maev@uwindsor.ca

M.P. André et al. (eds.), *Acoustical Imaging*, Acoustical Imaging 30,
DOI 10.1007/978-90-481-3255-3_2,

1 Introduction

Biometrics is the measurement of physical and biological characteristics which are unique to each individual for purpose of personal identification. Such identification is critical in situations requiring restricted access to areas, data and objects or in case of some medical emergencies. Direct measurement is supposed to be more foolproof and protected in comparison with classical linking some kind of tag (ID, key or password) to the person.

There are several techniques for biometrics authentication which are actively developing and promoting by different companies [1]. The oldest one is the face recognition which was performed manually during centuries. Formalization of this process in several complicated algorithms had lead to development of automatic systems; however they essentially rely on camera positioning and are known to not be fairly accurate due to fluctuations in person's appearance and weight. Hand shape recognition also is not reliable enough due to various changes in the dimensions and placement of the original measurements of the hand. Identification based on scanning of iris and retinal patterns is much more accurate but requires complicated positioning and can be affected by the contact lens.

All of the above methods provide data which are not compatible with existing law enforcement databases and information accumulated in criminal practice. Such compatibility exits for fingerprint biometrics. Widespread and long-term usage of this method gives essential experience and familiarity. Classical pen and ink are gradually replaced by more convenient and sophisticated devices utilizing the optical, capacitance and ultrasonic techniques [1–3]. Each of ten easily assessable unique fingerprints has relatively small area, what makes the scanning process fast and convenient.

This study extends scanning acoustic microscope technology for fingerprint imaging. The method is insensitive for surface contamination and allows use not only the surface grooves pattern, but also the internal structure of the fingers. Mapping of elements of this structure, such as sweat pores and scars, increase information and add security measurements.

2 Experimental Setup

The 3D acoustical data were acquired with Tessonics AM-1103 scanning acoustic microscope (Tessonics Corp., Canada) in short-pulse reflection mode [4]. The optimal transducer for fingerprint imaging, as follow from preliminary tests, is the 50 MHz a narrow-aperture focused ultrasonic lens which provides spatial resolution of about 15 μm. Scanning 10 mm × 10 mm area with resolution 25 mkm (corresponds to 1000 dpi image) takes 2–3 min for this general-purpose device. A specialized holder was designed to keep finger of volunteer motionless during this time. Finger surface was pressed against acoustically transparent polystyrene plate with thickness 2 mm (Fig. 1). Acoustic gel was used between the plate and finger for

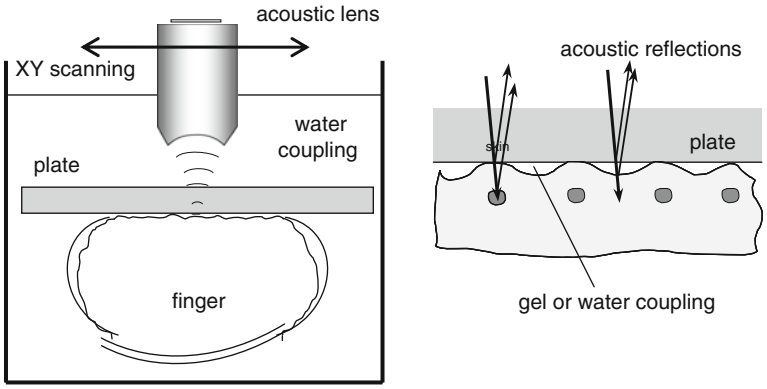

Fig. 1 Acoustical setup for fingerprints imaging

better acoustic contact. The whole assembly was submerged into water tank under the lens scanning plane (Fig. 2).

The output signal from transducer (A-scan) in the time interval 0–1 μs after bottom of the plate reflection includes a series of pulses representing sound reflection from skin elements along the axis. These signals obtained during one scanning stroke were compiled into two- dimensional B-Scan which resembles a 0.8 mm deep vertical cross section of the sample. Series of B-scans were further complied and stored into 3D matrix of information. A horizontal slice of this volume at chosen depth can be plotted as acoustic C-scan. This technique allowed us to only once

Fig. 2 Holder with volunteer's finger under acoustical microscope

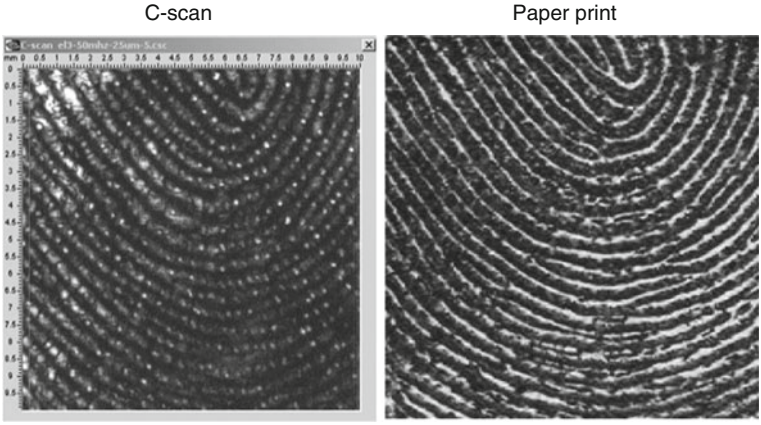

Fig. 3 Comparison of acoustical C-scan and standard ink-paper print

obtain a scan and then vary the C-scan gate position and width to visualize acoustic reflections from any appropriate depth inside the skin. Also, B-scans and A-scans can be recreated from any point. Therefore, this gives the total control over the visualization options.

3 Results

Example of raw acoustic images of a fingerprint, obtained in this manner versus the optical (ink-and-paper) image of the same finger area is shown on Fig. 3. The pattern is obviously identical; however the grooves in the acoustical image (light) and the optical one are inverted (dark). The white spots located along the ridges of dermis at acoustical image are sweat pores. Given that their distribution should be unique for each individual, this provides additional means of personal identification which is not affected by any changes (accidental or intentional) of the finger surface conditions.

Focusing on close undersurface layer reveals their position as well as depth and parameters of dermal layers (Fig. 4). This structure is consistent even in presence of mechanical distortions, like a scar (Fig. 5).

4 Conclusions

The acoustic scanning method for biometrics fingerprint characterization provides great insight and identification ability. The collected information can be directly compared to the very large already existing database of fingerprints. The method allows for not only the fingerprint pattern to be analyzed but also other dermis elements such as scars and sweat pores. These details are as unique as the print and unlike the surface cannot be surgically altered or removed.

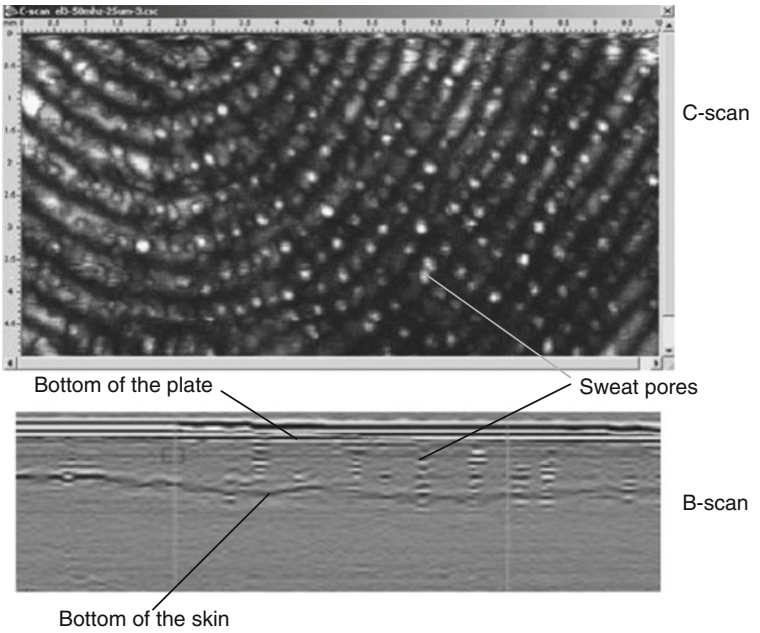

Fig. 4 A zoomed in C-scan where sweat pores are clearly visible along grooves of dermis. The dermal layers are visible in the B-scan along with the bottom of the plate

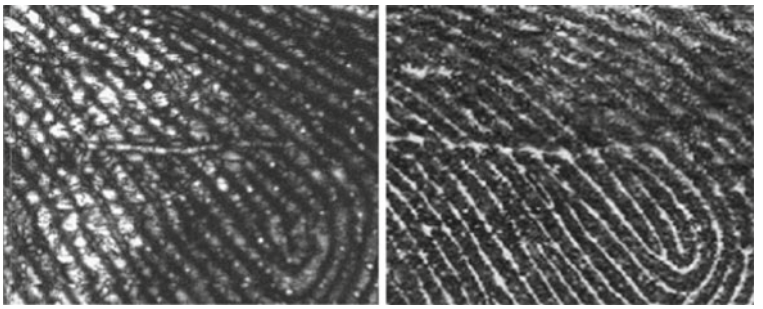

Fig. 5 A comparison between an acoustic image and an optical ink-and-paper image of a finger with scar tissue

The security of the method can be increased by the tracking of blood flow using Doppler Effect, what should distinguish real live finger from its replicas of any kind. The same technique can be applied to characterize the fingernail and its underlying tissue and characteristics which are also unique from one individual to another.

Design of specialized cylindrical multi-transducer scanner will make the method fast and convenient. The large area of the finger (nail to nail 2.5 cm $\times$ 2.5 cm) can be scanned less than in 5 s with the raw resolution up to 1000 dpi. The digitally

interpolated images can be enhanced allowing for even better resolution. The only downside is the use of a medium such as water or gel.

Acknowledgments This work was inspired and supported by The National Law Enforcement and Corrections Technology Center – West, The Aerospace Corporation (USA) and Tessonics Corporation (Canada).

References

1. Millard, K.: Developments on automatic fingerprint recognition, Proc. Int. Carnahan Conf. Security Technol. 173–178 (1983)
2. Schneider, J.K.: Surface Feature Mapping Using High Resolution C-Scan Ultrasonography, Ph.D. Dissertation, State University of New York at Buffalo, Electrical and Computer Engineering Dept. (1990)
3. Schmitt, R.M., Scott, W.G., Irving, R.D., Arnold, J., Bardons, C., Halpert, D., Parker, L.: Ultrasonic imaging of fingerprints using acoustical impediography, *IEEE Ultrasonics Symposium,* 680–688 (2004)
4. www.biometricscatalog.org

Ultrasonic Detection of Metastases in Dissected Lymph Nodes of Cancer Patients

E.J. Feleppa, J. Mamou, J. Machi, M. Hata, A. Coron, E. Yanagihara, and P. Laugier

Abstract Current histological methods can miss micrometastases (< 2.0 mm) in dissected lymph nodes because nodes are cut into sections that are at least 2-mm thick for examination, and the entire node volume cannot be evaluated microscopically. In this study, high-frequency, quantitative ultrasound (HFU, QUS) methods were applied to freshly dissected lymph nodes to detect micrometastases based on their microstructural properties. 3-D ultrasound data were acquired from 40 nodes from 22, colorectal-cancer patients using a single-element, 25 MHz transducer. Significant cancer was detected subsequently in 7 of the 40 nodes. Node images were segmented semi-automatically in 3-D, and echo signals were processed to yield basic spectral parameters (slope, intercept, and midband) values plus QUS estimates associated with tissue microstructural properties (scatterer size and acoustic concentration). Images were formed by expressing local QUS estimates as color-encoded pixels and overlaying the color on conventional, gray-scale ultrasound images. Linear discriminant analysis classified nodes based on intercept, midband, size, and acoustic concentration. ROC methods assessed classification performance. 3-D QUS images interactively displayed spectral-parameter and QUS values. Linear-discriminant methods produced an area under the ROC curve of 1.000 based on size and intercept; interestingly, the areas for size alone and for intercept alone were 0.986. These initial results appear to validate spectrum-analysis-based QUS methods for distinguishing cancerous from non-cancerous tissue in lymph nodes. The Areas under the ROC curves suggest that this approach can be valuable clinically to identify nodal micrometastases that current histologic methods can miss.

Keywords Colorectal cancer · Quantitative ultrasound · High-frequency ultrasound · Spectrum analysis · Lymph nodes · Metastasis · Micrometastasis · Maximum likelihood

E.J. Feleppa (✉)
Riverside Research Institute, New York, NY, USA
e-mail: feleppa@rrinyc.org

M.P. André et al. (eds.), *Acoustical Imaging*, Acoustical Imaging 30,
DOI 10.1007/978-90-481-3255-3_3,

1 Introduction

Lymph nodes of cancer patients who are have or are suspected of having metastatic cancer are dissected and examined histologically for the purpose of detecting possible metastases to the nodes and thereby staging the cancer and selecting treatment appropriate for the stage. Typically, nodes in the region considered to be draining the site of the tumor are removed surgically, cut into thick sections or blocks of 2–3 mm in depth, fixed and embedded. Thin sections of 3–4 μm in depth are cut by a microtome from the surfaces of the embedded thick sections, stained, and evaluated under a microscope by a pathologist. For some cancers, e.g., invasive breast adenocarcinomas, a modification of the typical procedure is used. In the modified procedure, only nodes termed "sentinel" nodes are dissected initially, and if they prove to be cancer containing, then a formal node dissection or lymphadenectomy is performed to remove and evaluate all regional nodes, e.g., the axillary node bed of a breast-cancer patient. Sentinel nodes are identified using a colored or radioactive dye injected into the site of the excised tumor, commonly at the time of tumor excision, which permits the dye-containing nodes to be detected, removed, and evaluated by frozen section or a cytological procedure termed "touch prep" while the patient remains in the operating room under anesthesia. (In the touch-prep procedure, dissected nodes are cut in half and the cut surfaces are pressed onto microscope slides for immediate cytological examination of cells that remain attached to the slide surface.) In the case of the axillary nodes of breast-cancer patients, three or four nodes may be identified by the dye and removed for examination, which spares the great majority of the nodes in the axillary bed. If sentinel-node metastases are detected at that time, then a formal dissection can be performed immediately. If metastases are not detected at that time, but are detected after a subsequent complete histological procedure, then the patient needs to be recalled to undergo a formal dissection. Sentinel-node procedures are attractive for many patients because, if the histology proves to be negative, then the often-severe side effects of a formal lymphadenectomy can be avoided if no metastases in fact exist.

Unfortunately, these procedures are prone to producing false negatives. Frozen-section and touch-prep procedures leave virtually the entire node unexamined, and easily can miss small metastases that are not located on or near the plane of the cut. Furthermore, typical full histological procedures only evaluate the thin sections taken from the surfaces of the 2- to 3-mm-thick blocks, which allow the small metastases lying between the cut surfaces to remain undetected. Therefore, a need exists for a method of evaluating the entire node and identifying suspicious regions that warrant more-detailed histology by the pathologist immediately after node dissection. If sufficiently reliable, the method also could be used to evaluate sentinel nodes upon dissection and to determine immediately whether a formal dissection is warranted.

The remainder of this article describes a method based on spectrum analysis of radio frequency (RF), high-frequency-ultrasound (HFU) echo signals that initially has demonstrated a very encouraging potential for discriminating cancerous from non-cancerous tissue in lymph nodes and for providing an urgently needed method to guide pathology, and, in particular, for supporting decisions regarding formal

node dissections in sentinel-node procedures. (Spectrum-analysis methods for tissue typing have been described in numerous publications [1–4], but are summarized very briefly in the Methods section below.)

2 Methods and Materials

Methods and materials are described in the sequence they occur clinically and subsequently off line. Clinical tasks, i.e., surgery and pathology, were performed at the Kuakini Medical Center of the University of Hawaii in Honolulu, HI; segmentation methods and software were developed at Université Pierre et Marie Curie and CNRS in Paris, France; signal analysis, tissue typing and imaging were performed at Riverside Research Institute in New York, NY. Data and results were transferred among research sites via the internet.

2.1 Node Dissection

Node dissections were performed in the operating room according to standard surgical procedures. Dissected nodes were placed in isotonic saline for transport to the pathology laboratory. In the pathology laboratory, individual nodes were selected and excess perinodal tissue was removed from each specimen. Nodes were pinned individually to a sound-absorbing pad by inserting pins through the thin layer of remaining fat. Pinned nodes were placed in a water bath filled with phosphate-buffered isotonic saline and scanned at room temperature for acquisition of RF echo signals as described below. In the case of sentinel nodes, each half node was pinned, immersed, and scanned. After echo-signal data were acquired, nodes were inked, as shown in Fig. 1, to provide orientation for subsequent 3D reconstructions and spatial matching of histology with ultrasonic results. The red of Fig. 1a, b indicates the node surface that was distal to the transducer; the blue ink of Fig. 1b indicates the surface that was proximal and the black indicates the origin of the x axis. Histological sections were obtained in the horizontal planes depicted in Fig. 1, as discussed below.

2.2 Data Acquisition

Data were acquired using a single-element transducer that had a center frequency of 25.6 MHz and a -6-dB bandwidth that extended from 16.4 to 33.6 MHz; its aperture was 6.1 mm and its focal length was 12.2 mm; i.e., its f-number was 2.0. The transducer position was adjusted in the z direction to place the focus in the center of the node or 2 mm deep within the node, whichever was less in terms of depth into the node. The transducer was translated in the x and y directions by positioning stages under computer control, and scan vectors were separated by 25 μm in both directions. RF echo-signal data were acquired at a sampling frequency of 400 MS/s. Scanning was performed at room temperature. In Fig. 1, the ultrasound transducer was located above the inked node and transmitted ultrasound was incident on the

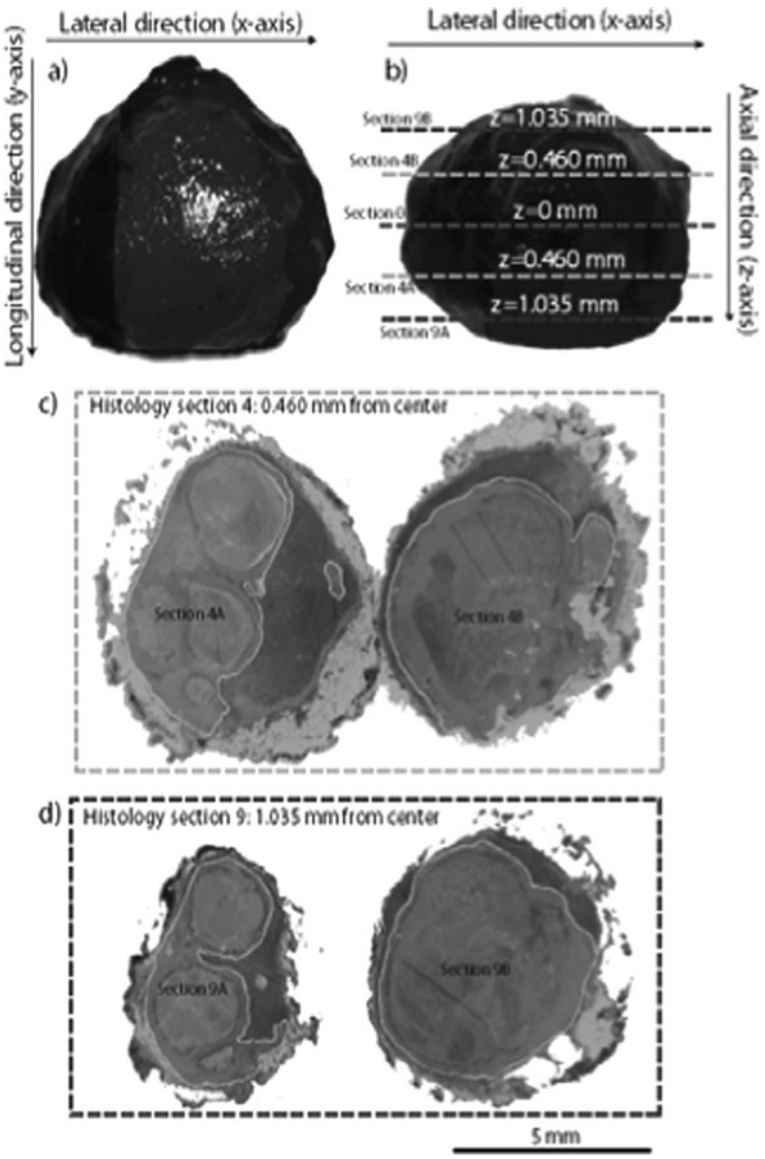

Fig. 1 Inked node and matching histology. (**a**) and (**b**) proximal and distal surfaces with 4th and 9th sectioning planes above and below the equator (boundary); (**c**) and (**d**) corresponding demarcated histology in Sections 4 and 9

surface that was subsequently inked blue; i.e., ultrasonic scan planes and histological scan planes were orthogonal to each other. The scanning apparatus is shown in Fig. 2. Figure 2a shows the complete apparatus, including the positioning stages; Fig. 2b shows a close up view of the pinned node on the sound-absorbing pad with the transducer coupled through the saline bath.

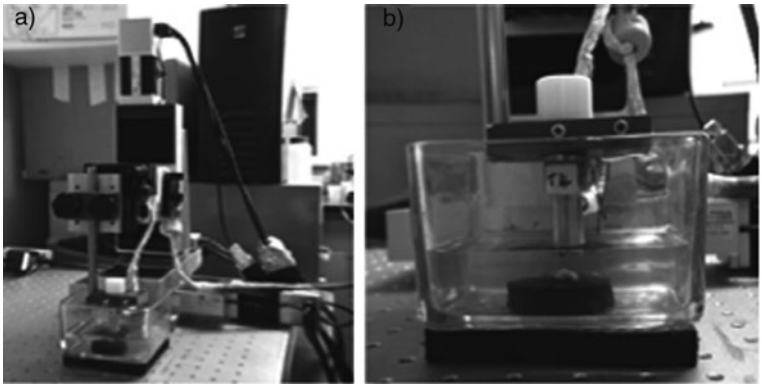

Fig. 2 Scanning setup. (**a**) broad view showing computer-controlled stages; (**b**) close-up view showing immersed node, transducer, and sound-absorbing pad in the water bath

To date, over 400 dissected nodes have been scanned using this data-acquisition method. Data have been acquired from nodes of patients with colorectal, breast, and stomach cancers. The most-common type of cancer in our data set was colorectal cancer; the data include approximately 250 nodes from approximately 90 colorectal-cancer patients. Accordingly, results described here were computed for 38 nodes dissected from 22 colorectal-cancer patients. Of the 38 colorectal-cancer nodes, 31 were entirely negative for metastases; 7 were positive for metastatic cancer in an estimated 65–100% of the node volume.

Ultrasound echo-signal data for calibration, i.e., normalization of spectra, were acquired from the weakly reflecting planar interface between water and type 710 oil (Dow Corning Corporation, Midland, MI), which is denser than water. This allows the transducer to be immersed in water, which obviates the necessity to correct for often severely temperature-dependent propagation properties of oils. Having a weakly reflecting interface of known reflectivity allowed the settings of the data-acquisition system (e.g., pulse power, damping, receiver gain, and digitizer sensitivity) to remain the same for calibration and tissue data acquisition, which obviated the possibility of having different transfer functions at different system settings.

2.3 Pathology

For the purposes of this study, the standard thick blocks were not used. Instead, all fixed nodes were cut in half, embedded, and sectioned in planes parallel to the cut surfaces. Thin sections having a 3- to 4-μm depth were obtained in horizontal planes separated by 115 or 57 μm; and, as shown in Fig. 1 above, histologic-section planes were orthogonal to the ultrasound scan planes. The 115-μm sectioning-plane spacing was used in larger nodes, such as the 3 × 5 × 5 mm node of Fig. 1. In smaller nodes, the spacing was reduced to 57 μm. Stained and mounted thin sections then were examined by a pathologist under high-power magnification. After high-power

examination, the sections were photographed with a high-quality digital camera, and the digital images were marked using a computer to delineate cancerous regions as shown in Fig. 1c, d.

2.4 Signal Processing

The first step in processing the acquired echo signals was segmenting the data into saline medium, perinodal fibro-adipose tissue, and nodal tissue. The second step was applying QUS methods based on spectrum analysis to compute QUS parameters such as spectral slope and intercept and estimates of scatterer size and acoustic concentration [1–3]. Acoustic concentration was defined by Lizzi as the number concentration times the square of the relative acoustic impedance of the scatterers compared to their surroundings [3].

A region-based semiautomatic 3D segmentation method was used. It involved a watershed-transform of the 3D gradient of the low-pass filtered, down sampled (by a factor of 8), log-compressed envelope of the 3D RF data [5]. The watershed regions were classified as saline, fat or tissue using a maximum-likelihood classifier based on the mean backscatter of each region. The maximum-likelihood classifier took into account transducer diffraction and then employed depth-dependent thresholds to classify the regions [5]. Finally, minor artifacts of the 3D segmentation were corrected by an expert using custom software.

Spectrum analysis occurred within the segmented nodal tissue using cylindrical regions of interest (ROIs) that were 1 mm in diameter and length. Spectral-parameter values and scatterer-property estimates were computed as the ensemble average of all scan-vector segments in the ROI. ROIs were applied only within perinodal tissue and were overlapped by 80% in x, y, and z directions, i.e., results for an entire ROI were presented for a cube (voxel) that was 200 μm on each side and was centered in the ROI. The axis of the ROI paralleled the beam axis and a Hanning window was applied to the raw, RF, echo signals. Normalized spectra were computed for every scan vector in the ROI using the method described by Lizzi [1–3]; scatterer-property estimates applied a Gaussian form factor using the method described by Insana [6]. Spectral slope values and scatterer size estimates were corrected for measured attenuation in the perinodal fat layer and for an assumed attenuation coefficient of 0.5 dB/MHz-cm within the node. Spectral amplitudes and parameter values were expressed in dBr, i.e., dB relative to values for a perfect reflector.

2.5 Image Generation

Voxel values were computed in 3D for spectral parameters and scatterer properties. An interactive GUI was developed that displayed the node volume as 3 orthogonal planes in the 3D volume of the node. Mouse movement controlled the position of a line cursor in any one of the 3 views, which controlled the display of the orthogonal plane corresponding to the line cursor.

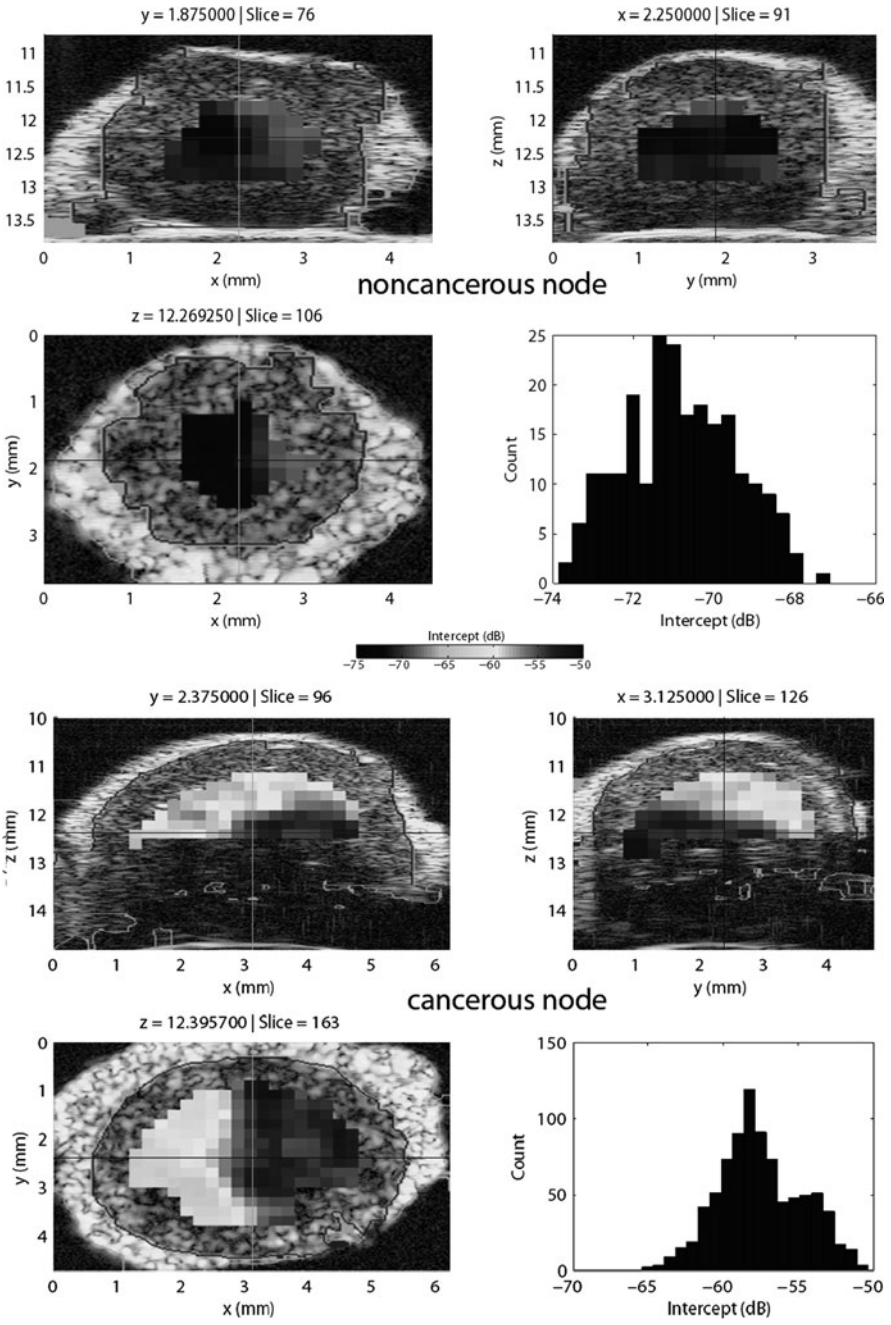

Fig. 3 Positive and negative nodes with color-encoded intercept values shown in 3 orthogonal planes. Voxels are 200-μm cubes. A histogram displays the intercept-value distribution for each node

Negative and positive nodes of a colorectal-cancer patient are shown in Fig. 3. The upper node is cancer free and the lower one contains cancer. The images display color-encoded spectral-intercept values along with the semi-automatically segmented saline, fibro-adipose, and nodal-tissue regions in each of 3 orthogonal planes. The displayed planes are selected by the cursors in either of the other pair of planes. The intercept value is depicted in grey scale with lighter values indicating intermediate values and darker indicating the greater deviations, lower (more-negative) or higher (more-positive) values. A calibrated grey bar is displayed between the nodes. Histograms depict the parameter-value distribution within the node.

2.6 Classification

Classification was performed using linear-discriminant methods and in some cases simply by computed spectral-parameter values and scatterer-property estimates. Classifier performance was expressed as the area under the ROC curve [7].

Linear discriminant analysis was performed to determine the classification performance possible using multiple variables and to determine objectively which variables contributed most to the classification [8]. To do this, the variables that visual inspection of means and standard deviations suggested might have value for discriminating between cancerous and noncancerous tissue were input into SPSS (SPSS, Chicago, IL); the selected variables were scatterer size, acoustic concentration, spectral slope, and spectral intercept. Discriminant-function values for each node then were input into SPSS ROC algorithms or into ROCKIT software (Charles Metz, University of Chicago, Chicago, IL) to derive classifier-assessing ROC curves. Furthermore, spectral-intercept values and scatterer-size estimates for positive and negative values were input individually into ROCKIT software to derive classifier-assessing ROC curves directly.

3 Results

Results include classification performance measures expressed as areas under the ROC curve and spectral-parameter and scatterer-property images computed in 3D.

3.1 ROC Analyses

ROC results obtained for spectral-intercept values, scatterer-size estimates, and discriminant-function values are shown in Table 1. In Table 1, Az is the area under the ROC curve, $\pm$ indicates the standard error in the area estimate, and 95% confidence interval (CI) is the 95% confidence interval. SPSS did not compute standard errors in the area estimates. Areas under the ROC curve were computed for all 3 types of variables using SPSS but only for intercept and size using ROCKIT because the performance of the discriminant-function variable was

Table 1 Results of ROC analyses

Method	Variable	Az	95% CI
SPSS	Discriminant score	1.000±0.000	1.000–1.000
SPSS	Scatterer size	0.986±0.016	0.955–1.018
SPSS	Spectral intercept	0.986±0.015	0.957–1.016
ROCkit	Scatterer size	0.9884±0.0167	0.8830–0.9996
ROCkit	Spectral intercept	0.9859±0.0158	0.9083–0.9989

considered indeterminate by ROCKIT, i.e., it was "perfect." Spectral-slope values and acoustic-concentration estimates contributed less to classification and are not shown in these results.

3.2 Images

Image results illustrated in Fig. 3 typify the trends apparent in the colorectal-cancer nodes. Cancerous tissue in the nodes tended to have larger scatterer sizes as well as the more-positive intercept values shown in these figures.

4 Discussion

Although the extremely encouraging results described above are preliminary in nature, they are consistent with results obtained a decade ago using lower, 10-MHz ultrasound frequencies [9]. Interestingly, the current results and those of a decade ago indicate that the attenuation-independent intercept parameter possibly can serve as a cancer-identifying parameter without requiring segmentation or attenuation correction. The results described here also are consistent with results published earlier for 4 nodes of an individual colorectal-cancer patient segmented using 2D rather than the current 3D approach; 10 in those data, 1 node was positive and 3 were negative for metastases, and the positive node exhibited larger scatterer-size estimates and higher intercept values. The current results offer the hope that results derived from a larger number of nodes, particularly cancer-containing nodes, will lead to an effective method of assessing dissected nodes. These assessments will enable targeted pathology evaluations of nodes in traditional histological procedures and will enable more-rapid decision making in sentinel-node procedures. In both applications, a reduction in false-negative determinations and improved staging of a wide variety of cancers will be valuable clinical benefits.

In the short term, future studies will emphasize processing of a greater number of positive nodes and thereby obtain a better representation of metastatic tissue in lymph nodes. These studies also will seek to automate the crucial segmentation algorithms and to automate them as much as possible. Classification methods will be evaluated by spatially comparing tissue-typing results with cancerous and non-cancerous regions demarcated by the pathologists and represented in 3D in our

data sets. This evaluation effort will require careful co-registration of histological and ultrasonic data using non-rigid deformation techniques to correct for distortions and shrinkage occurring during histological preparation. The evaluations will be crucial in validating the application of spectral properties associated with node-filling metastases to those of smaller, sometimes multiple foci within nodes – the micrometastases that are the object of this research.

In the long term, future studies will emphasize reducing the processing to clinically more-useful and practical means of imaging suspicious tissue in 3D. A reduction of processing time and the development of automated analysis and imaging tools will be essential for these methods to be acceptable and practical clinically.

5 Summary and Conclusions

Means of distinguishing cancerous from non-cancerous tissue in lymph nodes based on spectrum analysis of RF ultrasonic echo signals show promise for clinically detecting nodal micrometastases and thereby improving staging of disease. Although only 38 nodes from 22 patients have been evaluated to date, and only 7 of those nodes contained a significant cancer volume, areas under the ROC curves equaling 1.0 for combined parameters and closely approaching 1.0 for scatter-size estimates and particularly for the attenuation-independent intercept parameter offer strong encouragement that future studies will be able to develop clinically practical and useful implementations of this approach.

Acknowledgements The authors acknowledge the support provided by NIH grant CA100183 and the Riverside Research Institute Biomedical Engineering Research Fund.

References

1. Lizzi, F.L., Greenebaum, M., Feleppa, E.J., Elbaum, M., Coleman, D.J.: Theoretical framework for spectrum analysis in ultrasonic tissue characterization. J. Acoust. Soc. Am. **73**(4), 1366–1373 (1983)
2. Feleppa, E.J., Lizzi, F.L., Coleman, D.J., Yaremko, M.M.: Diagnostic spectrum analysis in ophthalmology: A physical perspective. Ultrasound Med. Biol. **12**(8), 623–631 (1986)
3. Lizzi, F.L., Ostromogilsky, M., Feleppa, E.J., Rorke, M.C., Yaremko, M.M.: Relationship of ultrasonic spectral parameters to features of tissue microstructure, *IEEE Transactions on Ultrasonics, Ferroelectrics, and Frequency Control*, UFFC-34, 319–329 (1987)
4. Feleppa, E.: Ultrasonic tissue-type imaging of the prostate: implications for biopsy and treatment guidance. Cancer Biomark. **4**(4–5), 201–212 (2008)
5. Coron, A., Mamou, J., Hata, M., Machi, J., Yanagihara, E., Laugier, P., Feleppa, E.J.: Three-dimensional segmentation of high-frequency ultrasound echo signals from dissected lymph nodes, *Proceedings of the 2008 Ultrasonics Symposium*, edited by K.R. Waters (Institute of Electrical and Electronics Engineers, Piscataway, 2008), pp. 1370–1373
6. Insana, M.F., Hall, T.J.: Parametric ultrasound imaging from backscatter coefficient measurements: Image formation and interpretation. Ultrason. Imaging **12**, 245–267 (1990)

7. Metz, C.E.: ROC methodology in radiologic imaging. Investigative Radiology **21**, 720–733 (1986)
8. McLachlan, G.J.: Discriminant analysis and statistical pattern recognition. Wiley, New York, NY (1992)
9. Tateishi, T., Machi, J., Feleppa, E.J., Oishi, R., Jucha, J., Yanagihara, E., McCarthy, L.J., Noritomi, T., Shirouzu, K.: *In vitro* diagnosis of axillary lymph node metastases in breast cancer by spectrum analysis of radio frequency echo signals. Ultrasound Med. Biol. **24**(8), 1151–1159 (1998)
10. Mamou, J., Coron, A., Hata, M., Machi, J., Yanagihara, E., Laugier, P., Feleppa, E.: High-frequency quantitative ultrasound imaging of cancerous lymph nodes. Jpn. J. Appl. Phys. **48**, 07GK08-1 (2009)

Measurement of Mechanical Properties of Soft Tissue with Ultrasound Vibrometry

I. Nenadich, M. Bernal, and J.F. Greenleaf

Abstract The cardiovascular diseases atherosclerosis, coronary artery disease, hypertension and heart failure have been related to stiffening of vessels and myocardium. Noninvasive measurements of mechanical properties of cardiovascular tissue would facilitate detection and treatment of disease in early stages, thus reducing mortality and possibly reducing cost of treatment. While techniques capable of measuring tissue elasticity have been reported, the knowledge of both elasticity and viscosity is necessary to fully characterize mechanical properties of soft tissues. In this article, we summarize the Shearwave Dispersion Ultrasound Vibrometry (SDUV) method developed by our group and report on advances made in characterizing stiffness of large vessels and myocardium. The method uses radiation force to excite shear waves in soft tissue and pulse echo ultrasound to measure the motion. The speed of propagation of shear waves at different frequencies is used to generate dispersions curves for excised porcine left-ventricular free-wall myocardium and carotid arteries. An antisymmetric Lamb wave model was fitted to the LV myocardium dispersion curves to obtain elasticity and viscosity moduli. The results suggest that the speed of shear wave propagation in four orthogonal directions on the surface of the excised myocardium is similar. These studies show that the SDUV method has potential for clinical application in noninvasive quantification of elasticity and viscosity of vessels and myocardium.

Keywords Tissue · Elasticity · Mechanical properties · Radiation force · Shear waves · Myocardium · Viscosity · Sound speed · Vessels · Vibrometry · Viscoelastic

1 Introduction and Background

According to the American Heart Association report the estimated direct cost of cardiovascular diseases in the United States for 2009 is $270 billion, the majority of which is attributed to treatment of coronary diseases, atherosclerosis, hypertension and heart failure [1]. These diseases have been related to stiffening of the vessels and myocardium. Decreased elasticity (stiffening) of the myocardium leads

I. Nenadich (✉)
Ultrasound Research Laboratory, Department of Physiology and Biomedical Engineering, Mayo Clinic College of Medicine, Rochester, MN, USA
e-mail: jfg@mayo.edu

M.P. André et al. (eds.), *Acoustical Imaging*, Acoustical Imaging 30,
DOI 10.1007/978-90-481-3255-3_4,

to decreased left ventricular (LV) relaxation, compliance and reduced passive filling which could lead to heart failure. Current clinical tools used for evaluation of diastolic function rely on measurements of ejection fraction using ultrasound Doppler imaging. Ejection fraction coefficient is not a reliable indicator of diastolic function since patients with normal ejection fractions and preserved systolic function often present with angina, edema and other symptoms of heart failure [2]. Decreased arterial elasticity (stiffening) can lead to hypertension and, according to Dolan, et al., can be used as an independent parameter for prediction of cardiovascular diseases [3].

Changes in mechanical properties of soft tissue due to pathological conditions have been known for centuries. In recent decades, significant effort has been directed towards producing a technique capable of non-invasive characterization of tissue elasticity. These techniques are mostly based on inducing tissue deformation and detecting the response with either magnetic resonance imaging or ultrasound [4, 5]. Unlike ultrasound techniques, MRI is not limited by focal length and acoustic window, but *is* fairly expensive and therefore unlikely to become widely available. Thus, the field of ultrasound elastography has developed and offers various methods of characterizing tissue viscoelasticity. Early techniques [6–9] were capable of producing relative tissue stiffness maps, but such information was sufficient only when the diagnosis of the diseases where the pathologic and healthy tissues present at the same time for comparison. Diffuse disorders such as liver fibrosis, left-ventricular free wall stiffening, and atherosclerosis affect the elasticity of the entire tissue and their diagnoses require methods capable of *quantifying* tissue stiffness.

Shear wave propagation velocity has been used to quantify tissue stiffness, [10–12] largely because the shear moduli from body tissues such as muscle, liver, dermis, cartilage and bone differ by several orders of magnitude [12]. Shear wave attenuation in soft tissue is fairly high which allows for high spatial resolution because of the use of high frequency waves. These techniques, however, neglect tissue viscosity and therefore underestimate the elasticity by ignoring the complex part of shear modulus. A liver fibrosis study by Huwart, et al., [13] shows that viscosity serves as another indicator of tissue health in addition to elasticity. Thus, a technique capable of quantifying both tissue elasticity and viscosity would be of great benefit in clinical settings.

Here, we describe a non-invasive ultrasound technique developed by our group that uses shear wave velocity dispersion to quantify both elasticity and viscosity of soft tissue [14, 15]. This technique uses harmonic radiation force to induce deformation and pulse-echo ultrasound to detect shear wave motion. This technique has been referred to as Shearwave Dispersion Ultrasound Vibrometry, or SDUV [15].

As previously reported by our group, *in vivo* measurements of liver viscoelastic moduli using SDUV are in good agreement with the values reported by other groups [15]. In addition to describing SDUV technique, we summarize the progress we have made in quantifying material properties of LV myocardium and large vessels.

2 Materials and Methods

2.1 SDUV Basic Principles

As described by Chen, et al. [14, 15], amplitude modulated (AM) ultrasound beam from a "push" transducer is focused on the medium to generate monochromatic radiation force in the range 50–500 Hz, and a pulse echo (or "detect") transducer is used to register motion (Fig. 1).

Due to narrow beamwidth and constant force along the beam axis (z-axis) near the focus the push transducer produces cylindrical shear waves [14]. Particle displacement due to harmonic cylindrical shear waves is mostly along the z-axis and for homogenous viscoelastic media is approximated by:

$$u_z(r,t) \approx \frac{i}{4}\sqrt{\frac{2}{\pi \tilde{h} r}}\, e^{i(\tilde{h}r - \omega t + \pi/4)} \tag{1}$$

where u is the particle displacement, r is the distance away from the excitation, ω is the frequency of the shear wave, t is the time and $\tilde{h}$ is the wave number for a shear wave in a viscoelastic material which can be calculated as:

$$\tilde{h} = \omega\sqrt{\frac{\rho}{\mu_1 - i\omega\mu_2}} \tag{2}$$

where μ_1 and μ_2 are the Voigt model elastic and viscous moduli.

Equation (1) shows that for large r (according to simulations, larger than one tenth of the shear wavelength) the phase delay and distance from the excitation are linearly related. Since $\omega = 2\pi f$, one can estimate the shear wave speed by measuring the phase shift $\Delta\phi = \phi_2 - \phi_1$ over distance traveled Δr:

$$c_s = \omega\frac{\Delta r}{\Delta\phi} \tag{3}$$

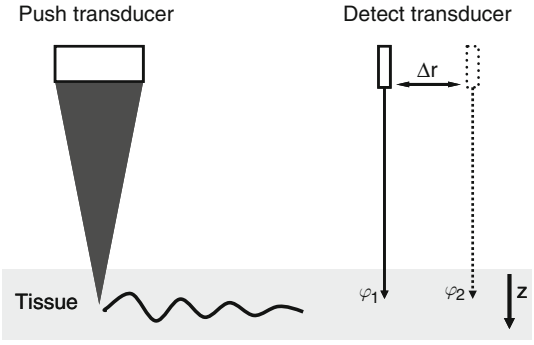

Fig. 1 Principle of SDUV: a push transducer is the source of a radiation force that induces monochromatic shear wave propagation in tissue; the motion is measured by a pulse echo transducer

Equation (3) requires phase measurements at multiple locations which can be accomplished by moving the detect transducer by Δr (Fig. 1). An alternative approach is to move the excitation point and keep the detect transducer in one location.

As mentioned above, a pulse echo ultrasound transducer is used to detect the motion. Ultrasound pulses are transmitted at the location of interest at a pulse repetition rate of few kilohertz. Each point in the time domain of the returning echo signal corresponds to a specific region of the tissue along the beam axis. Cross-spectral correlation of the echoes is used to calculate tissue displacement as a function of time [16]. A specialized Kalman filter is applied to the displacement versus time data to extract the motion at the excitation frequency of the push transducer and estimate the shear wave amplitude and phase [17].

2.2 Single Transducer SDUV

For a clinical application of the methodology described before, the SDUV technique needs to be incorporated in single transducer, where both the excitation and the motion detection are acquired "simultaneously". In commercial scanners it is possible to steer the ultrasound beam. This can be used for the steering of the pushing and the detection beam. The pushing beam is applied at a specific site in the tissue to generate a shear wave that propagates through it. After the excitation, the system changes to a pulse echo mode, where the detection echo beam is steered to at least 2 different positions in the area adjacent to the excitation to obtain phase differences for the propagating shear wave. As shown in Fig. 2, the pushing beam in SDUV is made of repeated push tonebursts, each with the duration of several microseconds (T_b). These toneburst are repeated at the repetition frequency (f_r), which is usually

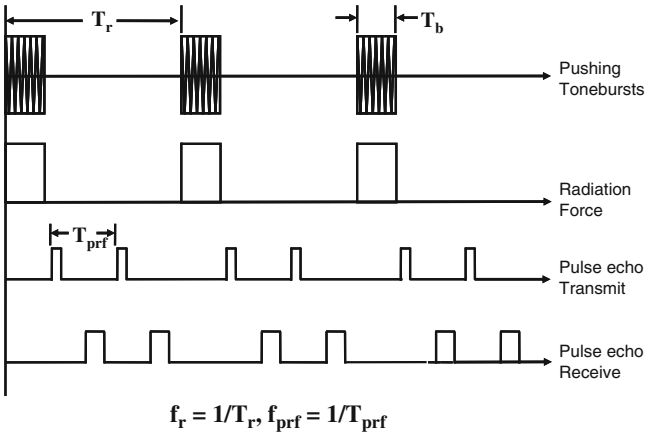

Fig. 2 SDUV excitation and detection sequence. Tr is the period of the pushing toneburst and Tb is the duration. Tprf is the period of the tracking sequence, the transmission of the pulse echo and the reception of the pulse echo. This figure is modified from Urban, et al. [18]

set to 50 or 100 Hz. After each of these push tonebursts, the system switches to the detection mode, and the pulse echo signal for tracking the motion is generated with a frequency (f_{prf}) of 1–4 kHz, depending on the application.

The motion of the tissue is extracted from the echo signal using cross spectrum correlation. Due to the repetition frequency of the pushing beam, the shear waves generated contain pure-tone frequencies harmonics of the repetition frequency up to 1 kHz, and all this can be recorded simultaneously. Therefore the shear wave velocity dispersion needed to characterize the viscoelastic properties of tissues can be easily obtained with one excitation sequence. This reduces the time of acquisition and the heating of the tissue, making it feasible to explore different points of the tissue during the same exam.

3 Results and Discussion

3.1 Porcine LV Study

A similar approach to the SDUV method described above was used to measure shear wave speeds at different frequencies in an excised porcine left-ventricular myocardium. The tissue sample was embedded in gelatin inside a container and mounted on a stand to provide stability. The gelatin was contained to the edges of the sample in order to eliminate coupling. In this set of experiments, the push transducer was replaced by a mechanical actuator to ensure large motion. The experimental set up was otherwise as in Fig. 1. The detect transducer was used to track motion at multiple locations in four orthogonal directions on the surface plane. Kalman filter and Equation (3) were used to estimate the speed at different frequencies. Shear wave speed at different frequencies (dispersion) measured in four orthogonal directions are shown in Fig. 3 (circles connected with lines).

The phase values of the particle displacement were fairly constant throughout the thickness (z-axis) which is characteristic for anti-symmetric Lamb wave motion. The experimental data were fitted with a Lamb wave mathematical model (solid lines) proposed by Kanai [19].

The measured shear wave speeds agree with previously reported values [19]. To our best knowledge viscoelastic coefficients are not well established in literature. These results suggest that the Lamb wave model can be used to fit the experimental results and that the porcine LV myocardium elasticity and viscosity are similar in four orthogonal directions. In the future, we intend to perform *in vivo* open chest studies in pigs to examine the capabilities of this method.

3.2 Carotid Artery Study

The SDUV method was used to study shear wave speed and mechanical properties of large vessels. Figure 4, shows the motion recorded on the wall of an excised pig carotid after exciting it with radiation force. The artery was mounted on a metallic frame, covered with gelatin to simulate the surrounding tissue of *in vivo* carotids,

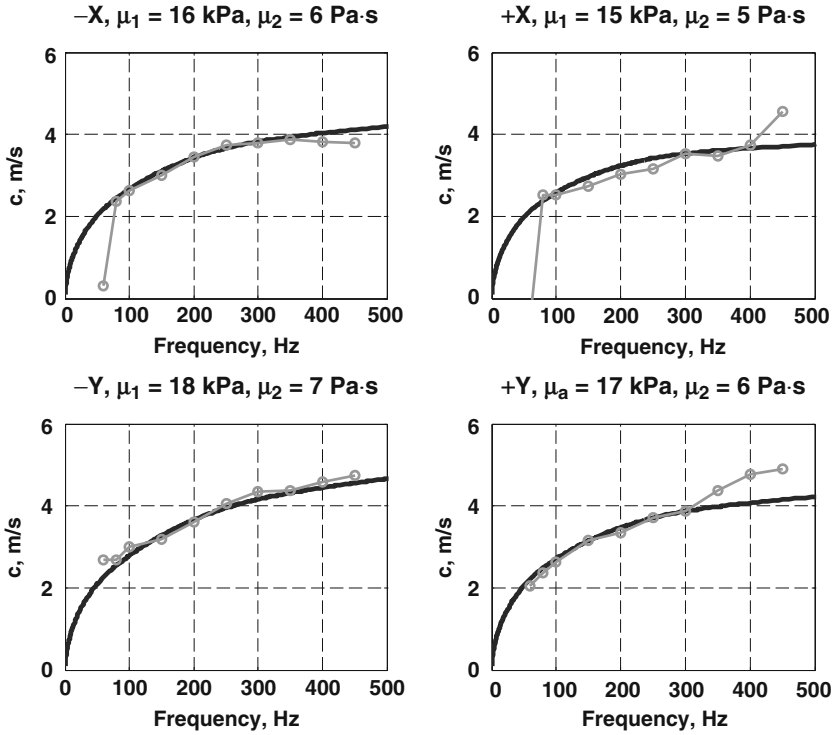

Fig. 3 Dispersion curves in four orthogonal directions on the surface of the excised porcine LV free wall. Experimental data are shown as *circles* connected with lines and Lamb wave model as *solid lines*

and pressurized to 50 mmHg using a column of water. Panel A shows the motion of front wall of the vessel created by a 100 μs toneburst of ultrasound which generated radiation force on the vessel wall. Panel B, similarly, shows the motion on the same wall when excited with the SDUV pushing sequence. In this case 4 tonebursts with a repetition frequency of 50 Hz and the toneburst length to 100 μs was applied. The total time of pushing sequence was 80 ms. Panel C shows the difference in the frequency components of the two signals presented in panel A and B. Notice how the magnitude of fast Fourier transform (FFT) of the SDUV signal has amplitude only at harmonics of the repetition frequency, 50, 100, 150, etc, up to 1 kHz, giving a better signal to noise ratio at the harmonics of the repetition frequency. Meanwhile the FFT of the impulse excitation shows continuous frequency values which are the envelope of the SDUV FFT.

In this experiment, the motion of the wall was measure at 41 different points spaced 0.5 mm apart from each other for a total of 2 cm. Cross correlation of the motion was performed to find the time shifts between consecutive distances. The time shift versus distance was fitted with a linear regression and the group velocity extracted from the slope of the fitted line. In the case of the pig carotid pressurize to 50 mmHg the group velocity was 8.097 m/s.

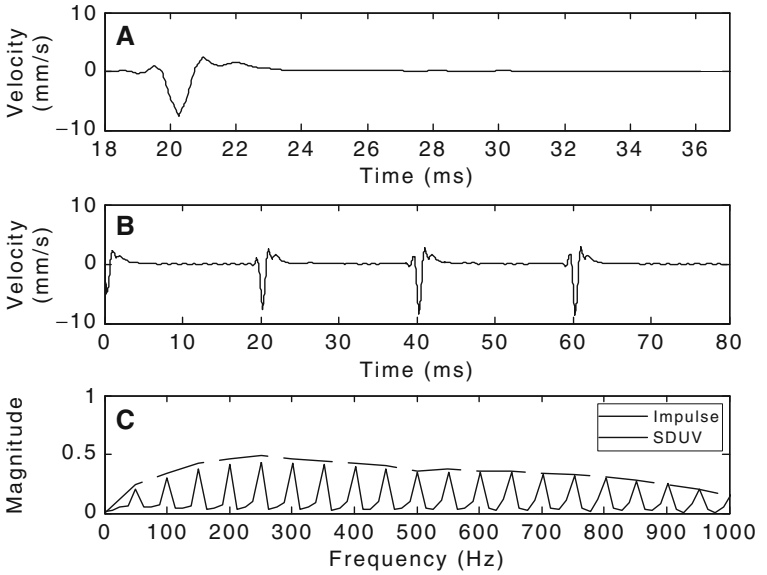

Fig. 4 Results of SDUV and impulse excitation on an excised carotid artery from a pig. Panel A shows the wall motion of the artery (velocity of motion) after pushing it with an 100 μs impulse toneburst. Panel B shows the SDUV excitation, where the repetition frequency was 50 Hz and the toneburst length 100 μs. Panel C shows the magnitude of the FFT of the motion of the wall when excited with the impulse or with the SDUV pushing sequence

Figure 5 shows the shear wave dispersion curve for the same carotid, pressurized to 70 mmHg. Using the FFT of the SDUV wall motion, we extracted the phase values for the repetition frequency, 50 Hz, and its harmonics up to 1 kHz for all the 41 locations. The phase-distance relationship for each frequency was fitted with a

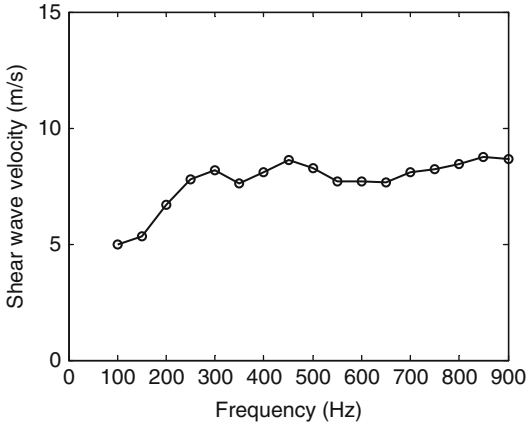

Fig. 5 Shear wave velocity dispersion curve for excise pig carotid, pressurize to 70 mmHg

liner regression and from there the phase velocity was calculated at each frequency value using Equation (3). Currently, our lab is working on a model to fit the dispersion data to get values of the elasticity and the viscosity of the vessels similar to the one described above for the myocardium.

4 Conclusion and Summary

SDUV is a method that uses radiation force to induce shear wave propagation in soft tissue and a pulse echo transducer to track the motion. Wave speed is estimated by fitting linear regression through the phase data at multiple points. Shear wave dispersion measurements are used to estimate tissue elasticity and viscosity. SDUV technique has been successfully used to estimate liver viscoelasticity in pigs *in vivo* and has potential for application in estimating elasticity and viscosity in vessels and myocardium.

References

1. American Heart Association. Heart Disease & Stroke Statistics - 2009 Update. Dallas, Texas: American Heart Association; 2009. ©2009, American Heart Association. Accessed on March 17, 2009. http://www.americanheart.org/statistics
2. Gary, R., Davis, L.: Diastolic heart failure. Heart Lung. **37**(6), 405–416 (2008)
3. Dolan, E., Thijs, L., Li, Y., et al.: Ambulatory arterial stiffness index as a predictor of cardiovascular mortality in the Dublin Outcome Study. Hypertension **47**, 365–370 (2006)
4. Gao, L., Parker, K.J., Lerner, R.M., Levinson, S.F.: Imaging of the elastic properties of tissue – A review. Ultrasound Med. Biol. **22**(8), 959–977 (1996)
5. Greenleaf, J.F., Fatemi, M., Insana, M.: Selected methods for imaging elastic properties of biological tissues. Annu. Rev. Biomed. Eng. **5**, 57–78 (2003)
6. Lerner, R.M., Huang, S.R., Parker, K.J.: Sonoelasticity images derived from ultrasound signals in mechanically vibrated tissues. Ultrasound Med. Biol. **16**(3), 231–239 (1990)
7. Ophir, J., Cespedes, I., Ponnekanti, H., Yazdi, Y., Li, X.: Elastography: A quantitative method for imaging the elasticity of biological tissues. Ultrason. Imaging **13**(2), 111–134 (1991)
8. Fatemi, M., Greenleaf, J.F.: Ultrasound-stimulated vibroacoustic spectrography. Science **280**, 82–85 (1998)
9. Nightingale, K.R., Palmeri, M.L., Nightingale, R.W., Trahey, G.E.: On the feasibility of remote palpation using acoustic radiation force. J. Acoust. Soc. Am. **110**(1), 625–634, (2001)
10. Nightingale, K., McAleavey, S., Trahey, G.: Shear-wave generation using acoustic radiation force: In vivo and ex vivo results. Ultrasound Med. Biol. **29**(12), 1715–1723 (2003)
11. Sandrin, L., Tanter, M., Gennisson, J.L., Catheline, S., Fink, M.: Shear elasticity probe for soft tissues with 1-D transient elastography. IEEE Trans. Ultrason. Ferroelectr. Freq. Control **49**(4), 436–446 (2002)
12. Sarvazyan, A.P., Rudenko, O.V., Swanson, S.D., Fowlkes, J.B., Emelianov, S.Y.: Shear wave elasticity imaging: A new ultrasonic technology of medical diagnostics. Ultrasound Med. Biol. **24**(9), 1419–1435 (1998)
13. Huwart, L., Peeters, F., Sinkus, R., Annet, L., Salameh, N., ter Beek, L.C., Horsmans, Y., Van Beers, B.E.: Liver fibrosis: Noninvasive assessment with MR elastography. NMR Biomed. **19**(2), 173–179 (2006)
14. Chen, S., Fatemi, M., Greenleaf, J.F.: Quantifying elasticity and viscosity from measurement of shear wave speed dispersion. J Acoust Soc Am. **115**(6), 2781–2785 (2004)

15. Chen, S., Urban, M.W., Pislaru, C., Kinnick, R., Zheng, Y., Yao, A., Greenleaf, J.F.: Shearwave dispersion ultrasound vibrometry (SDUV) for measuring tissue elasticity and viscosity. IEEE Trans Ultrason Ferroelectr Freq Control. **56**(1), 55–62 (2009)
16. Hasegawa, H., Kanai, H.: Improving accuracy in estimation of artery-wall displacement by referring to center frequency of RF Echo. IEEE Trans Ultrason Ferroelectr Freq Control **53**(1) (2006)
17. Zheng, Y., Chen, S., Tan, W., Kinnick, R., Greenleaf, J.F.: Detection of tissue harmonic motion induced by ultrasonic radiation force using pulse-echo ultrasound and kalman filter. IEEE Trans Ultrason Ferroelectr Freq Control **54**(2) (2007).
18. Urban, M.W., Greenleaf, J.F.: Harmonic pulsed excitation and motion detection of a vibrating reflective target. J Acoust Soc Am. **123**(1), 519–533 (2008)
19. Kanai, H.: Propagation of spontaneously actuated pulsive vibration in human heart wall and in vivo viscoelasticity estimation. IEEE Trans Ultrason Ferroelectr Freq Control **52**(11) (2005)

Vector Doppler Method Based on an Automatic Transverse Angle Tracking Procedure

A. Dallai, E. Boni, L. Francalanci, and P. Tortoli

Abstract Traditional Doppler methods only measure the axial component of the velocity vector. The lack of information on the beam-to-flow (Doppler) angle creates an ambiguity which can lead to large errors in velocity magnitude estimates. An original approach was recently introduced, in which two ultrasound beams with known relative orientation are directed towards the same vessel, one being committed to perform a Doppler measurement, while the second beam has the specific task of detecting the beam-to-flow angle. In this paper, an angle-tracking procedure allowing the Doppler angle to be automatically determined with high accuracy is presented. The procedure is based on the real-time estimation of suitable Doppler spectrum parameters obtained from an M-line associated to a sub-aperture of a linear array probe. Such parameters are used to steer the M-line towards a direction corresponding to a desired beam-flow angle. Knowledge of this angle is finally exploited to obtain the velocity magnitude through the classic Doppler equation related to the second beam. The implementation of the method on a new ultrasound machine and its validation through in vitro and in vivo tests are reported.

Keywords Vector Doppler · Dual-beam methods · Transverse Doppler · Doppler angle estimation · Velocity magnitude measurement

1 Introduction

One of the major limitations of Doppler imaging systems consists in the difficulty of estimating the orientation of blood flow with respect to the ultrasound (US) beam. According to the Doppler Effect, a flow with velocity magnitude $|v|$ impinged by a planar US wave with centre frequency f_o, generates echoes characterized by a frequency shift:

$$f_1 = \frac{2 f_0}{c} |v| \cos\ \theta \tag{1}$$

where c is the velocity of US and θ is the beam-to-flow angle. By measuring the frequency f_1, the axial component, $|v| \times \cos\theta$, of the velocity magnitude is estimated.

A. Dallai (✉)
Microelectronic Systems Design Laboratory, Electronics and Telecommunications Department, Università degli Studi di Firenze, Firenze, Italy
e-mail: piero.tortoli@unifi.it

M.P. André et al. (eds.), *Acoustical Imaging*, Acoustical Imaging 30,
DOI 10.1007/978-90-481-3255-3_5,

However, unless θ is known, it is not possible to estimate the individual contribution of $|v|$ or θ to this component.

The standard approach to obtain angle-independent blood velocity estimates is based on the combination of Doppler measurements taken along multiple US beams intersecting in the region of interest [1]. The same sample volume (SV) is insonified by two (or more) probes whose beam axes are oriented along directions describing a known inter-beam angle. The Doppler equations related to the frequencies obtained by the different probes, are then trigonometrically combined to provide an estimate of both the velocity magnitude and the flow direction.

A method employing the classic dual-beam configuration in an original way has been recently introduced [2]. Here, the two probes are devoted to perform distinct tasks: the "reference" probe is used to determine the flow direction only, while the other performs a classic Doppler frequency measurement.

The flow direction is identified by forcing the reference probe to be transversely oriented to the flow itself. This condition is known to produce Doppler spectra having unique features of symmetry around zero frequency. Once the flow direction has been identified, the second beam can be used to estimate the velocity magnitude through an angle-corrected Doppler frequency measurement.

Although the technique has been thoroughly validated in vitro, for its practical in vivo application it is useful that the needed transverse beam-flow angle is automatically achieved. In this paper, we present an automatic angle tracking method, based on the real-time computation of suitable Doppler spectral parameters. The method has been implemented in the programmable ULtrasound Advanced Open Platform (ULA-OP), an experimental system connected to a linear array probe, which was recently developed in our lab [3]. In vitro experiments conducted in both steady and pulsatile flow conditions are reported, showing that the flow direction can be identified with small errors whichever the initial Doppler angle is over a wide range.

2 Methods

2.1 Dual-Beam Method

Let us consider two transducers, hereinafter referred to as 'reference' and 'measuring' transducers, respectively, inspecting the same SV with steering angles α_1 and α_2, respectively. It is assumed that the inter-beam angle, δ, is always known (see Fig. 1).

The angle α_1 can be suitably steered, so that the reference direction is correspondingly fixed at 90° with respect to the flow. In that particular direction, in fact, the Doppler spectrum of the backscattered echo is substantially symmetrical around the zero frequency. This property of the Doppler spectrum, demonstrated through both in vitro and in vivo experiments [4], is derived from the transducer focusing features, which involve a set of effective beam-to-flow angles equally distributed around a nominal 90° angle.

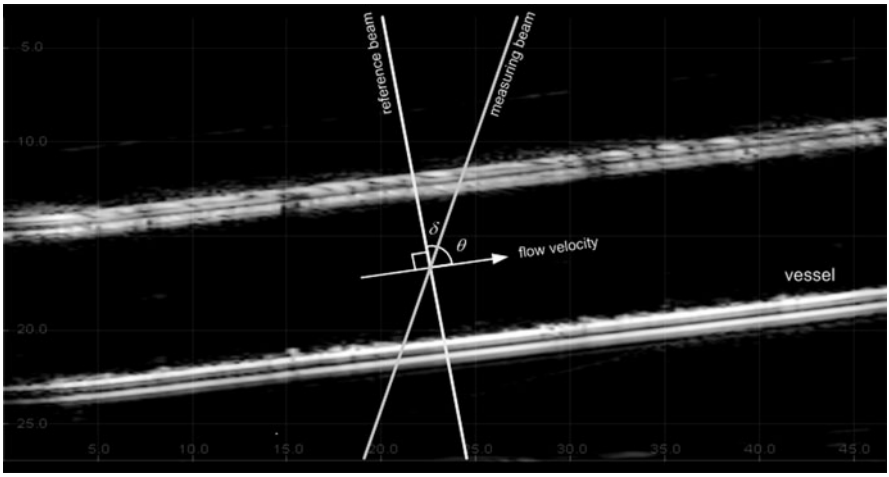

Fig. 1 Dual beam geometry: the reference beam (left) continuously tracks a transverse orientation to the flow direction

The extent at which the spectrum is actually symmetrical can be based on the evaluation of a Spectral Symmetry Index (SSI) defined as:

$$SSI(\%) = \frac{\text{Doppler power distributed over positive frequencies}}{\text{Doppler power distributed over negative frequencies}} \times 100 \qquad (2)$$

in which the numerator and denominator are exchanged when the ratio is > 1. At 90° beam-flow angle, the SSI should ideally be equal to 100%. Since the mean Doppler frequency of the received signal is proportional to the cosine of the nominal Doppler angle, even a small deviation from the desired transverse orientation causes a visible loss of symmetry, and the SSI correspondingly drops down. It was experimentally demonstrated that it is sufficient a $\pm 1°$ deviation from the preferred transverse angle to make the SSI lower than 80% [2]. This suggests that by keeping the SSI larger than a suitable threshold, the beam-flow angle can be maintained close to 90° with the desired accuracy.

Once the reference direction has been made transverse to the flow, the measurement beam-flow angle, θ, is given by:

$$\theta = 90° - \delta \qquad (3)$$

The mean velocity within the investigated SV can finally be directly evaluated through the Equation (1), in which f_I represents the mean frequency of the Doppler signal backscattered from the measuring line, and θ is the (known) beam-flow angle.

2.2 Automatic Angle-Tracking Method

The procedure needed to automatically track a transverse beam-flow angle can be suitably illustrated by making reference to the standard duplex mode of US machines using linear array probes. The procedure starts by fixing, within a B-mode image, the position of the Doppler SV to be investigated. The "reference" Doppler line is initially made coincident with the unsteered M-line crossing the selected SV. The spectrum of echo data received from the SV is monitored in a real-time spectrogram, and used to continuously provide the spectral symmetry index, SSI, and the spectral mean frequency, f_d.

The reference M-line steering angle is automatically modified in order to decrement f_d and to increment the SSI. The steering correction is initially made in coarse steps, which are progressively decreased while the SSI increases. Once the SSI has become larger than a suitable threshold, the steering angle is no more modified, and the flow direction is assumed to be perpendicular to the current reference M-line.

Among all possible beams crossing the SV of interest, the one which is maximally steered is elected as "measuring" beam. The corresponding spectral data are finally converted to velocity magnitude through the Doppler Equation (1).

2.3 Implementation in the ULA-OP System

The angle tracking technique has been implemented and tested through the ULA-OP system, a novel research platform whose architecture is described in detail in [5]. In this system, four high-density Field Programmable Gate Arrays (FPGAs) control 64 transmit/receive channels, which are connected to a 192-element linear array probe through a programmable switch matrix. The echo-signals are channeled through low noise amplifiers, sampled by 12-bit 50 Msps Analog-to-Digital Converters, and dynamically beamformed according to the desired steering angle and apodization factor. Real-time processing of beamformed signals is mainly implemented in a powerful Digital Signal Processor (DSP) by Texas Instruments (TMS320C6455, 750 MHz).

The ULA-OP system was programmed in such a way that two (reference and measuring, respectively) M-lines are simultaneously controlled, i.e., for each line it is possible to continuously set the corresponding group of active elements and steering angle.

While the FPGAs beamform and demodulate the echoes gathered by the probe, the DSP processes the samples related to the two M-lines separately. This is feasible thanks to the DSP firmware architecture that permits concurrent processing modules to coexist and run without hampering each other. Each module is connected to a different data stream and employs a distinct algorithm, therefore when activated the processing module that encapsulates the tracking algorithm is connected to the samples gathered by the reference M-line. For blood flow observation, other

modules, such as the one needed for spectrogram computation, can be allocated and connected to the measuring M-line.

The tracking algorithm continuously evaluates the spectrum of the signal backscattered along the reference M-line throughout 128-point FFTs. In order to increase stability, up to 128 consecutive and partially overlapped Doppler spectra are averaged to extract more robust spectral parameters. The *SSI* allows the DSP to find out if the reference M-line should be further steered and, eventually, to establish the step span. The optimal steering direction is determined according to the sign of f_d.

3 Experiments

The automatic tracking method has been tested in vitro by using a flow phantom which forced a blood mimicking fluid (BMF) to flow, either steadily or with pulsatile trend, through a plastic tube with 8 mm internal diameter.

The linear array probe was positioned to produce longitudinal scans of the tube (see Fig. 1). At the beginning of each experiment, the B-mode display of the ULA-OP system was used to set the SV at a convenient location (typically, in the center) of the tube.

The spectrograms obtained from the reference line was continuously monitored on the PC display and used to achieve the desired transverse beam-flow angle. Once the reference line had reached its final orientation, the real time spectrogram assumed a stable symmetrical behavior and the raw Doppler data related to the measuring line were acquired in a PC file to allow an off-line analysis.

The entire procedure was repeated several times, for a given volume flow, by changing each time the initial probe orientation. Three volume flow values were considered in steady flow conditions (150, 180, 240 mL/min).

The repeatability of the method was assessed by calculating, for each in vitro volume flow, the coefficient of variation (CV), i.e., the ratio between the measured standard deviation (SD) and mean velocity. Over 20 measurements made in steady flow conditions produced CVs between 1.4 and 2.3%.

Four groups of measurements, each corresponding to a different velocity profile, were obtained in pulsatile flow conditions. The velocity curves obtained from the acquisitions corresponding to the same pulsatile flow profile were also compared to each other. As an example, Fig. 2 reports 8 velocity curves measured for a same pump flow profile. The SD mean value, normalized with respect to the mean velocity, produced the CV for this group. CVs between 5.5 and 7.9% were obtained for the four data groups.

11 healthy volunteers (age range 22–31 years) were also recruited for preliminary in vivo application of the technique. All measurements were made by the same operator. The SV was located in the center of the right common carotid artery, at least 2 cm from the bifurcation. When the SSI resulted stably larger than 80%, the raw Doppler data from the M-lines were acquired and stored in a file. After

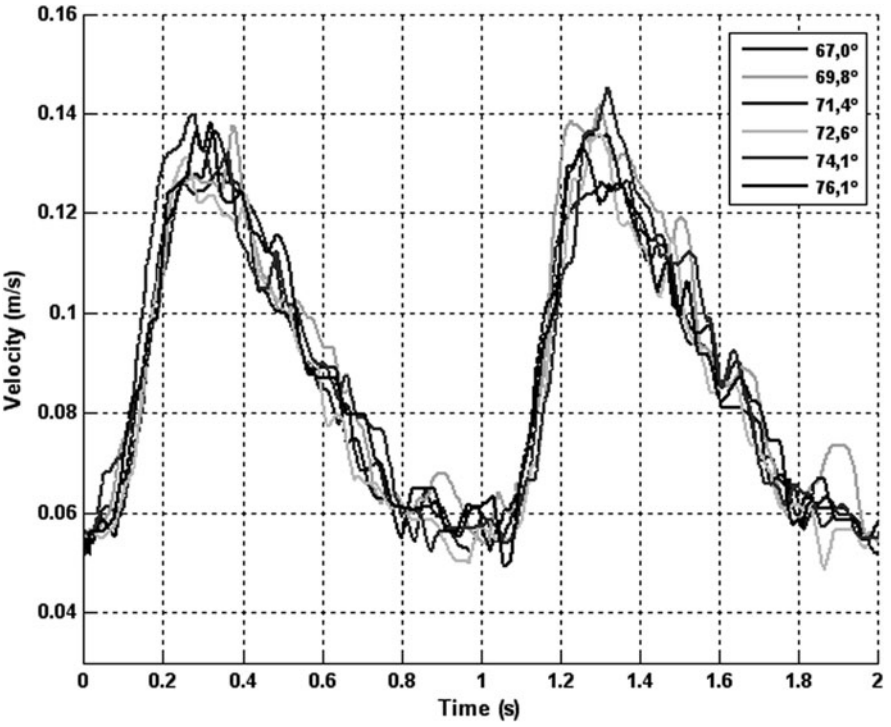

Fig. 2 Velocity curves obtained for a given pump flow profile and different initial probe-to-vessel angles. The indicated angles were estimated through the described procedure

removing the probe from the neck of the volunteer, the operator proceeded with the next acquisition. For each subject, 3 acquisitions were made, each including at least 3 cardiac cycles, depending on the heart rate. The peak systolic velocities measured in each acquisition were averaged to generate a mean value. The mean values obtained from different measurements on the same volunteer (see Fig. 3) were compared to each other. The measured velocities and the resulting CVs ranged between 0.7–1.0 m/s and 1–13%, respectively. The mean CV was 6.6%.

4 Conclusion

The results of the in vitro test demonstrate the tracking method suitable for automatically finding the correct reference line orientation without degrading the repeatability performance of the dual-beam technique. The preliminary experiments on volunteers suggest the method appropriate for in-vivo applications. In all cases where the desired transverse orientation is within the steering capabilities of the used linear array probe, the proposed method makes the proposed dual-beam technique suitable for clinical application in human vessels.

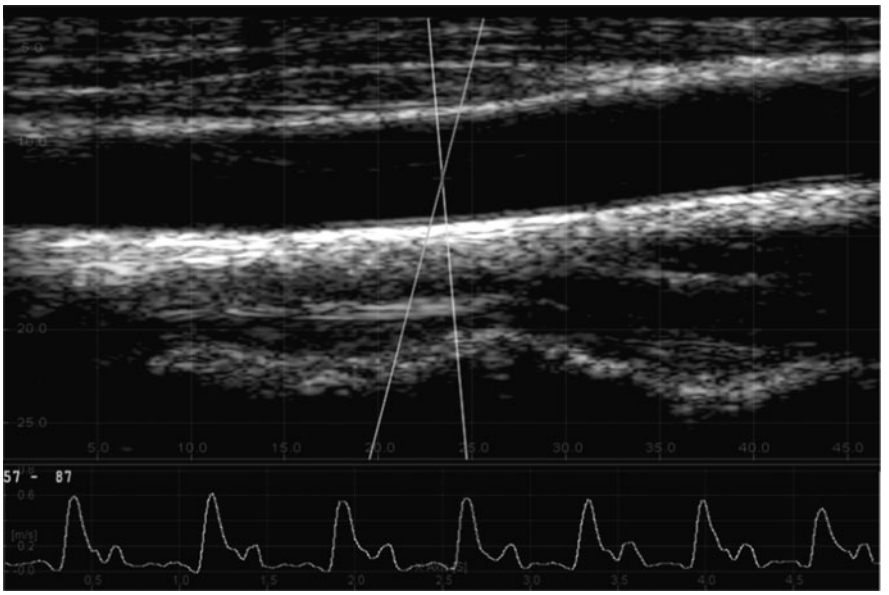

Fig. 3 During a CCA dual-beam exam, one beam is automatically oriented transverse to the flow lines, while the second is the maximally steered beam intercepting the selected SV. The velocity profile estimated through the measuring line is shown on the *bottom*

Acknowledgments The authors wish to thank all the staff of the Microelectronic Systems Design Laboratory, and in particular Stefano Ricci and Luca Bassi, for their great contribution to this work.

References

1. Dunmire, B., Beach, K.W., Labs, K.H., Plett, M., Strandness, D.E.: Cross-beam vector Doppler ultrasound for angle-independent velocity measurements. Ultrasound Med. Biol. **26**(8), 1213–1235 (2000)
2. Tortoli, P., Bambi, G., Ricci, S.: Accurate Doppler angle estimation for vector flow measurements. IEEE Trans. Ultrason. Ferroelect. Freq. Contr. **53**(8), 1425–1431 (2006)
3. Bassi, L., Boni, E., Dallai, A., Guidi, F., Ricci, S., Tortoli, P.: ULA-OP: A novel ULtrasound Advanced Open Platform for experimental research, 2007 IEEE Ultrasonics Symposium Proceed., 632–635, New York, (2007)
4. Tortoli, P., Guidi, G., Pignoli, P.: Transverse Doppler spectral analysis for a correct interpretation of flow sonograms. Ultrasound Med. Biol. **19**(2), 115–121 (1993)
5. Ricci, S., Bassi, L., Cellai, A., Guidi, F., Tortoli, P.: ULA-OP: A fully open ultrasound imaging/Doppler system, Proceedings of the 30th International Symposium on Acoustical Imaging, Monterey, 1–3 March 2009

Proposal for Blood-Flow Imaging by Contrast Echo Using Counter-Crossed Beams

T. Eura, K. Yoshida, Y. Watanabe, T. Takayasu, K. Nakamura, and I. Akiyama

Abstract We propose a new contrast-echo method using counter-crossed beams of two ultrasonic frequencies as an ultrasound diagnostic for cancer. We call this the Counter-Cross Beam Contrast-Echo (C-CBCE) method. Sum and difference frequency components derived from nonlinear vibration of the contrast agents (microbubbles) driven by dual-frequency ultrasound are used in the C-CBCE method. In this study, we used Sonazoid microbubbles as we attempted to detect the sum frequency component generated by Sonazoid fixed in agar gel. We also measured the in-channel flow velocity of the Sonazoid.

Keywords Contrast-echo method · Dual-frequency drive · Contrast agents · Nonlinear vibration · Microbubbles · Sum frequency component

1 Introduction

A contrast-echo imaging method [1–3], in which administrated contrast agents can enhance echo intensity thus permitting effective visualization of the distribution of the microvascular, is the prevailing technology. In the contrast-echo imaging method, all echo signals except those from microbubbles can be eliminated by using secondary signals generated by nonlinear vibration of the microbubbles (contrast agents) [4]. Thus, the distribution of the microvascular system is generally determined by a harmonic-imaging method that visualizes the second-harmonic component in the echo signals. However, a second-harmonic component is generated during propagation through biological soft tissues as well as by nonlinear vibration of the microbubbles. In particular, when measuring a slow blood flow velocity such as in the diagnosis of hepatocellular carcinoma, the influence of the propagation through biological soft tissues cannot be ignored. Therefore, separation of the echoes caused by microbubbles in the blood flow from echoes received from biological soft tissues is an important issue.

In order to address this issue, we propose a new contrast-echo imaging method using counter-crossed beams of two different ultrasonic frequencies. The flow of

T. Eura (✉)
Faculty of Engineering, Doshisha University, Kyoto, Japan
e-mail: akiyama@iwaki.org

M.P. André et al. (eds.), *Acoustical Imaging*, Acoustical Imaging 30,
DOI 10.1007/978-90-481-3255-3_6,

microbubbles can be visualized by using sum and difference frequency components generated by nonlinear vibration of the microbubbles in the crossed area. We call this method the "Counter-Crossed Beam Contrast-Echo method" (C-CBCE method). In this study, we attempted to detect the sum frequency component generated from microbubbles fixed in agar gel. In addition, we measured the flow velocity of the microbubbles in the channel.

2 Principles of the C-CBCE Method

The basic principle of the C-CBCE method is as follows. Two transducers with different resonant frequencies face each other. A broad ultrasonic beam with a frequency of f_1 is formed by a transducer. Another transducer forms a narrow ultrasonic beam with a frequency of f_2. Due to the nonlinear vibration of the microbubbles, sum and difference frequency components (f_1+f_2, f_1-f_2) are generated in the crossed area of the two ultrasonic beams. By extracting these frequency components from the received echo signal, we can measure very slow blood velocities associated only with the contrast echo. The continuous transmission of ultrasound with frequency f_1 from a fixed transducer and a conventional scan featuring repeated transmission of pulsed ultrasound waves with frequency f_2 can be combined to visualize the spatial distribution of blood velocity.

3 Detection of the Sum Frequency Component

We experimentally examined the sum frequency component generated by the nonlinear vibration of microbubbles driven by dual-frequency ultrasound in the crossed area. We used Sonazoid for the microbubbles. The experiment system is described below. Two concave ceramic transducers face each other in degassed water in a water tank. One transducer is driven by 50 cycles of a sinusoidal wave at 2 MHz with sound pressure amplitude at the focal point of 180 kPa. The other transducer is driven by 14 cycles of a sinusoidal wave at 2.8 MHz with sound pressure amplitude at the focal point of 180 kPa. The Sonazoid was fixed in agar gel and arranged in the crossed area. The ultrasound wave was scattered by the Sonazoid in the agar gel and received by a needle-type hydrophone with a diameter of 1.5 mm. We compared the result for the agar gel with microbubbles with that for the agar gel with particulates.

Figure 1a, b plot the respective frequency spectra of the signals received from the agar gel with particulates and with Sonazoid, where $f_1 = 2.8$ MHz and $f_2 = 2$ MHz. Here, a Hamming window is used on the received signal before carrying out a Fast-Fourier transform in order to eliminate the transient response of the transducer from the echo signal. The amplitude is normalized by the fundamental component (f_2), as seen in Fig. 1a. Only the fundamental components f_1 and f_2 are observed in Fig. 1a. However, harmonics ($2f_1$, $2f_2$) and the sum frequency component (f_1+f_2) were observed in addition to the fundamental components in Fig. 1b. Therefore, these harmonic components and the sum frequency component are generated by nonlinear vibration of the microbubbles in the area where the beams cross. The sum

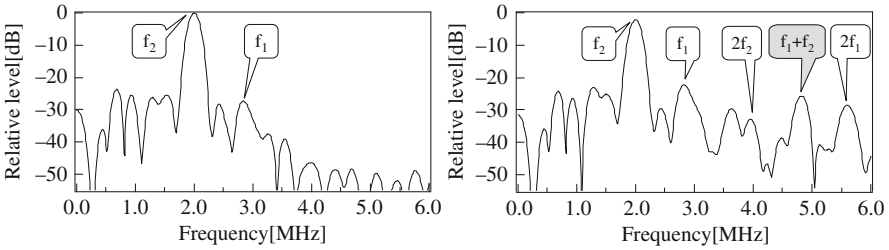

Fig. 1 Spectra of signals received from agar gel phantom

frequency component is larger than all the other components due to the nonlinear vibration of the microbubbles.

4 Measurement of Flow Velocity by C-CBCE Method

Figure 2a presents an overview of the experiment setup for measuring the flow velocity. In order to explain the experiment setup in detail, the front view of a water tank is depicted in Fig. 2b, and the corresponding side view is depicted in Fig. 2c. As seen in Fig. 2b, a concave transducer and a flat transducer face each other. The

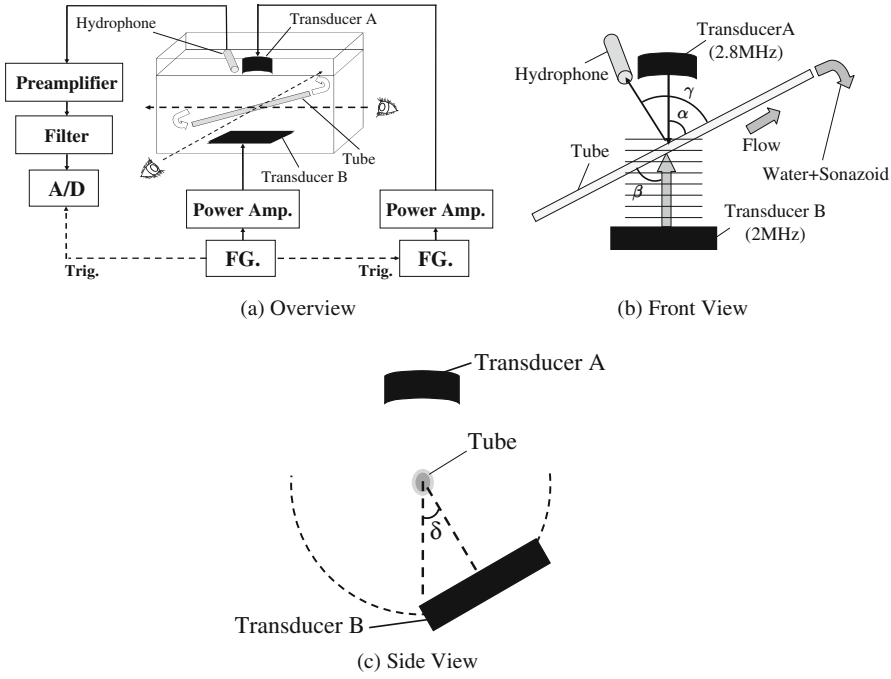

Fig. 2 Experimental setup

flat transducer is driven by 30 cycles of a sinusoidal wave at 2 MHz, and the concave transducer is driven by 10 cycles of a sinusoidal wave at 2.8 MHz. The cycle period of the input signals is 1 ms. A silicon rubber tube with an internal diameter of 4 mm is located at the focal point of the concave transducer, and Sonazoid flows into the tube with degassed water. The ultrasound wave is scattered by the Sonazoid in the tube and is received by a PVDF hydrophone near the concave transducer. As seen in Fig. 2c, the flat transducer can be rotated around the tube. δ is the angle of rotation, as seen in Fig. 2c. In this experiment, the values of δ are 0°, 30°, and 60°.

The received signals are analyzed as follows. Each scattered wave from the Sonazoid is put through a gate function and subjected to quadrature detection by the sum-frequency component (4.8 MHz). Clutter signals, such as the reflected wave from the tube, are eliminated with a Moving Target Indicator (MTI) filter. The scattered signals are arranged to produce a two-dimensional signal whose horizontal axis is time and whose vertical axis is repetition time. The cycle period of the input signals is 1 ms, and thus the repetition time interval is 1 ms. The two-dimensional signal is subjected to Fourier transforms in the direction of the repetition time axis. We used a period of high intensity to calculate the centroid frequency. Finally, we determined this value as a Doppler shift frequency in order to calculate the flow velocity in the tube.

Figure 3 presents a map of the spectrum vs. time with a setup flow velocity of 23 mm/s, after carrying out a Fourier transform in the direction of the repetition time axis. In Fig. 3, the centroid frequency was 28 Hz; we determined this value as the Doppler shift frequency of the sum frequency component (4.8 MHz) in order to calculate the flow velocity.

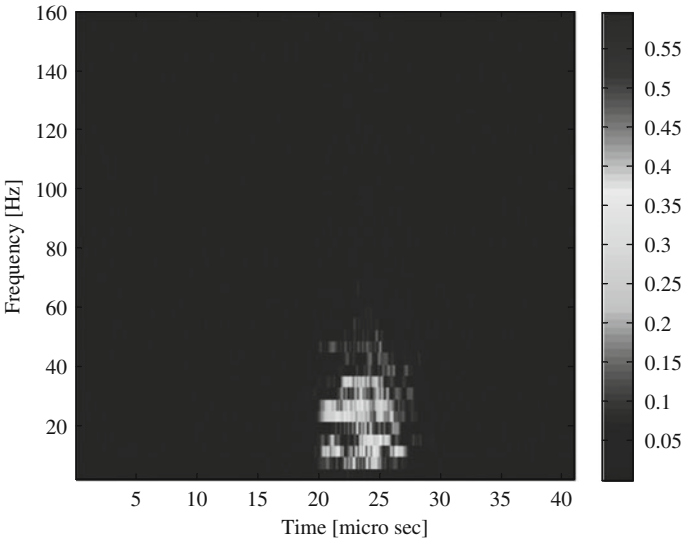

Fig. 3 Map of spectrum vs. time

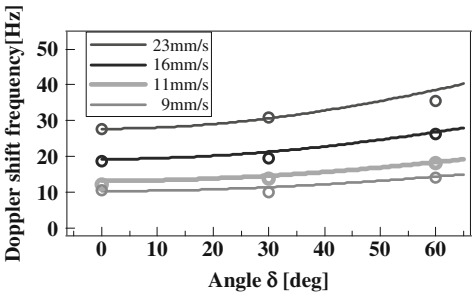

Fig. 4 Relation between the measured and theoretical values of Δf_+

As seen in Fig. 2b, α is the angle between the blood flow direction and the sound wave from Transducer A. β is the angle between the blood flow direction and the sound wave from Transducer B. γ is the angle between the blood flow direction and the sound wave toward the hydrophone. The relation between the Doppler shift frequency of the sum frequency component and the flow velocity is expressed by

$$\Delta f_+ = \frac{v}{c}\left\{ f_1(\cos\alpha + \cos\gamma) + f_2(\cos\gamma - \cos\beta\cos\delta)\right\} \tag{1}$$

where Δf_+ is the Doppler shift frequency of the sum frequency component, c is the sound velocity, and v is the flow velocity in the tube.

In this experiment, we set α and β to 45°, and γ to 75°. We calculated the theoretical value of Δf_+ with Equation (1). The theoretical value of Δf_+ with a setup flow velocity of 23 mm/s was approximately 28 Hz. Therefore, the theoretical value of Δf_+ agreed with the measured value. Figure 4 illustrates the relation between the measured value of Δf_+ and the theoretical value calculated by Equation (1). In Fig. 4, the vertical axis represents the Doppler shift frequency of the sum frequency component Δf_+, and the horizontal axis represents the angle of rotation δ. We succeeded in measuring the flow velocity in the range of 9–23 mm/s. As seen in Fig. 4, the measured values of the Doppler shift frequency of the sum frequency component agreed with the theoretical values calculated by Equation (1).

5 Summary

In this study, we attempted to detect the sum frequency component generated from microbubbles fixed in agar gel. We also measured the flow velocity of microbubbles in a silicon rubber tube. In our result, we extracted the sum frequency component generated by the nonlinear vibration of microbubbles from the echo signals. The measured values of flow velocity agreed with those of the actual velocity over the range of 9–23 mm/s.

Acknowledgements This work was supported by KAKENHI (20300181).

References

1. Akiyama, I., Ohya, A., Saito, S.: Speckle noise reduction by superposing many higher harmonic images. Jpn. J. Appl. Phys. **44**, 4631–4636 (2005)
2. Tanaka, S., Kitamura, T., Fujita, M., Nakanishi, K., Okuda, S.: Color Doppler flow imaging of liver tumors. Am. J. Roentgenol. **154**(3), 509–514 (1990)
3. Akiyama, I., Yoshimoto, N., Yoshida, K., Watanabe, Y.: Measurement of secondary waves generated by nonlinear vibration of microbubbles in the crossed beams of two ultrasonic frequencies, nonlinear acoustics-fundamentals and applications. In: Enflo B.O., Hedberg C.M., Kari L. (eds.) AIP Conference Proceedings, New York, USA, pp. 432–435 (2008)
4. Tanaka, S., Hamada, Y., Ioka, T., Sugiyama, T., Akamatsu, I., Takakura, R., Yoshioka, F., Nakaizumi, A., Ishida, T.: Contrast-enhanced multiphase dynamic ultrasonography for the characterization of liver tumors. J. Med. Ultrason. **32**(2), 57–63 (2005)
5. Leighton, T.G.: The Acoustic Bubble. Academic Press, London, pp. 413–424 (1994)
6. Young, F.R.: Cavitation. McGraw-Hill Companies, London, pp. 115–136 (1990)
7. Watanabe, R., Matsumura, M., Chen, C.J., Kaneda, Y., Fujimaki, M.: Characterization of Tumor Imaging with Microbubble-Based Ultrasound Contrast Agent, Sonazoid, in Rabbit Liver. Biol. Pharm. Bull. **28**(6), 972–977 (2005)

Inverse Scattering Theory

J. Wiskin, D. Borup, and S. Johnson

Abstract This paper discuss a fully 3D nonlinear algorithm that results in a 3D quantitative estimate of breast tissue characteristics and a refraction corrected reflection algorithm (RFCR) that utilizes these estimates. The data are obtained from a specially designed clinical ultrasound breast scanner and processed on the device. We discuss the data collection process, a fast solution to the forward problem and a concomitant fast inverse scattering solution for the imaging problem. We show how the resulting 3D tissue map is used in a refraction corrected reflection algorithm.

Keywords Full wave · Nonlinearity · Inverse scattering · Ultrasound · Breast cancer · Helmholtz wave equation · Ribiere-Polak coefficient · Whole breast ultrasound

1 Introduction

It has been pointed out in André, et al. [1], in 2008 that the full inverse scattering solution has multiple advantages over conventional breast sonography. However, the attainment of an inversion or imaging algorithm that utilizes the full waveform and the inherent nonlinearity of the inversion process, in a potentially useful time frame, has been lacking. Furthermore, the inversion should take place on a computational engine that can accompany the data acquisition device, and be reasonably inexpensive, if the device is to be clinically useful as a self-contained device.

This paper will give a physical motivation for just such an algorithm, using a fast forward solver, and concomitant algorithms for implementation of a very large ($\sim$20 million unknowns) minimization of a functional (shown below) F, that yields a solution to the inverse scattering problem.

Specifically the minimization is based on the Ribiere-Polak version of nonlinear conjugate gradients [2], therefore it requires a fast way to calculate the gradient of F and the step length. These calculations are shown below.

J. Wiskin (✉)
Techniscan Medical Systems, Inc., Salt Lake City, UT 84106, USA; Department of Bioengineering, University of Utah, Salt Lake City, UT 84106, USA
e-mail: jwiskin@techniscanmedical.com

M.P. André et al. (eds.), *Acoustical Imaging*, Acoustical Imaging 30,
DOI 10.1007/978-90-481-3255-3_7,

The inversion algorithm is based on a type of approximate factorization of the Helmholtz wave equation that leads to a form of the phase screen approach (described in U.S. patent 6,636,584) [4].

2 Materials and Methods

2.1 Data Collection

The data are collected on a clinical device constructed by Techniscan Medical Systems (TMS), Inc, shown below in Fig. 1.

The water bath contains a "tri-channel scanning head" that holds a pair of transmission arrays, and three reflection arrays (not shown above). The transmitter sends out a broadband chirp signal from 0.350 to 2.0 MHz, centered at ~1.1 MHz. This signal passes through the water bath, into the breast and finally reaches the receiver array on the opposite side of the breast. This array consists of 160 horizontal elements and 6 rows vertically. The columns are 0.8 mm wide, and the rows vary in height: 4.6 mm, 1.9 mm, and 1.45 mm.

The reflection data are collected on three separate transceivers with different focal lengths of 2.5, 4.0 and 7.5 mm (Fig. 2). The purpose of the variable focal lengths is to allow overlapping focal regions resulting in greater depth of focus than one transceiver alone. The three transceivers rotate 360°, and reflection data are collected every 6°, for a total of 60 views. The bandwidth of the transceivers is 2–8 MHz.

The three transceivers are placed at 48° azimuth angle increments and are tilted upward 10° from the horizontal to obtain data near the chest wall.

Data collection occurs with the patient lying prone on the examination table, with the breast hanging pendant through the hole in the table, into the water bath, and between the transducer arrays. The breast is constrained against movement via a snap/magnet device that is attached via medical grade adhesive to the

Fig. 1 TMS, Inc. Whole Breast Ultrasound (WBU) clinical device

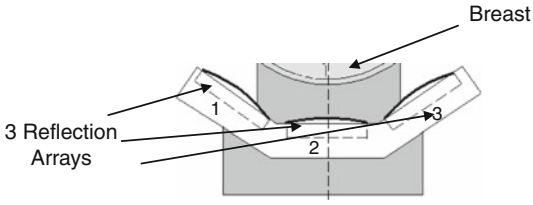

Fig. 2 Placement of three transceivers on U-arm in water bath for collecting reflection data

areolar region of the breast. As the breast is lowered into the water bath, the magnet is attracted to the top of the retention rod (Fig. 1) located in the center of the tri-channel scanning head.

2.2 Inverse Scattering Imaging Algorithm

The inverse scattering algorithm is based on the minimization of the functional F (Equation 1), which is a function of the object function $\gamma(\mathbf{x}) \equiv (1/k_o)(k(\mathbf{x}) + i\alpha(\mathbf{x}))$, where $k_o \equiv \omega/c_o$, and $k(\mathbf{x}) \equiv \omega/c(\mathbf{x})$, are the wave-numbers in water and inhomogeneous tissue, respectively, at frequency $\omega = 2\pi f$, and α is the attenuation coefficient in Nprs/mm.

$$\min F_{\omega_j}(\gamma(\mathbf{x})) = \min \frac{1}{2} \sum_{\substack{\theta = 1,...N_{views} \\ l = 1,...,N_{levels}}} \overline{\mathbf{r}^l_{\omega_j\theta}(\gamma)}\mathbf{r}^l_{\omega_j\theta}(\gamma) \tag{1}$$

at successive frequencies, ω_j, $j = 1,...N_{freq}$. We proceed from low frequencies to high frequencies to avoid local minima. We image at 0.35, 0.4, 0.45, 0.5, 0.6, 0.7, and 0.8 MHz successively for the 2D case, and 0.5, 0.6, 0.7, 0.8, 0.9, 1.0, 1.1, 1.2, and 1.25 MHz successively for the 3D volume image. The vectors $\mathbf{r}^l_{\omega\theta}(\gamma) \equiv \left(\hat{\mathbf{d}}^l_{\omega\theta}(\gamma) - \mathbf{d}^l_{\omega\theta}\right) \in C^{N_R}$ represent the residual between the predicted field, $\hat{\mathbf{d}}^l_{\omega\theta}(\gamma)$, and the measured field, $\mathbf{d}^l_{\omega\theta}$, at each receiver position, for each transmitter position, θ, level *l, and* at the fixed frequency ω. Note that this functional involves all views, and all levels simultaneously, that is, it is a true 3D algorithm.

The algorithm at the highest level is described in Wiskin, et al. [2]. It is a series of updates to γ. $\gamma^{(n+1)} = \gamma^{(n)} + \alpha_n \mathbf{d}_n$, where the descent direction $\mathbf{d}_n \equiv -\mathbf{g}_n + \beta_n \mathbf{d}_{n-1}$, where $\mathbf{g}_n$ is the gradient, $\beta_n \equiv \frac{(\mathbf{g}_n - \mathbf{g}_{n-1})^T \mathbf{g}_n}{\|\mathbf{g}_{n-1}\|^2}$ is the Ribiere-Polak coefficient ($\beta_0 = 0$), and α_n is the step-length. The calculation of the step-length and the gradient are detailed below.

2.2.1 Initial Estimates

Due to the minimization nature of the algorithm, an initial estimate is required. First a time of flight algorithm is used to create a series of initial distribution for speed of sound and attenuation *at each level.* These initial estimates are used in a series of 2D inverse scattering algorithms to create a series of 2D inverse scattering images at

each level, which are the distributions which minimize the functional (Equation 1), for *one particular level, l*. These 2D images are then concatenated together to form a 3D volume. This 3D volume is the *starting estimate* for the full 3D inverse scattering algorithm. The 3D algorithm is required to account for energy that is refracted out of plane. The 2D-algorithm gives an anomalously high result for the attenuation estimate.

2.2.2 Forward Problem

We require a very fast solution of the forward problem. To achieve this we rewrite the Helmholtz equation:

$$\frac{\partial^2 p\left(\mathbf{x}\right)}{\partial x^2}+\frac{\partial^2 p\left(\mathbf{x}\right)}{\partial y^2}+\frac{\partial^2 p\left(\mathbf{x}\right)}{\partial z^2}+\left(k\left(\mathbf{x}\right)+i\alpha\left(\mathbf{x}\right)\right)^2 p\left(\mathbf{x}\right)=0 \tag{2}$$

$$\text{as } \left[\left(A+iB\right)\left(A-iB\right)-i\left[B,A\right]\right]p\left(\mathbf{x}\right)=0 \tag{3}$$

where: $A\equiv\frac{\partial}{\partial x}$, is a partial differential operator, and

$B\equiv\sqrt{\frac{\partial^2}{\partial y^2}+\frac{\partial^2}{\partial z^2}+k^2\left(x,y,z\right)}$, is a pseudo-differential operator, and $[B,A]$ is the commutator of these operators.

Under the assumption that this commutator can be ignored, we can approximately "factor" the Helmholtz equation to yield:

$$\frac{\partial}{\partial x}p\left(x,\mathbf{r}_\perp\right)=i\mathbf{H}\left(x,\mathbf{r}_\perp\right)p\left(x,\mathbf{r}_\perp\right) \tag{4}$$

a "Schrödinger" equation in "time" x, with the unusual "Hamiltonian,"

$$\mathbf{H}(x,\mathbf{r}_\perp)=\sqrt{\frac{\partial^2}{\partial y^2}+\frac{\partial^2}{\partial z^2}+k^2(x,y,z)} \tag{5}$$

in transverse co-ordinates $\mathbf{r}_\perp\equiv(y,z)$, x (the direction of propagation) plays the role of time.

A symbolic solution for the propagator from initial state (wave field) at x_o to final state (wave field) at x, is given as the phase-space path integral [3]:

$$\left\langle p\left(x,\mathbf{r}_\perp\right)\left|p\left(x^o,\mathbf{r}_\perp^o\right)\right.\right\rangle=\int D\mathbf{r}_\perp\left(x\right)\int D\mathbf{p}_\perp\left(x\right)e^{iS\left(\mathbf{r}_\perp,\mathbf{p}_\perp\right)} \tag{6}$$

with "action", $S\left(\mathbf{r}_\perp,\mathbf{p}_\perp\right)\equiv\int_{x^o}^{x}dx\left(\mathbf{p}_\perp\frac{d\mathbf{r}_\perp}{dx}-\mathbf{H}\left(x,\mathbf{r}_\perp,\mathbf{p}_\perp\right)\right)$

Discretizing the "time" from x_0 to x, $x_0<x_1<\cdots<x_{N-1}<x_N<x_{N+1}=x$, and utilizing standard properties of the exponential gives for the propagator:

$$\prod_{j=1}^{N}\int d\mathbf{p}_j\,e^{i\mathbf{r}_{j+1}\mathbf{p}_j}e^{-i\mathbf{H}\left(x,\mathbf{r}_j,\mathbf{p}_j\right)\Delta x}\int d\mathbf{r}_j e^{-i\mathbf{r}_j\mathbf{p}_j} \tag{7}$$

We approximate this with the following form of the propagator acting on the initial field at x_o: $p\left(x_o, \mathbf{r}_o^{\perp}\right)$, to give the total field at the receivers:

$$p\left(x_N, \mathbf{r}_N^{\perp}\right) = \prod_{j=1}^{N} t\left(x_j, \mathbf{r}_{\perp}\right) \odot \mathbf{F}^{-1} P \odot \mathbf{F} p\left(x_o, \mathbf{r}_o^{\perp}\right) \tag{8}$$

The $\odot$ indicates element-wise multiplication of two matrices: i.e. if $A_{\lambda\mu}, P_{\lambda\mu}$ are components of 2D matrices, $(P \odot A)_{\lambda\mu} \equiv \left(P_{\lambda\mu} A_{\lambda\mu}\right)$. $\mathbf{F}$ indicates Fourier Transform. P is the 2D matrix with elements, $P_{\lambda\mu} \equiv e^{i\varepsilon\sqrt{k_0^2-(\lambda\Delta_k)^2-(\mu\Delta_k)^2}}$, ε is step length in x, Δ_k is step length in transform space: k_y, k_z. and

$t\left(x_j, \mathbf{r}_{\perp}\right) \equiv t_j(y,z) \equiv e^{i\varepsilon\left(k\left(x_j,y,z\right)-k_0\right)} \equiv e^{i\varepsilon k_0\left(\gamma\left(x_j,y,z\right)-1\right)}$ is the "phase mask" element-wise multiplication operator [4].

2.2.3 Gradient of Functional, *F*

The Polak-Ribiere version of the nonlinear conjugate gradient algorithm requires the gradient of functional F:

$$\frac{\partial}{\partial \overline{\gamma}} F(\gamma) = \sum\nolimits_{l\theta} \left(\overline{\frac{\partial}{\partial \gamma} \mathbf{r}_{l\theta}}\right)^T \mathbf{r}_{l\theta} \equiv \overline{J}_{\omega}^T \mathbf{r}, \tag{9}$$

where $J \equiv \frac{\partial \mathbf{r}_{l\theta}}{\partial \gamma}$ is the Jacobian operator. This is obtained in the following manner. $\delta\gamma_j^{\omega\theta} = \mathbf{v}_j \odot f_{\mathbf{r}_{\omega\theta}}^j$ is the contribution to the gradient, from view angle θ and *x-coordinate, x_j*. It is the point-wise product of two 2-dimensional arrays of size (N_y, N_z). viz., $\mathbf{v}_j \equiv \mathbf{F}^{-1} P \odot \mathbf{F} p\left(x_{j-1}, \mathbf{r}_{j-1}^{\perp}\right)$, the total field at propagation distance *j−1,* propagated through water, to propagation distance *j*. $f_{\mathbf{r}_{\omega\theta}}^j$ is the field at x_j, resulting from treating all receivers, at tomographic view angle θ, as transmitters, at frequency ω. The strength of each "transmitter" is: $f_{\mathbf{r}_{\omega\theta}}^N \equiv \overline{\delta \mathbf{f}}_N$, i.e., the difference between the measured and predicted fields at the receivers, and we recursively define $f_{\mathbf{r}_{\omega\theta}}^j = \mathbf{F}^{-1}\overline{P} \odot \mathbf{F}\overline{\mathbf{t}_j} f_{\mathbf{r}_{\omega\theta}}^{j+1}$, for *j=N-1,. . . ,0.*

2.2.4 Step Length Calculation for Ribiere-Polak Conjugate Gradients

Step length $\alpha_n \approx \frac{\mathbf{g}_n^T \mathbf{d}_n}{\|J_n \mathbf{d}_n\|^2}$, $\mathbf{d}_n$ is the RP descent direction. $\mathbf{g}_n$ is the gradient of the functional *F,* and $J \equiv \frac{\partial \mathbf{r}_{l\theta}}{\partial \gamma}$ is the associated Jacobian.

The action of the Jacobian on the descent direction is given by

$$J_n \mathbf{d}_n = \left[\frac{\partial \mathbf{r}_{l\theta}}{\partial \gamma}\right] \mathbf{d} = \delta \mathbf{p}_N \tag{10}$$

where: $\delta \mathbf{p}_j = \mathbf{A}\mathbf{p}_{j-1} \odot \delta \mathbf{t}_j + t\left(x_j, \mathbf{r}_{\perp}\right) \odot \mathbf{A}\left(\delta \mathbf{p}_{j-1}\right)$, *j=1,..,N,* and where $\mathbf{A} \equiv \mathbf{F}^{-1} P \odot \mathbf{F}$ propagates a field a distance ε through water, and $\delta \mathbf{t}_j\left(\mathbf{r}^{\perp}\right) \equiv i\varepsilon k_0 \mathbf{t}_j(y,z)\, \delta\gamma\left(x_j, y, z\right)$ from the definition of the phase mask $\mathbf{t}_j$.

2.2.5 Update for Image Volume γ

Having determined the step length and descent direction the update is given by $\gamma^{(n+1)} = \gamma^{(n)} + \alpha_n \mathbf{d}_n$.

2.3 3D Refraction Corrected (RC) Reflection Algorithm

The speed of sound and attenuation images resulting from the 3D inverse scattering algorithm are used to correct for refraction effects in the reflection algorithm. The canonical ray-tracing equations derived from the eikonal equation [5]

$$\frac{d}{ds}\left(n\frac{d\mathbf{r}}{ds}\right) = \nabla n, n\,(\mathbf{x}) = c_o/c\,(\mathbf{x}) \tag{11}$$

are solved to give the energy path corrected for refraction due to speed variation. The attenuation images are used to adjust the amplitude of the energy along the computed ray.

A data driven back-projection algorithm is used to place the reflected energy at its place of origin, via ray tracing, at each of 60 views, which are then compounded. The resulting back-projected reflection image is a 360° compound B-scan.

3 Results

The compounded B-scan (RFCR) gives accurate morphology to less than 1 mm resolution. However, no quantitative tissue characteristics are recovered. The transmission inverse scattering, on the other hand, yields quantitative estimates of the speed of sound and attenuation coefficient tissue characteristics at ~1.5 mm resolution horizontally. André, et al. [1], have shown that the speed of sound estimates are well correlated ($R^2 = 0.9918$) with known values. The attenuation images are thought to be less accurate, due to the poorer numerical conditioning of the attenuation inversion problem.

Figure 3 shows a fibro-adenoma exhibiting characteristic high speed, low to medium attenuation, and little internal structure in the reflection mode. Further results from patient-volunteers, and discussion, are shown in the accompanying paper in these proceedings.

4 Conclusions

Using a simple parallelization, it is possible to create 3D speed of sound and attenuation images, with ~1.5 mm resolution [1] in approximately 45 min for a typical breast size, using the algorithm described here, and a cluster of 6 Pentium CPU's. These images are then used with 3D ray tracing to create a RFCR reflection image. Additionally, these images could be used in a clinical setting, the topic of the following paper in these proceedings.

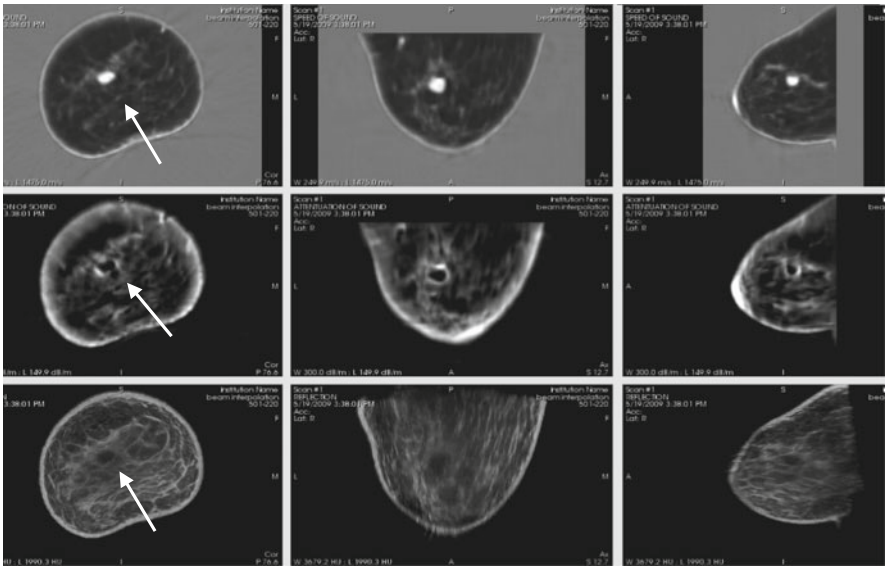

Fig. 3 Screenshot of 220-R with fibroadenoma, showing correlated views of speed, (*top*), attenuation (*center*) and reflection (*bottom*) reconstructions, in correlated coronal, axial, and sagittal views (*left* to *right*)

The somewhat faster convergence of the speed image, over the attenuation image is thought to be due to the fact that the speed of sound of the image is more closely tied to the phase information encoded within the data, whereas the attenuation image is more closely tied to the amplitude data.

The speed of sound and attenuation maps produced can be used to create a refraction corrected reflection image. The refraction correction improves spatial resolution by allowing large angle compounding, which reduces speckle. Furthermore, the refraction correction allows the compounding to be carried out for a full 360°, so that the resolution is based on the axial resolution, and not the lateral, thereby giving the above mentioned high resolution < 1 mm.

References

1. André, M.P., Barker, C.H., Sekhon, N., Wiskin, J., Borup, D., Callahan, K.: Pre-clinical experience with full wave inverse scattering for breast imaging. In: Akiyama, I. (ed.) Acoustical Imaging, vol. 29. Springer, Dordrecht (2008)
2. Wiskin, J., Borup, D.T., Johnson, S.A., Berggren, M., et al.: Full wave non-linear inverse scattering. In: André, M. (ed.) Acoustical Imaging, vol. 28, p. 183. Springer, Dordrecht (2007)
3. Bailin, D., Love, A.: Introduction to Gauge Field Theory, Ch. 2, eqn. 2.18. Institute of Physics Publishing, Bristol (1993)
4. Johnson, et al.: Acoustic imaging using inverse scattering techniques, US Patent #6,636,584
5. Born, M., Wolf, E.: Principles of Optics, 7th edn. Cambridge University Press, Cambridge (1999)

Inverse Scattering Results

J. Wiskin, D. Borup, K. Callahan, Y. Parisky, J. Smith, M.P. André, and S. Johnson

Abstract We discuss the results obtained using the inversion and refraction corrected reflection (RFCR) algorithms described in the companion paper in these proceedings. We show images for three patients created with these algorithms, from data collected with our clinical device. We discuss their potential clinical relevance, and their relationship to other, more conventional imaging modalities.

Keywords Quantitative images · Speed of sound · Attenuation · Clinical · Ultrasound · Inverse scattering breast sonography · Mammography · Breast cancer · Fibroadenoma · Complicated cyst · Infiltrating ductal carcinoma

1 Introduction

Ultrasound has been proposed as an adjunct diagnostic modality for over 30 years [1–3]. There have been two major types of ultrasound data processed: transmission data, and reflection data, with standard ultrasound utilizing reflection data. However, since most inversion algorithms avoid the inherent nonlinearity of the inversion process, the images tend to lack quantitative accuracy. Furthermore, the reflection based images are not generally corrected for refractive effects, since a quantitatively accurate detailed speed of sound map is generally not available.

The transmission inversion algorithm described in the previous paper in these proceedings yields a quantitatively accurate estimate of the tissue characteristics to approximately 1.5 mm in-plane resolution, known as the Whole Breast Ultrasound (WBU) image [4–6]. The speed and attenuation maps that resulted from these inversions were then utilized in a refraction corrected reflection (RFCR) algorithm to yield the images shown below.

The data were collected at the University of California, San Diego, (UCSD), and Techniscan, Inc. (TSI), in Salt Lake City.

J. Wiskin (✉)
Techniscan Medical Systems, Inc., Salt Lake City, UT 84106, USA; Department of Bioengineering, University of Utah, Salt Lake City, UT 84106, USA
e-mail: jwiskin@techniscanmedical.com

M.P. André et al. (eds.), *Acoustical Imaging*, Acoustical Imaging 30,
DOI 10.1007/978-90-481-3255-3_8,

2 Materials and Methods

The transmission and reflection data were collected in approximately 15 min per breast. The transmission inversion process is a very large minimization, involving approximately 20 million unknowns. The precise inversion and reflection algorithms are given in the companion paper (Wiskin et al.) to this one in this volume.

The cases presented below represent female patients who presented for routine screening mammograms, and had some indeterminate mass. They were given an appropriate BI-RADS category score for the mammogram, and the follow-up hand held ultrasound. After this, the patients who gave their consent were scanned on our system. In the instances below, when the patient underwent biopsy the scan on the TechniScan Whole Breast Ultrasound (WBU) device was carried out before the biopsy was performed.

3 Results

3.1 Case 501-169-L

Figures 1 and 2 show images for a 50 year old female who had a tender, palpable mass in the 6–7 o'clock position of the left breast. The patient had heterogeneously dense breast parenchyma and a strong family history of breast cancer (2 sisters diagnosed with breast cancer).

The TSI WBU images (Fig. 3) is a screenshot of the viewer designed specifically by TSI to portray all three modalities in a registered fashion. It contains speed (top row), reflection (middle) and attenuation images (bottom row) in coronal (left column), axial (middle), and sagittal (right column) views. These views and modalities are completely registered with one another. The speed and attenuation images are quantitative: High speed and high attenuation are shown as light grey or

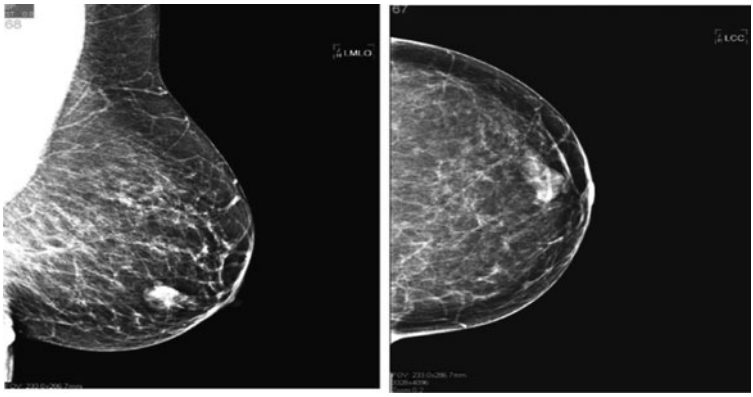

Fig. 1 Case 501-169-L, mammography images show palpable mass (left MLO, left CC)

Fig. 2 Case 501-169-L ultrasound image, left breast, 3 o'clock

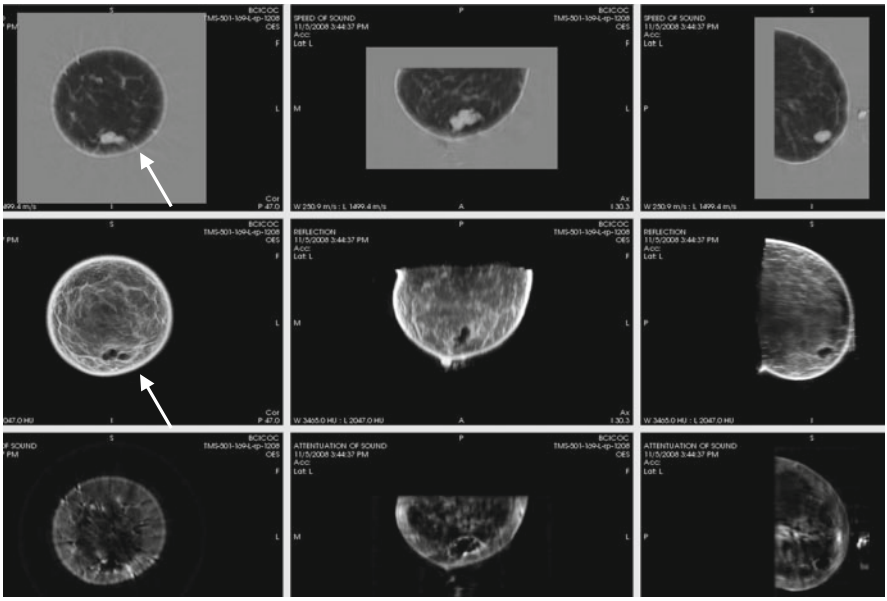

Fig. 3 TechniScan WBU Images of 501-169-L: speed (*top*), reflection (*middle*), attenuation (*bottom*), in coronal (*left*), axial (*middle column*), and sagittal (*right*) views. The complicated cyst has high sound speed, low attenuation and is hypo-echoic

white and low speed and attenuation values are shown as dark grey or black. The speed of sound in the water bath is shown as grey (~1.5114 mm/μsec). Fatty tissue appears dark (~1.40–1.48 mm/μsec) and the complex cyst as a very light grey (~1.60 mm/μsec). In our attenuation image, the cyst shows up as a dark interior with a defined border of relatively high attenuation.

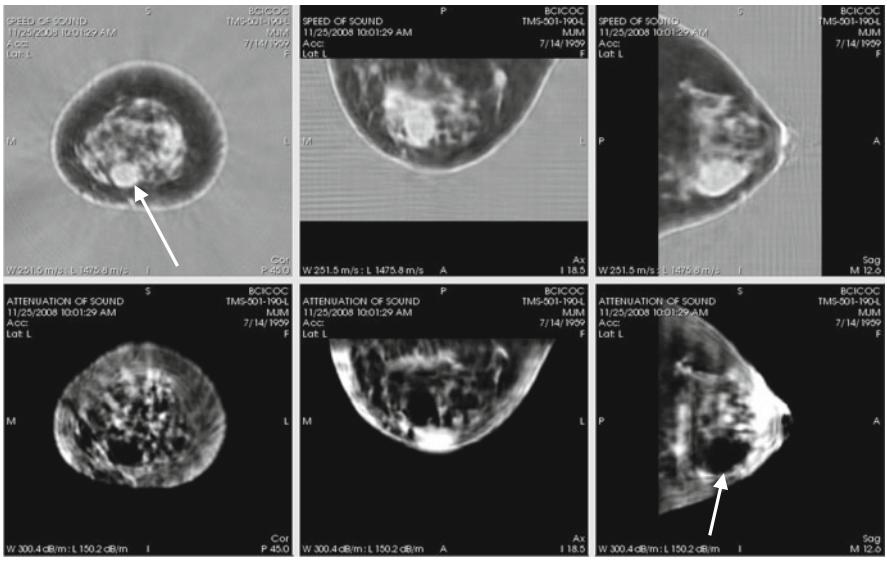

Fig. 4 WBU speed and attenuation images in coronal, axial and sagittal views (*left* to *right*), showing speed of sound similar to water and no attenuation, (Case 501-190-L)

3.2 Case 501-190-L

Figure 4 is a 50 year old female who presented in Fig. 4 with a tender palpable mass in the 6–7 o'clock position of the left breast. This patient had a heterogeneously dense breast parenchyma and a family history of breast cancer (2 sisters diagnosed).

This was determined to be a cyst measuring 2 cm in size, and was successfully aspirated, resulting in removal of 5 cc of thick whitish fluid with complete cyst collapse.

3.3 Case 501-187-R

This patient (Figs. 5, 6, 7) was 12 years post-treatment for breast cancer in the right breast. She had a benign biopsy in the surgical site 3 years prior. The mammograms show an area of increased density close to the chest wall, with a somewhat irregular margin. The breast itself has scattered fibrous and glandular tissue. The Ultrasound B-scan image shows a discrete hypo-echoic mass at the 9 o'clock position that is wider than tall with central vascularity. This was given a BI-RADS category 5 (highly suspicious), and the biopsy confirmed infiltrating, invasive ductal carcinoma.

The WBU image shows the high speed of sound region, with irregular border both in the speed image and the attenuation image. Furthermore the attenuation image has a highly attenuating border that is thick. We have noted that there is a

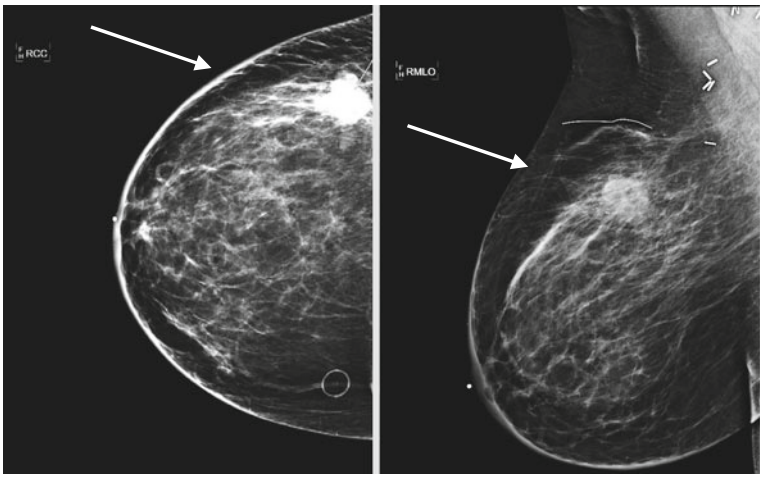

Fig. 5 501-187-R Mammogram RCC and RMLO, showing increased density close to chest wall

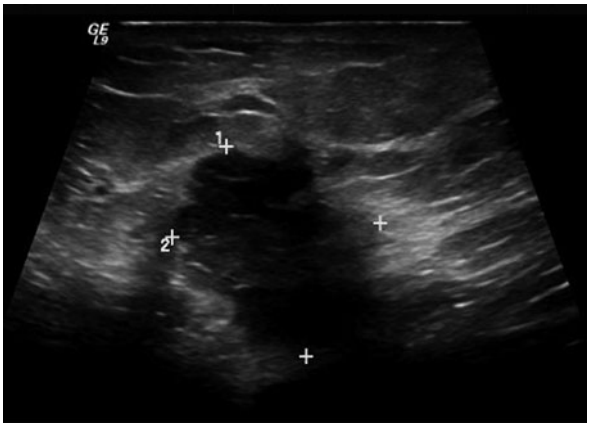

Fig. 6 501-187-R B-Scan Right Breast at 9 o'clock showing shadowing indicating an attenuating mass

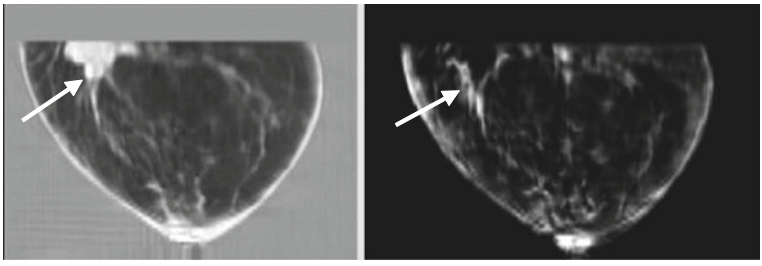

Fig. 7 Speed of sound (*left*) and attenuation (*right*) for 501-187-R. The lesion has a high speed of sound (indicated by light color), and a border of high attenuation surrounding a low attenuation region. This was infiltrating ductal carcinoma

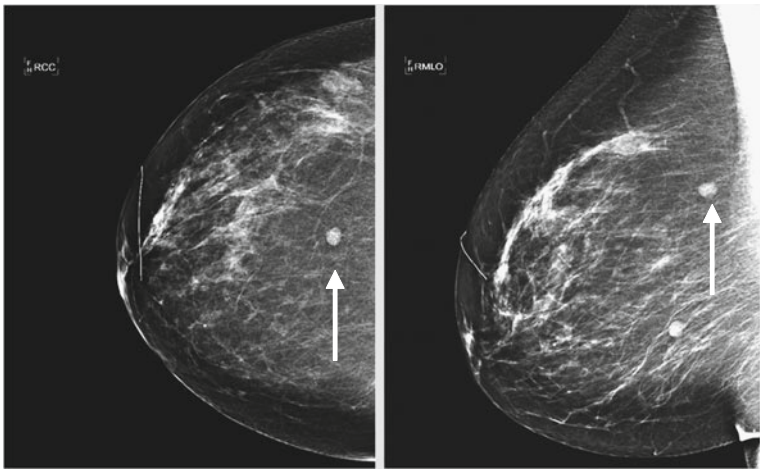

Fig. 8 501-174-R CC and MLO Mammograms showing lesions of interest

Fig. 9 Right breast, 501-174-R, 10 o'clock lesion showing lobulation, inhomogeneity and complex posterior shadowing

higher attenuation value at the border of any object. This is to be expected, due to the fact that the algorithm does not account for reflected energy and therefore, the reflected energy at a border will be interpreted as attenuation. However, in such a case, the attenuation should have thin spatial extent, whereas this lesion has thick spatial extent, it is not thin.

3.4 Case 501-174-R

A 39 year-old patient presented for screening mammography (Fig. 8). There were 3 indeterminate masses in the right breast at 7, 9 and 10 o'clock and the breast tissue was fatty. Using ultrasound (Fig. 9), the lesions at 9 and 10 o'clock were shown

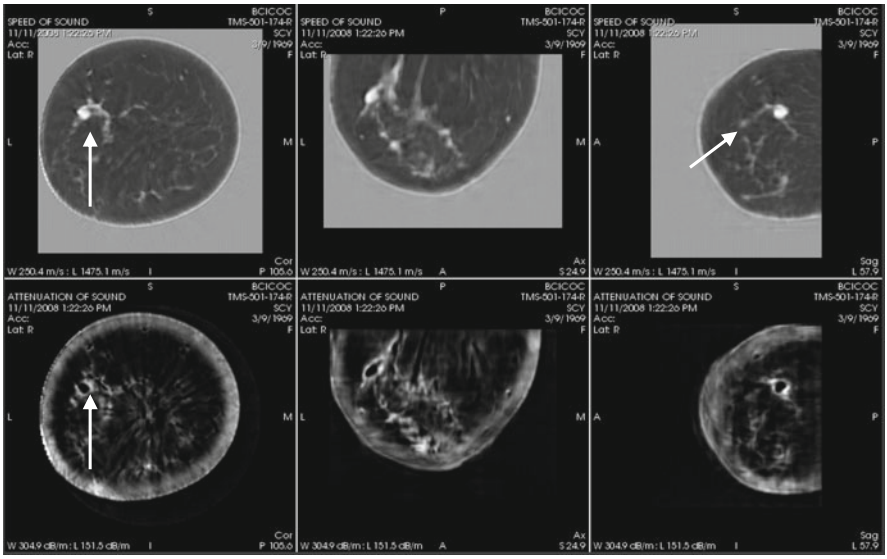

Fig. 10 501-174-R WBU Image: coronal, axial, and sagittal views (L to R). The mass appears as a region showing high speed (*top*), high attenuation border but low attenuation interior, surrounded by lower speed fatty tissue

to be considerably lobulated and biopsy was recommended (BI-RADS 4). WBU shows a distinct mass with very high sound speed at 9 o'clock (Fig. 10). Pathology determined the lesions to be fibro-adenomas/fibroses.

4 Conclusions

We have observed that objects of interest (complicated cysts, cancers, fibro-adenomas) appear in sound speed images as bright regions. They are especially well defined when they occur in fatty tissue, and less so when they occur in ductal tissue, or breast parenchymal tissue, which itself has higher speed of sound than water. However, the quantitative estimates of the speed of sound may allow a differentiation of the lesion even in this case. Further clinical studies are underway to test this claim.

In particular, we observed that lesions generally showed a high attenuation border, with a low attenuation interior. We are still investigating the ramifications of this, and if it is possible to distinguish between the benign and malignant lesions with the aid of quantitative attenuation values.

We noted that the object of interest in 501-169-L above was described as being at 3 o'clock, whereas in our image the absolute position of the complex cyst was closer to 6 o'clock in the coronal image. Interestingly, in retrospect the annotation of 3 o'clock turned out to be an error, thereby validating our image. One of the advantages of our device is the absolute and reproducible positioning of the breast in the water-bath, leading to more accurate reporting of the lesions' positions and

perhaps aiding the diagnostic follow up of multiple masses. Furthermore, if aspiration or surgery is required, knowledge of the absolute position of the lesion is beneficial. High Intensity Focused Ultrasound (HIFU) is another treatment that is potentially aided by our images. The speed of sound map can be used to accurately focus the acoustic energy onto the relevant lesion, thereby minimizing damage to surrounding healthy tissue.

References

1. Greenleaf, J.F., Bahn, R.C.: Clinical imaging with transmissive ultrasonic computerized tomography. IEEE Trans. Biomed. Eng. **BME-28**(2), 231 (1981)
2. André, M.P., Janée, H.S., Otto, G.P., et al.: High speed data acquisition in a diffraction tomography system with large-scale toroidal arrays. Int. J. Imaging Syst. Technol. **8**, 137 (1997)
3. Duric, N., Littrup, P., Poulo, L., Babkin, A., Pevzner, R., Holsapple, E., Rama, O., Glide, C.: Detection of breast cancer with ultrasound tomography: First results with the computed ultrasound risk evaluation prototype. Med. Phys. **34**(2), 773–785 (2007)
4. André, M.P., Barker, C.H., Sekhon, N., Wiskin, J., Borup, D., Callahan, K.: Pre-clinical experience with full-wave inverse-scattering for breast imaging. Acoustical Imaging **29** (2009)
5. Johnson, S.A., Abbott, T., Bell, R., Berggren, M., et al.: Non-invasive breast tissue characterization using ultrasound speed and attenuation. Acoustical Imaging **28**, 147 (2007)
6. Wiskin, J., Borup, D.T., Johnson, S.A., Berggren, M., et al.: Full-wave, non-linear, inverse scattering: High resolution quantitative breast tissue tomography. Acoustical Imaging **28**, 183 (2007)

Multiple Scattering Contribution to Trabecular Bone Backscatter

J. Wójcik, J. Litniewski, and A. Nowicki

Abstract Integral equations that describe scattering on the structure with stependly changing physical parameters, have been numerically solved on example of the trabecular bone model. The model consists of several hundred elements with randomly selected parameters. The spectral distribution of scatter coefficients in subsequent orders of scattering has been presented.

Keywords Multiple scattering · Absorbing medium · Complex random structure · Back scatter coefficients · Trabecular bone

1 Introduction

The evaluation of bone strength requires not only the knowledge of its mean density but also of its microscopic structure. The ultrasound signals that have been scattered in trabecular bone contain information of the properties of the bone structure, and hence the analysis of the backscatter could be useful in assessment of the microscopic architecture of the bone. It has been demonstrated that the use of the backscattering models of bone enabled an assessment of some micro-structural characteristics from the experimental data.

Starting from Wear's work [1], to the best of the authors' knowledge almost all of the reported bone scattering models assumed, not precisely speaking, the Born approximation and consequently the multiple scattering within the bone trabeculae was neglected. Trabecular bone consists of trabeculae whose mechanical properties differ significantly from the surrounding marrow and therefore the ultrasonic wave is strongly scattered. The work of Bossey, et al. [2], presents analytically advanced approach. The scattering structure corresponds to the real one. Unfortunately this approach does not enable determination of the influence of multiple scattering on the total field. Wear's work contains the review of methods and problems of bone sonometry [3].

The aim of the presented paper was the evaluation of the contribution of the first, second and higher order scattering (multiple scattering) into total scattering of the

J. Wójcik (✉)
Institute of Fundamental Technological Research, Polish Academy of Sciences, Warsaw 00-049, Poland

M.P. André et al. (eds.), *Acoustical Imaging*, Acoustical Imaging 30,
DOI 10.1007/978-90-481-3255-3_9,

ultrasounds in the trabecular bone. The scattering, due to interconnections between thick trabeculae, usually neglected in trabecular bone models, has been also studied. Our model is fully scaled.

The basic element in our model of trabecular bone was an elastic cylinder with varying finite-length and diameter as well as orientation. The density and speed of sound were similar to those of the bone tissue. The cylinder was applied in building of the multi-element structures, similar to the architecture of the trabecular bone, taking into account variation of elements size and spatial configuration. The field scattered on the bone model was evaluated by solving numerically the integral form of the Sturm-Liouville equation in the version that describes longitudinal wave in inhomogeneous media.

For the calculated scattered fields the effective cross-sections as well as the Broadband Ultrasonic Backscatter (BUB), directly related to the detected echo-signal level, were determined. Calculations were performed for the frequency ranging from 0.5 to 3 MHz.

2 Basic Equations

Lame's equation for longitudinal *disturbances* of stress in non-homogeneous and isotropic medium can be written as [4]

$$g\nabla\cdot\left(\frac{\nabla P}{g}\right)-\frac{1}{c^2}\partial_{tt}P-2\mathbf{A}\partial_t P=0, \tag{1}$$

where: $P=P(\mathbf{x},t)$ is normalized stress: $g=g(\mathbf{x})$, $c=c(\mathbf{x})$are respectively: normalized density and speed of sound of the longitudinal waves, $(\mathbf{x},t)$ are normalized coordinates in space and time, whereas ∇, $\nabla\cdot\ \partial_t$ are normalized operators of gradient, divergence and derivation in respect to time. The normalization was performed as follows: $P\equiv\overline{\mathrm{P}}/P_0$, $g\equiv\bar{g}/g_0$, $c\equiv\bar{c}/c_0$, $\mathbf{x}\equiv K_0\,\bar{\mathbf{x}}$, $t\equiv\omega_0\,\bar{t}$, $\nabla\equiv\overline{\nabla}/K_0$, $\partial_t\equiv\partial_{\bar{t}}/\omega_0$. P_0 is the reference pressure; g_0, $c_0$are density and speed of sound in reference medium respectively (in our case – volume dominant). It means that $c=1$ and $g=1$ for reference medium. The dimensional variables are accented. The characteristic wave number K_0 and pulsation ω_0 are restricted by the relation: $K_0c_0=\omega_0$, $\omega_0\equiv 2\pi/T_0$, where T_0 is reference time (e.g. Time window). A consequence of the applied normalization method is equality of non-dimensional pulsation and frequency n, and the wave number $n\equiv\omega/\omega_0$. Most often for solid body Equation (1) is written for displacement vector $\boldsymbol{\zeta}(\mathbf{x},t)$. The Equation (1) was derived on the basis of the relation $P=\lambda\,\nabla\cdot\boldsymbol{\zeta}$ and $c^2=\lambda/g$. $\mathbf{A}$ is the convolution type operator describing the absorption [5]. We assume that for solid state $\mathbf{A}\equiv 0$. So called absorption coefficient $a(n)=\mathrm{F}[A(t)]$. $\mathrm{F}[\bullet]$ is the Fourier transform of time, while $A(t)$ is the kernel of $\mathbf{A}$. In dimensional units $\bar{a}=K_0a$. After Fourier transform respect time, the Equation (1) can be written as follows:

$$\Delta C+k^2C=VC+\mathbf{Q}\cdot\nabla C,\quad C=C(\mathbf{x},n)=\mathrm{F}[P(x,t)]\,, \tag{2}$$

$$\mathrm{V}(\mathbf{x}) \equiv n^2\left(1-\frac{1}{c(\mathbf{x})^2}\right) \quad \mathbf{Q}(\mathbf{x}) \equiv \frac{\nabla g}{g} \tag{3}$$

Complex wave number k is given by $k(n) \equiv n\sqrt{1+i2a(n)/n} \cong n + ia(n)$. Equation (2) was written when Helmholtz operator $\Delta + k^2$was distinguished for dominant reference medium surrounding regions of material parameter disturbances. Equation (3) is based only on the assumption that in the reference medium $a(n) \neq 0$.

3 Medium Construction and Potentials

We assume that reference medium surrounds L regions υ_l of space. The regions are bounded by surfaces $s_l, l = 1, \ldots, L$. Each region υ_l is filled with homogeneous medium and its density $g_l = const \neq 1$, as well as sound speed $c_l = const \neq 1$. The multiple-theory sum of the υ_l *sets* describes the structure being submerged in reference medium. We assume that elements of structure do not cross in a sense of 3D measure of volume $d^3(\cdot)$.

$$\upsilon = \bigcup_l \upsilon_l, \quad s = \bigcup_l s_l, \quad d^3\left(\upsilon_l \bigcap \upsilon_m\right) = 0 \tag{4}$$

Thus spatial distributions of sound speed and density have a form:

$$c(\mathbf{x})^2 = 1 + \sum_l \mathrm{d}c_l(\mathbf{x})^2 = 1 + \sum_l \chi_l({c_l}^2 - 1) \tag{5}$$

$$g(\mathbf{x}) = 1 + \sum_l \mathrm{d}g_l(\mathbf{x}) = 1 + \sum_l \chi_l(g_l - 1) \tag{6}$$

Where $\chi_l \equiv \chi(\upsilon_l)$ characteristic function of υ_l, $\chi = 1$ for $\mathbf{x} \in \upsilon_l$, $\chi = 0$ for $\mathbf{x} \notin \upsilon_l$. $\chi(s) = \sum_l \chi(\upsilon_l)$ is the characteristic function of the structure.

Neglect detailed discussion, we have

$$\mathbf{Q} \equiv \mathrm{Q}(\mathbf{x})\mathbf{u}(\mathbf{x})\delta(\mathrm{s}) = \left(\sum_l \sigma_l\left(\frac{1}{g_l} - 1\right)\right)\mathbf{u}(\mathbf{x})\delta(s) = \left(\sum_l \mathrm{Q}_l\right)\mathbf{u}(\mathbf{x})\delta(s) \tag{7}$$

$$\mathrm{V} \equiv \sum_l \chi_l \mathrm{V}_l = \sum_l \chi_l n^2\left(1-\frac{1}{{c_l}^2}\right), \quad \mathrm{V} = \chi(\upsilon)\mathrm{V} \tag{8}$$

Where: $\delta(s) \equiv \sum_l \delta(s_l)$ Dirac distribution, $\sigma_l(\mathbf{x}) \equiv \chi(\upsilon_l(\mathbf{x} \in s_l))$, $\mathbf{u}(\mathbf{x})$ the field of the unit externally normal vectors to the surface s.

4 Scattering Equations

For the assumed model of structure of medium the Equation (2) takes the form

$$\Delta C + k^2 C = VC + QB\delta(s), B(\mathbf{x}, n) \equiv \mathbf{u}(\mathbf{x}) \cdot \nabla C(\mathbf{x}, n) \tag{9}$$

The field B is determined only on surface s of the structure υ. Further, if it will not make misunderstanding the non-dimensional pulsation will be neglected in the argument list. When transforming Equation (9) into integral equation and using features of distributions $\delta(s)$ and $\chi(\upsilon)$ we obtain

$$\begin{aligned} C(\mathbf{x}) = C^0(\mathbf{x}) &- \int_{\upsilon} G(r(\mathbf{x}, \mathbf{x}'))\mathrm{V}(\mathbf{x}')C(\mathbf{x}')d\upsilon \\ &- \int_{s} G(r(\mathbf{x}, \mathbf{x}'))\mathrm{Q}(\mathbf{x}')B(\mathbf{x}')ds \end{aligned} \tag{10}$$

Where: $G(r, n) \equiv \exp(ik(n)r/4\pi r)$, $r = r(\mathbf{x}, \mathbf{x}') = |\mathbf{r}|$, $\mathbf{r} = \mathbf{x} - \mathbf{x}'$, and $d\upsilon$ is a elementary volume in υ, ds is a elementary surface on s. $C^0(\mathbf{x}) \equiv C^0(\mathbf{x}, n)$ is a solution of Helmholtz equation in reference medium (incident field), $G(r(\mathbf{x}, \mathbf{x}')) = G(r(\mathbf{x}, \mathbf{x}'), n)$ is the Green's function of the Helmholtz equation. The integrals in Equation (10) describe the scattering of incident field on potentials V and Q of the structure. It is sufficient to determine the equation for $\mathbf{x} \in \upsilon$ in order to solve it. When the solution is substituted to the integrals in Equation (10) it gives solution in whole medium. Applying $\mathbf{u}(\mathbf{x}) \cdot \nabla$ to the both sides of Equation (10) we get equation for the field B.

$$\begin{aligned} B(\mathbf{x}) = B^0(\mathbf{x}) &- \int_{\upsilon} \partial G(r(\mathbf{x}, \mathbf{x}'))\mathrm{V}(\mathbf{x}')C(\mathbf{x}')d\upsilon \\ &- \int_{s} \partial G(r(\mathbf{x}, \mathbf{x}'))\mathrm{Q}(\mathbf{x}')B(\mathbf{x}')ds \end{aligned} \quad , \mathbf{x} \in \upsilon, s \subset \upsilon \tag{11}$$

$$B^0 = \mathbf{u} \cdot \nabla C^0, \partial G(r) = \mathbf{u}(\mathbf{x}) \cdot \mathbf{e}(\mathbf{r})\partial_r G, \mathbf{e}(\mathbf{r}) = \nabla r = \mathbf{r}/r \tag{12}$$

By grouping the functions and their normal derivatives in vector function

$$\overline{\mathrm{C}} \equiv \begin{pmatrix} C \\ B \end{pmatrix}, \overline{\mathrm{C}}^0 \equiv \begin{pmatrix} C^0 \\ B^0 \end{pmatrix}, \overline{\mathrm{G}} \equiv \begin{pmatrix} G \\ \partial G \end{pmatrix}, \mathrm{W} \equiv \begin{pmatrix} \mathrm{V}d\upsilon \\ \mathrm{Q}ds \end{pmatrix} \tag{13}$$

and introducing the scattering field $\mathrm{E} \equiv \overline{\mathrm{C}} - \overline{\mathrm{C}}^0$, we may rewrite Equations (10–11) in the compact form

$$(\mathbf{I} + \mathbf{GW})\,\mathrm{E} = -\mathrm{E}^0 \quad \mathbf{GW}\overline{\mathrm{C}} \equiv \int \left(\overline{\mathrm{G}} \circ \mathrm{W}\right)\overline{\mathrm{C}} \tag{14}$$

where, the kernel of operator $\mathbf{GW}$ is 2×2 matrices determined by dyadic vectors product signs by $\circ$, $\mathrm{E}^0 = \mathbf{GW}\overline{\mathrm{C}}^0$. $\mathbf{I}$ is the identity operation $\mathbf{I}\mathrm{E}(\mathbf{x}') = \mathrm{E}(\mathbf{x})$. Equivalent form of the operator $\mathbf{GW}$ is

$$\mathbf{GW} \equiv \begin{pmatrix} \int d\upsilon \mathrm{V} G & \int ds \mathrm{Q} G \\ \int d\upsilon \mathrm{V} \partial G & \int ds \mathrm{Q} \partial G \end{pmatrix} \tag{15}$$

Integration domains are clearly determined by $d\upsilon$ and ds. Because $\mathrm{E} = \sum_l \chi_l \mathrm{E} = \sum_1 \mathrm{E}_l$ then the operator $\mathbf{GW}$ can be presented as the sum of the cells $\mathbf{GW} = \bigcup_{l,m} \mathbf{GW}_{lm}$, where $\mathbf{GW}_{lm}$ is given by Equation (14) or (15) for $\mathrm{W}_m = \chi_m \mathrm{W}$ and $\mathbf{x} \in \upsilon_l$. For $\mathbf{x}, \mathbf{x}' \in \upsilon_l$ and $\mathbf{x} = \mathbf{x}'$, $\mathbf{GW}_{lm} = \mathbf{0}$ (no self interaction). We set $\mathbf{GW}_l \equiv \mathbf{GW}_{ll}$ for diagonal cells $l = m$.

5 Solution Method

We seek the solution of Equation (14) for $\mathbf{x} \in \upsilon$ in the form

$$\mathrm{E} = \sum_l \mathrm{E}_l^1 + \mathrm{R}^2 \tag{16}$$

where E_l^1 is the solution of Equation (14) in *l- th* element of the structure under the assumption that the only scattering field in υ_l is $\mathrm{E}_l^0 = \chi_l \mathrm{E}^0$ produced by incident field $\overline{\mathrm{C}}_l^0 = \chi_l \overline{\mathrm{C}}^0 \quad \mathrm{E}_l^0 = \mathbf{GW}_l \overline{\mathrm{C}}_1^0$.

$$(\mathbf{I} + \mathbf{GW}_l)\, \mathrm{E}_l^1 = -\mathrm{E}_l^0 \tag{17}$$

$$\mathrm{E}_l^1 = -\mathbf{H}_l \mathrm{E}_l^0 = -\mathbf{H}_l \mathbf{GW}_l \bar{C}_l^0 \quad l = 1, \ldots, L$$

where $\mathbf{H}_l \equiv (\mathbf{I} + \mathbf{GW}_l)^{-1}$ denotes inverse operator. The fields E_l^1 determine a field in medium in the first order of scattering (single scattering). The reminder R^2 denotes a field in structure created due to interaction between structure elements in the second and higher orders of the scattering (multi-scattering). The R^2 satisfies equation

$$(\mathbf{I} + \mathbf{GW})\, \mathrm{R}^2 = -\sum_l \mathbf{GW}_l \left(\sum_{m,\, m \neq l} E_m^1 \right) \quad E_m^1 = \mathbf{GW}_{lm} \mathrm{E}_m^1 \tag{18}$$

The field E_m^1 is calculated as the field from the *m*- th element failing on *l*-th element. Then we repeat the described above procedure. We suppose that $\mathrm{R}^2 = \sum_l \mathrm{E}_l^2 + \mathrm{R}^3$ and E_l^2 satisfy Equation (19) with source in the form of l^{th} component on right side in Equation (24). Then we have

$$\mathrm{E}_l^2 = -\mathbf{H}_l \mathbf{GW}_l \sum_{m \neq l} E_m^1, \tag{19}$$

and after substitution $E_m^2 \rightarrow E_m^1 \mathrm{R}^3$ satisfies Equation (18). Generally, in j^{th} order of the scattering $\mathrm{R}^j = \sum_l \mathrm{E}_l^j + \mathrm{R}^{j+1}$

$$\mathrm{E}_l^j = -\mathbf{H}_l \mathbf{G} \mathbf{W}_l \sum_{m \neq l} E_m^{j-1} \tag{20}$$

Then in point $\mathbf{x}$ of the medium the total j^{th} order component of the scattered field takes the form

$$E^j(\mathbf{x}) = -\sum_l \mathbf{G} \mathbf{W}_l \mathrm{E}_l^j(\mathbf{x}') \quad \mathbf{x}' \in \upsilon_l \tag{21}$$

The total scattered field is given by sum of the $E^j(\mathbf{x})$. We obtain the discrete (numerical) representation of the above procedure when W is replaced by the weight system $W(j_l)$ for numerical integration's respect sampling structure vector $\mathbf{x} \rightarrow \mathbf{x}(j_l)$. Where j_l is the sample index in l^{th} element of the scattered structure.

6 Results

The skeletal of the model of trabecular bone structure, applied in scattering field calculations, is presented in Fig. 1a. One of skeletal structures parallel to the x-z plane (*horizontal respect incident field*) is shown in Fig. 1b. The cylinder with Φ and length d was adopted as the model of trabecular. Each segment of the skeleton is the axis of cylinder.

The skeleton was obtained randomly by displacement of nodes in each layers of regular structure built of cuboids. Their dimensions are 2 mm in the **y** direction and 1×1 mm in the **x** and **z** directions. The uniform probability was assumed for displacements in range (−0.15; 0.15) mm. The horizontal structures were adjusted to new *node* positions. Then some elements were randomly (uniform probability) eliminated from the structure. The results are similar to those which were presented in Reference 6.

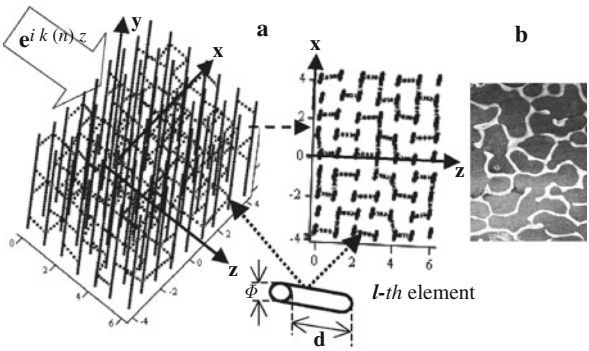

Fig. 1 (**a**) Left: full skeleton of the trabecular bone model; right: one of horizontal substructures in the skeleton. (**b**) The cross-section of the real trabecular bone structure

Values of sound speed and densities of each trabecular were selected based on Gamma distribution. Maximum deviation from mean values 4,000 m/s and 2,000 kg/m^3 was assumed as $\pm 5\%$. For trabecular, in $\boldsymbol{y}$ direction and in horizontal planes, mean values $\Phi = 0.05$ and 0.04 mm with deviations $\pm 20\%$ and $\pm 25\%$ respectively, were assumed.

For surrounding medium (*marrow,* fluid filler) as well as surrounding space $g_0 = 1,000$ kg/m^3, $c_0 = 1,500$ m/s. The absorption parameter for fluid filler was $2.3 \cdot 10^{-4}$ Np/MHz Total number of elements (trabecular) was 409. The unit plane wave was assumed as incident field $C^0 = \exp(ik(\nu)z)z \geq 0$, $\nu \in [0.5,\ 3]$ MHz with step 0.333 MHz. Dimensionless frequency is $n = 15, 16, \ldots, 90$.

6.1 Scattering Field Distribution

Exemplary distributions of scattering fields in subsequent orders and for selected frequencies were shown in Fig. 2. Brightness refers logarithmic scale of values. Contour of the scattering structure and its location is shown by white rectangle whereas white narrow indicates direction of incident wave. The represented area is the rectangle with location $[-30,\ 20]$ mm in $\boldsymbol{z}$ direction and $[-15,\ 15]$ mm in $\boldsymbol{x}$ direction.

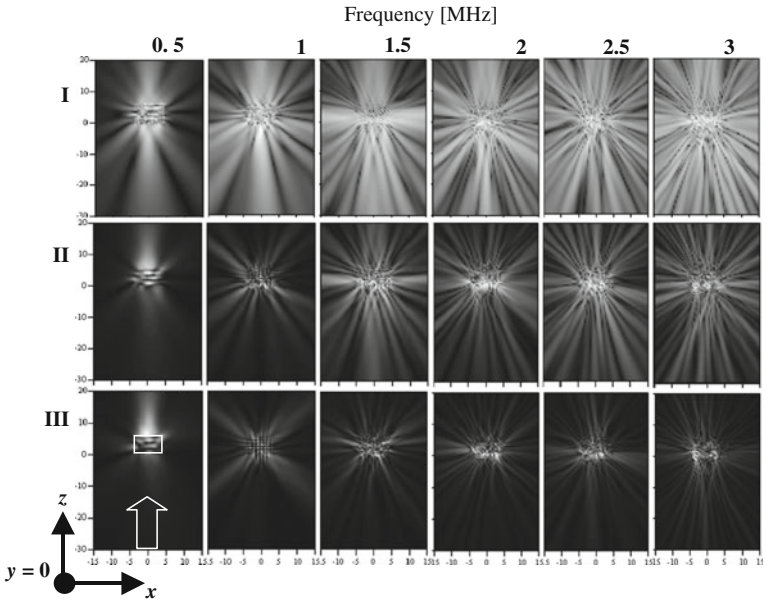

Fig. 2 Distributions of fields in subsequent orders of scattering in rows: I, II, III, while in function of frequency from 0.5 to 3 MHz they are shown in columns

6.2 Backscatter Coefficients

We define substructures: horizontal (denoted by "h") as a set of all trabecular that are situated in planes being parallel to the ***x*-*z*** plane, and vertical (denoted by "y") as a set of all trabecular which are parallel to the ***y*** axis.

In Fig. 3, S is a sum of S1, S2 and S3, the effective backscatter cross-section coefficients that were obtained in subsequent orders of scattering and in function of frequency ν. Multiplication factors, 50 and 5,000, were applied for better representation. In the nearness of frequency $\nu = 1.5$ MHz, the estimated relations between values S1:S2:S3 from Fig. 3 are as 1:(0.01):(0.0001). The S1, 2, 3 are characteristics of the second order in respect to field. In case of characteristics linear in respect to field the proportions will be as 1:(0.1): (0.01) or even higher.

In Fig. 4a–c the contribution of substructures **h** and **y** to effective backscatter cross-sections in subsequent orders of scattering is presented. Let us notice the validity change of substructures in transition from the first order to higher orders of scattering. It is visible in Fig. 4a, b (the transition occurs for $\nu > 1.3$ MHz).

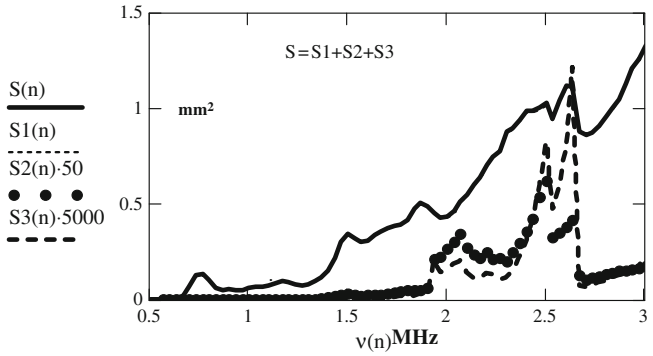

Fig. 3 Effective backscatter cross-section decomposition in respect to scattering order

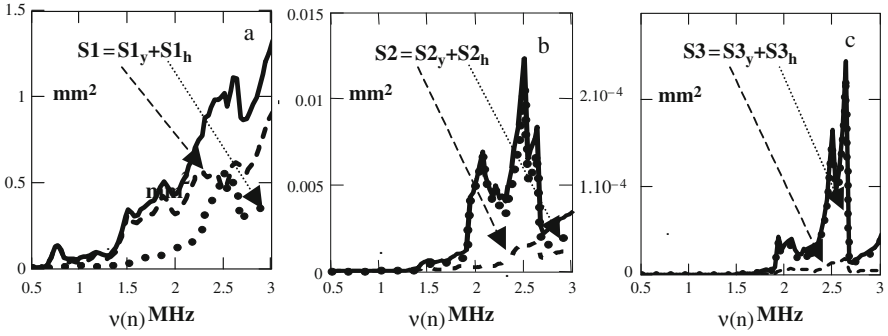

Fig. 4 Contribution of substructures **h** and **y** in subsequent orders of scattering as well as in respect to frequency

In Fig. 4a the resonance for $\nu = 0.75$ MHz is observed, it is fully created by y substructure in which the trabecular length is 2 mm. It corresponds to the resonance frequency. Similar analysis can be performed for other resonances using higher scattering orders.

7 Conclusions

In space-frequency range the method of solving of longitudinal wave scattering equations has been developed. It is convergent for high potentials and multi-element structures in numerical applications. The method is *accurate* in each order of scattering that means the calculated fields in subsequent order do not make *corrections* in scattering fields of former order. The Neumann's iteration of integral equations of scattering produces the asymptotically converged series (if it is converging). This means that each subsequent element of series *includes* improving accuracy corrections to former field elements for the selected structure element. The developed algorithm enables the analysis of the scattering field characteristics taking into account not only the scattering order but also the influence of selected substructures. The examples of this effect have been presented.

In the range up to 1.5 MHz the influence of higher scattering orders on characteristics of the first order in respect to the field is less than few percent. In the range above 1.5 MHz one can observe in higher orders even several percent resonance effect of scattering.

Acknowledgements This work is supported by Ministry of Science and Higher Education (grant No. 0219/T02/2007/32)

References

1. Wear, K.: Frequency dependence of ultrasonic backscatter from human trabecular bone: theory and experiments. J. Acoust. Soc. Am. **106**(6), 3659–3664 (1999)
2. Bossy, E., Padilla, F., Peyrin, F., Laugier, P.: Three-dimensional simulation of ultrasound propagation through trabecular bone structures measured by synchrotron micro-tomography. Phys. Med. Biol. **50**, 5545–5556 (2005)
3. Wear, K.: Ultrasonic scattering from cancellous bone: A review. IEEE Trans. Ultrason. Freq. Contr. **55**(7), 1432–1441 (2008)
4. Brekhovskikh, L.M., Godin, O.A.: Acoustics of layered media I, ISBN 3-540-51038-9, pp. 1–14. Springer-Verlag Berlin Haidelberg, New York (1990)
5. Wójcik, J.: Conservation of energy and absorption in acoustic fields for linear and nonlinear propagation. J. Acoust. Soc. Am. **104**(5), 2654–2663 (1998)
6. Hosokawa, A.: Development of numerical cancellous bone model for finite-difference time-domain simulations of ultrasound propagation. IEEE Trans. Ultrason. Ferro. Freq. Contr. **55**(6), 1219–1233 (2008)

ULA-OP: A Fully Open Ultrasound Imaging/Doppler System

S. Ricci, L. Bassi, A. Cellai, A. Ramalli, F. Guidi, and P. Tortoli

Abstract Experimental research in Imaging/Doppler ultrasound frequently involves new transmission strategies, non-conventional beamforming techniques, custom data processing. This flexibility is not available on commercial equipment designed for clinical use but only on few existing research platforms which, on the other hand, are typically characterized by cumbersome and expensive electronics. In this paper, we present a novel ULtrasound Advanced Open Platform (ULA-OP), designed in the effort to overcome the aforementioned drawbacks. ULA-OP hardware and software are described in detail and the system capabilities are shown with two preliminary, non-conventional applications.

Keywords Open ultrasound system · Research platform · Ultrasound imaging · Arbitrary waveform generation · Digital beamforming

1 Introduction

There is an increasing need for fully "open" Imaging/Doppler systems in ultrasound (US) research [1]. High flexibility is requested to test arbitrary transmission (TX) strategies, collect the corresponding echo data at different points along the receiver (RX) chain, and/or applying original real-time processing methods.

Special research kits or software interfaces that partially compensate this problem can be added to some commercial echographs. For example, the Axius Ultrasound Research Interface (URI) adds to Sonoline Antares™ (Siemens Medical Solutions, Inc., Mountain View, California, USA) the possibility of accessing beamformed radio-frequency (RF) data and other control parameters [2]. However, full control of the TX/RX process and full access to pre-beamformed data are possible only in few existing dedicated research platforms. One of these is the RASMUS system [3] that is characterized by cumbersome and expensive electronics that hampers the duplication and prevents use out of the lab where it is installed.

In this paper, we present a novel ULtrasound Advanced Open Platform (ULA-OP), which has been entirely developed in our laboratory. The system was designed

S. Ricci (✉)
Microelectronic Systems Design Laboratory, Electronics & Telecommunications Department, University of Florence, Firenze, Italy

M.P. André et al. (eds.), *Acoustical Imaging*, Acoustical Imaging 30,
DOI 10.1007/978-90-481-3255-3_10,

by taking into account the need of balancing between computational power and cost/dimensions, programmability and friendly use. By using last generation Field Programmable Gate Arrays (FPGAs) and Digital Signal Processor (DSP), all electronics was integrated in two fully programmable boards, coupled to a host PC through standard USB 2.0. A powerful, compact, portable and relatively cheap architecture was thus obtained. ULA-OP features include the possibility of transmitting arbitrary waveforms to 64 elements sorted out of a 192-element array probe, access to pre-beamforming and beamformed data, programmable beamformer, the possibility to add custom data processing on DSP and real-time result visualization.

ULA-OP has been designed to be employed not only by advanced technical users, e.g., US researchers, but also by non-specifically trained staff working, for example, in a clinical environment. This goal was pursued by developing suitable software tools.

The flexibility of ULA-OP is here shown with some example. The capability of the TX section of producing a self-designed acoustic field is shown together with the match between the measured and simulated field. A non-conventional Doppler application of the new system is also presented.

2 ULA-OP Description

ULA-OP is integrated in a "box" where the specialized hardware is assembled and connected to a PC, either laptop or desktop (see Fig. 1). This choice allows not only to limit the rack dimensions to only $34 \times 23 \times 14$ cm and the weight to 5 kg but also to take advantage of the friendly and well-established Windows® interface.

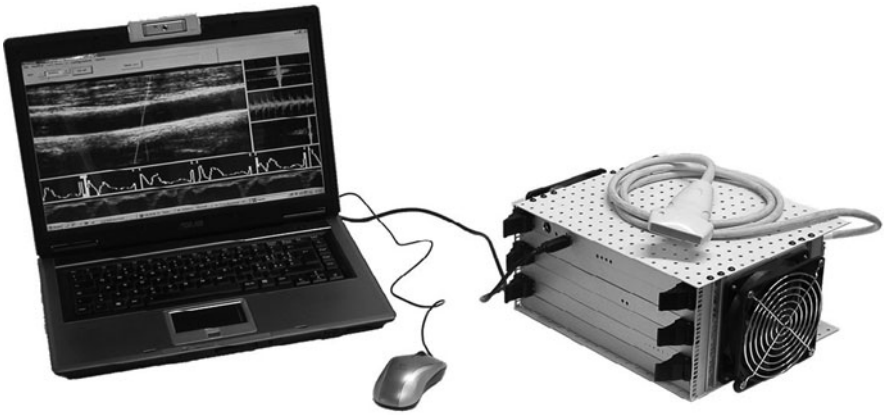

Fig. 1 ULA-OP consists of an easy-to-handle rack connected through a USB 2.0 link to a PC where a set of tools allows advanced and quick use

2.1 The Hardware

The hardware of ULA-OP is composed by two specialized boards (an analog board and a digital board) connected by a backplane. A third board provides the needed power. All hardware is collected in a compact rack refreshed by two lateral fans. External connections are limited to a connector for a 192-element array probe, the 12 V unstabilized power input and a USB 2.0 channel toward the host PC. The rack is designed for holding other boards for future expansion.

The analog board includes the RF front-end while the digital board carries out the requested numeric signal processing. In particular, the latter is based on 5 state-of-the-art FPGAs from Stratix family (Altera, San Jose, CA, USA) and a hi-end DSP from 320C6455 family (Texas Instruments, Austin, TX, USA).

The TX section integrates a bank of arbitrary waveform generators (AWGs) that synthesize 64 independent excitation signals through the sigma-delta technique [4]. The signals, ranging between 1 and 16 MHz, are passed through 64 linear amplifiers. A programmable switch-matrix maps the excitation signals to a part of the 192 array elements. During the TX and RX phases the switch-matrix can select either the same or a different group of array elements. The received signals are processed through Low Noise Amplifiers (LNA) and Programmable Gain Amplifiers (PGA) with Time-Gain Compensation (TGC) control. The gain of each channel is programmable in the range 6-46 dB. The 64 channels feed the digital board where a bank of Analog-to-Digital (AD) converters work at 50 Msps. Four FPGAs are devoted to programmable beamforming, with possible apodization and dynamic focusing. The 5th FPGA, together with the DSP elaborates the beamformed signal. In particular, this FPGA contains 4 coherent demodulators, filters, decimators and other calculation-intensive modules which can be optionally inserted in the signal processing chain. The firmware architecture running on the DSP supports several concurrent processing modules each devoted to a standard elaboration, like B-mode or spectral Doppler processing, or to a novel experimental method. Each module formats the results in a frame that is transferred to the host PC through the USB channel.

During system operation, at each Pulse Repetition Interval (PRI), the DSP programs all the ULA-OP aforementioned functions to obtain the TX/RX desired behaviour. For example, for each PRI, the TX waveforms and relative delays, the TX probe aperture, the RX aperture, the channel gains, the beamformer dynamic apodization and focus, the digital processing chain, etc can be changed under software control.

One of the most requested features in a research platform is the capability of accessing data in multiple points of the RX chain. Figure 2 reports the ULA-OP resources for data extracting and storing. The digital board reserves up to 1 GB of SDRAM memory for saving the raw data acquired from the 64 input channels. Here, the data flow rate is near 40 Gb/s. Hence, depending on the PRI and ROI extension, up to 1 s of raw data can be saved. The DSP can access a 256 MB memory, where

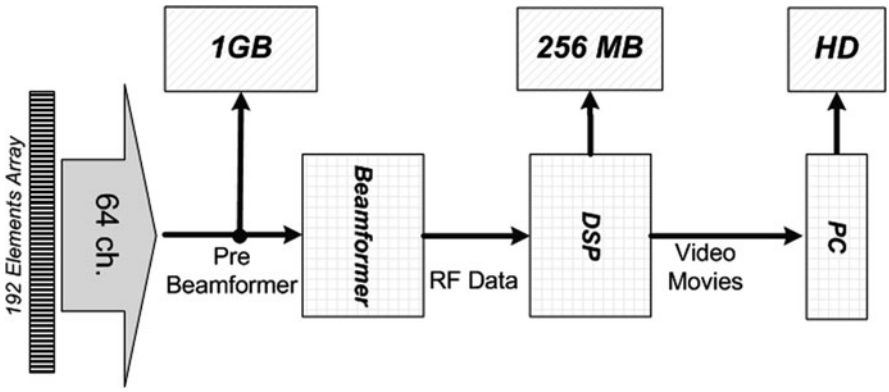

Fig. 2 OLA-OP memory capability for data saving

beamformed and/or DSP-processed data can be saved. Since the throughput rate is here much lower, several seconds of data can be saved. Finally, the video data moved to the PC can be continuously saved, with the only limit of hard-disk capacity. At any moment the on-board memories can be downloaded to the PC into an open-format file, provided the real-time acquisition is temporarily halted.

2.2 Software Tools

The ULA-OP is supported by suitable software tools (see Fig. 3). A Matlab®-based toolbox for predicting the US field associated with the ULA-OP system

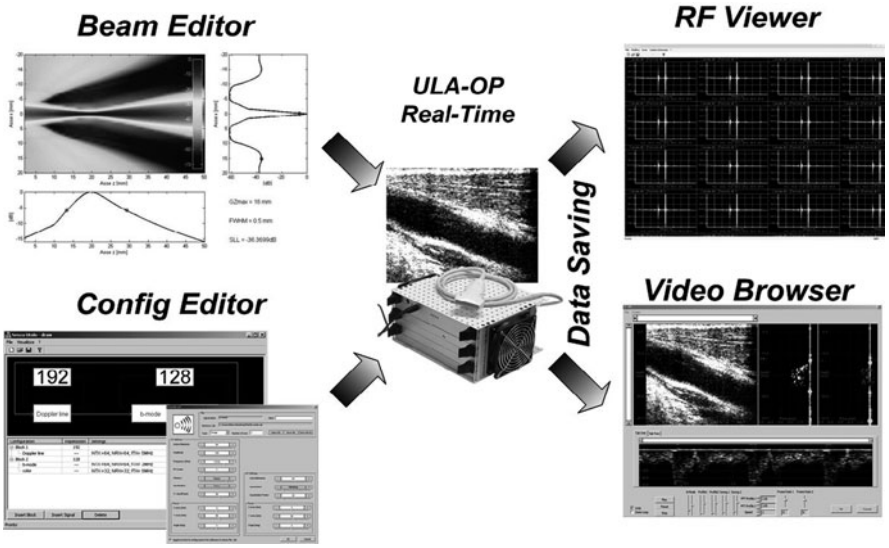

Fig. 3 ULA-OP software environment

was developed (*Beam Editor*). The program allows setting all significant physical and electrical parameters of the linear array probe, as well as the system settings which influence the TX. The *Config Editor* can be used to build particular, non standard system configurations. For example it is possible to customize several TX/RX parameters (e.g. TX waveforms, probe aperture, beamforming apodization and focalization curves, TGC, etc), set the PRIs sequence with different customizations, and associate each PRI with the desired data processing (e.g. B-mode, Color, or custom). The tool saves the configuration in a file that can be loaded in the real-time scanning session. The real-time software starts the ULA-OP scanning session with a standard, pre-defined configuration or by loading a custom file arranged with the aforementioned tools.

The real-time software allows the user to manage the current scanning session, and allows halting the session to save the acquired raw data. This data is saved with a documented open format, so that the user can develop their own software, for example in Matlab, for reading and processing them. An *RF Viewer* that quickly displays the pre-beamforming data, and a *Video Browser* that reconstructs the B-mode and up to two M-line displays starting from demodulated data, are also available.

3 Examples of Applications

The first example of ULA-OP application illustrates a steered beam which was first designed and simulated using the *Beam Editor* and then compared with the acoustic field measured by a hydrophone (see Fig. 4).

The beam was produced by exciting the 64 central elements of a 192-element (LA523) linear array probe with 6.5 MHz, 5 cycles Hanning windowed bursts. The relative delays were calculated for a 9° steering and 20 mm focal depth. Hanning

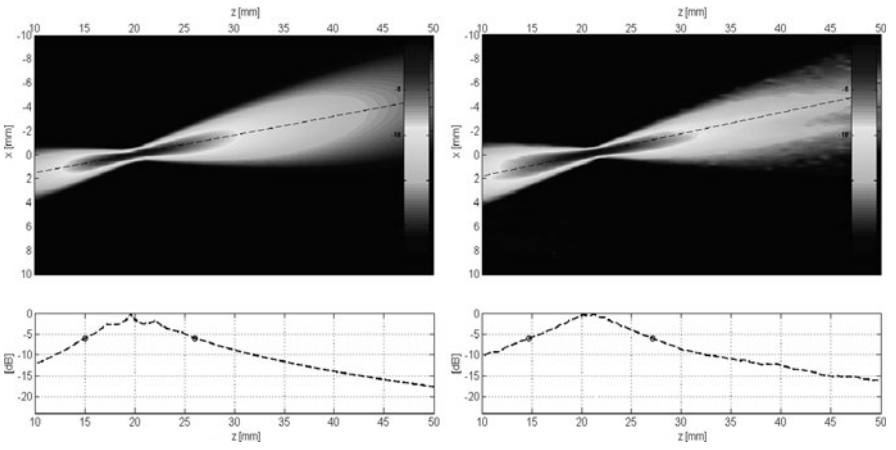

Fig. 4 One-way simulated (*left*) and measured (*right*) beam plots obtained for a 9° steering angle. Bottom graphs show the beam profiles along the propagation direction

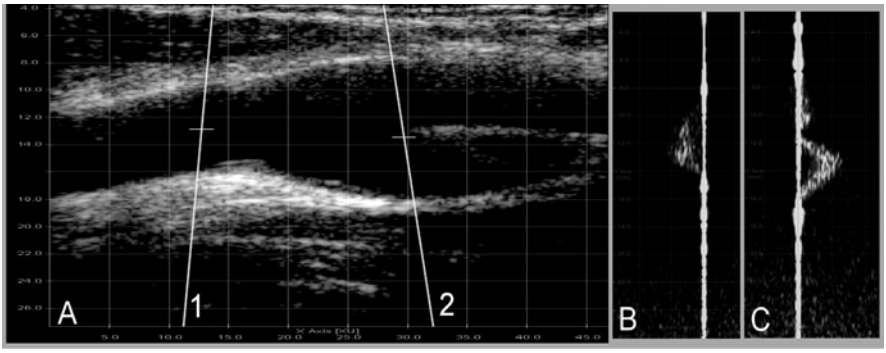

Fig. 5 ULA-OP simultaneously provides standard B-mode images (**a**) and two spectral profiles (**b**, **c**). The spectral profiles, here obtained from the scan lines 1 and 2, respectively, report the distribution of Doppler spectral components along the investigated depth (original in color)

apodization was also applied on the active elements to reduce the sidelobes. The acoustic field measured over the probe plane shows good agreement with simulation, although some low-level noise on the right side is present, probably because of some residual mismatch between receiver channels.

In the second example of application, ULA-OP was used to investigate the blood flow in a carotid artery bifurcation through the so-called Multigate Spectral Doppler (MSD) method [5], which allows detecting the blood velocity profiles within the intercepted vessels. Figure 5a shows the B-mode image with two highlighted scan lines (1, 2) which intercept the vessel in different bifurcation regions. The signals backscattered along the scan lines were processed through 128-point FFTs, color-coded and presented on the display together with the B-mode (a screenshot is visible in Fig. 5a–c). In this example, a total of 512 FFTs were calculated in real-time for each frame and each scan line. In particular the profile visible in Fig. 5b shows the typical parabolic flow in the common carotid artery investigated by the scan line 1, while in Fig. 5c the two profiles originated by the two branches of the bifurcation are visible.

For each display the frame rate was maintained at about 40 fps. The computational load associated to MSD- and B-mode has been estimated below 3% and 1%, respectively, of the overall DSP-FPGA computational power. This confirms that a considerable amount of unused computational resources can be partitioned for new processing modules.

4 Conclusion

This paper has presented a novel US system characterized by high programmability and wide access to raw data, made compatible with compact size and reasonable cost. ULA-OP was completely implemented in our lab through the development of two dedicated boards exploiting the latest digital electronic technology. This

choice allowed us to avoid undesired performance or functionality limitations, while making the system available to researchers of other laboratories.

In principle, any TX-RX strategy to simultaneously control a maximum number of 64 elements could be implemented in the ULA-OP system. The DSP-FPGA computational power is high enough to guarantee that a large class of processing methods can be implemented in real-time. Saving data with an open and documented format from three levels of the RX chain (i.e. pre-beamforming, post-beamforming, frame-level) is feasible. A complete set of software tools are designed not only for accessing the advanced ULA-OP features but also for facilitating a quick and friendly use.

Applications of ULA-Op system such as the test of novel coded transmission methods [6], focussing/beamforming [7] and apodization techniques [8], contrast agents investigations [9] have already been scheduled in our laboratory. The system portability also promotes its use in any other laboratory interested to make the experimental test of novel ideas or methods.

Acknowledgments The authors wish to acknowledge valuable technical support by Enrico Boni, Paolo Palchetti and Fabio Andreuccetti, Firenze, Italy.

References

1. Tortoli, P., Jensen, J.A.: Introduction to the special issue on novel equipment for ultrasound research. IEEE Trans. Ultrason. Ferroelect. Freq. Contr. **53**, 1705–1706 (2006)
2. Brunke, S.S., Insana, M.F., Dahl, J.J., Hansen, C., Ashfaq, M., Ermert, H.: An ultrasound research interface for a clinical system. IEEE Trans. Ultrason. Ferroelect. Freq. Contr. **54**, 198–210 (2007)
3. Jensen, J.A., Holm, O., Jensen, L.J., Bendsen, H., Nikolov, S., Tomov, B.G., Munk, P., Hansen, M., Salomonsen, K., Hansen, J., Gormsen, K., Pedersen, H.M., Ammelmark, G.K.: Ultrasound research scanner for real-time synthetic aperture data acquisition. IEEE Trans. Ultrason. Ferroelect. Freq. Contr. **52**, 881–891 (2005)
4. Ricci, S., Bassi, L., Boni, E., Dallai, A., Tortoli, P.: Multichannel FPGA-based arbitrary waveform generator for medical ultrasound. Electron. Lett. **43**(24), 1335–1336 (2007), ISSN: 0013-5194. doi:10.1049/el:20072859
5. Tortoli, P., Guidi, F., Guidi, G., Atzeni, C.: Spectral velocity profiles for detailed ultrasound flow analysis. IEEE Trans. Ultrason. Ferroelect. Freq. Contr. **43**, 654–659 (1996)
6. Misaridis, T., Jensen, J.A.: Use of modulated excitation signals in ultrasound. Part I: Basic concepts and expected benefits. IEEE Trans. Ultrason. Ferroelect. Freq. Contr. **52**(2), 192–207 (2005)
7. Zhou, S., Hossack, J.A.: Dynamic-transmit focusing using time-dependent focal zone and center frequency. IEEE Trans. Ultrason. Ferroelect. Freq. Contr. **50**(2), 142–152 (2003)
8. Tomov, B.G., Jensen, J.A.: Compact implementation of dynamic receive apodization in ultrasound scanners. In Proceedings of SPIE-Medical Imaging, pp. 260–271 (2004)
9. Miller, A.P., Nanda, N.C.: Contrast Echocardiography. Ultra. Med. Biol. **30**(4), 425–434 (2004)

The Use of Quality Metrics in Ultrasonic Strain Imaging

A.H. Gee, G.M. Treece, L. Chen, and R.W. Prager

Abstract Deformation estimation by block matching plays a central role in most ultrasonic elastography systems. However, not all matches are equally reliable, since the data in many blocks may be severely decorrelated for a number of reasons, including electrical noise, intra-window strain and out-of-plane motion. Conventionally, an estimate of the match quality is derived from the post-alignment similarity metric and used to reject poor matches. This paper moves beyond such rejection thresholds in two ways. First, a displacement tracking strategy is described, in which the tracking direction is not fixed in advance but is generated dynamically according to the quality metric. Second, a nonparametric regression technique is used to smooth the resulting strain images, with more smoothing in low quality regions and less in high quality regions. Simulation and *in vivo* results show how these two innovations help to improve the accuracy and intelligibility of the strain images.

Keywords Strain imaging · Elastography · Displacement · Deformation

1 Introduction

At the heart of most ultrasonic elastography systems, including all those based on the quasistatic and shear wave paradigms, can be found algorithms for estimating the deformation from one frame to the next. These typically rely on block matching of some sort, using the correlation coefficient or perhaps a phase-based similarity metric to identify the optimal alignment of radiofrequency (RF) data windows in pre- and post-deformation frames. However, not all matches are equally reliable. The quality of a match is affected by many factors, including electrical noise, intra-window strain and out-of-plane motion.

An estimate of the match quality can be derived from the post-alignment similarity metric and used to guide various stages of the strain imaging process. For example, the literature is replete with algorithms that use the correlation coefficient to reject poor matches, and perhaps replace them with alignments interpolated from nearby, superior matches (e.g., [1]). In this paper, novel uses of the match quality

A.H. Gee (✉)
Department of Engineering, University of Cambridge, Cambridge, CB2 1PZ, UK

M.P. André et al. (eds.), *Acoustical Imaging*, Acoustical Imaging 30,
DOI 10.1007/978-90-481-3255-3_11,

are described, moving beyond conventional rejection thresholds to further improve the accuracy and intelligibility of the resulting strain images.

We consider two measures of the match quality. It was shown in [2] that, under certain simplifying assumptions, the precision $p\psi$ of the displacement estimates (i.e., the reciprocal of the measurement variance) can be derived from the real part of the complex cross-correlation ρ of matched pre- and post-deformation windows. For two matched signals, $r_1 e^{i\theta_1}$ and $r_2 e^{i\theta_2}$,

$$p \approx \frac{\rho}{1-\rho} \text{ where } \rho = \Re\left[\frac{\sum r_1 r_2 e^{i(\theta_1-\theta_2)}}{\sqrt{\sum r_1^2 \sum r_2^2}}\right] \tag{1}$$

For strain imaging algorithms that match using the correlation coefficient, ρ is available at each matched window without any processing overhead. However, when using a phase-based algorithm [3], it is more efficient to use instead the weighted variance σ_θ of the residual phase differences:

$$\sigma_\theta = \frac{\sum r_1 r_2 (\theta_1 - \theta_2)^2}{\sum r_1 r_2} \tag{2}$$

Under certain weak assumptions [4], it can be shown that

$$\rho \approx 1 - \frac{\sigma_\theta}{2} \tag{3}$$

In this way, the phase variance provides a minimal overhead route to estimate p for phase-based algorithms.

2 Precision-Guided Displacement Tracking

Strain estimation algorithms typically start by obtaining the displacement between the pre- and post-deformation frames at a number of seed points, perhaps using correlation-based exhaustive search. It is then common to employ some sort of tracking algorithm to propagate these seeds into the remainder of the frame while enforcing a degree of continuity. The direction of propagation is usually fixed in advance: for example row-to-row [5, 6], column-to-column [7] or diagonal [8]. The problem with such approaches is that a poor displacement estimate inevitably causes further errors in the downstream tracking direction. However, by switching to a dynamically generated tracking path, the match quality can be used to prevent this sort of error propagation.

The precision map may be represented as $p(x, y)$, where y and x are indices in the axial and lateral directions respectively. The tracking algorithm maintains a set S which contains points that have been initialized and are ready for processing. In the first step, $S_1 = \{s_1, s_2, s_3, \ldots, s_n\}$ contains the n seeds. The seeds are not all

processed at once: instead, only the one with the maximum precision is selected as the current point Pt_1

$$Pt_1 = \arg\max\left(p\left(s_1\right), p\left(s_2\right), p\left(s_3\right), ..., p\left(s_n\right)\right) \tag{4}$$

where Pt_1 refers to the current point to be processed (1 denotes the index of the step), and the arg max() operator extracts the point with the maximum precision value from S. The point Pt_1 is then processed, by which we mean refining its displacement from the initial guess, using any suitable displacement estimation method [5, 9–13].

In the second step, the point set is updated by removing Pt_1 from S and adding its four neighbors, whose initial displacement estimates and qualities are assigned according to Pt_1's values. S now contains the four neighbors of Pt_1 and the remaining seeds not yet processed. Once again, the next point to be processed is selected from S according to the maximum precision criterion. This recursive process continues and can be described as

$$S_{k+1} = S_k + \text{Neighbour}(Pt_k) - Pt_k \tag{5}$$

$$Pt_{k+1} = \arg\max\left(p\left(s\right) | s \in S_{k+1}\right) \tag{6}$$

where the Neighbor() operator extracts a point's 4-way neighbors that are not in S and have not yet been processed. For any neighbor that is already in S, a comparison is made between its precision value and that of the current point. If the current point's precision is greater, the neighbor's initial displacement estimate is replaced by the current point's displacement. This simply reflects the fact that a better displacement estimate is now available. The algorithm terminates when the point set S is empty, which indicates that all points in the frame have been processed.

This strategy tends to mean that high quality regions are processed first, while low quality regions are avoided at an early stage. The advantage is twofold. Firstly, accurate estimation in high quality regions is propagated to other points, thus facilitating subsequent processing. Secondly, initialization errors (bad seeds) frequently encountered in low quality regions are prevented from propagating. Figure 1

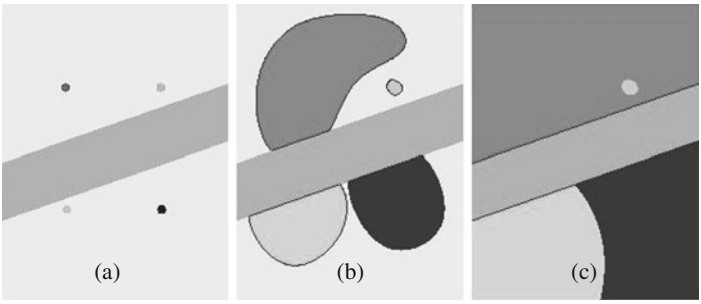

Fig. 1 Illustration of the precision-guided tracking algorithm

illustrates these properties. The frame contains a diagonal band of decorrelated data (medium grey), that separates the good quality data into two disjoint regions. In Fig. 1a, only four seeds are shown for clarity; there will typically be more. Suppose that the dark grey (upper left), lighter grey (lower left) and black seeds (lower right) are good, while the medium grey (upper right) seed is bad, even though the correlation is high. In Fig. 1b, the bad seed does not propagate very far, since neighbouring windows do not match well at the incorrect displacement. The three good seeds grow steadily, though they do not penetrate the poorly correlated region. The active point set $S\psi$ is shown in black as a circumscribed line around the regions. Towards the end of tracking Fig. 1c, all the good quality data has been processed; all that remains is for the dark grey, light grey and black fronts to penetrate the decorrelated region. The small region of poor displacement estimates, surrounding the bad seed, can be corrected in a second pass of the tracking algorithm with negligible computational overhead; full details can be found in [14].

The precision-guided tracking algorithm is used in a hybrid displacement estimation method [15], that combines elements of multi-level correlation and phase-based displacement tracking to achieve the noise tolerance of the former and the speed of the latter. The algorithm was evaluated using three finite element simulations (Abaqus 6.7, Simulia, Rhode Island, USA): a stiff inclusion embedded in a homogeneous background, with normal compression of the material; the same materials but with tilted compression, modelling uneven pressure distribution across the face of the probe; and a three-layer specimen with slip planes between the layers. For each simulation, two frames of simulated RF echo data were obtained, pre- and post-deformation, using Field II [16]. The experimental protocol involved corrupting the simulated RF echo data with additive noise at six signal-to-noise ratios in the range 4 dB to -1 dB. The displacement tracking method was evaluated 200 times (with different random noise) at each noise level. After each test, the estimated axial displacement field was compared with the known ground truth and the average absolute point-wise difference $d\psi$ was recorded. The results in Fig. 2 are presented in terms of the mean and standard deviation of d across the 200 trials. For comparison, results are also shown for a pure tracking approach (Stradwin, [17]) and a pure multi-level search approach [1]. The superior performance of the hybrid algorithm is further evident in the *in vivo* example in Fig. 3. The hybrid algorithm requires 38 ms per frame, running on a 2.4 GHz Intel Core 6600 processor. This compares with 41 ms for Stradwin and 109 ms for the multi-level method.

3 Precision-Guided Nonparametric Regression

Following displacement estimation, strain is calculated by differencing adjacent displacement estimates and the precision is adjusted accordingly. The strain data is then normalised to account for variations in probe movement, and the precision updated to account for this normalisation, as described in [2].

Local fluctuations in the precision of the strain estimates can make strain images hard to interpret. For example, in the strain images in Fig. 3 there are noisy estimates

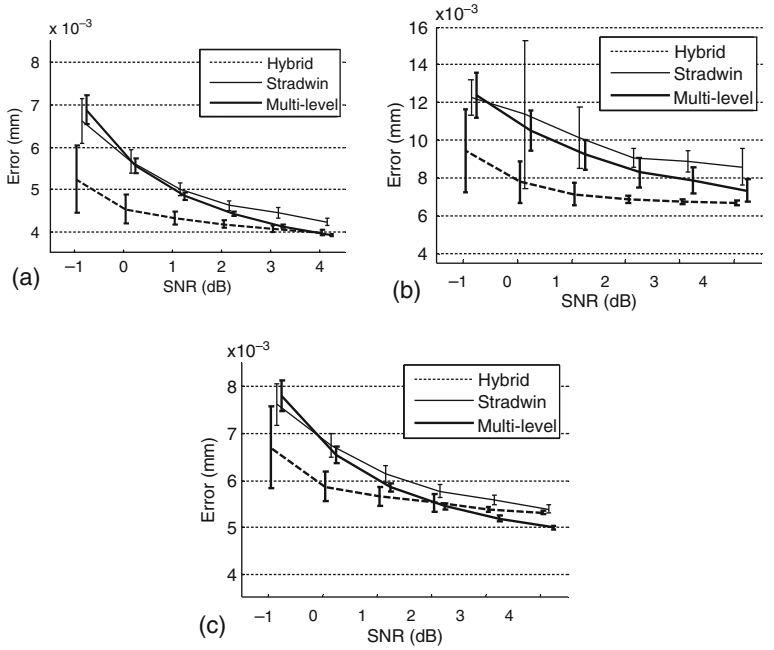

Fig. 2 Results for the finite element simulations. (**a**) Normal compression with stiff inclusion. (**b**) Tilted compression with stiff inclusion. (**c**) Normal compression with slip planes

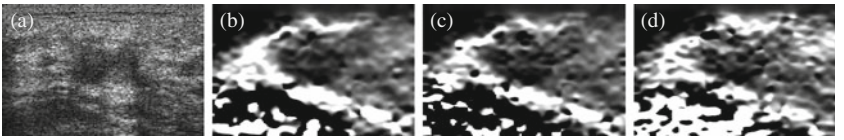

Fig. 3 (**a**) B-mode image of the breast with stiff fibroadenoma. Axial strain images calculated using (**b**) the hybrid method, (**c**) Stradwin and (**d**) the multi-level method. Dark is hard and bright is soft

at the bottom left of the frame. Low precision regions can be visually suppressed by use of a suitable colour wash [2]. Alternatively, we present here a method for producing strain images with uniform *precision* and varying *resolution*, rather than uniform *resolution* and varying *precision*. Such images may be easier to interpret: lack of precision in strain images leads to regions which falsely appear to have strong fine scale stiffness variation, whereas lack of resolution leads to high levels of blurring, which is less prone to misinterpretation. In this case, a colour wash can additionally be used to suppress areas with very low resolution (rather than low precision as before). Whether this approach is indeed better is clearly somewhat subjective, hence the results are presented in visual form, so that readers can judge for themselves.

Uniform precision images can be obtained in a nonparametric regression (NPR) framework. We consider one cost function of many possibilities

$$C = \iint \left(w_{xy}(s - \tilde{s})^2 + r \left[\left(\frac{\partial \tilde{s}}{\partial x} \right)^2 + \left(\frac{\partial \tilde{s}}{\partial y} \right)^2 \right] \right) \mathrm{d}x\mathrm{d}y \tag{7}$$

where x and y denote lateral and axial distance, s and $\tilde{s}$ are the raw and regressed strain data respectively, which are multiplied by data weights, w_{xy}. The roughness penalty consists of squared partial first derivatives in the x and y directions. Hence C penalizes strain data which is not reasonably constant, where r controls the degree of "reasonableness".

In practice, we do not have a continuous description of the raw strain data, and we do not require a continuous function for the regressed strain. Our aim is simply to replace the raw data with a filtered version of the data. In this case, Equation (7) can be expressed in a discrete matrix form:

$$C \approx (\mathrm{s} - \tilde{\mathrm{s}})^T \mathbf{W} (\mathrm{s} - \tilde{\mathrm{s}}) + r \tilde{\mathrm{s}}^T \mathbf{M}^T \mathbf{M} \tilde{\mathrm{s}} \tag{8}$$

W is now a diagonal matrix of data weighting factors, with one entry per data point. s and $\tilde{\mathrm{s}}$ are vectors listing are vectors listing the raw and regressed strain data respectively. **M** is a matrix which extracts every first difference, in both x and y directions. A formula for the regression surface is found by setting $\nabla C = 0$, differentiating with respect to the value at every point on the regression surface, $\tilde{\mathrm{s}}$, which gives , which gives

$$\left(\mathbf{W} + r \mathbf{M}^T \mathbf{M} \right) \tilde{\mathrm{s}} = \mathbf{W} \mathrm{s} \tag{9}$$

For 2D kernels, we can keep the precision of the regressed data constant by setting each of the diagonal elements of **W** to a value $w(x, y)$ equal to the precision $p(x, y)$ of the corresponding raw data [4]. The precision of the entire regressed image will then scale with r. A similar analysis in 3D shows that we should set $w(x, y) = p(x, y)^{2/3}$ to maintain uniform precision. For a 2D strain image, Equation (9) can be solved in less than 30 ms (2.16 GHz Intel Core2 processor) using a tailored multi-grid technique [4]. Typical 3D data sets require 3–4 s[4].

Results are presented using a commercially available breast biopsy phantom (CIRS model 052A, Computerized Imaging Reference Systems, Inc, Virginia, USA), containing randomly positioned stiff inclusions which were also visible in ultrasound B-mode images. In Fig. 4, the ultrasound signal strength is good throughout the data, but the probe movement is predominantly rotational, about an axis orthogonal to the image plane roughly at the top centre of the images. This results in a high degree of variation in the applied stress field, and no axial strain in a vertical line down the centre of the image. In contrast, Fig. 5 is a scan with good ultrasound signal strength and good probe motion. Results are presented for NPR and, by way of comparison, more conventional Gaussian filtering, with the adjustable Gaussian kernel size providing a variable degree of smoothing akin to the NPR parameter r.

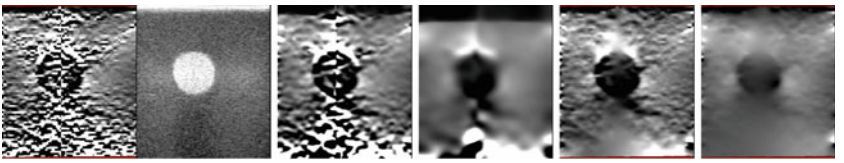

Fig. 4 Strain images of the CIRS breast biopsy phantom. (**a**) The raw high resolution strain image and associated B-mode image. The remaining images show lightly filtered (*left*) and heavily filtered (*right*) versions of the strain data. (**b**) and (**c**) use Gaussian filtering, (**d**) and (**e**) use NPR

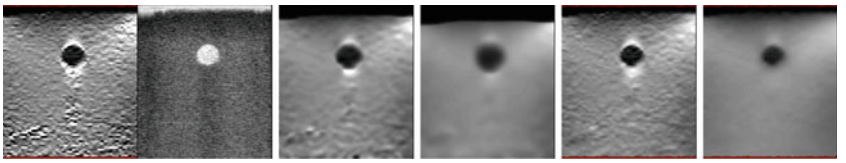

Fig. 5 Strain images of the CIRS breast biopsy phantom. (**a**) The raw high resolution strain image and associated B-mode image. The remaining images show lightly filtered (*left*) and heavily filtered (*right*) versions of the strain data. (**b**) and (**c**) use Gaussian filtering, (**d**) and (**e**) use NPR

In Fig. 4, Gaussian filtering does not cope well with the vertical band of zero strain (and hence very low precision) down the centre of the image. A sharp vertical feature is still evident in the filtered data, even with heavy filtering. NPR effectively ignores the data at the centre of the image and smoothes over this region. Figure 5 contains higher quality raw data, and in this case both filtering algorithms produce reasonable strain images, particularly with light filtering. Differences can still be seen in the small noisy regions at the bottom left and underneath the inclusion: these are better suppressed in Fig. 5d, e than in Fig. 5b, c. Furthermore, with heavy filtering, the Gaussian method in Fig. 5c makes the inclusion appear significantly larger. In contrast, with NPR the inclusion remains much the same size.

Figure 6 is a clinical 3D scan from a breast examination. Here the patient was scanned with 2D strain imaging first, to establish the general area of interest, before a 3D scan was performed. Two low strain (black) regions are very obvious in the strain images, in an area unrelated to the larger black region in the B-mode image (which was what initially drew the clinician's attention). However, the presentation is confused in the Gaussian-filtered image of Fig. 6b by a distracting fine scale pattern of strain variation apparent in most of the views. The NPR image in Fig. 6c draws attention much more clearly to the real low strain region.

4 Conclusions

When estimating displacement as a precursor to strain imaging, the block matching quality (or, more formally, the estimation precision) is as valuable a measure as the displacement estimates themselves. We have shown how the precision can be

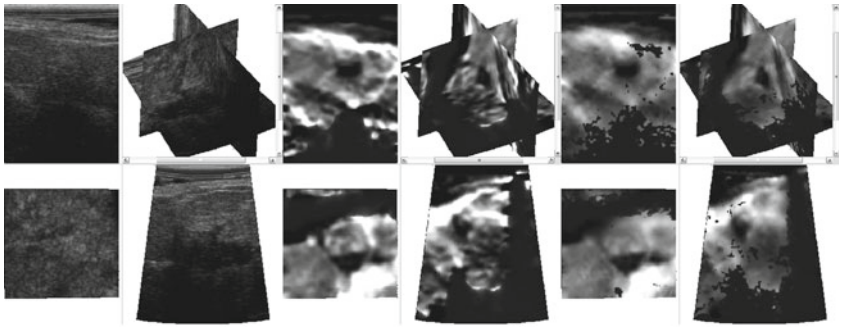

(a) (b) (c)

Fig. 6 3D data from a clinical breast examination. Each image shows three orthogonal views and a combined 3D view. (**a**) B-mode data for a possible invasive ductal carcinoma, (**b**) strain data using Gaussian filtering and (**c**) using NPR. For Gaussian filtering, the *grey color wash* indicates lack of data precision, whereas with NPR it indicates lack of resolution

used to guide a tracking algorithm for displacement estimation, and then to obtain uniform precision strain images in an NPR framework. Other uses of the match quality include precision-weighted strain normalization and temporal persistence, and precision-based display [18].

References

1. Shi, H., Varghese, T.: Two-dimensional multi-level strain estimation for discontinuous tissue. Phys. Med. Biol. **52**, 389–401 (2007)
2. Lindop, J.E., Treece, G.M., Gee, A.H., Prager, R.W.: Dynamic resolution selection in ultrasonic strain imaging. Ultrasound Med. Biol. **34**(5), 809–823 (2008a)
3. Lindop, J.E., Treece, G.M., Gee, A.H., Prager, R.W.: Phase-based ultrasonic deformation estimation. IEEE Trans. Ultrason. Ferroelect. Freq. Contr. **55**(1), 94–111 (2008c)
4. Treece, G.M., Lindop, J.E., Gee, A.H., Prager, R.W.: Uniform precision ultrasound strain imaging. Tech. Rep. CUED/F-INFENG/TR 624, Cambridge University Department of Engineering (2009)
5. Pesavento, A., Perrey, C., Krueger, M.H.E.: A time efficient and accurate strain estimation concept for ultrasonic elastography using iterative phase zero estimation. IEEE Trans. Ultrason. Ferroelect. Freq. Contr. **46**(5), 1057–1067 (1999)
6. Zhu, Y., Hall, T.J.: A modified block matching method for real-time freehand strain imaging. Ultrason. Imag. **24**, 161–176 (2002)
7. Jiang, J., Hall, T.J.: A parallelizable real-time motion tracking algorithm with applications to ultrasonic strain imaging. Phys. Med. Biol. **52**, 3773–3790 (2007)
8. Zahiri-Azar, R., Salcudean, S.E.: Motion estimation in ultrasound images using time domain cross correlation with prior estimates. IEEE Trans. Biomed. Eng. **53**, 1990–2000 (2006)
9. Langeland, S., d'Hooge, J., Torp, H., Bijnens, B., Suetens, P.: Comparison of time-domain displacement estimators for two-dimensional RF tracking. Ultrasound Med. Biol. **29**, 1177–1186 (2003)
10. Ophir, J., C´Espedes, I., Ponnekanti, H., Yazdi, Y., Li, X.: Elastography: A quantitative method for imaging the elasticity of biological tissues. Ultrason. Imag. **13**(2), 111–134 (1991)

11. O'Donnell, M., Skovoroda, A.R., Shapo, B.M.: Measurement of arterial wall motion using Fourier based speckle tracking algorithms. In: Proceedings of the IEEE Ultrasonics Symposium, pp. 1101–1104 (1991)
12. O'Donnell, M., Skovoroda, A.R., Shapo, B.M., Emelianov, S.Y.: Internal displacement and strain imaging using ultrasonic speckle tracking. IEEE Trans. Ultrason. Ferroelect. Freq. Contr. **41**, 314–325 (1994)
13. Viola, F., Walker, W.F.: A comparison of the performance of time-delay estimators in medical ultrasound. IEEE Trans. Ultrason. Ferroelect. Freq. Contr. **50**, 392–401 (2003)
14. Chen, L., Treece, G.M., Lindop, J.E., Gee, A.H., Prager, R.W.: A quality-guided displacement tracking algorithm for ultrasonic elasticity imaging. Med. Image Anal., in press (2009)
15. Chen, L., Housden, R.J., Treece, G.M., Gee, A.H., Prager, R.W.: A hybrid displacement estimation method for ultrasonic elasticity imaging. Tech. Rep. CUED/FINFENG/TR 615, Cambridge University Department of Engineering (2008)
16. Jensen, J.A.: Field: A program for simulating ultrasound systems. In: Proceedings of the 10th Nordic-Baltic Conference on Biomedical Imaging. Tampere, pp. 351–353 (1996)
17. Treece, G.M., Lindop, J.E., Gee, A. H., Prager, R.W.: Freehand ultrasound elastography with a 3-D probe. Ultrasound Med. Biol. **34**(3), 463–474 (2008)
18. Lindop, J.E., Treece, G.M., Gee, A., Prager, R.W.: An intelligent interface for freehand strain imaging. Ultrasound Med. Biol. **34**(7), 1117–1128 (2008b)

Applying Echoes Mean Frequency Shift for Attenuation Imaging in Tissue

J. Litniewski, Z. Klimonda, and A. Nowicki

Abstract The purpose of this study was to develop the attenuation parametric imaging technique and to apply it for in vivo characterization of tissue. Local attenuation coefficient was determined by evaluating the frequency downshift that encounters the amplitude spectrum of the interrogating ultrasonic pulse during propagation in the absorbing tissue. Operation and accuracy of the processing methods were verified by assessing the size-independent region of interest (ROI) for attenuation determination and calculating the attenuation coefficient distribution for experimentally recorded tissue-phantom scattered waveforms. The Siemens Antares scanner equipped with Ultrasound Research Interface unit allowing for direct radiofrequency (RF) signals recording was used for B-scan imaging of the tissue- mimicking phantom in vitro and liver *in vivo*. RF data were processed to determine attenuation coefficient along the B-scan lines. Also, the preliminary studies of backscattered signals from skin recorded using a skin scanner were performed to calculate parametric-attenuation images.

Keywords Attenuation imaging · Parametric imaging · Tissue attenuation · Amplitude spectrum

1 Introduction

It has been emphasized in many publications that ultrasound attenuation is closely related to the type and pathological state of the tissue. Liver is the most usual example. The in vivo characterization of this organ is often restricted to its attenuation properties and it has been proved that the ultrasonic attenuation coefficient increases as the amount of pathological fat in the liver increases [1]. Also, the study of excised cancer tissue revealed the differences in acoustic attenuation among cancer types and degrees of pathology [2]. However, in most conventional applications of clinical ultrasonic scanners only the peak amplitude echogenicity is used to create the image. Moreover, signal envelope detection destroys potentially useful

J. Litniewski (✉)
Institute of Fundamental Technological Research, Polish Academy of Sciences, Warsaw 00-049, Poland
e-mail: jlitn@ippt.gov.pl

M.P. André et al. (eds.), *Acoustical Imaging*, Acoustical Imaging 30,
DOI 10.1007/978-90-481-3255-3_12,

information about frequency dependence of acoustic properties of tissue comprised in RF backscattered echoes.

In this pilot study, we explored the possibility of extracting information of the tissue attenuation coefficient from the ultrasonic B-scans obtained with high frequency skin scanner and conventional ultrasonograph. To find in vivo estimates of the attenuation from ultrasonic echo signals we assumed that the attenuation of tissue increases linearly with frequency and that the backscattered signals have a Gaussian shaped spectrum. Thus, the attenuation coefficient was determined from the downshift (Δf) of the backscattered spectrum center frequency ($\Delta f = \alpha \cdot \sigma^2 \cdot \Delta z$, where α is attenuation coefficient, σ^2 is Gaussian variance, and Δz is distance traveled in the medium).

2 Materials and Methods

2.1 Acquisition of Data

Two types of ultrasonic data were considered, the B-scan RF images of the skin recorded with the skin scanner and the RF images of the tissue mimicking phantom and the liver obtained with Siemens Antares ultrasonography system equipped with the Ultrasound Research Interface (URI). The URI enabled direct access to RF echo signals.

The skin scanner was developed in our laboratory. It performed a sector scan with the image frame rate up to 10 Hz. The transmitted and scattered echoes (sinusoidal or encoded) were sampled at 200 MHz frequency with 12 bit resolution. The received sequences were envelope detected (prior compressed, if necessary) and displayed. Simultaneously, the RF data were stored separately. In this study we have used a 20 μm thick spherical transducer made of modify PZT 37 deposited on PZT substrate with thick film technology (Ferroperm, Denmark). This 3 mm diameter transducer was focused at 8.6 mm. RF B-scans of skin at the nape of the neck were recorded with the focus located 1.6 mm beneath the skin surface and were processed to extract the information about attenuating properties of the skin tissue.

Also, a study with conventional ultrasonography B-scans was performed. The RF data from a tissue mimicking phantom (DFS, attenuation coefficient $= 0.51 \pm 0.02$ dB/MHz·cm at 4 MHz) and from liver *in vivo* were stored using URI. We have used a convex probe (Siemens CH6-2) operating at 4 MHz, with programmed single, 80 mm long focus.

2.2 Analysis of Data

When the ultrasonic pulse with the Gaussian amplitude spectrum propagates in the medium that attenuation is linearly depended on frequency then, the pulse instantaneous mean frequency is continuously shifted to lower frequencies. Prior to determine this shift the RF echo signals were processed to equalize the amplitude of strong reflection within the sample with averaged amplitude of scattered signal. To

determine the mean frequency (MF) along the propagation path we have applied the MF correlation estimator (I/Q algorithm adopted from the Doppler technique). The results obtained from several adjacent B-scan echo-lines were averaged. The number of averaging scan lines and the length of the time window applied for frequency determination were calculated from the size of selected regions of interest (ROIs). For details see the next section. Then the overall mean-frequency shift (MFS) trends were calculated using Single Spectrum Analysis (SSA). We have decided to applied SSA technique to trend extraction because it requires no model specification of time series and trend, extracts trend of noisy time series containing oscillations of unknown period and is robust to outliers [3]. The MFS trends were converted into attenuation coefficient distributions and finally, by assigning the gray scale levels to the attenuation coefficient values the parametric images were computed.

2.3 Selection of ROI Size

The goal of this investigation was to convert the standard B-scan images into attenuation coefficient distributions with the special resolution of the area of region of interest. To find the size of ROIs necessary to give ROI size-independent attenuation coefficients we have used a B-scan image of a homogenous part of a tissue-mimicking phantom (Siemens Antares image) and a homogenous part of a skin B-scan (skin scanner image). A set of concentric ROI squares was selected with the length defining the I/Q algorithm window length and the width qualifying number of averaged adjacent mean frequency lines. Each square was analyzed for their respective average attenuation coefficient. For the skin scanner, it was found that 1 mm $\times$ 1 mm ROI box is sufficient (see Fig. 1, left) what corresponded to 1.3 μs long time window and averaging over 25 scan lines. In the case of Antares images,

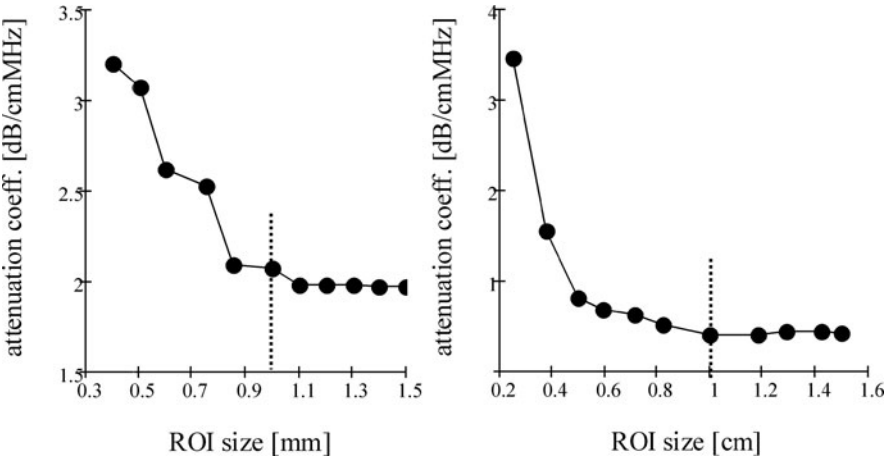

Fig. 1 Measured attenuation coefficient versus size of the rectangular ROI for (*left*) skin B-scan and (*right*) Antares image of tissue-phantom. *Dotted lines* show the minimal area assumed to give ROI size-independent attenuation coefficients

the corresponding ROI box was 10 mm × 10 mm, setting the time window length and the number of averaged lines to 13 μs and 22 respectively (Fig. 1, right).

2.4 Correction for Diffraction

It is important to compensate for the effects of focusing when using the downshift in center frequency to estimate the attenuation coefficient from the backscattered signals emitted by focused sources [4]. The depth of focus depends on frequency and is shorter for the high frequency waves than for the long waves. Thus when the acoustic pulse is approaching the focus the amplitude of pulse high frequency components increases faster than the amplitude of lower frequencies and consequently the shifting up of the pulse spectrum together with its center frequency occurs. For the diverging beam the opposite effect takes place. Otherwise, in regions in front of the focus the attenuation is underestimated and in regions beyond the focus is overestimated. In our study we compensated for diffraction or focusing by obtaining echoes from a rigid plane located in water at different locations along the beam axis and calculating the frequency shifts of the echoes spectrum center frequency. It was assumed that the same effect takes place in tissue but quantitatively MFS are different because the focusing occurs in attenuating medium that shifts down the pulse frequency spectrum. Thus to obtain corrected values of attenuation coefficient the MFS correction calculated for water was transformed to new values accounting for more realistic frequency contents of propagating pulse. The calculated correction curves for tissue attenuation determination from the skin scanner and Antares B-scans are presented in Fig. 2. The pulses emitted by multi-element probe consist of a number of elementary pulses fitted in time and space. As such a fitting is never perfect the calculated amplitude spectra reveal complicated structure resulting in some departure from Gaussian shape that probably disturbed our measurements of the mean frequency curve. Thus, the correction curve for Antares scanner (Fig. 2, left) was additionally adjusted to recover correctly the overall attenuation of the tissue-mimicking phantom.

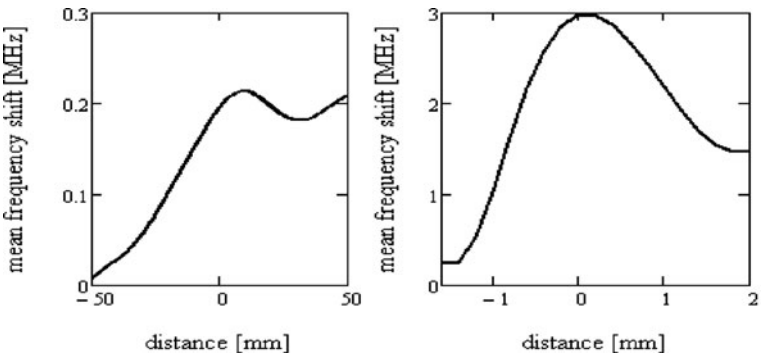

Fig. 2 The curves correcting the effects of focusing for (*left*) Antares scanner with the probe focusing at 80 mm and (*right*) skin scanner with the spherical transducer with 8.6 mm focal length

3 Results and Discussion

The effect of applying the MFS correction to compensate focusing is clearly visible in Fig. 3 where the mean frequency of the phantom scattered signals is displayed in the gray scale. The monotonic MF decrease with propagation depth reflects uniform distribution of attenuation coefficient within the phantom.

In Fig. 4 the B-scan image of the skin recorded at the nape of the neck together with the equivalent attenuation distribution image is presented. Because the skin can be regarded as the layered structure the time window used for the MF determination was set to 0.5 mm and averaging over 60 scans was applied. Thus, ROI

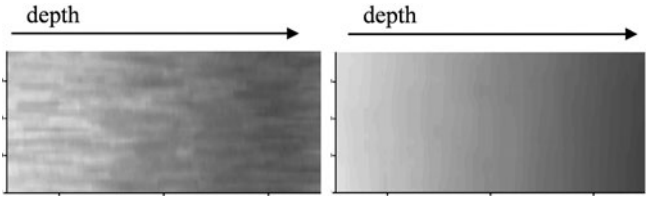

Fig. 3 Mean frequency (MF) distribution images calculated from the phantom B-scan (*left*) without and (*right*) with the correcting for focusing

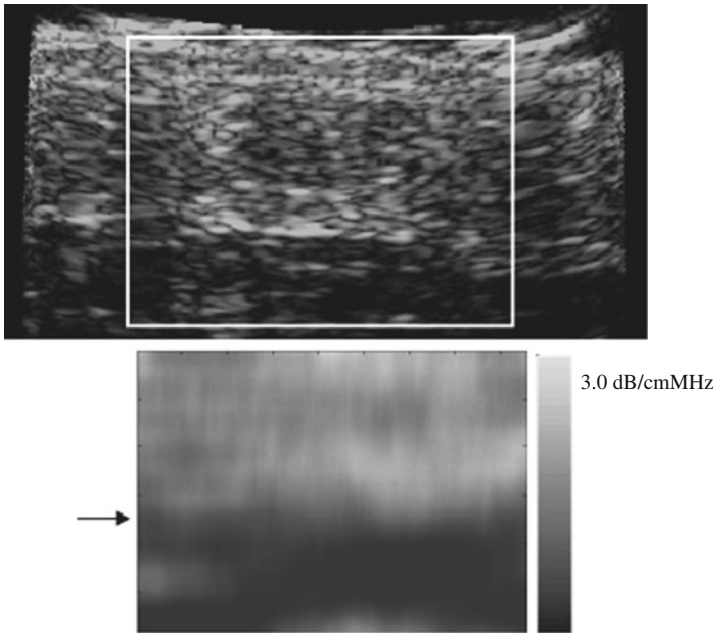

Fig. 4 B-scan image (*top*) and calculated attenuation coefficient distribution (*bottom*) obtained in vivo for the skin of the neck. Rectangle market on the B-scan shows the area where the attenuation was calculated. An *arrow* shows an approximate location of the interface between dermis and hypodermis

area was similar to the ROI box area selected in Fig. 1 and we have checked that it produced the same results as the square ROI. The attenuation distribution images calculated from the skin B-scans show two oblong areas highly differing in attenuation coefficient value. Significant decrease of attenuation begins approximately 2 mm from the skin surface. A difference can be also seen on the B-scan image. The sudden jump in reflectivity at the depth of 2 mm corresponds to dermis and hypodermis interface. The mean attenuation coefficient calculated for these two distinct parts of the image along with the standard deviation was equaled to 1.865 ± 0.23 dB/cm·MHz and 0.77 ± 0.69 dB/cm·MHz for dermis-area and hypodermis-area respectively what corresponds well with the published data [5, 6]. The high value of attenuation standard variation in this innermost and thickest layer of the skin reflects complicated structure of hypodermis that consists primarily of loose connective tissue and lobules of fat.

The image of the liver was obtained in vivo with the scanner settings described in the Acquisition Section and is presented together with the calculated attenuation coefficient distribution (Fig. 5). The spatial resolution in attenuation image can be assumed to be approximately similar to the ROI size equal to 1 cm^2. The attenuation coefficient values are much higher for the areas corresponding to the liver tissue comparing to the areas outside of the liver. The coefficient averaged over the liver

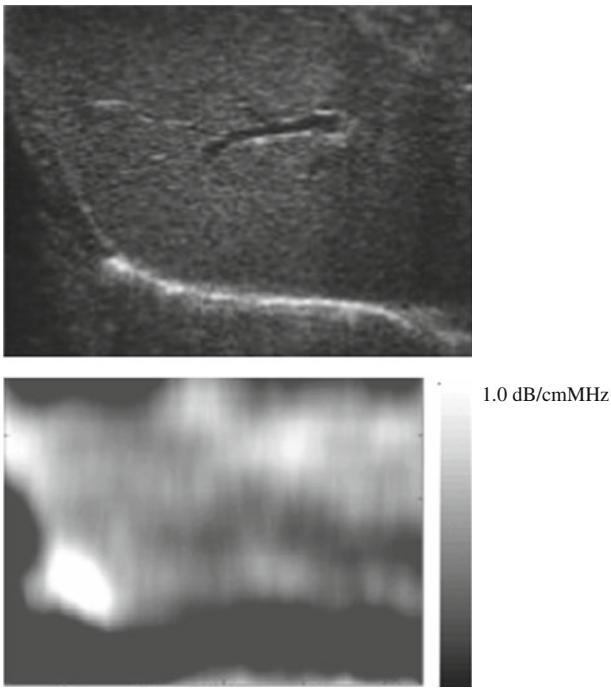

Fig. 5 B-scan image (*top*) and calculated attenuation coefficient distribution (*bottom*) obtained in vivo for the liver

tissue was equal to 0.59 ± 0.27 dB/cm·MHz what also corresponds well with published data [7, 8, 9]. An increase of the attenuation coefficient at the maximal depth (Fig. 5, bottom) was probably caused by the noise that limits the depth of attenuation determination to approximately 12 cm. Some variation of attenuation within the liver tissue could be of natural reasons as well as could be caused by not satisfactory focusing compensation. Very high attenuation shown at the liver left border could be caused by reflections at the interface.

4 Conclusions

The frequency dependent attenuation is an interesting acoustic parameter for tissue characterization. Usually, tissue-attenuating properties averaged over large areas are presented. However, it has been shown that imaging is the best diagnostic technique. Conventional ultrasonic imaging as well as other medical visualization methods is successfully applied in all medical fields. Their usefulness is closely connected with physician's experience, not with numerical data that can be extracted from ultrasonic waves or another kind of radiation applied for examination. Thus, it could be anticipated that also parametric attenuation imaging is a promising diagnostic technique.

We have shown that RF B-scans can be converted into parametric attenuation images with the spatial resolution defined by the size of experimentally selected ROI. The attenuation value resolution depends on the backscattered signal quality. Noise is the most disturbing factor, highly increasing the MF value and limiting the imaging depth. Also, the focusing effects can seriously degrade the parametric image, as the absolute correction is often impossible. Finally, we can deduce from our experience that accurate, in vivo imaging of tissue attenuating properties is only possibly with the scanners developed with intension of parametric imaging.

Acknowledgements This work was partly supported by the Polish Ministry of Science and Education, projects N N518388234 and 3 T11E 011 30.

References

1. Lu, Z., Zagzebski, J., Lee, F.: Ultrasound backscatter and attenuation in human liver with diffuse disease. Ultrasound Med. Biol. **25**(7), 1047–1054 (1999)
2. Saijo, Y., Sasaki, H.: High frequency acoustic properties in tumor tissue. In: Dunn, F. (ed.) Ultrasonic tissue characterization. Springer, Tokyo (1996)
3. Golyandina, N., Nekrutkin, V., Ahigljavsky, A.: Analysis of time Series Structure: SSA and related techniques. CRC Press, Boca Raton, FL (2001)
4. Bigelow, T., McFarlin, B., O'Brien, W., Oelze, M.: In vivo ultrasonic attenuation slope estimates for detecting cervical ripening in rats: Preliminary results. J. Acoust. Soc. Am. **123**(3), 1794–1800 (2008)
5. Baldewec, T., Laugier, P., Berger, G.: Ultrasonic attenuation estimation in highly attenuating media: Application to skin characterization. In: Tortoli, P., Masotti, L. (eds.) Acoustical Imaging, pp. 341–348. Plenum Press, New York (1996)

6. Raju, B., Srinivasan, M.: High-frequency ultrasonic attenuation and backscatter coefficient of in vivo normal human dermis and subcutaneous fat, Ultrasound Med. Biol. **27**(1), 1543–1556 (2001)
7. Fujii, Y., Taniguchi, N., Itoh, K., Shigeta, K., Wang, Y, Tsao, J-W., Kumasaki, K., Itoh, T.: A new method for attenuation coefficient measurement in the liver. J. Ultrasound Med. **21**, 783–788 (2002)
8. Maklad, N., Ophir, J., Balsara, V.: Attenuation of ultrasound in normal liver and diffuse liver disease in vivo. Ultrason. Imag. **6**, 117–125 (1984)
9. Garra, B., Insana, M., Shawker, T., Russel, M.: Quantitative estimation of liver attenuation and echogenicity: Normal state versus diffuse liver disease. Radiology **162**(1), 61–67 (1987)

Part II
Acoustic Microscopy

Visualization of Microvessels in Skin by Three-Dimensional Ultrasound Microscope

Y. Saijo, K. Kobayashi, N. Hozumi, A. Tanaka, and S. Sakai

Abstract A non-invasive imaging technique capable of visualizing microvessels through epidermis to subdermis has been strongly desired. A PVDF ultrasonic transducer with the central frequency of 100 MHz and the focal length of 3.2 mm was mechanically scanned over the objects by two linear servo motors controlled by a personal computer. A microvessel model was made of a tungsten wire with a diameter of 100-microns and placed in the water tank. The microvessel model was clearly visualized by 3D ultrasound microscope. In cases of skin imaging, conventional echo gel was used as the coupling medium between transducer and skin surface. *In vivo* 3D skin morphology was also clearly visualized. In dermis, a microvessel may be shown as small, round, lucent echo areas continuously observed in the serial sections. 3D structure of hair-follicle was also visualized from the skin surface to the bud of hair-follicle in dermis. The 3D ultrasound microscope noninvasively provides important information on the distribution of microvessels in skin.

Keywords Skin · Epidermis · Dermis · Microvessel · Three-dimensional ultrasound microscope

1 Introduction

Application of acoustic microscopy in medicine and biology has three major features and objectives [1–5]. First, it is useful for intra-operative pathological examination because staining is not required. Second, it provides basic acoustic properties to assess the origin of echo in clinical ultrasonic images. Third, it provides information on biomechanics of the tissues and cells at a microscopic level. However, conventional usage of acoustic microscope in medicine and biology has been limited for visualization of thinly sliced tissues or cells cultured as a single layered structure. Thus, ultrasonic visualization of microstructures of *in vivo* tissue has been desired for years. Recently, hardware of high frequency ultrasound and software of signal processing and imaging techniques have been matured for the development of next generation acoustic microscopy.

Y. Saijo (✉)
Graduate School of Biomedical Engineering, Tohoku University, Sendai, Japan
e-mail: saijo@idac.tohoku.ac.jp

M.P. André et al. (eds.), *Acoustical Imaging*, Acoustical Imaging 30,
DOI 10.1007/978-90-481-3255-3_13,

Three-dimensionally regenerated skin with epidermis, dermis, hair follicle, lipid gland and capillary is being developed for the treatment of large burn or for plastic surgery. Microvasculature of skin is important for maintaining viability of grafted skin including regenerated skin. Recently, optical coherence tomography (OCT) has provided high resolution imaging of skin including microvasculature [6]. However, OCT cannot visualize the structures deeper than approximately 600-micron because light has a limitation in penetrating depth. Clinical ultrasound skin imaging using 20 MHz transducer visualizes the deep layer morphology but cannot visualize fine structures such as microvessels or hair-follicles. Thus, non-invasive imaging technique capable of visualizing microvessels through epidermis to subdermis is strongly desired.

In the present study, three-dimensional ultrasound microscope with the central frequency of 100 MHz was developed and applied for imaging of 3D structure of microvessel model and microvessels in human skin.

2 Methods

2.1 Instrumentation

Figure 1 shows the schematic illustration of the 3D ultrasound microscope system. An electric impulse was generated by a high speed switching semiconductor. The start of the pulse was within 400 ps, the pulse width was 2 ns, and the pulse voltage was 40 V. The frequency of the impulse covered up to 500 MHz. The electric pulse was used to excite a PVDF transducer with the central frequency of 100 MHz. The ultrasound spectrum of the reflected ultrasound was broad enough

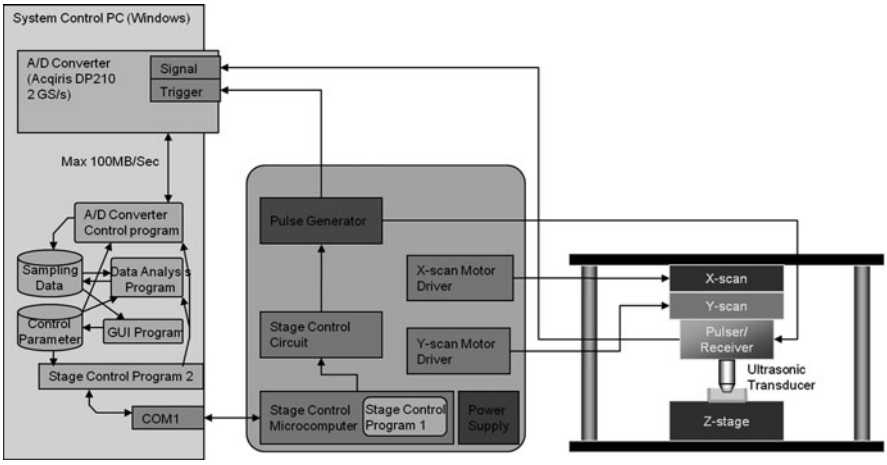

Fig. 1 Block diagram of the 3D ultrasound microscope

to cover 50–160 MHz (-6dB). The reflections from the tissue was received by the transducer and were introduced into a Windows-based personal computer (PC, Pentium D, 3.0 GHz, 2 GB RAM, 250 GB HDD) with a high-speed A/D converter (Acqiris DP210, Geneva, Switzerland). The frequency range was 500 MHz, and the maximum sampling rate was 2 GS/s. Eight pulse-echo sequences with 2,000 sampling points were averaged for each scan line in order to increase the signal-to-noise-ratio. The transducer was mounted on the X-Y scanner with two linear servo motors that were controlled by a microcomputer board connected to the serial port of the PC.

In classical acoustic microscopy, the focal length is short because the ultrasound pulse should be tightly focused on the glass. However, working range is expected to be longer for B-mode imaging because the ultrasound should be penetrated deeply into the tissue. Thus, design of the transducer was modified from that of our conventional acoustic microscopy. A PVDF transducer with the diameter of 2.4 mm and the focal length of 3.2 mm was fabricated for B-mode imaging (Fig. 2, right) while the diameter of 1.2 mm and the focal length of 1.5 mm was used for conventional acoustic microscopy (Fig. 2, left). Figure 2 shows the schematic illustration of the geometry and acoustic field of two kinds of transducer.

2.2 Signal and Image Processing

Obtained RF signal of each scanning line was converted to B-mode image by a conventional image processing algorithm of echography. The scan area was 2.4 mm wide (X-axis) and 1.5 mm deep (Z-axis) with 300 × 300 pixels. Three-hundred sequential B-mode images with 8-micron intervals were obtained for 3D ultrasound data set. For visualization of the microvessel model or surface morphology of the skin, volume rendering technique was used. For visualization of the inner structure of the skin, multiplanar reconstruction method was used.

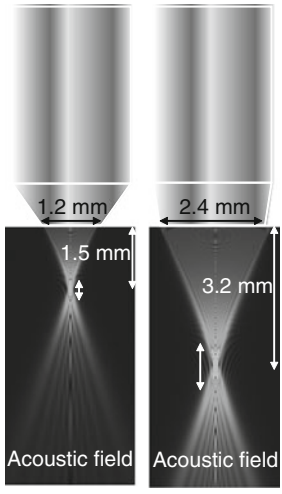

Fig. 2 Schematic illustration of the two kinds of transducer geometry and acoustic fields

2.3 Imaging Objects

The microvessel model was made of a tungsten wire with a diameter of 100-microns and placed in a water tank. In cases of skin imaging, conventional echo gel was used as the coupling medium between transducer and skin surface. Surface of the skin was stabilized during the 3D ultrasound measurement by a specially made stabilizing instrument.

3 Results

3.1 Volume Rendering Mode

Figure 3 shows 3D ultrasound microscope image of the microvessel model displayed as the volume rendering mode. Crossing of the two wires and some micro bubbles attached to the wire are clearly shown.

3.2 Multi-Planar Reconstruction Mode

Figure 4a shows the B-mode (X-Z plane) image of the skin at the forearm. Keratinocytes at the epidermis shows strong echo. Tubular hypo-echoic area is observed in the dermis. X-Y plane (parallel to the skin surface) images at the lines A, B, C and D were shown in Fig. 4b–e, respectively.

Figure 4b may indicate the grain of the skin. Round lucent echo areas (V) are seriously observed through Fig. 4c–e, and they are considered as a microvessel. Hair follicle (H) is also observed through Fig. 4c–e. The round dark area (S) located at the same position may be acoustic shadow of the surface microbubble.

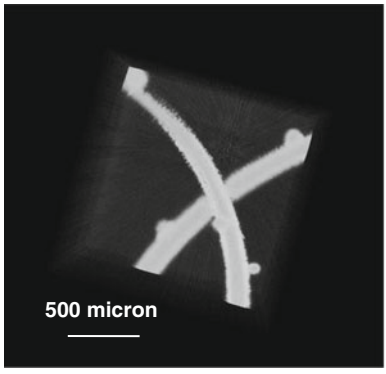

Fig. 3 3D ultrasound microscope image of the microvessel model (Volume rendering mode)

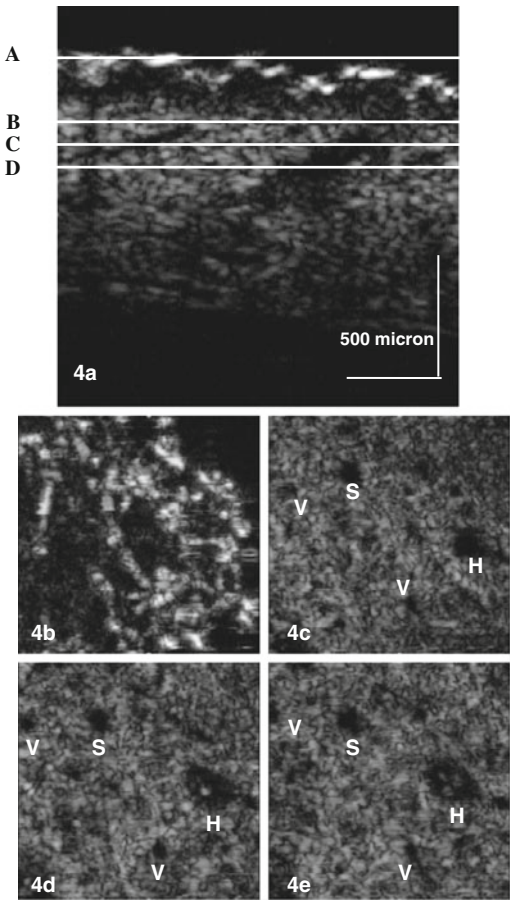

Fig. 4 3D ultrasound microscope images of *in vivo* skin (Multiplanar reconstruction mode)

4 Discussion

The microvessel model with the diameter of 100-micron was clearly visualized by the 3D ultrasound microscope. *In vivo* skin morphology was also clearly visualized by the system. Stratum corneum showed highest intensity while the epidermis showed less intense signals than the dermis. The epidermis was distinguished from stratum corneum. X-Y plane displayed by multiplanar reconstruction mode clearly showed that the grain of the skin surface was affected by the collagen fiber arrangement in the epidermis. In dermis, small, round, lucent echo area was continuously observed in the serial sections and it can be considered as the microvessel. A hair-follicle containing a hair was clearly captured from the skin surface to the deeper layer in dermis.

A group in Bochum has also developed some high frequency B-mode imaging systems for skin and visualized surface 3D morphology of the skin [7–8]. Compared

with those studies, the present study was unique to show the 3D morphology of the microvessels in dermis. The realistic resolution of the system was comparable to those of OCT although the ideal resolution was lower than OCT. This was because the ultrasound was not interfered by pigments in skin while the pigments caused large noise in OCT imaging.

5 Conclusion

Three-dimensional ultrasound microscope was developed for investigation of microstructures of the skin. Both microvessel model and microvessels of *in vivo* skin were successfully visualized. The 3D ultrasound microscope noninvasively provides important information of the skin that is not provided by OCT. The 3D ultrasound microscope is suitable for the follow up study after implantation of the regenerated skin. The application may cover various fields such as dermatology, plastic surgery and cosmetic industries.

Acknowledgements This work was supported in part by Grants from New Energy and Industrial Technology Development Organization (06001905-0), Grants-in-Aid for Scientific Research (Scientific Research (B) 19300179) from the Japan Society for the Promotion of Science and Sendai Advanced Preventive Health Care Services Cluster from the Ministry of Education, Culture, Sports, Science and Technology.

References

1. Saijo, Y., Tanaka, M., Okawai, H., Dunn, F.: The ultrasonic properties of gastric cancer tissues obtained with a scanning acoustic microscope system. Ultrasound Med. Biol. **17**(9), 709–714 (1991)
2. Saijo, Y., Tanaka, M., Okawai, H., Sasaki, H., Nitta, S., Dunn, F.: Ultrasonic tissue characterization of infarcted myocardium by scanning acoustic microscopy. Ultrasound Med. Biol. **23**(1), 77–85 (1997)
3. Saijo, Y., Sasaki, H., Sato, M., Nitta, S., Tanaka, M.: Visualization of human umbilical vein endothelial cells by acoustic microscopy. Ultrasonics **38**(1–9), 396–399 (2000)
4. Saijo, Y., Miyakawa, T., Sasaki, H., Tanaka, M., Nitta, S.: Acoustic properties of aortic aneurysm obtained with scanning acoustic microscopy. Ultrasonics **42**(1), 695–698 (2004)
5. Saijo, Y., Hozumi, N., Kobayashi, K., Okada, N., Santos Filho, E.D., Sasaki, H., Yambe, T., Tanaka, M.: Ultrasonic tissue characterization of atherosclerosis by a speed-of-sound microscanning system. IEEE Trans. Ultrason. Ferroelect. Freq. Contr. **54**(8), 1571–1577 (2007)
6. Gambichler, T., Moussa, G., Sand, M., Sand, D., Altmeyer, P., Hoffmann, K.; Applications of optical coherence tomography in dermatology. J. Dermatol. Sci. **40**(2), 85–94 (2005)
7. El Gammal, S., El Gammal, C., Kaspar, K., Pieck, C., Altmeyer, P., Vogt, M., Ermert, H.: Sonography of the skin at 100 MHz enables in vivo visualization of stratum corneum and viable epidermis in palmar skin and psoriatic plaques. J. Invest. Dermatol. **113**(5), 821–829 (1999)
8. Vogt, M., Ermert, H.; In vivo ultrasound biomicroscopy of skin: spectral system characteristics and inverse filtering optimization. IEEE Trans. Ultrason. Ferroelect. Freq. Contr. **54**(8), 1551–1559 (2007)

Technique for Visualization of Anisotropy of Biomedical Tissue by Shear Wave Acoustic Microscopy

B.R. Tittmann, C. Miyasaka, E.Y. Maeva, and R.Gr. Maev

Abstract The motivation for this work is the improvement in discrimination between anomalous biological tissue vis-à-vis normal tissue. When ultrasonically visualizing tissue surrounding a cancerous portion it is useful for medical diagnosis when the portion has a different contrast in the image. The cancer tends to grow with its own direction typically different from normal tissue. Therefore, if we could ultrasonically visualize both isotropy and anisotropy of the tissue, the cancerous tissue may be discriminated from the normal tissue.

Keywords Acoustic microscopy · Anisotropy · Shear waves · Polarized shear wave transducer · Tissue · Cancer

1 Introduction

Our methodology is the use of an acoustic lens with a shear wave transducer [1] to visualize the anisotropy of the biological tissue. The center frequency of the acoustic lens transducer combination was 75 MHz. The shear polarized transducer was made of PZT and was deposited on the top of a fused quartz buffer rod. The shear wave propagated through the rod and was mode-converted into a longitudinal wave having a particular direction at the interface between the spherical recess located at the bottom of the rod and the coupling medium (i.e., de-ionized water). The acoustic beam that was excited in the water with the shear wave transducer has a directionality that allows for the measurement of anisotropy and makes it possible to measure variations in the surface wave velocity with a spatial resolution that is an order of magnitude better that achieved with a traditional lens. The polarized longitudinal wave is focused onto the tissue. The focal distance has been theoretically calculated for optimizing quality in acoustical image. The tissue includes a group of breast cancer cells. The tissue has been fixed and sliced with the thickness of 15 micrometer by a microtome, and deposited onto the optical slide glass, but not stained. Stained thinly sliced tissue was also prepared for indicating the group of cancer cells with optical microscopy.

B.R. Tittmann (✉)
The Pennsylvania State University, University Park, PA, USA
e-mail: brt4@psu.edu

M.P. André et al. (eds.), *Acoustical Imaging*, Acoustical Imaging 30,
DOI 10.1007/978-90-481-3255-3_14,

The acoustic lens with the shear polarized transducer was found to clearly be discriminated the cancer portion with high contrast in the acoustical image. The contrast was changed when changing the angle of the transducer. The results have been compared to images obtained by conventional acoustic lenses with different frequencies.

2 Technical Approach

Figure 1a is an optical image of an Eosin and Hematoxylin stained tissue section showing tumor cells in blue and fibrous stromal tissue in pink. The thickness of the tissue is 15 μm. Figure 1b is a magnified image of the cells. Higher power optical microscope examination of the breast tumor IS showing infiltrative growth of malignant cells, which are seen in irregular nest in the fibrous stroma. Frequent mitotic features, such as pleomorphic nuclei are indicative of a high grade carcinoma.

Figure 2a is an acoustic image (C-scan) obtained with a pulse-wave mode scanning acoustic microscope (SONIX). A conventional acoustic lens (250 MHz) was used to form the image. The specimen was sliced from the same tissue used for optical microscopy, and not stained. The comparison between the optical image (i.e., Fig. 1a), and the acoustic image shows that the acoustic image does not depict the cells so clearly. Therefore, the image is less useful for medical diagnosis. Figure 2b is the waveform of the reflected signal, and it's FFT. We used an input frequency of 250 MHz, but the output was found to be 56.64 MHz. Since the pulse wave is broadband, the high frequency components apparently were attenuated. Therefore, the image was actually formed with an operating frequency of 56.64 MHz, and not 250 MHz when gating the entire signal. The deterioration of the resolution was caused by this fact. It means that we need to use a different approach to acoustically form highly resolved images of the biological tissue for medical diagnosis.

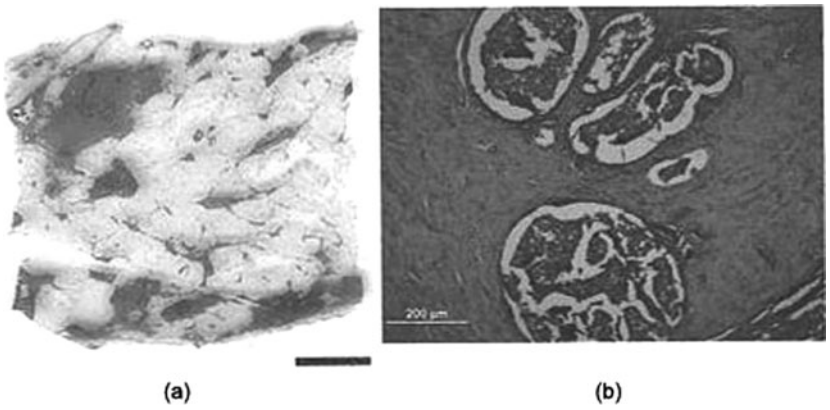

Fig. 1 Optical images; (**a**) The image was formed by the stereoscopic microscope (Olympus, SZX16). Bar is 4 mm; (**b**) The image was formed by the upright microscope (Olympus, BX61)

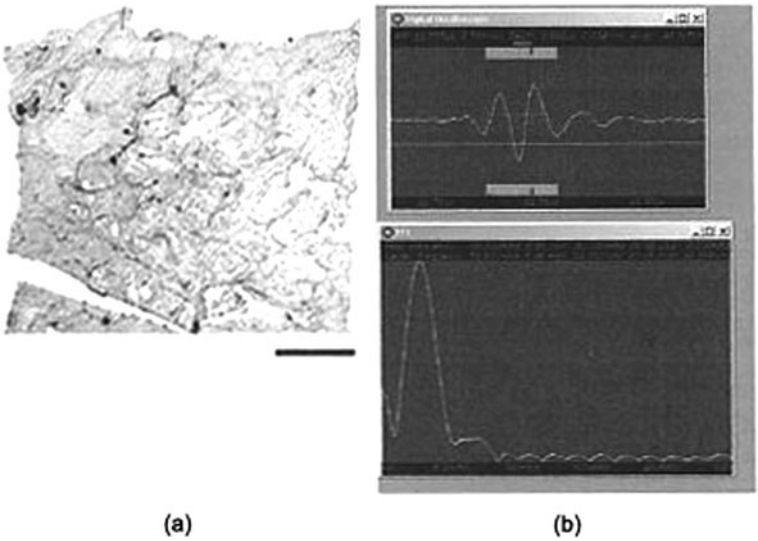

Fig. 2 (**a**) Acoustic image. Bar is 4 mm; (**b**) The upper part of the graph is a reflected signal from the specimen located on the slide glass, and lower part of the graph is the FFT of the reflected signal

3 Gate Positioning and Width Adjustment

Since the reflected signal (Fig. 2b upper part) is mixture of frequency components, the image quality may be improved by choosing the appropriate width of the gate and its position. Figure 3a is an acoustic image formed by adjusting its width and its position. Figure 3b is a magnified image of the portion including the cancer cells. Resolution and contrast in the images are improved. However, it takes several hours

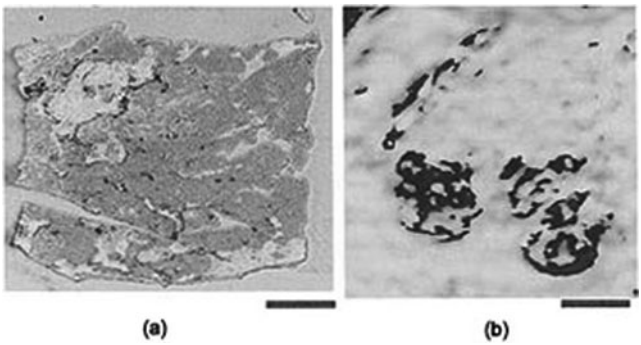

Fig. 3 (**a**) Acoustic image formed by adjusting gate width and position. The acoustic lens (SONIX, 250 MHz) was used. The bar is 4 mm; (**b**) the magnified image showing *arrow* in Fig. 3(**a**). The bar is 1 mm

to find the width and the position to form the image. Therefore, this method is not practical to use for medical diagnosis.

4 Shear Polarized Acoustic Lens

Figure 4 is a schematic diagram of a shear polarized acoustic lens. The acoustic lens comprises a buffer rod made of fused quartz, a shear polarized piezoelectric transducer (PZT) deposited on the rod. The opposite end of the rod has a spherical recess (i.e., a lens). Application of voltage across the transducer excites a shear polarized wave in the rod shown in Fig. 4 by the arrow. The wave travels downward to the lens. Mode conversion at the interface between the lens and the coupling medium excites the longitudinal wave. The wave is focused into the specimen via the coupling medium. The pattern of excitation of the longitudinal wave in the coupling medium is directional. Therefore, the anisotropy of a specimen can be visualized. The center frequency of the acoustic lens is 75 MHz.

5 Visualization of Anisotropy

Figure 5 shows images of the breast cancer tissue. The images were formed by the shear polarization acoustic lens. The specimen was rotated with three different angles (i.e., 45°, 90° and 180°). The contrast of the image was changed in accordance with the direction of anisotropy. The left image clearly shows the group of the cancer cells. Applying this method to form the C-scan image of the breast cancer tissue, we do not need to think about the gate width and the gate position. Further, we do not need to care about the decrease in the frequency of the pulse wave due to attenuation.

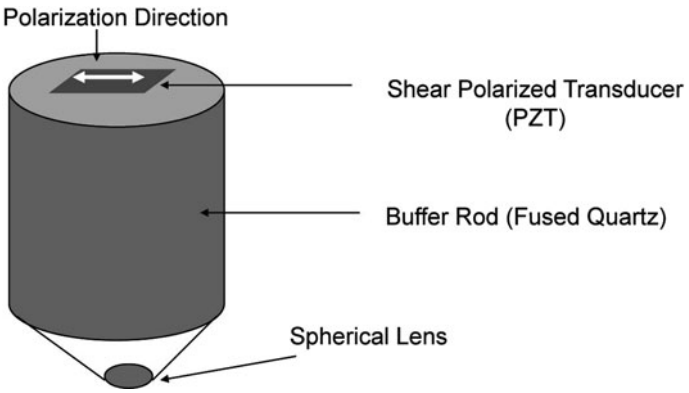

Fig. 4 Schematic diagram of a shear polarized acoustic lens

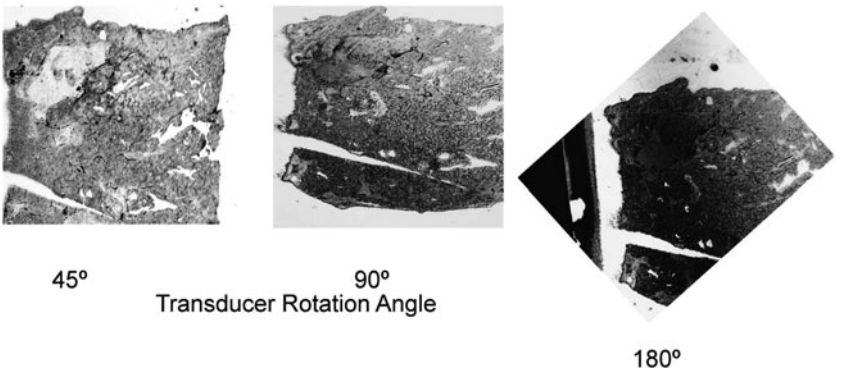

Fig. 5 Visualization of anisotropy of breast cancer tissue. The bar is 4 mm

6 Conclusion

When ultrasonically visualizing tissue surrounding a cancerous portion it is useful for medical diagnosis when the portion has a different contrast in the image. The cancer tends to grow with its own direction typically different from normal tissue. Therefore, if we could ultrasonically visualize both isotropy and anisotropy of the tissue, the cancerous tissue may be discriminated from the normal tissue.

We showed that a spherical acoustic lens with the shear polarization transducer (SPT) can visualize anisotropy of a biological tissue. The acoustic lens with the shear polarized transducer was found to clearly discriminate the cancer portion with high contrast in the acoustical image. The contrast was changed when changing the angle of the transducer. The results have been compared to images obtained by conventional acoustic lenses with different frequencies.

The high contrast obtained with the SPT gives positions of cancer cells within the tissue for use in medical diagnosis.

References

1. Khuri-Yakub, B.T., Chou, C.-H.: Acoustic microscope lenses with shear wave transducers. IEEE Proceedings of Ultrasonics Symposium, 741–744 (1986)
2. Ebert, A., Tittmann, B.R., Du, J., Scheuchenzuber, W.: Technique for rapid in vitro single-cell elastography. Ultrasound Med. Biol. **32**(11), 1687–1702 (2006)
3. Tittmann, B.R., Miyasaka, C., Mastro, A.M., Mercer, R.R.: Study of cellular adhesion with scanning acoustic microscopy. IEEE Trans. Ultrason. Ferroelect. Freq. Contr. **54**(8), 1502–1513 (2007)
4. Maeva, E., Severin, F., Miyasaka, C., Tittmann, B.R., Maev, R.Gr.: Acoustic imaging of thick biological tissue. IEEE Trans. Ultrason. Ferroelect. Freq. Contr. **56**(7), 1352–1358 (2009)

High Frequency Ultrasound Imaging of Cartilage-Bone Complex

Y. Hagiwara, Y. Saijo, A. Ando, K. Kobayashi, A. Tanaka, N. Hozumi, K. Hatori, and E. Itoi

Abstract High frequency ultrasound microscope with central frequency of 100 MHz was developed. The system was capable of (1) conventional C-mode acoustic microscope imaging of thinly sliced tissue, (2) ultrasound impedance imaging of the surface of *in vitro* thick tissue and (3) 3D ultrasound imaging of inside of the *in vitro* tissue. In the present study, cylindrical cartilage-bone unit specimens were removed from rat knee joints and evaluated with the equipment. The resolution was enough to visualize the articular cartilage surface morphology and the subchondral bone. Compared with histological sections observed by optical microscope, it can also differentiate the non-calcified zone and calcified zone of the articular cartilage. High frequency ultrasound microscope will provide important information of the structural changes of the articular cartilage.

Keywords Ultrasound · Articular cartilage · Subchondral bone · 3-D imaging · Ultrasound microscopy · Osteoarthritis

1 Introduction

Osteoarthritis (OA) has been a prevalent musculoskeletal disease causing pain, disability and stiffness [1]. Evaluation of the articular cartilage in OA is quite important to make treatment strategies. Histological evaluation using samples from patients or animals is the gold standard to precisely assess a degree of the articular cartilage degeneration. Non-invasive procedures to evaluate the articular cartilage, such as computed tomography and magnetic resonance imaging (MRI), have been developed but they have some drawbacks regarding high cost and limited accessibility. Ultrasonography (US) is also a non-invasive and inexpensive method widely accepted in daily clinical use. However, because of low central frequency in ordinary equipment, its resolution for evaluating the articular cartilage was not sufficient to supersede a histological examination. The purpose of the present study was to determine how useful our newly developed high frequency ultrasound imaging system was in evaluating the articular cartilage-bone complex from a matured rat knees in comparison with the histological evaluation.

Y. Hagiwara (✉)
Department of Orthopaedic Surgery, Tohoku University School of Medicine, Japan

M.P. André et al. (eds.), *Acoustical Imaging*, Acoustical Imaging 30,
DOI 10.1007/978-90-481-3255-3_15,

2 Materials and Methods

2.1 Animals

The protocol for this experiment was approved by the Animal Research Committee of Tohoku University. Three adult male Sprague-Dawley rats (CLEA Japan Inc., Tokyo, Japan) weighing from 500 to 540 g were used. After administration of an overdose of sodium pentobarbital, the capsule of the knee was cut with a surgical knife and the joint was opened. Bilateral menisci and peri-articular tissues were resected.

2.2 Tissue Preparation

A cartilage-bone complex (3 mm in diameter) was obtained from the medial mid-condylar regions of the tibia with a cylindrical bar (Trephine Bur, Technika Inc., Tokyo, Japan). The specimens were immediately immersed in a saline at room temperature before scanning with high frequency ultrasound microscope (HFUM). After the scanning with HFUM, the specimens were immersed in 4% paraformaldehyde in 0.1 M phosphate-buffer, pH 7.4 overnight at 4 °C. The fixed specimens were then decalcified in 10% EDTA in 0.01 M phosphate-buffer, pH 7.4 for 1 week at 4 °C. After dehydration through a graded series of ethanol solutions, the specimens were embedded in paraffin. The embedded tissue was cut into 5-μm sagital sections from the medial to the lateral side of the joint. The serial sections, stained by hematoxylin and eosin, were prepared for histological evaluation. The optical and ultrasound images were compared to ensure morphological congruence.

2.3 High Frequency Ultrasound Microscope

2.3.1 System Setup

The schematic illustration of HFUM was shown in Fig. 1. An electric impulse was generated by a high speed switching semiconductor. The start of the pulse was within 400 ps, the pulse width was 2 ns, and the pulse voltage was 40 V. The electric pulse was used to excite a PVDF transducer with the central frequency of 100 MHz. The ultrasound spectrum of the reflected ultrasound was broad enough to cover 50–160 MHz (-6dB). The reflections from the tissue was received by the transducer and were introduced into a Windows-based PC (Pentium D, 3.0 GHz, 2 GB RAM, 250 GB HDD) via a high-speed A/D converter (Acqiris DP210, Geneva, Switzerland). The frequency range covered was up to 500 MHz, and the sampling rate was 2 GS/s. Eight pulse echo sequences were averaged for each scan point in order to increase the signal-to-noise-ratio. The transducer was mounted on an X-Y stage with a microcomputer board that was driven by the PC through RS232C. The Both X-scan and Y-scan were driven by linear servo motors.

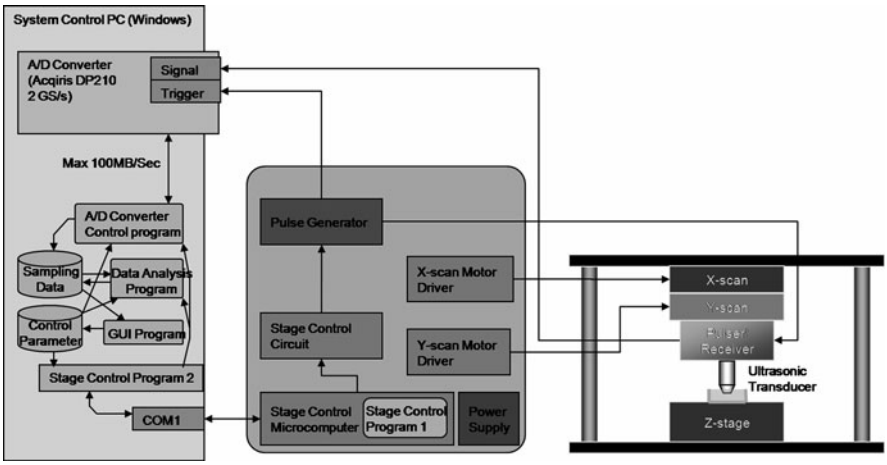

Fig. 1 Schematic illustration of high frequency ultrasound microscope

2.3.2 Transducer

Because the ultrasound should be penetrated deeply into the tissue, a PVDF transducer with the diameter of 2.4 mm and the focal length of 3.2 mm was fabricated (Fig. 2).

2.3.3 Signal Processing

RF signal of each scanning line was converted to B-mode image (*x*-scan with *z*-axis depth) by a conventional image processing algorithm. The scan area was 2.4 mm × 3.0 mm with 300 × 4,000 sampling points. The *y*-scan interval was available with 8 / 16 / 24 / 64-micron steps to obtain 3D data set.

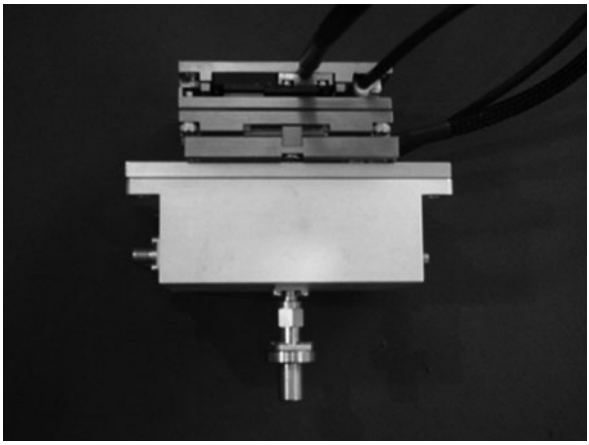

Fig. 2 Appearance of PVDF transducer

3D image was reconstructed by sequential B-mode images with the intervals of 8-micron step using specially developed 3D image software.

3 Results

3.1 B-Mode Image

The resolution was enough to visualize surface morphology of the articular cartilage and the subchondral bone. Compared with histological sections observed by optical microscope, the intensity distribution within the articular cartilage corresponded well with the non-calcified and calcified zone (Fig. 3).

3.2 3D-Reconstruction Image

HFUM provides microscopic surface morphology of the articular cartilage (Fig. 4).

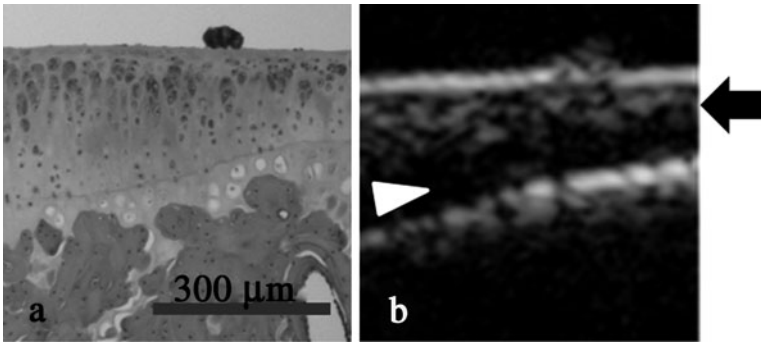

Fig. 3 Comparison of optical image with stored HFUM image. (**a**) hematoxylin and eosin stain. (**b**) B-mode image. *Arrow*: non-calcified zone. *Arrow heads*: calcified zone

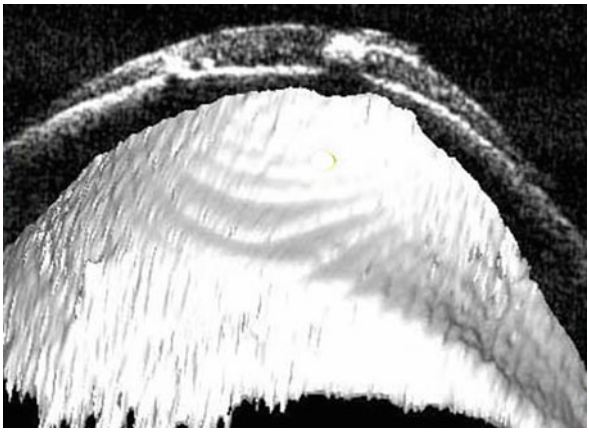

Fig. 4 3D-reconstruction image of the articular cartilage

4 Discussion

OA has been a prevalent musculoskeletal disease usually causing pain and disability [2]. Radiography is a frequently used image modality evaluating joint space narrowing [3]. However, the degree of joint space narrowing does not correlate with clinical symptoms. Arthroscopy is a direct approach to assess cartilage lesions but it is an invasive procedure.

Non-invasive approaches to evaluate the articular cartilage are computed tomography (CT), MRI and US [4]. However, CT cannot depict the articular cartilage very well. Though MRI was shown to detect glycosaminoglycan content of the articular cartilage recently [5], it has some drawbacks regarding high cost and limited accessibility. US is also a non-invasive and inexpensive method in daily clinical use. However, because of low central frequency in ordinary equipment, its resolution for evaluating the articular cartilage was not enough to distinguish its structure [1, 2].

Acoustic microscopy for medicine and biology has been developed for more than 20 years at Tohoku University [6–11]. High frequency ultrasound is suitable for non-invasive evaluation of tissues because it can obtain both morphological and biomechanical information [12]. The group lead by Foster et al., has already commercialized high frequency (40–60 MHz) B-mode imaging device as ultrasound biomicroscope for animal experiment [2]. However, they assess morphology or defect of the articular cartilage. In the present study, specially developed HFUM can distinguish the non-calcified and calcified zone of the articular cartilage. This is the first report of evaluating structural differences of the articular cartilage. Further, 3D-reconstruction image can provide useful information of congruity of the articular cartilage.

HFUM has potential to evaluate *in-vivo* imaging of early lesions of OA and monitoring of the disease.

References

1. Tsai, C.Y., Lee, C.L., Chai, C.Y., Chen, C.H., Su, J.Y., Huang, H.T., Huang, M.H.: The validity of in vitro ultrasonographic grading of osteoarthritic femoral condylar cartilage–a comparison with histologic grading. Osteoarthritis Cartilage **15**, 245–250 (2007)
2. Spriet, M.P., Girard, C.A., Foster, S.F., Harasiewicz, K., Holdsworth, D.W., Laverty, S.: Validation of a 40 MHz B-scan ultrasound biomicroscope for the evaluation of osteoarthritis lesions in an animal model. Osteoarthritis Cartilage **13**, 171–179 (2005)
3. Mazzuca, S.A., Brandt, K.D., Katz, B.P.: Is conventional radiography suitable for evaluation of a disease-modifying drug in patients with knee osteoarthritis?' Osteoarthritis Cartilage **5**, 217–226 (1997)
4. Martel, W., Adler, R.S., Chan, K., Niklason, L., Helvie, M.A., Jonsson, K.; Overview: new methods in imaging osteoarthritis. J. Rheumatol. **18**(Suppl 27), 32–37 (1991)
5. Peterfy, C.G., Schneider, E., Nevitt, M.: The osteoarthritis initiative: report on the design rationale for the magnetic resonance imaging protocol for the knee. Osteoarthritis Cartilage. **16**, 1433–1441 (2008)
6. Tanaka, M., Okawai, H., Chubachi, N., Kushibiki, J., Sannomiya, T. Propagation properties of ultrasound in acoustic microscopy through a double-layered specimen consisting of thin biological tissue and its holder. Jpn. J. Appl. Phy. **23**, 197–199 (1984)

7. Saijo, Y., Tanaka, M., Okawai, H., Dun, F.: The ultrasonic properties of gastric cancer tissues obtained with a scanning acoustic microscope system. Ultrasound Med. Biol. **17**, 709–714 (1991)
8. Sasaki, H., Tanaka, M., Saijo, Y., Okawai, H., Terasawa, Y., Nitta, S., Suzuki, K.: Ultrasonic tissue characterization of renal cell carcinoma tissue. Nephron **74**, 125–130 (1996)
9. Saijo, Y., Sasaki, H., Sato, M., Nitta, S., Tanaka, M.: Visualization of human umbilical vein endothelial cells by acoustic microscopy. Ultrasonics **38**, 396–399 (2000)
10. Hozumi, N., Yamashita, R., Lee, C.K., Nagao, M., Kobayashi, K., Saijo, Y., Tanaka, M., Tanaka, N., Ohtsuki, S.: Time-frequency analysis driven ultrasonic microscopy for biological tissue characterization. Ultrasonics **42**, 717–722 (2004)
11. Hagiwara, Y., Saijo, Y., Ando, A., Chimoto, E., Suda, H., Onoda, Y., Itoi, E.: Ultrasonic intensity microscopy for imaging of living cells. Ultrasonics **49**, 386–388 (2009)
12. Saijo, Y., Kobayashi, K., Okada, N., Hozumi, N., Hagiwara, Y., Tanaka, A., Iwamoto, T.: High frequency ultrasound imaging of surface and subsurface structures of fingerprints. Conf. Proc. IEEE Eng. Med. Biol. Soc. **1**, 2173–2176 (2008)

Ultra-High Resolution Thin Film Thickness Delineation Using Reflection Phase-Sensitive Acoustic Microscopy

E.A. Mohamed, A. Kamanyi, M. von Buttlar, R. Wannemacher, K. Hillmann, W. Ngwa, and W. Grill

Abstract The acoustic phase and magnitude data of a planar homogenous sample of smoothly varying thickness deposited on a glass substrate can best be represented by a polar plot. In this work, the method is extended to achieve topographical mapping of thin films with a height resolution beyond the diffraction limit of optical confocal microscopy. The radial dependence of the polar graph describes the regression of the magnitude of the reflected signal due to the attenuation. The later increases with the gradual increase of the thickness and is additionally influenced by interference effects. The angular dependence of the polar plot reveals the rotation of the phase angle of the signal due to reflection from different thicknesses of the sample. Model calculations are employed, and input values are varied until an optimum agreement with the measurement data points is achieved and the primary acoustic properties (speed of longitudinally polarized ultrasound, mechanical density of the sample and the attenuation within the material) are obtained. The model manifests the variation of the magnitude and phase of the reflected signal due to variation in thickness. After optimum adjustment of the model parameters, the thickness corresponding to each measured value of the reflectivity is obtained.

Keywords Phase-sensitive · Acoustic microscopy · Polar · Height profile · Thin film thickness · Ultraresolution

1 Introduction

Phase-sensitive acoustic microscopy has long been known as a high- resolution non-contacting height profiling tool [1, 2]. The topographical mapping is mainly based on measuring the phase of the returned echo from the reflecting surface. Liang et al. [3] applied a topographic mapping technique by detecting the large acoustic path difference between the reflected signal of the focused beam and that of the ring beam which is transmitted and received through the flat edge of the acoustic lens. This method is direct and accurate regarding application to thick homogenous

E.A. Mohamed (✉)
Institute of Experimental Physics II, University of Leipzig, Leipzig D-04103, Germany

M.P. André et al. (eds.), *Acoustical Imaging*, Acoustical Imaging 30,
DOI 10.1007/978-90-481-3255-3_16,

objects. With thin films this technique suffers, however, from the additional contribution to the phase change gained from the complex reflection coefficients of the two interfaces involved. Some other previous studies on film thickness relied on the V(z) method. Hänel [1] measured the height profile of a thin film sample. They measured the perturbation in the Rayleigh velocity using out of focus measurements with large defocusing sufficient for substantial time difference between the on-axis reflection signal and the Rayleigh wave path reflection signal. The relative phase change was directly related to the change in surface wave velocity caused by the thickness variation of the thin film. This method suffered from the interferences between the Rayleigh and the on-axis reflections. Film thickness on isotropic substrates was measured by comparing the measured Rayleigh velocity with the calculated one [4]. Thickness of films on an anisotropic substrate was estimated [5] by V(z), as obtained by a lens with an assumed point focus, under the assumption that the main factor affecting the V(z) function is the average Rayleigh wave velocity. The film thickness can also be measured [6] by comparing the calculated reflectance function obtained by inverse Fourier transform of V(z) with the reflectance function derived from the V(z) obtained with a point focus lens.

In this work we demonstrate a method that provides height profiling of deposited samples using the polar representation method in an extension to earlier works [7, 8] where the polar method was used to determine the mechanical properties.

For the data obtained by 1.2 GHz reflection mode phase-sensitive acoustic microscopy, the contrast in magnitude and phase depends on the properties of the substrate, the coupling fluid and on the elastic properties of the sample under observation. For homogenous and sufficiently planar samples of smoothly varying thickness deposited on a planar substrate, the magnitude and phase contrast will depend only on the actual thickness.

If the magnitude and phase data are plotted in polar coordinates, such that the phase data corresponds to the angular coordinate and the magnitude data corresponds to the radial part, the magnitude and phase data gained from the acoustic image will be plotted in a single curve, with the data points distributed spatially depending on the variation of the thickness of the material. The signature of the deposited object can be fitted based on a model that simulates propagation of sound in the various media: the coupling fluid, the sample and the substrate resulting in the determination of sample properties with a resolution of less than 1% [7]. The thickness corresponding to spatially distributed points can inversely be mapped from the adjustment of the model parameters for an optimum fit to the measured data as will be presented.

2 Theory

The model employed in the calculations uses the approach outlined by Liang et al. [9]. Since in this work imaging was always carried out in focus, the variation of complex output voltage V dependence on the defocusing distance z, V(z), has

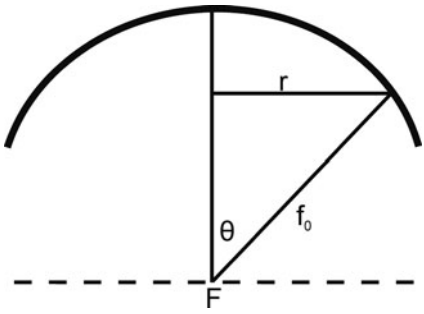

Fig. 1 Schematic of a focusing acoustic lens. F is the focal point, f_0 is the focal distance, θ is the angle of a ray in the coupling medium to the lens axis and r is the distance from the lens surface to the axis

been replaced by the variation of the thickness, V(d), in a similar way as used by Reinholdtsen et al. [10].

$$V(d) = \int P^2\left(\frac{r}{f_0}\right) R\left(\frac{r}{f_0}, d\right) e^{-i2kd\sqrt{1-\left(\frac{r}{f_0}\right)^2}} \frac{r}{\sqrt{1-\left(\frac{r}{f_0}\right)^2}} dr \qquad (1)$$

here it is assumed that the focus of the lens is set to the interface between the sample and the substrate. The transmission through the spherical surface of the lens is described by a pupil function $P(r/f_0)$ which is assumed to be of Gaussian form and takes into account the non-uniform excitation of the transducer and any aberration effects. $R(r/f_0, d)$ is the thickness-dependent reflection coefficient of the studied layer and $(r/f_0) = (k_r/k)$, where k_r is the lateral component of the wave vector k in the coupling fluid and the variables r and f_0 are described in Fig. 1.

The layer reflection coefficient which was plugged in Equation (1) has been calculated as the infinite sum of a geometrical progression that is built from the reflection from the top of the layer and multiple contributions from the transmission through the surface of the layer, reflection from the sample-substrate interface and transmission back into the coupling fluid [11] (Fig. 2 and Equations (2) and (3)) within a wedge-shaped sample. Lateral shifts and related delayed signal arrival

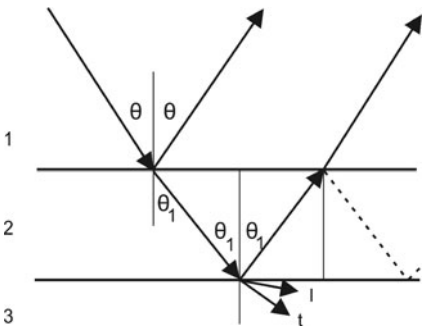

Fig. 2 Reflections at the sample-coupling fluid and the sample–substrate interfaces, transmission through both interfaces, and multiple reflections within the sample are shown. l and t denotes longitudinal and transverse waves in the solid substrate respectively. The substrate is assumed to be isotropic. (1) denotes the coupling fluid, (2) the sample and (3) the substrate

time were ignored because tone bursts long compared to the round trip time in the layer were employed in the experiments. In our model, lateral walk-off for tilted incidence is neglected. This is reasonable in cases where at least one of the involved reflection factors is sufficiently low, such as for the observed sample. Moreover, the inhomogeneity of waves in the absorbing layer (Re(k) not being parallel to Im(k)) has been neglected here.

2.1 Calculation of the Total Reflection Coefficient of the Sample

The approximation as a locally plane parallel sample is used [12], which is reasonable for soft materials with acoustic longitudinal velocity close to that of water as the coupling medium and vanishing shear velocity, as it may be assumed, for the sample under study [13].

The total reflection R (θ, d) results from summing up all waves as:

$$R(\theta,d) = r_{12}(\theta) + w(\theta)r_{23}(\theta_1)\hat{w}(\theta_1)e^{2ik_{2n}d} + w(\theta)r_{23}^2(\theta_1)\hat{w}(\theta_1)\left(e^{2ik_{2n}d}\right)^2\hat{r}_{12}(\theta_1) + w(\theta)r_{23}^3(\theta_1)\hat{w}(\theta_1)\left(e^{2ik_{2n}d}\right)^3\hat{r}_{12}^2(\theta_1) + \ldots\ldots\ldots \quad (2)$$

here, $r_{12}(\theta)$ is the reflection coefficient corresponding to the coupling fluid-sample interface, $r_{23}(\theta)$ is the reflection coefficient corresponding to the sample-substrate-interface, $w(\theta)$ is the transmission coefficient of the coupling fluid-sample interface. $\hat{w}(\theta)$ is the reverse transmission coefficient, and $\hat{r}_{12}(\theta_1)$ is the reflection coefficient of the coupling fluid-sample interface for a beam incident from within the sample, k_{2n} represents the component of the wave vector in the sample normal to the interface, and d is the local sample thickness. The total reflection coefficient is obtained as the infinite sum of the geometrical progression build from the layer [11]:

$$R(\theta,d) = r_{12}(\theta) + \frac{(1 - r_{12}^2(\theta))r_{23}(\theta_1)e^{2ik_{2n}d}}{1 + r_{12}(\theta_1)r_{23}(\theta_1)e^{2ik_{2n}d}} \quad (3)$$

2.2 Determination of the Thickness

The model calculations simulate the reflection from a thin film that has a thickness varying from a minimum value d_{min} to a maximum value d_{max} in n_z steps of thickness intervals d_s such that:

$$d_s = \frac{(d_{max} - d_{min})}{n_z - 1} \quad (4)$$

Inputs to the software are trial values for the parameters of the sample (density, attenuation and speed of longitudinal sound wave) supplied iteratively, until the best agreement between the calculated and measured data is achieved. The thickness

corresponding to a calculated value of the complex reflection coefficient is ascribed to the nearest measured point in the polar plot, such that the distance between the measured and calculated points, in the polar graph, t as calculated by Equation (5) assumes a minimum.

$$t = \sqrt{(X_c - X_m)^2 + (Y_c - Y_m)^2} \tag{5}$$

where (X_m, Y_m) are the Cartesian coordinates of the measured value and (X_c, Y_c) corresponds to the coordinates of the nearest calculated value, polar co-ordinates converted into Cartesian coordinates (X_c, X_m) denotes the real parts of the complex numbers and (Y_c, Y_m) denotes the imaginary parts.

The definition of the distance (t) is extended into a three-dimensional parameter space with the height as the third dimension using a tracking routine which takes the distance between the height of the current point and that of the subsequent adjacent point as the third dimension such that,

$$t = \sqrt{(X_c - X_m)^2 + (Y_c - Y_m)^2 + N(h_l - h)^2} \tag{6}$$

where h is the thickness of the current point and h_l is the thickness of the preceding point. As the 2D (x, y) coordinates of each point are the Cartesian coordinates and the third coordinate is derived by the height in micrometers, the term (h_l-h) is multiplied by an empirical correction factor (N) which is in the order of $10^{12}/\mu m$ and is chosen such that the third term in Equation (6) gains a weight comparable to the first two terms. In this way the calculated value with the smallest distance in (X, Y) space and the smallest distance to the previously determined height is found.

3 Materials and Methods

The thin chitosan film was prepared from an acetic acid based chitosan solution and imaged by a phase-sensitive acoustic microscope in reflection at a working frequency of 1.2 GHz. Materials, sample preparation, and the detection scheme were described in a preceding publication [7].

4 Results and Discussion

An acoustic image of a thin film of chitosan deposited on a glass substrate is depicted in Fig. 3. The focus was adjusted to the surface of the substrate. The signal reflected from the glass substrate-coupling fluid interface has maximum magnitude. The signal from bare glass without a deposited layer serves as reference for the phase. The signal reflected from areas where the substrate is covered by the thin film derives mostly from reflections from the interface between the substrate and the sample. A signal of lesser magnitude results from reflections from the top of the chitosan film sample. Within the film, the signal suffers attenuation due to scattering

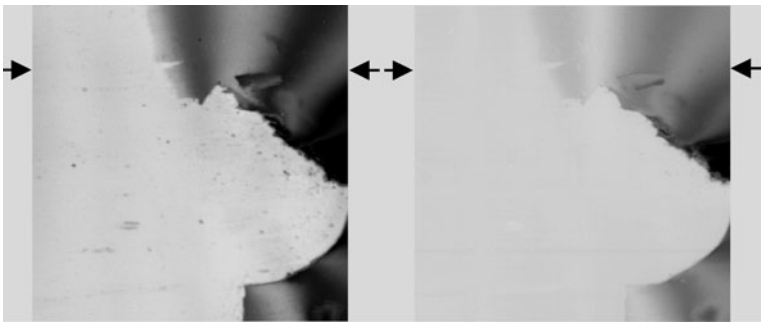

Fig. 3 Images in magnitude contrast (*Left*, black representing zero signal) and phase contrast (*right*, full gray scale of the image representing 2π) of a chitosan layer of variable thickness on a glass substrate. The data has been evaluated for the line between the arrows and for the area above that line

and absorption by the material. The attenuation increases with increasing thickness. The overall detected reflected signal is a result of interference and therefore the amplitude strongly depends on the phases of the reflected waves. The interference patterns can be recognized in the images (Fig. 3) where alternating dark and bright bands are obvious.

The experimental magnitude and phase data taken for each pixel of the acoustic image along the line between the arrows as indicated in the images and for each pixel within the area above the line were plotted in a polar diagram. The model described above is applied. Manual adjustments for the relevant parameters were applied for a thickness varying from 0 (at bare glass) to maximum value (corresponds to the largest thickness investigated of the sample), until an optimum fit to the data was obtained as shown in Fig. 4. By this procedure the speed and attenuation of sound and the density of the sample were determined. Different to earlier published results [7], existence of a residual layer of 0.06 μm was assumed and an empirical fitting was applied. This resulted in a better fitting of the measured data in the polar graph where the signal is influenced by interferences. Speed of sound

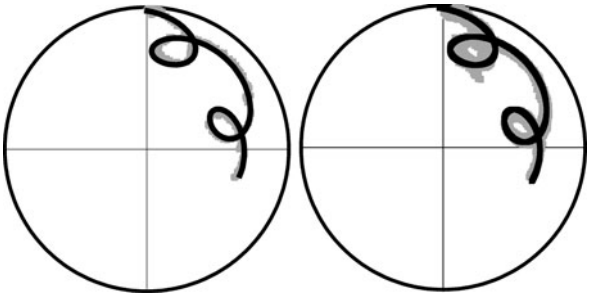

Fig. 4 Polar diagrams of the magnitude and phase of the reflected signal for data taken along the line between the arrows as indicated in the chitosan images (*left*) and from the area above the line between the arrows (*right*). Experimental values are in gray squares and the *black solid line* represents the fit of the experimental data

and attenuation coefficient obtained in this way differ by about 1% and 18% from the speed and attenuation values (respectively), obtained for the same sample previously [7]. The thickness of the sample for each measured value is obtained from the thickness used for calculation of the closest fitting value.

Figure 5 shows the magnitude and phase in response to variation in the thickness as calculated by the model for the line enclosed between the arrows as indicated in Fig. 3.

The oscillations in the magnitude (Fig. 5, left) manifest the interferences and are represented in the polar plots by the two rotations. Except for interferences, the power of the reflected signal decreases exponentially with the gradual increasing thickness following Lambert-Beer's law:

$$I_d = I_0 e^{-\alpha 2d} \tag{7}$$

here, I_0 is the intensity of the acoustic signal at depth zero and I_d is the intensity of the ultrasound signal after distance, or thickness (d) in the medium and α is the extinction coefficient or attenuation coefficient given in (Nepers/cm) or alternatively in dB/cm [14]. The measured phase changes, even at the maximum film thickness, correspond to less than one complete rotation (Fig. 5, right). This indicates that there is no step in height that could reach a quarter of the wavelength of the acoustic wave, which could lead to problems in the fitting procedure.

The height profile of the chitosan thin film for the line corresponding to the data used to plot the polar graph in Fig. 4, left as calculated by the model is shown in Fig. 6, left and is compared to the thickness obtained by counting [15] interference fringes (Fig. 6, right). The applied method provides a continuous line profile of height whereas, the interference fringes method provides the height profile only at discrete points separated by an interference fringe.

The height profile was also calculated for the area (140 μm × 28.2 μm) above the arrows in the images in Fig. 3, in the same manner as done for the line data. The mapped height profile is represented by a gray scale so that each thickness value is

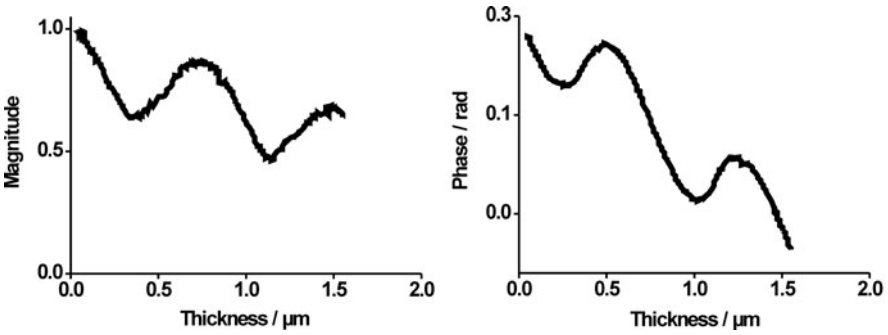

Fig. 5 The variation of the magnitude (*left*) and phase (*right*) of the reflected signal with the variation in the thickness of the reflecting sample

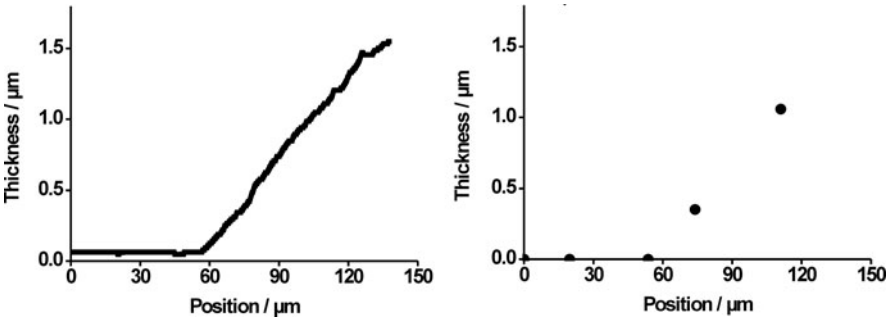

Fig. 6 Height profile of the chitosan film as calculated by the model (*left*) and as calculated by counting the interference fringes (*right*). The height profiles were plotted for same data used to plot the polar graph in Fig. 4, left

Fig. 7 Height as calculated by the model is mapped in gray scale for each point in the marked area in the images. The size of the image is 140 µm × 28.2 µm

assigned a certain gray scale level gradually from black at zero thickness to maximum brightness at maximum height (Fig. 7). A waterfall representation of the data of Fig. 7 is shown in Fig. 8. The distance t, (as defined in Equation (5)), between the measured and calculated data points is mapped in gray scale (Fig. 9), such that

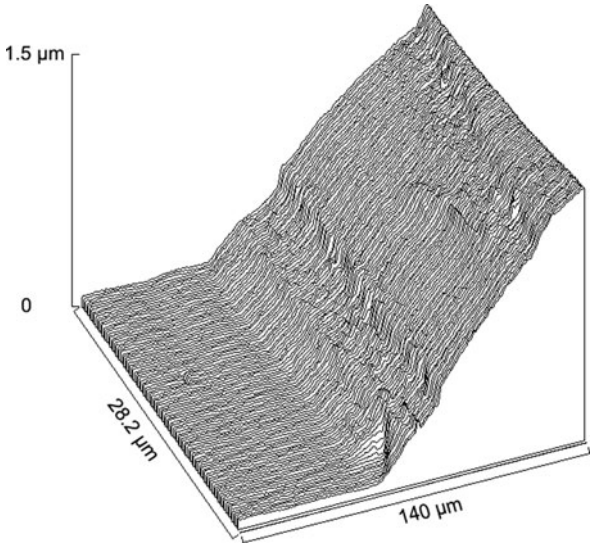

Fig. 8 Waterfall representation of the same area as in Fig. 7 with the height as calculated for each point

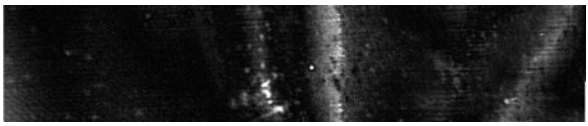

Fig. 9 Mapping of the distance t between the measured and calculated points (with the height as the third dimension). The highest brightness corresponds to the largest difference between the measured and calculated values

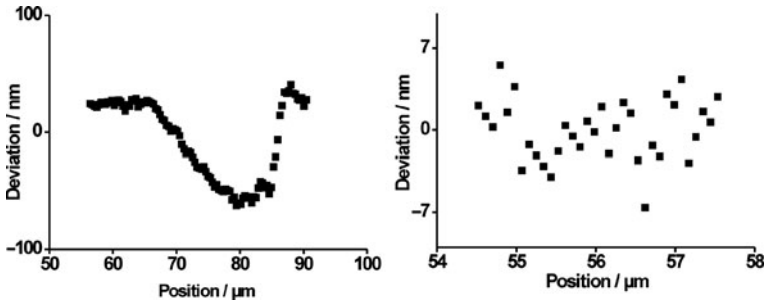

Fig. 10 Estimation of the systematic (*left*) and statistical (*right*) errors

black corresponds to the coincidence of calculated and measured points (full agreement) and brighter scale indicates gradual departure from perfect coincidence. The brightest points in Fig. 9 could be attributed to artifact in the chitosan thin film and areas of interferences which is not perfectly fitted.

The height profile of all of the parallel lines in Fig. 8 has fluctuations that could be attributed to artifacts in modeling where plane parallel sample was assumed. Possible sources of systematic errors could also be the lateral walk-off of the beam, which leads to a non-negligible phase error and to a tilt of the laterally displaced reflected beams in the lens, relative to the lens axis, and, therefore, to a partial cancellation of the contribution of the multiply reflected waves on the transducer.

The systematic error was evaluated from the deviation of calculated height values from an assumed and fitted linear rise (Fig. 10) to be 33 nm. For parts of the line where the systematic error defined in this way vanishes, the deviations from optimum linear fit is attributed to statistical errors, which were about 2.6 nm for the data taken a long a line of about 5 μm. This indicates that the resolution for height mapping as provided by the current method is higher than could be achieved by most of the available optical confocal microscopic techniques.

5 Conclusions

The described method is used to map the thickness variations of a chitosan film from few nanometers up to about 1.5 wavelengths (in water and at an acoustic frequency of 1.2 GHz) using phase sensitive acoustic microscopy, provided that the thickness

variation is smooth. The method uses both the phase and magnitude information, rather than using either alone. The height profile is obtained by the method with sub-Abbe resolution, beyond the diffraction limit, while the mechanical properties are simultaneously obtained.

References

1. Hänel, V.: Determination of sound velocity and thickness of thin samples by time-resolved acoustic microscopy. J. Appl. Phys. **84**, 668–670 (1998)
2. Liang, K., Bennett, S.D., Khuri-Yakub, B.: Precision measurement of Rayleigh wave velocity perturbation. Phys. Lett. **41**, 1124–1126 (1982)
3. Liang, K., Khuri-Yakub. B., Dennett, S., Kino, S.: Phase measurements in acoustic microscopy. *IEEE Ultrasonic Symposium*, 599–604 (1983)
4. Weglein, R.D.; Acoustic microscopy applied to SAW dispersion and film thickness measurement. IEEE Trans. Sonics Ultrason. **27**, 82–86 (1980)
5. Crean, G., Waintal, A.: Average Rayleigh-wave velocity of a computer simulated crystallographic plane. J. Appl. Cryst. **19**, 181–186 (1986)
6. Sasaki, Y., Endo, T., Yamagishi, T., Sakai, M.: Thickness measurement of a thin–film layer on an anisotropic substrate by phase-sensitive acoustic microscope. IEEE Trans. Sonics Ultrason. **39**, 638–642 (1992)
7. Ahmed Mohamed, E., Kamanyi, A., von Buttlar, M., Wannemacher, R., Hillmann, K., Ngwa, W., Grill, W.: Determination of mechanical properties of layered materials with vector contrast scanning acoustic microscopy by polar diagram image representation, *Proceedings of SPIE* **6935**, 69351Z-69351Z-8 (2008)
8. Hillmann, K., Grill, W., Bereiter-Hahn, J.: Determination of ultrasonic attenuation in small samples of solid material by scanning acoustic microscopy with phase contrast. J. Alloy. Comp. **151**, 211–212 (1994)
9. Liang, K., Kino, G., Khuri-Yakub, B.: Material characterization by the inversion of V(z). IEEE. Trans. Sonics Ultrason. **32**, 213–224 (1985)
10. Reinholdtsen, P., Chou, C-H., Khuri-Yakub, B.: Quantitative acoustic microscopy using amplitude and phase imaging. *IEEE Ultrasonic symposium*, pp. 807–811 (1987)
11. Brekhovskikh, L.: Waves in Layered Media, 2nd edn., pp. 5–46. Academic Press, INC, New York (1980)
12. Litniewski, J., Bereiter-Hahn, J.: Measurements of cells in culture by scanning acoustic microscopy. J. Microsc. **158**, 95–107 (1990)
13. Ngwa, W., Grill, W., Kundu, T.: Bio-soft-matter imaging and micrometrology by phase-sensitive ultrasonic microscopy. Proc. SPIE. **5394**, 263–272 (2004)
14. Cloostermans, M., Verhoef, W., Thijssen, J.: Generalized description and tracking of the frequency dependent attenuation of ultrasound in biological tissue. Ultrason. Imag. **7**, 133–141 (1985)
15. Kundu, T., Bereiter-Hahn, J., Karl, I.: Cell property determination from the acoustic microscope generated voltage versus frequency curves. Biophys. J. **78**, 2270–2279 (2000)

Signal Processing for Time-Lapse Cell Imaging with Vector-Contrast Scanning Acoustic Microscopy

M. von Buttlar, E.A. Mohamed, and W. Grill

Abstract Non-invasive and marker-free monitoring of living cells can be accomplished by vector contrast scanning acoustic microscopy. In this paper, the signal processing required for creating time-lapse movies of mesenchymal stem cells is discussed. This includes electronic signal processing, autofocusing and image processing. Prior to each recorded image the focusing transducer is moved away from the sample until no echo signal is received. This allows direct measurement of the offset vector caused by internal lens echoes. The offset vector can then be subtracted from the following vector-contrast image. For subsequent autofocusing the transducer is moved closer to the sample until the maximum of the signal in reflection is passed. The transducer position for the maximum reflected signal is determined by respective software and adjusted accordingly. Autofocusing is a requirement for tiled scans where a piezo-scanner and an automatic microscope stage are combined to increase the field of view. As there are typically thousands of images involved in a single movie, batch image processing routines are required. Customized plugins for ImageJ were developed to combine specialized functions for vector contrast data processing with standard image processing capabilities. The motility of a population of ovine mesenchymal stem cells was continuously recorded for 8 h. The detection scheme including experimental details is presented and applications including time-lapse imaging are demonstrated and discussed.

Keywords Phase-sensitive · Scanning acoustic microscopy · Cell imaging · Stem cells · Time-lapse movies · Autofocus · Vector-contrast · PSAM · Stem cells

1 Introduction

Scanning acoustic microscopy has been applied to biological samples and living cells soon after first systems were available [1]. The resolution at operating frequencies above 1 GHz is comparable to light microscopy and the acoustic contrast of cells, which is related to their mechanical properties, is well pronounced. The mechanical properties of cells are of substantial interest and respective differences

M. von Buttlar (✉)
Institute of Experimental Physics II, University of Leipzig, Leipzig D-04103, Germany

M.P. André et al. (eds.), *Acoustical Imaging*, Acoustical Imaging 30,
DOI 10.1007/978-90-481-3255-3_17,

between cell populations (for example cancer cells and healthy cells) have been described in the literature [2].

Acoustic microscopy is a non-contact and non-invasive method suitable for imaging and mechanical characterization of cells. Due to the pulsed operation, the average acoustic power to which observed cells are exposed during imaging is low, about 1 μW [3], and believed to be harmless for the cells [4]. Most of the other methods are invasive because the cells are either directly touched (for example by an AFM cantilever, A-Hassan et al. [5] or acted upon by means of beads attached to the cell membrane (magnetic twisting cytometry [6]. Optical stretching of cells in suspension is another newly developed method [7].

Several techniques for quantitative scanning acoustic microscopy of living cells have been developed, including time-resolved short pulse scanning acoustic microscopy [4], acoustic microscopy with frequency variation [8] or with variation of the focusing distance [9]. A summary of the relevant methods can be found in the literature [10].

The focus of this paper is on imaging living stem cells for several hours with a vector-contrast scanning acoustic microscope operating at a frequency of 1.2 GHz in reflection. Newly developed hardware and software reduce artifacts and automatically adjust the focus position, which is a prerequisite for time-lapse imaging. Vector-contrast scanning acoustic microscopy has the advantage of providing two contrasts in a single measurement: the magnitude of the echo signal, which relates to the extinction of the ultrasonic wave, and the phase, which relates to the time-of-flight (TOF) of the ultrasonic wave [3, 11].

2 Methods

2.1 Vector-Contrast Scanning Acoustic Microscope

The vector-contrast scanning acoustic microscope is operated in reflection with a Lemons/Quate type [12] focusing acoustic transducer (KSI, Germany, Type 525 002, 0.8–1.3 GHz operating frequency, 100° full opening angle). The transducer physically scans over the sample. Sinusoidal bursts with 60 oscillations at a mean frequency of 1.2 GHz are cut out from a sine wave generator and applied via a switch to the focusing transducer. The acoustic echo signal is converted back into an electrical signal by the transducer, amplified and the real- and imaginary signals $\mathrm{Re}(x, y, t)$ and $\mathrm{Im}(x, y, t)$ are determined from the RF signal. This is accomplished by mixing the echo signal with the sine and cosine signal outputs of the signal generator (quadrature demodulation). A Boxcar integrator averages the received echo signals over several burst repetitions (burst repetition rate: 900 kHz) and across the oscillations of each burst. The continuous output signals $\mathrm{Re}(x, y)$ and $\mathrm{Im}(x, y)$of the boxcar integrator are sampled by a two-channel data acquisition card which also controls the movement of the piezo scanner. Magnitude $M(x, y)$ and phase $\Phi(x, y)$

of the echo signal are calculated for each pixel position from the real and imaginary signals according to Equations (1–2).

$$M(x,y) = \sqrt{\mathrm{Re}(x,y)^2 + \mathrm{Im}(x,y)^2} \tag{1}$$

$$\Phi(x,y) = \tan^{-1}(\mathrm{Im}(x,y)/\,\mathrm{Re}(x,y)) \tag{2}$$

The conversion to polar coordinates described by Equation (2) requires additional processing steps to take the quadrant of the vector into account. More details can be found in Grill et al. [3] and [13].

2.2 Combination of Acoustic and Optical Microscopy

Several systems with combinations of acoustic microscopy and optical fluorescence [14], confocal laser scanning [15] or two-photon microscopy [16] have been described so far. For this work the acoustic microscope was attached to a commercially available confocal laser scanning microscope (LSM510 with an Axiovert 200 M inverted microscope, Zeiss, Germany).

A three axes piezo scanner (Tritor 400, piezosystem jena GmbH, Germany) with 400 µm scanning range in all dimensions was attached to the inverted microscope. By a mechanical tilting mechanism the piezo scanner with the attached focusing transducer can be removed from the Petri dish to allow access to the sample (Fig. 1). The alignment between the optical and acoustical images has a high repeatability with a standard deviation of 2.26 µm in the x axis and 1.21 µm in the y axis (optically determined by 53 consecutive cycles of opening and closing). The fixation to

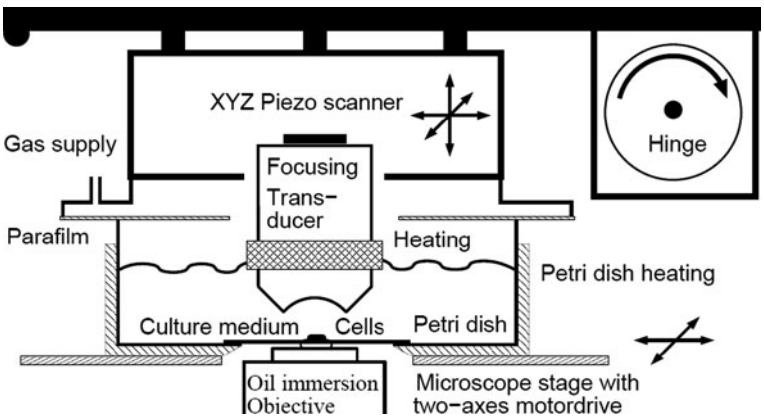

Fig. 1 System for simultaneous acoustical (*upper half*) and optical imaging (*lower half*) with live support chamber for cells (*central part*). The acoustic microscope is attached to an inverted microscope (not shown). It can be removed by tilting

the base of the microscope results in higher stability than in the previous construction described by Kamanyi et al. [15]. The phase signal is sensitive to vibration and therefore the microscope has been placed on a 2nd order active and passive vibration damping system. The live-support system for cells consists of separated heating systems for the acoustic lens and for the Petri dish. The temperature of the focusing transducer is controlled by an aluminum collar around the lens which is heated by resistance wire. The temperature is measured and regulated with a temperature controller (Lakeshore 330, Westerville, Ohio). The Petri dish fits into an aluminum holder whose temperature is controlled with a custom-designed computer controlled regulator. A cover glass (VWR International, Cat. 631-0177) is fitted into a hole cut in the bottom of a Petri dish to allow optical high-resolution microscopy. For providing a CO_2 and oxygen regulated atmosphere, a flexible plastic film (Parafilm, Menasha, WI, USA) is used to seal the atmosphere inside the chamber from the outside. The sealing film is attached to the housing of the piezo scanner and automatically seals the Petri dish when the scanner is operated. Pre-mixed gas can be filled into the chamber which is required for many live cell experiments. The live support system with the Petri dish is placed on the microscope stage. Wide range scanning with the motor driven 2D scanner of the optical microscope allows an extension of the field of view of the combined microscope by tiled scanning or the scanning of selected regions of interest.

2.3 Z Scan for Zero Correction and Autofocus

One problem encountered in phase-sensitive scanning acoustic microscopy is the offset vector caused by internal lens echoes [17]. It determines the origin of the complex plane used for quadrature detection and drifts of the offset vector can lead to erroneous reading of magnitude and phase values.

To solve this problem a zero correction procedure operated prior to the recording of each new image was introduced. The focusing transducer is moved more than 100 μm away from the sample to assure that no echo signal from the sample can be detected (Fig. 2). This corresponds to zero volts applied to the z-axis of the piezo scanner and takes less than 1 s. The remaining signal corresponds to the offset vector caused by internal lens echoes.

The vector is memorized (magnitude and phase) and subsequently subtracted from all measurement values. Changes of the mean frequency or the magnitude of the excitation burst signal also result in changes of the offset vector and can be compensated by the described method.

Drift of the distance between the focusing transducer and the sample is a common problem in time-lapse microscopy because it causes out-of-focus images. An autofocus procedure for acoustic microscopy was developed operating in two steps. First, the magnitude signal is recorded for a focal distance from $z = 80$ μm to $z = -10$ μm (Fig. 2 from $t = 1.2$ s to $t = 1.8$ s). Then, the z axis is positioned to the corresponding maximum of the recorded magnitude curve ($t = 1.6$ s in Fig. 2). In the second step the z position is modulated with a saw tooth wave and adjusted

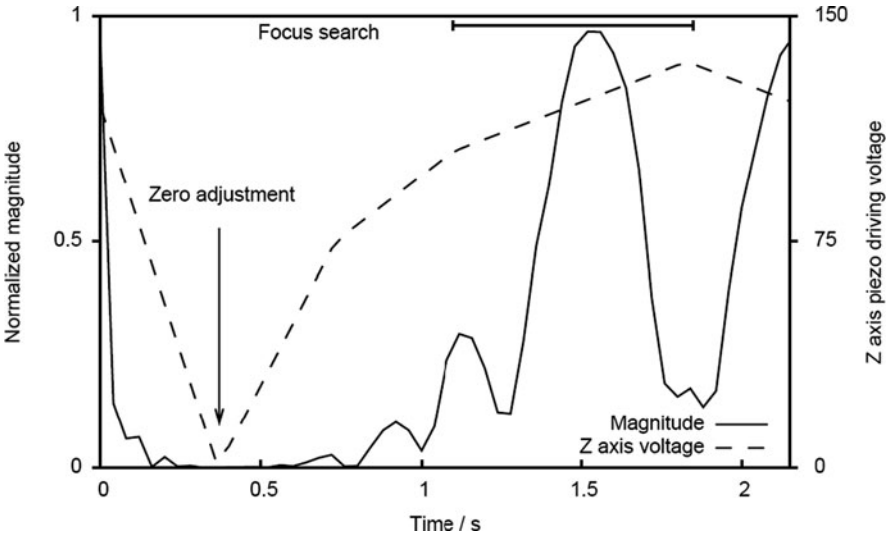

Fig. 2 Acoustic magnitude signal and the corresponding z-axis drive voltage which regulates the focal position during autofocusing. First the offset vector is measured at t = 0.4 s and then the optimal focus position is determined between t = 1.2 s and t = 1.8 s

to center the maximum of the measured curve. The fine adjustment procedure also takes the phase of the echo signal into account and adjusts the final focus position to a given phase value.

2.4 Image Processing

A time-lapse movie may contain thousands of images. To process the raw data into a 3D movie, specialized batch image processing is required. The open-source image processing software ImageJ [18] was extended for vector-contrast image processing by several plug-ins. These include zero adjustments to compensate for the offset vector drifts, phase unwrapping, background subtraction of scanning artifacts, and conversion of phase images into TOF images. The TOF image and the magnitude image can be combined to form a pseudo-3D image of the cells. Under the simplifying assumptions that the sound velocity of cells has a constant value and that echo signals from the top surface of the cells are negligible the TOF is proportional to the height of the cells and the TOF image can be interpreted as a height map. The Persistence of Vision Raytracer (POV-Ray, http://www.povray.org/, version 3.5) creates pseudo 3D computer graphics from height and texture maps and allows batch processing of the images for a time-lapse movie. The images in magnitude contrast are used as the texture. The position of the observer and the direction of viewing can be placed arbitrarily. For all images displayed here the illumination was chosen directly from above.

3 Time-Lapse Imaging of Mesenchymal Stem Cells

Ovine mesenchymal stem cells were harvested from bone marrow of sheep and cultured under an atmosphere of 5% CO_2 and 5% oxygen in an incubator at a temperature of 37 °C as described by Zscharnack et al. [19]. The cells were grown on a collagen coated glass cover slip and imaged with the described acoustic microscope equipped with the live cell imaging system. The total observation time was 8 h with one frame recorded every 40 s. The size of the images is 306 μm × 225 μm.

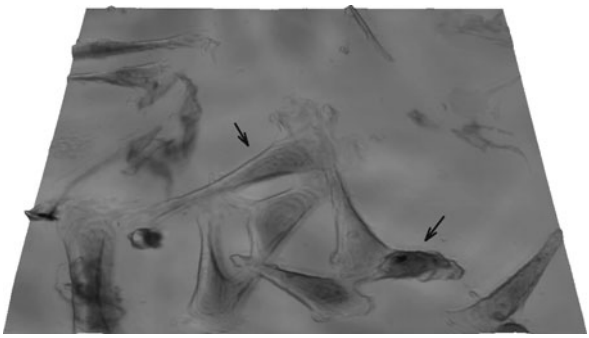

Fig. 3 Image of the cells 380 min after the start of the time-lapse movie. The two marked cells adhere flat to the substrate. The image size is 306 μm × 225 μm

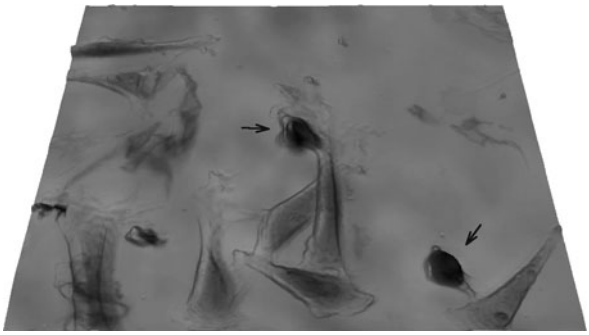

Fig. 4 The cells 392 min after the start of recording with the marked in the contracted state. The image size is 306 μm × 225 μm

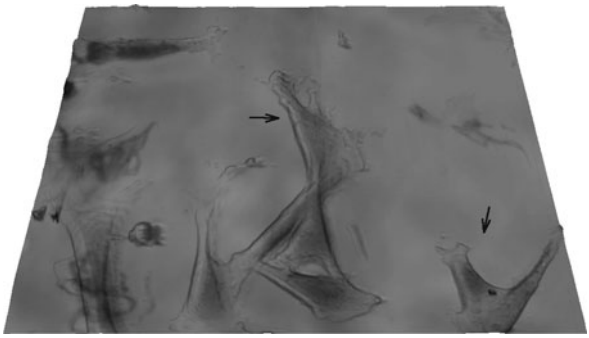

Fig. 5 Images of the cells 411 min after the start of recording; the marked cells adhere flat to the substrate again. The image size is 306 μm × 225 μm

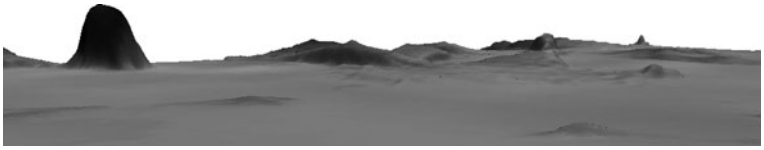

Fig. 6 View of a single contracted cell on the left side and multiple flat cells on the right side. The observer was positioned close to the substrate

Figures 3, 4 and 5 show three frames of the movie as an example. A population of typically 10 cells can be observed. The two marked cells change their shape from one image to the other. First they are observed in the contracted (tall) state. After that they spread out into the more distributed (flat) state. This change of shape can happen in less than 40 s. Figure 6 shows a magnified visualization taken from the same time-lapse image sequence. The observer is placed near the surface of the substrate. A single, contracted cell can be seen on the left side and several flat cells on the right side.

4 Conclusions

Automatic zero correction and focusing increases the quality of time-lapsed PSAM movies by reduction of offset errors and focal drifts. Long-term monitoring of stem cells can thus be performed and cell behavior can be studied by visualization as pseudo-3D movies. For batch image-processing a combination of open-source software (ImageJ) and specially developed plug-ins for vector-contrast scanning acoustic microscopy have lead to the presented results.

Acknowledgments We would like to thank Matthias Zscharnak, Claudia Pösel and Frank Peinemann for providing the cells and the Federal Ministry of Education and Research (BMBF grant 0313836, MS CartPro) for financial support.

References

1. Hildebrand, J.A., Ruger, D., Johnston, R.N., Quate, C.F.: Acoustic microscopy of living cells. PNAS **78**(3), 1656–1660 (1981)
2. Cross, S., Jin, Y., Rao, J., Gimzewski, J.: Nanomechanical analysis of cells from cancer patients. Nat. Nanotechnol. **2**, 780–783 (2007)
3. Grill, W., Hillman, K., Würz, K.U., Wesner, J. In: Briggs, A., Arnold, W. (ed.) Advances in Acoustic Microscopy, vol. 2, pp. 167–218. Plenum Press, New York (1996)
4. Briggs, G.A.D., Wang, J., Gundle, R.: Quantitative acoustic microscopy of individual living human cells. J. Microsc. **172**, 3–12 (1993)
5. A-Hassan, E., Heinz, W.F., Antonik, M.D., D'Costa, N.P., Nageswaran, S., Schoenenberger, C-A., Hoh, J.H.: Relative microelastic mapping of living cells by atomic force microscopy. Biophys. J. **74**, 1564–1578 (1998)
6. Fabry, B., Maksym, G.N., Butler, J.P., Glogauer, M., Navajas, D., Taback, N.A., Millet, E.J., Fredberg, J.J.: Time scale and other invariants of integrative mechanical behavior in living cells. Phys. Rev. E **68**(4), 041914 (2003)

7. Wottawah, F., Schinkinger, S., Lincoln, B., Ananthakrishnan, R., Romeyke, M., Guck, J., Käs, J.: Optical rheology of biological cells. Phys. Rev. Lett. **94**(098103), 1–4 (2005)
8. Kundu, T., Bereiter-Hahn, J., Karl, I.: Cell property determination from the acoustic microscope generated voltage versus frequency curves. Biophys. J. **78**, 2270–2279 (2000)
9. Kundu, T., Bereiter-Hahn, J., Hillmann, K.: Measuring elastic properties of cells by evaluation of scanning acoustic microscopy v(z) values using simplex algorithm. Biophys. J. **59**, 1194–1207 (1991)
10. Bereiter-Hahn, J., Blase, C.: Ultrasonic characterization of biological cells. In: Kundu, T. (ed.) Ultrasonic Nondestructive evaluation, pp. 725–759. CRC Press, Boca Raton, FL (2003)
11. Liang, K.K., Bennett, S.D., Kino, G.S.: , Precision phase measurement with short tone burst signals in acoustic microscopy. Rev. Sci. Instrum. **57**, 446–452 (1986)
12. Lemons, R.A., Quate, C.F.: Acoustic microscope - scanning version. Appl. Phys. Lett. **24**(4), 163–165 (1974)
13. Grill, W., Hillmann, K., Kim, T.J., Lenkeit, O., Ndop, J., Schubert, M.: Scanning acoustic microscopy with vector contrast. Physica B **263**, 553–558 (1999)
14. Lemor, R.M., Weiss, E.C., Pilarczyk, G., Zinin, P.V.: Measurements of elastic properties of cells using high-frequency time-resolved acoustic microscopy. IEEE Ultrasonics Symposium, pp. 762–765 (2003)
15. Kamanyi, A., Ngwa, W., Betz, T., Wannemacher, R., Grill, W.: Combined phase-sensitive acoustic microscopy and confocal laser scanning microscopy. Ultrasonics **44**, e1295–e1300 (2006)
16. Schenkl, S., Weiss, E.C., Stracke, F., Sauer, D., Stark, M., Riemann, I., Lemor, R.M., König, K.: In-vivo observation of cells with a combined high-resolution multiphoton-acoustic scanning microscope. Microsc. Res. Tech. **70**, 476–480 (2007)
17. von Buttlar, M., Twerdowski, E., Grill, W.: Offset correction for scanning acoustic microscopy with phase contrast. Proc. Int. Congr. Ultras., Paper ID 1698 (2007)
18. Rasband, W.S.: ImageJ, U. S. National Institute of Health, Bethesda, Maryland, USA, http://rsb.info.nih.gov/ij/ (1997–2009)
19. Zscharnack, M., Poesel, C., Galle, J., Bader, A.: Low oxygen expansion improves subsequent chondrogenesis of ovine bone-marrow-derived mesenchymal stem cells in collagen type I hydrogel. Cells Tissues Organs. doi:10.1159/000178024 (2008)

Acoustic Microscopy Study of Properties and Microstructure of Synthetic and Natural Fiber Composite Materials

I. Severina, J. Sadler, and E.Y. Maeva

Abstract Bio-fiber based composites are gaining acceptance in today's industries. Aimed to replace synthetic fiber-reinforced composite materials, natural fiber composites significantly differ from them in microstructure. Development of new bio-composites shows necessity for effective studies of their mechanical properties. In this paper, properties of bio-composites with different content of wheat straw fillers are analyzed. Microstructure of the composites, its relation to material composition and distribution of the filler phase in the polymer matrix is investigated with acoustic microscopy. The obtained results help to deeper understand structure-property relationship for bio-composite materials and provide feedback for development of new materials with properties satisfactory for industrial needs.

Keywords Bio-fibers · Composites · Acoustic microscopy · Microstructure

1 Introduction

Fiber-reinforced composites have intense application in construction, aerospace, automotive, marine, electronics, and biomedical and other high-technology areas [1]. A traditional composite structure, which consists of fibers incorporated in polymer resin matrix, provides increased strength and stiffness. New environmental regulations and depletion of and uncertainty about petroleum resources have revive interest in composite materials from natural sources. Natural fibers in composite materials include straw, stems, and hulls from wheat, oat, barley, corn and other crops. These materials provide comparable with synthetic materials stiffness, strength, and toughness at reduced cost. Lower density and weight give additional advantage, especially important in automotive industry.

Mechanical properties of the most of bio-composites are similar to the properties of the wood [2] but composite material provides uniform distribution of these properties compared with wood. Properties of the composite are determined by the properties of its components, morphology of the system and nature of the interface

I. Severina (✉)
The Institute for Diagnostic Imaging Research, University of Windsor, Windsor, ON N9B 3P4, Canada
e-mail: seviary@uwindsor.ca

M.P. André et al. (eds.), *Acoustical Imaging*, Acoustical Imaging 30,
DOI 10.1007/978-90-481-3255-3_18,

between two phases. Compared with synthetic fiber composites, bio-composites represent another level of material organization. While synthetic fibers are, long and uniform in diameter, natural fibers are short particles with wide variations in dimensions. Characterization and visualization of the composites microstructure is essential for the developing new materials as their mechanical properties are determines by the composition, microstructure and arrangements of the composite elements.

The objective of this work was to characterize microstructure of the composite materials reinforced with synthetic and natural fibers by acoustic methods.

2 Theoretical Modeling of Sound Propagation in Oriented Fiber Composite Materials

Using the principles of acoustics (Christoffel's equations and boundary conditions) one can produce the equations for the reflection and transmission coefficients at a variable strength boundary between two materials with hexagonal anisotropy. This anisotropy corresponds to an overall longitudinal fiber direction, where the fibers are oriented parallel to the interface, but may be at different orientations in the plane in each layer of the sample. In this case the reflection and transmission coefficients at each interface are:

$$T_1 = \frac{2\rho^I c_1^I}{\rho^{II} c_1^{II} + \rho^I c_1^I - i\rho} \qquad R_1 = 1 - \frac{\rho^{II} c_1^{II}}{\rho^I c_1^I} T_1$$
$$T_1 = \frac{2\rho^I c_1^I}{\rho^{II} c_1^{II} + \rho^I c_1^I - i\rho^{II} c_1^{II} \rho^I c_1^I / K_x} \quad R_1 = 1 - \frac{\rho^{II} c_1^{II}}{\rho^I c_1^I} T_1 \tag{1}$$

where ρ = density, c = sound velocity, R = reflection coefficient, T = transmission coefficient, K_x is a variable bonding parameter describing the level of bonding between the two layers. Figure 1 shows a plot of this reflection coefficient vs. the inverse bond parameter ($1/K_x$) for the case where the layers of the sample are made up of the same material.

Theoretical modeling of sound propagation in oriented fiber composite materials can be performed, allowing the multiple reflections within the composite plate to be calculated, and in turn the expected A-Scan of the material can be produced for different levels of disbonding. As an example consider the case producing the A-Scans shown in Fig. 2. For this simulation the theoretical composite is made up of identical materials (density 1.008 g/cm^3, velocity 1,660 m/s, and attenuation 9.1 dB/cm), where partial bonding of the composite occurs creating two layers. (In this case the top layer has thickness 0.3 mm and the bottom 0.7 mm). Here the figures show three specific cases from the fully bonded case (Fig. 2a), where the response is that of a solid material; next a partially disbonded case (Fig. 2b), where the additional reflections are seen to noticeably alter the A-Scan; and finally a nearly 100% disbonded material (Fig. 2c), where the response is largely that of the thinner top layer of the composite.

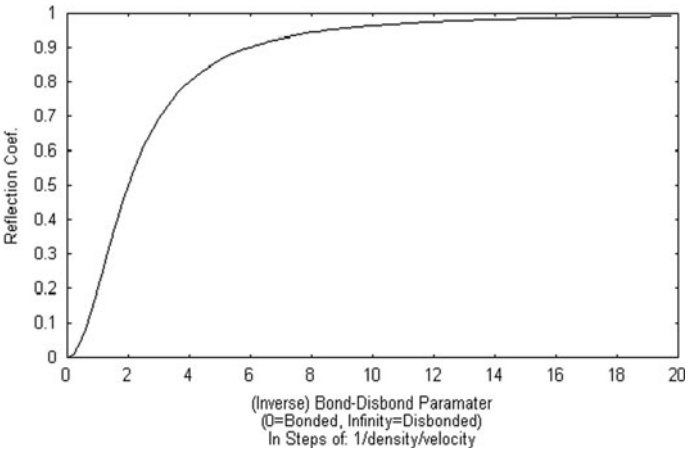

Fig. 1 Plot of the reflection coefficient with varying bond strength

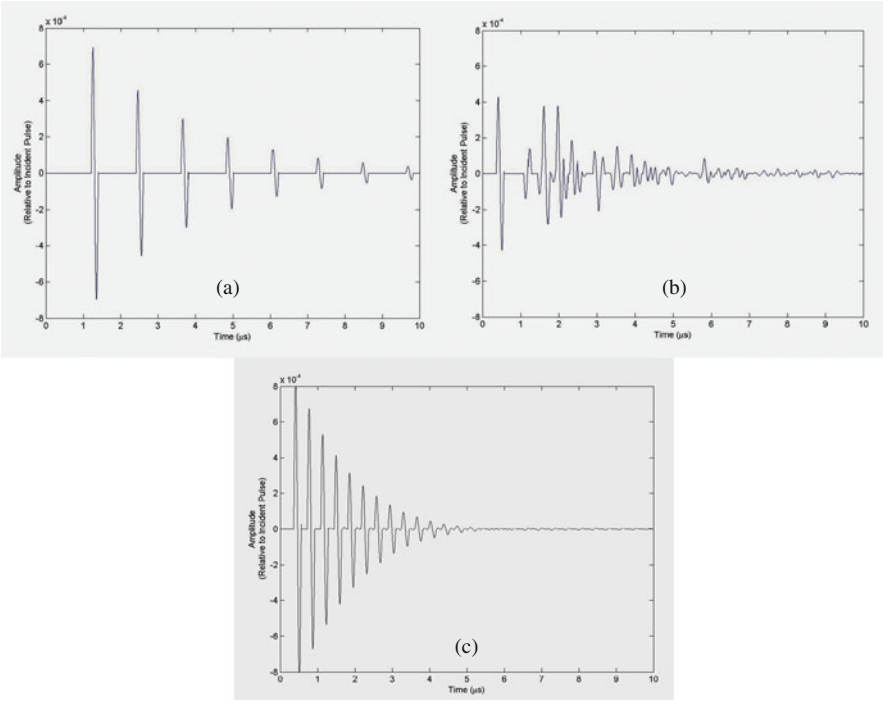

Fig. 2 Theoretical modeling of sound propagation. **(a)** Fully bonded material, **(b)** partially disbonded material (50% reflection), **(c)** nearly 100% disbonded materail

3 Evaluation of Microstructure of Synthetic Fiber Composites

An acoustic microscopy is able to distinguish an interface between the polymer matrix and synthetic fiber as a result of their significantly different acoustic and elastic properties. The acoustic microscope with short pulse mode and spherically focused acoustic lens at frequency of 25 MHz was used for analyzing the internal microstructure of laminated and randomly oriented synthetic composites. This frequency provides high spatial resolution and sufficient penetration depth. Short ultrasonic pulses are sent through a coupling liquid (water) into the sample with the beam focus positioning on different depths. Received echo signals are used for image creation. Bright color on the image usually corresponds to the areas with higher reflection at the interfaces while darker areas correspond to the regions with high attenuation or some acoustic shadows.

The interface region between an embedded fiber and a surrounding polymer matrix is an important factor with respect to the mechanical behavior of composite materials. The effect of the microstructure of this region on the fiber–matrix stress transfer characteristics is an important property of the composite materials.

The acoustic images of the internal structure of the laminates and randomly oriented composites are presented on the Figs. 3 and 4, correspondingly. On the Fig. 3, first three images represent the virtual horizontal cross-sections made on different depth and the forth one is the integral image made by capturing the signal reflections

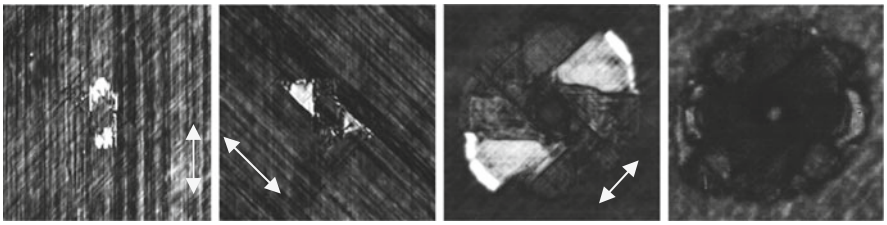

Fig. 3 Acoustic C-scans of the laminated composite specimen made on depth of 2^{nd}, 4^{th} and 6^{th} and 15^{th} layers. *Arrows* show the fibers orientation in each ply layer. 2×2 cm scanning area

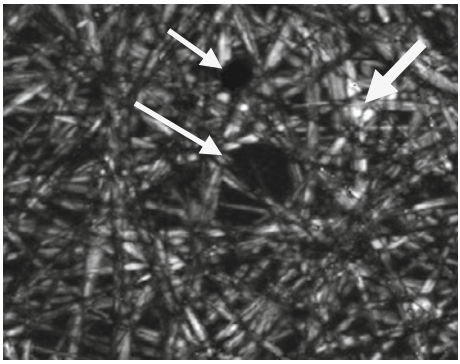

Fig. 4 The internal structure of the randomly orientated synthetic fiber composite. 2×2 cm scanning area, 25 MHz acoustic lens. *Thick arrows* show poor contact on the fiber/matrix interface and the *thin arrows* show areas without fibers

from the bottom of the sample. Direction of the fibers orientation on each composite's ply is clearly visible and some delaminations between plies are detectable at these C-scans as a bright spots. Image of the 6^{th} ply shows the helical-type shift of the delaminations on each ply level. This occurs due to the fact of fibers different orientation on each layer. The defect blocks reflection from the bottom signal and appears as black area on the corresponding image.

The acoustic image of the composite with random fiber orientation (Fig. 4) shows the internal structure of the material, direction of the fiber orientations and distribution of the fiber in the matrix. The image reveals some areas with poor contact on the fiber-matrix interface (thick arrows), as well as areas with an absence of fibers (thin arrows).

4 Study of Natural Fibers Distribution Within the Polymer Matrix

Natural fiber-reinforced composites have a significantly different morphology compared with synthetic fibers. The fibers are rather short particles with wide variations in all dimensions. The dispersion of the fibers in composites is determined by chemical and mechanical interactions between the fiber and matrix. The uniform distribution of the filler phase is an important parameter which determines composite mechanical properties which increase with good dispersion due to material's homogeneity. Heterogeneity of the composite structure or presence of morphological defects may lead to the appearance of the micro-cracks and further material degradation.

There is no effective method for visualization of the particle dispersion within the matrix [3]. However, an acoustic microscopy technique can be successfully used to study the overall distribution of the elements in composite materials. It can also detect the internal defects such as non-uniform fiber distribution, improper contact on the matrix-fiber interface, cracks, micro voids, etc that are also of great importance.

Composite materials used in this study are polypropylene (PP)-based composites filled with wheat straw fibers as filler phase. Fiber's size is in the range below 1,000 μm. The specimen dimensions are $0.3 \times 1.2 \times 3$ cm. Ultrasonic testing was performed with Sonix HS-1000 acoustic microscope. Specimens were scanned at various acoustic frequencies. It was found that 10 MHz frequency focused acoustic lens provides the satisfying visualization of the sample structure without resolving individual fibers. The beam focus and imaging electronic gate were positioned on the bottom of the specimens. As PP has quite low acoustic impedance, it allows more acoustic power to penetrate into the material what improves the interior structure investigation. Obtained C-scans contain the information about integral distribution of the specimen structure. The brightness of the pixel on the C-scan is determined by the amplitude of the reflected signal and is affected by the acoustic impedance of the material, its attenuation and presence of any flaws. The polished surface of the specimen eliminates the scattering at the interface so most of changes in color on the C-scans are assumed to be due to uniformity of filler distribution within the polymer

matrix or porosity. As longitudinal acoustic waves are relatively slow, it is possible to distinguish the reflections from the layers at different depth of the material with time resolved technique [4]. Therefore, the analysis of the C-scans was combined with the B-scans cross-sections to study the material's structure in the most efficient way and to visualize the position of any flaws or defects.

The polypropylene specimen shows the uniform distribution of its properties (Fig. 5a). The image of PP/clay composite (Fig. 5b) also demonstrates the uniform dispersion of the clay nanoparticles in the PP matrix. The acoustic scans of composite with wheat straw filler show more complex internal structure compared with pure polymer matrix (Fig. 6). Images do not show completely uniform distribution of the filler inside the polymer matrix. Some darker areas present; they indicate regions with higher ultrasound attenuation what may caused by fiber clusters in that

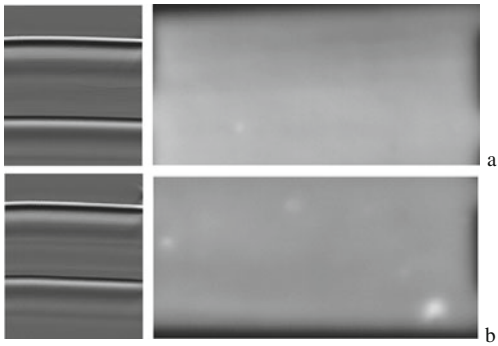

Fig. 5 The acoustic B- (*left*) and C- (*right*) scans of internal structure of polypropylene (**a**) and PP/clay composite (**b**)

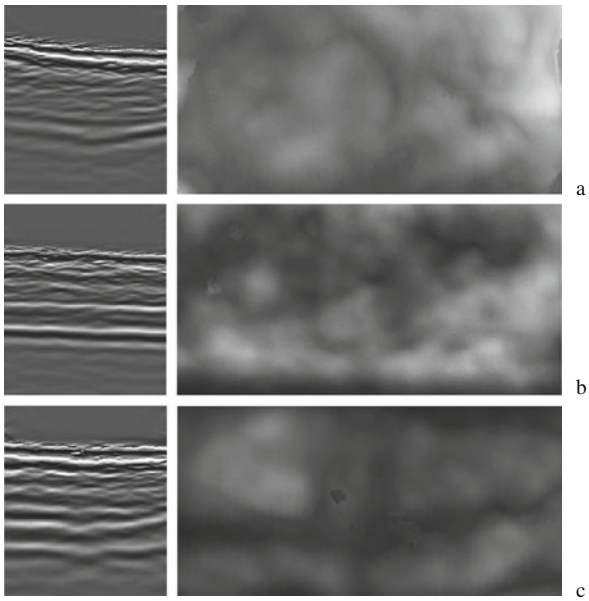

Fig. 6 The acoustic B- (*left*) and C- (*right*) scans of internal structure of PP/clay/wheat straw filler. Wheat straw content is 30% (**a**), 40% (**b**), 50% (**c**)

areas, presence of the fiber particles with dimensions larger than usual or presence of trapped air (microvoids). The frequency used for scanning does not allow us to distinguish between these factors. Increase of filler content in material composition corresponds to increase of darker areas on the acoustic images. This observation correlates with the increase in attenuation with more filler content in composite which will be discussed further.

Direct comparison of the images' brightness does not reflect a real difference in the material's attenuation as the images were made with different settings. However, the quantitative analysis is possible with corresponding recalculation included all parameters. The longitudinal sound velocity gradually decreases with adding the clay into the PP and increasing the fibers content (Fig. 7). This fact can be attributed to increase of the material's heterogeneity and decrease of its elasticity and/or crystallinity. Compared this data, it seems that ultrasound in the composites propagates along the continuous phase of PP matrix.

Acoustic attenuation, in contrary, grows with increasing of the fibers content (Fig. 8). The same effect was shown for coir fibers in polyester resin matrix [5]. It is interesting to note that adding of the 30% of wheat straw to the PP increases composite's attenuation more than two times. Further increase in fiber content up to 40% leads to slight rise in attenuation and no difference are shown in attenuation

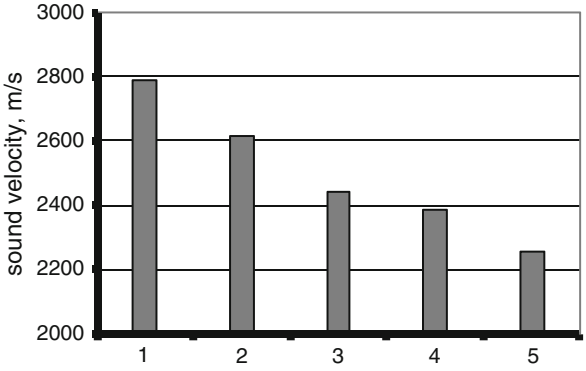

Fig. 7 Sound velocity in natural fiber composite materials. 1-PP, 2-PP/clay, 3-PP/clay/30% wheat straw, 4-PP/clay/40% wheat straw, 5-PP/clay/50% wheat straw

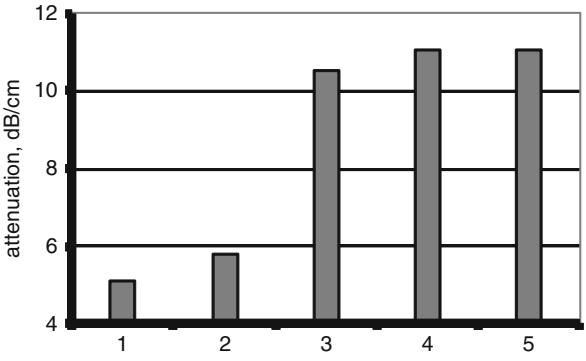

Fig. 8 Attenuation in natural fiber composite materials. 1-PP, 2-PP/clay, 3-PP/clay/30% wheat straw, 4-PP/clay/40% wheat straw, 5-PP/clay/50% wheat straw

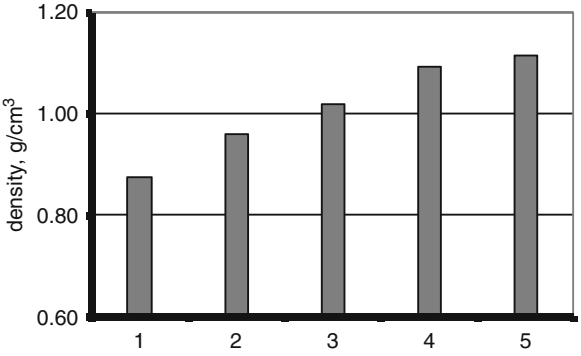

Fig. 9 Density of natural fiber composite materials. 1-PP, 2-PP/clay, 3-PP/clay/30% wheat straw, 4-PP/clay/40% wheat straw, 5-PP/clay/50% wheat straw

containing 40 and 50% of wheat straw. Figure 9 shows that density of the composites grows as well with increase of the wheat straw content.

5 Conclusions

Scanning acoustic microscopy was used for the analysis of the composite materials reinforced with synthetic and natural fibers. The study shows that unlike the visualization of the synthetic fiber composites, it is more challenging to visualize the individual natural fibers due to their irregular shape and higher attenuation in the material. However, the integral structure of the composites can be revealed. Polypropylene and PP/clay composite show very uniform structure while adding wheat straw fibers in the composition leads to appearance of the areas with higher acoustic attenuation. This may be due to presence of the trapped air or not uniform distribution of the filler phase.

Acknowledgments This project was supported by Ontario BioCar Initiative. The authors are grateful to Dr. Christine Moresoli, University of Waterloo and Dr. Mohini Sain, University of Toronto for providing the natural fiber composite materials.

References

1. Mohatnty, A.K., Mistra, M., Hinrichsen, G.: Biofibers, biodegradable polymers and biocomposites: an overview. Macromal. Mater. Eng. **276/277**, 1–24 (2000)
2. Sun, X.S. In: Wool, R., Sun, X.S. (eds.) Bio-Based Polymers and Composites, pp. 15–32. Elsevier Academic Press, San Diego, CA (2005)
3. Kulkarni et al., S.M.: Analysis of filler-fiber interaction in fly ash fillers short fibre-epoxy composites using ultrasonic NDE. Bull. Mater. Sci. **25**(2), 137–140 (2002)
4. Briggs, A.: Acoustic Microscopy. Claredon Press, Oxford (1992)
5. Lee, S.M.: Handbook of Composite Reinforcements. J Wiley & Sons, New York (1992)
6. Piche, L., Massines, F, Lessaard, G., Hamel, A.: Ultrasonic characterization of polymers as function of temperature, pressure and frequency, Ultrasonic symposium, 1987 in Ultrasonic Symposium Proceedings, IEEE, pp. 1125–1130 (1987)

Part III
Non-Destructive Evaluation

A Defect Localization Procedure Based on Warped Lamb Waves

L. De Marchi, A. Marzani, S. Caporale, and N. Speciale

Abstract Passive defect location procedures based on ultrasonic guided waves are widely used for structural health monitoring purposes of plate-like structures. Approaches based on the measured time-of-flight delay of propagating waves recorded at different locations are generally adopted. In these approaches, uncertainties are due to the fixed speed assumed for the incoming waves to convert their time delay in distances. These distances are next used to solve a triangulation scheme that leads to the defect location. In this paper, this inconvenient is avoided by processing the time transient measurements acquired at the different locations with a "Warped Frequency Transform" (WFT) that is capable to reveal the distance travelled by dispersive waves. In fact, by means of the WFT the recorded time waveform is converted into the incipient pulse at a distance from the origin which is proportional to the distance travelled by a mode within the signal, thus fully compensating its dispersive effect. Then, the processed time waveforms recorded from simple sensors can be used for locating defects by means of classical triangulation procedures.

Keywords Guided waves · Time-frequency transforms · Defect localization · Lamb waves

1 Introduction

Sonic and ultrasonic stress waves are a wonderful tool to probe materials and structures. A clear advantage of probing with sounds is that the examination can be carried out in a total non-destructive manner and also that some inspections can be executed without moving out of duty the structure. It is, however, well known that the interpretation of probing with sounds is not always clear or straightforward, especially when guided waves (GWs) are used. In this case, in fact, the number of waves as well as their propagative features, such us group velocity, attenuation and wavefront, depend on the frequency of propagation. In fact, because of the interference between the wave's wavelength and the finite dimension of the component, guided waves' features modify varying the frequency of propagation (dispersive behaviour). Dispersion leads in general to non-stationary multimodal time transient events (time-waveforms) when the waveguide is excited by a broadband pulse [1].

L. De Marchi (✉)
ARCES-DEIS, University of Bologna, 40136, Bologna, Italy

M.P. André et al. (eds.), *Acoustical Imaging*, Acoustical Imaging 30,
DOI 10.1007/978-90-481-3255-3_19,

The use of GWs for remote and real time defect detection and location has interested several researchers in the last decades (see for example, Zhongqing et al. [2]). Among the several, major efforts have been devoted to detect defects in beam and plate-like structures, largely used in the aerospace industry. In general, a network of sensors (generators and detectors) embedded or installed on a side of the structural component is used actively or passively to locate defects. In active network, in general one sensor is used to generate GWs and the remaining sensors work as a waves detectors. In this case the receivers can be triggered on the sensor used as actuators and the time-of-flight of waves, eventually scattered by a defect, easily calculated.

In a passive network, instead, all the sensors are continuously recording and discarding data. When the acoustic energy released by an excited defect crosses a certain threshold in one of the sensors, the trigger information is sent to all sensors (acoustic emission system). At this point, depending on an assumed time delay, part of the data is recovered at each sensor and the waves time-of-flight next reconstructed.

In both cases eventual defects in the plate-like structure are localized by classical triangulation, like those used in seismology, by converting the waves time-of-flight in distances from the sensors. To this aim, is important to select an appropriate velocity for the propagating waves. This is not an easy task since the guided wave speed depends on the waveguide geometry, on the guided mode that is being detected as well as on its frequency of propagation. To skip these complexities, in general, source location techniques assume improperly a constant waves velocity in a material.

Here, instead, we proposed a totally new approach capable to extract the distance travelled by a non-stationary dispersive signal. The approach is based on a unitary transformation, namely the Warped Frequency Transform (WFT), which reveals the distance travelled by a dispersive guided mode within the recorded time-waveform in force of its group velocity covariant property.

Thanks to its versatility the developed tool could pave a new class of procedures to locate defects as well as waves sources in waveguides.

2 Warped Frequency Transform

Given a discrete-time signal, the WFT introduces a deformation of the periodic frequency axis *f* with a proper warping function *w(f)*. In order to guarantee invertibility, *w(f)* must be chosen so that it maps the f axis on itself, which is:

$$\dot{w}(f) > 0 \quad a.e. \quad \Rightarrow \quad \exists w^{-1}, w^{-1}(w(f)) = f \tag{1}$$

where $\dot{w}(f)$ represents the first derivative of the map $w(f)$. In addition, in order to guarantee that a real signal is transformed into a real signal, $w(f)$ must be an odd function. The frequency warping operator can be defined as:

$$\mathcal{W} = \mathcal{F}^{-1}\mathcal{F}_w \tag{2}$$

where $\mathcal{F}^{-1}$ is the inverse Discrete-Time Fourier Transform and $\mathcal{F}_w$ is a modified Discrete-Time Fourier Transform that, for a given discrete signal $s(n)$, is defined as:

$$[\mathcal{F}_w s](f) = \sqrt{\dot{w}(f)} \sum_{n \in \mathbb{Z}} s(n) e^{-j2\pi n w(f)} \tag{3}$$

In Equation (3) the factor $\sqrt{\dot{w}(f)}$ has been introduced to render the operator unitary, i.e., to preserve orthogonality. However, the numerical implementation of Equation (3) involves unfeasible continuous operations along the frequency axis. So we introduced a sampling operation on M discrete frequencies to get a modified Discrete Fourier Transform:

$$[\mathsf{F}_w s](f_k) = \sqrt{\dot{w}(f)} \sum_{n \in \mathbb{Z}} s(n) e^{-j2\pi n w(f_k)} \tag{4}$$

The final discrete warped frequency operator is defined as:

$$\mathsf{W} = \mathsf{F}_M^{-1} \mathsf{F}_w \tag{5}$$

where F_M^{-1} is the inverse of the Discrete Fourier Transform of size M. Through this decomposition of the frequency warped operator we can achieve a fast computation. In fact Equation (4) can be efficiently factorized with the Non-uniform Fast Fourier Transform algorithm [3].

It has been proven [4] that a group delay shift covariant representation could be obtained by designing the warping map according to this formula:

$$K \frac{dw^{-1}(f)}{df} = \tau(f) \tag{6}$$

where $\tau(f)$ is the group delay of the dispersive system. In our approach [5], $\tau(f)$ is assumed as the inverse of the dispersive group velocity curve of a particular guided mode. In particular, in Fig. 1 is represented the sampling of the time-frequency (TF) plane induced by this warping, obtained by considering a warping map designed on the group velocity dispersion curve of the fundamental symmetric mode (S0) for an aluminium plate of thickness 2.54 mm. The group velocity dispersion curve for the S0 mode was obtained by using the semi-analytical formulation proposed in [6].

Because of frequency warping, the n-th tile is delimited by $[(n - 1/2)\mathrm{Dw} - 1, (n+1/2)\mathrm{D}w - 1]$ (solid lines), where D represents the derivative according to Euler's notation. This transformation produces a time sampling which matches the spectro-temporal structure of the S0 guided wave.

3 Artificially Simulated Lamb Waves

Artificial time-waveforms related to Lamb waves propagating in an aluminium plate were obtained by means of an opportune time transient Finite Element Simulation. In force of the problem symmetry an x-y plane strain condition was assumed. A plate of length $l = 1,000$ mm and thickness $h = 2.54$ mm was considered. A notch

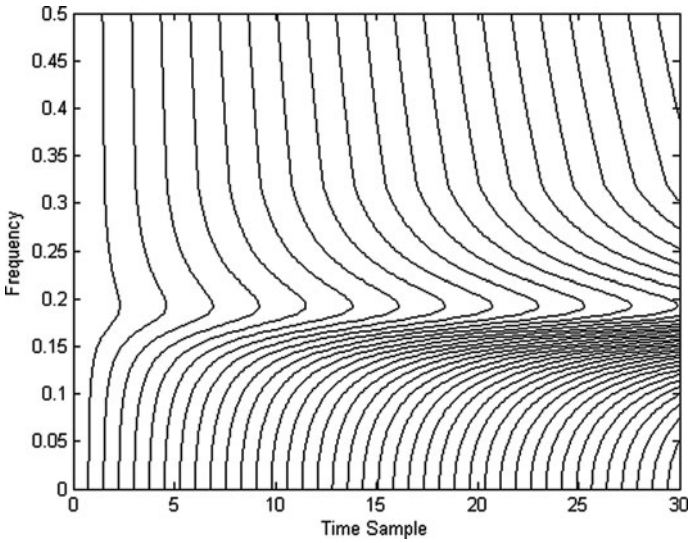

Fig. 1 Sampling of the time-frequency plane in according to the S0 mode time delay

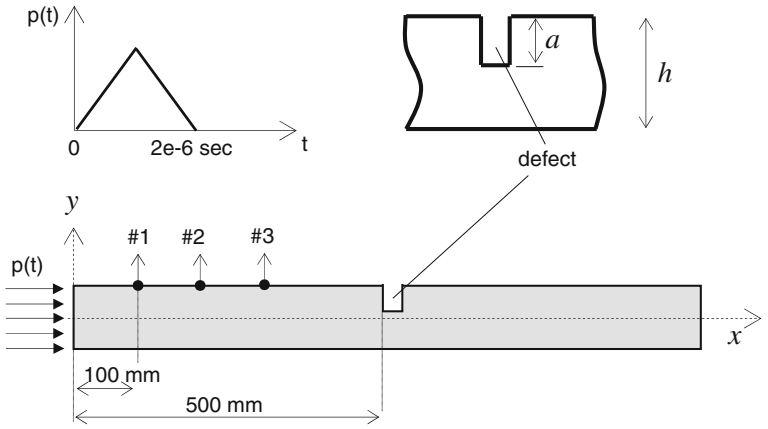

Fig. 2 Schematic representation of the aluminum damaged plate used in the time-transient Finite Element simulations

of width 0.254 mm and depth a, placed on the top side at the mid span of the plate ($x = 500$ mm), was considered, as shown in Fig. 2. In the simulations, several depth of the notch were analyzed, namely a/h=0.1, 0.2, 0.3 and 0.4.

Lamb waves were excited by imposing an impulsive force distributed on the left hand edge of the plate towards the plate mid-plane in order to mainly generate the symmetric S0 mode. The force was shaped in time as a triangular window with a total duration of 2 μs, as shown in Fig. 2, in order to excite consistent Lamb waves up to 500 kHz. The time-dependent y out-of-plane displacement was recorded at three points on the top side of the plate, namely #1, #2 and #3, located between

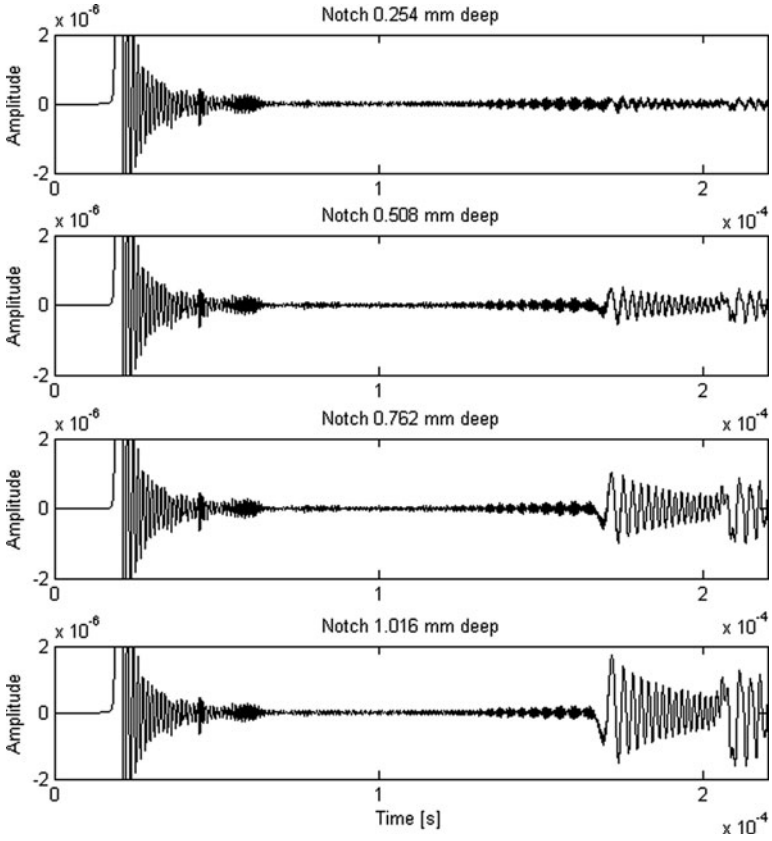

Fig. 3 Signal acquired by the first sensors #1 for different notch depths

the left edge and the defect at $x = 100$ mm, $x = 200$ mm and $x = 300$ mm, respectively.

The recorded signal was lasting enough to fully capture both the incoming wave from the left edge, mainly S0 due to the excitation type, and the waves reflected by the defect.

For example, in Fig. 3 are depicted the signals acquired by sensor #1 for the different notch depths. As it can be seen from Fig. 3, as expected, the deeper the notch the bigger is the amplitude of the reflected waves. These signals were next processed by the proposed WFT to prove the capability of extracting the distance notch-receiver.

4 Results

By means of the WFT the recorded time waveform is converted into the incipient pulse at a distance from the origin which is proportional to the distance travelled by the mode, thus fully compensating the dispersive effect. Plate's defect and edges

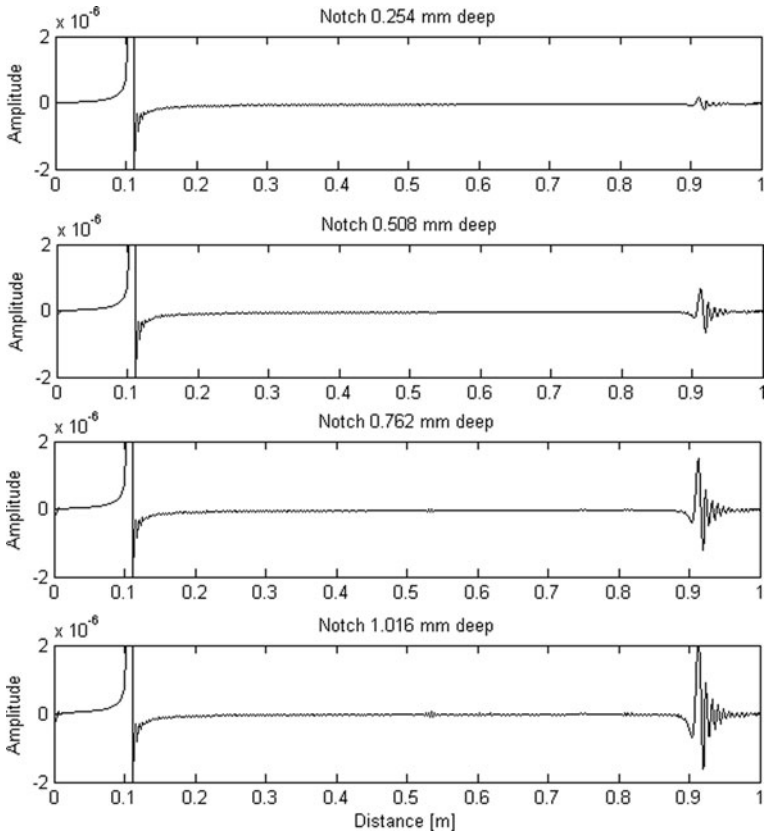

Fig. 4 Warped signal acquired at sensor #1 for different notch depths

locations can thus be extracted from a recorded time waveform. In Fig. 4 are represented the four signals of Fig. 3 processed by the described WFT. The warping map was designed on the S0 group velocity dispersion curve in order to highlight the lowest order symmetrical mode (S0). In this plots clearly emerge the presence of the S0 mode at a distance of 0.1 m as well as at 0.9 m.

Obviously, the first spike in the warped signal is related to the first arrival of the S0 mode travelling from the left edge to the sensor #1, while the second spike, at 0.9 m, is related to the S0 mode reflected back from the notch to sensor #1. It is interesting to note, that the WT reveals also the smallest defect of 0.254 mm depth, as visible in the upper plot of Fig. 4. From this plots, it can be observed that the amplitude of the spike in the warped signal could be also used to estimate the size of defect.

In Fig. 5 are plotted the warped signals for a 1.016 mm deep notch as acquired from the three different sensors. Also in this case, it can be seen that the WFT clearly detect either the distance of the S0 traveling from the left edge of the plate to the

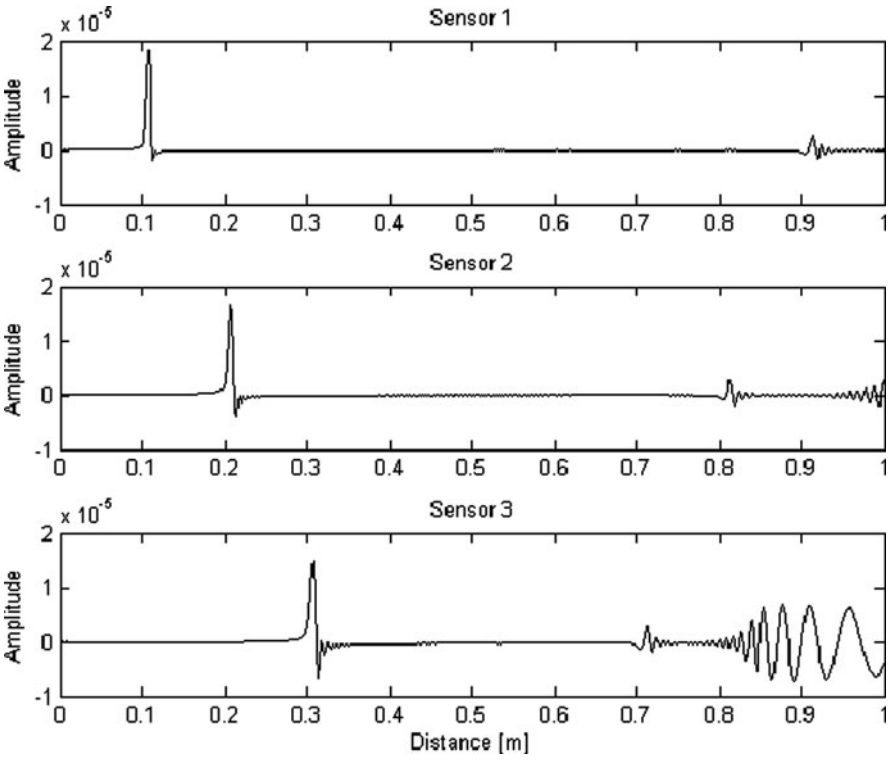

Fig. 5 Warped signals detected at sensor #1 (*top*), #2 (*middle*) and #3 (*bottom*)

notch and the S0 reflected from the notch (please note that the scale of amplitude in Figs. 4 and 5 are different).

In the signal acquired by the third sensor #3 also emerges the presence of the A0 mode, slower of the S0 wave, which is generated by the defect. The presence of the A0 mode could complicate the detection of the defect distance from the warped signal. However, by simply processing the warped waveforms by means of the Short-Time Fourier Transform (STFT), the presence of the S0 mode at several frequencies would avoid any mistake. For example, by analyzing the reassigned STFT of the warped signal detected at sensor #3 (Fig. 6), the S0 wave is clearly highlighted as a straight vertical lines for a distance source-receiver of 0.3 m and 0.7 m. The vertical lines in Fig. 6 denote the fact that within the warped signal the dispersive behavior of the S0 mode was fully compensated. The compensation of the S0 mode dispersion does not compensate the behavior of the A0 mode that still presents its dispersive behavior, traveling faster at higher frequencies.

Therefore, by means of pattern recognition techniques in the time-frequency domain (e.g., Barbarossa [7]), and combining the proposed WFT and STFT, we can always extract the distance traveled by a dispersive mode within a time-transient measurement.

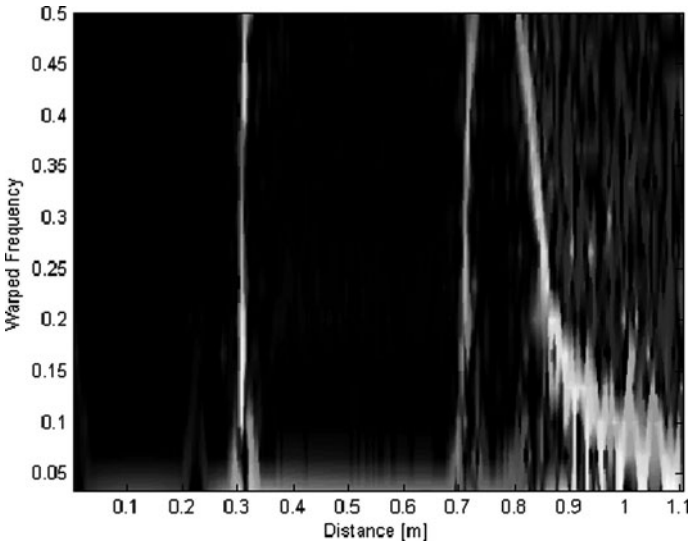

Fig. 6 Reassigned Short-Time Fourier Transform of the warped signal detected at sensor #3 represented at the bottom of Fig. 5

In real scenarios, the processed time waveforms recorded from simple sensors can thus be used for locating defects by means of classical triangulation procedures.

5 Conclusions

In this work a new signal processing tool capable to extract the distance travelled by non-stationary multimodal signals was presented. As non-stationary signals, in particular, time transient events related to propagating stress guided waves were considered.

The tool consists in a novel transformation that in force of its group velocity covariant property allows us to reveal the distance travelled by a dispersive guided mode within a recorded multimodal time-waveform. This appealing property has been used to detect the distance of a defect from the point where the time-waveform was acquired in an aluminium plate. For the several depths of the notch considered, the proposed procedure was capable to reveal the distance source-receiver accurately. Thanks to its versatility, also coupled to the STFT in a pattern recognition framework, the developed tool could pave a new class of procedures to locate defects in waveguides.

References

1. Marzani, A.: Time-transient response for ultrasonic guided waves propagating in damped cylinders. Int. J. Solid Struct. **45**, 6347–6368 (2008)

2. Zhongqing, S., Lin, Y., Ye, L.: Guided lamb waves for identification of damage in composite structures: A review. J. Sound Vib. **295**, 753–780 (2006)
3. Ware, A.: Fast approximate fourier transforms for irregularly spaced data. SIAM Rev. **40**(4), 838–856 (1998)
4. Papandreou-Suppappola, A., Murray, R., Iem, B., Faye Boudreaux-Bartels, G.: Group delay shift covariant quadratic time-frequency representations. IEEE Trans. Sig. Proc. **49**, 3–48 (2001)
5. De Marchi, L., Marzani, A., Caporale, S., Speciale, N.: Ultrasonic guided-waves characterization with warped frequency transforms. Proceedings of the 2008 IEEE International Ultrasonics Symposium (IUS), pp. 188–191 (2008)
6. Bartoli, I., Marzani, A., Lanza di Scalea, F., Viola, E.: Modeling wave propagation in damped waveguides of arbitrary cross-section. J. Sound Vib. **295**, 685–707 (2006)
7. Barbarossa, S.: Analysis of multicomponent LFM signals by a combined Wigner-Hough transform. IEEE Trans Sig. Proc. **43**(6), 1511–1515 (1995)
8. Caporale, S., De Marchi, L., Speciale, N.: Analytical computation of fast frequency warping. In: Proceedings IEEE ICASSP, pp. 3793–3796 (2008)

Second Harmonic Detection Generated from Fastened Bolt

M. Fukuda and K. Imano

Abstract The second harmonic components before/after the bolt was fastened were detected by using double-layered piezoelectric transducer (DLPT). The resonance frequency of DLPT changes to 1 MHz ($f_0/2$) when connected in parallel, but remains at 2 MHz (f_0) when connected in series. An effective fundamental transmission (1 MHz) is obtained when the DLPT is electrically connected in parallel while efficient second harmonic reception (2 MHz) is obtained when the DLPT is connected in series. In our system, the pulse inversion averaging (PIA) method was applied to enhance the second harmonic component. A hexagon head bolt (the diameter of a screw: 12 mm, the length: 100 mm) was used in experimental. The bolt was fastened by 40 N-m. The detected second harmonic component after the bolt was fastened was increased by approximately 10 dB compared with before the bolt was fastened.

Keywords Fastened bolt · Second harmonic · Pulse wave · Non-destructive testing · Double-layered piezoelectric transducer · Pulse echo

1 Introduction

Bolt conclusion is frequently used for the assembly of the machine structure. Since breakage of a bolt, slack, and superfluous bolting lead to an accident, maintenance check of a bolt is required. Bolt axial force, the ultrasonic method, the distortion gauge method, the load cell method, etc. are known as the inspection method [1]. In ultrasonic techniques, the contact between ultrasonic transducer and bolt using acoustic coupling medium becomes a source of error [2]. Thus, the novel measuring method for the bolting condition in which an acoustic coupling medium does not affect the measurement is required. Recently, new methods such as electromagnetic acoustic transducer (EMAT) [2], piezo cable [3], and smart washer using piezoelectric material [4] for the measurement of bolt axial force have been presented.

Nonlinear ultrasonic wave, second harmonic, etc., has been studied for use in NDE [5–9]. The second harmonic component is generated by nonlinear vibrations of

M. Fukuda (✉)
Department of Electrical and Electronic Engineering, Faculty of Engineering and Resource Science, Akita University, Akita 010-8502, Japan

M.P. André et al. (eds.), *Acoustical Imaging*, Acoustical Imaging 30,
DOI 10.1007/978-90-481-3255-3_20,

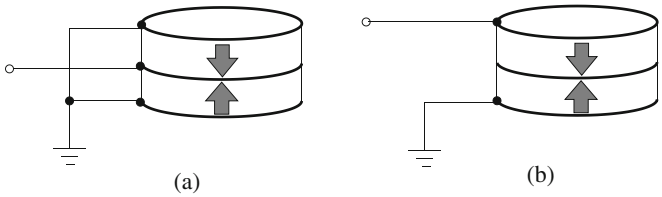

Fig. 1 DLPTs electrically connected (**a**) in parallel and (**b**) in series. *Bold arrows* denote the direction of polarization

closed cracks with the finite-amplitude ultrasonic waves having fundamental components. When the structure is bolted, the bolt stretches and tensile strength is loaded with the bolt. When the tensile strength exceeds the elastic yield point, a part of bolt is plastically deformed, or the fractures may be generated.

A real time detection system for second harmonic components [10, 11] or subharmonic components using double-layered piezoelectric transducers (DLPT) [12] has recently been constructed by the authors. The authors also analyzed the effective detection of second harmonic components or subharmonic components generated by plastic-deformed metals using the DLPT [11, 12].

In this study, the second harmonic component generated from the bolt is detected before and after the fastening of a bolt with a nut using a double-layered piezoelectric transducer (DLPT).

2 Double-Layered Piezoelectric Transducer

To construct a simple pulse-echo system, the DLPT which transmits finite-amplitude ultrasonic waves and receives a second harmonic component was used. The DLPT is composed of two $PbTiO_3$ (PT) thickness-mode piezoceramic plane disks that have the same characteristics (resonance frequency $f_0 = 2$ MHz). Both disks are stacked and bonded together with electroconductive silver paint so that their respective polarizations were bonded to each other in opposite directions. The DLPT can be electrically connected in parallel or in series as shown in Fig. 1a, b, respectively. Frequency-admittance characteristics of the DLPT when connected in parallel and in series are shown in Fig. 2a, b, respectively. The resonance frequency changes to 1 MHz ($f_0/2$) when connected in parallel, but remains at 2 MHz (f_0) when connected in series. An effective fundamental transmission (1 MHz) is obtained when the DLPT is electrically connected in parallel while efficient second harmonic reception (2 MHz) is obtained when the DLPT is connected in series.

3 Method of Experiment

In our system, the pulse inversion averaging (PIA) method [10] was applied to enhance the second harmonic component. Two pulse waves of opposite phase were transmitted alternately in the PIA method. The received waves were time-averaged

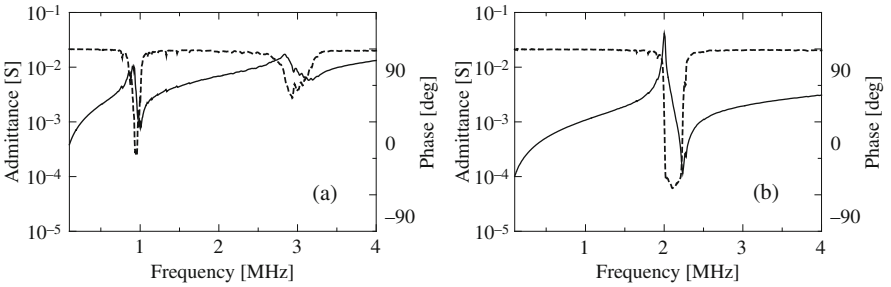

Fig. 2 Frequency-Admittance characteristics of DLPT electrically connected (**a**) in Parallel and (**b**) in series. *Solid lines* indicate the absolute value of admittance and *dotted line* the phase of admittance

to cancel out the fundamental and odd harmonic components of the waves [10]. This method is also used in medical diagnostic equipment for harmonic imaging [13–15]. The driving voltage waveform for the PIA was produced in an arbitrary waveform generator (Hewlett Packard, HP33120A). The driving voltage waveform was designed for 20 cycles of a 1 MHz burst sine (burst duration time: 20 μs). After an appropriate interval, T, the next inverted signal was applied to the DLPT. The interval of each signal was determined to be $T = 500$ μs. PIA was automatically carried out by averaging every interval T.

The system of employing DLPT is shown in Fig. 3. An electronic switch was used to detect second harmonic components automatically [10]. The switch was inserted between the electrode of the back surface and the ground. When the switch is turned on, the electrode of the back surface is grounded and the DLPT was connected in parallel (1 MHz). The DLPT was connected in series (2 MHz) when the switch was turned off and thus the electrode on the back surface was open. When

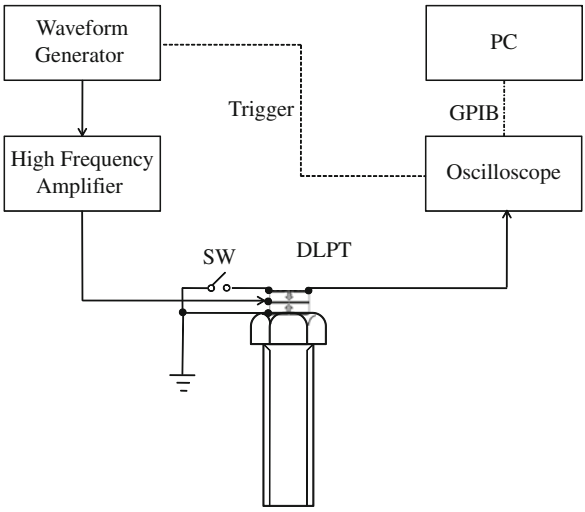

Fig. 3 Experimental setup. Nut was removed when the experiment was carried out

the switch is turned on, voltage is not applied directly to the switch. In this case, the switch only makes a short circuit connection between the electrode of the DLPT and the ground. On the other hand, when the switch is turned off in receiving mode, the switch allows the DLPT to receive a low level signal. The DLPT of opposite polarization direction can thus use a conventional switch to generate and detect second harmonic components.

Transmission signals were generated using an arbitrary waveform generator and their amplitudes were amplified to 150 V with a high-frequency power amplifier (Thamway, 145-4715B). The switch was turned and a parallel connection for the transmission of a 1 MHz ultrasonic pulse wave was produced. Ultrasonic pulses of 1 MHz were transmitted through the bolt. Before reflected pulse waves reached the DLPT transducer the switch was turned off to enable the series connection for efficient reception of second harmonic waves (2 MHz). The resultant pulse waveform and spectrum were captured by an oscilloscope (Agilent, Infinium 54845A) and second harmonic components could be observed in real time using the FFT function of the oscilloscope. Finally, the received pulse waveforms were digitized and fed into a personal computer via a general purpose interface bus (GPIB).

A hexagon head bolt (the diameter of a screw: 12 mm, the length: 100 mm) was used in experimental. The bolt was fastened by 40 N-m (general torque of intensity classification 4.8) to a nut using a torque wrench.

4 Results and Discussion

The received waveform and its spectrum before fasten bolt are shown in Fig. 4a, b, and the received waveform and its spectrum after fasten bolt are shown in Fig. 4c, d, respectively. These waveforms were carried out PIA to cancel the fundamental components. The amplitudes of these spectra were normalized by the amplitudes of fundamental component before PIA. The detected result of second harmonic component after the bolt was fastened was increased by approximately 10 dB compared with before the bolt was fastened.

Bolt axial force in case of the bolt was fastened by the torque of 40 N-m might be approximately 10–20 kN. The previous report for detecting second harmonic components using plastic-deformed metal rods have been also increased as the tensile strain [5]. The bolt axial force was increased as the bolt was fastened, and the inside of the bolt might be plastic-deformed as the bolt axial force was increased. The second harmonic detection will be applied to evaluation of conditions of the bolts, such as slack of a bolt, and superfluous bolting.

5 Conclusions

The second harmonic components before/after the bolt was fastened were detected by using double-layered piezoelectric transducer (DLPT). The detected second harmonic component after the bolt was fastened was increased by approximately 10 dB compared with before the bolt was fastened.

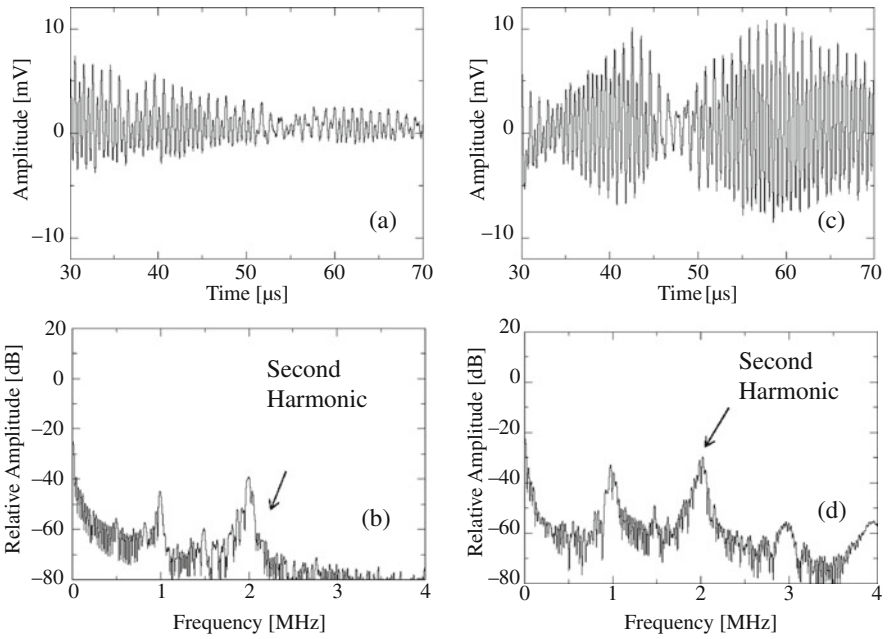

Fig. 4 (**a**) The received waveform and (**b**) its spectrum before fasten bolt. (**c**) The waveform and (**d**) its spectrum after fasten bolt. These results were carried out with pulse inversion averaging

It is not certain in whether to have reached to yield stress with the torque in the experiment, since the coefficient of friction of a bolt was not clear. In the future, quantitative consideration such as changing torque will be required.

Acknowledgements This work was supported by Grant-in-Aid for Young Scientists (Start-up) (No. 20860020) from Japan Society for the Promotion of Science.

References

1. Sakai, T.: Zouho Neji Teiketsu Gairon, pp. 108–114. Yokendo Ltd., Tokyo (2005) [in Japanese]
2. Ogi, H., Hirao, M., Yasui, H.: Ultrasonic measurement of bolt-axial stress by a shear-wave electromagnetic acoustic transducer. Hihakai Kensa **47**(5), 331–336 (1998) [in Japanese]
3. Kurosaki, S., Sasaki, Y., Izumi, S.: Trial of measurements for axial force of bolt using piezo cable. Hihakai Kensa **56**(7), 149–154 (2007) [in Japanese]
4. Okugawa, M., Egawa, K.: Study on smart washer using piezoelectric material for bolt loosening detection. Hihakai Kensa **52**(9), 511–516 (2003) [in Japanese]
5. Ohara, Y., Yamamoto, S., Mihara, T., Yamanaka, K.: Ultrasonic evaluation of closed cracks using subharmonic phased array. Jpn. J. Appl. Phys. **47**(5), 3908–3915 (2008)
6. Kawashima, K., Murase, M., Shibata, K., Ito, T.: Backscattered transverse wave imaging of cracked-faces with linear and nonlinear ultrasonics. Mater. Trans. **48**(6), 1202–1207 (2007)
7. Cantrell, J.H.: Dependence of microelastic-plastic nonlinearity of martensitic stainless steel on fatigue damage accumulation. J. Appl. Phys. **100**(063508), 1–7 (2006)

8. Alippi, A., Bettucci, A., Germano, M., Passeri, D.: Harmonic and subharmonic acoustic wave generation in finite structures. Ultrasonics **44**, e1313–e1318 (2006)
9. Solodov, I., Wackerl, J., Pfleiderer, K., Busse, G.: Nonlinear self-modulation and subharmonic acoustic spectroscopy for damage detection and location. Appl. Phys. Lett. **84**(26), 5386–5388 (2006)
10. Fukuda, M., Nishihira, M., Imano, K.: Real time extraction system using double-layered piezoelectric transducer for second-harmonic ultrasonic pulse waves. Jpn. J. Appl. Phys. **45**(5B), 4556–4559 (2006)
11. Fukuda, M., Nishihira, M., Imano, K.: Real time detection of second-harmonic components generated from plastic-deformed metal rod using double-layered piezoelectric transducer. Jpn. J. Appl. Phys. **46**(7B), 4529–4531 (2007)
12. Fukuda, M., Nishihira, M., Imano, K.: Novel detection system using double-layered piezoelectric transducer in same polarization direction for sub-harmonic components generated from plastic-deformed metal rod. Jpn. J. Appl. Phys. **47**(5B), 3899–3903 (2008)
13. Burns, P.N., Simpson, D.H., Averkiou, M.A.: Nonlinear imaging. Ultrasound Med. Biol. **26**(1), S19–S22 (2000)
14. Simpson, D.H., Chin, C.T., Burns, P.N.: Pulse inversion doppler: A new method for detecting nonlinear echoes from microbubble contrast agents. IEEE Trans. Ultrason. Ferroelect. Freq. Contr. **46**(2), 372–382 (1999)
15. Simm, F.C.: Phase inversion wideband non-linear imaging: Applications to tissue harmonic imaging. J. Med. Ultrason. **26**(4), 285 (1999)

In-line Ultrasonic Array System for Monitoring Dynamic of Coating Forming by Cold Spray Process

M. Lubrick, S. Titov, V. Leshchynsky, and R.Gr. Maev

Abstract This study attempts to test the viability of studying the cold spray process using acoustic methods, specifically testing during the actual spray process itself. Multiple composites studied by flat and multi channel transducers as well as actual online measurements are presented. It is shown that the final thickness as well as the dynamics of buildup can be evaluated (including plotting rates of buildup). Cross sections of the coating thickness are also easy to obtain and show true profiles of the coating. The data can also be used to generate real estimates for nozzle speed and spray diameter. Finally comparisons of real thickness and acoustically estimated thickness show a close linear relationship with the y intercept seeming to depend on the composition. The data clearly shows that online acoustic measurement is a viable method for estimating thickness buildup.

Keywords Cold spray · Ultrasonic array · Thickness determination · In-situ material characterization

1 Introduction

Cold Spray (CS) is a rapidly developing coating and manufacturing technology in which the spray particles (in the range of 10–150 μm) are fed into a supersonic gas stream and accelerated to a high velocity, and are deposited on a substrate in solid state [1–5]. The severe plastic deformation of the particles on impact produces a deposit that is very dense, with low oxide content and no thermally induced tensile stresses. A typical feature of CS is the relatively low temperature of driving gas compared with the conventional thermal spray techniques. Accordingly, the temperature of spray particles prior to impact is much lower than their melting point. Other important advantages, especially when compared to thermal spraying techniques are the low oxygen content within the material, the relatively high deposition rates (10–30 kg/h) achievable and the compressive residual stresses after deposition as solidification shrinkage and shrinkage on cooling are avoided. The low temperature characteristic of CS makes it possible to deposit the coating of the materials without

M. Lubrick (✉)
The Institute for Diagnostic Imaging Research, University of Windsor, Windsor, ON N9B 3P4, Canada
e-mail: lubrick@uwindsor.ca

M.P. André et al. (eds.), *Acoustical Imaging*, Acoustical Imaging 30,
DOI 10.1007/978-90-481-3255-3_21,

any significant change in the microstructure of feedstock. Most metals, such as Cu, Al, Ti and their alloys, have been deposited by CS [6–8], and even cermets [9] and ceramic particles [2, 10] could be embedded into a metallic substrate to form a thin layer coating.

A glance at the recent literature on different coating processes shows increased interest in depositing composite coatings with precise control of a buildup process. Being relatively new there is not a lot of data describing the buildup process, especially for the low pressure case focused on by our group. In fact, other than previous papers by the authors, there seems to be no acoustic measurements of any type. Acoustic studies allow for the nondestructive determination of properties especially if models are developed to relate acoustic and structural properties. Even more important, this paper discusses the development of online monitoring (during spraying) of the process using acoustics methods. The focus is on the thickness build up of the coating and demonstrating the feasibility of monitoring this acoustically.

2 Procedure

Commercially available aluminum (Al), alumina (AlO), and zinc (Zn) powders were mixed in the amounts shown in Table 1 (here after referred to by their names in Table 1). The composites were then applied using a portable apparatus equipped with an SST Centerline gun [11]. This system utilizes the injection of powder into the divergent part of a supersonic nozzle. The powder mixtures were supplied by a powder hopper and were injected into the supersonic portion of the nozzle near the throat area by means of a negative pressure developed by an accelerated stream of compressed air passing through the nozzle. The injected particles are accelerated in the high velocity air stream by the drag effect. To increase the air velocity and, ultimately the particle velocity, the compressed air can be preheated within a range from 100 to 700° C. The pressure and temperature of the compressed air were monitored

Table 1 Materials used and particulars of study

Name	Composition (wt %)	Substrate	Transducer	Notes
1	Al+10% Al_2O_3	Steel	Flat contact	1 sample multiple points
2	Al+25% Al_2O_3 +10%Zn	Steel	Flat contact	1 sample multiple points
3	Al+30%Al_2O_3	Steel	Flat contact	1 sample multiple points
4	Al	Steel	Flat contact	3 samples off substrate
9 samples	Al+25% Al_2O_3 +25%Zn	Steel	Multi element transducer (1 channel)	9 samples
Online	Al+25% Al_2O_3 +25%Zn	Aluminum	Multi element transducer (1 channel per point)	Results obtained during online measurement

by a pressure gauge and a thermocouple positioned inside the gun. The gun was installed on an X-Y manipulator to scan the air-powder jet over the substrate surface.

The acoustic studies used two types of transducers but had the same procedure. The ultrasonic probe is attached to the opposite surface of the substrate (except for 4 – pure aluminum the samples broke from substrate). It sends ultrasonic waves through a coupling media and substrate to the area where the spray process takes place (or coating for non online samples). A hard delay line wetted with ultrasonic gel was used as the coupling media. The wave passes through the substrate, is reflected from the upper surface of the sprayed layer, and travels back to be received by the probe. Measuring the time of flight of the ultrasonic pulse and knowing the sound velocity in the deposited material it is possible to calculate the thickness of the material at the particular point and time. The main distinction between the two transducers used, was the number of channels/elements (to generate a distinct signal). The flat transducer referred to in Table 1 had just a single element generating a 15 MHZ signal and had a diameter of roughly 6.7 mm. The multi element transducer had 52 elements (it is possible to use some and turn off others) with central frequency and relative bandwidth of the elements 15 MHz and 60%, respectively. Also dimensions are shown in Fig. 1a. Figure 1b shows the dimensions/direction of the applied coating relative to the transducer elements. The grey region is the total coating with lines 1 and 2 showing the middle of the coating and highest point of the coating respectively (details follow).

As can be seen in the Table 1, the samples had a variety of compositions as well as unique ways in which they were studied. For all the sets of samples the time for the signal to propagate within the coating as well as coating thickness was measured (thickness was measured via a depth gauge with accuracy 10 μm). The first 3 types of samples were sprayed over large areas and then the top surface was ground and polished to give a smooth surface for sound to reflect back off. They were than studied with the flat transducer in 15 completely separate sections to generate a set of data points. The 4^{th} set of samples had three smaller samples (one data point per) all of which broke from the substrate. Both the top and bottom surfaces were polished and then were also studied with the flat transducer. The “9 samples” were a set of three samples that were each cut in thirds leaving 9 pieces. Again the top surface was ground and polished but this time the studies were conducted using a single channel of the multi element transducer (each piece correlated to one data point). The final “online” samples were the most important. These acoustic measurements were conducted during the actual spraying process. The setup for this online monitoring is shown in Fig. 2. The multi element transducer is kept in tight contact with the substrate. The spray is than simply directed diagonally across the sample and over the transducer while data is recorded.

3 Results

Figure 3 shows an example of the type of data that is generated by the channels within the online measurement. It is referred to as a d-scan, which is multiple b-scans (cross sectional signals) over a period of time. The data is a gray scale image

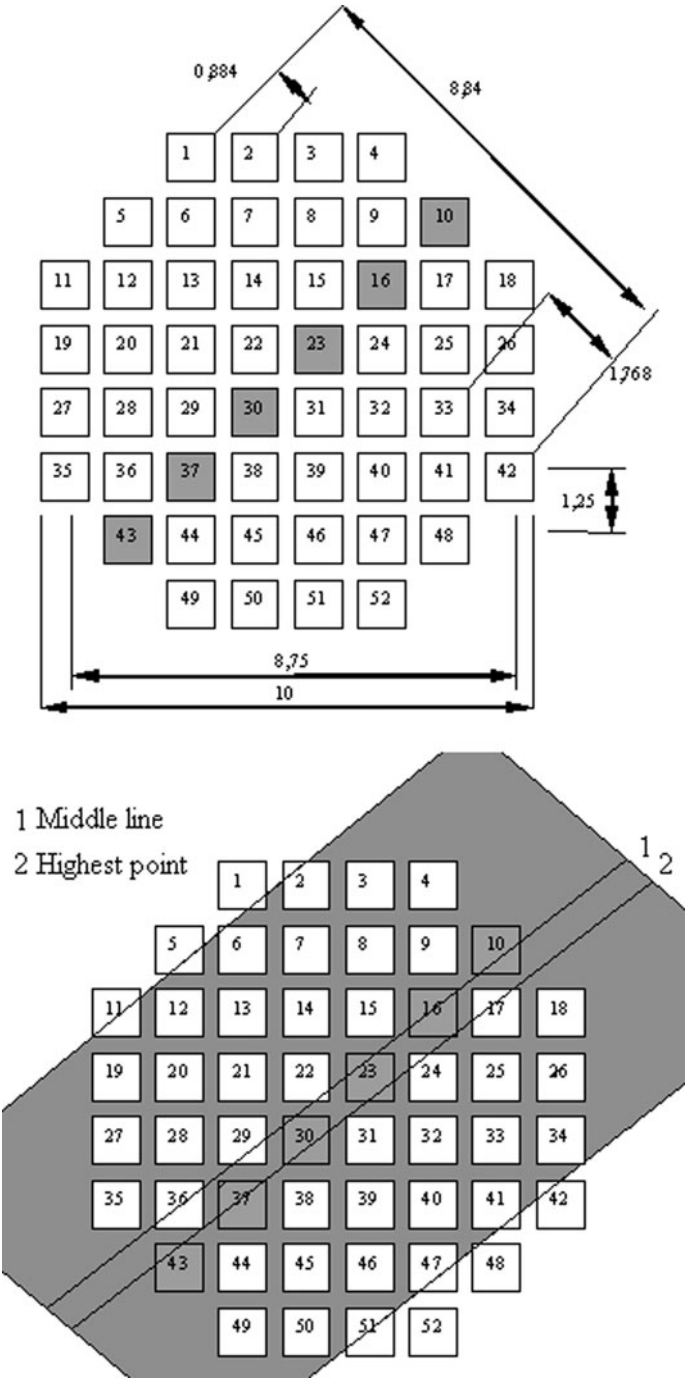

Fig. 1 Layout of transducer channels (distances in mm), (*top*) and applied coating and regions of interest (*bottom*)

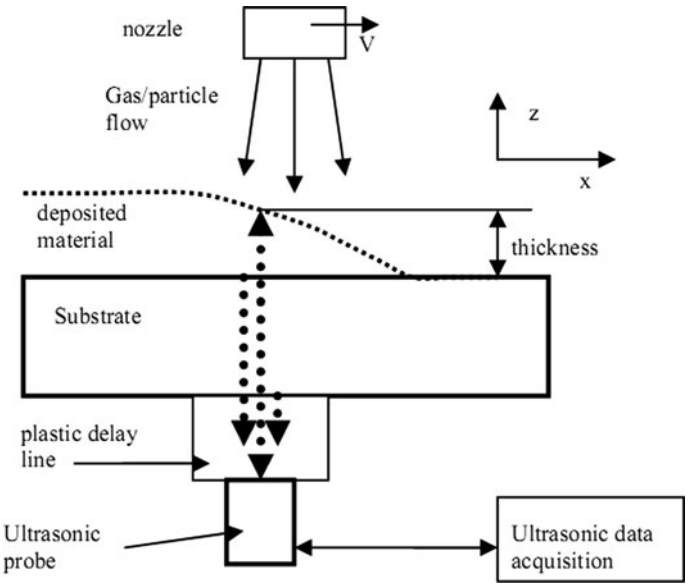

Fig. 2 Online acoustic measurement setup

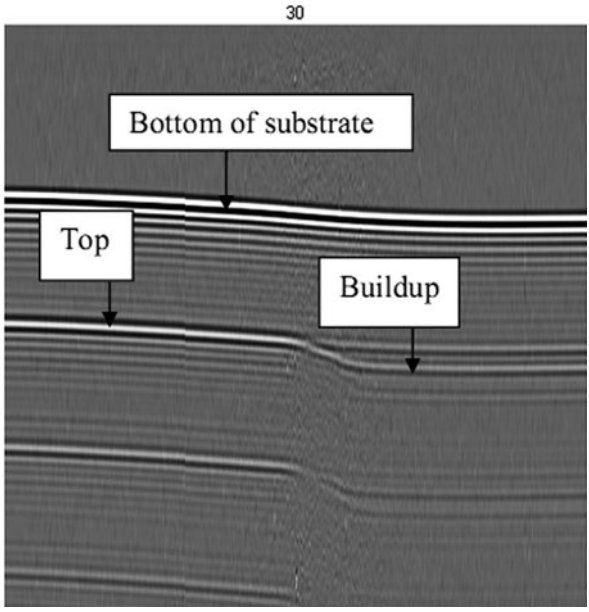

Fig. 3 D-scan generated during online measurement

where bright pixels correspond to a high level of the signal, dark pixels correspond to negative values, and zero signal looks like gray background. The frequency with which the images are taken is controlled by the number of channels used at any time and the length of the d scans. Here channels recorded data 40 times per second

(25 ms period). To understand the d-scan it is necessary to read it from top to bottom. The top line shows the reflection from the bottom of the substrate while the next line shows the reflection from the top plate (the other lines are just secondary reflections and can be ignored). It can be clearly seen by studying the second line that over time we get a second reflection which is from the buildup of the coating itself.

Much of the d-scan shows time where nothing is happening (before or after spray reaches element). Figure 5 therefore shows the important data, that of the actual coating buildup for each of the channels considered. It shows the thickness of the coating as a function of the distance that the spray nozzle has traveled. To get the acoustic thickness measurements we used the time of flight and the theoretical velocities for the fully dense composites as calculated in a previous paper [12]. Also, each channel records thickness build up at different distances since the spray nozzle is traveling and therefore passes across each channel at a different time. This difference in fact allows us to estimate the nozzle speed during spraying simply by comparing the time at which buildup begins for channels in a line (by choosing a line parallel to spray direction). The theoretical value that was calculated was averaged to 4.2 mm/s as compared to the actual measured speed of 5 mm/s.

Figure 5 shows the time derivative of thickness (Δthickness / Δtime) plotted against the nozzle distance for selected channels. Also shown is 2^{nd} degree polynomial fits to the data for each channel. This plot thus shows the rate of buildup of the coating as the nozzle moves along. It can be seen that the polynomial fit for all the channels is similar. This is true as well for the channels that were omitted (they were omitted to make the plot easier to read).

Figure 6 shows a distribution of the sample thickness generated from the online measurements. The position is measured as diagonal distance from the center of channel 7 (therefore measures the thickness at the middle point of each element). As can be seen from Fig. 1 plot 5 takes data from 2 lines of elements. This was done so as to have more data points and a more detailed cross section. The measurement results in the figure show the ratio of width of spray from the left side to the peak compared to peak to right side (at the same thickness). The final plot, arguably the most important, compares the actual thickness of the samples to the thickness calculated acoustically.

4 Discussion

Much of the results are fairly self explanatory, but the important thing is to determine whether acoustic analysis, especially in real time, is a viable method for studying the cold spray process. Figures 3 and 4 clearly show that we can actually detect the buildup of the coating as it takes place. Not only that but we can also plot and see how it builds up over time (Fig. 5). For each channel the 2^{nd} degree polynomial fit gives a similar shape. It shows that initially there is slow buildup, followed by a region of rapid buildup and finally it again experiences slow growth. This implies that the deposition at the outer regions of the spray takes place slowly (most likely due to lower powder concentration). These considerations can be expanded on even

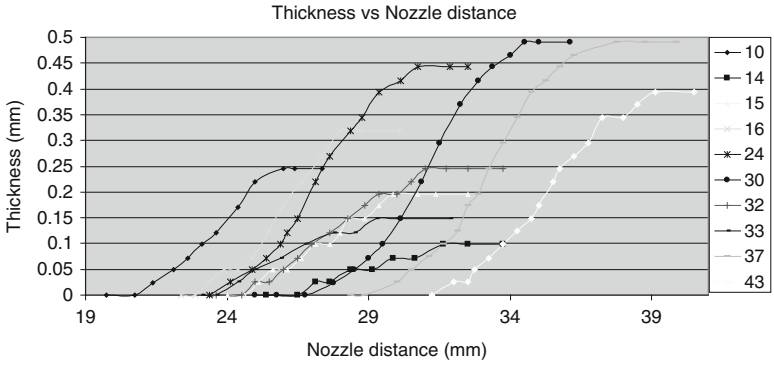

Fig. 4 Plot of thickness against distance moved by nozzle for multiple channels

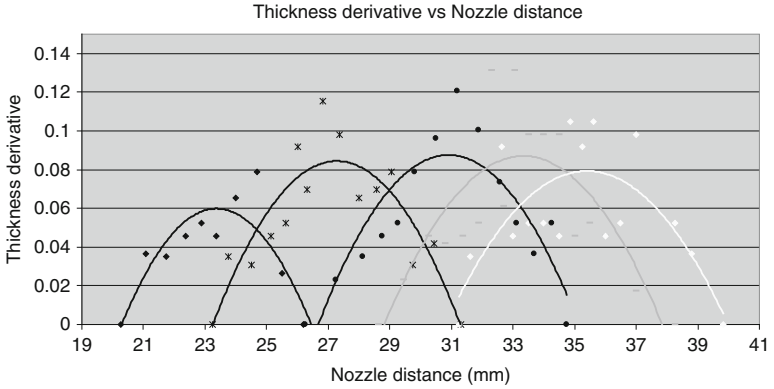

Fig. 5 Time derivative of thickness vs. nozzle distance and 2nd degree polynomial fit of data

more through a close examination of Fig. 4. By subtracting the time at which buildup initially begins from the time at which buildup stops, we get the time for the spray to traverse across the channel. Multiplying this by the actual speed of the nozzle, then leads us to an estimate of the spray diameter. It is important to remember from Fig. 1 that the spray does not lay directly along a line of elements. Therefore some of the elements will give a random cord of the spray diameter and underestimate. Therefore it seems prudent to consider the channels with the largest thickness since they likely indicate the regions with the longest time and most direct spray passing over them. The channels 30 and 37 seem the most likely and they do give the highest estimates of diameter (as well as 43). The calculated value is 7–7.6 mm. This can be compared against the measured width of the coating after spraying which gave a value of 7.8 mm. This slight underestimation is most likely due to the spray not being perfectly aligned across the channels and/or the edge of the coating being too thin to give a proper reflection. Knowing that the nozzle diameter is 5 mm and the standoff distance was 15 mm it is possible to accurately describe the spray profile.

It can be seen that the spray spreads out in a cone shape and thus it is very logical that the outer regions will have less powder concentration as mentioned above.

A comparison between the actual nozzle speed and that estimated acoustically seemed to give somewhat poor results. However, this can be explained quite easily due to the direction of the spray. As stated above, Fig. 1 showed the direction of spray is not perfectly along the line of transducers. This could be seen by looking at the samples themselves but also can be shown by carefully studying plot 4. If the spray was perfectly diagonal, then the channels in that line should all be approximately the same final height. It is clear though that channels 30 and 37 are higher and the other channels drop off (channel 23 is not shown since it had poor imaging most likely due to a lack of coupling fluid at that point) with channel 10 having the smallest thickness of all in that line. Since the actual direction of spray is different than theorized, the spray must travel a further distance from initial channel to final and therefore it is logical that we get a smaller velocity than it actually moved at.

Figure 6 shows a cross section of thickness for a portion of the cold sprayed samples. The profile that it creates matches very well with the shape of our sprayed samples. Figure 7 shows an optical cross section. However we may only compare shape instead of actual thickness dimensions since it was not aligned perfectly with where the cross section was taken (would be impossible since the acoustic cross section relies on two lines of elements). Even still one can see a very odd relation which is even clearer in Fig. 8. For the cold sprayed samples created the highest point of the coating is not actually directly in the middle (the exact reason for this

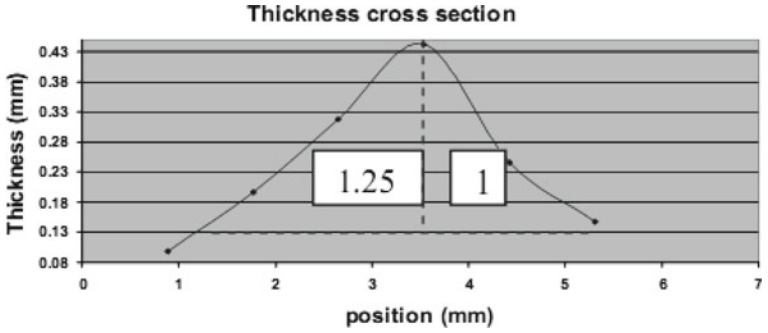

Fig. 6 Cross section of coating thickness (channels 14, 15, 16, 24, 32, 33 respectively)

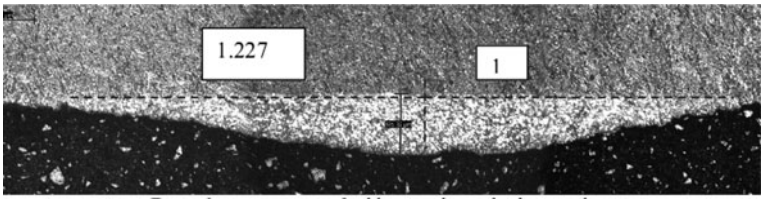

Fig. 7 Cross section of cold sprayed sample showing dimensions

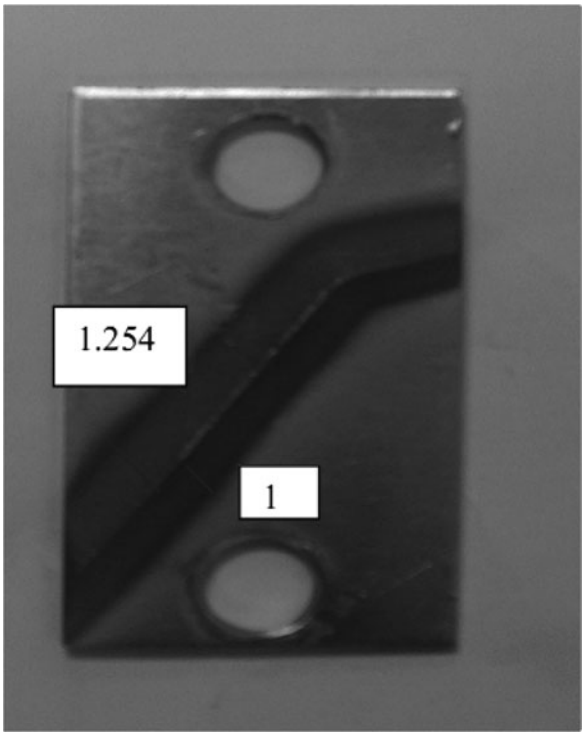

Fig. 8 Cold sprayed sample showing ratio of dimensions

still needs to be explored but is likely due to the fact that the spray is injected from one side of the gun only). In fact, by measuring it can be shown that the ratio of the left most side of the coating to the peak and that of the rightmost side to the peak is approximately 1.254:1. This agrees well with the values of 1.227:1 for the cross section. However, the most exciting aspect of this is the rough ratio predicted acoustically. In Fig. 6 it shows the measurement process. The midpoint of the two left most data points had the same thickness as the rightmost data point. Therefore by comparing the distance from each to the center we can get an approximate ratio of left side to right side as above. The value predicted acoustically was 1.25:1. This matches up extremely well with the ratios measured in the other two methods. This shows that a very realistic cross section of the coating is created even demonstrating the oddities of the process.

Figure 9 truly demonstrated the potential of acoustic analysis. For all the sets of samples there is a good fit between acoustically determined thickness and real thickness. In this case a good fit does not necessarily mean that the values are the same, but instead means a linear relationship. The actual values might be off since as said before we estimated the thickness based on the fully dense composites which is not the case here. This may not seem important, however, we have found that the acoustic velocity for the porous cold sprayed composites is usually lower than

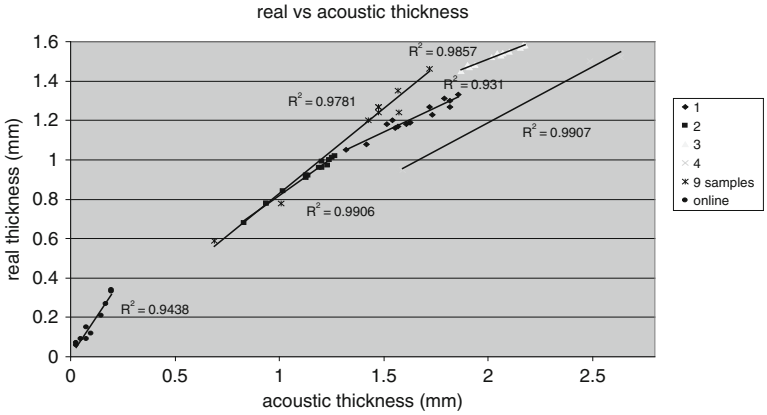

Fig. 9 Plot of real thickness against acoustically measured thickness

the fully dense case (results to be published later). Thus, the values might not be the exact same but the linear relationship for various data points shows that this is viable. Another important point to note is that many of our data sets will not have y intercepts close to 0, which one would expect since a 0 real thickness means no coating and obviously should lead to no acoustic thickness. This will obviously mean that some type of correction factor will have to be introduced to set the intercept at 0 but this is not something which has been done as yet. Also it may not even be necessary if a database of points is made since that it will be clear that a given acoustic reading corresponds to a set real thickness. That being said, a look at the online measurements shows some very promising data. The linear fit is fairly good at about 94% but also we get a y-intercept of 0.0072. This means the online data is giving the closest fit to what is expected between acoustic and real thickness, in fact by introducing the point (0,0) into the data the fit is improved with $R^2 = 0.9551$, and the y intercept = 0.0052. It is important to be cautious, however, in concluding whether this is due to the measurement process or composite itself since data sets 2 and "9 samples" had similar compositions and fairly good y-intercepts as well (0.0767 and 0.0331 respectively).

5 Conclusion

While this was only a preliminary study and focused more on presenting the results than analyzing them a few conclusions may still be drawn. Not only can the final value of thickness be estimated, it is also possible to see the dynamics of how the buildup takes place in real time. Figure 5 demonstrated that the buildup process is fairly universal across the spray, with slower buildup at the outer extremities of the coating. Estimates of nozzle speed and spray diameter matched fairly well with the actual values and should be easy to improve by aligning the spray completely parallel to the line of channels considered. Also the cross sectional thicknesses show

very accurate profiles of the actual coating structure. Most importantly it was shown that comparing real and acoustic thickness led to a reliably linear fit for all data points. It will be important in future work to add a correction factor to zero the y intercept for aesthetics and so it fits with common logic, but it clearly is shown that thickness estimates from acoustic data is a viable method.

References

1. Rocheville, C.F., US Patent 3,100,724
2. McCune, R.C., Donlon, W.T., Popoola, O.O., Cartwright, E.L.: Characterization of copper layers produced by cold gas-dynamic spraying. J. Thermal Spray Technol. **9**(1), 73–81 (2000)
3. Alkimov, A.P., Kosarev, V.E., Papyrin, A.N.: A method of cold gas-dynamic deposition. Dokl. Akad. Nauk SSSr **318**, 1062–1065 (1990)
4. McCune, R.C., Donlon, W.T., Cartwright, E.L., Papyrin, A.N., Rybicki, E.E., Shadley, J.R. In: Berndt, C.C. (ed.) Thermal Spray: Practical Solutions for Engineering Problems, pp. 397–403. ASM International, Materials Park, OH (1996)
5. Bhagat, R.B., Amateau, M.F., Papyrin, A.N., Conway JL, J.C., Stutzman JL, B., Jones, B. In: Berndt, C.C. (ed.) Thermal Spray: A United Forum for Scientific and Technological Advances, pp. 361–367. ASM International, Materials Park, OH (1997)
6. Papyrin, A.N., Alkimov, A.P., Koserev, V.E.: Spraying current conducting coatings on electrotechnical units by CGS method. Proceedings of United Thermal Spray Conference, pp. 288–290, Dusseldorf, Germany(1999)
7. Karthikeyan, J., Kay, C.M., Lindeman, J., Lima, R.S., Berndt, C.C. In: Berndt, C.C. (ed.) Thermal Spray:Surface Engineering via Applied Research, pp. 255–262. ASM International, Materials Park, OH (2000)
8. Stoltenhoff, T., Kreye, H., Richter, H.J., Assadi, H. In: Berndt, C.C., Khor, K.A., Lugscheider, E.E. (eds.) Thermal Spray 2001: New Surfaces for a New Millenium, pp. 409–416. ASM International, Materials Park, OH (2001)
9. Karthikeyan, J., Kay, C.M, Lindemann, J., Lima, R.S, Berndt, C.C. In: Berndt, C.C., Khor, K.A., Lugscheider, E.E. (eds.) Thermal Spray 2001: New Surfaces for a New Millenium, pp. 383–387. ASM International, Materials Park, OH (2001)
10. Yang, G.J., Han, F., Li, C.J.: Deposition characteristics of titanium coating in cold spraying, Proceedings of the Fifth International Seminar and the Sixth China national Thermal Spraying Conference, Anshan, China, 56-61 May 21–25, 2002 (in Chinese)
11. CenterLine (Windsor) Limited, http://www.cntrline.com, as on 16 June (2008)
12. Lubrick, M., Maev, R.Gr., Leshchynsky, V.: Development of cold spray composite coatings non destructive characterization, MS&T 2008 Pittsburgh, Pennsylvania (CD proceeding)

An Experimental Comparison of Thermographic and Acoustical Methods for Evaluation of Layered Structures

R.Gr. Maev, D. Gavrilov, G. Ghodsi, and E.Y. Maeva

Abstract Analytical capabilities of thermographic methods have been studied and compared to those of scanning air-coupled acoustic methods of control. Both advantages and disadvantages of these approaches have been discussed, with reference to basic theoretic models. For several samples with and without defects, both methods' detection capabilities were evaluated. Separately, the possibilities of application of both methods for analysis of objects of art were discussed. For this purpose samples of typical support-ground configuration were prepared and tested. It was demonstrated that both techniques are capable for finding delaminations and degradation of materials preceding the decay of the art objects. An example of real paintings analysis was presented.

Keywords Non-destructive evaluation · Industrial applications · Material characterization · Air coupled

1 Introduction

The role of nondestructive evaluation (NDE) in modern world can hardly be overestimated since nowadays it is used almost everywhere. On its new frontiers, industry tends to produce superfine structures with novel physical properties, such as composite materials, nanostructures and others. These new technologies are used in production of details for various precise scientific devices, industrial equipment; more and more often on the quality of such materials health and life of people depend. In the other cases, the quality and the state of material is important for preserving expensive objects from being destroyed.

Evaluation and maintenance of the quality of materials, details, for reporting on the current defects and properties of structures – all these directions require testing technologies. And in most of cases the technology is supposed to be nondestructive for performing in-situ analysis, without destroying the tested sample.

R.Gr. Maev (✉)
Chrysler/NSERC Industrial Research Chair in Applied Solid State Physics and Material Characterization, The Institute for Diagnostic Imaging Research, University of Windsor, Windsor, ON N9B 3P4, Canada
e-mail: maev@uwindsor.ca

M.P. André et al. (eds.), *Acoustical Imaging*, Acoustical Imaging 30,
DOI 10.1007/978-90-481-3255-3_22,

By the moment numerous methods have been developed for almost any application. These utilize different physical principles such as spectroscopic and different kinds of imaging techniques (using various bands of electromagnetic spectrum). All of them serve to different purposes, demonstrate different precision and suitability.

1.1 NDE in Art Analysis

Evaluation of conservation state of objects of artworks becomes more and more important problem for preservation of cultural heritage. For performing efficient preservation measures conservators often experience necessity in exact location of defects, developing delaminations and degradations. Especially acute this problem is for those museums and galleries exhibiting collections to public, and/or transport collections between the places of exhibition [1–3].

Another important task in art analysis is art forgery detection. The professional level of modern forgeries reaches such high levels that even top experts may perform improper attribution. Such forgeries imitate the style of the real author, his palette, sometimes even the canvases, and sometimes can be really considered as masterpieces [2].

Successful fakery detection now requires full scientific arsenal including material analysis, brushstrokes analysis, any kinds of the author's signatures and symbols, and so on. A connoisseur possessing all this information will have the highest chance to provide proper attribution service.

In this article we will review and discuss two of NDE methods, namely, scanning acoustical and thermographic imaging techniques. Like most of NDE techniques both these methods assume application of certain kind of excitation to the sample, be it focused sound impact or a heat pulse, and subsequent study of the reaction of the sample, which carries information on its properties and structure.

Both of the methods can be applied for wide range of samples, among which metals, plastics, composite materials are the most common examples. Also the capabilities of these techniques allow them to be used as an inspection tool for such delicate structures as works of art, where nondestructive methods are especially important [1, 4].

2 Acoustics and Thermography in NDE

In basic acoustic inspection a signal is delivered to the sample by means of an acoustical transducer, generating a sound wave. The sound wave is delivered to the sample's surface, partly reflects from it, partly penetrates into the bulk of the sample and interacts with internal structure. The later reflections carry the information on the defects inside, which can be delaminations, impurities, different kinds of inclusions, etc. Analyzing the parameters of the detected reflections one can make a decision on the integrity of the sample. Other applications of acoustic inspection

may include the study of elastic properties of materials, based on the analysis of reflections, time of flight delays, changes of spectrum and other parameters [5].

In acoustical raster imaging the image is formed point-by-point by means of acoustical scanning in a number of points of the sample. Spatial resolution in this case is described by the precision of the transducer and the distance between the points scanned. A good example of the device performing acoustical raster scanning is scanning acoustic microscope, basically consisting an acoustical lens (a focused acoustic generator for better resolution) fixed on a scanning frame driven by stepper motors [5, 6].

Scanning acoustical imaging may be performed in different regimes. In pulse-echo scheme a single transducer generates a pulse of finite duration and then receives the "echoes" reflections from the surface and/or the structure of the sample examined [5–7]. Another realization of reflection mode utilizes two transducers, one of which generates the sound, and the other registers the reflections (Fig. 1). This scheme allows continuous-wave generation, making the signal spectrum to be narrower than in case of pulse-echo mode. But this scheme forbids normal incidence of acoustical wave as the two transducers must be geometrically separated.

In through-transmission regime, two transducers are involved, one at each side of the sample (Fig. 2). In terms of attenuation this method has its advantages as the wave generated by the first transducer passes the sample's thickness only once before being detected by the other one.

The disadvantage of the scheme is more difficult extracting the depth information. Generally, through-transmission scans are "shadow" images, only containing the projection image of defects distribution, while the reflection scheme results often contain important information related to the depth of the defect.

Frequency of the sound is determined by the desired spatial resolution, sound attenuation in material and the coupling media. Higher frequencies are better for high-resolution imaging, though due to higher attenuation of them, a compromise must be found between the depth and the resolution. Also, to deliver high-frequency ultrasound to the sample, a coupling medium (water or special gel) is required. The absence of special coupling limits the working frequency [6].

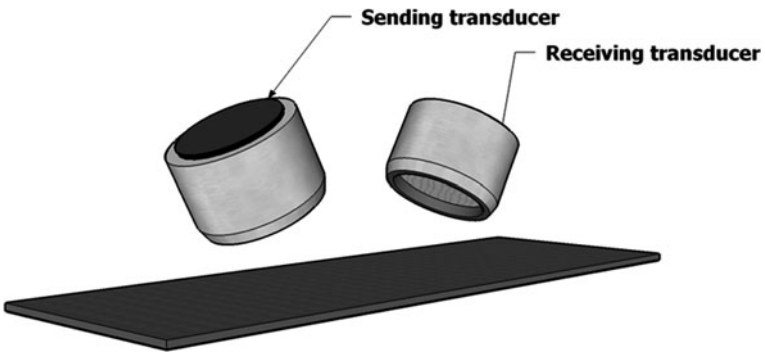

Fig. 1 Single-side transducer configuration for acoustic scanning

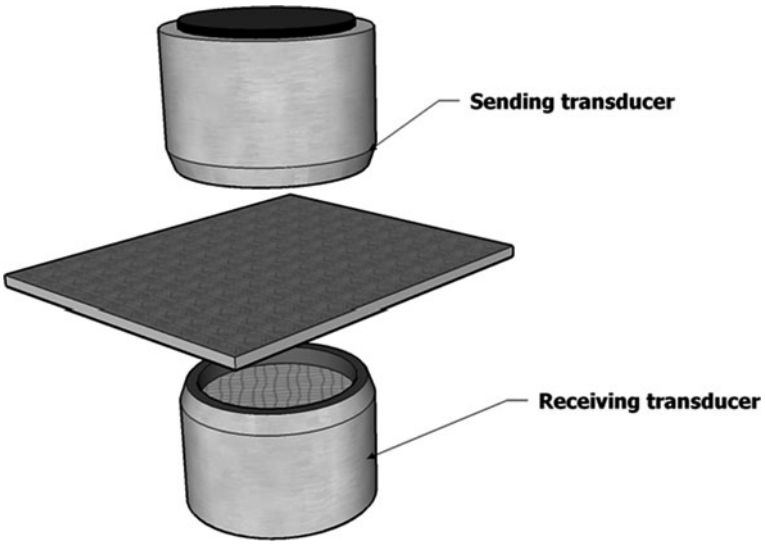

Fig. 2 Through-transmission transducers configuration for acoustic scanning

Thermography is a different kind of inspection. Basically this kind of NDE is dependent on thermomechanical properties of material tested, though in defectoscopy it has a lot of common with acoustic NDE.

Except certain kinds of testing, such as buildings, electric circuits and some other kinds of monitoring, thermographic testing requires application of an external heat pulse. This so called active thermography is the main type of thermographic testing. The heat pulse of known configuration is applied to the surface of the sample, and the surface temperature is monitored with a thermal imager for a certain period of time [8]. Evidently, if the field of view of the camera is large enough, the necessity in actual spatial scanning is eliminated.

Among all the kinds of active thermography there are pulsed thermography (PT), lock-in thermography (LT), shown in Fig. 3, and pulsed phase thermography (PPT) shown in Fig. 4. The fastest (and simplest) kind, pulsed thermography, is basically the monitoring of the heat distribution on the surface of the sample. After the heat is applied, the temperature front propagates into the bulk of the sample until the thermal equilibrium is reached. Until the front reaches any discontinuities (delaminations, inclusions, etc), the temperature on the surface decreases uniformly, as all the regions have similar heat sink. When there is a feature, blocking the heat propagation, the temperature of the surface becomes slightly higher than that of adjacent regions. The time after the flash and the detection of the defect is proportional to the square of its depth [8, 9].

In Lock-In thermography the heat is applied as a harmonic signal. In fact, one of the solutions of heat propagation equation is a decaying harmonic:

$$T(x,t) = T_0 \exp\left(-\frac{x}{\mu}\right) \exp\left(i\left[\omega t - kt\right]\right), \tag{1}$$

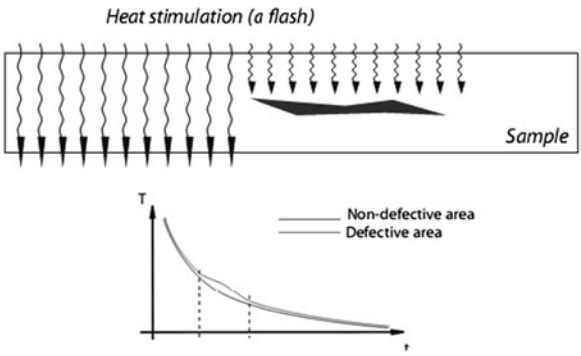

Fig. 3 Explanation of basics of pulsed thermography

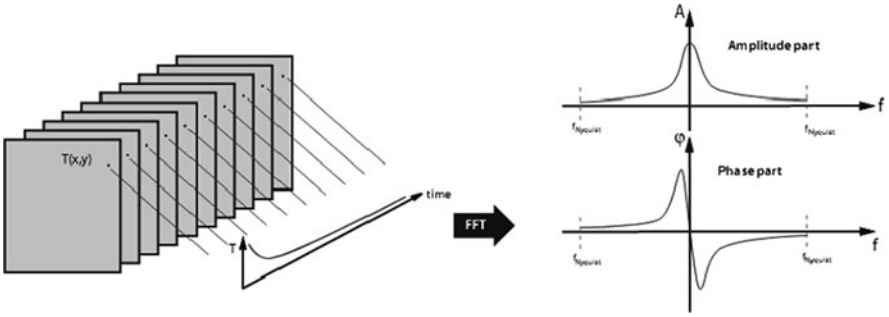

Fig. 4 Explanation of pulsed phase thermography

where x is the depth, t is the time of observation, ω is the angular frequency of the heat wave, k is the wave vector and μ is called "diffusion length" and is determined by thermal properties of the material as

$$\mu = \sqrt{\frac{\alpha}{\pi f}}, \tag{2}$$

where α is thermal diffusivity and f is the frequency of heat wave. It can be seen that the rate of the decay is determined by the frequency of the thermal wave. In fact, the lower harmonics propagate deeper than the higher [8, 10, 11].

Evidently, the temperature of the sample's surface changes according to harmonic law. It was demonstrated [12], that the phase part of these oscillations is affected by the presence of the defect in case if it is not deeper than the distance at which the wave decays. The locations of the defects are observable on images formed of extracted phases of the harmonic signals. Changing the stimulation frequency and building new phase image, one can extract information on the defects distribution on different depths. Also, the phase of the oscillations was proven to have been less affected by non-uniform heating of the surface [9, 12].

On the other hand, LT requires testing the sample with different frequencies, which is often time-consuming and inconvenient. An alternative way, Pulsed Phase thermography (PPT) is based on idea that a heat pulse can be represented as a number of harmonic signals by Fourier transformation, as well as the detected surface response. In practice, PPT requires one short pulse rather than a series of continuous harmonic signals and mathematical processing of collected array of data (thermal snapshots) [8, 9]. Each row of the 3D array of data represents a time evolution for a particular point on the surface. This temperature evolution curves can be processed individually and the phase part of Fourier-transformation will provide the phases of individual harmonics. Selecting the lowest harmonic in the spectrum allows detecting the deepest defects at the depths comparable to the diffusion length, μ.

Active thermal analysis, as well as acoustic scanning is widely used for studies of layered samples, measurements of thermal properties, defectoscopy of different kinds of materials.

3 Equipment

For the purposes of acoustic inspection the authors used VN Instruments air-coupled acoustic scanning system, equipped with SecondWave Systems transducers with frequencies 200 kHz, 500 kHz and 1,000 kHz. The system consists of the SIA-7 acoustical system and DaVinci-3 scanning frame for performing raster imaging.

The device can be operated in different modes including through-transmission, pulse-echo reflection configuration, and continuous-wave reflection mode.

In order to perform thermographic testing, an ultra fast thermal imager FLIR SC4000 sensitive in 3–5 μm infrared band was used. The material of the detector is InSb, detector resolution 320×256, maximum frame rate – up to several kHz.

The heating was generated by a single Speedotron 206VF 4800 Watt flash lamp.

4 Objects of Inspection

One kind of samples tested was adhesive steel joints, represented by two steel plates connected with epoxy glue (Fig. 5). An artificial “defect” was created by the absence of the adhesive in the center of the joint layer (Fig. 6). The sample was used for demonstration of qualitative detection of thee delamination.

Wooden plates with artificial delaminations were utilized for imitation of ground layer detachment in panel paintings. Several paintings, two panel and two canvas-based ones, were used for demonstration of applicability of thermographic and acoustical techniques for defectoscopy and authentication.

Though acoustic analysis is evidently nondestructive, pulsed thermography remains risky for inspection of paintings. Following results for the artworks were performed in such a way that the surface temperature did not exceed 40–45°C for 1/175 s time duration, which was considered safe [1, 2].

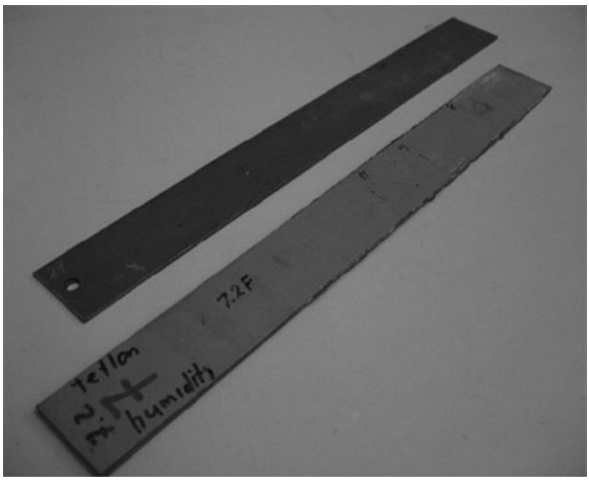

Fig. 5 The samples to be tested

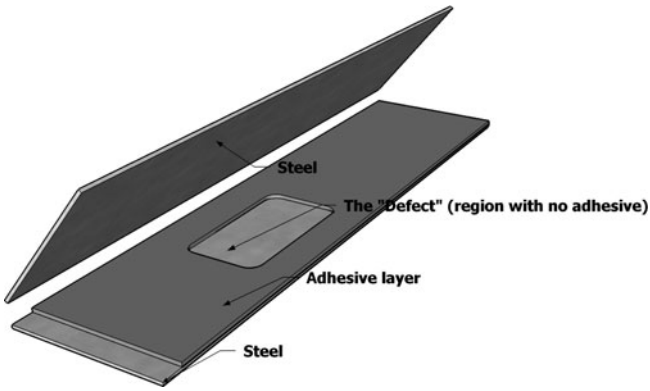

Fig. 6 The scheme of the adhesive joints tested

5 Experimental Results

The results for the adhesive joint sample illustrate good correspondence between the two methods (Fig. 7). The defect was found by both methods, which indicates sensitivity of both methods to serious delaminations.

In case of simulated ground layer detachments again, both methods demonstrate quite similar results (Figs. 8 and 9).

To demonstrate the real applicability of the methods to art analysis, let us discuss the results of real paintings analysis. The first sample, an early twentieth century oil canvas painting, was altered by a restorer (Fig. 10). Namely, the genuine signature was concealed. In visible light there are no signs of fakery. Using the PPT method,

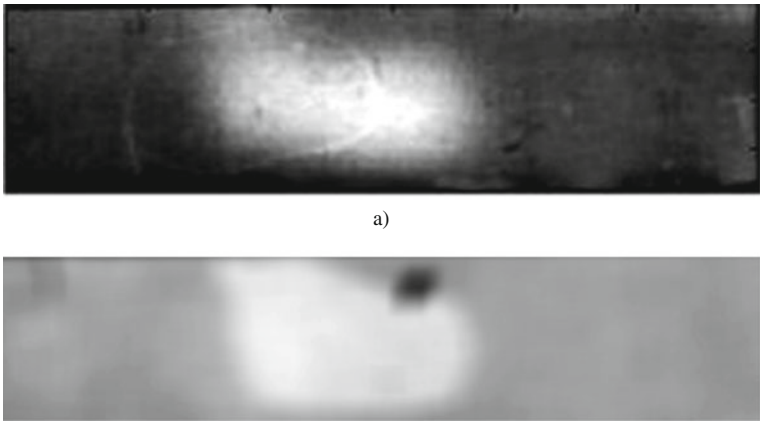

a)

b)

Fig. 7 The results of testing: (**a**) thermographic, (**b**) acoustical

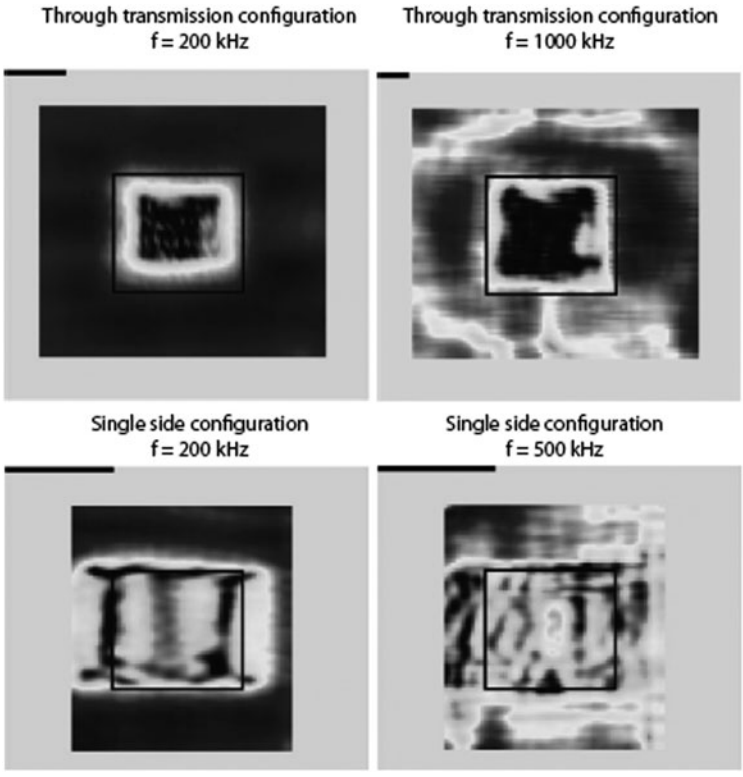

Fig. 8 The results of the acoustic testing

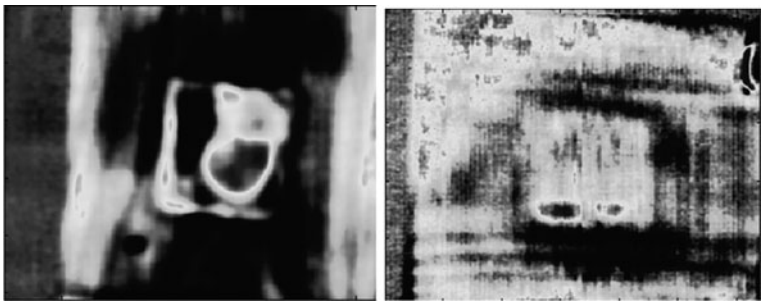

Fig. 9 The results of thermographic testing

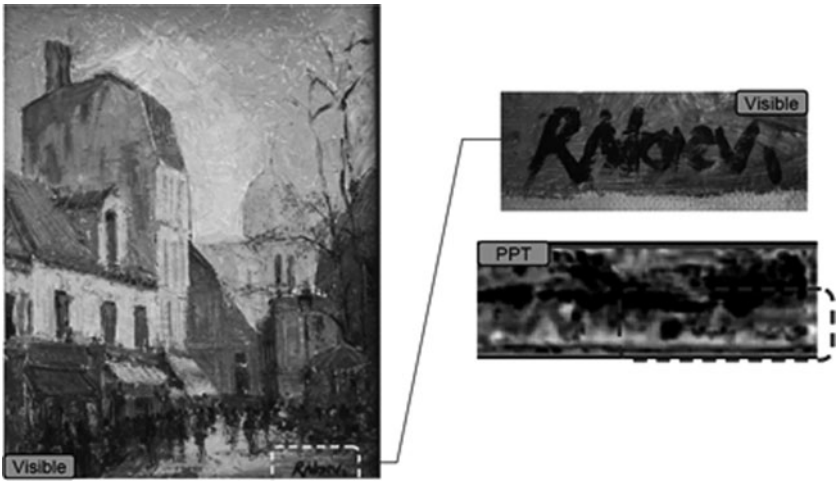

Fig. 10 The painting to be examined

explained above, it was possible to reveal the traces of the concealed signature, which appears twice smaller than the over-painted one.

The second painting, a variation of P. P. Rubens' "Cimon and Pero," demonstrates the alterations made in the central part of the painting (Fig. 11). As a comparison, there is an "Amsterdam version" of the same painting.

Acoustic inspection demonstrates its power in inspection of the panel paintings (Fig. 12). The results collected in single-sided configuration demonstrate the presence of delaminations, which locations can be clearly revealed by threshold processing of the data. Thus, the delaminations found represent the cracks in wood panel caused by aging.

Acoustic inspection demonstrates its power in inspection of the panel paintings (Fig. 12). The results collected in single-sided configuration demonstrate the presence of delaminations, which locations can be clearly revealed by threshold

Fig. 11 The "Cimon and Pero" thermographic test. Below is the painting by the same author from Amsterdam museum

processing of the data. Thus, the delaminations found represent the cracks in wood panel caused by aging.

6 Conclusion

Several examples of acoustic and thermographic inspection were discussed. As it can be seen, both acoustic and thermographic methods are suitable for the search of delaminations in adhesive steel joints. By now these methods are quite common for industry and science [5, 8].

But for the art field both methods are more or less exotic. Nevertheless, they demonstrate enough precision to be applied in art diagnostics. A couple of examples were presented on the application of acoustic and thermographic methods in art analysis. These have demonstrated that both techniques are suitable for detection of detachments in ground layers, where they give comparable results.

On additional examples it was demonstrated that the acoustic scanning is also sensitive to the presence of hollows in wood support, caused by aging. Thermographic analysis illustrated its sensitivity to certain kinds of under-paintings, which confirms the applicability of these methods in art NDE.

Fig. 12 The wooden paintings examined and the results of the acoustic analysis

References

1. Maev, R.Gr., Gavrilov, D., Maeva, A., Vodyanoy, I.: Modern non-destructive physical methods for paintings testing and evaluation, Proceedings of 9th International Conference on "Non-Destructive Investigations and Microanalysis for the Diagnostics and Conservation of Cultural and Environmental Heritage", Jerusalem, Israel (2008)
2. Gavrilov, D., Ibarra-Castanedo, C., Maeva, E., Grube, O., Maldague, X., Maev, R.Gr.: Infrared methods in noninvasive inspection of artwork, Proceedings of 9th International Conference on "Non-Destructive Investigations and Microanalysis for the Diagnostics and Conservation of Cultural and Environmental Heritage", Jerusalem, Israel (2008)
3. Maldague, X.P.: Theory and Practice of Infrared Technology for Nondestructive Testing. Wiley, New York (2001)
4. Maev, R.Gr.: Acoustic Microscopy: Fundamentals and Applications. Wiley-VCH, Weinheim (2008)
5. Maev, R.Gr., Green, R.R., Siddiolo, A.M.: Review of advanced acoustical imaging techniques for nondestructive evaluation of art objects. Res. Nondestr. Eval. **17**, 191–204 (2006)
6. Murray, A., Mecklenburg, M.F., Fortunko, C.M., Green, R.E.: Air-coupled ultrasonic system: A new technology for detecting flaws in paintings on wooden panels. J. Am. Inst. Conservat. **35**(2), 145–162 (1996)

7. Ibarra-Castanedo, C.: Quantitative subsurface defect evaluation by pulsed phase thermography: Depth retrieval with the phase, *PhD thesis*, Universite Laval, Quebec (2005)
8. Breitenstein, O., Langenkamp, M.: Lock-In Thermography: Basics and Use for Functional Diagnostics of Electronic Components. Springer, Berlin (2003)
9. Taft, W. S., Mayer, J.W.: The Science of Paintings. Springer, New York (2000)
10. Ibarra-Castanedo, C., Maldague, X: Defect depth retrieval from pulsed phase thermographic data on plexiglas and aluminum samples. Proc. SPIE, 5405 (2004)
11. Gavrilov, D., Maeva, E., Grube, O., Ibarra-Castanedo, C., Maldague, X., Maev, R.Gr.: Nondestructive diagnostics of paintings with infrared techniques, CAP Congress, Quebec, Canada (2008)
12. Wu, D., Busse, G.: Lock-in thermography for nondestructive evaluation of materials, Revue générale de thermique **37**, 693–703 (1998)

Acoustic Microscope Inspection of Cylindrical Butt Laser Welds

R.Gr. Maev and F. Severin

Abstract Presented work was made in order to develop the ultrasound technique for quality control of critical butt laser welds in automotive production. The set of powertrain assemblies was tested by high resolution acoustic microscopy method. The pulse-echo Tessonics AM 1102 scanning acoustic microscope was modified to accommodate cylindrical configuration of the parts. The spherically focused transducers with frequencies 15, 25 and 50 MHz were used; ultrasonic beam was focused on the joint area. Three-dimensional acoustic images were obtained and analyzed. The clear distinction between weld seam and remaining gap was demonstrated on the B- and C-scans representation. Seam depth varying from 0 up to 3.2 mm was measured along the weld. Different types of defects (porosity, cracks, lack of fusion) were detected and classified. The optimized analytical procedures for signal processing and advanced seam visualization were determined. The results were used as a basis for development of specialized instrumentation for inspection of this kind of parts in industrial environment. The technical requirements were established and the general design of new cylindrical acoustical scanner was made.

Keywords Laser weld · Butt weld · Seam crack · Acoustic microscopy · Non-destructive evaluation

1 Introduction

Linear weld seam is a classical object for nondestructive evaluation. A wide range of applications and variety of welding conditions provides a permanent challenge and requires a new solution for each particular problem. Ultrasound methods also are a classical solution for welds defectoscopy, but each new geometrical configuration of the joints leads to rebuilding of an acoustic inspection scheme [1]. The implementation of new metal alloys into production as well as new more sophisticated welding technologies provide even bigger number of topics for non-destructive evaluation (NDE) research.

R.Gr. Maev (✉)
Chrysler/NSERC Industrial Research Chair in Applied Solid State Physics and Material Characterization, The Institute for Diagnostic Imaging Research, University of Windsor, Windsor, ON N9B 3P4, Canada
e-mail: maev@uwindsor.ca

M.P. André et al. (eds.), *Acoustical Imaging*, Acoustical Imaging 30,
DOI 10.1007/978-90-481-3255-3_23,

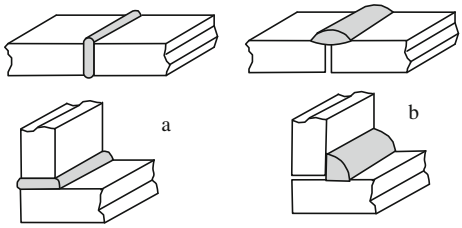

Fig. 1 The butt weld (**a**) and fillet weld (**b**) geometry

The objective of this work was to prove applicability of high-resolution acoustic imaging methods for ultrasonic evaluation of the laser weld seam joining the massive automotive powertrain parts. This is a first and essential stage in adaptation of the technique for industrial use. The next proposed step should be a prototype design and building of a specialized inspection device with perspective integration into production line.

2 Laser Butt Welding

The welds are classified as butt welds if the seam with added material is located between two welded parts (Fig. 1). That position differ it from the fillet weld, when filler metal forms a buildup seam out of surfaces of parts. Generally, the butt welds are more expensive to make than the fillet welds as they may require some additional shaping of the joining surfaces. However, the fillet weld is quite difficult to examine volumetrically using non-destructive testing techniques to confirm its internal soundness. Therefore, the same reliance on the joint integrity should not be placed on the fillet welds as it may be placed on the fully inspectable butt weld.

Heating from laser radiation with filler metal supply can be effectively used for creating of the fillet type of weld seam. However, the most advantages of the laser welding become apparent in case of butt welds. Precisely measured and focused, heating gives an ability to create a weld seam with minimal redistribution of the material and distortion of the parts shape. This fact is especially valuable in the manufacturing of automotive powertrain components where the composite rotating parts (shafts, axles, gears) should be assembled with minimal imbalance. High quality of these assemblies is critical for whole vehicle safety. An accidental equipment malfunction or adjustment problems can cause serious defects like incomplete seam penetration and total lack of fusion [2]. Residual stress appearing during metal melting-solidifying cycle can create cracks in weld area. For this reason, an intensive use of laser welding in the production should be accompanied by reliable testing procedures [3]. The acoustic scanning microscopy with corresponding implementation can serve as convenient NDE inspection technique.

3 Acoustic Scanning of Powertrain Parts

The samples for technology development were provided by MAGNA Powertrain AG & Co KG (Austria). They consist of a flange welded to a cylindrical drum (both made of C60 steel) with laser technology (Fig. 2). The weld seam with nominal

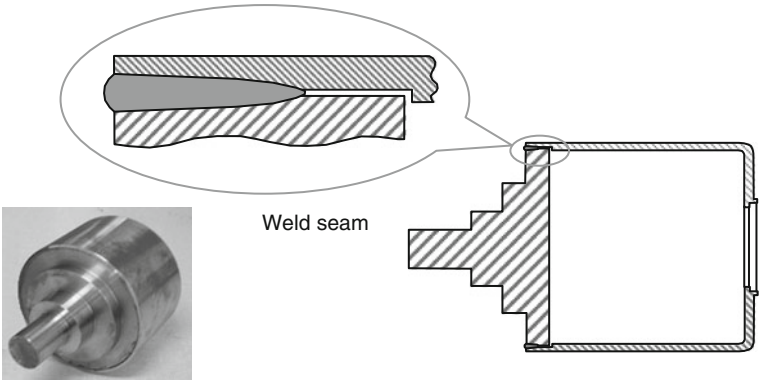

Fig. 2 Structure of the samples

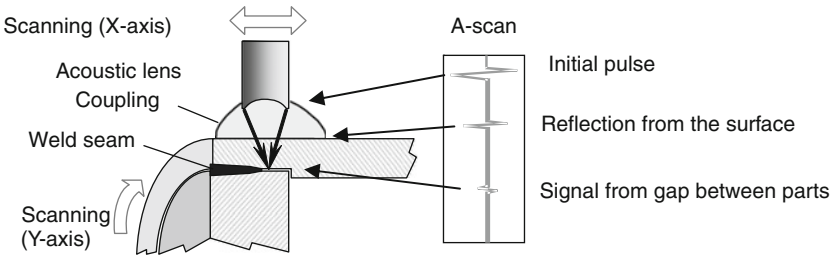

Fig. 3 Acoustical inspection of the weld seam

depth of melting 5–6 mm and width of 1.5–2.5 mm was located 2 mm under side surface. The samples contain intentionally some formed segments of defective welding.

The samples were tested using Tessonics AM 1103 acoustic microscope. Short pulses of focused ultrasound from 50 MHz acoustic lens were sent through a coupling liquid (water) into the sample (Fig. 3). The beam focus was positioned on the gap between two components of the sample. The welded area shows good ultrasound penetration and gives no reflection whereas the unbounded regions completely reflect the sound pulses [4, 5]. The typical B-scan representing the vertical cross-section of the weld seam in the samples is shown on Fig. 4.

The external surface of the drum, the gap between the sample components and, finally, the internal surface of the drum are clearly visible on the scan. The weld seam is represented on the image as absence of the gap and its depth can be measured as a distance between end of the gap and edge of sample. A B-scan like shown above can be obtained in any point along the weld and a corresponding measurement of the weld width can be done. A special rotating fixture was fabricated in order to provide the access to all the points along the weld. Rather than moving the scanning arm across the sloping surface, it was decided to rotate the sample in its place. The sample was mounted onto a metal platform which is rotated by a stepper motor. This keep the welded area of interest fixed in the focal plane of the acoustic lens. The scanner was then rewired so that the Y-control of Tessonics AM 1103 acoustic

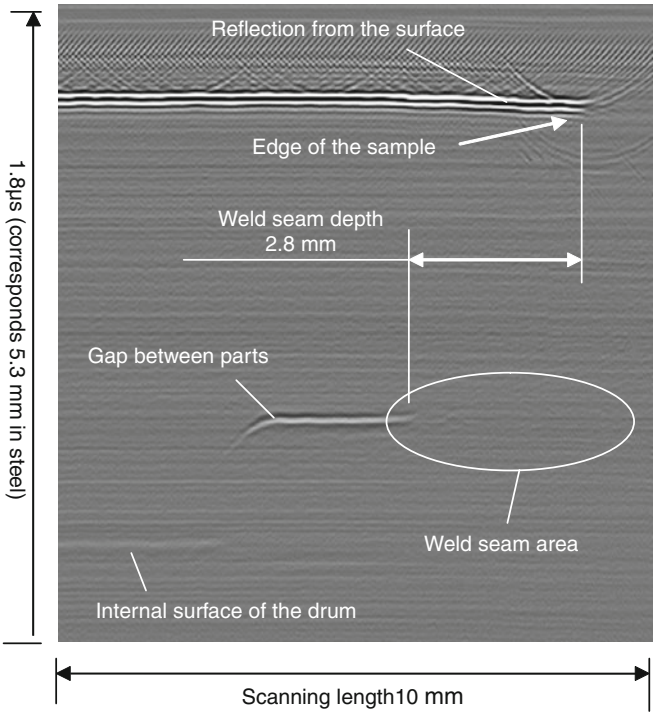

Fig. 4 Elements of B-scan

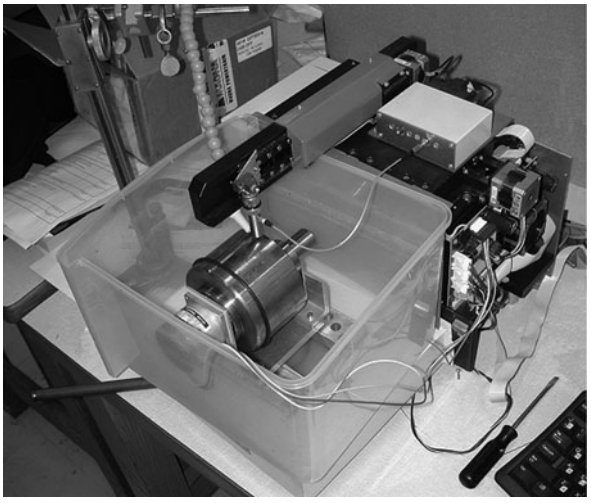

Fig. 5 Experimental setup for inspection of cylindrical parts

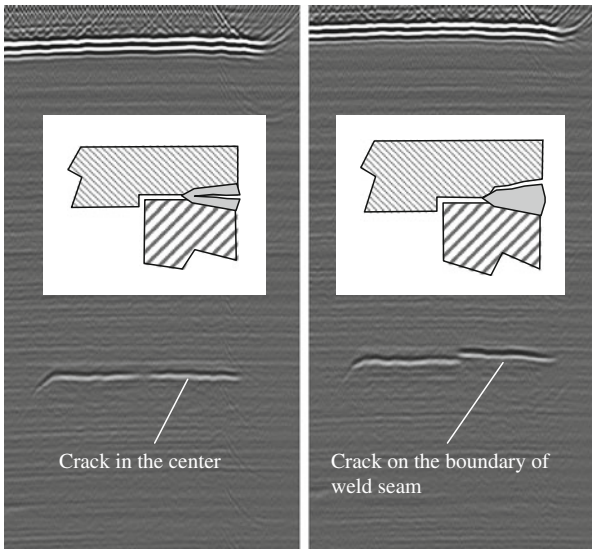

Fig. 6 Cracks appearance on B-scans

microscope, which would normally have moved the scanning arm laterally, would instead drive the motor to rotate the sample at equivalent increments. As the motor could not be submerged in water, a pump system was used to deliver water into the area of acoustic contact (Fig. 5).

4 Acoustic Images of the Weld Seam

The cracks and porosities appear at the B-scans as lines and spots in seam area (Fig. 6). The character of the defect and its exact position can be determined from the analysis of B-scan. Two-dimensional scanning is preferable to find defect distribution along the seam. For every B-scan made by the lens, the cylinder was rotated by an angle of 0.1125 degrees which corresponds to a linear step of 0.1 mm along the weld. As a result, the C-scans that showed welding details all around the sample were obtained. The examples of such C-scans are represented in Fig. 7. The images are stretched along the short side because of big difference in their dimensions, 5 mm width and 340 mm length. Dark areas on the scans represent the properly welded regions, whereas the light areas – completely unbounded regions. The scan in Fig. 7a shows a lot of porosity inside the weld seam and two areas (approximately 20°–70° and 290°–350°) with very low weld penetration. The average depth of the weld is 2.9 mm. The scan in Fig. 7b had a different pattern of the weld penetration; part of the circle contains a good weld with penetration depth of 3.2 mm whereas the rest of the weld shows a huge thermally induced crack inside with few opening to the surface. Defects in both cases are clearly visible and easy to identify.

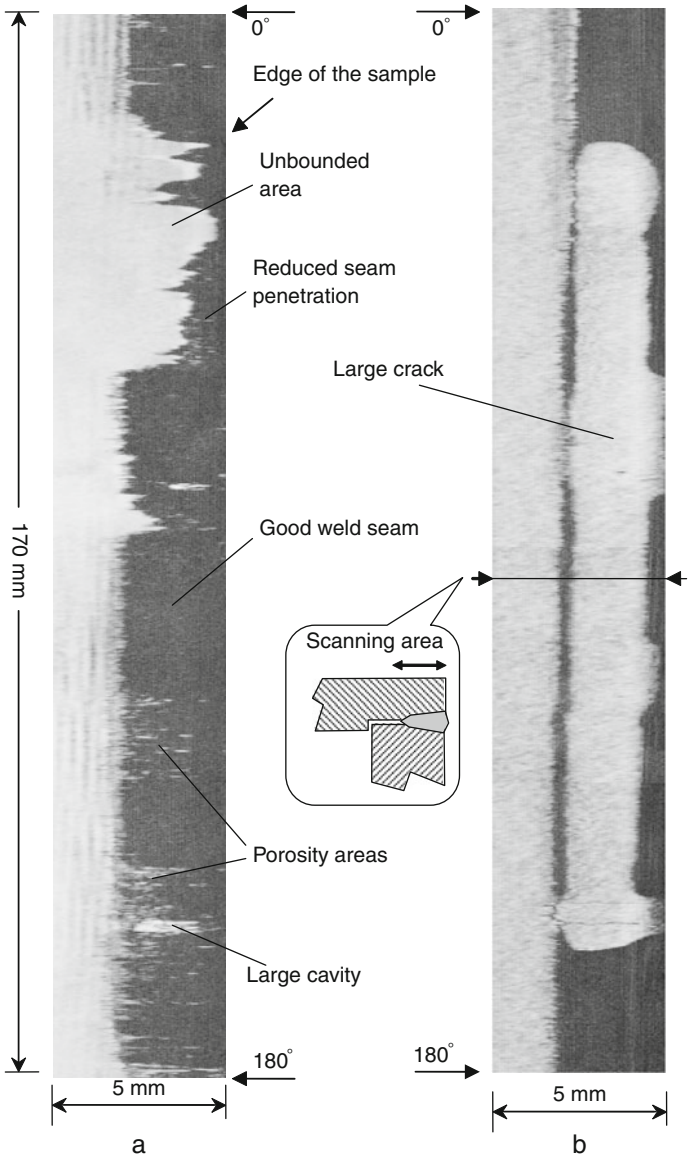

Fig. 7 Cylindrical C-scans with welding defects (**a**) and crack (**b**)

5 Conclusions

An ultrasonic method provides excellent results for nondestructive testing of the laser welds in thick steel automotive parts. Scanner modification gives us ability to accommodate the cylindrical shape of the weld seam and to obtain high resolution

acoustic B- and C-scans. Various types of seam defects including lack of fusion, porosity, cracks, insufficient depth were observed on acoustical images and classified. This methodology can be easily incorporated into production routine as a laboratory off-line inspection or, with corresponding equipment development, as a total in-line screening procedure.

Acknowledgments The authors are grateful to the Magna Powertrain AG & Co. KG (Lannach, Austria) for providing of samples, attention and support to the project.

References

1. ASM Handbook Volume 17: Nondestructive evaluation and quality control. ASM International **795** (1989)
2. Ghasempoor, A., Wild, P., Auger, M., Mueller, R.: Automatic detection of lack of fusion defects in CO_2 laser gear welding. J. Laser Appl. **15**(2), 77–83 (2003)
3. Carrasco, M.A., Mery, D.: A robust algorithm for nondestructive testing of weld seams. In: Chen, C.H. (ed.) Ultrasonic and Advanced Methods for Nondestructive Testing and Material Characterization, pp. 635–658. World Scientific, New York (2007)
4. Maev, R.Gr.: Scanning Acoustical Microscopy. Theory and Application. Wiley, New York (2008)
5. Bisbee, L.H., Nottingham, L.: Longitudinal seam weld characterization by focused ultrasound. In: Prager, M., Tittley, R. (eds.) Proceedings of SPIE, vol. 2947, Nondestructive Evaluation of Utilities and Pipelines, pp. 88–99 (1996)

Part IV
Systems Analysis

Intracardiac Forward-Looking Ultrasound Imaging Catheters Using Capacitive Micromachined Ultrasonic Transducers

A. Nikoozadeh, I.O. Wygant, D.-S. Lin, Ö. Oralkan, K. Thomenius, A. Dentinger, D. Wildes, G. Akopyan, K. Shivkumar, A. Mahajan, D.N. Stephens, M. O'Donnell, D. Sahn, and P.T. Khuri-Yakub

Abstract Atrial fibrillation is the most common sustained arrhythmia that now affects approximately 2.2 million adults in the United States alone. Minimally invasive catheter-based electrophysiological interventions have revolutionized the management of cardiac arrhythmias. We are developing forward-viewing ultrasound imaging catheters based on two types of transducer arrays using the capacitive micromachined ultrasonic transducer technology: A 10-MHz, 24-element MicroLinear (ML) array with a footprint of 1.7 mm × 1.3 mm, and a 10-MHz, 64-element annular ring array with an outside diameter of 2.6 mm and inner diameter of 1.6 mm. Both arrays are integrated with custom-designed front-end electronic circuitry to overcome the performance degradation associated with long cables in the catheter. The ML and ring arrays provide real-time 2-D and 3-D images, respectively, in front of the catheter tip. Using the ML array, we demonstrated ex-vivo images of the left atrial appendage in an isolated Langendorff-perfused rabbit heart model and in-vivo images of heart through the open chest in a porcine animal model. We used the ring array to demonstrate 3-D images of coronary stents and an anatomic cast of a left atrial model.

Keywords Intracardiac imaging · Intracardiac echocardiography · Ultrasound imaging · Forward looking · Cardiac electrophysiology · Capacitive micromachined ultrasonic transducer (CMUT) · Catheter

1 Introduction

Atrial fibrillation is the most common type of cardiac dysrhythmia that now affects approximately 2.2 million adults in the United States alone [1]. Minimally-invasive catheter-based electrophysiological (EP) interventions provide valuable information about the electrical behavior of the cardiac muscle that yields to better diagnosis and treatment of arrhythmias. Catheter-based radio-frequency (RF) ablation, which is the most common ablation therapy, is often used to destroy a small amount of

A. Nikoozadeh (✉)
Stanford University, Stanford, CA, USA
e-mail: aminn@stanford.edu

M.P. André et al. (eds.), *Acoustical Imaging*, Acoustical Imaging 30,
DOI 10.1007/978-90-481-3255-3_24,

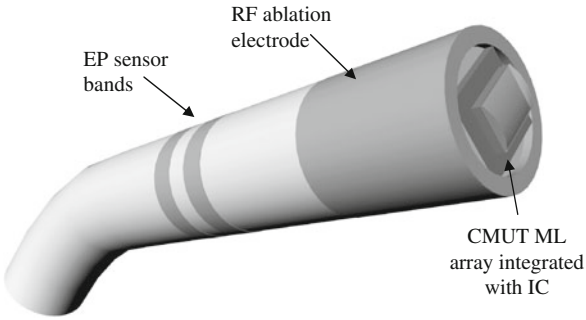

Fig. 1 Conceptual drawing of the multifunctional EP-ICE ML catheter. This catheter is capable of forward-looking imaging and is equipped with EP sensor bands and RF ablation electrode

the malfunctioning tissue that causes the arrhythmia. Multiple catheters are used for electrophysiology assessment and ablation.

Currently, fluoroscopy is the standard method for navigating catheters throughout these procedures. This guidance method exposes both the patient and the practitioner to hazardous ionizing radiation that could take tens of minutes. Also the poor soft-tissue resolution of fluoroscopy, even with the use of contrast agents, does not provide adequate anatomical information for precise catheter positioning in the heart [2].

We are developing forward-looking intracardiac ultrasound imaging catheters for real-time guidance and monitoring of EP interventions. These are multi-function catheters that are integrated with EP electrodes and ablation devices (Fig. 1). These catheters not only simplify interventions in the heart and improve the procedural success but also reduce the undesirable use of fluoroscopy.

2 Methods

2.1 CMUT Arrays

We are developing forward-viewing ultrasound imaging catheters based on two types of transducer arrays using the capacitive micromachined ultrasonic transducer (CMUT) technology: MicroLinear (ML) array and ring array. Both these transducers are designed for a center frequency of 10 MHz. For the design of the CMUT arrays we used the linear CMUT equivalent circuit model [3]. Some of the parameters required for this circuit were derived using the analytical calculation of the membrane displacement [4]. Table 1 summarizes the design parameters of these transducer arrays.

The ML array is a 1-D transducer array composed of 24 elements with an element pitch of 63 μm (Fig. 2). The device measures about 1.3 mm × 1.7 mm. This device provides real-time 2-D images in front of the catheter tip. The ring array is composed of 64 elements that are approximately 100 μm × 100 μm in size (Fig. 3). The outer diameter of the device is about 2.6 mm and the inner diameter measures

Table 1 Design parameters of the CMUT arrays

CMUT ML array		CMUT ring array	
Center frequency	10 MHz	Center frequency	10 MHz
Number of elements	24	Number of elements	64
Element pitch	63 μm	Element size	100 μm × 100 μm
Device size	1.3 mm × 1.7 mm	Outer/inner diameter	2.6 mm/1.6 mm

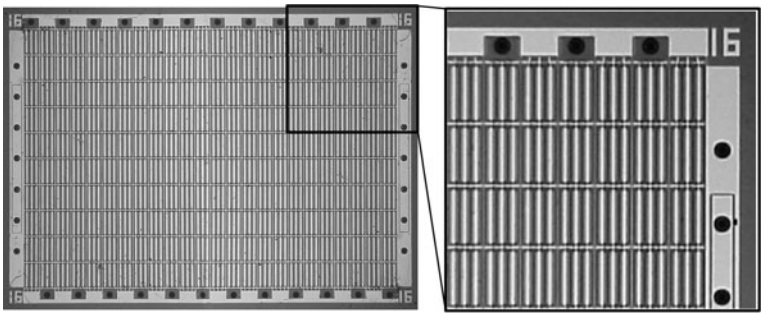

Fig. 2 Photograph of the front side of a CMUT ML array

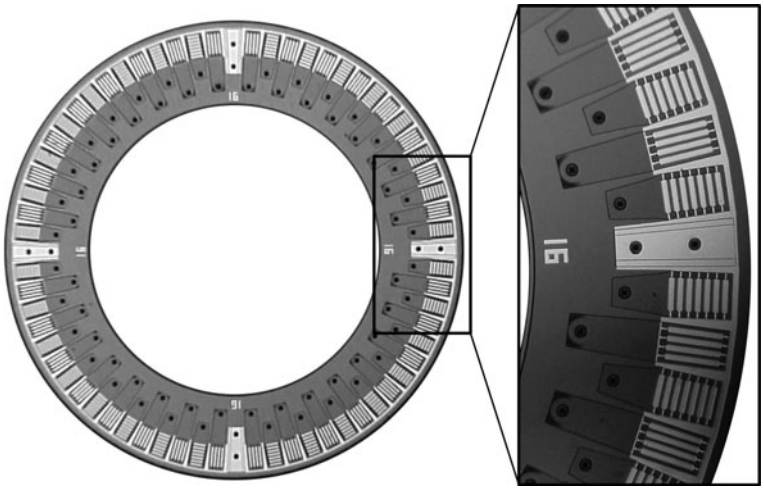

Fig. 3 Photograph of the front side of a CMUT ring array

about 1.6 mm in diameter. This device is capable of providing real-time volumetric images in front of the catheter tip. Also the central lumen available in the ring array geometry enables a variety of other applications such as high intensity focused ultrasound, photoacoustic imaging, laser and RF ablation, etc.

The CMUT arrays were fabricated using the standard polysilicon sacrificial layer process with through-wafer via interconnects [5]. The silicon nitride membrane is

0.5-μm thick, the thickness of the bottom electrode insulation layer is 180 nm, and the vacuum gap height measures 150 nm. The through-wafer via interconnects provide electrical connection to individual array elements from backside pads. These pads facilitate the tight integration with the front-end supporting electronics through flip-chip bonding.

2.2 Custom-Designed Front-End Electronics

Catheter cables usually account for a capacitance of approximately 100 pF/m. Each element of the CMUT array has a capacitance of about 1–2 pF. Therefore direct connection of the transducer elements to the imaging system will result in performance degradation. A closely integrated front-end electronics with the transducer array enhances the SNR and hence the image quality.

We designed a custom front-end electronics composed of 24 transmit/receive channels. Each channel is composed of a pulser, a switch, a transimpedance amplifier and a buffer (Fig. 4a, b). The pulser can provide up to 25-V unipolar pulses. The switch is used to isolate the low-voltage amplifier from the pulser during the transmit cycle. The transimpedance amplifier provides low impedance for the transducer while providing a better noise performance than a simple resistive load termination. This integrated circuit (IC) has matching pads with the CMUT ML array for flip-chip bonding.

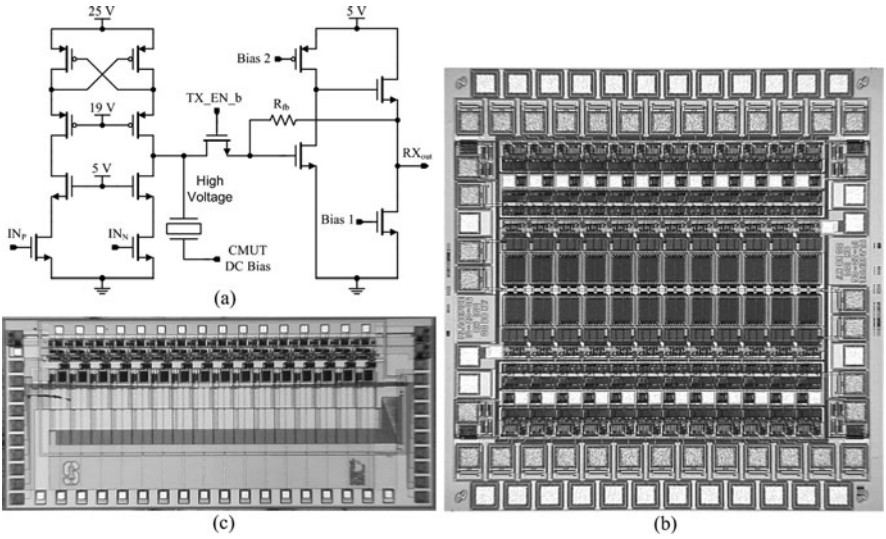

Fig. 4 (**a**) Schematic of the main components of one channel of the custom front-end IC, (**b**) 24-channel design for ML array, (**c**) 16-channel preliminary design for ring array

A 16-channel version of the same circuit topology was used for an early assessment of the ring array imaging capability (Fig. 4c). Four IC's were wire-bonded to the 64-element ring array in a ceramic package.

3 Imaging Results

3.1 ML Array

For preliminary experiments, we flip-chip bonded an ML array to the 24-channel custom IC and then wire-bonded the IC pads to a ceramic package. A commercial imaging system was used for imaging experiments. Additional electronic circuitry was designed to interface the imaging system to the custom IC.

The assembly was used to image standard phantoms and an *ex vivo* rabbit heart. Figure 5a shows an image of a contrast resolution test phantom (rubber-based soft tissue-mimicking material, ATS Laboratories, Inc., Bridgeport, CT). Figure 5b shows an image of a standard point resolution test phantom (Model RMI 404GS LE gray scale phantom, Gammex, Inc., Middleton, WI). Figure 5c shows one frame of the real-time image of the left atrial appendage of an isolated Langendorff-perfused rabbit heart.

3.2 Ring Array

For preliminary experiments, we wire-bonded a ring array to four 16-channel custom IC's in a ceramic package. A PC-based data acquisition system was used to collect the data. Volumetric images were reconstructed offline with the full 64×64 set of data using synthetic phased-array image reconstruction method. Norton's weightings [6] and cosine apodization [7] were applied to obtain the full-disk resolution and to suppress the side-lobes, respectively.

Figure 6a, b show cross-sectional and 3-D rendered images of an undeployed stent and an anatomical cast of atrial model, respectively.

4 Conclusion

We demonstrated real-time ultrasound imaging with a 1-D forward-looking CMUT array. We also confirmed the volumetric imaging capability of a forward-looking CMUT ring array. These results show that using the CMUT technology we can make high-frequency, miniature transducer arrays with different geometries that are readily integrated with electronics to guide catheter-based intracardiac and intravascular interventions.

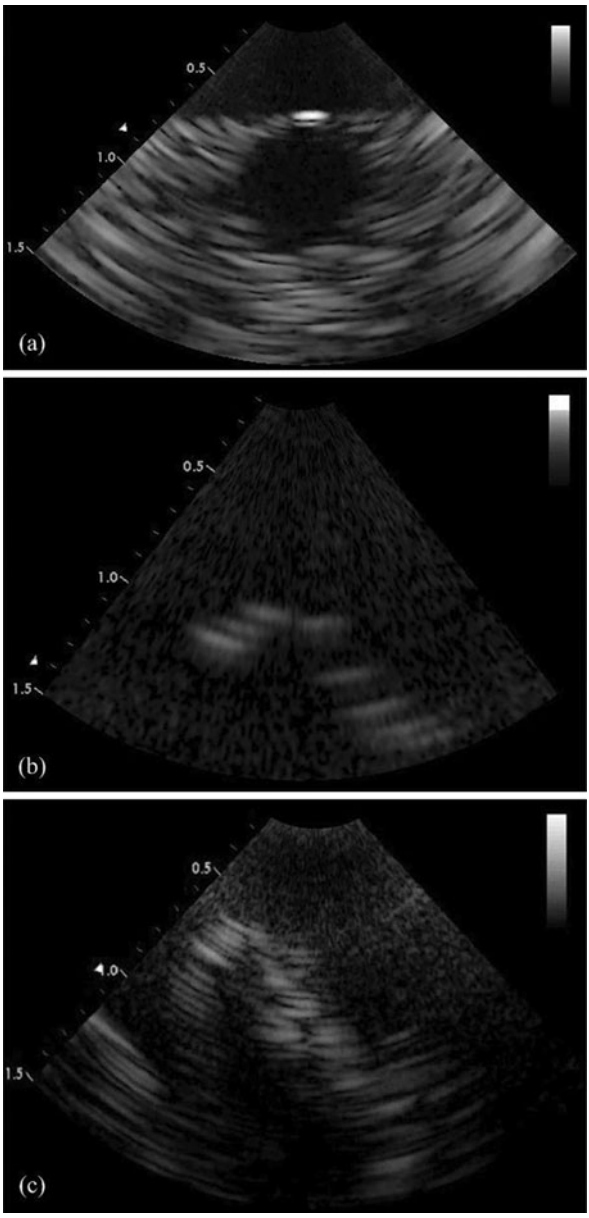

Fig. 5 Images with the CMUT ML array assembly in the PGA package. (**a**) An image of a contrast resolution test phantom. (**b**) An image of a point resolution test phantom. (**c**) An image of the left atrial appendage of an isolated Langendorff-perfused rabbit heart

We are currently working on the full integration of the arrays and the custom front-end IC's within the catheter for forward-looking imaging. We are also working on a second generation front-end electronics that would allow for direct connection to the commercial imaging systems to take full advantage of their capabilities.

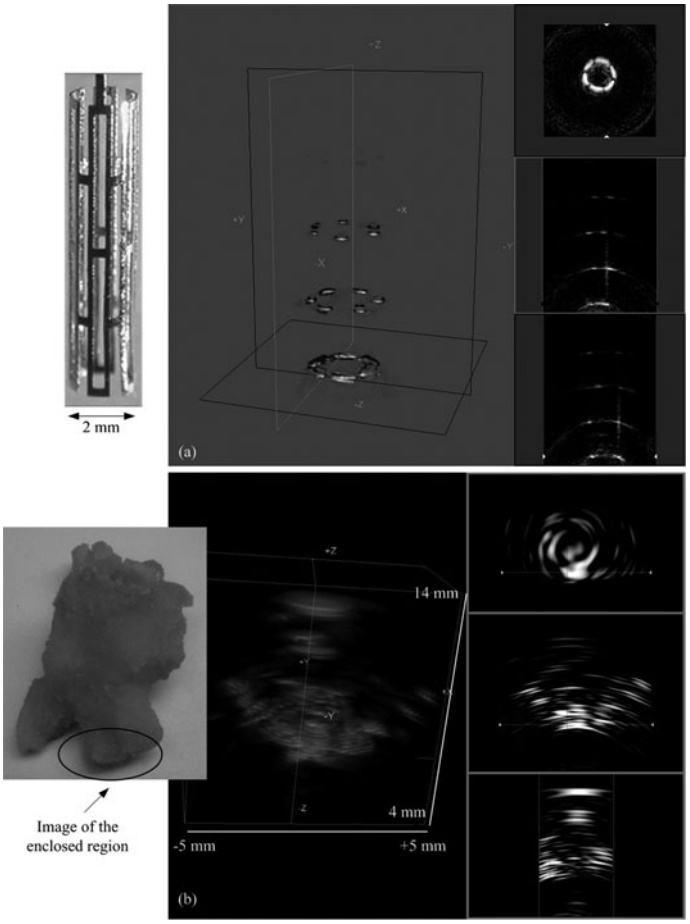

Fig. 6 Images of (**a**) an undeployed stent, and (**b**) an anatomic cast of left atrial model

Acknowledgments This work was supported by the National Institutes of Health under grant HL67647, USA. We thank National Semiconductor (Santa Clara, CA) for their valuable support in the design and fabrication of the IC. CMUT fabrication was done at the Stanford Nanofabrication Facility (Stanford, CA), which is a member of National Nanotechnology Infrastructure Network. Pac Tech USA, Inc. (Santa Clara, CA) provided electrodeless Ni/Au UBM plating and solder bumping.

References

1. Go, A.S., Hylek, E.M., Phillips, K.A., et al.: Prevalence of diagnosed atrial fibrillation in adults: National implications for rhythm management and stroke prevention: The anticoagulation and risk factors in atrial fibrillation (ATRIA) study. JAMA **285**(18), 2370–2375 (2001)

2. Burke, M.C., Roberts, M.J.D, Knight, B.P.: Integration of cardiac imaging and electrophysiology during catheter ablation procedures for atrial fibrillation. J. Electrocardiol. **39**(4), S188–S192 (2006)
3. Lohfink, A., Eccardt, P.-C.: Linear and nonlinear equivalent circuit modeling of CMUTs. IEEE Trans. Ultrason. Ferroelect. Freq. Contr. **52**(12), 2163–2172 (2005)
4. Nikoozadeh, A., Bayram, B., Yaralioglu, G.G., et al.: Analytical calculation of collapse voltage of CMUT membrane [capacitive micromachined ultrasonic transducers]. Proceedings of the IEEE Ultrasonics Symposium, vol. 1, 256–259 (2004)
5. Ergun, A.S., Huang, Y., Zhuang, X., et al.: Capacitive micromachined ultrasonic transducers: Fabrication technology. IEEE Trans. Ultrason. Ferroelect. Freq. Contr. **52**(12), 2242–2258 (2005)
6. Stephen, J.N.: Annular array imaging with full-aperture resolution. J. Acoust. Soc. Am. **92**(6), 3202–3206 (1992)
7. Brunke, S.S., Lockwood, G.R.: Broad-bandwidth radiation patterns of sparse two-dimensional vernier arrays. IEEE Trans. Ultrason. Ferroelect. Freq. Contr. **44**(5), 1101–1109 (1997)

Conformal Ultrasound Imaging System

R.S. Singh, M.O. Culjat, M. Lee, D.B. Bennett, S. Natarjan, B.P. Cox, E.R. Brown, W.S. Grundfest, and H. Lee

Abstract A conformal ultrasound imaging system has been developed that may potentially provide improved acoustic signal acquisition by wrapping around objects with increased angular coverage. The system features a conformal ultrasound transducer array, with bulk ceramic PZT elements mounted on etched silicon islands connected by patterned flexible polyimide joints, customized portable transmit/receive electronics, and backward propagation based image reconstruction techniques. The system was used to image a cylindrical tissue phantom, demonstrating successful operation and the feasibility of the conformal ultrasound approach.

Keywords Conformal · Imaging system development · Flexible transducer · Lead zirconate titanate (PZT)

1 Introduction

Flexible or conformal ultrasound transducer arrays have previously been proposed as alternatives to rigid multi-element transducers for medical imaging and non-destructive evaluation (NDE) [1–4]. Flexible transducer arrays can wrap around objects or curved body surfaces with increased angular coverage relative to rigid transducers or handheld medical probes. The larger aperture and conformal nature of flexible transducers may allow for improved detection of objects or defects that are outside of the direct sight lines of rigid transducers by collecting additional acoustic information (Fig. 1). Flexible transducers may also eliminate the need to manually translate and rotate transducers to locate landmarks, therefore reducing or eliminating the expertise associated with handheld mechanical scanning. While various flexible transducers have been proposed or fabricated, no dedicated flexible transducer-based imaging systems have been developed to date, and therefore the viability of the approach has yet to be determined.

This paper presents a complete ultrasound imaging system, including a micro-fabricated conformal transducer, dedicated transceiver electronics, and customized

R.S. Singh (✉)
Department of Electrical and Computer Engineering, University of California, Santa Barbara, CA, USA
e-mail: rsingh@soe.ucsc.edu

M.P. André et al. (eds.), *Acoustical Imaging*, Acoustical Imaging 30,
DOI 10.1007/978-90-481-3255-3_25,

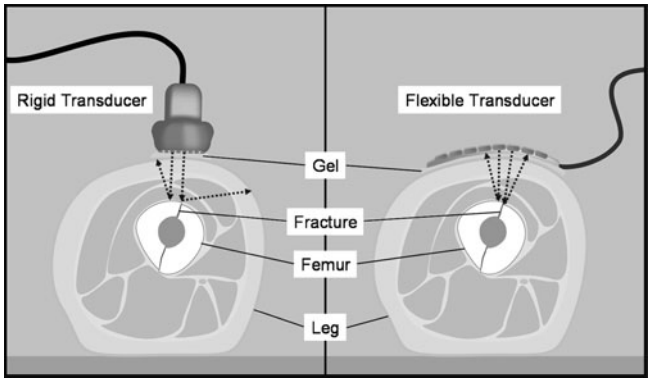

Fig. 1 Conformal ultrasound transducer concept illustrated (placed upon a leg) in comparison to traditional, rigid ultrasounds transducer arrays

image reconstruction techniques, as well as preliminary imagery from a cylindrical tissue phantom. The transducer array was fabricated on a flexible substrate comprised of silicon islands attached together with microfabricated polyimide joints. Ceramic lead zirconate titanate (PZT) piezoelectric elements were used to operate in thickness mode at a fundamental (center frequency) of 11.4 MHz, with a backing layer to improve bandwidth and dual parylene coatings to improve soft tissue matching and structural integrity of the device. A portable, lightweight transceiver was developed consisting of a microcontroller, a superhetrodyne down converter, a pair of 14-bit A/D converters for the I and Q channels, and 14-bit D/A to construct arbitrary transmit waveforms. Pulse-CW signals were used with a pulse width of 200 ns, corresponding to a width of 1.8 μs in water for the experiments. Both experimental and simulated data was used to test and validate the image reconstruction algorithms developed for the system. Image reconstruction was performed using a backward propagation-based algorithm. Phantom imagery was obtained using custom image reconstruction algorithms. While preliminary, the resulting images fundamentally demonstrate the feasibility of the conformable ultrasound array concept.

2 Conformal Ultrasound Transducer Array

Flexible ultrasound transducers have previously been proposed and fabricated using a number of techniques. Flexible transducers were constructed by embedding ceramic rods in a passive polymer matrix, with the authors reporting a design tradeoff between aspect ratio and flexibility [5, 6]. Capacitive microfabricated ultrasound transducers (CMUTs) were fabricated on a sectioned wafer with the etch trenches refilled with polydimentysiloxane (PDMS) [3, 4]; these arrays had high flexibility, but were reported to have limited robustness due to cracking of the electrical traces bridging the PDMS-refilled trenches. In another approach, a high temperature transducer for nondestructive evaluation (NDE) was fabricated by iteratively

air-brushing sol-gel PZT through a shadow mask directly onto thin-film steel foils, and was reported to be robust and resilient even at high temperature [5, 6]. However, both sol-gel PZT and CMUTs are known to have lower electromechanical efficiency than bulk piezoelectrics.

Several recent fabrication strategies have employed rigid bulk piezoelectric materials and packaged them onto flexible substrates or assemblies. Fabrication methods have included attaching bulk piezoelectrics onto flexible printed circuits [5], transferring bulk piezoelectrics from polydimethylsiloxane (PDMS) templates to flexible substrates with adhesive films [6], and mounting transducers onto spring-loaded probe matrices [7, 8]. Some of these bulk piezoelectric fabrication strategies have yielded fully-packaged flexible devices, but with limitations in uniformity and scalability. The approach outlined here focuses on transducer arrays featuring bulk piezoelectric elements mounted on a microfabricated array of silicon islands, connected with flexible polyimide joints.

2.1 Fabrication Process

8 × 1 element conformal transducer arrays were fabricated with flexible polyimide joints. Polyimide was selected because it is mechanically strong, readily patternable by photo-lithographic techniques, and resistant to chemicals used in microfabrication processes [5]. It has a low coefficient of thermal expansion and adheres well to many materials through broad temperature latitude. The transducer featured bulk lead zirconate titanate (PZT) elements mounted on silicon islands that were connected by flexible polyimide joints and reinforced with parylene (Fig. 2). Bulk PZT was selected due to its piezoelectric properties, especially in terms of electro-acoustic efficiency. The silicon islands were 2.5 mm × 2.5 mm and the PZT elements were 1.8 mm × 1.8 mm.

A silicon wafer was sectioned via deep reactive ion etching (DRIE) to produce an array of silicon mesas. A polyimide layer was spin coated and cured onto the bottom side of the wafer. The silicon on the top-side of the wafer was etched to

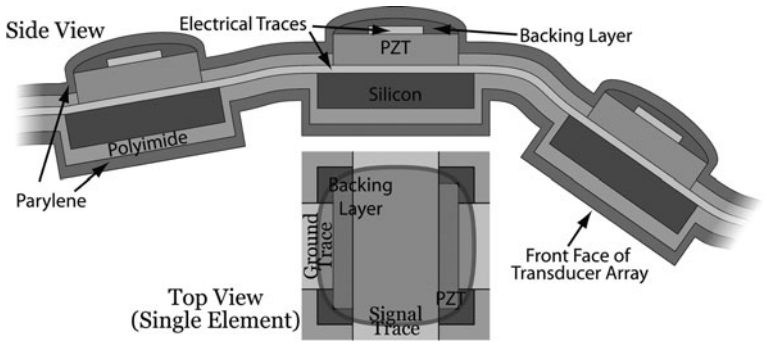

Fig. 2 Illustration of conformal ultrasound transducer cross section and top view

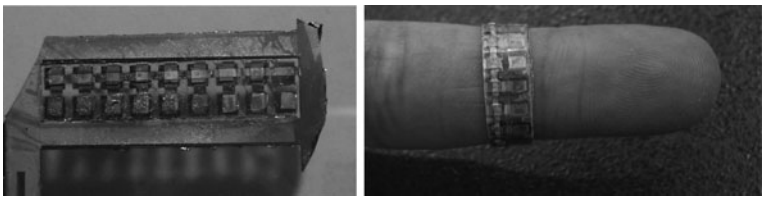

Fig. 3 Image of the completed transducer in its silicon frame (*left*), shown without backing layer for clarity, and wrapped around index finger (*right*)

release a flexible substrate of silicon islands with polyimide joints. An aluminum electrode film was sputtered and patterned onto the flexible substrate, and an additional polyimide layer was cured and patterned atop the wafer to encapsulate and protect the electrodes, reinforce the flexible joints, and serve as alignment trenches for the placement of piezoelectric elements on the silicon islands (Fig. 3).

Ceramic PZT elements were diced and attached to the silicon islands using thin layers of silver paste, and a conformal parylene layer was added and patterned to both mechanically secure and electrically isolate the bottom electrode and traces of the PZT. Via holes were etched into the top PZT electrodes using oxygen plasma. A second set of electrical leads composed of chromium and gold were patterned by electron beam evaporation through a shadow mask of Kapton film, connecting to the top electrode through the via holes in the parylene. A tungsten-loaded epoxy acoustic backing layer and an additional parylene film were then added.

The silicon elements served as the mechanical substrate for the piezoelectric elements and, in combination with the parylene, achieved acoustic impedance matching to soft tissue. The polyimide formed the flexible joints between the silicon islands, and also supported the aluminum and gold electrical interconnections. A column of gold solder pads was fabricated adjacent to the column of piezoelectric elements in the linear arrays.

2.2 Conformal Transducer Characterization

The transducer joints were mechanically characterized by measuring the stiffness coefficient and examining the joints and electrical interconnects following multiple bending cycles. Stiffness of the polyimide/parylene joints, determined by bending the joints with a known force, was 24.5 N/m, comparable to 10 μm thick aluminum foil. Durability was confirmed after microscopic and electrical examination revealed no visible or measureable electrical deterioration of the thin-film traces following 10,000 bending cycles.

The transducers were electrically characterized by recording S_{11} reflectance data using a vector network analyzer (HP 3577B Network Analyzer, Hewlett Packard, Inc). The average fundamental thickness mode resonant frequency was measured as 11.4 MHz, and the 3 dB bandwidth was measured to be 27%. The average characteristic impedance was 43 Ω. The measured acoustic pulse (Fig. 4) width was 1.8 μs

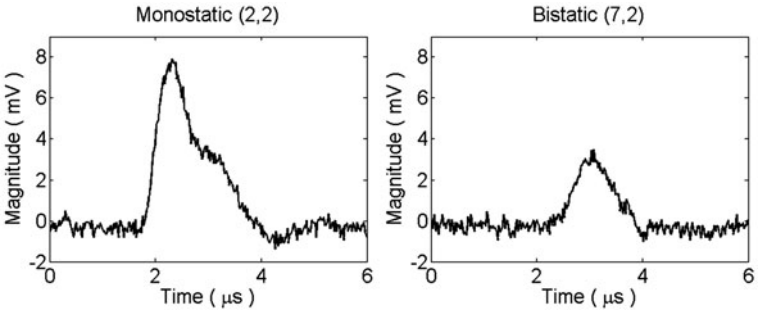

Fig. 4 Representative acoustic pulse-echo data from transducer wrapped around a steel rod in a phantom. Monostatic data is shown from (2,2) transmit/receive element pair (*left*) and bistatic data from (7,2) element pair

in water, upon excitation with a 200 ns, 2.5 V_{pp} continuous wave pulse. The operating (or sensor) signal-to-noise ratio (SNR) of the monostatic pairs (maximum SNR) was 39 dB using a low noise amplifier (Minicircuits ZFL-1000LN) for the receiver.

3 System Electronics

The conformal imaging system was designed to be low cost, portable, and adaptable to various applications. In order for portability to be achieved, it is important not only to reduce the size of the system but to minimize overall system power needs. Bulk ceramic PZT materials were used to maximize electro-acoustic efficiency so as to reduce drive voltages, and the transducers were designed with input impedance near 50 Ω in order to leverage widely available off-the-shelf RF electronics.

The imaging system has been designed to use both a pulse-CW and step FMCW format. FMCW signaling illuminates a volume of interest with a sequence of continuous waves. While the step FMCW operating modality differs from pulse-echo systems with regard to the form of the received data, both ultimately provide range estimation data for image reconstruction. In fact, it has been shown that the step FMCW and pulse-echo modalities are time-frequency counterparts, whose data formats can be interchanged using FFTs and scaling operations [3].

3.1 Transceiver and System Electronics

A custom transceiver was developed and integrated with the conformal transducer array. The transceiver (Fig. 5) was comprised of an arbitrary waveform transmitter, a super-heterodyne down-converter, and 65 MSample A/D converters, controlled and connected to laptop via USB. The transmitter is comprised of a 166 MSamples/s D/A converter connected via USB to a laptop. This laptop connection allows for arbitrary signal generation by first designing the waveform on the laptop and then downloading it to the transmitter where it is converted to an analog waveform. The

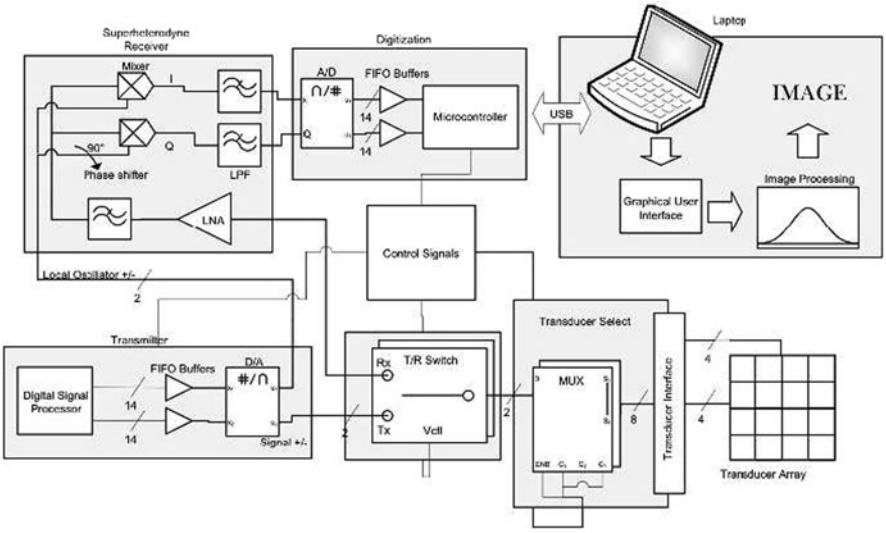

Fig. 5 Block diagram for system electronics

analog waveform is then routed to the desired firing element through a 16 channel multiplexer (MUX) and T/R switch controlled by the laptop. To transmit and receive through a pair of transducer elements, first the T/R switch is put into the transmit position and the MUX is configured to connect to the desired transmitting element. After the transmit waveform is applied to the element, the T/R switch is then put into the receive position and the MUX is configured to connect to the receive element. The received waveform is then down-converted from the RF frequency (same as the center frequency of operation) to baseband through the super-heterodyne down-converter. The receiver is comprised of two mixers and low pass filters (i.e., classical I-Q demodulator architecture) so as to extract the in-phase and quadrature phase baseband signals. The baseband signals are then digitized using the A/Ds and the digital waveforms are uploaded to the laptop via USB.

3.2 Signal Acquisition

The conformal ultrasound transducer functions multi-statically. For FMCW, during a frequency step within an illumination cycle, one element transmits CW while all elements, including the transmitter, are in receive mode. This repeats as another element assumes the role of the transmitter. Therefore, an M-element transducer array will produce M^2 received complex data sequences, one for each permutation of element pairs including monostatic data. For pulse-CW operation, the principle is the same, with one element selected and connected to the transmitter through the MUX. Once the signal is transmitted, the T/R switches to the receiver position and the MUX is reconfigured to select any element to record the reflected acoustic

signals. Each of the transmit and receive element pairs are cycled through to collect a complete data set for the image reconstruction algorithms.

4 Image Reconstruction

A space-time image reconstruction technique was used in the conformal ultrasound imaging system. The technique is based upon the backward propagation method [3]. The image reconstruction algorithm was developed to account for arbitrary transducer array geometries due the flexible nature of the array. Simulations were performed to test the viability of and further examine the space-time image reconstruction algorithm in the step FMCW environment. Various atypical transducer element configurations, mimicking a range of possible transducer conformations, and point target distributions were conceptualized on a 2D range bin matrix. A simple soft tissue phantom with a stainless steel rod in the center (to mimic bone) was imaged to evaluate the conformal ultrasound imaging concept.

4.1 Image Reconstruction Algorithms

As previously noted, mathematical formulation of the step FMCW data acquisition format showed that time-delay profiles are obtained through IFFTs of the acquired spectral data sequences. Since a unique spectral data sequence is collected for each pair of elements, there is a unique time-delay profile associated with each pair. The time-delay profiles are scaled by the propagation speed and a linear phase term to give range profiles for the space-time image reconstruction.

Given the coordinates of the transducer elements, space-time image reconstruction is achieved by mapping multistatic range profiles onto a discrete 2D matrix of range bins. From the perspective of a particular element pair, each bin is characterized by a total range distance $R_{total} = R_1 + R_2$. That is to say, if a point target existed at that bin location, R_{total} denotes the range traveled by the acoustic wave from the transmit element, to the target, and back to the receive element. The range profile for that element pair is referenced, and the complex magnitude located at the index R_{total} is added to the bin location of the image matrix.

This procedure repeats and information provided by each element pair is superimposed onto the image matrix. Increasing target energy causes SNR to rise and improves the target's visibility. Consider a point target occupying a single bin in the image matrix, surrounded by a circular aperture of array elements. Theoretically, each range profile would exhibit a sharp peak, signifying target presence. Mapping a profile onto the image matrix visually results in the demarcation of a thin ellipse with its foci located at the two element positions. This ellipse indicates all possible locations of the single target. As other element pairs contribute their respective ellipses (or circles, as in the case of a monostatic pair), the target emerges in its proper location as the single bin's value grows in correspondence to the areas of

repeated intersection. The extent to which non-target bin values also increase is dictated by the relative sharpness and prominence of the range profile peak, and is governed in large part by system bandwidth.

The image reconstruction algorithm developed for the conformal imaging system accommodates various array geometries and is capable of producing high quality imagery.

4.2 Simulated Data

Based on the element locations, theoretical range profiles for the targets were generated for each element pair, and then scaled to time-delay profiles according to a typical soft tissue propagation speed of 1,490 m/s. Each 2048-point time-delay profile was selected to accommodate a maximum delay of 50 μs, setting the sampling frequency at 40.96 MHz.

The time-delay profiles were converted to step FMCW data through the FFT operation, and appropriate frequency components in the spectra were selected to model the desired limited bandwidth of the system. The modified spectra were then converted back to give bandlimited time-delay profiles, which were used to reconstruct the image based on the process outlined in Section 4.1.

The reconstructed image shown in Fig. 6 represents a 3 cm by 3 cm area (150 by 150 range bins), with elements depicted in bright white. The dimension of each range bin was selected to reflect the scale of the range resolution, with the understanding that exceedingly large matrices, though never detrimental to the image,

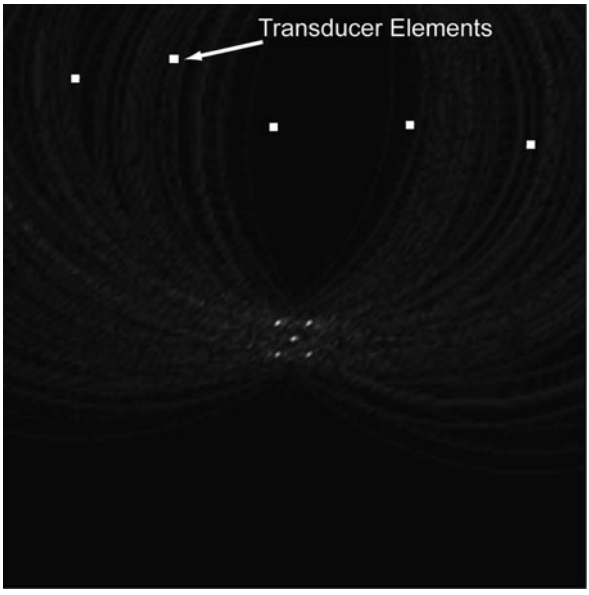

Fig. 6 A distribution of five point targets imaged fewer than five irregularly spaced transducer elements with a 4 MHz of bandwidth. Element locations (near *top* of image) are denoted in *bright white* and indicated by the *arrow*. Higher magnitudes are denoted by brighter regions

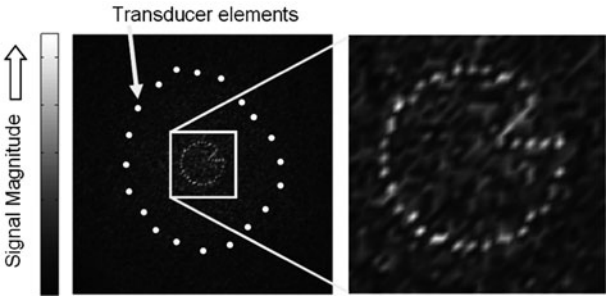

Fig. 7 A distribution of point targets (mimicking a bone with crack) imaged under irregularly spaced transducer elements (mimicking conformal wrapping) with a 0.5 MHz of bandwidth. Element locations are denoted in *bright white* and indicated by the *arrow*. Higher magnitudes are denoted by brighter regions

require more processing time. Figure 6 shows the simulated reconstruction of a dense group of five point targets, as close as 1.1 mm apart, located near the center of each image. The elliptical patterns from contributing element pairs could be clearly observed. Background artifacts were due to the bandlimiting of the time-delay profiles.

Similarly, full 360° element coverage around a distribution of point targets arraigned to mimic a bone with crack, shown in Fig. 7, resulted in excellent target clarity with only 0.5 MHz bandwidth. Though this arrangement encapsulated the concept of a conformal, inward imaging array, the same reconstruction algorithm can be applied in an outward manner.

4.3 Phantom Image Reconstruction

Experiments were performed to determine the feasibility of 2D imaging using the 8×1 conformal transducer array and imaging system to image a simple soft tissue phantom. A stainless steel rod was embedded into a cylindrical soft tissue phantom (diameter = 2 cm) to simulate a bone of simple geometry. The transducer was partially wrapped (160°) around the phantom (Fig. 8) and coupled with acoustic scanning gel. Each element of the array was sequentially fired using the transceiver, with each of the 64 transmit/receive pairs (including monostatic and bistatic data) captured on a laptop. Pulse-CW was used for the phantom because of the simpler signal processing needed to better assess the system operation. Despite this departure from step FMCW, the theoretical equivalence between the two modalities allows the experiment to address the performance of the conformal array while retaining the described space-time approach.

A 2D image reconstruction (Fig. 8) was performed using the space-time backward propagation algorithm. The rod was represented by the bright (high signal) region in the image, where the ellipses terminated. The curved lines appearing in the image are due to the limited number of transmit/receive pairs in the backward

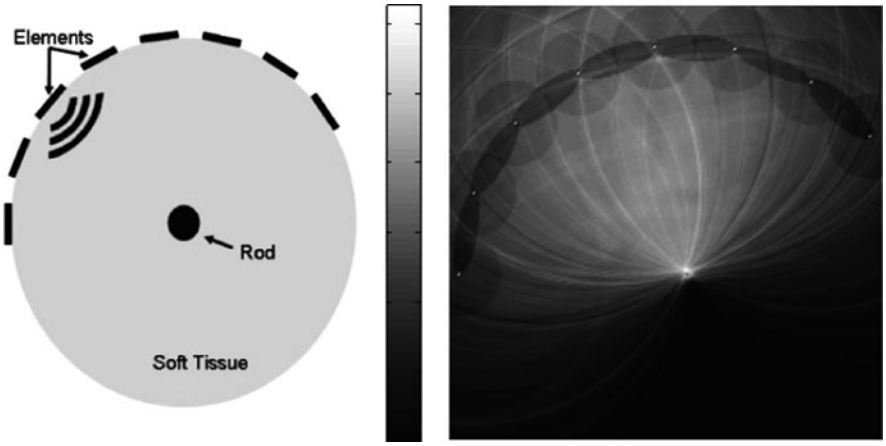

Fig. 8 Illustration of conformal ultrasound transducer array mounted on cylindrical soft tissue phantom with embedded rod (*right*). Resulting image reconstruction of soft tissue phantom and aluminum rod (*left*)

propagation model. Despite this limitation in element density, the results suggest that high quality imagery can be obtained using the conformal ultrasound system.

5 Discussion and Conclusion

A conformal ultrasound imaging has been designed, developed, and initial imagery has been acquired. The use of polyimide and parylene enabled fabrication of transducers with high flexibility and durability, while also supporting a two-layer electrode network across both materials, as well as across PZT. The fabrication process can be extended to two dimensions, and can be scaled to produce architectures tailored to specific applications. While the initial approach presented here was focused on small cylindrical targets such as fingers, future applications may be extended to abdominal imaging, craniofacial imaging, and ultrasound guidance procedures. In addition to scaling, future efforts will focus on increasing array density in order improve image quality by decreasing target location ambiguity and increasing SNR. Ongoing research is also underway to enable active registration of element positioning and array curvature using various techniques, including electrical cross-talk, adaptive image reconstruction, and integration of strain gauges into the transducer substrate. Further testing and incorporation of the FMCW signal processing will also be performed.

Together, these advances may enable a new approach to ultrasound imaging, allowing high quality imagery to be obtained with little or no expertise for a variety

of medical applications. The imaging system presented is an initial development success that will be further refined and improved to potentially realize a medical conformal imaging system for clinical use.

Acknowledgements The authors would like to thank Dr. E. Carmack Holmes and Cheryl Hein for their support of this project. The authors wish to also thank Dr. Ratnakar R. Neurgaonkar for his help on piezoelectric materials. Additional thanks goes to Priyamvada Tewari, Kimani Williams, Zachary Taylor, Jon Suen, David Goldenberg, and Christopher Cham. This work was supported by the Telemedicine and Advanced Technology Research Center (TATRC) / Department of Defense under award numbers W81XWH-07-1-0672 and W81XWH-07-1-0668.

References

1. Singh, R.S., Culjat, M.O., Vampola, S.P., Williams, K., Taylor, Z.D., Lee, H., Grundfest, W.S., Brown, E.R.: Simulation, fabrication, and characterization of a novel flexible, conformal ultrasound transducer array. Proc. IEEE Ultrason. Symp., 1824–1827 (2007)
2. Culjat, M.O., Singh, R.S., Utley, C.D., Vampola, S.P., Sharareh, B., Lee, H., Brown, E.R., Grundfest, W.S.: A flexible, conformal ultrasound array for medical imaging. Stud. Health Technol. Inf. **132**, 95–97 (2008)
3. Roy, O., Chatillon, M.S.: Ultrasonic inspection of complex geometry component specimen with a smart flexible contact phased array transducer: modeling and applications. Proc. IEEE Ultrason. Symp. **1**, 763–766 (2000)
4. Casula, O., Poidevin, C., Cattiaux, G., Dumas, P.: Control of complex components with smart flexible phased arrays. Ultrason. **44**(1), e647–e651 (2006)
5. Powell, D.J., Hayward, G.: Flexible ultrasonic transducer arrays for nondestructive evaluation applications. I. The theoretical modeling approach. IEEE Trans. Ultrason. Ferroelect. Freq. Contr. **43**(3), 385–392 (1996)
6. Powell, D.J., Hayward, G.: Flexible ultrasonic transducer arrays for nondestructive evaluation applications. II. Performance assessment of different array configurations. IEEE Trans. Ultrason. Ferroelect. Freq. Contr. **43**(3), 393–402 (1996)
7. Zhuang, X., Lin, D.S., Oralkan, O., Khuri-Yakub, B.T.: Flexible transducer arrays with through-wafer electrical interconnects based on trench refilling with PDMS. Proceedings Of IEEE MEMS Conference 73–76 (2007)
8. Zhuang, X., Lin, D.S., Oralkan, O., Khuri-Yakub, B.T.: Fabrication of flexible transducer arrays with through-wafer electrical interconnects based on trench refilling with PDMS. J. Microelectromech. Syst. **17**(2), 446–452 (2008)
9. Kobayashi, M., Cheng-Kuei, J., Levesque, D.; Flexible ultrasonic transducers. IEEE Trans. Ultrason. Ferroelect. Freq. Contr. **53**(8), 1478–1486 (2006)
10. Kobayashi, M., Jen, C.K.: Integrated and flexible high temperature ultrasonic transducers. 4th International Workshop Ultrason. Adv. Methods Nondestr. Test. Mater. Charact., 25–36 (2006)
11. Bowen, C.R., Bradley, L.R., Almond, D.P., Wilcox, P.D.: Flexible piezoelectric transducer for ultrasonic inspection of non-planar components. Ultrasonics **48**(5), 367–375 (2008)
12. McGough, R.J., Owens, A.M., Cindric, D., Heim, J.W., Samulski, T.V.: The fabrication of conformal ultrasound phased arrays for thermal therapy. Proceedings of the 22nd Annual EMBS International Conference, 3, 1617–1620 (2000)
13. Chatillon, S., Cattiaux, G., Serre, M., Roy, O.: Ultrasonic non-destructive testing of pieces of complex geometry with a flexible phased array transducer," Ultrasonics **38**(1–8), 131–134 (2000)

14. Roy, O., Mahaut, S., Casula, O.: Development of a smart flexible transducer to inspect component of complex geometry: modeling and experiments. Proc. Am. Inst. Phys. **21**, 908–914 (2002)
15. Stieglitz, T., Beutel, H., Schuettler, M., Meyer, J.U.: Micromachined, polyimide-based devices for flexible neural interface. Biomed. Microdevices **2**(4), 283–294 (2000)
16. Lee, M., Singh, R.S., Culjat, M.O., Natarajan, S., Cox, B.P., Brown, E.R., Grundfest, W.S., Lee, H.: Waveform synthesis for the design and image reconstruction of step FMCW ultrasound imaging systems with conformal transducer arrays. Proc. SPIE Medical Imaging: Ultrason. Imag and Signal Proc. 7–12 February 2009, Lake Buena Vista, FL (2009, in press)
17. Lee, H.: Formulation of the generalized backward projection method for acoustical imaging. IEEE Trans. Sonics Ultrason. **31**(3), 157–161 (1984)

Air-Coupled Vibrometry

Making Linear and Nonlinear Sound in Air Visible

D. Döring, I. Solodov, and G. Busse

Abstract Sound and ultrasound in air are the products of a multitude of different processes and thus can be favorable or undesirable phenomena. Development of experimental tools for non-invasive measurements and imaging of airborne sound fields is of importance for linear and nonlinear nondestructive material testing as well as noise control in industrial or civil engineering applications. One possible solution is based on acousto-optic interaction, like light diffraction imaging. The diffraction approach usually requires a sophisticated setup with fine optical alignment barely applicable in industrial environment. This paper focuses on the application of the robust experimental tool of scanning laser vibrometry, which utilizes commercial off-the-shelf equipment. The imaging technique of air-coupled vibrometry (ACV) is based on the modulation of the optical path length by the acoustic pressure of the sound wave. The theoretical considerations focus on the analysis of acousto-optical phase modulation. The sensitivity of the ACV in detecting vibration velocity was estimated as $\sim$1 mm/s. The ACV applications to imaging of linear airborne fields are demonstrated for leaky wave propagation and measurements of ultrasonic air-coupled transducers. For higher-intensity ultrasound, the classical nonlinear effect of the second harmonic generation was measured in air. Another nonlinear application includes a direct observation of the nonlinear air-coupled emission (NACE) from the damaged areas in solid materials. The source of the NACE is shown to be strongly localized around the damage and proposed as a nonlinear "tag" to discern and image the defects.

Keywords Acousto-optics · Air-coupled · Laser vibrometer · Non-destructive evaluation · Nonlinear acoustics · Leaky waves

1 Introduction

The acousto-optic effect in the ultrasonic frequency range is often only seen as the interaction of an extended laser beam with an acoustic field whose wavelength is far shorter than the laser beam size. This leads to light diffraction phenomena that

D. Döring (✉)
Department for Non-Destructive Testing (IKT-ZfP), Institute for Polymer Technology, Universität Stuttgart, Stuttgart, Germany

M.P. André et al. (eds.), *Acoustical Imaging*, Acoustical Imaging 30,
DOI 10.1007/978-90-481-3255-3_26,

were predicted in the early twentieth century [1, 2] and can be described as a Bragg-type diffraction at layers of varying optical density. The periodical variation of the refractive index can also be described as a phase grating and thus as a means to manipulate a light beam. However, these methods require a very regular acoustic field to be applicable and are quite demanding in respect to the laser properties.

From the viewpoint of applied acoustics the typical sonic wavelength is in the sub-millimeter to centimeter range and thus far outside the applicability of the diffraction approach. Here a technique based on frequency modulation of a narrow laser beam by acoustic oscillations can close the gap for extended, low-frequency and non-uniform fields. The use of a raster imaging system based on a commercial laser vibrometer supplies a robust laboratory and application solution.

2 Theoretical Background

2.1 Photoelasticity in Air

The photoelasticity of air is caused by the dependence of the refractive index n on the local mass density ρ which can be modulated by a number of phenomena like air flow, vortices and sound. With n_o being the normal refractive index in air and ρ_o the undisturbed density, this relation can be approximated [3, 4] as:

$$\Delta n = n - n_o \approx (n_o - 1)\frac{\Delta\rho}{\rho_o} \tag{1}$$

The change in density $\Delta\rho$ can be caused by the wave pressure $\Delta p = p - p_o$ of an ultrasonic wave, p_o being the ambient atmospheric pressure. They are linked via the adiabatic condition $p\rho^{-\gamma} = const$, where $\gamma = C_p/C_v$ is the ratio of specific heats, of wave propagation and the velocity of sound $V = \sqrt{\gamma p_o/\rho_o}$ to form the relation

$$\Delta p = \rho_o V^2 \frac{\Delta\rho}{\rho_o} \tag{2}$$

Introduction of Equation (2) into Equation (1) yields the photoelastic relation for acoustic waves in air:

$$\Delta n = (n_o - 1)\frac{\Delta p}{\rho_o V^2} \tag{3}$$

2.2 Air-Coupled Vibrometry: Phase Modulation

A change in refractive index is equivalent to a variation of the velocity of light in the medium ($n = c/c_{air}$, c being the vacuum light velocity):

$$n = n_o + \Delta n = n_o\left(1 + \frac{\Delta n}{n_o}\right) = n_o\left(1 + \frac{\Delta c_{air}}{c_{air}}\right) \tag{4}$$

If the refractive index variation is caused by acoustic waves, Equations (3) and (4) can be combined to:

$$\frac{\Delta c_{air}}{c_{air}} = \frac{(n_o - 1)\Delta p}{n_o \rho_o V^2} \tag{5}$$

From Equation (5), a quite intense wave of $\Delta p \approx 1Pa$ yields a change in velocity of only $\Delta c_{air}/c_{air} \cong 2 \cdot 10^{-9}$. To be detectable, this small change requires a sensitive interferometric system. The use of a laser vibrometer for the optical measurement (Fig. 1) supplies such a setup: a narrow laser beam crosses the acoustic wave field with an interaction length (aperture) L, is then reflected at a fixed screen and detected in a sensitive heterodyne interferometer (Polytec PSV 300) based on mixing with an internal reference beam and analysis of the resulting beating [5].

Assuming a simplified acoustic field consisting of only one spatial component (plane wave) described by $\Delta p = \Delta p_{\sim} \cos(\Omega t - Kz)$, one can use Equation (3) to calculate the temporal variation of the refractive index at a given fixed position (e.g., $z = 0$):

$$\Delta n = \frac{n_o - 1}{\rho_o V^2} \Delta p_{\sim} \cos \Omega t \tag{6}$$

A light wave traveling orthogonal to the assumed acoustic wave (along the x-axis) will traverse the sound field parallel to the wavefronts and thus at a fixed value of Δn.

As the light wave can be described as $\tilde{\exp}[i\varphi] = \exp[i(\omega t - kx)]$, with $k_{air} = \omega/c_{air}$ being the optical wave number in air, the phase of the light wave returning to the vibrometer is

$$\varphi = \omega t - \int \tilde{k}_{air} dx = \omega t - 2\tilde{k}_{air} L = \omega t - 2k_{air} L \left(1 - \frac{\Delta \tilde{c}_{air}}{c_{air}}\right) \tag{8}$$

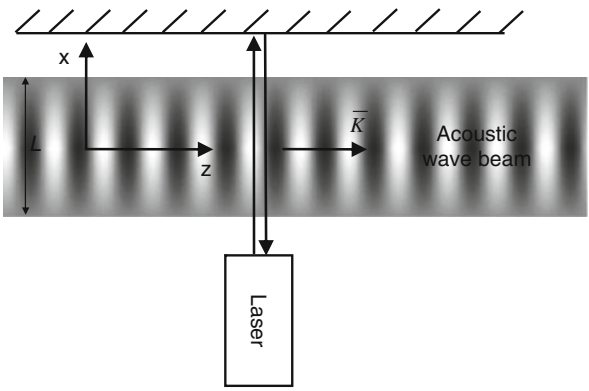

Fig. 1 Setup for air-coupled vibrometry

where $\tilde{k}_{air}$ and $\Delta\tilde{c}_{air}$ are the terms that include the variations induced by the acoustic wave. By using Equation (5), the phase variation takes the form of

$$\varphi = \omega t - 2k_{air}L\left(1 - \frac{n_o - 1}{n_o \rho_o V^2}\Delta p_\sim \cos\Omega t\right) \tag{9}$$

so that the received light experiences a phase modulation with the frequency Ω of the acoustic wave. The instantaneous frequency f_i of this wave is found as:

$$f_i = \frac{1}{2\pi}\frac{\partial\varphi}{\partial t} = f\left(1 - \frac{(n_o - 1)L\Omega}{n_o \rho_o V^2}\Delta p_\sim \cos\Omega t\right) \tag{10}$$

According to Equation (10), the received light is frequency modulated (or color shifted) to a degree proportional to the local sound pressure.

The case of spatial components of the acoustic wave field that are not orthogonal to the laser beam has previously been studied theoretically and experimentally [6] and leads to additional sinc-modulation of the measured intensity.

2.3 "Doppler" Vibrometry and Absolute Measurements

The laser vibrometer used for air-coupled vibrometry (ACV) is designed to measure vibration velocities in reflection ("Doppler Vibrometry"). The light reflection from a vibrating surface is accompanied by propagation path variations $\tilde{L} = L_o + L_\sim \cos(\Omega t)$, which cause the phase modulation at the receiver:

$$\varphi_D = \omega t - 2k_{air}L_o\left(1 + \frac{L_\sim}{L_o}\cos\Omega t\right) \tag{11}$$

and the frequency modulation of the reflected beam:

$$f_i = f\left(1 + 2\frac{v_{ref}}{c_{air}}\sin\Omega t\right) \tag{12}$$

Here $v_{ref} = L_\sim\Omega$ is the peak velocity of the reflecting surface. The maximum frequency deviation (modulation index) is $\Delta f = \pm 2f\, v_{ref}/c_{air}$, commonly known as the "Doppler" frequency shift. In the ACV experiment, a "Doppler" vibrometer therefore measures an apparent vibration velocity of the virtual reflector. From Equations (10) and (12), it is related to the acoustic pressure that actually causes the frequency modulation measured in the AC:

$$v_{ref} = \frac{n_o - 1}{n_o}\frac{\Omega L}{\rho_o V^2}\Delta p_\sim \tag{13}$$

This result is similar to the one obtained in a "virtual vibration" approach [7, 8]. Since in a plane wave $\Delta p_\sim = v_p \rho_o V$, the acoustic wave particle velocity measured by ACV is related to the vibrometer read-out (v_{ref}) as follows:

$$v_p = \frac{n_o}{(n_o - 1)KL} v_{ref} \tag{14}$$

A reliable detection of vibrations with a Doppler vibrometer starts at $v_{ref} = 10\,\mu$m/s. For $n_o \approx 1.0003$ and $KL \approx 33$ the scaling factor in Equation (14) is 100, so the ACV sensitivity is estimated to be ≈ 1.0 mm/s. This motion velocity corresponds to an acoustic wave pressure of $\Delta p_{\sim}^{\min} = 0.4\,Pa$ or an intensity of $2 \cdot 10^{-4}$ W/m^2.

3 Experimental Results

3.1 AC Transducer Field Imaging and Quantification

For the field image presented in Fig. 2, an air-coupled transducer (circular aperture of $2a = 11$ mm diameter, Airstar AS200) was driven with a 10 V (amplitude) sine wave at its resonance frequency of 200 kHz. The field shows the expected properties of a relatively small, non-focused source (Rayleigh distance $\pi a^2/\lambda \approx 60$ mm): a strong but slightly divergent main lobe and some indication of symmetrical side lobes. The readout of the vibrometer software (apparent reflector velocity) was measured as $v_{ref} = 2.0$ mm/s at a typical working distance of 2 cm from the transducer surface. Using Equations (13) and (14) for $KL = 33$, the particle velocity and acoustic pressure amplitude are found to be $v_p \approx 0.2$ m/s, $\Delta p \approx 0.34\,Pa$.

To verify these data, a radiometry experiment was carried out. For the same input voltage, the radiation force exerted by the ultrasonic wave on a small reflector (light Al-foil pendulum) was measured to be $\approx 1\mu N$ providing a radiation pressure of $P_{rad} \approx 0.027$ Pa. The particle velocity derived from the value of radiation pressure is

$$v_p = \sqrt{2P_{rad}/\rho_o} = 0.14 m/s \tag{15}$$

the result is in fair agreement with the particle velocity derived from the ACV measurement. The major source of the error for measurements of the absolute velocity values in the ACV experiment is apparently concerned with uncertainty of the KL value for acoustic fields.

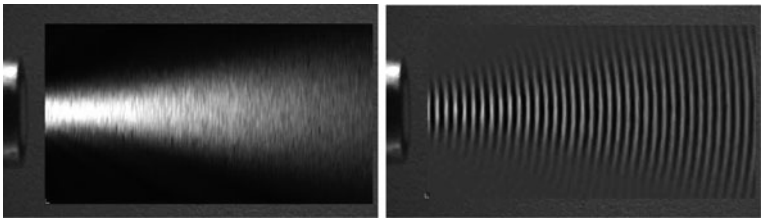

Fig. 2 ACV image of the field radiated by an air-coupled ultrasound transducer, magnitude (*left*) and real part ("snapshot," *right*) of the motion

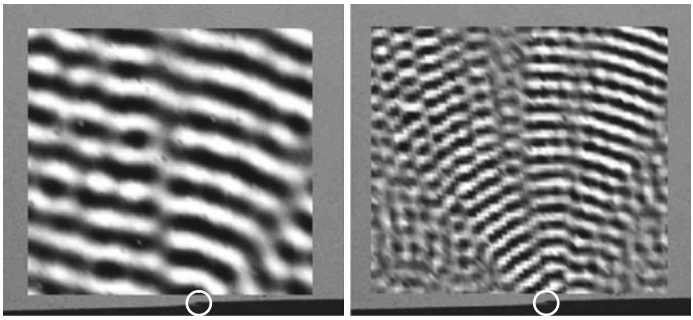

Fig. 3 Leaky wave in air at the fundamental frequency (40 kHz, *left*) and non-linear air-coupled emission at the 2nd harmonic (80 kHz, *right*) from a cracked defect marked by a *white circle*

3.2 Imaging of Linear and Nonlinear Air-Coupled Emission

A plate wave propagating in a plate-like specimen is known to radiate longitudinal waves into a surrounding liquid or gas at an angle Θ (from the surface normal) given by $\sin\Theta = v_{air}/v_{plate}$. The leaky wave in air was studied for a 40 kHz flexural plate wave (propagating from left to right) in a carbon fiber reinforced plastic (CFRP) rod and which was excited by a point-like contact transducer (Fig. 3, left). The ACV image shows the typical pattern of Cherenkov's radiation: plane airborne waves propagating at $\Theta = 15°$, that brings about the value of the guided wave velocity in the specimen $v_{plate} = 1.3$ km/s.

Cracked defects, like closed cracks, poor gluing, "kissing bonds" in welds, etc. are known to have strongly nonlinear elastic properties. They generate nonlinear spectral components (harmonics, subharmonics, frequency pairs, etc.) while driven with an intense acoustic wave. These vibrations have been found to be efficient localized sources of non-linear air-coupled emission (NACE) that has been proposed as a method for defect detection [9]. For the cracked CFRP rod, the ACV signal was found to comprise the higher harmonics of the driving frequency (40 kHz) within the bandwidth of the instrument (1 Hz–1 MHz). A fast Fourier transformation (FFT) was applied to select the nonlinear frequency components of interest which visualize airborne ultrasound radiated by nonlinear vibrations of the crack. The ACV image presented in Fig. 3 (right) was filtered for the second harmonic component (80 kHz). This wave field clearly indicates a localized nonlinear source at the position of the crack. The nonlinear ACV image is a new signature of the damage induced defects which suggests further application as a new non-linear acoustic imaging technique for non-destructive testing.

3.3 ACV Imaging of Nonlinear Airborne Ultrasound

When an intense acoustic wave is traveling in a nonlinear medium, each point of its waveform moves with a different phase velocity [10]:

$$V = V_o + \beta v_p \tag{16}$$

which depends on the particle velocity v_p in that point. The factor β (nonlinear parameter) includes the two sources of nonlinearity from the adiabatic equation of state and the continuity of a deformed medium. For air, $\beta = (\gamma + 1)/2 = 1.2$, where γ is the ratio of specific heat capacities. During propagation in a nonlinear medium the wave acquires a growing distortion that can be described as a built-up of the higher harmonic components. In a dissipative medium (characterized by the attenuation constant α), this linear growth is counteracted by an exponential decay of both the fundamental wave and the higher harmonics. For small Mach numbers $M = v_{po}/V_o << 1$, the major nonlinear contribution comes from the second harmonic so that the nonlinear plane wave field can be written as [10]:

$$v_p(x,t) = v_{po}e^{-\alpha_o x}\sin(\omega t - kx) + \frac{\beta\omega M^2}{4\alpha_o}\left[e^{-2\alpha_o x} - e^{-4\alpha_o x}\right]\sin\left[2\left(\omega t - kx\right)\right]$$
$$= v_{po}^{\omega}(x)\sin(\omega t - kx) + v_{po}^{2\omega}(x)\sin\left[2(\omega t - kx)\right]. \quad (17)$$

Figure 4 shows the ACV images of a freely propagating 200 kHz fundamental wave in air. The interpolation of the fundamental wave amplitude decay with propagation distance (Fig. 4, bottom left) enables to evaluate the attenuation coefficient as $\alpha \approx 0.1\,\mathrm{cm}^{-1}$. The second harmonic displays a classical behavior: its amplitude grows with propagation distance (due to nonlinearity) and then decays due to dissipation. According to Equation (17) the 2ω-component reaches maximum at the so-called stabilization distance $x_{stab} = \ln 2/2\alpha$. For $\alpha \approx 0.1\,\mathrm{cm}^{-1}$, the expected value of the stabilization distance is $x_{stab} = 35\,\mathrm{mm}$. The experimental data in Fig. 4 (bottom, right) shows that $x_{stab} = 33\,\mathrm{mm}$, which is in a good agreement with the theoretical estimation.

The ratio or the second harmonic amplitude to the fundamental wave also grows with propagation distance and reaches maximum in the neighborhood of x_{stab}. For the input voltage 120 V_{pp}, the ACU measurements yield: $v_{po}(0) = 9 \times 10^3$ mm/s, $M = 2.6 \times 10^{-3}$, so the estimate from Equation (17) is $v_p^{2\omega}(x_{stab})/v_p^{\omega}(x_{stab}) = 13\%$.

The experimental data (Fig. 4, bottom) enables to estimate the measured second harmonic content at $x = x_{stab}$. In the experiment $KL = 33$ for the fundamental wave

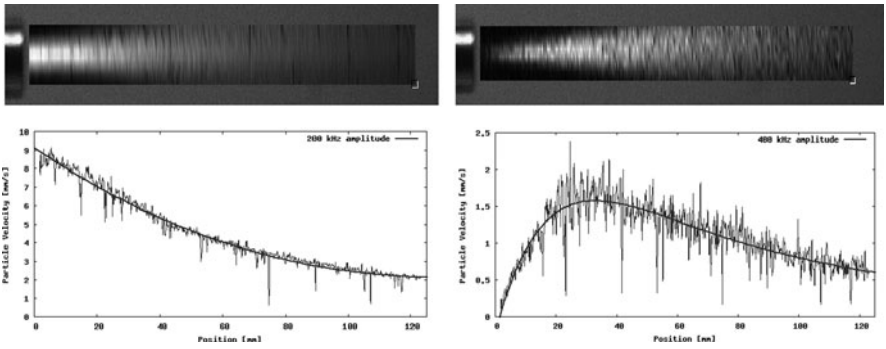

Fig. 4 Images (*top*) and particle velocity amplitude along the beam (*bottom*) at the fundamental frequency (200 kHz, *left*) and the 2nd harmonic (400 kHz, *right*)

and is assumed to be twice as large for the second harmonic field. By using the data of Fig. 4 in Equation (14), the values of the particle velocities for the fundamental wave and its second harmonic are found to be: $v_p^{\omega}(x_{stab}) = 6.3 \times 10^2$ mm/s and $v_p^{2\omega}(x_{stab}) = 90$ mm/s. The ratio $v_p^{2\omega}(x_{stab})/v_p^{\omega}(x_{stab}) = 14\%$ agrees well with the theoretical estimate.

4 Conclusions

In contrast to other acoustic imaging techniques based on acousto-optic interaction, the ACV is applicable to visualization and quantification of airborne fields in the laboratory and possibly even in industrial environments. This is due to the use of a phase/frequency modulation measured with a robust commercial instrument (Laser Doppler Vibrometer). The ACV implements non-invasive, quantitative measurements of sound fields in linear and nonlinear acoustics in the frequency range up to the a few hundred kHz. For classical nonlinear acoustics it gives a unique possibility to "tap" into the ultrasonic field at any given distance from the source without disturbing the field, making it easy to probe nonlinear wave components. The ACV imaging of linear and nonlinear air-coupled radiation patterns from cracked defects is a new NDE tool for detection and localization of damage.

Acknowledgements The authors are grateful to the German Research Foundation (DFG) for supporting this work as part of the project Bu 624/26–1 ("Development and application of a new non-contact method for mapping of elastic anisotropy using air-coupled plate and surface waves").

References

1. Yarif, A.: Optical Electronics. Saunders, Philadelphia, PA (1971)
2. Korpel, A.: Acousto-Optics. Marcel Dekker, Oxfordshire, UK (1988)
3. Williams, C.C.: High resolution optical probe. In Proceedings of the IEEE Ultrasonics Symposium, vol. 1, pp. 951–955 (1983)
4. Dürr, W.: Acousto-optic interaction in gases and liquid bases in the far infrared. Int. J. Infrared Millim. Waves **7**, 1537–1558 (1986)
5. Polytec Inc., "Vibrometry Basics," http://www.polytec.com/usa/158_942.asp
6. Solodov, I., Döring, D., Busse, G.: Air-coupled laser vibrometry: analysis and applications. Appl Optic **48**(7) (2009)
7. Zipser, L.: Refraktovibrometrie zur Messung und Visualisierung akustischer, fluidischer und spannungsmechanischer Phänomene, http://www.polytec.com/ger/_files/07_Zipser_Refraktovibrometrie.pdf
8. Zipser, L., Franke, H.: Laser-scanning vibrometry for ultrasonic transducer development. Sens. Actuators A **110**, 264–268 (2004)
9. Solodov, I., Busse, G.: Nonlinear air-coupled emission: the signature to reveal and image microdamage in solid materials. Appl. Phys. Lett. A **91**, 251910 (2007)
10. Beyer, R.T.: Nonlinear Acoustics. ASA, Sewickley, PA (1997)

A Hybrid Kirchhoff Migration Direction-of-Arrival Method for Underwater Imaging of Complex Objects Using Sparse Sensor Arrays

J.-F. Dord and C. Farhat

Abstract This paper considers the problem of imaging a complex object submerged in shallow waters using a sparse surface sensor array and a hybrid signal processing method. This method is constructed by refining the Kirchhoff migration technique to incorporate a zoning of the sensors and an analysis of multiple reflections, and combining it with the direction of arrival estimation method. Its performance is assessed and analyzed with the shape identification of a mockup submarine by numerical simulation. The obtained numerical results highlight the potential of this approach for detecting underwater intruders.

Keywords Complex object · Direction of arrival · Gathers · Kirchhoff migration · MUSIC · Underwater acoustics

1 Introduction

Migration or coherent summation techniques are popular for many imaging applications. They can be viewed as methods for solving inverse obstacle problems. They are often applied with the Kirchhoff (or ray theory) approximation. Their origin goes back to the seminal 1954 paper by Hagedoorn [1], which described a heuristic for seismic reflector imaging. During the last decades, they have been extended to applications of increasing complexity [2–5], and have led to related imaging methods such as Delay and Sum (DAS) beamforming [6], and Synthetic Aperture Focusing Technique (SAFT) [6]. Migration methods have also undergone several refinements, for example, to incorporate gathers [7] and later super-gathers which simultaneously improves image quality and reduces computational cost, and to enable the identification of geometric irregularities in layered media [4]. More recently, these methods have also been equipped with the analysis of multiple reflections [8] to compensate for limited aperture and exploit multiple paths in a complex medium. A mathematical analysis of such methods applied to the imaging of a point object in random media is also available in the literature [9].

J.-F. Dord (✉)
Department of Mechanical Engineering, Department of Aeronautics and Astronautics, Stanford University, Stanford, CA, USA
e-mail: jfdord@stanford.edu

M.P. André et al. (eds.), *Acoustical Imaging*, Acoustical Imaging 30,
DOI 10.1007/978-90-481-3255-3_27,

To the best of the authors' knowledge, most if not all of the aforementioned refined migration methods have been developed and/or applied in the context of coherent or phased sensor arrays. In particular, the successful imaging of complex (non-convex) extended objects by a migration method has been successfully demonstrated in the very specific context of phased sensor arrays [10]. However, such arrays can be impractical in many applications including non-destructive testing and underwater surveillance, to mention only a few. For this reason, this paper presents a hybrid migration method based on combining a refined Kirchhoff summation technique and a Direction Of Arrival (DOA) estimation method and demonstrates its potential for imaging complex objects using sparse surface sensor arrays. To this effect, the remainder of this document is organized as follows.

In Section 2, the Kirchhoff migration method is overviewed and then equipped with a sensor zoning. An analysis of multiple reflections is also incorporated in this technique before combining it with the DOA estimation method to construct a more capable hybrid imaging method. Section 3 reports on the simulation of the imaging of an underwater intruder shaped like a mockup submarine using this method and a sparse surface sensor array. The obtained numerical results highlight the merits of the proposed hybrid imaging algorithm even when used with a sparse surface sensor array, and lead to the conclusions formulated in Section 4.

2 Kirchhoff Migration and Refinements

2.1 Principles and Outline of the Method

Let D denote a bounded domain in R^3, let X=(x, y, z) in D denote a point in this domain with coordinates x, y and z, and let S and R denote two sets of sources s_i and receptors r_j deployed in R^3, respectively. In the sequel, any element of S or R is also referred to as a sensor. Let t denote time, and t_i^0 denote the offset time for source s_i to fire (measured from the reference instant $t = 0$). Let $p_{ij}(t)$ denote the value of the pressure recorded at time t by r_j when source s_i fires. Finally, let $t_t(X)$ denote a travel-time defined here as the time elapsed between the instant at which a wave – in the context of this paper, a pressure wave – is emitted from a source point s_i, and the instant at which it is received at a receptor r_j after bouncing on an hypothetic surface $\partial\Omega_S$ embedded in D at the point X. For the sake of simplifying the notation, $t_t(X)$ is not written with its indices i and j as $t_t(X)$ is always associated to a measure of pressure p_{ij} and therefore $t_t(X)$ is non ambiguous. The migration method is based on the simple idea that for all sources s_i and receptors r_j, the pressure values $p_{ij}(t_t(X) + t_i^0)$ should show a maximum amplitude when X is on the surface $\partial\Omega_S$ of the scatterer Ω_S.

Hence, the migration technique consists of generating an intensity scalar field K(X), which after rendering allows to recover Ω_S. From the above discussion, it follows that K(X) is given by:

$$K(X) = \sum_{s_i \in S} \sum_{r_j \in R} p_{ij}(t_t(X) + t_i^0) \tag{1}$$

More specifically, the maxima of K(X) reveal, in principle, the surface $\partial\Omega_S$ of the scatterer Ω_S located in D.

The Kirchhoff approximation allows the estimation of the travel-time $t_t(X)$ by assuming that the medium in which the wave propagates is uniform and is characterized by a constant wave speed c. With this approximation, the travel-time can be estimated as:

$$t_t(X) = (||X_i - X||_2 + ||X - X_j||_2)/c \tag{2}$$

where X_i and X_j denote the locations of sensors s_i and r_j, respectively.

In the context of this work, D is a search zone in a shallow region of an ocean whose floor is assumed to be flat, S and R overlap and form a sparse array of cross-shaped active broadband sonobouys, and the array is assumed to be deployed right under the top surface of the ocean. Furthermore, each pressure value p_{ij} inputted to the function K corresponds to the difference δp_{ij} between the pressure values recorded in the presence of the scatterer Ω_S and that measured in its absence. Working with δp_{ij} instead of p_{ij} eliminates the effects of the ocean's free surface. When using simulated pressure data, it also eliminates the potentially spurious effects of absorbing boundary conditions when these are introduced in the numerical computations. Hence, working with δp_{ij} instead of p_{ij} reduces the data noise and therefore can be expected to produce better images.

2.2 Sensor Zoning

In general, the basic Kirchhoff migration method outlined above images point-like objects far better than extended ones [9]. The main reason is that the reflected waves on the surface of an extended scatterer do not necessarily combine properly.

Depending on the spacing between the sensors and on the curvature of the scatterer's surface, the combination of reflected waves can smear their peaks, thereby weakening contrast and leading to an image of poor quality. To prevent this from happening, R and S can be collectively organized in clusters of neighboring sensors – a process referred to here as zoning. Then, the Kirchhoff migration method can be applied using each pair of sensor clusters independently, and the partial images produced by these sensor clusters can be combined to produce a more accurate image of the scatterer. In this case, every partial image $K_{Zs,Zr}$ is created by the partial intensity field

$$K_{Z_s,Z_r}(X) = \sum_{i \in Z_s} \sum_{j \in Z_r} p_{ij}(t_t(X)) \tag{3}$$

where Z_s and Z_r are two subsets of S and R, respectively. The complete image is obtained by combining these partial images as follows

$$K_{zoning}(X) = \max_{Z_s, Z_r} \frac{K_{Z_s,Z_r}(X)}{\max_X K_{Z_s,Z_r}(X)} \tag{4}$$

Hence, the final image is generated by computing the maximum of the normalized partial images as the main objective is to highlight the brightest reflectors in every partial image.

2.3 Analysis of Multiple Reflections

In a subsurface scanning of the ocean, pressure waves are reflected not only by scatterers, but also by the seabed which can be responsible for the most energetic reflections. This calls for an adaptation of the travel-time estimate embedded in the function K(X) to account for multiple reflections on the ocean's floor. For applications relying on surface sensors only, accounting for multiple reflections also compensates the lack of full aperture by conveying to the sensors information about the sides, bottom, and other hidden surfaces of the scatterer. More specifically, assuming that the sensors are deployed in a plane above the scatterer, one reflection on the ocean's floor can provide images of the sides of a complex scatterer, and two such reflections can provide an image of its bottom.

Using sensor zoning, the incorporation of the effect of multiple reflections in the basic image function K leads to

$$\begin{aligned} K^{(0)}_{Z_s,Z_r}(X) &= K_{Z_s,Z_r}(X) \\ K^{(1)}_{Z_s,Z_r}(X) &= \sum_{i\in Z_s}\sum_{j\in Z_r} p_{ij}\left(t_t^{(1)}(X)\right) \\ K^{(2)}_{Z_s,Z_r}(X) &= \sum_{i\in Z_s}\sum_{j\in Z_r} p_{ij}\left(t_t^{(2)}(X)\right) \end{aligned} \tag{5}$$

where the superscripts (0), (1), and (2) specify zero, one, or two reflections on the seabed, and the travel-times $t_t^{(1)}$ and $t_t^{(2)}$ associated with one and two reflections, respectively, are estimated by

$$\begin{aligned} t_t^{(1)}(X) &= (||X_i - X||_2 + ||X - X_{g1}||_2 + ||X_{g1} - X_j||_2)/c \\ t_t^{(2)}(X) &= (||X_i - X_{g1}||_2 + ||X_{g1} - X||_2 + ||X - X_{g2}||_2 + ||X_{g2} - X_j||_2)/c \end{aligned} \tag{6}$$

In the above equations, Xg_1 and Xg_2 denote two points of reflection on the ocean's floor.

Then, the final image is constructed by normalizing every partial image and selecting that with the brightest reflectors. This process is captured by the following definition of the new image intensity field:

$$K_{Z_s,Z_r}(X) = max\left[\frac{K_{Z_s,Z_r}(X)}{\max_X K_{Z_s,Z_r}(X)}, \frac{K^{(1)}_{Z_s,Z_r}(X)}{\max_X K^{(1)}_{Z_s,Z_r}(X)}, \frac{K^{(2)}_{Z_s,Z_r}(X)}{\max_X K^{(2)}_{Z_s,Z_r}(X)}\right] \quad (7)$$

2.4 Computational Aspects

In addition to enhancing an image's quality, sensor zoning also reduces drastically its computational cost. Indeed, in the absence of sensor zoning, the construction of one image using the function K requires $N_s{}^*N_r$ signal processing tasks, where N_s and N_r denote the number of sources and number of receptors, respectively. This cost grows quadratically with the number of sensors. With sensor zoning, the number of signal processing tasks becomes $N_{pz}{}^*N_z/N_z{}^*N_z/N_z$, where N_z and N_{pz} denote the number of zones and number of pairs of zone source and zone receptor, respectively, and $N_{pz} \leq N_z^2$. Hence, this number of tasks can be significantly reduced by choosing appropriately N_{pz}, for example, by pairing only sensor zones that touch each other in which case $N_{pz} = O(N_z)$. Finally, it is worthwhile mentioning that all partial images can be processed in an embarrassingly parallel fashion.

2.5 Combination with a Direction of Arrival Estimation Method

The refinements outlined in Section 2.2 and 2.3 improve significantly the quality of an image produced by the base Kirchhoff migration method applied to the shape identification of a submerged complex object. However, by reducing the aperture of the sensors in each partial image and creating multiple partial images, the amount of high intensity information increases and the recovery of the surface of the object becomes very dependent on the choice of an arbitrary threshold. The impact of this drawback can be considerably reduced if a DOA analysis is performed at every receptor on the measured signal. In this paper, the DOA is determined using the classical MUSIC algorithm [10].

3 Application

The potential of the hybrid method described above for imaging underwater obstacles using a sparse surface sensor array is assessed in this paper by numerical simulations. All the pressure time-histories have been generated on a Linux cluster using a massively parallel higher-order finite element wave equation solver.

3.1 Problem Setup

The strait is assumed to be 95 m deep with a constant speed of sound equal to 1,500 m/s. As stated earlier, the seabed and ocean's surface are assumed to be flat. The intruder to be detected is a mockup submarine that is 100 m long, 16.35 m large and 22.2 m high. Its geometrical center is at a depth of 65 m.

3.2 Signal Emissions

The active broadband sonobuoys are assumed to lie on a flat surface at a depth of 13 m; they are scattered on two overlapping regular grids creating a non-regular net of sensors. They emit perfectly spherical waves with the following time history (Fig. 1):

The central wavelength of the emitted pulse is 3 m. Hence, the mockup submarine is 33 wavelengths long while its tower is 2.5 wavelengths long.

The strategy for ensonifying the ocean is that where every sources fires only when the echoes of the previous emission have vanished.

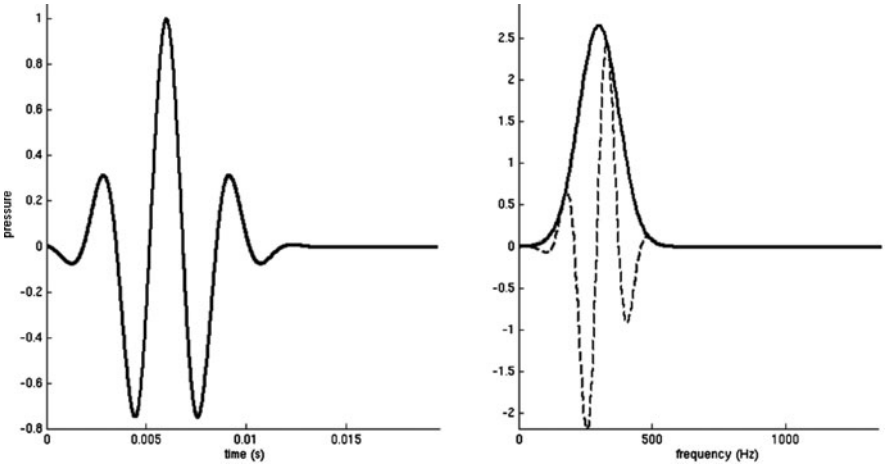

Fig. 1 Time history of the signal (on the right, its Fourier transform)

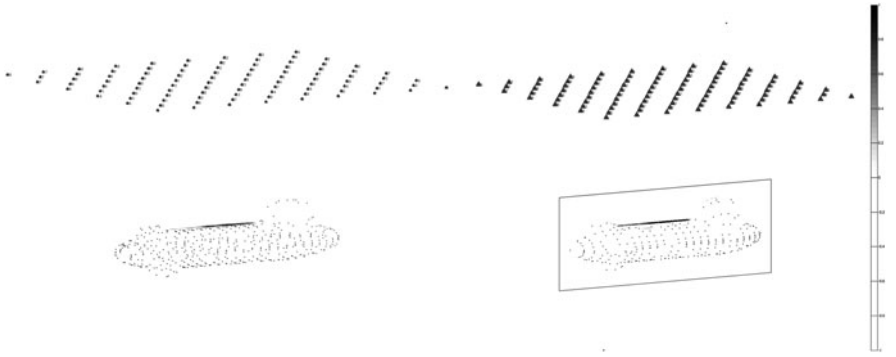

Fig. 2 Base Kirchhoff migration

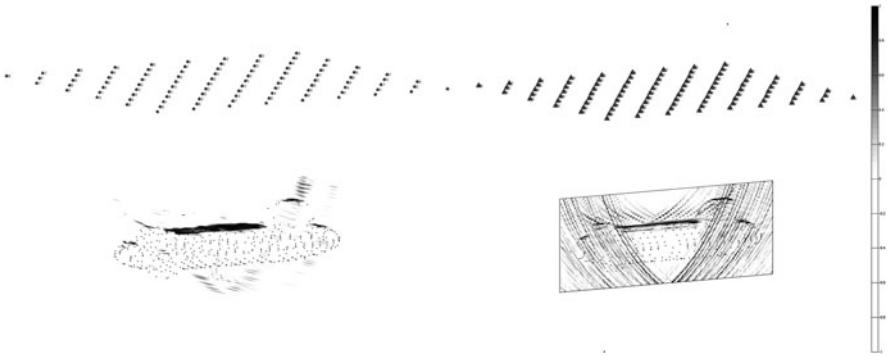

Fig. 3 Kirchhoff migration with sensor zoning

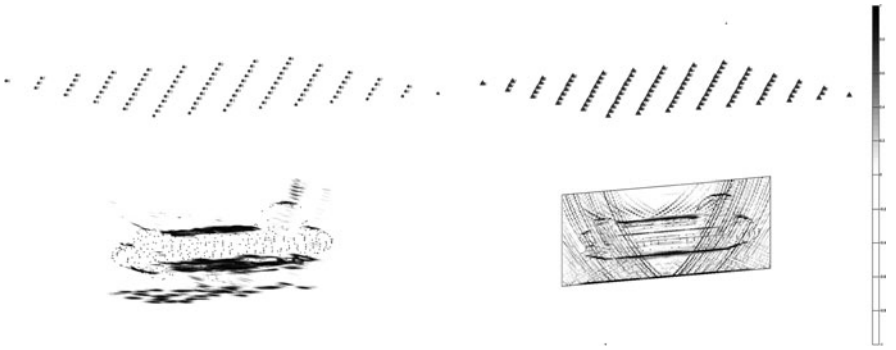

Fig. 4 Kirchhoff migration with sensor zoning and multiple reflection analysis

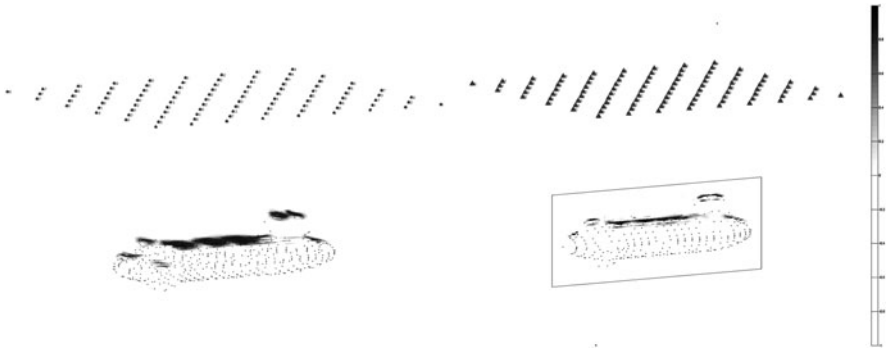

Fig. 5 Kirchhoff migration with sensor zoning and DOA filter

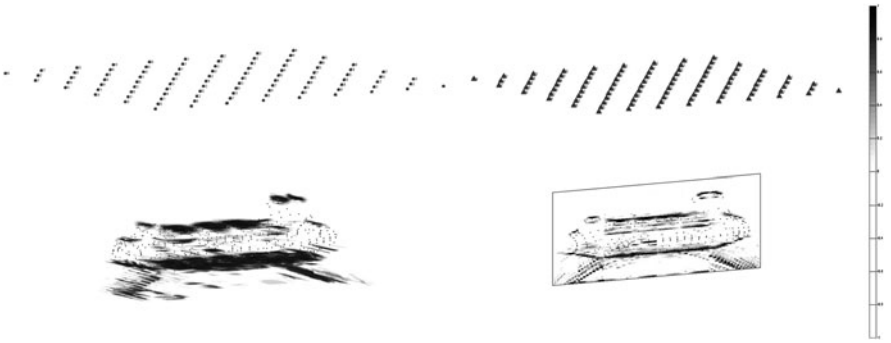

Fig. 6 Kirchhoff migration with sensor zoning, multiple reflection analysis, and DOA filter

3.3 Data Collection

The pressure is measured at seven points on each sonobuoy. The seven points are at the extremities and at the center of a three-dimensional latin-type cross.

3.4 Imaging of a Submerged Mockup Submarine

The Figs. 2–6 highlight the performance of the migration method and the effect of its different refinements. Two views are shown for each imaging strategy; on the left, the 3D view of the iso-surface at approximately 95% of the maximum of K, and on the right, a vertical cut of the intensity field K that passes through the center of the submarine. On every image, some tiny dots appear where the real surface of the mockup submarine is; they are visual artifacts that allow a convenient assessment of the quality of the surface's recovery.

4 Conclusions

The Kirchhoff migration method equipped with sensor zoning, multiple reflection analysis, and a direction of arrival filter has a strong potential for underwater imaging using a sparse surface sensory array. The image it produces is rich enough to allow a surface reconstruction, or initialize a non-linear inversion Newton-type method [11] to accelerate the generation of a more detailed image. The incorporation of multiple reflection analysis in the method reduces drastically the shadow zone [12].

Acknowledgments The authors acknowledge partial support by the Office of Naval Research under Grant N00014-05-1-0204-1, and partial support by the National Science Foundation under Grant CNS-0540419.

References

1. Hagedoorn, J.G.: A process of seismic reflection interpretation. Geophys. Prosp. **2**, 85–127 (1954)
2. Bleistein, N.: Hagedoorn: Kirchhoff migration and inversion. The Leading Edge **18**, 918–927 (1999)
3. Claerbout, J.: Imaging the earth's interior, Report of the Stanford Exploration Project #40 (1985)
4. Biondi, B.L.: 3D seismic imaging, Investigations in Geophysics #14 by Society of Exploration Geophysicists (2006), Chapter 2
5. Aastroem, T.: From fifteen to two hundred NDT methods in fifty years, Proceedings of the 17th World Conference on Nondestructive Testing, Shanghai (2008)
6. Dougherty, R.P.: Advanced time-domain beamforming techniques, 10th AIAA/CEAS Aeroacoustics conference (2004)
7. Bancroft, J.C., Geiger, H.D., Foltinek, D.S., Wang, S.: Prestack migration by equivalent offsets and CSP gathers, CREWES Research Report (1995)
8. Berkhout, A.J., Verschuur, D.J.: Imaging multiple reflections: The concept. Geophysics **71**(4), SI209–SI220 (2006)
9. Borcea, L., Papanicolaou, G., Tsogka, C.: Coherent interferometric imaging in clutter. Geophysics **71–74**, 165–175 (2006)
10. Marengo, E.A., Gruber, F.K., Simonetti, F.: Time-reversal MUSIC imaging of extended targets. IEEE Trans. Image Process. **16**, 1967–1984 (2007)
11. Farhat, C., Tezaur, R., Djellouli, R.: On the solution of three-dimensional inverse obstacle acoustic scattering problems by a regularized Newton method. Inverse Probl. **18**, 1229–1246 (2002)
12. National Academy of Sciences: Beyond discovery: Sounding out the ocean's secrets (2003)
13. Lopez-Sanchez, J.M., Fortuny-Guasch, J.: 3D radar using range migration techniques. IEEE Trans. Antenn. Propag. **48**(5), 728–737 (2000)
14. Sternlicht, D., Pesaturo, J.F.: Synthetic aperture sonar: Frontiers in underwater imaging. Sea Tech. **45** (2004)

Multi-View Acoustic Sizing and Classification of Individual Fish

P.L.D. Roberts and J.S. Jaffe

Abstract Estimating biophysical parameters of fish populations in situ such as size, orientation, shape, and taxa is a fundamental goal in oceanography. Towards this end, acoustics is a natural choice due to its rapid, non-invasive capabilities. Here, multi-view methods are explored for classification, size and orientation estimation, and 2D image reconstruction for individual fish. Size- and shape-based classification using multi-view data is shown to be accurate (~10% error) using kernel methods and discriminant analysis. For species-based classification in the absence of significant differences in size or shape, multi-view methods offer significant (~40%) reduction in error, but absolute error rates remain high (~20%) due to the lack of discriminant information in acoustic scatter. Length and orientation estimation are investigated using a parameter-based approach with a simple ellipsoidal scattering model. Good accuracy is obtained when the views span the full 360°. When the span is limited to less than 60°, incorporating a prior constraint on possible body shapes can lead to reduced uncertainty in the estimated parameters. Finally, using views that span the full 360°, sparse Bayesian learning coupled with a conventional Radon transform yields accurate two-dimensional, projected images of the fish.

Keywords Acoustics · Fish classification · Scattering · Size estimation · Radon transform · Bayesian learning · Distorted wave Born approximation

1 Introduction

The advantages of acoustic methods for studying fish populations are rapid and non-invasive assessment that can be cost effective, operate over long ranges, and operate in complete darkness. In pelagic fisheries applications, acoustics has become the standard means for abundance assessment [1]. However, despite these advantages, acoustic methods generally lack specificity, and are highly sensitive to fish orientation [2, 3]. Since fish orientation is typically unknown during the time of insonification, this presents a potential problem for translating measured energy into abundance. In the case of individual fish, acoustic scattering is highly sensitive to

P.L.D. Roberts (✉)
Department of Electrical and Computer Engineering, University of California,
San Diego, CA 92093-0238, USA
e-mail: plrobert@ucsd.edu

M.P. André et al. (eds.), *Acoustical Imaging*, Acoustical Imaging 30,
DOI 10.1007/978-90-481-3255-3_28,

fish size, shape, and orientation. This limits the inferences that can be made with conventional single-frequency and single-view methods.

In the context of zooplankton classification, broadband scattering measurements recorded at several different angles can offer dramatic improvements in the discrimination capabilities over both narrowband and single-view methods [4, 5]. Here, the key aspect of improvement is a result of exploiting characteristic shape differences across multiple views for different zooplankton classes. Although fish typically share more shape similarity between classes than zooplankton, these methods can be naturally extended to fish classification with appropriate modifications to the learning algorithms.

In addition to classification, it is useful to estimate physical parameters of the fish such as size, shape, orientation, and perhaps even internal structure. Such an approach has been presented [6] for estimating swimbladder length from multiple views using narrow or wideband scattering. This method was based on analysis of variability in echo magnitude as a function of view angle and frequency. In this document, an alternative approach is investigated based on echo duration. Here, the echo duration from multiple views is converted into a "thickness." These thickness estimates are then compared to an ellipsoid model to yield an estimate for ellipsoidal shape.

In addition, it is shown that both echo energy and echo duration can be combined to create a two-dimensional reconstruction that is a projected image of the fish. The method is investigated using full aperture scattering measurements and incorporates a procedure for aligning and windowing these data.

2 Laboratory Scattering Experiments

In order to observe multi-view broadband scattering measurements a laboratory system for recording these data was constructed.

2.1 Multi-View Scattering Apparatus

The details of the scattering apparatus and its calibration are described in Roberts and Jaffe [5]. The system used here is similar in configuration, except that the transmit frequencies are lower, and the fish are harnessed in the field of view under sedation (protocol approved by the University of California, San Diego – IACUC #S07191). Broadband, bistatic scattering is recorded simultaneously on eight receivers for a single transmit pulse.

As shown in Fig. 1, the receiver array is positioned at mid-depth in a large elliptical tank, 1.25 m off the bottom. The transmitter and receivers are aligned so that their beams intersect at a common location that is at a distance of 1.14 m from the array. The field of view varies with frequency, however, it is at least 5 cm^3. Two cameras record the position and orientation of the fish under observation. During the experiment, the fish is held mostly horizontal in the plane of the array where it is rotated about the vertical axis.

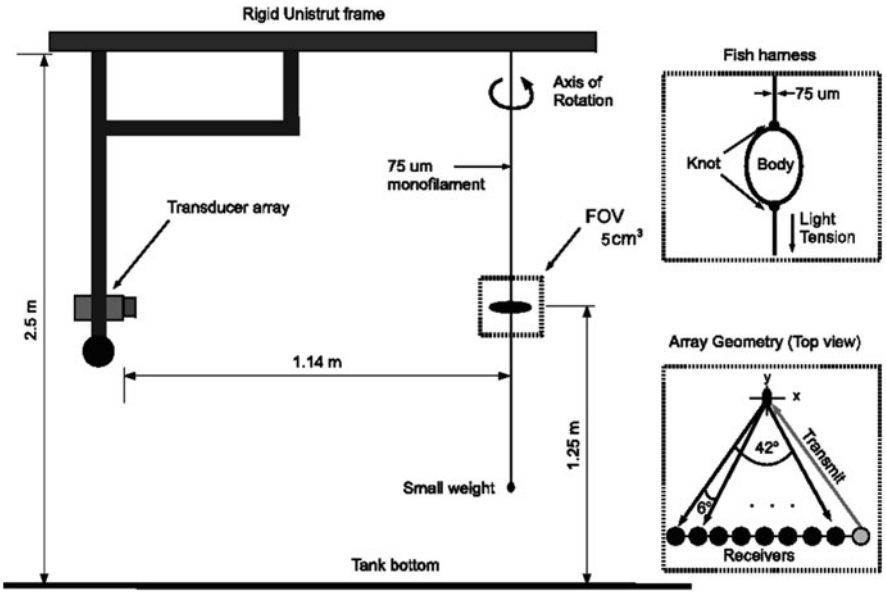

Fig. 1 Two-dimensional drawing of the experimental setup showing the geometry of the problem, the harness used to hold fish in the field of view, and the array geometry with 6° spacing and a full aperture of 42°

2.2 Fish Scattering Experiments

Two sets of experiments were performed using broadband linear frequency-modulated (LFM) chirps, one in February 2007 with a bandwidth of 250 kHz and a center frequency of 500 kHz. The second experiment took place in September 2007 with 250 kHz of bandwidth and a center frequency of 750 kHz. In total, 36 specimens were observed both visually and acoustically with the system. Requirements for usable data were that the orientation of the fish was primarily horizontal during insonification, the fish stayed alive during the entire experiment, and data were free from artifacts due to bubbles or other contaminants.

Scattering data were preprocessed by matched filtering raw echoes with a transmit signal model [7]. The matched filter output was then windowed around the peak with a 100 μs duration window. Windowing was applied to each receiver independently to account for differences in travel time between the transmitter and receiver. Video data provided an estimate for the orientation of the fish during each ping.

3 Multi-View Fish Classification

There has been substantial research in the area of multi-view target classification during the past decade [8–10]. This has lead to a progression towards methods that combine both discriminant and probabilistic algorithms [10].

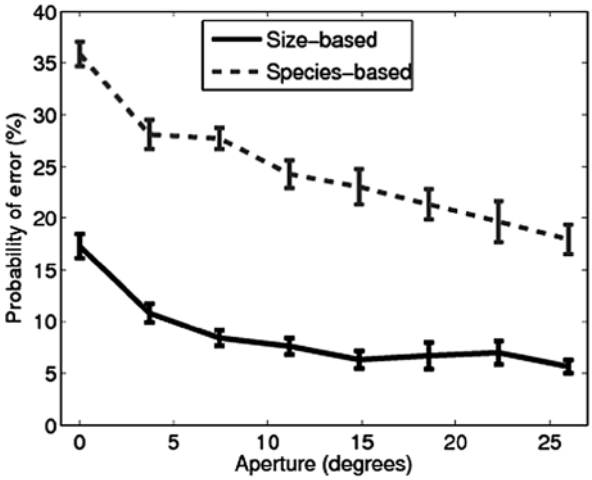

Fig. 2 Probability of error for the size- and species-based classification problems with three classes. The error is plotted as a function of the effective aperture in degrees resulting from increasing the number of views. Error bars denote one standard deviation. Fractional reductions in error for both problems are above 40% using all eight views

The classification algorithm used in this work is a network-based algorithm applying a cascade of multi-layer perceptions (MLP) and a single support vector machine (SVM) to combine probabilistic predictions from the individual views. The features used were discrete cosine transform (DCT) coefficients computed from the envelope of received echoes.

The algorithm was evaluated on two three-class problems where the algorithm was trained using a subset of available data and tested on the remaining data. Average error rates were obtained by repeating this process five times using different sets for training and testing.

The classification results for the two problems are shown in Fig. 2. Size-based classification is accurate (~10% error), and significant (~40%) reductions in error are obtained using a small number of views. In the case of species-based classification, the absolute error is significantly higher, yet the fractional error reduction remains at roughly 40%. In addition, the error curve does not level out after eight views indicating that further reduction in error could be achieved by acquiring additional views.

4 Multi-View Size and Orientation Estimation

4.1 Ellipsoid Model

Multi-view echo data were combined with an ellipsoid scattering model to estimate fish size and orientation. The scattering model is a special case of the distorted wave Born approximation (DWBA) [11] which assumes the scatterer is an ellipsoid. For a single ellipsoid, the DWBA has been shown to be a spherical Bessel function of the first kind (Dezhang Chu, personal communication, 2007)

$$S(\mathrm{k}) = C(g,h,\alpha)\mathrm{k}_1^2 abc\frac{j_1(\mathrm{kP_t})}{\mathrm{kP_t}}, \tag{1}$$

where

$$P_t = \sqrt{a^2\cos^2(\varphi)\sin^2(\theta) + b^2\sin^2(\varphi)\sin^2(\theta) + c^2\cos^2(\theta)}, \tag{2}$$

and a, b, and c are the principle radii of the ellipsoid and φ, and θ define the direction of the wave vector with wavenumber k with respect to the principle axes of the ellipsoid. The scaling term $C(g,h,\alpha)$ is a function of the gamma contrasts of the scatterer [11]. The parameter φ was assumed to be zero since the fish rotates in the plane of the array, and the parameter b was dropped from the model. The P_t term is a "thickness" parameter, and can be related to an "equivalent spherical radius" due to the fact that the DWBA for a sphere of radius r can be obtained from Equation (1) by substituting $r = P_t$ and $r^3 = abc$ (Roberts, unpublished).

4.2 Posterior Parameter Estimation

The unknown ellipsoid parameters were assumed to be random and unknown. A factorized prior was assumed over the model of the form

$$p(a,c,\theta) = p(a,c)p(\theta), \tag{3}$$

where

$$p(a,c) = \frac{1}{\sqrt{(2\pi)^2|\Sigma|}}\exp\left(\left(\begin{bmatrix}a\\c\end{bmatrix} - \mu\right)^T \Sigma^{-1}\left(\begin{bmatrix}a\\c\end{bmatrix} - \mu\right)\right), \tag{4}$$

and p(θ) is uniform.

The likelihood function was assumed to be Gaussian with unknown variance which was estimated from data. The error for the i^{th} view was computed as

$$e_i = \hat{P}_t^i - P_t^i(a,c,\theta), \tag{5}$$

where $\hat{P}_t^i$ is estimated from echo data using frequency domain analysis and $P_t^i(a,c,\theta)$ is the ellipsoid model output for the i^{th} view and the given parameters.

Examples of marginal posterior pdfs for a, c, and θ are shown as a function of the number of views of the fish, when the views cover 360° (Fig. 3), and also when the views are increasingly limited (Fig. 4). In the case of the limited views, a size proportional prior (Equation 4) is used to constrain the posterior pdfs. As can be seen, the estimates are tightly peaked near the true parameter values when a complete set of views are available (Fig. 3). In contrast, when the aperture is decreased, the distributions stay peaked until the aperture decreases below 60°. When the aperture is highly limited (Fig. 4, bottom row), the distributions are quite broad demonstrating a fundamental uncertainty between length and thickness of the fish at limited aperture.

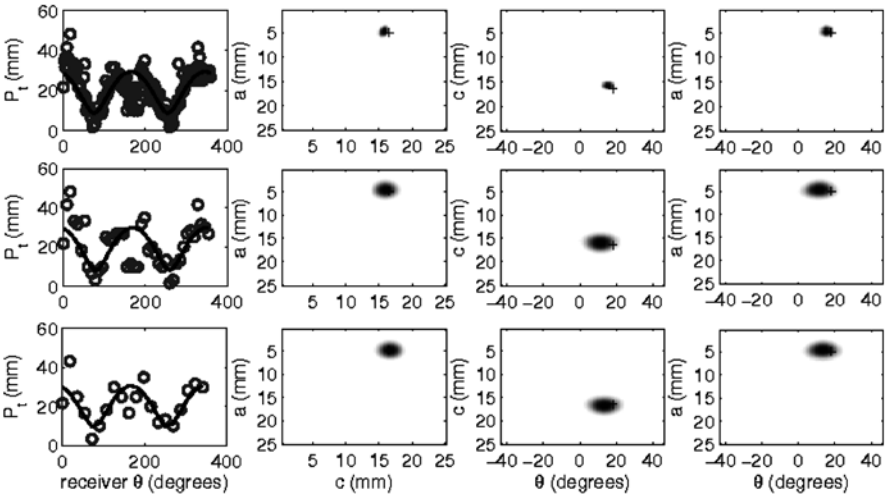

Fig. 3 Marginal posterior pdfs for different angular sampling frequencies (rows). The left column shows the modeled (*black line*) and estimated thickness (*gray circles*) and the other columns show the marginal pdfs. Going from the top to the bottom row, the angular sampling frequency is reduced by 50% at each step. The measured parameters are shown by the black "+" signs

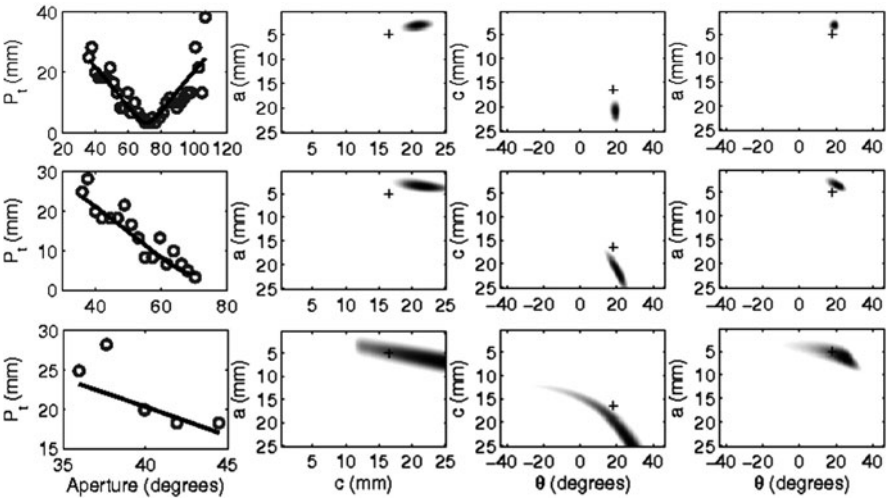

Fig. 4 Marginal posterior pdfs for different apertures (rows). The left column shows the modeled (*black line*) and estimated (*gray circles*) thickness and the other columns show the marginal pdfs. Going from the top to the bottom row, the aperture is 60, 30, and 10 degrees. The measured parameters are shown by the *black* "+" signs

5 Fish Shape Reconstruction

In this section, the reconstruction of the projected 2D image of the fish (as viewed from above) is investigated using the full 360° of backscattering over 250 kHz of bandwidth centered at 750 kHz.

Due to the limited bandwidth, and the use of backscatter, the range of spatial frequencies sampled by the system is limited to an annulus centered at the origin with width radial frequencies varying from 650 to 900 kHz. This prevents direction reconstruction from echo data as no low frequency data is available. To mitigate this problem, the echo envelope is used to approximate the impulse response of the fish at a given observation angle. This is similar to creating a time of flight image of strong scatterers on the fish body.

The laboratory experiments were not designed with this type of reconstruction in mind, and the echoes must first be registered for different fish orientations. To align and window echoes, sparse Bayesian learning [12, 13] is used to estimate an impulsive impulse response $\mathbf{w}$ from echo data $\mathbf{y}$ which satisfies

$$p(\mathbf{y}|\mathbf{w},\sigma^2) = \frac{1}{\sqrt{\left(2\pi\sigma^2\right)^N}} \exp\left(-\frac{1}{2\sigma^2}||\mathbf{y}-\mathbf{\Phi}\mathbf{w}||^2\right), \tag{6}$$

where $\mathbf{\Phi}$ is a transmit signal model matrix and the prior on $\mathbf{w}$ has the form

$$p(\mathbf{w};\boldsymbol{\gamma}) = \prod_{i=1}^{N} \frac{1}{\sqrt{2\pi\gamma_i}} \exp\left(-\frac{w_i^2}{2\gamma_i}\right). \tag{7}$$

These constraints on $\mathbf{w}$ enforce a sparse solution [13] which was found to yield excellent results for aligning echoes and windowing them. The echoes were windowed by setting all elements of $\mathbf{y}$ outside the index of the first and last nonzero coefficient of $\mathbf{w}$ to zero. The echoes were then aligned by centering them about the midpoint between the index of the first and last nonzero coefficient of $\mathbf{w}$. Given the aligned and windowed echo envelopes for all 360°, the image of the fish was reconstructed using an inverse Radon transform [14] (Fig. 5).

6 Conclusions

In this article, the application of multi-view acoustic methods to sizing and classifying individual fish has been presented. It has been shown that observing multiple views of scattering offers significant advantages for classifying fish both in terms of size classes and species classes. The absolute error in species-based classification is much higher due to the lack of discriminant information in the echoes.

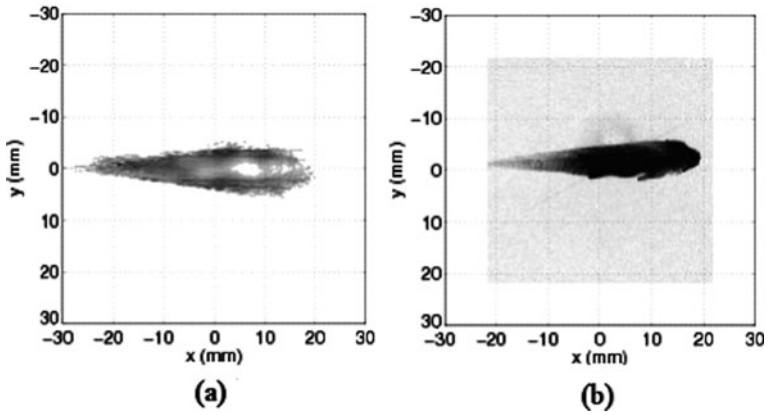

Fig. 5 Reconstructed 2D projected image of a damselfish (**a**) showing internal structure in the reconstruction and very good agreement with the corresponding video image (**b**)

Results of this study show that size-based classification is mostly likely to be a viable and accurate strategy for inferring information from limited view data. When full-aperture data is available, the inverse Radon transform approach performed better than the parametric approach due to mismatch between the ellipsoid model and the true shape of the fish. However, the ellipsoid model was also able to yield accurate estimates when full-aperture data was used.

These results highlight some promising areas of research in applying multi-view methods problems in fisheries and oceanography.

Acknowledgements This work was supported by the California Sea Grant. The authors would like to thank Eddie Kisfaludy, Robert Glatts, Fernando Simonet, Ben Maurer, Erdem Karakoylu, and the SIO machine shop for help with the design and implementation of these laboratory experiments.

References

1. Simmonds, J., MacLennan, D.: Fisheries Acoustics: Theory and Practice (Fish and Aquatic Resources). Wiley-Blackwell, New York, NY (2006)
2. McClatchie, S., Alsop, J., Ye, Z., Coombs, R.F.: Consequence of swimbladder model choice and fish orientation to target strength of three New Zealand fish species. ICES J. Mar. Sci. **53**, 847–862 (1996)
3. McQuinn, I., Winger, P.D.:, Tilt angle and target strength: Target tracking of Atlantic cod (gadus morhua) during trawling. ICES J. Mar. Sci. **60**, 575–583 (2003)
4. Roberts, P.L.D., Jaffe, J.S.: Multiple angle acoustic classification of zooplankton. J. Acoust. Soc. Am. **121**, 2060–2070 (2007)
5. Roberts, P.L.D., Jaffe, J.S.: Classification of live, untethered zooplankton from observations of multiple-angle acoustic scatter. J. Acoust. Soc. Am. **124**, 796–803 (2008)
6. Jaffe, J.S.: Using multiple-angle scattered sound to size fish swim bladders. ICES J. Mar. Sci. **63**, 1397–1404 (2006)

7. Kay, S.M.: Fundamentals of Statistical Signal Processing, Vol. 2: Detection Theory. Prentice Hall, Upper Saddle River, NJ (1998)
8. Azimi-Sadjadi, M.R., Yao, D., Huang, Q., Dobek, G.J.:, Underwater Target classification using wavelet packets and neural networks. IEEE T. Neural Networ. **11**(3), 784–794 (2000)
9. Dasgupta, N., Runkle, P., Carin, L., Couchman, L., Yoder, T., Bucaro, J., Dobeck, G.: Class-based target identification with multi-aspect scattering data. IEEE J. Ocean. Eng. **28**(2), 271–282 (2003)
10. Robinson, M., Azimi-Sadjadi, M., Salazar, J.: Multi-aspect target discrimination using hidden Markov models and neural networks. IEEE T. Neural Networ. **16**(2), 447–459 (2005)
11. Lavery, A.C., Stanton, T.K., McGehee, D.E., Chu, D.Z.: Three-dimensional modeling of acoustic backscattering from fluid-like zooplankton. J. Acoust. Soc. Am. **111**, 1197–1210 (2002)
12. Tipping, M.E.: Sparse Bayesian learning and the relevance vector machine. J. Mach. Learn. Res. **1**, 211–244 (2001)
13. Wipf, D.P., Rao, B.D.: Sparse Bayesian learning for basis selection. IEEE T. Signal Proces. **52**(8), 2153–2164 (2004)
14. Deans, S.R.: The Radon Transform and Some of Its Applications. Wiley, New York (1983)

Acoustic Image Models for Obstacle Avoidance with Forward-Looking Sonar

T. Masek and M. Kölsch

Abstract Long-range forward-looking sonars (FLS) have recently been deployed in autonomous unmanned vehicles (AUV). We present models for various features in acoustic images, with the goal of using this sensor for altitude maintenance, obstacle detection and obstacle avoidance. First, we model the backscatter and FLS noise as pixel-based, spatially-varying intensity distributions. Experiments show that these models predict noise with an accuracy of over 98%. Next, the presence of acoustic noise from two other sources including a modem is reliably detected with a template-based filter and a threshold learned from training data. Lastly, the ocean floor location and orientation is estimated with a gradient-descent method using a site-independent template, yielding sufficiently accurate results in 95% of the frames. Temporal information is expected to further improve the performance.

Keywords Sonar · Acoustic image analysis

1 Introduction

Autonomous underwater vehicles (AUVs) are becoming a standard mapping tool for marine research, exploration, and for the military. These missions require the vehicle to maintain a constant altitude above the ocean floor, typically 3 m. Operating at low altitudes, the AUV is at risk of colliding with obstacles on the ocean floor. Forward looking sonar (FLS) can be used as an effective tool for avoiding possible collisions. However, identifying objects in the image is difficult because the intensity and shape of the possible obstacles is unknown. Furthermore, background noise due to gain and backscatter can hide objects that have a faint return, and the sonar is susceptible to artificially introduced artifacts caused by other acoustic sources such as micro modems. Proper identification of the ground location and orientation has the benefit of being able to extract vehicle state information, such as pitch and altitude.

One technique used to track features in FLS data is to compare the movement of a possible feature from one frame to another and relate it to the vehicle movement to filter out false positives. A more complex implementation of this technique was successfully used for underwater SLAM [1] and obstacle avoidance [2] and obstacle avoidance without vehicle motion knowledge [3]. However, these techniques require

T. Masek (✉)
Naval Postgraduate School, Monterey, CA, USA
e-mail: tdmasek@nps.edu

M.P. André et al. (eds.), *Acoustical Imaging*, Acoustical Imaging 30,
DOI 10.1007/978-90-481-3255-3_29,

multiple frames and only track static objects. Two-view homography was used with FLS images to estimate 3-D motion parameters and target tracking [4]. Again, stationary targets are assumed and techniques discussed were beyond our current onboard processing resources. By describing features in the FLS data obstacles could be detected in a single frame regardless if the obstacle is static or moving.

Our approach to detecting obstacles was to first model and identify four common artifacts in the BlueView 450X-R100 FLS image: background noise, artifacts caused by the micro modem and a pulse-like artifact generated from an unknown source. Next, we searched for and estimated the ground position and orientation. A blend of pixel-based and spatial (neighborhood, template-based) models were utilized depending on the object or effect. Section 2 introduces the acoustic image models, Section 3 presents the experiments, and results are discussed in Section 4 followed by conclusion in Section 5.

2 Acoustic Image Models

The four models, described in the following subsections, were applied independently to the original sonar image after smoothing with a 5×5 Gaussian filter. Remaining pixels that were not well described were grouped by proximity to see if they were large enough to pose a collision hazard. The complete model for the entire image is a mixture of source models P_i:

$$I(x, y) = \max(P_i(x, y)) \tag{1}$$

2.1 Acoustic Noise Background Model

Acoustic background noise is characterized by low intensity random signals. A uniform image-wide threshold is insufficient for describing the background because the average intensity of the background noise varies by angle across the field of view, a typical characteristic of this technology.

Using a set of images in polar space containing only the background, an intensity histogram was created for each angle. Visual observation suggested a Gaussian noise distribution. The model parameters ($\mu_\alpha, {\sigma_\alpha}^2$) for each angle α were estimated with the sample mean and variance. A pixel was marked as background ($p_{bg} = 1$) if the intensity of the pixel fit within 3 standard deviations of the Gaussian models mean for that angle.

$$P_{bg}(\alpha, r) = \begin{cases} 1 \text{ if } & |I_{\alpha,r} - \mu_\alpha| < 3\sigma_\alpha \\ 0 \text{ if } & |I_{\alpha,r} - \mu_\alpha| > 3\sigma_\alpha \end{cases} \tag{2}$$

2.2 Acoustic Interference Noise Models

Acoustic noise from an unknown source (in ~1% of the frames) appears as a digital pulse, confined to a small band of the image. Noise from the acoustic modem (present in ~7% of the frames) appears as small rectangles of varying intensities. Both of these artifacts are easier to analyze in the polar space (see Fig. 1).

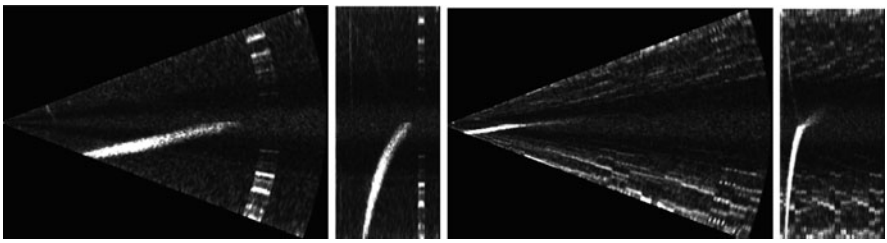

Fig. 1 Far Left: Pulse artifact from unknown source and ground in Cartesian space. *Left*: Same image in polar space. *Right*: Modem noise and ground in Cartesian space. Far Right: Same image in polar space

2.2.1 Acoustic Pulse Noise

The pulse noise had a predictable size and shape but a varying digital pattern. Template matching using a sum of absolutes difference (SAD) was used to detect the noise. Since the pulse noise was most prominent in the top of the image, the search was limited to that area to reduce computation time.

$$SAD(x,y) = \sum_{i=0}^{rows} \sum_{j=0}^{cols} |(x+i, y+j) - (i,j)| \tag{3}$$

Templates P_{ff}, P_{lc}, P_{sd}, and P_{pc} were site-specific and created by averaging five sub-images containing only top-pulse noise from an individual site P_{av}. The fifth template was created by averaging the four templates together, see Fig. 2.

The score from the detection test was used to classify images as containing pulse noise. Once an image was classified as having pulse noise the pixels within the area of the up-pulse and bottom-pulse template at the detected distance were set as being caused by pulse noise.

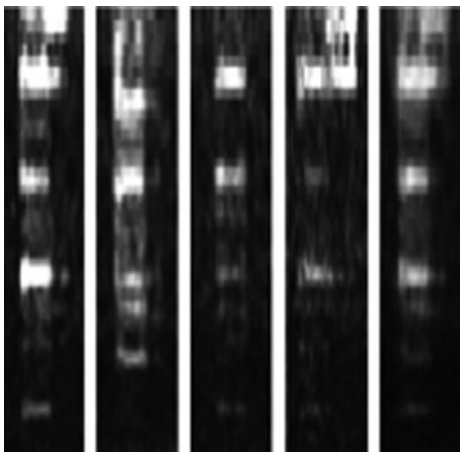

Fig. 2 Five pulse templates tested, $P_{sd}, P_{pc}, P_{lc}, P_{ff}$, and P_{av}

2.2.2 Modem

Two approaches were tested to detect images that contain modem noise. The first technique matched a template of an approximately 60 degree downward sloping "digital" pattern against parts of the image. The correlation was scored with Normalized Cross Correlation (NCC) [5]. The second technique was calculating the mean and median intensities of the top 20% and bottom 20% of the image.

$$NCC(x,y) = \frac{\sum_{x,y}\left[f(x,y) - \bar{f}_{u,p}\right]\left[t(x-u,y-v) - t\right]}{\left\{\sum_{\{x,y\}}\ \left[f(x,y) - \bar{f}_{u,v}\right]^2 \sum_{x,y}\ \left[t(x-u,y-v-t)\right]^2\right\}^{0.5}} \tag{4}$$

Five different templates were tested. Again, the first four were cropped directly from randomly sampled images from each site and the fifth the average of these four, see Fig. 3.

If modem noise was detected, pixels within an angle-specific intensity range were marked as modem noise. This range was determined by finding the mean of the brightest pixels for each angle of a set of 20 annotated images only containing modem noise. The lower limit was $3\sigma_\alpha$ above the mean background at angle α.

For each angle the probability is set to 1 if intensity for the pixel (angle dist) is less than intensity threshold value, as in

$$P_{mn}(\alpha, r) = \begin{cases} 1 \text{ if } I(\alpha, r) > t_{bg} \text{ and } I(\alpha, r) < t_{mn} \\ 0 \text{ otherwise} \end{cases} \tag{5}$$

2.3 Ground Model

The ground feature changes position and rotation relative to the vehicle and is better represented in a Cartesian space image. The shape and intensity varies with different bottom types but is similar enough to describe with a common template. Ground model parameters were translation (x, y), rotation, and anisotropic scale, fitted to

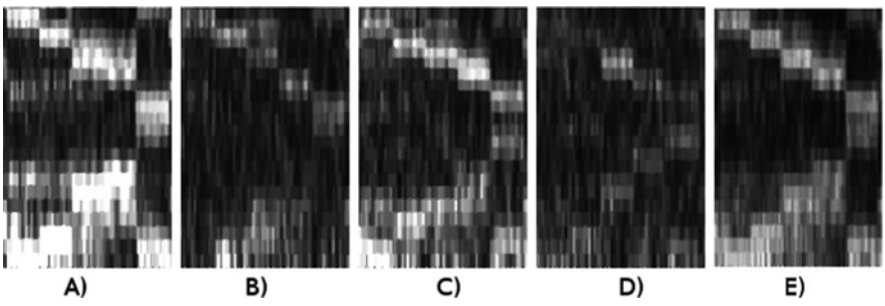

Fig. 3 Five modem templates tested, M_p, M_f, M_{sd}, M_{lc}, and M_{av}

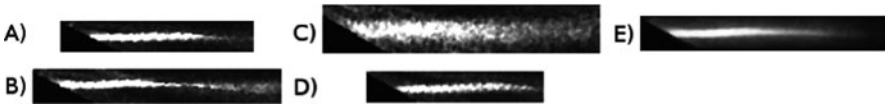

Fig. 4 Five ground model templates tested. A)G_{sd} B)G_{pc} C)G_{lc} D)G_{ff} E)G_{av}

the image using Nelder-Mead [6] non-linear optimization using NCC as the criterion for fit.

Five ground templates were created and tested (see Fig. 4). Again, the first four were cropped from an image from each of the four sites. The image in each run was chosen to be a good representative to the given run. The fifth template was created by averaging forty ground images together, ten images from each site.

Parameter initialization is critical due to the many local minima. To locate initial conditions the previous noise description techniques were applied to the corresponding polar image. The polar image was then transformed to Cartesian space. Pixels not described with noise models were clustered by proximity. The center points of clusters larger than 300 pixels were used as the starting location for the ground template. The default template size was used for the initial scale. Six degrees was chosen as the initial rotation because the sonar has a five degree tilt down and the vehicle tends to operate with a one degree down.

The usefulness of the ground template fit depends largely on the accuracy at the *top* of the ground. Hence, to quantify the results, a weighted score was calculated by summing the number of pixels of the ground in the template above the annotated ground ($Pixels_t$) with the number of pixels of the annotated ground that were above the template ground ($Pixels_a$). This implicitly accounts for rotation error. That score was then multiplied by the percent of annotated ground not covered by the ground template plus one.

$$e_{ground_{fit}} = (Pixels_t + Pixels_a) * (P_{g-not} + 1) \tag{6}$$

3 Experimental Results

Data for the experiments were captured over the last year from four sites (see Table 1 and Fig. 5), chosen due to varying factors such as bottom type and water temperature. Different sites were chosen to compare how well the models behaved in varying environments.

Four different background models were created and tested (BG_1, BG_{10}, BG_{25}, BG_{50}). The first four models were created from randomly sampling 1, 10, 25 and 50 images from a set of 87 images sampled from each site and smoothed with a 5×5 Gaussian filter. The background models' ability to separate background noise from other artifacts was compared to using a global threshold value on the remaining 37 annotated images.

Table 1 Characteristics of the four sampling sites, numbers are frame counts

Site	Depth (m)	Bottom type	Pings	Modem	Pulse
Fisherman Flats(FC)	15	Sandy with 3 m rock	1,860	146	62
Lovers Cove(LC)	5	Rocky with kelp forest	673	38	14
Shell Island(PC)	20	Flat, fine grain sand	4,384	332	142
Silver Strand(SD)	20	Flat sandy	5,376	362	187

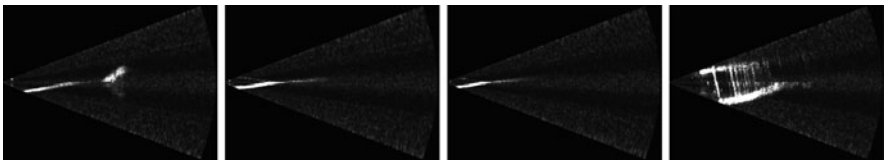

Fig. 5 Sample images from the four sites. *Far Left*: Fisherman Flats (FF) *Left*: Panama City (PC) *Right*: San Diego (SD) *Far Right*: Lovers Cover (LC)

The five different pulse noise templates were applied to 552 test images, half of which contained pulse noise. The templates were compared by their ability to detect the presence of pulse noise. Five modem templates were applied to the bottom of 676 test images and scored using NCC, 338 images contained modem noise. The mean and median of the top and bottom third of the image were also calculated for the test data set.

The ground model dataset was comprised of 40 annotated Cartesian-space images, ten from each of the four sites. Each set from the different sites contained two images with modem noise and one image with pulse noise. Some of the images contained unclassified objects. The five ground templates.

Templates G_{ff}, G_{lc}, G_{sd}, G_{pc}, G_{av} were fit to the 40 test images. The weighted score was calculated for each of the 200 experiments. The final weighted scores were then used to judge template fit. A score of less than 200 was considered an excellent fit. Scores less than 500 were considered a good fit, scores between 500 and 1,000 were poor and any score greater than 1,000 was an unacceptable fit.

4 Discussion

The results show that the models explain the observed patterns well. Figure 6 shows a ROC curve of the background classification. The ROC curve shows the percent of pixels correctly classified as background over the percent of non background pixels incorrectly classified as background, by changing the model ${\sigma_\alpha}^2$ from 0.01 to 17. Also shown is a curve for an image-wide threshold. Modeling background noise performed better than using an image-wide threshold. All background noise models performed roughly the same regardless of how large the training set was.

Figure 7 contains the ROC curve that shows how many images were correctly described as having pulse noise to false positives using the SAD correlation score

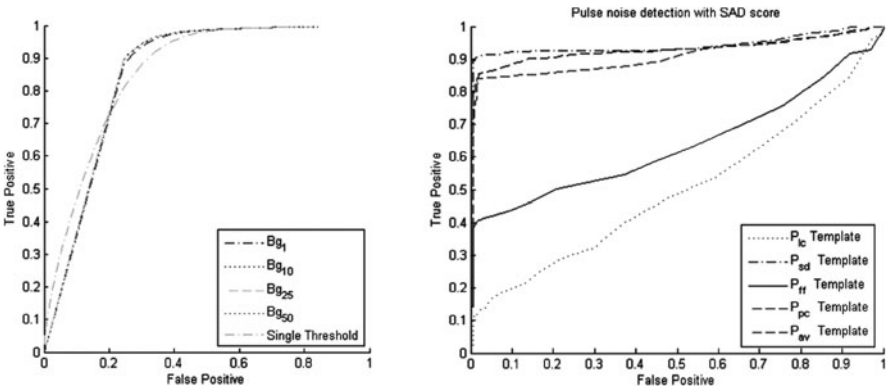

Fig. 6 *Left*: ROC plot of background detection models. *Right*: ROC plot of templates ability to detect pulse noise

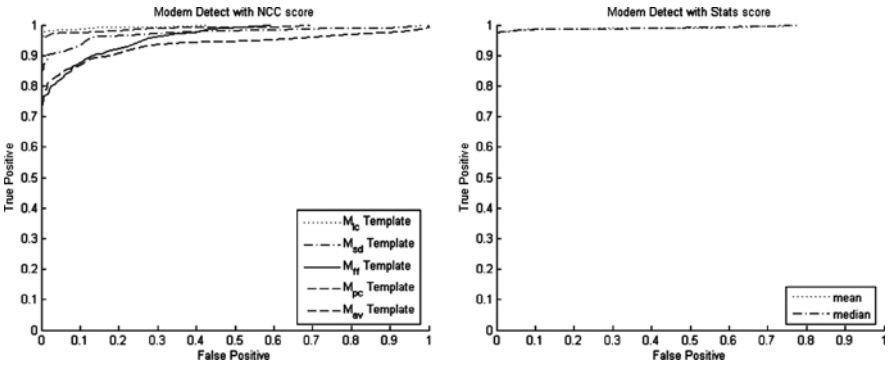

Fig. 7 *Left*: ROC plot of templates ability to detect modem noise. *Right*: ROC plot of statistical methods to detect modem noise

as the threshold. The template-based pulse noise detection performs well using the P_{SD} template matched with SAD. This was able to classify images containing pulse noise correctly 92% of the time with less than a 3% false positive rate. Template matching using SAD is a reliable way to detect pulse noise, but the choice of the template is important.

Modem noise detection proved robust with any of the three techniques. With template-based modem noise detection with NCC, all five of the modem templates M_{ff}, M_{lc}, M_{sd}, M_{pc}, M_{av} accurately detected images with modem noise more than 80% of the time with less than 5% false positives. Calculating the mean and the median were both very reliable at detecting images with modem noise 98% of the time with less than 2% false positive.

Being able to accurately identify images with modem noise is important because the noise affects such a large area of the image. If an image is misclassified as not having modem noise then the large unknown area will be classified as objects and

Table 2 Ground template weighted score summery for each site

Template	Excellent	Good	Poor	Unacceptable
Fisherman Flats				
G_{ff}	6	2	2	0
G_{lc}	0	2	4	4
G_{sd}	4	5	1	0
G_{pc}	0	9	1	0
G_{av}	0	4	4	2
San Diego				
G_{ff}	3	7	0	0
G_{lc}	0	4	3	3
G_{sd}	5	5	0	0
G_{pc}	1	9	0	0
G_{av}	0	0	10	0
Panama City				
G_{ff}	3	6	1	0
G_{lc}	0	3	6	1
G_{sd}	2	7	1	0
G_{pc}	0	4	6	0
G_{av}	0	2	7	1
Lovers Cove				
G_{ff}	0	1	2	7
G_{lc}	0	0	2	8
G_{sd}	0	0	2	8
G_{pc}	0	0	1	9
G_{av}	0	1	2	7

possible collisions. During the ground-template-fitting stage a ground model will be fit to each one of these objects. This will increase the run time of the ground-template-fitting stage dramatically.

The method for ground position and orientation estimation with a generic template was successful in most cases. Refer to Table 2 for a summary of how each template performed at the different sites. The G_{ff} and G_{sd} templates performed the best at multiple sites. One interesting result was that the G_{ff}, G_{sd} performed the best at their corresponding site, but G_{pc}, G_{lc} did not. Also, the G_{av} was one of the poorest performing templates over all the sites. Using template matching to find the ground worked well at specific sites but did not do well at describing the ground at the Lovers Cove site. The ground at this site is very rocky and dynamic and difficult to describe with a template.

5 Conclusions

The use of models has been shown to successfully detect common features in FLS images. Being able to describe features allows the vehicle to detect obstacles and removes many of the false positives that need to be filtered. This allows obstacles to be classified much faster than using filtering alone. Improved feature models will

allow the vehicle to react to obstacles seen in a single frame, improving navigation abilities and reaction time.

References

1. Folkesson, J., Leonard, J., Leederkerken, J., Williams, R.: Feature tracking for underwater navigation using Sonar. IEEE/RSJ International Conference on Intelligent Robots and Systems Proceedings (2007)
2. Horner, D., Yakimenko, O.: Recent developments for an obstacle avoidance system for a small AUV. Paper presented at IFAC Conference on Control Applications in Marine Systems, Bol island Brac, Croatia (2007)
3. Petillot, Y., Tena Ruiz, I., Lane, D.M.: Underwater vehicle obstacle avoidance and path planning using a multi-beam forward looking sonar. IEEE J. Ocean. Eng. **26**, 240–251 (2001)
4. Sekkati, H., Negahdaripour, S.S.: 3-D motion estimation for positioning from 2-D acoustic video imagery. Lect. Notes Comput. Sci. **4478**, 80–88 (2007)
5. Haralick, R.M., Shapiro, L.: Computer and Robot Vision, vol. 2. Addison-Wesley, Boston, MA (1993)
6. Nelder, J., Mead, R.: A simplex method for function minimization. J. Computer **7**, 308–313 (1965)

Underwater Acoustical Imaging and Sensing Systems for Homing, Docking, Navigation and Collision Avoidance

H. Lee

Abstract This paper presents a simple high-performance algorithm for underwater geolocation and navigation. The simplicity of the algorithm provides excellent stability, accuracy, and computation efficiency. In addition, the paper also describes the reversed version of the system for the enhancement of system performance, and the conversion to active system for UUV collision avoidance.

Keywords Geolocation · Underwater navigation · Bearing angle · Collision avoidance

1 Introduction

This paper presents the development of a novel algorithm for underwater geolocation and navigation. The resultant algorithm came from a sequence of seemingly unrelated projects. Upon close examination, the convergence of signal processing procedures to a surprisingly simple form is most interesting.

At the early stage of the projects, the goal was to improve the accuracy and stability of the conventional polarity estimation algorithm for unmanned underwater vehicle (UUV) homing and docking exercises. The assumption is that the relative left-right position of the UUV to the base stations can be estimated from the polarity of the beacon waveforms. The traditional technique conducts the polarity estimation based on the phase term of the first peak of the received beacon signal. In the underwater environment, this approach has been problematic with low stability and accuracy, because of the difficulty especially in the locating the first peak from the interference signal pattern under substantial multi-path and background noise. After a series of trials for improving existing algorithms, the effort was then redirected toward the design and development of algorithms with simple structures. As a result, the *double-integration method* was developed and the results showed superior stability and accuracy.

During the investigation, it was also noted that the reversed version of the existing system could be even more effective. This involves the reversal of the

H. Lee (✉)
Department of Electrical and Computer Engineering, Center for Advanced Surgical and Interventional Technology (CASIT), University of California, Santa Barbara, CA 93106, USA
e-mail: hualee@ece.ucsb.edu

M.P. André et al. (eds.), *Acoustical Imaging*, Acoustical Imaging 30,
DOI 10.1007/978-90-481-3255-3_30,

configuration of the transmitter and receiver. The alternative arrangement further simplifies the hardware and software. Besides, the new configuration enables us to continue the improvement of system performance with added receiver elements without increasing the computation complexity.

One important extension is the conversion of the existing system to the active modality by placing the transmitter at the center of the circular receiver array. Because the transmitted signal is available as the reference waveform, this enables us to integrate the estimation of the range distance into the algorithm. For the superior computation efficiency in dynamic sensing, this system will be an excellent candidate for added applications to collision avoidance.

2 Sensor Unit

In mobile autonomous sensing, the geolocation capability for navigation and guidance can be achieved by estimating the position of the sensor unit with respect to the underwater base stations. The locations of the underwater base systems are constantly estimated and updated with respect to the interface stations over the ocean surface. The interface stations are supported by the GPS systems with the direct microwave link to surface communication infrastructure. Thus, one of the most critical elements is the mobile sensor's capability of dynamic estimation and updating of its relative position with respect to the underwater base stations. In three-dimensional underwater geolocation tasks, the objective parameters include mainly the *range distance* and a multi-dimensional *bearing angle vector*.

Figure 1 shows the laboratory prototype of the three-component transmitter of the base stations. Each of the three components consists of four small square transmitting elements. With the three transmission components, the transmitter unit sends out a sequence of three signals, $\{T_1(t), T_2(t), T_3(t)\}$. The first signal $T_1(t)$, from the top transducer element, is an in-phase reference signal, of which all four elements send out the same signal. The second signal $T_2(t)$, from the middle transducer, is a beacon signal, transmitting a pair of signals with a left-right polarity of 180-degree phase offset, for the estimation of the bearing angle in the horizontal direction.

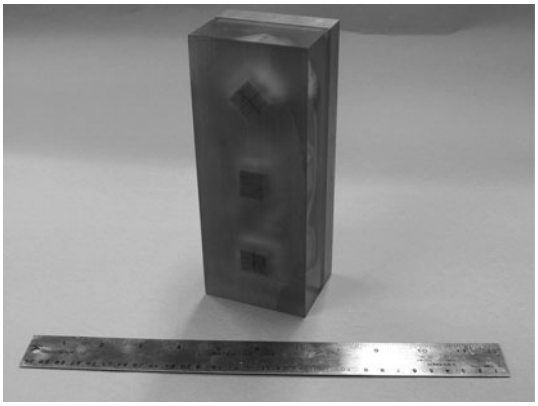

Fig. 1 Laboratory prototype of the three-component transmitter

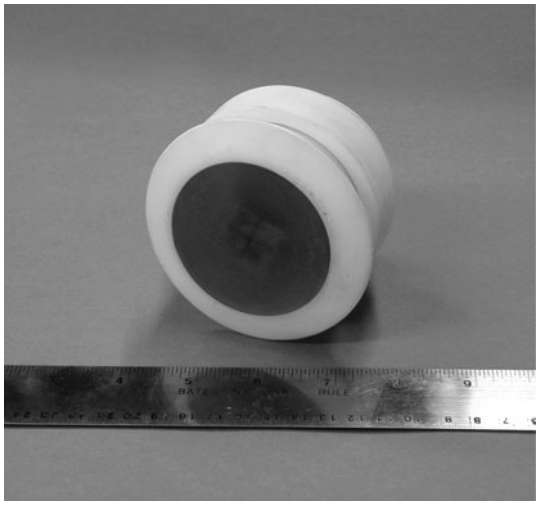

Fig. 2 Single-element receiver

Similarly, the third signal $T_3(t)$, from the bottom transducer, is with a top-bottom polarity of a 180° phase offset for the estimation of the bearing angle in the vertical direction. And Fig. 2 is the single-element receiver at the mobile sensor.

Because of the complexity and sensitivity of the underwater acoustic propagation and serious multi-path interference, the accuracy of geolocation has been an extremely difficult problem. For the estimation of polarity, the conventional approach is to search for the first peak of the matched-filtered received signal and identify its phase term. Figure 3 shows a typical result of the horizontal bearing

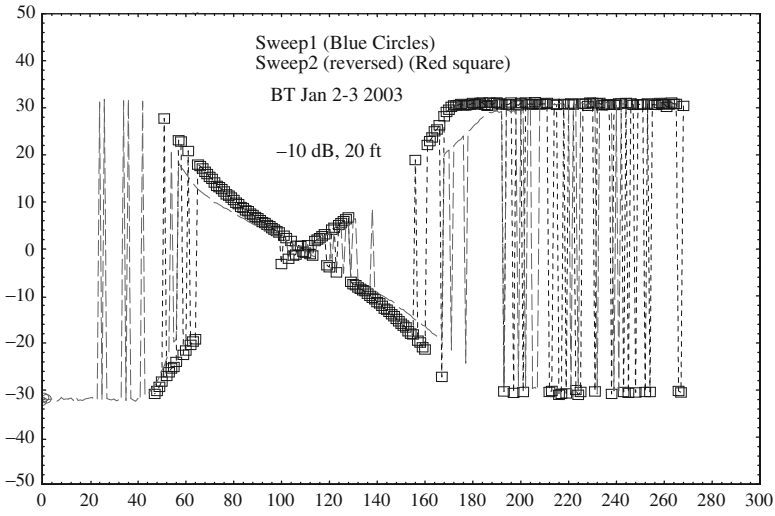

Fig. 3 Bearing angle estimation experiment with the conventional method

angle estimation experiment with the conventional method. The experiment was conducted in a laboratory pool. The receiver unit scans along a circular path with a 60° angular span. The horizontal axis is the bearing angle, and the vertical axis is the estimate. The ideal result is a monotonically increasing pattern. The rapid hopping between the top and bottom curves represents the failure of correctly estimating the bearing angle. This difficult task has long been regarded as the bottleneck of high-precision underwater geolocation and navigation.

3 Double-Integration Method

As we start, we examine the basic structure of the received beacon signal. From a particular receiver position, the beacon signal, with the polarity of 180° phase offset, from the transmitter array can be written in the form of

$$\begin{aligned} T_2(t) &= [h(t + \Delta/2) - h(t - \Delta/2)] \\ &= [\delta(t + \Delta/2) - \delta(t - \Delta/2)] * h(t) \end{aligned} \tag{1}$$

where *h(t)* is the designated transmission waveform. For the laboratory experiments, the signal *h(t)* has a center frequency of *73.9 KHz* with a *15.8 KHz* bandwidth. The positive-polarity term $h(t + \Delta/2)$ is transmitted from the element at the right, and the negative-polarity term from the left transmitter element is $-h(t - \Delta/2)$.

The time-delay term Δ is the relative propagation lag due to the separation distance D between the transmitter elements

$$\Delta = \frac{D}{v} sin(\theta) \tag{2}$$

where θ is the bearing angle and v is the propagation speed. The width of the separation D is 1 cm. It is important to point out that the term Δ can be either positive or negative. If the receiver is at the right-hand side of the transmitter, the angle θ is positive and Δ becomes a positive value accordingly. Then the positive-polarity term $\delta(t + \Delta/2)$ arrives at the receiver first, followed by the negative-polarity term $-\delta(t - \Delta/2)$, Δ seconds later. On the other hand, when the receiver is at the left-hand side of the transmitter, the angle θ becomes negative, and so is Δ. Then the negative-polarity term, $-\delta(t - \Delta/2)$ arrives at the receiver first, followed by the positive-polarity term $\delta(t + \Delta/2)$.

The objective of the algorithm is the accurate estimation of the term Δ, which gives the estimate of the polarity as well as the bearing angle. The detected signal at the receiver is in the form of

$$s(t) = T_2(t - d) = c[\delta(t - d + \Delta/2) - \delta(t - d - \Delta/2)] * h(t) \tag{3}$$

where d is the time delay due to the propagation from the center of the transmitter-array unit to the receiver, and c is the attenuation factor due to propagation loss [1–3].

At the receiving end, matched filtering is first applied to the received signal. Mathematically, the matched filtering process can be formulated in the form of a convolution with $h^*(-t)$

$$\begin{aligned} r_0(t) &= s(t) * h^*(-t) \\ &= c[\delta(t-d+\Delta/2) - \delta(t-d-\Delta/2)] * [h(t) * h^*(-t)] \\ &= c[\delta(t-d+\Delta/2) - \delta(t-d-\Delta/2)] * R_0(t) \\ &= c[R_0(t-d+\Delta/2) - R_0(t-d-\Delta/2)] \end{aligned} \tag{4}$$

where $R_0(t)$ is the auto-correlation of *h(t)*. Because $R_0(t)$ is zero at $t = \pm\infty$, the initial and final value of the matched-filtered signal $r_0(t)$ are also zero,

$$r_0(-\infty) = r_0(\infty) = 0 \tag{5}$$

Now we introduce a new function $r_1(t)$ by integrating $r_0(t)$,

$$\begin{aligned} r_1(t) &= \int_{-\infty}^{t} r_0(\tau)d\tau = c[u(t-d+\Delta/2) - u(t-d-\Delta/2)] * R_0(t) \\ &= \pm c p_\Delta(t-d) * R_0(t) \end{aligned} \tag{6}$$

where $p_\Delta(t)$ is a pulse of unit amplitude with pulse duration Δ. Note that the duration of the pulse is independent of the time delay term d. The $\pm$ polarity of the term depends solely on the value of Δ. And the polarity of the term follows exactly the sign of the time-delay Δ.

This equation also shows $r_1(t)$ is the result of a convolution of the auto-correlation function $R_0(t)$ with a finite-length pulse with a $\pm$ polarity. If we perform the second integration, it results in,

$$\begin{aligned} r_2(t) &= \int_{-\infty}^{t} r_1(\tau)d\tau = \pm c p_\Delta(t-d) * \int_{-\infty}^{t} R_0(\tau)d\tau \\ &= \pm c p_\Delta(t-d) * R_1(t) \end{aligned} \tag{7}$$

where $R_1(t)$ is the result of integration of $R_0(t)$,

$$R_1(t) = \int_{-\infty}^{t} R_0(\tau)d\tau \tag{8}$$

Thus, the final value of $R_1(t)$ is the DC term of $R_0(t)$. Since $R_0(t)$ is the auto-correlation of *h(t)*, the DC term of $R_0(t)$ is $|H(0)|^2$, where $H(j\omega)$ is the Fourier spectrum of *h(t)* [4]. Hence,

$$R_1(\infty) = |H(0)|^2 \tag{9}$$

Subsequently, we find the final value of $r_2(t)$ as

$$\begin{aligned} \textit{Final value} = r_2(\infty) &= c\,\Delta \cdot R_1(\infty) = c\,\Delta \cdot |H(0)|^2 \\ &= c\frac{D\sin(\theta)}{v}|H(0)|^2 \\ &= \frac{cD}{v}|H(0)|^2 sin(\theta) \end{aligned} \tag{10}$$

Note that separation of the transmitter elements D, propagation velocity v, propagation attenuation c, and $|H(0)|^2$ are all real and positive constants. So, the final value of $r_2(t)$ is linearly related to $sin(\theta)$. This means the final value of $r_2(t)$ can uniquely characterize the polarity of the signal as well as the bearing angle of the receiver with respect to the transmitter.

4 Normalization

The parameters, D, v, and $|H(0)|^2$ are fully defined from the system design. The propagation-loss term c is the only uncertain element. The propagation loss is known to be a function of the range distance. When the mobile sensor unit changes its position, the range distance varies and the value of the c term changes also as a result, which introduces ambiguity to the estimation of the bearing angle. Thus, to achieve high-precision estimation of the bearing angle, the c factor needs to be isolated from the estimation process.

The reference signal, the first pulse from the transmitter array, is in the form of

$$\begin{aligned} T_1(t) &= [h(t+\Delta/2) + h(t-\Delta/2)] \\ &= [\delta(t+\Delta/2) + \delta(t-\Delta/2)] * h(t) \end{aligned} \tag{11}$$

The corresponding detected signal at the receiver is in the form of

$$s(t) = T_1(t-d) = c[\delta(t-d+\Delta/2) + \delta(t-d-\Delta/2)] * h(t) \tag{12}$$

After matched filter, the signal is

$$\begin{aligned} r_0(t) = s(t) * h^*(-t) &= c[\delta(t-d+\Delta/2) + \delta(t-d-\Delta/2)] * R_0(t) \\ &= c[R_0(t-d+\Delta/2) + R_0(t-d-\Delta/2)] \end{aligned} \tag{13}$$

After one integration, it becomes

$$\begin{aligned} r_1(t) = \int_{-\infty}^{t} r_0(\tau)d\tau &= c\int_{-\infty}^{t} R_0(\tau-d+\Delta/2) + R_0(\tau-d-\Delta/2)d\tau \\ &= c[R_1(t-d+\Delta/2) + R_1(t-d-\Delta/2)] \end{aligned} \tag{14}$$

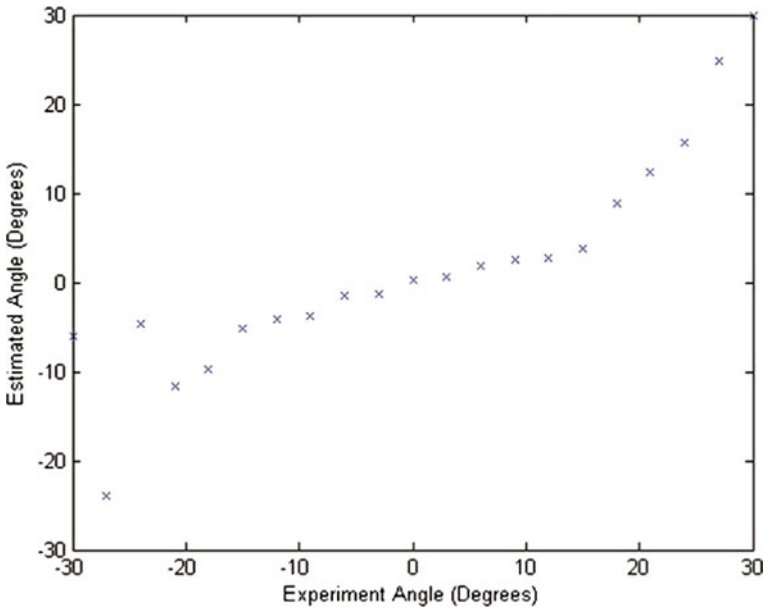

Fig. 4 Results of the bearing-angle estimation

Then the final value of $r_1(t)$ is

$$\textit{Final value} = r_1(\infty) = 2cR_1(\infty) = 2c|H(0)|^2 \tag{15}$$

Now it can be seen that the ratio of the final values, after the double integration of the beacon signal and the first integration of the reference waveform, is

$$\rho = \frac{D}{2v} sin(\theta) \tag{16}$$

The normalization removes the ambiguity factor due to propagation loss and as a result isolates the bearing-angle estimation from sources of errors. Since the separation distance D and propagation speed v are known, the the bearing angle can be estimated with high accuracy.

This algorithm was applied to the same data set and the result is documented in Fig. 4, which shows superior performance and accuracy.

5 Conclusion

In this paper, a simple algorithm was presented for bearing-angle estimation for UUV geolocation and navigation. The algorithm was originally designed as the replacement for the conventional peak-phase approach for the systems with twin

transmission waveforms and the polarity of 180° phase offset. The accuracy, stability, and especially the simplicity of this algorithm made the system, in both hardware and software, significantly more effective.

It turns out that this algorithm can also function effectively with the reversed version of the system. The conventional techniques for passive multi-receiver acoustic arrays were largely structured, based on the computationally extensive cross-correlation method. This simple algorithm showed remarkable system performance in laboratory tests and the simplicity in computation remains for large number of receiver elements.

The most interesting extension of this simple signal processing technique is the application to the active version of the system, with combined transmitter and receivers in the same unit. The accuracy, stability, and computational efficiency make it an excellent system for UUV collision avoidance. The analysis in the paper has been organized in the pulse-echo mode. Yet, with slight modifications, this algorithm can function equally well with FMCW signaling formats.

Acknowledgments This research project was supported by UC MICRO Program, Sonatech, and ONR STTR Program.

References

1. Lee, H., Wade, G.: Imaging Technology. IEEE Press, New York, NY (1986)
2. Lee, H., Wade, G.: Modern Acoustical Imaging. IEEE Press, New York, NY (1986)
3. Goodman, J.W.: Introduction to Fourier optics. McGraw Hill, New York, NY (1968)
4. Whalen, A.D.: Detection of Signals in Noise, pp. 39–41. Academic Press, San Diego, CA (1971)

Part V
Signal Analysis and Image Processing

Resolving the Location of Acoustic Point Sources Scattered Due to the Presence of a Skull Phantom

J. Sadler, K. Shapoori, E. Malyarenko, A. DiCarlo, J. Dech, F. Severin, and R.Gr. Maev

Abstract This paper considers resolving the location of a foreign object in the brain without the removal of the skull bone by detecting and processing the acoustic waves emitted from the foreign object modeled as point source. The variable thickness of the skull bone causes propagation acoustic waves to be scattered in such a manner that the acoustic wave undergoes a variable time delay relative to its entry point on the skull. Matched filtering can be used to detect the acoustic wave front, the time delay variations of the skull can be corrected for, and matched filtering time reversal algorithms can then detect the location of the acoustic source. This process is examined experimentally in a water tank system containing an acoustic source, custom-made skull phantom, and receiver. The apparatus is arranged in transmission mode so that the acoustic waves are emitted from the source, scattered by the phantom, and then received by a second transducer. The skull phantom has been designed so that the acoustic properties (velocity, density, and attenuation correspond approximately to those of a typical human skull. In addition, the phantom has been molded so that the surface closest to the acoustic source has smoothly oscillating ridges and valleys and a flat outer surface, approximately modeling a real-world skull bone. The data obtained from the experiment is processed to detect and extract the scattered acoustic wave front and correct for the time of flight variations in the skull. This re-creates the approximate wave front of a point source, whose location can be resolved via a matched filtering time reversal algorithm. The results of this process are examined for cases where there is no phantom present (no scattering), and with the phantom present. Comparison of these results shows a correlation between the calculated locations of the acoustic source and the expected location.

Keywords Point source · Skull phantom · Ultrasound · Time reversal · Matched filtering · Attenuation · Sound speed · Scattering

J. Sadler (✉)
The Institute for Diagnostic Imaging Research, University of Windsor, Windsor, ON N9B 3P4, Canada
e-mail: jsadler@uwindsor.ca

M.P. André et al. (eds.), *Acoustical Imaging*, Acoustical Imaging 30,
DOI 10.1007/978-90-481-3255-3_31,

1 Introduction

This paper examines the possibility of utilizing the time reversal match filtering method [1] to locate the position of an acoustic source in the brain, without the removal of the skull bone. Here the skull bone is theoretically approximated as a variable thickness object (with specific material properties), such that an acoustic wave traveling through the object undergoes a variable time delay dependant on the entry point of the acoustic wave into the skull. Time reversal [1–3] predicts that if this delay can be measured, a time reversed wave can be created, which will focus back on the source position. When examined mathematically, this process can be described by performing the convolution of the delayed wave, with the time-reversed wave, where the expected output is a uniform planar wave [1], which produces constructive interference when summed over the individual waves.

This technique will be adapted for solving the problem of locating the acoustic source by measuring the acoustic wave transmitted through a custom made skull phantom, in a traditional transmission mode data. In this paper, the time reversal matched filtering technique is adapted to find the source by first correcting for the measured delay properties of the phantom, thus obtaining an estimation of the unscattered wave front. This technique can then be used to quantitatively determine the expected location of the point source by examining the output of the technique over a range of possible locations for the source. The wave fronts emitted from those locations closest to the true location of the source will be the most similar to the corrected wave front, and the matched filtering process will yield a maximum result (relative to other test positions). By examining wave fronts (instead of arbitrary waves) not only allows the delay of the scattered wave to be corrected for, but also simplifies the mathematics of the matched filtering process. Here, the convolution of the two waves (the corrected, and test position waves) becomes a simple addition.

2 Experimental Setup

The set up of the experimental system is as shown in Fig. 1, and forms a typical water tank immersion system. The apparatus is arranged in transmission (pitch-catch)

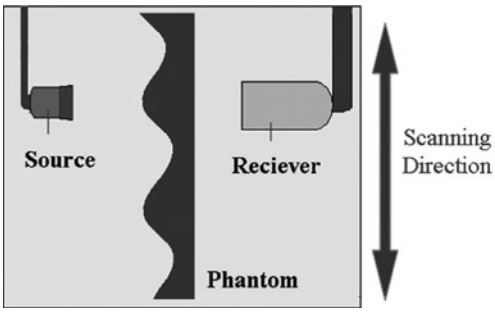

Fig. 1 Source, phantom and receiver of transmission immersion system

Table 1 Acoustic properties of human skull and custom skull phantom

	Velocity (m/s)	Density (kg/m^3)	Attenuation (dB/m)	Thickness (mm)
Phantom	2,350	1,898	2,417	6–9
Skull	2,060	1,800	3,300	2.8–9.5

mode so that the ultrasonic waves emitted from the source, travel through an object (a skull phantom), before being received by a second transducer. The source in this case is a small aperture planar transducer, with a UTEX pulser-receiver providing the signal to generate the acoustic wave. The receiver used for the results in this paper is a large diameter focused transducer (2.5 MHz central frequency, 0.75 inch diameter, 1.25 inch spherical focus). The receiver is mounted to a four-axis scanner, which allows the position of the transducer to be carefully controlled, so that the acoustic field behind the phantom can be measured. This acoustic signal received by this transducer is pre-amplified by the same UTEX pulser-receiver before being digitized with a 14-bit, 65 MS/s analogue to digital converter (Instrument Systems). The control for the scanning system and pulser-receiver is coordinated via a computer, such that a B-Scan along the scanning axis shown in Fig. 1 is obtained. The phantom used in this experiment was specifically designed to approximately replicate the acoustic properties of a human skull [4–6] as shown in Table 1. In addition, the phantom is molded such that it possesses a flat outer surface (for minimal refraction) and an undulating inner surface similar to what is shown in Fig. 1. This creates a situation similar to the real world skull bone, which has an internal undulating surface, and a smooth other surface.

While an equivalent system can be made with a linear array, using a single receiver allows the step size of the measurements to be altered (currently 256 points at 0.300 mm separation are taken). In addition, the use of the focused transducer as the receiver allows the experiment to be quickly changed to a pulse-echo mode of operation. This allows the time delay of the phantom to be measured without changing transducers, ensuring the phantom is measured at the same points the acoustic wave was received during the transmission mode experiment.

3 Time Reversal Match Filtering Methodology

Fink [1] has previously explained the method of time reversal matched filtering both from the experimental perspective of using a phased array (time delay array), and the mathematical equivalent using the convolution operation, both in cases with and without a variable thickness medium causing a time delay. The methodology presented used in this paper is based on a similar mathematical approach, but with two important changes. First this method performs an initial filtering step to extract the wave front from the received waveform, where in this particular experiment, the wave front can be detected via wave's large distinctive minimum. Alternatively, the maximum of the correlation of each time domain scan with an estimate of the incident waveform can be used to extract the wave front. This extraction procedure

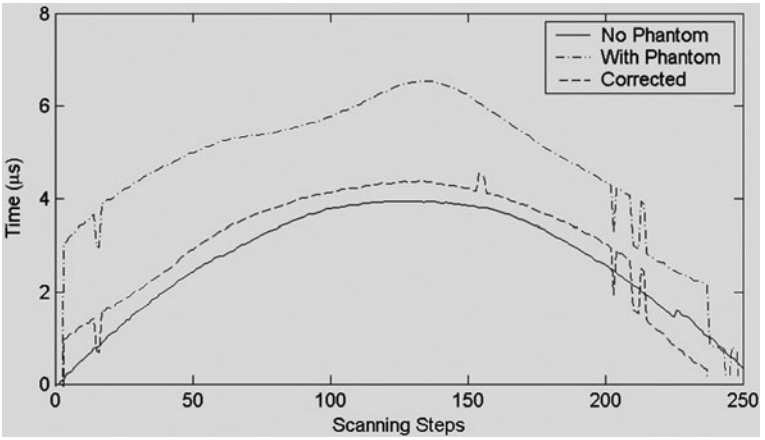

Fig. 2 Extracted wave fronts with and without phantom, and the corrected wave front

allows the complicated convolution operation of the time reversal matched filtering technique to be changed into a simple addition of two wave fronts, allowing for a faster calculation process. Secondly, the B-Scan of the phantom made during the experiment allows the variable time delay information to be extracted from the scan. (The reflections from the front, and back surfaces produce two distinct wave fronts, which can be detected similar to the transmitted waves). Using this information, the delay of the phantom can be corrected for, and the altered wave front returns to the approximate form as when no phantom was present. (One example of the delayed, undelayed (original), and corrected wave fronts are shown in Fig. 2). In the results to be shown in this paper the transducer is close enough to the phantom that a one-to-one relation can be used to map the receiving position of the transducer, to the corresponding time delay measurement position, thus necessary time delay correction is known approximately. A range of test points for the position of acoustic source is then tested and the maximum result from the time reversal matched filtering process indicates the most likely position for the source. The extraction of the wave fronts simplifies the superposition process into a phasor (vector component) addition operation. The process of testing with a range of points theoretically allows the technique to resolve multiple source locations; as well the result can be represented by a color scale plot to visualize the location of the source.

4 Results And Discussion

4.1 Calibration

Before examining the situation where the phantom is present, a series of calibration tests were performed in order to ensure the location of the acoustic source could reasonably be resolved when the phantom is not present. As well as testing the reliability of the resolving technique, these results also serve as method to calibrate the

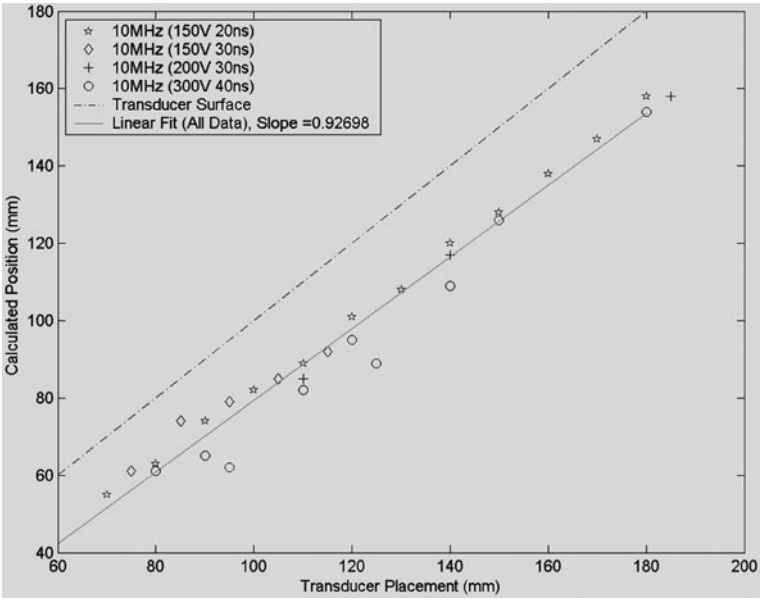

Fig. 3 Resolved position of source with no phantom present

experiment. Such calibration is necessary, since even though the piston transducer's acoustic field can be approximated as a point source in the far field region, it is not a true point source. Thus, the acoustic field will likely not focus exactly at the transducer's surface, and this offset must be measured. Consistency in the results will verify that the source serves as a reliable point source, as well as calibrating for the point source when the phantom is present.

The calibration tests are preformed at a variety of settings available on the pulser-receiver (changes in voltage, and pulse width), as well as at a range of distances between the source and the receiver. Figure 3 shows the resolved location for each of these tests, along with a line of best fit for the data, and a second line representing the location of the front surface of the piston transducer (the acoustic source). Examining the data finds that on average the point source is resolved at a distance of 22 mm behind the transducer's surface, and fits along linear slope nearly parallel to that of the transducer's surface. The line of best fit has slope of 0.927 ± 0.30, with a coefficient of linear correlation (r-value) of 0.987, where ideal values are 1.0 for both quantities. The data is found to consistently fit this line over a variety of pulse settings, with data taken at lower voltage settings (star data set) providing more linear results than the largest voltage reading (circle data set).

4.2 Resolving the Point Source

At the same time data was obtained for each of the experiments when no phantom was present, an additional set of data was taken but with the phantom now located

between the source and the receiver. A millimeter guide on the immersion tank ensures the source is returned to the same location as was used in the case when no phantom was present, with accuracy of less than 1 mm. It is noted that the location of the receiver has not been moved between the two sets of measurements. In addition to changing the distance between the source and receiver, and the electronic signal for the source transducer, the location of the source along the scanning axis was altered from experiment to experiment and in some cases measured at multiple locations during a single experiment. The alteration ensures the location of the source is resolvable for any location along the scanning axis. Finally, it is noted that in all the results that will be examined, the receiver is at a distance from the phantom less than the transducer's focal length.

The results of the above cases with the phantom present are shown in Fig. 4, where again a linear fit of the data, and a line representing the surface position of the source transducer are also plotted. The linear fit of the results with no phantom is also included for reference. Again the data is found to consistently follow a line of best fit (slope 0.901 ± 0.037 and r-value 0.970) parallel to the transducer's surface over a variety of pulse settings (changes in voltage, and pulse width), although the maximum deviation from the line is now larger than in the case with no phantom. This line of fit remains relatively parallel to the surface of the transducer, and more importantly is statistically parallel to the line of best fit calculated for the resolved position when no phantom was present. Overall, the point is resolved closer to the transducer surface, where on average the offset is 12.5 mm, or the point source is resolved 9.5 mm closer to the transducer's surface when the phantom is added.

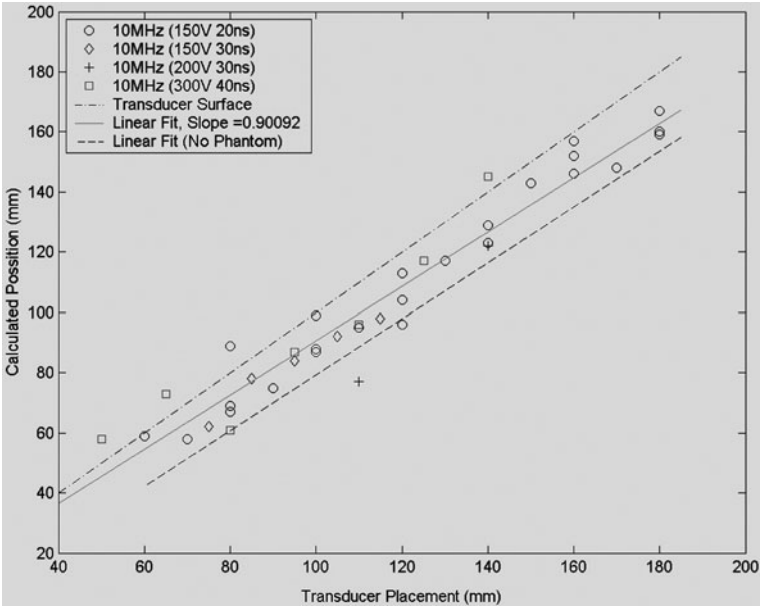

Fig. 4 Resolved position of scattered source (phantom present)

With promising results showing an overall correlation between the resolved position for the point source with and without a phantom, it is also useful to examine a single set of experimental data more clearly in order to analyze the results without varying experimental parameters. The above results not only used different signal voltages, but different receiver positions, electronic gains, and overall noise levels. One such case for the result for a single experimental data set, along with the lines of best fit for the data, and the position of the transducer surface as shown in Fig. 5. Here the lines of best fit yield a slope of 0.932±0.010 with r-value 0.999 for the data obtained with no phantom, and a slope of 0.986±0.045 with r-value 0.990 for the case data obtained with the phantom present. From these calculations one observes these two lines of best fit are considered parallel within the error calculated. In addition, the two data sets are on average separated by a distance of 3.5 mm, thus indicating an excellent overall agreement between the unscattered data (no phantom) and the scattered and corrected data (phantom present). The resolved position for the scattered and corrected data (phantom present) does appear to diverge from the unscattered data (no phantom present) as the distance between the source and receiver increases, particularly the data points in the 140–160 mm region. However, for the next two points resolved (170 and 180 mm distances), the scattered and unscattered data return to fitting almost exactly again. Examining the previous data (Fig. 4) the problematic data points likely do not conform to some overall trend; additional measurements will confirm this, as well improvements in the signal analysis routines of the time reversal matched filtering technique may be able to adjust the resolved location of these points.

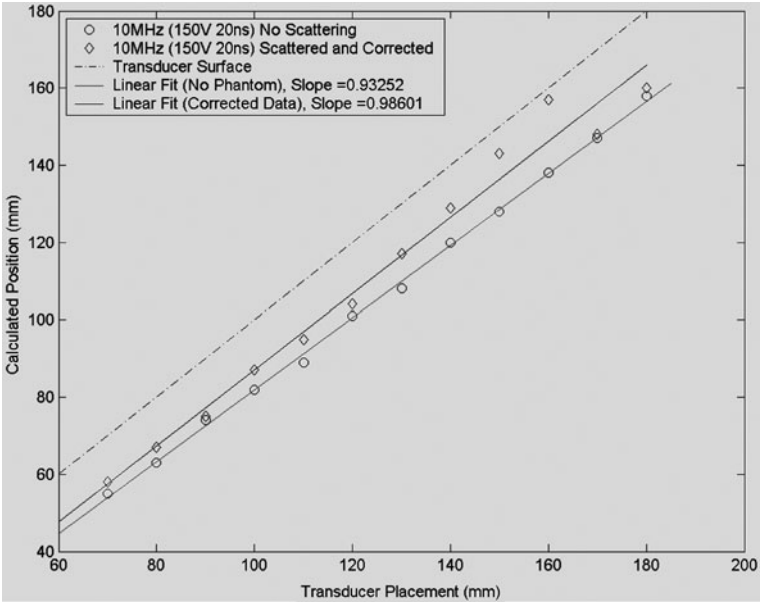

Fig. 5 Direct comparison of a single data set with and without phantom

5 Conclusion

This paper has briefly discussed the experimental method, and corresponding match filtering time reversal technique, which has been successfully used to resolve the location of a point source scattered due to the time delay properties of a non-uniform thickness object with acoustic properties similar to the human skull. Here by measuring the time delay of the phantom, and correcting for this delay in the scattered wave, one can obtain an approximate prediction of the unscattered wave front. Extraction of the wave front, allows the time reversal matched filtering process to quickly test a range of locations for the location of the point source, allowing the expected position of the source to be determined.

The technique is validated by comparing the resolved position of the delayed waveform, to the cases where no delay is present (no phantom), as well as the position of the transducer's surface used to generate the ultrasonic wave. Finally, a direct quantitative comparison of two data sets (with and without the phantom) showed the resolved positions of the two cases correlate well, fitting on statistically parallel lines when plotted with respect to resolved position versus transducer placement. In addition, it is found that these two data sets on average are currently separated by 3.5 mm. Advances in the signal processing routines, and the calculations used to correct for the time delay of the phantom, are expected improve the ability of the technique to resolve the location of point source further, where our goal is to reduce this separation to 0.5 mm.

Acknowledgements The authors would like to express thanks to the Office of Naval Research, USA for providing the funding for this research.

References

1. Fink, M.: Time reversal of ultrasonic fields – Part I: Basic principles. IEEE Trans. Ultrason. Ferroelect. Freq. Contr. **93**(5), 555–566 (1992)
2. Wu, F., Thomas, J.L., Fink, M.: Time reversal of ultrasonic fields – Part II: Experimental results. IEEE Trans. Ultrason. Ferroelect. Freq. Contr. **39**(5), 567–578 (1992)
3. Cassereau, D., Fink, M.: Time reversal of ultrasonic fields – Part III: Theory of the closed time-reversal cavity. IEEE Trans. Ultrason. Ferroelect. Freq. Contr. **43**(6), 1112–1129 (1996)
4. Fry, F.J., Barger, J.E.: Acoustical properties of the human skull. J. Acoust. Soc. Am. **63**(2), 1567–1590 (1978)
5. Gross, S.A., Johnston, R.L., Dunn, F.: Comprehensive compilation of empirical ultrasonic properties of mammalian tissues. J. Acoust. Soc. Am. **64**(2), 423–457 (1978)
6. Gross, S.A., Johnston, R. L., Dunn, F.: Compilation of empirical ultrasonic properties of mammalian tissues II. J. Acoust. Soc. Am. **68**(1), 93–108 (1980)

Reflection and Scattering of Acoustical Waves from a Discontinuity in Absorption

J.P. Jones, S. Leeman, E. Nolan, and D. Lee

Abstract The reflection and transmission of a plane acoustical wave from a planar boundary at the interface between two homogeneous media of different acoustical properties is a classical problem in acoustics that has served as a basis for many developments in acoustics for over 100 years. This problem, detailed in virtually every textbook on acoustics, provides us with the acoustical analogue to Snell's Law in optics and gives us correspondingly simple results. Classical acoustics predicts that a reflection from a boundary occurs only if the characteristic acoustical impedances of the two media are different. Here we show that a reflection also occurs if the media have the same impedances but different absorption coefficients. Our analysis yields some surprising results. For example, a reflection will occur at a discontinuity in absorption even if the impedance is uniform and continuous across the interface. In addition, a discontinuity in impedance at an interface between two media that have constant and equal, but non-zero absorption, results in a reflection coefficient that is dependent on absorption as well as impedance. In general, reflection coefficients now become frequency dependent. To experimentally test our results, we measured the reflection at the interface between water and castor oil, two liquids with similar impedances but very different absorption coefficients. Measurement of the reflection coefficient between 1 and 50 MHz demonstrated a frequency dependence that was in good agreement with our analysis.

Keywords Plane wave · Reflection · Absorption · Scattering

1 Reflection from a Change in Impedance

The reflection of a plane acoustical wave from a planar boundary is perhaps the most famous boundary value problem in acoustics and is detailed in virtually every textbook on acoustics [1, 2] In the simplest formulation of the problem, we consider a plane acoustical wave propagating in a homogeneous medium of uniform density and of constant velocity. This wave is then incident on the boundary between the first medium and a second medium that is also assumed to be homogeneous but has

J.P. Jones (✉)
Department of Radiological Sciences, Irvine Medical Center, University of California, Orange, CA 92868, USA
e-mail: jpjones@uci.edu

M.P. André et al. (eds.), *Acoustical Imaging*, Acoustical Imaging 30,
DOI 10.1007/978-90-481-3255-3_32,

different acoustical properties. The boundary between the two media is assumed to be normal to the direction of propagation of the wave and of infinite extent. If we solve the simple boundary value problem, which requires that the pressure and normal particle velocity be equal on either side of the boundary, we find that the wave is both reflected and transmitted at the boundary and that this reflection/transmission process is dependent upon the acoustical properties of the two media. Since the calculations related to this classic boundary value problem are detailed in the standard acoustical literature and the results are well known, we simply state them here.

The pressure reflection coefficient, r, is given by

$$r = (\rho_2 c_2 - \rho_1 c_1)/(\rho_2 c_2 + \rho_1 c_1) \tag{1}$$

where ρ is the density, c is the speed of sound, and the sub-scripts denote medium 1 and medium 2. The pressure transmission coefficient, τ, is given by

$$\tau = 1 + r \tag{2}$$

Repeating this calculation in terms of intensity or energy rather than pressure we find that the intensity (or energy) reflection coefficient, R, is given by

$$R = r^2 \tag{3}$$

and the intensity transmission coefficient, T, is given by

$$T = 1 - R \tag{4}$$

Note that $R + T = 1$, which is the conservation of energy.

2 Reflection from a Discontinuity in Absorption

Although classical acoustics considered the reflection of a plane wave from a discontinuity in impedance, the tacit assumption was made that no reflection would occur from a discontinuity in absorption. Linsay [3], explicitly considered reflection from a change in absorption but because of a sign error concluded incorrectly that no refection would occur.

Let us now consider the general case of reflection of a plane wave that is normally incident on a plane boundary between two media of different impedances and different absorptions. Let us assume that medium 1 is characterized by $\{\rho_1, c_1, \alpha_1\}$ while medium 2 is characterized by $\{\rho_2, c_2, \alpha_2\}$ where ρ is the density, c is the speed of sound, and α is the absorption coefficient. Note that the specific acoustical impedance is defined as $Z = \rho c$. The incident wave is given by

$$p_r = A_1 e^{i(\omega t + k_1 x)} e^{+\alpha_1 x} \quad \text{for } x \leq 0, \tag{5}$$

the reflected wave is given by

$$p_r = B_1 e^{i(\omega t + k_1 x)} e^{+\alpha_1 x} \quad \text{for } x \leq 0, \tag{6}$$

and the transmitted wave is given by

$$p_t = A_2 e^{i(\omega t - k_2 x)} e^{-\alpha_2 x} \quad \text{for } x \geq 0. \tag{7}$$

The boundary conditions for this case are of course the same as the classical problem for reflection from a discontinuity in impedance, the results for which are given in Section 1. Although including absorption makes the boundary value problem somewhat more complicated, the calculation is straightforward and follows exactly the classical case of reflection from an impedance boundary. Since the details of the calculation are lengthy, here we only state the results. Although the general reflection coefficient is complex, the physically meaningful quantity is the real part of the reflection coefficient, Re(r), which is

$$\mathrm{Re}(r) = \frac{(\omega/c_1c_2)^2(\rho_2c_2 - \rho_1c_1)(\rho_2c_2 + \rho_1c_1) + (\rho_2\alpha_1 - \rho_1\alpha_2)(\rho_2\alpha_1 + \rho_1\alpha_2)}{(\omega/c_1c_2)^2(\rho_2c_2 + \rho_1c_1)^2 + (\rho_2\alpha_1 + \rho_1\alpha_2)^2} \tag{8}$$

Equation (8) is the general expression for the reflection of a plane wave from a planar discontinuity in absorption and impedance. Further analytical details for some of these results are given by Nolan [4].

3 Selected Cases of Reflection

It is useful to check Equation (8) for several special cases. First, we note that if $\alpha_1 = \alpha_2 = 0$ then Equation (8) reduces to Equation (1), which is the standard result of classical acoustics.

Secondly, if $\alpha_1 \neq \alpha_2 \neq 0$ but $\rho_1 = \rho_2 = \rho$ and $c_1 = c_2 = c$ then Equation (8) reduces to the following

$$\mathrm{Re}(r) = [(\alpha_1 - \alpha_2)(\alpha_1 + \alpha_2)]/[(2k)^2 + (\alpha_1 + \alpha_2)^2] \tag{9}$$

Thus, a discontinuity in absorption along with no discontinuity in impedance will produce a reflection. Note that the reflection coefficient is also frequency dependent, unlike the case in classical acoustics.

Thirdly, let us consider the case where we have a discontinuity in impedance only, but where the magnitude of the absorption is constant and non-zero. That is, $\alpha_1 = \alpha_2 = \alpha$. Now Equation (8) becomes

$$\mathrm{Re}(r) = \frac{(\omega/c_1c_2)^2(\rho_2c_2 - \rho_1c_1)(\rho_2c_2 + \rho_1c_1) + \alpha^2(\rho_2 - \rho_1)(\rho_2 + \rho_1)}{(\omega/c_1c_2)^2(\rho_2c_2 + \rho_1c_1)^2 + \alpha^2(\rho_2 + \rho_1)^2} \tag{10}$$

Note that a constant but non-zero absorption alters the reflection from a discontinuity in impedance and that the reflection process is now frequency dependent. This is a surprising result, which is totally unexpected from classical acoustics.

It is worth considering two special cases of Equation (10). First, let us assume that $\rho_1 = \rho_2 = \rho$. That is, we have a discontinuity in velocity only with a constant but non-zero absorption. Then Equation (10) becomes

$$\mathrm{Re(r)} = [(k_1)^2(1 - (c_1/c_2)^2)]/[(k_1)^2(1 + c_1/c_2)^2 + 4\alpha^2] \tag{11}$$

where $k_1 = \omega/c_1$. Note that if $\alpha = 0$ then the result of classical acoustics is obtained.

As a second special case of Equation (10) let us assume that $c_1 = c_2 = c$. That is, we have a discontinuity in density only with a constant but non-zero absorption. Then Equation (10) becomes

$$\mathrm{Re(r)} = (\rho_2 - \rho_1)/(\rho_2 + \rho_1) \tag{12}$$

that is identical to the classical result. The presence of constant non-zero absorption therefore alters the reflectivity only in the case of a discontinuity in velocity but not for the case of a discontinuity in density.

4 Experimental Considerations

Although the analysis given here has shown that acoustical waves can be reflected from a discontinuity in absorption, it is useful to explore what impact such an effect might have on experimental observations. First it should be noted that the absorption coefficient used here is completely general, the only limitation on it being that the absorption is assumed to be exponential with depth. It can be considered to include thermal absorption and other mechanisms, and may be a function of frequency or velocity.

For soft biological tissue it is found that, to a good approximation, the absorption varies linearly with frequency and the velocity does not vary much with frequency (i.e., there is very little dispersion). When considering the interface between two tissues, then, we may express the absorption coefficients as $\alpha_1 = a_1 f$ for the first medium and $\alpha_2 = a_2 f$ for the second, where f is the frequency. If we substitute these into the general expression for the real part of the reflection coefficient, Equation (8), we have

$$\mathrm{Re(r)} = \frac{(2\pi/c_1c_2)^2(\rho_2c_2 - \rho_1c_1)(\rho_2c_2 + \rho_1c_1) + (\rho_2a_1 - \rho_1a_2)(\rho_2a_1 + \rho_1a_2)}{(2\pi/c_1c_2)^2(\rho_2c_2 + \rho_1c_1)^2 + (\rho_2a_1 + \rho_1a_2)^2} \tag{13}$$

and the reflection coefficient for soft biological tissues is not a function of frequency.

For homogeneous media with characteristic acoustical impedances and absorption coefficients similar to those of tissue, the difference between the new reflection

coefficient and the classical one is small and does not vary significantly with frequency. This does not mean, however, that these results have no implications in medical imaging. On the contrary, in medical imaging we rarely encounter planar surfaces between homogeneous media, and such simple reflections as we have considered here seldom occur. However, we have shown that a planar discontinuity in absorption leads to a reflection and this implies that a small discontinuity or occlusion in absorption will lead to scattering. Scattering from occlusions in density and compressibility have been studied at length and are well understood [5, 6] but the possibility of an occlusion in absorption has only recently been investigated [7–9]. While the reflection at a planar surface due to an absorption discontinuity may be small, the scattering due to a small occlusion in absorption may be large and comparable to other scattering effects.

To experimentally test our analysis we considered the reflection at an interface between two liquids that have similar acoustical impedances but very different absorption coefficients. Data from the literature [10, 11] suggest that water and castor oil would be appropriate, since $Z(\text{water}) = 1,479,676\ \text{kg/m}^2\text{s}$, $Z(\text{castor oil}) = 1,419,594\ \text{kg/m}^2\text{s}$, $\alpha(\text{water}) = 25.3\times10^{-15}\text{s}^2/\text{m}$, $\alpha(\text{castor oil}) = 10.1\times10^{-12}\text{s}^2/\text{m}$. Since these liquids have an absorption that varies approximately as frequency squared, we can substitute these parameters into Equation (8) and calculate the reflection coefficient as a function of frequency and determine the relative difference between the new reflection coefficient (including absorption) and the classical reflection coefficient for an interface between water and castor oil. At 1 MHz this difference is only 0.003%, at 10 MHz the difference is 0.7%, and at 50 MHz the difference is 18%. Although preliminary experiments suggest differences on the order of 10%, more careful and extensive studies are required to validate our findings.

References

1. Kinsler, L., Frey, A.: Fundamentals of Acoustics. Wiley, New York, NY (1962)
2. Morse, P.M., Ingard, K.U.: Theoretical Acoustics. McGraw-Hill, New York, NY (1968)
3. Linsay, R.B.: Mechanical Radiation, p. 77. McGraw-Hill, New York, NY (1960)
4. Nolan, E.: Reflection of acoustic waves from a discontinuity in absorption, MS Thesis, University of California Irvine (1988)
5. Leeman, S.: Ultrasound pulse propagation in dispersive media. Phys. Med. Biol. **25**, 481 (1980)
6. Cho, Z.H., Jones, J.P., Singh, M.: Foundations of Medical Imaging, p. 511–518. Wiley, New York, NY (1993)
7. Hutchins, L., Leeman, S., Jones, J.P.: Bounded pulse propagation. In: Alais, P., Metherell, A. (eds.) Acoustical Imaging, vol. 10, p. 427. Plenum Press, New York (1981)
8. Leeman, S., Peyman, A.: The maxwell model as a soft tissue descriptor. In: Halliwell, M., Wells, P.N.T. (eds.) Acoustical Imaging, vol. 25, p. 357. Kluwer/Plenum, New York (2000)
9. Leeman, S., Jones, J.P.: Visco-elastic models for soft tissue. In: Iwaki, A. (ed.) Acoustical Imaging, vol. 29. Springer, Dordrecht, Netherlands (2008)
10. American Institute of Physics Handbook. McGraw-Hill, New York, NY (2007)
11. Handbook of Chemistry and Physics. CRC, Boca Raton, FL (2008)

Automatic Regions of Interest Segmentation for Computer Aided Classification of Prostate Trus Images

M. Scebran, A. Palladini, S. Maggio, L. De Marchi, and N. Speciale

Abstract Transrectal ultrasound (TRUS) plays two central roles in prostate cancer diagnosis, prostate examination and measurement and biopsy guidance, but its sensitivity and specificity need improvement. This paper presents one possible method to improve TRUS detection and biopsy guidance using computer-aided diagnosis techniques for ultrasound images. The method uses automated segmentation of regions of interest followed by a supervised classifier. It was tested on a database of 37 prostate TRUS RF scans (22 with cancer). Average sensitivity was 78%, average specificity was 92% and average accuracy was 90% in discriminating normal from cancerous tissue.

Keywords Ultrasound · Segmentation · Tissue characterization · Computer aided diagnosis (CAD) · Prostate cancer · Transrectal ultrasound (TRUS)

1 Introduction

Prostate cancer is one of the most frequent cancers in man and one of the major causes of mortality in developed countries. Due to its high incidence but low aggressiveness, its detection at early stages is crucial for a successful treatment. Prostate cancer is typically diagnosed through a complex screening procedure which comprises: clinical data analysis, digital rectal examination, evaluation prostate cancer specific antigen levels, imaging of the prostate gland and biopsy. Although the screening procedure is composed of different steps, due to the lack of accuracy of the mentioned tests, the diagnosis process unavoidably ends with a histological confirmation by means of biopsy.

Within this context, the role of transrectal ultrasound (TRUS) examination is central and twofold: first it is one of the privileged imaging techniques for prostate inspection and volume assessment, thanks to its inexpensiveness and non-invasiveness and second, thanks to its real time imaging procedure it's the standard guidance tool for biopsy. In spite of this, TRUS still needs improvement in sensitivity and specificity. One possible way of improving TRUS-guided cancer detection and biopsy is the development of computer aided diagnosis (CAD) techniques for

M. Scebran (✉)
ARCES-DEIS, University of Bologna, 40136 Bologna, Italy

M.P. André et al. (eds.), *Acoustical Imaging*, Acoustical Imaging 30,
DOI 10.1007/978-90-481-3255-3_33,

ultrasound images. CAD techniques relaying on imaging are typically based on segmentation of the given image in regions of interest (ROI) and this task is usually performed by an expert radiologist. In order to make image classification independent by radiologists' skills and give them and additional tool for making diagnosis, ROI segmentation must be possibly automated.

In this work, we developed a two step CAD technique for prostate tissue classification based on an automatic ROI segmentation procedure, followed by a supervised classifier. The ROI segmentation procedure consists in two phases: feature calculation and image segmentation. In the feature calculation phase the radio frequency (RF) signal is used to compute spectral, statistical and textural features over a rough selection of the prostate gland that can be performed also by non trained personnel. These features are then used in the segmentation procedure, based on an unsupervised Bayesian learning technique, for assign each image pixel to a class. The assignment is realized by a K-means clustering followed by an iterative Bayesian regularization algorithm. Such algorithm imposes spatial smoothness constraints in the solution, minimizing the energy function derived by modeling the signal features with a multivariate Gaussian and the pixel segmentation class with a Markov random field. The contiguous pixels forming a closed region are then identified as a ROI. Finally, each ROI is classified as normal or suspicious, by a support vector machine classifier trained with a selection of relevant features for prostate cancer identification.

2 Proposed Method

Ultrasound image segmentation is strongly influenced by signal quality as well as by the tissue imaged. The characteristic artifacts of ultrasound images like attenuation, speckle, shadows and signal dropouts, missing boundaries due to the orientation dependence of acquisition, make the segmentation task complicated. While in other areas of medical imaging (e.g., computed tomography, magnetic resonance imaging) application of general image processing methods is sufficient, in the case of ultrasound signals more complex and specialized methods are needed in order to obtain satisfactory results.

In the literature, there are a large number of papers describing segmentation procedures applied to ultrasound images.

For a complete review of the state of the art of medical and ultrasound image segmentation methods see References [1] and [2]. Most of the techniques presented in literature concern prostate boundary segmentation, while only few works about region of interest segmentation have been published. Moreover, most of the methods depend on human interaction and their performances are user dependent. Therefore, to overcome the limitations of the existing procedures, new procedures should ideally be: user independent, independent on training images, focused on region of interest segmentation.

According to the review on the published methods for prostate segmentation and tissue characterization, relying on the paradigm of Fig. 1 a new procedure for

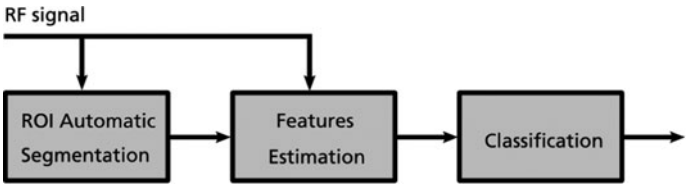

Fig. 1 Schematic representation of the proposed procedure for computer aided classification of TRUS images

ultrasound aided prostate cancer diagnosis is proposed. The method is based on three steps: automatic segmentation of prostate in ROIs, feature estimation on the segmented ROIs, and characterization of ROIs through a classifier.

2.1 Regions of Interest Segmentation

The automatic ROIs segmentation procedure is composed of four sequential steps as summarized in Fig. 2: feature estimation, clustering, Markov random field based regularization and ROIs selection.

Since many boundary estimation algorithms are available in literature, a rough estimation of prostate boundary performed by automatic algorithm or done manually by non-trained personnel is considered as given. Feature estimation is then performed pixel-wise only inside the prostate gland, by means of a sliding window. The estimation is done following a multi-feature approach, i.e., different classes of features are estimated starting from the radio frequency signal before time gain compensation and envelope detection. B mode features are estimated after envelope detection and log compression of the radio frequency signal. Among the features proposed in literature we employed texture parameters (Unser's features) [3] and B mode statistical modeling (Nakagami fitting) [4].

The estimated features are then used to segment the image by mean of a clustering procedure. Clustering techniques are unsupervised learning technique that easily allows the combination of multiple description parameters and data mining in a high dimension space, with a feasible computational cost [5]. In this work we

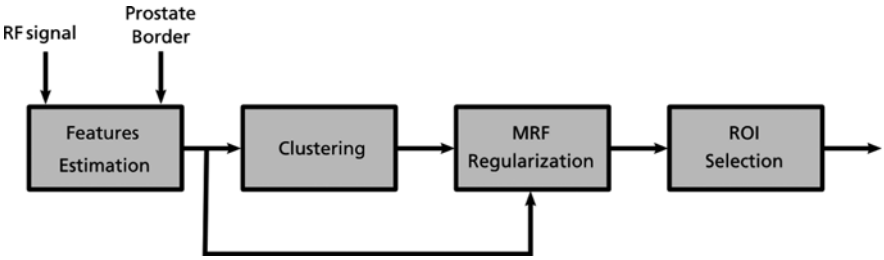

Fig. 2 Schematic representation of ROI segmentation algorithm

adopted K-means algorithm, a based clustering method which evaluate the similarity of pixels by means of their distance in feature space. More precisely pixel portioning is obtained by minimizing the following energy function:

$$W(C) = \frac{1}{2} \sum_{k=1}^{K} \sum_{C(i)=k} d(x_i, \bar{c}_k) \tag{1}$$

where C represents the clustering of all the data points i in K predetermined number of clusters, $C(i) = k$ stands for the assignment of the assignment of the i-th data point to the k-th cluster with center c_k, and d(.,.) is the distance. The K means algorithm minimize the functional *W(c)*, with a two steps iterative procedure: for a given clustering *C, W(C)* is minimized with respect to cluster centers $\{c_1, \ldots, c_k\}$ yielding the mean of the point currently assigned to each clusters; given a current set of means $\{c_1, \ldots, c_k\}$ the function *W(C)* is minimized assigning each data point to the nearest cluster center c_k, with respect to distance *d(.,.)*. Such procedure is repeated until convergence is reached.

The main drawback of clustering techniques is the lack of spatial information, which in the case of ultrasound images causes noisy segmentations, with irregular jagged-edges, wrong classified pixel and small isolated ROIs. Such issue can be mitigated applying a MRF based regularization algorithm on the segmentation obtained with the clustering procedure, as proposed in Reference [6]. Image segmentation is formulated as a MAP estimation problem: the observed features vector $Y_i = \{Y_{i,1}, \ldots, Y_{i,N}\}$ for each image pixel i are modeled as a Gaussian Markov random field on a 2D rectangular grid and the data to be estimated is the assignment of each pixel i to a class k, indicated as $X_i = k$. Since the MAP estimation is computationally unfeasible, a complexity reduction is mandatory. One of the most used suboptimal minimization algorithm is the Iterated Conditional Modes (ICM), first proposed in Reference [6] and applied in different medical image segmentation problems. The ICM minimizes the MAP estimator no more on the entire grid, but pixel-by-pixel. In other words, we have to minimize for every pixel with respect to the assignment $x_i = k$ the functional:

$$U(x_i|\mathbf{Y}) = \sum_j \left[\ln(\sigma_{i,j}^k) + \frac{(Y_{i,j} - \mu_{i,j}^k)^2}{2(\sigma_{i,j}^k)^2} \right] + \sum_{c \in \delta_i} V_c(X) \tag{2}$$

where δ_i is the neighborhood system centered on the pixel I and V_c is the MRF potential function defined over a second order neighborhood system. This results in an iterative algorithm which drastically reduces computational requirements, and it provides a local optimum very close to the global one, if initialized with K-means segmentation.

The algorithm was implemented following the adaptive methodology proposed in Reference [6]; conditional mean $\mu_{i,j}^k$ and conditional variance $\sigma_{i,j}^k$ are estimated over windows whose size is reduced after a certain number of iteration until algorithm

convergence is reached, i.e. either the number of modified pixels is lower than a fixed threshold or the maximum number of iteration has been reached.

Finally, the different clusters are examined and further divided according their spatial distribution: all the pixel that forms a connected and closed area are identified as a single region of interest. If ROI of a minimum size are required, all the regions smaller than a fixed number of pixel are reassigned to the adjacent regions applying a morphological erosion operator on them.

2.2 Regions of Interest Classification

The last stage of the proposed method is a supervised classifier. In this phase, the selected ROI are classified by means of a new set of features estimated over them. The result of the classification will be displayed over the standard B mode image: position and extension of all cancerous ROIs are marked with false colors. Such information can be used by radiologist in guiding biopsy protocols.

Beside Unser's textural features, we adopted also Haralick and Fractal textural features [3], radio frequency signal statistical modeling (generalized Gaussian) [7] and spectral parameters (central frequency, midband and slope [8], polynomial fitting of wavelet spectrum [9]). Since the complete feature set of all parameters mentioned before would have a huge dimensionality of about 140 attributes a first selection step is performed keeping for each group of features only those highly correlated to the ground truth class, and so to the pathology, discarding the other ones. In this application a hybrid feature selection algorithm is used to rank and prune the initial feature set [10]. The selected and ranked feature for the available dataset is constituted of 54 attributes, where the first 20 features are meant to be the most relevant.

Among the possible supervised machine learning techniques a Support Vector Machine (SVM) classifier was adopted [11]. As reported in the literature, nonlinear classifier seems to be preferable for prostate tissue characterization and SVM have been proved to be a good choice. In order to obtain a nonlinear SVM classifier a Gaussian radial basis function was adopted as kernel. All the simulations were performed using the publicly available software implementation of SVM classifiers called *svmlight* [12].

3 Experimental Results

The proposed method for prostate tissue classification was applied to a database of in vivo scans in order to assess its accuracy. The experimental database was provided by the University of Florence and is formed by TRUS images of prostate sagittal section. All the signals were acquired with a commercial Esaote ultrasound machine using a transrectal broadband probe, with central frequency of 7.5 MHz, sampling at 50 MHz the radio frequency signal before time gain compensation with

a resolution of 12 bits. The dataset contains 37 different cases of prostate pathologies, 22 cases of prostate carcinoma and 15 cases of benign hyperplasia, acquired before biopsy. For each case, ten consecutive image frames were recorded. All the malignant cases have cancerous regions marked on the B mode image by radiologist after histological verification. All the cancer foci were identified during the histological examination. These labels constitute the ground truth for both segmentation algorithm tuning and classifier training. In Fig. 3 an example of the reference images is shown. Since, unless radical prostatectomy is performed, with high probability the portion of tissue sampled during biopsy is smaller than the true cancer extension, the available ground truth must be considered as an incomplete labeling. The learning problem is not fully supervised and specificity of the classification can't be evaluated in a reliable way.

However, since the main goal of computer methods for prostate cancer diagnosis is the identification of all the cancer foci for guiding biopsy, possible overestimations of the size of cancerous region does not affect the clinical performance of the computer aided diagnosis procedure. Thus, the main goal is the development of a high sensitivity classification method which is able to identify all the cancer foci with an average level of specificity.

For pursuing the mentioned goals the learning problem was formulated in the following way: the whole images database is segmented using the proposed segmentation method, obtaining about 300 ROI; all the examples of normal ROI are taken only form the benign cases while only the ROI marked by radiologist as pathological are used as examples of cancerous regions in the learning phase. The classifier was then trained above a random subset of the available data using stratified 10-fold cross validation, leaving the remaining data for test.

Since ROI have different sizes, the classification results must be normalized in order to take into account the size of each ROI. Therefore, classification

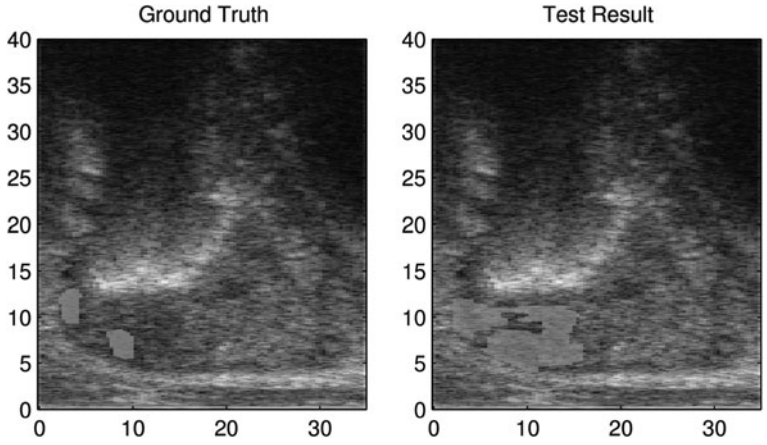

Fig. 3 Examples ground truth reference images (*left panel*) and classification results displayed above B mode prostate sagittal scans as visual guidance for biopsy (*right panel*)

performance is evaluated in terms of correctly classified pixels inside the prostate border. Typical measures to assess classifier performances are sensitivity (SE), specificity (SP), accuracy (Acc) defined as:

$$\begin{aligned} SE &= \frac{TP}{TP + FN} \\ SP &= \frac{TN}{TN + FP} \\ Acc &= \frac{TP + TN}{TP + TN + FP + FN} \end{aligned} \tag{3}$$

where TP are true positive pixels, TN are true negative pixels, FP are false positive pixels and FN are true negative pixels.

Since, in the segmentation phase and in other investigation performed on the same dataset, some malignant cases were proved to be source of errors, two different data set where created: dataset 1, which comprises all the available cases; dataset 2, where 4 malignant cases where excluded during the training phase.

The average classification performances obtained by the proposed procedure on the two dataset are resumed in Table 1. The classification results confirm that the first 20 features are the most relevant: while increasing the number of features from 10 to 20 a significant performance improvement is noted, only slightly improvement are obtained when the complete set of feature is used. Among the most relevant features we found textural features (Unser's and fractal), statistical features (Nakagami and Nakagami fitting on the diffused component extracted from the B mode image) and spectral (slope, intercept), confirming that a multi-feature approach is fundamental. Moreover, the results confirm that excluding the ambiguous case form the training set improve significantly the sensitivity of the method.

The high value of sensitivity obtained (always > 80%) suggests that the proposed method is able to identify most of the known cancer locations. As said before, since only partial information about the real extension of cancerous areas is available and since classification where performed above the whole image, the specificity value obtained is not fully reliable and it gives just quantitative information about method performance. However, analyzing the results obtained on the benign cases we observed that the number of false positive is extremely low and we can therefore conclude that the low specificity value is due to the over estimation of cancer size in malignant images. Since the classification results are meant to be used for guiding

Table 1 Classification performance of the proposed tissue characterization method

Settings	Sensitivity (SE)	Specificity (SP)	Accuracy (Acc)
Set 1–10 features	0.80	0.71	0.75
Set 1–20 features	0.93	0.73	0.87
Set 2–54 features	0.95	0.74	0.89
Set 2–54 features	0.90	0.84	0.87

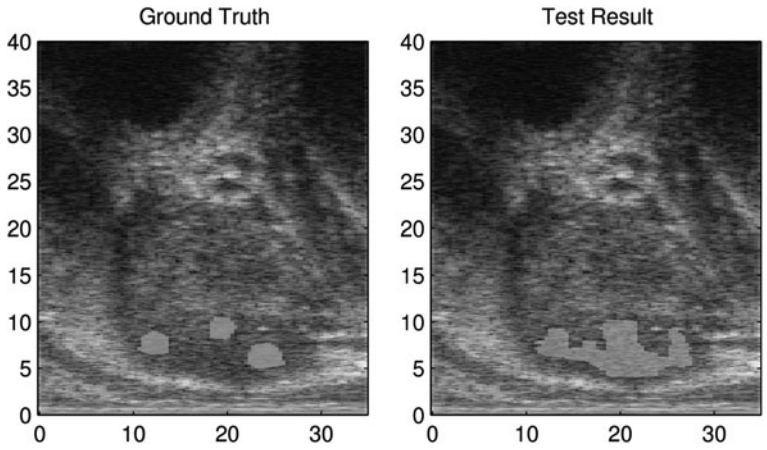

Fig. 4 Examples ground truth reference images (*left panel*) and classification results displayed above B mode prostate sagittal scans as visual guidance for biopsy (*right panel*)

biopsy, an over estimation of the tumor size is less problematic than false positive on benign cases, which would causes unnecessary additional biopsies. Finally, in Figs. 3 and 4 examples of the classification results displayed above the B mode scans as visual guidance for biopsy are given.

4 Conclusions

In this work, we developed a two step CAD technique for prostate tissue classification based on an automatic ROI segmentation procedure, followed by a supervised classifier. Both segmentation and classification procedures are based on a multi-feature approach.

References

1. Noble, J.A., Boukerroui, D.: Ultrasound image segmentation: A survey. IEEE Trans. Med. Imag. **25**(8), 987 (2006)
2. Pham, D.L., Xu, C., Prince, J.L.: Current methods in medical image segmentation. Annu. Rev. Biomed. Eng. **2**(1), 315–337 (2000)
3. Wagner, T.: Texture Analysis. Handbook of Computer Vision and Application, pp. 275–308. Academic Press, San Diego (1999)
4. Shankar, P.M., Dumane, V.A., Piccoli, C.W., Reid, J.M, Forsberg, F., Goldberg, B.B.: Classification of breast masses in ultrasonic B-mode images using a compounding technique in the Nakagami distribution domain. Ultrasound Med. Biol. **28**(10), 1295–300 (2002)
5. Theodoridis, S., Koutroumbas, K.: Pattern Recognition. Academic Press, San Diego, CA (2006)
6. Pappas, T.N.: An adaptive clustering algorithm for image segmentation. Signal Processing. IEEE Trans. Acoust. Speech Signal Process. **40**(4), 901–914 (1992)

7. Varanasi, M.K., Aazhang, B.: Parametric generalized Gaussian density estimation. J. Acoust. Soc. Am. **86**, 1404 (1989)
8. Lizzi, F.L., Feleppa, E.J., Alam, S.K., Deng, C.X.: Ultrasonic spectrum analysis for tissue evaluation. Pattern Recogn. Lett. **24**(4–5), 637–658 (2003)
9. Masotti, L., Biagi, E., Granchi, S., Breschi, L., Magrini, E., Di Lorenzo, F.: Tissue differentiation based on radiofrequency echographic signal local spectral content. Ultrasonics, 2003 IEEE Symposium on, 1, pp. 1030–1033 vol. 1, October 2003
10. Liu, H., Yu, L.: Toward integrating feature selection algorithms for classification and clustering. IEEE Trans. Knowl. Data Eng. **17**(4), 491–502 (2005)
11. Tibshirani, R., Walther, G., Hastie, T.: Estimating the number of clusters in a dataset via the gap statistic. J. Roy. Stat. Soc. B **63**(2), 411–423 (2001)
12. Joachims, T.: SVMLight: Support Vector Machine. SVM-Light Support Vector Machine http://svmlight.joachims.org/, University of Dortmund (1999)
13. Besag, J.: On the statistical analysis of dirty pictures. J. Roy. Stat. Soc. B **48**(3), 259–302 (1986)

Determination of *B/A* of Biological Media by Measuring and Modeling Nonlinear Distortion of Pulsed Acoustic Wave in Two-Layer System of Media

T. Kujawska, J. Wójcik, and A. Nowicki

Abstract Knowledge of the acoustic nonlinearity parameter, *B/A*, of biological fluids or soft tissues is necessary whenever high intensity pressure fields are induced. A numerical model recently developed in our lab is capable of fast predicting the nonlinear distortion of pulsed finite-amplitude acoustic waves generated from axisymmetric sources propagating through multilayer attenuating media. Quantitative analysis of the obtained results enabled developing the alternative method for determination of the *B/A* of biological media. First, the method involves measuring the nonlinear waveform distortion of the tone burst propagating through water. Then, it involves numerical modeling (in frequency domain) using the Time-Averaged Wave Envelope (TAWE) approach. The numerical simulation results are fitted to the experimental data by adjusting the source boundary conditions to determine accurately the source pressure, effective radius and apodization function being the input parameters to the numerical solver. Next, the method involves measuring the nonlinear distortion of idem tone burst passing through the two-layer system of parallel media. Then, we numerically model nonlinear distortion in two-layer system of media in frequency domain under experimental boundary conditions. The numerical simulation results are fitted to the experimental data by adjusting the *B/A* value of the tested material. Values of the *B/A* for 1.3-butanediol at both the ambient (25°C) and physiological (36.6°C) temperatures were determined. The obtained result ($B/A = 10.5 \pm 5\%$ at 25°C) is in a good agreement with that available in literature. The $B/A = 11.5 \pm 5\%$ at 36.6°C was determined.

Keywords Nonlinearity parameter measurement · *B/A* · Nonlinear propagation · Biological media · PVDF membrane hydrophone

1 Introduction

Nonlinear effects incidental to the finite-amplitude acoustic wave propagation in thermo-viscous fluids are systematically studied theoretically and experimentally in many laboratories around the world because of extensive possibilities of their

T. Kujawska (✉)
Institute of Fundamental Technological Research Polish Academy of Sciences,
Warsaw 00-049, Poland

M.P. André et al. (eds.), *Acoustical Imaging*, Acoustical Imaging 30,
DOI 10.1007/978-90-481-3255-3_34,

practical applications, especially for medical purposes. Knowledge of the *B/A* of media through which the acoustic wave propagates is indispensable for predicting nonlinear pressure fields in order to assess safety of modern US medical equipments or to improve image quality using the Tissue Harmonic Imaging (THI) technique. The therapeutic ultrasound techniques, such as the High Intensity Focused Ultrasound (HIFU) or lithotripsy, also produce the nonlinear waveform distortion leading to enhanced local heating or thermal ablation of tissues at the focal region.

The purpose of this work was to develop an alternative, relatively simple in use method for determining the nonlinearity parameter, *B/A*, of biological liquids or soft tissues. The proposed method is based on the comparison of the simulated numerically (in frequency domain under experimental boundary conditions) nonlinear waveform distortion of the pulsed acoustic wave propagating through the two-layer system of parallel media: water–tested material with the measured one. Water is used as the reference medium with known nonlinear properties in order to calibrate the experimental setup. The numerical model used accounts for the effects of absorption, diffraction, nonlinear interactions of harmonics as well as for the reflection and transmission at the media interfaces. The source boundary condition parameters such as the pressure on the surface, effective radius, initial acoustic pulse pressure-time waveform, radiating aperture apodization function as well as the tested material linear parameters such as density, sound velocity, frequency-dependent attenuation law are introduced as input data to the numerical model after their preliminary measuring.

2 Numerical Model

The numerical model used for describing the nonlinear waveform distortion of the pulsed finite-amplitude sound wave propagating through a nonlinear lossy medium accounts for the effects of diffraction, absorption and nonlinear interactions of harmonics and is comprehensively described in Reference [1]. The model was made computationally efficient by means of replacing the Fourier–series solution approach by the Time-Averaged Wave Envelope (TAWE) algorithm. The computer implementation of the numerical model for axisymmetric cases in a form of the 3D numerical solver, capable of predicting pulsed nonlinear acoustic fields from plane or focused circular acoustic sources in a multilayer system of parallel media with arbitrary attenuation law, was the powerful research instrument for studying properties of the nonlinear acoustic fields produced in various biological media from various ultrasonic transducers.

3 Methods and Materials

The degree of nonlinear waveform distortion of the pulsed finite-amplitude wave generated from the acoustic source and propagating through the attenuating medium depends on the nonlinear properties of this medium as well as on the source operating parameters. The source parameters required for the numerical model

include the pressure amplitude on the surface, effective radius, focal length, frequency, initial pulse waveform and apodization function. The medium parameters required for the numerical model include density, sound velocity, absorption coefficient, its frequency-dependent power-law and nonlinearity parameter, *B/A*. If boundary condition parameters of the source and linear parameters of the medium are determined experimentally then the *B/A* of the medium can be determined by fitting the calculated axial pressure variation of the fundamental and first two harmonics of the propagating tone burst to the measured one. The principle of measuring the nonlinearity parameter, *B/A*, of the medium being examined involves:

1. Determining the linear parameters of the medium being examined by measuring its density, ρ, sound velocity, c, small-signal attenuation coefficient, α, attenuation coefficient frequency-dependence law $\alpha(f)$ at chosen temperature T;
2. Determining the transducer boundary condition parameters: effective radius a, pressure amplitude P_0 at the surface, initial pressure-time waveform of the acoustic pulse and radiating aperture apodization function by measuring the axial and radial distributions of both the peak- to-peak and harmonics pressure amplitudes in water and fitting the numerically simulated results to the experimental data by adjusting the source boundary conditions parameters. This preliminary measurements calibrate the experimental setup and determines an accuracy of the proposed method;
3. Measuring nonlinear waveform distortion of the tone burst propagating through the two-layer system of parallel media: water–tested material using the method of the fixed path-length through the water layer and the variable path-length through the layer of the tested material [2, 3];
4. Introducing the input parameters into the numerical model and fitting the theoretical results obtained for the two-layer system of media to the experimental data by adjusting the *B/A* value of the tested material.

3.1 Experimental setup

The experimental set-up used for the measurements is shown in Fig. 1.

The measurements were carried out at both the 25°C and 36.6°C temperatures with the 16 mm diameter, 2.2 MHz central frequency, focused (focal length $F = 100$ mm) piezoceramic (Pz27 Ferroperm, Norway) transducer immersed in temperature-controlled distilled degassed water. The transducer had a quarter-wavelength matching layer, was back-loaded and positioned on the translation stage driven by computer-controlled stepper motors allowing its motion in horizontal and vertical planes with varied steps (from 0.1 to 5 mm). The output signals were recorded by the broadband (calibrated up to 40 MHz) bi-laminar polyvinylidene difluoride (PVDF) membrane hydrophone (Sonora Medical, Inc. S/N S5-153, P-159 preamplifier) with the 0.414 mm diameter of the active element. The hydrophone was immersed in water and fixed on the acoustic axis. To maximise the signal to noise ratio at the measurement of the 18$^{\text{th}}$ harmonic the transducer were driven by 8-cycle tone bursts from an Arbitrary Function Generator (Ritec Advanced Measurement System RAM-10000, Warwick, RI, USA). The amplitude of the

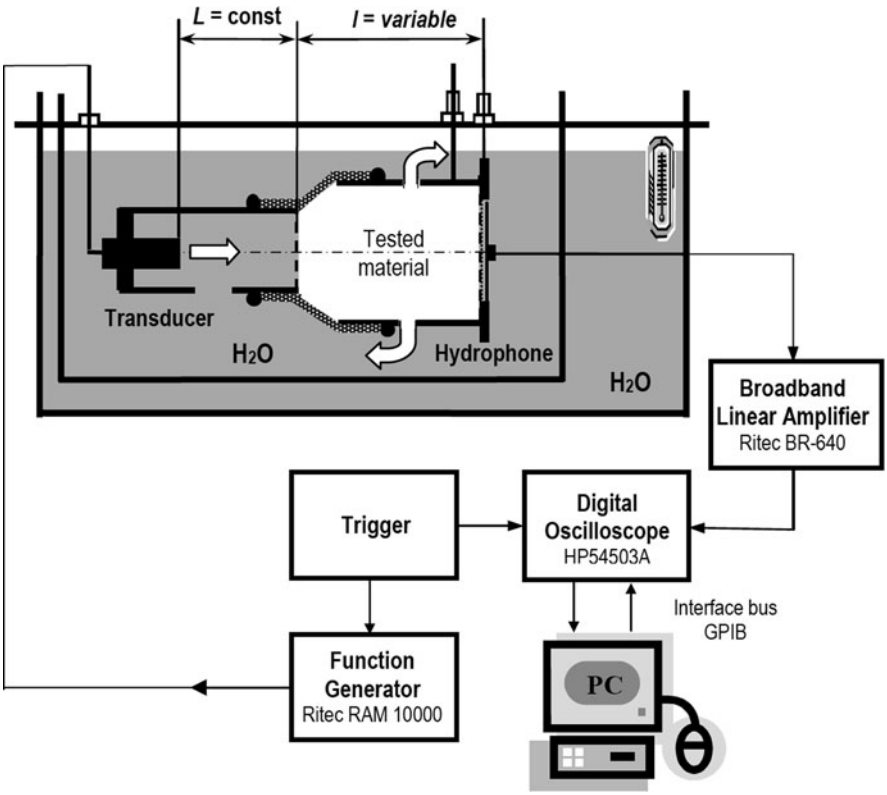

Fig. 1 Schematic diagram of the experimental setup

excitation voltage, frequency and duration of the tone bursts were controlled by PC. Nonlinear fields were produced when excitation level at the output of the generator was 178.9 V_{pp}. (producing source pressure of 0.225 MPa). The hydrophone output was additionally amplified by 20 dB using the linear broadband amplifier (Ritec BR-640, Warwick, RI, USA) and then fed to the input of an 8-bit digital oscilloscope (HP54503A, Hewlett Packard, Colorado Springs, CO, USA) with a 500 MHz sampling frequency. The received signals were digitised and averaged over 16 consecutive waveforms in the oscilloscope memory and then transferred for spectral analysis to PC. The amplitude of the measured harmonic components was corrected for the hydrophone sensitivity dependence on frequency.

3.2 Methodology of Measurements

Initially, the preliminary measurements are carried out in water in order to determine the acoustic axis as well as the input data to the numerical model. The acoustic axis was accurately determined from symmetry of the acoustic beam patterns that were

visualized as isobar contour lines. The input data included the acoustic parameters of water: density, ρ, sound velocity, c, attenuation coefficient, α_1, frequency-dependent attenuation law, $\alpha(f) = \alpha_1 \cdot f^2$, nonlinearity parameter, B/A, as well as the transducer boundary condition parameters: effective radius, a, focal length, F, source pressure P_0, pressure-time waveform, $P(t)$, of the initial tone burst that best reproduced the tone burst measured on the acoustic axis close to the transducer surface, radiating aperture apodization function, $g\,(r)$, which produced the radial pressure distribution close to the transducer that best reproduced this measured.

The apodization function, source pressure and pressure-time waveform of the initial tone burst as the input data to the numerical solver were determined at lower excitation level by measuring the radial and axial pressure distributions and pressure-time waveform of the tone burst close to the radiating surface (at $5 \div 15$ mm axial distance). The pulse waveforms measured along the acoustic axis were processed by the FFT technique, corrected for the hydrophone frequency-dependent sensitivity characteristic and then the axial variation of the fundamental and first two harmonics were compared with those numerically simulated by the 3D numerical solver while keeping both the effective radius and apodization function constant and varying the source pressure. The best agreement between calculation and measurement results determined the value of the source pressure.

Figure 2 illustrates very good agreement between the calculated results and experimental data in water for the source considered which produced 0.225 MPa pressure on the surface. Degree of these results agreement, determined by the ratio of the fundamental to the 2nd or 3rd harmonics amplitude as a function of the axial distance from the transducer face, was equal to 0.96 ± 0.034 for all points measured. These results validated correctness and accuracy of the numerical model proposed and calibrated the experimental setup.

To measure nonlinear waveform distortion of the tone burst propagating through the two-layer system of parallel media: water–tested material the method of fixed

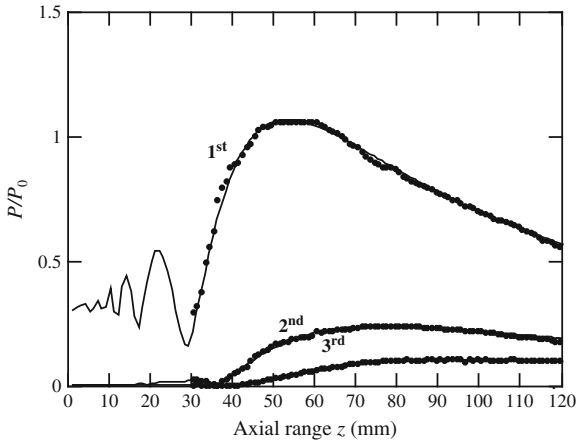

Fig. 2 Axial pressure variation of the fundamental (1st), 2nd and 3rd harmonics for the 8-cycle tone burst propagating in water. Fundamental frequency 2.2 MHz, source pressure 0.225 MPa. Experiment (points), theory (*solid lines*)

path-length in water and variable path-length in the tested material was used. In previous publications [4, 5] the specific feature of pulsed nonlinear fields in water, generated from circular sources of chosen dimensions and frequency, was proved. Namely, the distance from the source at which the rapid increase of amplitude of the 2nd harmonics (in the spectrum of the propagating tone burst) begins is specific for this source and does not dependent on the source pressure. This characteristic property of the nonlinear fields in water was used to develop an alternative method for determination of the nonlinearity parameter *B/A* of biological media.

The main principle of the proposed method is based on predicting numerically nonlinear waveform distortion (in frequency domain and under experimental boundary conditions) for the tone burst propagating through the two-layer system of parallel media: water–tested material and then fitting the obtained numerical simulation results to the experimental data by adjusting the *B/A* of the tested medium. For each source with chosen dimensions and central frequency the thickness of water layer in the two-layer system of media is specific and equal to the axial distance from the source at which a rapid increase of the 2nd harmonics and appearance of the 3rd harmonics for the tone burst propagating in water occurs. For the transducer considered here this distance was found to be 4 cm (see Fig. 2). Thickness of the tested medium layer may be chosen arbitrarily, however, soft tissues are highly attenuating media, and thus thickness of 1.3-butanediol layer was chosen to be 9 cm.

To determine experimentally nonlinear waveform distortion of the tone burst propagating through the two-layer system of media: water–tested material the method of a fixed path-length through the water layer and variable path-length through the tested material layer was used. In practice this requirements were fulfilled by enclosing water in a fixed-length chamber and tested fluid in a variable-length chamber. The design of the chambers was based on two coaxially mounted plastic pipes with different diameter and acoustically transparent polyethylene window at the output end. The smaller pipe was fixed coaxially with the transmitting probe and ensured the position of the transducer face at the desired distance from its output window and in parallel with it. The larger pipe was connected with the smaller one by a reduction rubber sleeve and fixed to the water tank. The output window of the larger pipe was mounted in parallel with the membrane of the PVDF hydrophone. Although the larger pipe had only one degree of freedom the transducer and hydrophone had tree degrees of freedom that allowed us to minimize alignment problems. Figure 1 illustrates the experimental setup for generating and recording nonlinear waveform distortion of the tone burst propagating through the two-layer system of fluids. The axial movement of the transducer to the hydrophone with the step of 0.1 mm was achieved using the translation stage controlled by a PC *via* GPIB bus interface. The tested fluid path-length was varying from 4 to 9 cm. The outer tank was filled with tap water. To provide the temperature control in the inner tank filled with distilled water the immersion heating circulator (Julabo

ME-6, Labortechnik GmbH, Germany) was mounted on the wall of the outer tank. The distorted electric signals were recorded by hydrophone, sampled and processed by the FFT. The amplitudes of obtained harmonics were corrected accordingly to the hydrophone frequency-dependent sensitivity characteristic (V/μPa) and fitted to those numerically predicted by adjusting the *B/A* value of the tested material. The numerical simulation results best fitted to the measured data determined the nonlinearity parameter of the medium under examination.

4 Results

The 1.3-butanediol (99%, Sigma-Aldrich Chemie GmbH, Steinheim, Germany) was considered as the tested material. Two different values of the *B/A* of this medium was determined by two different authors which used two different methods. The value measured by Chavrier, et al., ($B/A = 11$) [6] is different from the value estimated by Granz ($B/A = 7.3$) [7]. Our measurements were done at both the 25°C and 36.6°C temperatures. The acoustic parameters of water and 1.3-butanediol assumed for calculations are quoted in Table 1. They were available from literature for water at both temperatures and for 1.3-butanediol at 25°C. They were measured at 36.6°C.

Numerical simulations were made for the *B/A* of tested material varying from 7 to 11 with a step of 0.5. The axial variation of the fundamental (1^{st}), 2^{nd} and 3^{rd} harmonics calculated for the 8-cycle tone burst generated from the source considered and propagating through the two-layer system of media including 4 cm of water and 9 cm of 1.3-butanediol is presented in Fig. 3 for the axial range from 8 to 13 cm. In this case both the measured and calculated ratio of the $1^{st}/2^{nd}$ and $1^{st}/3^{rd}$ harmonics versus the axial range corresponding to the tested material layer are shown in Fig. 4.

The best correlation coefficient (0.986) between measured and calculated results for 1.3-butanediol was obtained for the value of the $B/A = 10.5$ at 25°C and $B/A = 11.5$ at 36.6°C. The proposed method allows us to get results with a reasonable degree of accuracy, ± 5%.

Table 1 Acoustic parameters of water and 1.3-butanediol at 25°C and 36.6°C

Material	Temperature (°C)	Density (kg/m^3)	Sound velocity (m/s)	Attenuation coefficient ($Np/m \cdot Hz^2$)	*B/A*
Distilled water	25	1,000	1,497	$2.8 \cdot 10^{-14}$	5.2
Distilled water	36.6	1,000	1,524	$2 \cdot 10^{-14}$	5.5
1.3-butanediol	25	1,005	1,530	$127 \cdot 10^{-14}$	$7 \div 11$
1.3-butanediol	36.6	1,005	1,560	$95 \cdot 10^{-14}$	$7 \div 11$

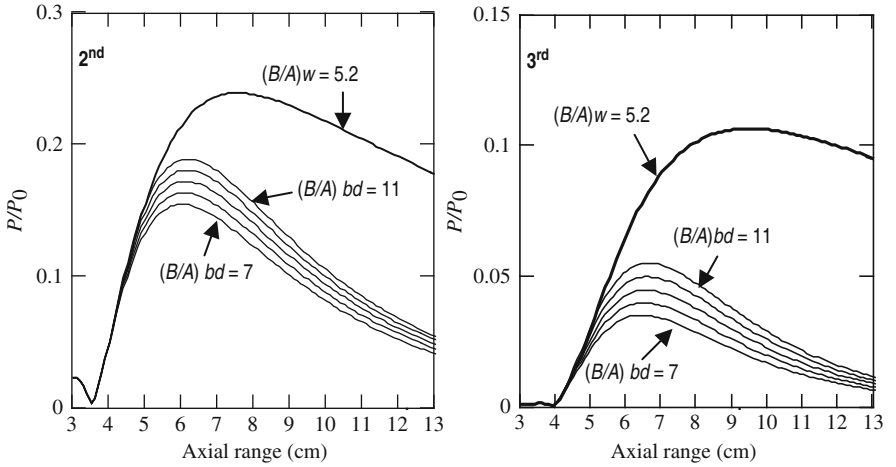

Fig. 3 Calculated axial variation of the second (2^{nd}) and third (3^{rd}) harmonics for the 8-cycle tone burst propagating through water (*thick lines*) and through the two-layer system of 4 cm of water +9 cm of 1.3-butanediol for $(B/A)_{bd}$ varying from 7 to 11 with a step of 1

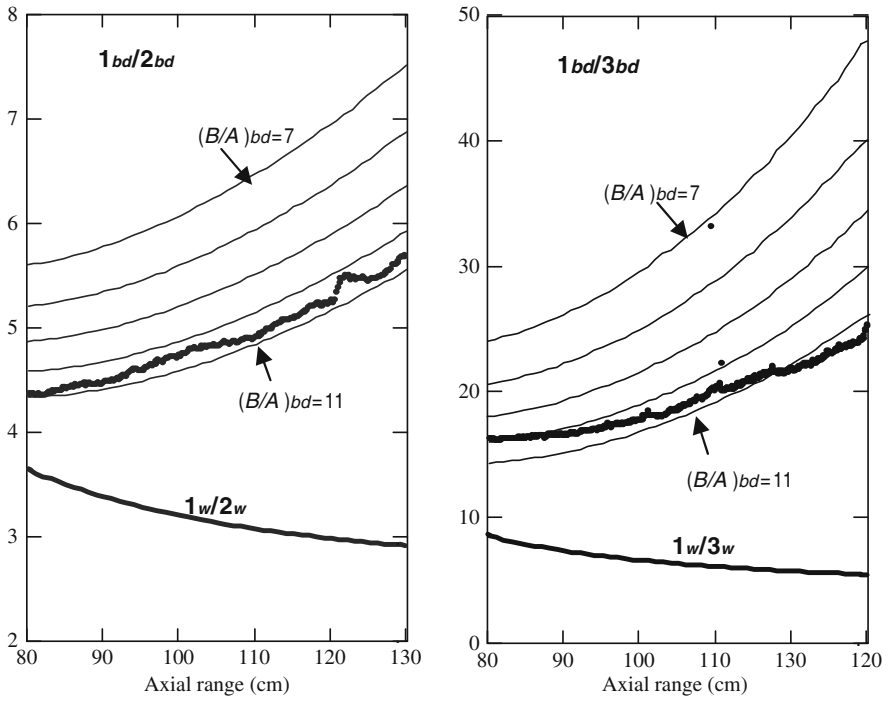

Fig. 4 Axial variation of the ratio of the 1^{st} to 2^{nd} and 1^{st} to 3^{rd} harmonics for the 8-cycle tone burst propagating through water (with index *w*) or through two-layer system including 4 cm of water +9 cm of 1.3-butanediol for $(B/A)_{bd}$ varying from 7 to 11 with a step of 1. Experiment (points) and calculation (*lines*) results

Acknowledgements This work was supported in part by the Ministry of Science and Higher Education (Grant Nr N N518 402734).

References

1. Wójcik, J., Nowicki, A., Lewin, P.A., Bloomfield, P.E., Kujawska, T., Filipczyński, L.: Wave envelopes method for description of nonlinear acoustic wave propagation. Ultrasonics **44**, 310–329 (2006)
2. Verma, P.K., Humphrey, V.F., Duck, F.A.: Broadband measurements of the frequency dependence of attenuation coefficient and velocity in amniotic fluid, urine and human serum albumin solutions. Ultrasound Med. Biol. **31**(10), 1375–1381 (2005)
3. Verma, P.K., Humphrey, V.F., Duck, F.A.: Broadband attenuation and nonlinear propagation in biological fluids: An experimental facility and measurements. Ultrasound Med. Biol. **31**(12), 1723–1733 (2005)
4. Kujawska, T., Wójcik, J.: Harmonic ultrasound beams forming by means of radiating source parameters. Hydroacoustics **7**, 135–142 (2004)
5. Kujawska, T.: A new method for determination of the acoustic nonlinearity parameter B/A in multilayer biological media. Proceedings of the 5th World Congress on Ultrasound, Paris, 81–84 (2003)
6. Chavrier, F., Lafon, C., Birer, A., Barriere, C., Jacob, X., Cathignol, D.: Determination of the nonlinear parameter by propagating and modelling finite amplitude plane waves. J. Acoust. Soc. Am. **119**(5), 2639–2644 (2006)
7. Grantz, B.: Measurement of shock wave properties after the passage through a tissue-mimicking material. Proceedings of the Ultrasonics Symposium, Cannes, 1847–1851 (1994)

A Consideration of Multi-Dimensional Simulation of Nonlinear Acoustic Wave Propagation Using the CIP Method

M. Konno, K. Okubo, T. Tsuchiya, and N. Tagawa

Abstract In this study, numerical simulation of nonlinear sound wave propagation in a time domain is demonstrated using the Constrained Interpolation Profile/ Cubic-Interpolated Pseudo-particle (CIP) method. That novel numerical scheme proposed by Yabe, et al., is a method of characteristics (MOC) and a low-dispersion and stable scheme. Actually, CIP method is suitable for analyses of nonlinear wave propagation including weak shock formation because a rapid pressure change such as a shock front easily causes numerical dispersion error in a conventional numerical scheme. Some of the authors have reported application of CIP method to one-dimensional nonlinear sound wave propagation in air. Furthermore, we demonstrate some numerical calculations of nonlinear sound wave propagation for a two-dimensional acoustic field.

Keywords Constrained interpolation profile (CIP) · MOC · Nonlinear acoustic field analysis · Wave propagation · Simulation

1 Introduction

To date, several numerical schemes have been applied to investigations of sound wave propagation. Development of accurate numerical schemes is an important technical issue [1–5]. At present, the finite difference time domain (FDTD) method is probably the most popular numerical method for the solution of linear wave propagation in acoustics. In FDTD method, central finite-differences for the space and time derivatives are used to approximate the continuous derivatives of the governing equations. However, it is known that this scheme easily causes error because of numerical dispersion. Therefore, the scheme is unsuitable for analysis of nonlinear sound wave propagation including shock formation: numerical simulation for nonlinear sound wave propagation necessitates a low-diffusion scheme.

The constrained interpolation profile (CIP) method is a novel numerical scheme proposed recently by Yabe, et al.; it is a kind of method of characteristics (MOC). It is a numerical scheme with high accuracy that only slightly causes numerical dispersion error. It uses not only the value of the acoustic field but also their derivatives at

M. Konno (✉)
Faculty of System Design, Tokyo Metropolitan University, Tokyo 191-0065, Japan

M.P. André et al. (eds.), *Acoustical Imaging*, Acoustical Imaging 30,
DOI 10.1007/978-90-481-3255-3_35,

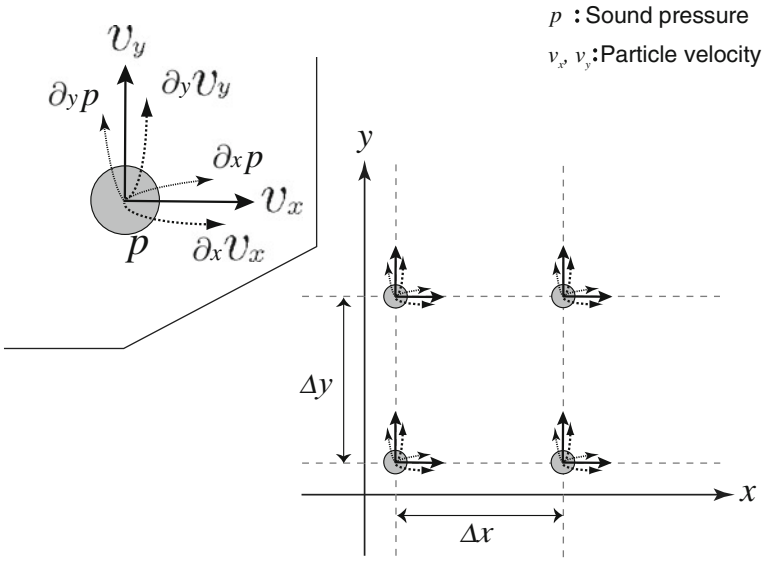

Fig. 1 Numerical model (2-D)

the grid point to solve the problem of sound wave propagation [6]. Figure 1 presents a two-dimensional numerical grid model in which $p$signifies the pressure, v_x and v_y respectively denote particle velocities in the x-direction and y-direction, and ∂_x, ∂_y respectively represent $\partial/\partial x$, $\partial/\partial y$. Some of the authors reported application of CIP method to one-dimensional (1-D) nonlinear sound wave propagation in air [7]. In this report, we first describe some numerical simulations using CIP method for two-dimensional (2-D) nonlinear sound propagation in air under the weak shock assumption and demonstrate this scheme's effectiveness.

2 Formulation

The governing equations for nonlinear acoustic fields with velocity dispersion under the assumption of weak shock are given as follows [8]. Equation (1) is a continuity equation and Equation (2) is the equation of motion.

$$\frac{\partial p}{\partial t} + \rho_0 c_0^2 \nabla \cdot \vec{v} = \frac{\delta_1}{\rho_0 c_0^2} \frac{\partial^2 p}{\partial t^2} + \frac{\beta}{\rho_0 c_0^2} \frac{\partial p^2}{\partial t} \tag{1}$$

$$\frac{\partial \vec{v}}{\partial t} + \frac{1}{\rho_0} \nabla p = \frac{\delta_2}{\rho_0} \nabla^2 \vec{v} \tag{2}$$

In those equations, $p$is the pressure, $\vec{v}$ is the particle velocity, ρ_0 is the ambient medium density, $c_0 = \sqrt{K/\rho_0}$ is the sound velocity of small amplitude, and β is the nonlinearity parameter. Moreover, K is assumed as the bulk modulus. Furthermore, δ_1 and δ_2 are given respectively as

$$\delta_1 = \chi\left(\frac{1}{c_v} - \frac{1}{c_p}\right), \delta_2 = \zeta + \frac{4}{3}\eta. \tag{3}$$

In those equations, χ is the thermal conductivity, ζ is the bulk viscosity, η is the shear viscosity, and c_v and c_p respectively signify the specific heat at constant volume and that at constant pressure.

In Equations (1) and (2), the left-hand expression is the advection phase and the right-hand expression is the non-advection phase. In 2-D acoustic field analysis using the CIP method, the formulation of the advection phase and the non-advection phase is done separately. The method is called the method of fractional steps [9].

2.1 Advection Phase

First, we designate the advection phase. Using the direction splitting method for solving the 2-D acoustic field, we separately calculate the sound wave propagation of the x-direction and the y-direction. Then, assuming $\vec{v} = (v_x, 0, 0)$ to analyze sound wave propagation of the x-direction, we can obtain the following equations from Equations (1) and (2).

$$\frac{\partial p}{\partial t} + c_0 \frac{\partial (Zv_x)}{\partial x} = 0 \tag{4}$$

$$\frac{\partial (Zv_x)}{\partial t} + c_0 \frac{\partial p}{\partial x} = 0 \tag{5}$$

Then, by addition and subtraction of these two equations, we obtain

$$\frac{\partial f_\pm}{\partial t} \pm c_0 \frac{\partial f_\pm}{\partial x} = 0. \tag{6}$$

In those equations, $f_\pm$ are defined as $f_\pm = p \pm Zv_x$, where Z represents the characteristic impedance (i.e. $Z = \sqrt{\rho_0 K}$) and c_0 represents the sound velocity in the medium (i.e., $c_0 = \sqrt{K/\rho_0}$).

In addition, through simple spatial differentiation of the equations, the equations of the derivatives are given as

$$\frac{\partial g_\pm}{\partial t} \pm c_0 \frac{\partial g_\pm}{\partial x} = 0. \tag{7}$$

Therein, $\partial_x = \frac{\partial}{\partial x}$, $g_\pm = \partial_x p \pm \partial_x Z v_x$.

Then, Equations (6) and (7) are advection equations of $p \pm Zv_x$ and $\partial_x p \pm Z\partial_x v_x$. Consequently, applying the CIP method to these equations yields a solution of the advection phase of acoustic field propagation in the x-direction.

Moreover, considering advection of $p + Zv_y$, $\partial_y p + Z\partial_y v_y$, we can calculate propagation in the y-direction as well as in the x-direction. The CIP method supports a solution of 2-D sound wave propagation.

2.2 Non-Advection Phase

Next, we describe the non-advection phase. The advection phase is solved by MOC; the non-advection phase is solved using finite difference method. Therefore, it is necessary that the formulation of p, v_x and v_y be done separately. Considering the dispersion and nonlinear terms, the equations of the non-advection terms are given as follows.

$$h_p = \frac{\delta_1}{\rho_0}\left(\frac{\partial^2 p}{\partial x^2} + \frac{\partial^2 p}{\partial y^2}\right) - 2\beta p\left(\frac{\partial v_x}{\partial x} + \frac{\partial v_y}{\partial y}\right) \tag{8}$$

$$h_{v_x} = \frac{\delta_2}{\rho_0}\left(\frac{\partial^2 v_x}{\partial x^2} + \frac{\partial^2 v_x}{\partial y^2}\right) \tag{9}$$

$$h_{v_y} = \frac{\delta_2}{\rho_0}\left(\frac{\partial^2 v_y}{\partial x^2} + \frac{\partial^2 v_y}{\partial y^2}\right) \tag{10}$$

For those equations, we use the linear relation $\nabla \cdot \vec{v} = (-1/(\rho_0 c_0^2))\partial p/\partial t$, $\partial \vec{v}/\partial t = (-1/\rho_0)\nabla p$ and $\nabla^2 = c_0^{-2}\partial^2/\partial t^2$. Those non-advection phases are calculated after calculation of the advection phase.

3 Discretization in the Cip Scheme

The advection phase and the non-advection phase are also treated separately. First, we consider the advection equations in Equations (6) and (7). After the advection phase is calculated, we solve the equation with which the dispersion and nonlinear terms are considered.

3.1 CIP Method

First, we calculate the advection Equations (6) and (7) using CIP method. For simplicity, the field values $f_\pm$ are defined at the one-dimensional grid points. For propagating waves $f_\pm$ along $\pm x$ directions, the field values $f_\pm^n(x_i \mp c_0\Delta t)$ are advected to point x_i after time step Δt.

$$f_\pm^{n+1}(x_i) = f_\pm^n(x_i \mp c_0\Delta t) \tag{11}$$

Here, f^n represents $f$at time step n. The field values $f_\pm^n(x_i \mp c_0\Delta t)$ are not defined at the grid points. They are interpolated using the field values at the grid points as

$$f_\pm^{n+1}(x_i) \cong F_{i\pm}^n(x_i \mp c_0\Delta t). \tag{12}$$

Therein, $F_{i\pm}(x)$ is the interpolation function defined for the interval $[x_{i\mp 1}, x_i]$.

Applying CIP method to $F_{i\pm}(x)$ yields the following equations related to propagation to the $\pm x$-direction:

$$F_{i\pm}^{n}(x) = a_{\pm}X_i^{\,3} + b_{\pm}X_i^{\,2} + c_{\pm}X_i + f_{\pm}^{n}(x_i), \tag{13}$$

where $X_i = x - x_i$. Then the derivative of the field value at the grid point is also advected using CIP method. The interpolation function for derivative for interval $[x_{i\mp1}, x_i]$ is given as

$$G_{i\pm}^{n}(x) = 3a_{\pm}X_i^{\,2} + 2b_{\pm}X_i + c_{\pm}. \tag{14}$$

Here,

$$a_{\pm} = \pm\frac{2\left\{f_{\pm}^{n}(i\mp1) - f_{\pm}^{n}(i)\right\}}{\left(\Delta x^3\right)} + \frac{g_{\pm}^{n}\,(i\mp1) + g_{\pm}^{n}\,(i)}{\left(\Delta x^2\right)}, \tag{15}$$

$$b_{\pm} = \pm\frac{3\left\{f_{\pm}^{n}(i\mp1) - f_{\pm}^{n}(i)\right\}}{\left(\Delta x^2\right)} + \frac{g_{\pm}^{n}\,(i\mp1) + 2g_{\pm}^{n}\,(i)}{\Delta x}, \text{ and} \tag{16}$$

$$c_{\pm} = g_{\pm}^{n}\,(i)\,, \tag{17}$$

where $f(i)$ and $g(i)$ are the field value and its derivative at $x = i\Delta x$ and Δx is the distance between grid points. Using Equations (13) and (14), the field values and their derivatives at the next time step $n+1$ are expressed as

$$f_{\pm}^{n+1}(x_i) \cong F_{i\pm}^{n}(x_i + \xi) = a_{\pm}\xi^3 + b_{\pm}\xi^2 + g_{\pm}^{n}(i)\xi + f_{\pm}^{n}(i) \tag{18}$$

$$g_{\pm}^{n+1}(x_i) \cong G_{i\pm}^{n}(x_i + \xi) = 3a_{\pm}\xi^2 + 2b_{\pm}\xi + g_{\pm}^{n}(i), \tag{19}$$

where $\xi = \mp c_0\Delta t$.

3.2 Non-Advection Phase

We next consider the dispersion and the nonlinearity terms shown in Equations (8), (9) and (10). The sound pressure and the particle velocity at the grid point are calculated separately (Figs. 1–3). Using the value calculated in the advection phase, we obtain the equations shown below.

$$\frac{\partial}{\partial t}p^* = h_p^* = \frac{\delta_1}{\rho_0}\left(\frac{\partial^2 p^*}{\partial x^2} + \frac{\partial^2 p^*}{\partial y^2}\right) - 2\beta p^*\left(\frac{\partial v_x^*}{\partial x} + \frac{\partial v_y^*}{\partial y}\right) \tag{20}$$

$$\frac{\partial}{\partial t}v_x^* = h_{v_x}^* = \frac{\delta_2}{\rho_0}\left(\frac{\partial^2 v_x^*}{\partial x^2} + \frac{\partial^2 v_x^*}{\partial y^2}\right) \tag{21}$$

$$\frac{\partial}{\partial t}v_y^* = h_{v_y}^* = \frac{\delta_2}{\rho_0}\left(\frac{\partial^2 v_y^*}{\partial x^2} + \frac{\partial^2 v_y^*}{\partial y^2}\right) \tag{22}$$

Here, p^*, $v_x{}^*$ and v_y^* is the middle value calculated in advection phase.

Therefore, using the finite difference method for those equations, the sound pressure and the particle velocity at the next time step $n+1$ are given as follows.

$$
\begin{aligned}
p^{n+1}(i,j) &= p^*(i,j) \\
&\quad + \frac{\delta_1 \Delta t}{\rho_0} \left(\frac{\partial_x p^*(i+1,j) - \partial_x p^*(i-1,j)}{2\Delta x} \right. \\
&\quad \left. + \frac{\partial_y p^*(i,j+1) - \partial_y p^*(i,j-1)}{2\Delta y} \right) \\
&\quad - 2\beta \Delta t p^*(i,j) \left(\partial_x v_x^*(i,j) + \partial_y v_y^*(i,j) \right)
\end{aligned} \tag{23}
$$

$$
\begin{aligned}
{v_x}^{n+1}(i,j) &= v_x^*(i,j) \\
&\quad + \frac{\delta_2 \Delta t}{\rho_0} \left(\frac{\partial_x v_x^*(i+1,j) - \partial_x {v_x}^*(i-1,j)}{2\Delta x} \right. \\
&\quad \left. + \frac{v_x^*(i,j+2) - 2v_x^*(i,j) + {v_x}^*(i,j-2)}{4\Delta y^2} \right)
\end{aligned} \tag{24}
$$

$$
\begin{aligned}
{v_y}^{n+1}(i,j) &= v_y^*(i,j) \\
&\quad + \frac{\delta_2 \Delta t}{\rho_0} \left(\frac{v_y^*(i+2,j) - 2v_y^*(i,j) + v_y^*(i-2,j)}{4\Delta x^2} \right. \\
&\quad \left. + \frac{\partial_y v_y^*(i,j+1) - \partial_y v_y^*(i,j-1)}{2\Delta y} \right)
\end{aligned} \tag{25}
$$

Here, $p(i,j)$ and $v(i,j)$ are the sound pressure and the particle velocity at $(x,y) = (x_i, y_j)$.

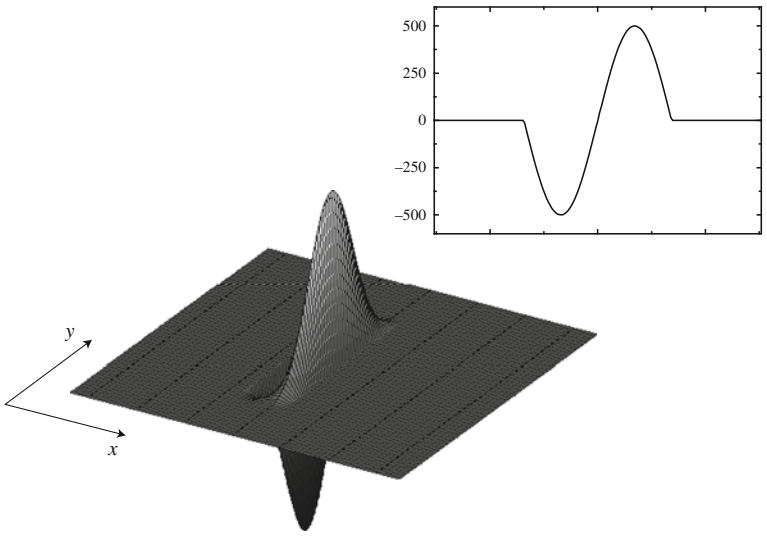

Fig. 2 Initial sound pressure distribution

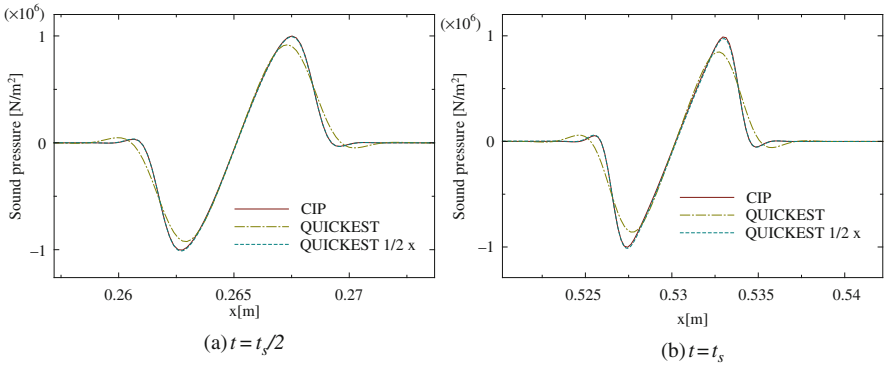

Fig. 3 Distribution of the sound pressure in water

Then the derivatives at the next time step are also calculated, simply differentiating Equations (20), (21) and (22).

4 Results And Discussion

We evaluated the calculation performance of 2-D analysis for nonlinear sound wave propagation using CIP method. Figure 4 portrays the spatial distribution of the initial pressure field.

Figure 5 portrays the sound pressure distribution obtained through CIP calculation at $1/2t_s$ and t_s, where t_s is the shock formation time given as

$$t_s = \frac{\rho_0 c_0^2}{\beta \omega p_0}. \tag{26}$$

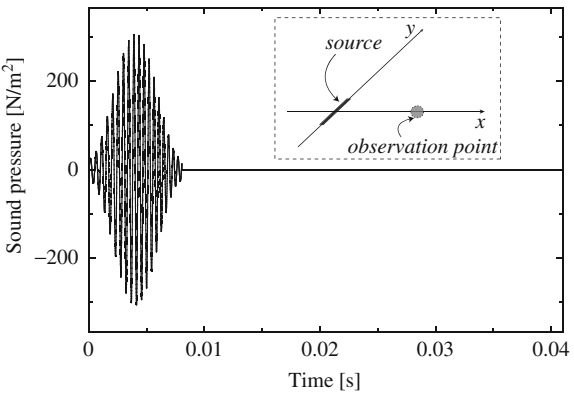

Fig. 4 Initial pressure waveform

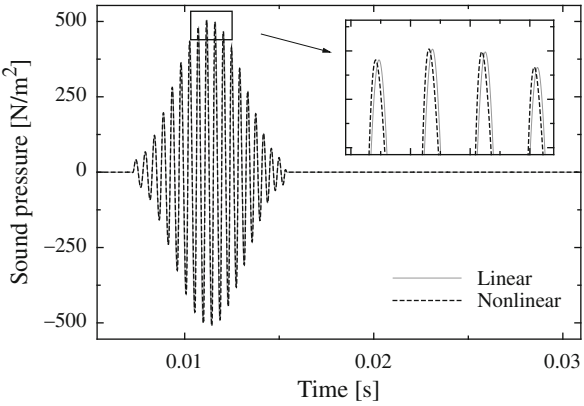

Fig. 5 Sound pressure versus time

A single-shot pulse of sinusoidal whose amplitude and frequency are 1 MPa and 200 kHz is given around $(x, y) = (0, 0)$ m. Here, the Blackman window is applied in the y-direction. Other numerical parameters are the following: grid size, $\Delta x = 0.19$ [mm]; time step, $\Delta t = 64$ ns; sound speed, $c_0 = 1,490$ m/s; and the nonlinearity parameter, $\beta = 4.96$. Figure 6 presents the spatial distribution of the sound pressure along the x-axis at times $t = t_s/2$ and $t = t_s$. In this figure, the results of the nonlinear sound wave propagation by the CIP method and QUICKEST is shown. The CIP results show the shock fronts associated with nonlinear acoustic wave propagation.

In the calculation shown below, the sound pressure source is driven as a line source on the y-axis. Equation (31) was used as an initial pressure; its waveform is depicted in Fig. 2.

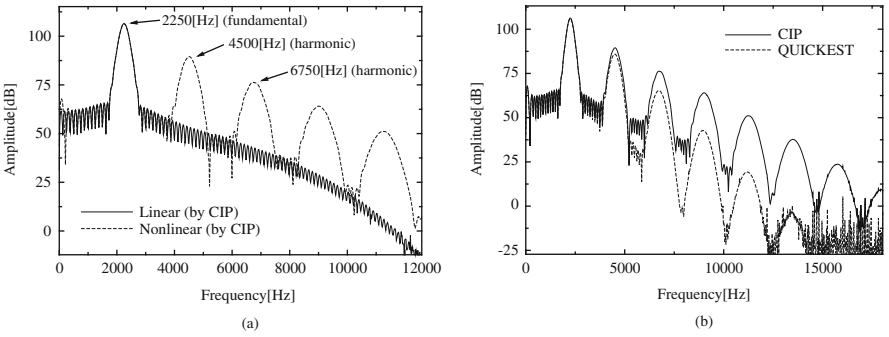

Fig. 6 Amplitude characteristics versus frequency: (**a**) Comparison between nonlinear results and linear results obtained using CIP calculation, (**b**) Comparison between CIP and QUICKEST scheme

$$p_i(t) = \begin{cases} A \sin\left\{2\pi\left(f_0 + \dfrac{f_1 - f_0}{2}\dfrac{t}{T_t}\right)t\right\} \cdot \left\{0.54 - 0.46\cos\left(2\pi\dfrac{t}{T_t}\right)\right\} & (0 < t \le T_t) \\ 0 & (t > T_t) \end{cases} \quad (27)$$

Here, T_t is the duration time of the initial signal. In those equations, $f_0 = 2$ kHz, $f_1 = 2.5$ kHz, $A = 500$ Pa and $T_t = 8.0$ ms, i.e., the frequency band of the chirp signal is from 2 to 2.5 kHz. Here, the Hamming window is used in the time region. Other analytical parameters are identical in the case of sinusoidal analysis.

Figure 3 portrays the sound pressure versus time. The observation point is $(x, y) = (5, 0)$ m: the azimuthal angle is 0 deg. Next, Fig. 6a presents amplitude characteristics versus frequency. The difference between the nonlinear result and the linear result is readily apparent. The results demonstrate the generation of the higher harmonic components with nonlinear wave propagation. Figure 6b presents a comparison between CIP and QUICKEST scheme. The result obtained using QUICKEST has more numerical dissipation than that of the CIP scheme. These results suggest that CIP analysis provides higher accuracy for calculating the nonlinear effect than that obtained using the conventional QUICKEST scheme.

5 Conclusions

This study first applies the CIP method to 2-D nonlinear acoustic wave propagation analysis in a time domain under the assumption of a weak shock. Numerical demonstrations are made for 2-D nonlinear sound propagation in air, which verified that the shock front and the harmonic components are clearly calculable using CIP method. That result demonstrates the feasibility of this method. Based on these results, we intend to investigate actual 3-D models in the near future.

References

1. Frederic, P., Emmanuel, P., Pascal, L.: Jpn. J Appl. Phys. **45**, 6496 (2006)
2. Virieux, J.: Geophysics. **49**(11), 1933–1942 (1984)
3. Botteldooren, D.: J. Acoust. Soc. Am. **98**(6), 3302–3308 (1995)
4. Sato, M.: Jpn. J. Appl. Phys. **45**, 4453 (2006)
5. Sakamoto, S., Seimiya, T., Tachibana, H.: Acoust. Sci. Tech. **23**(1), 34–39 (2002)
6. Yabe, T., Feng, X., Utsumi, T.: J. Comput. Phys. **169**, 556 (2001)
7. Tsuchiya, T., Okubo, K., Takeuchi, N.: Jpn. J Appl. Phys. **47**, 3952 (2008)
8. Kamakura, T.: Fundamentals of Nonlinear Acoustics, p. 61. Aichi Publishing, Tokyo (1996) [in Japanese]
9. Yanenko, N.N.: The Method of Fractional Steps, p. 42. Springer, New York (1971)

A Study of Similarity Measures for In Vivo 3D Ultrasound Volume Registration

U.Z. Ijaz, R.W. Prager, A.H. Gee, and G.M. Treece

Abstract Most of the conventional ultrasound machines in hospitals work in two dimensions. However, there are some applications where doctors would like to be able to gather ultrasound data as a three-dimensional (3D) block rather than a two-dimensional (2D) slice. Two different types of 3D ultrasound have been developed to meet this requirement. One type involves a special probe that can record a fixed block of data, either by having an internal sweeping mechanism or by using electronic steering. The other type of 3D ultrasound uses a conventional 2D ultrasound probe together with a position sensor and is called freehand 3D ultrasound. A natural progression of the mechanically-swept 3D ultrasound system is to combine it with the free hand sensor. This results in an extended field of view. There are two major problems with using a position sensor. Firstly, line-of-sight needs to be maintained between the sensor and the reference point. Secondly, the multiple volumes rarely register because of tissue displacement and deformation. Therefore, the objective of this paper is to get rid of the inconvenient position sensor and to use an automatic image-based registration technique. We provide an experimental study of several intensity-based similarity measures for the registration of 3D ultrasound volumes. Rather than choosing a conventional voxel array to represent the 3D blocks, we use corresponding vertical and horizontal image slices from the blocks to be matched. This limits the amount of data thus making the calculation of the similarity measure less computationally expensive.

Keywords Similarity measures · 3D ultrasound · Automatic registration

1 Introduction

In recent years, it has become more and more common to produce intrinsically 3D ultrasound (US) probes. Volumetric imaging has matured because of the possibility of capacitive micro-machined US transducers and 2D phased arrays. It is anticipated that some clinical applications offered by 3D US will replace X-ray computed tomography (CT) with greater safety and will replace magnetic resonance imaging (MRI) at lower cost. By acquiring 3D volumes from different viewpoints

U.Z. Ijaz (✉)
Department of Engineering, University of Cambridge, Cambridge, CB2 1PZ, UK

M.P. André et al. (eds.), *Acoustical Imaging*, Acoustical Imaging 30,
DOI 10.1007/978-90-481-3255-3_36,

and subsequently aligning them to create mosaics, volumes can be created with an extended field-of-view, as well as potentially better data quality, both of which can give more useful information to clinicians. Essentially, there are two ways to acquire 3D US scans. The first option is to use a 3D probe that when placed on the skin scans a small fixed volume underneath. The alternative is to use a freehand system which sweeps a conventional 2D probe over the region-of-interest resulting in a 3D volume. The probe has an additional position sensor to record the position and orientation of each image frame. Even though the position sensor, if calibrated well, is able to locate the B-scans within a sweep, there are additional problems associated with determining the relative positions of B-scans in an overlapping sweep. The main reason is the displacement and deformation of the underlying anatomy when scanned from different directions in multiple views. Furthermore, the position sensor is mounted on the probe, which makes it somewhat inconvenient to use. For example, line-of-sight may need to be maintained between the sensor and a reference point. It is also difficult to use a position sensor in certain 3D US screening methods, for example, with endoscopic, intravascular, trans-rectal, and trans-vaginal 3D US probes.

A possible solution is to use an automatic registration technique that uses a matching algorithm to register overlapping data. In literature on automatic ultrasound image registration, various similarity measures are used to calculate the six rigid-body transformation parameters (three for rotation and three for translation) and optionally include scale factors (including course-to-fine scale [1]) and deformation maps (including thin-splines [2] and B-splines [3]). These similarity measures may include mutual information [4], cross-correlation [5], Bhattacharyaa's coefficient [6], mean square of intensities [7], correlation ratio [8], and sum of squared differences [5]. There also exist some studies that consider the above mentioned similarity measures for multimodality fusion of US images with MRI [9] and CT [10]. Other noteworthy approaches include similarity energy for free-form deformation [11], variational approaches [12], segmentation-based approaches [10], probe pressure correction [13], and joint volume reconstruction with image alignment [14]. Some of the US-specific similarity measures [5] are based on a maximum likelihood framework and model ultrasonic speckle as multiplicative Rayleigh distributed noise (in the case of envelope-detected US B-mode data), or as signal-dependent Gaussian noise (in the case of displayed US image data that has undergone logarithmic compression, low and high-pass filtering, post-processing, etc.).

2 Intensity-Based Similarity Measures

We have restricted this study to intensity-based similarity measures which treat the intensity pairs taken from corresponding spatial locations in two images as independent and identically distributed samples of two random variables. With these assumptions, statistical concepts such as correlation, mutual information, and distance between joint and independent distributions are used as similarity measures

by estimating the statistical properties of the samples. The probabilistic similarity measures are particularly useful for multi-modal image registration since they do not assume any functional relationship between the two image values and have an inherent degree of robustness. These measures may not be statistically efficient, i.e., the registration variability due to noise can be larger than the sample correlation coefficient, but since US images have a low signal-to-noise ratio, they are well suited to the registration task. However, this comes at the cost of increased computational burden. In comparison to automatic-landmark-based image registration techniques, where the landmarks are generated once and only their spatial locations are matched for corresponding volumes, the similarity-measure-based registration techniques require the data to be re-interpolated for matching at each iteration of the search algorithm.

A solution that we propose is to consider only pair-wise image slices as opposed to voxel arrays as shown in Fig. 1. We generate the vertical and horizontal pair-wise slices through the region of interest based on nearest-neighbour interpolation of the B-scans. By finding the minimum number of image slices for satisfactory registration performance, the time for interpolation can be reduced substantially. Using this approach, two sets of images are obtained for two sweeps across the region-of-interest on which we apply some of the most popular similarity measures as shown in Table 1. Here $f = \{f_1, f_2, \ldots, f_n\}$ and $F = \{F_1, F_2, \ldots, F_n\}$ represent the one dimensional lists of brightness values for the target and the source image. The images of the target volume represent the pixels values when the target

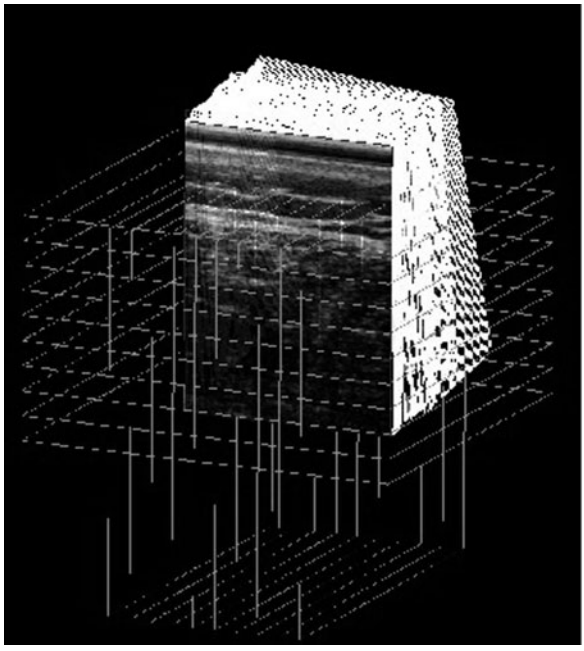

Fig. 1 Horizontal and vertical image pair boundaries are shown for two overlapping volumes obtained using a mechanically-swept 3D US probe

Table 1 Similarity measures [14] including correlation coefficient and probabilistic measures

Similarity measure	Description
Normalized Cross-correlation Coefficient (NCC)	$\text{NCC} = \frac{\sum_{i=1}^{n}(F_i - \bar{F})(f_i - \bar{f})}{\sqrt{\sum_{i=1}^{n}(F_i - \bar{F})^2}\sqrt{\sum_{i=1}^{n}(f_i - \bar{f})^2}}$
Normalized Mutual Information (NMI)	$\text{NMI} = \frac{H(X)+H(Y)}{H(X,Y)}$ where $H(X) = -\sum_i p_i \log p_i$ and $H(X,Y) = -\sum_i \sum_j p_{ij} \log p_{ij}$
Kolmogorov's distance	$\text{V} = \frac{1}{2}\sum_i \sum_j \lvert p_{ij} - p_i p_j \rvert$
χ^2-Divergence	$\text{R} = \frac{1}{2}\sum_i \sum_j \frac{(p_{ij} - p_i p_j)^2}{p_i p_j}$
Hellinger's distance	$\text{H}^2 = \frac{1}{2}\sum_i \sum_j (\sqrt{p_i p_j} - \sqrt{p_{ij}})^2$
Bhattacharyaa's distance	$\text{B} = -2\log \sum_i \sum_j \sqrt{p_{ij} p_i p_j}$

volume is already aligned to the source volume. $\bar{F}$ and $\bar{f}$ represent the mean values. Probabilities are denoted with: $p_i = P_f(f(T(\mathbf{x})) = i)$, $p_j = P_f(F(\mathbf{x}) = j)$, and $p_{ij} = P_{f,F}(f(T(\mathbf{x})) = i, F(\mathbf{x}) = j)$ where T represents a transformation over spatial coordinates $\mathbf{x}$. The two images are thus considered as random variables taking their values between grayscale levels 1 and 256.

In Fig. 1 the probe is positioned at the top and the direction of insonification is downwards. The image pairs are generated uniformly over the source and target volumes and located with reference to the first B-scan in the target volume. The vertical image pairs are generated over the whole volume up to a 10 pixel margin at either side and a 70 pixel margin at the top. The margins for horizontal image pairs are 70 pixels at the top and 10 pixels at the bottom. The dimensions of the image slices are 470 × 470 pixels, whereas the dimensions of the B-scans are 266 × 352 pixels. The scale is 0.01 cm/pixel.

3 Results

Ultrasound data (Fig. 2) was recorded with a GE RSP6-12 mechanically swept 3D probe interfaced to a Dynamic Imaging Diasus ultrasound machine. The depth setting was 3 cm with a single focus at 1.5 cm. Analogue RF echo signals were digitized after receive focusing and time-gain compensation, but before log-compression and envelope detection, using a Gage Compuscope CS14200 14-bit digitizer (http://www.gage-applied.com). The RF data was then converted

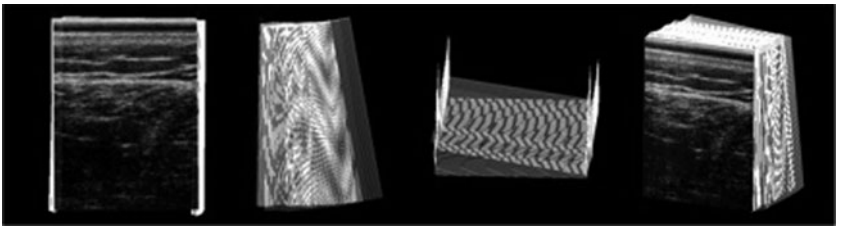

Fig. 2 Dataset used for comparison of similarity measures consisting of two overlapping volumes. The data is obtained through a mechanically-swept ultrasound probe with a sweeping angle of 10 degrees. Here, a front-view, side-view, top-view and perspective-view are presented

to B-scan images using Stradwin software (http://mi.eng.cam.ac.uk/~rwp/stradwin). The volumes were acquired with the probe held stationary during each sweep and repositioned by hand in between with some amount of overlap between the two volumes. Each B-scan's position and orientation was recorded using a Northern Digital Polaris optical tracking system (http://www.ndigital.com), with spatial and temporal calibration performed according to the techniques in Treece [13]. Each acquired volume consisted of 50 frames of data swept over 10 degrees. In order to test the performance of the similarity measures, the two volumes were first aligned based on the alignment obtained from the position sensor. For probabilistic similarity measures, the number of histogram bins was set to 128. A total of 10 horizontal and 10 vertical image pairs were generated. The positions and orientations of one volume were then changed while keeping the second volume fixed. The similarity measures were tested over a range of transformations (-9 to 9 mm in translation, and -9° to 9° in rotation). An extremum of the similarity measure was then designated as the registration position.

Figure 3 provides examples of typical behavior of some of the similarity measures and shows the probabilistic similarity measures to be more robust. Here, it can be seen that at the ground truth (established through the position sensor), the similarity measures achieve the maximum values. Next, we selected Kolmogorov's distance for detailed analysis. In Fig. 4, results are provided by varying the number of histogram bins for Kolmogorov's distance. It is shown that with a smaller number of histogram bins, the peaks are more prominent at ground truth. Therefore, the use of 32 histogram bins is recommended. Similarly in Fig. 5, it can be seen that with at least 5 horizontal and 5 vertical image pairs, Kolmogorov's distance works well (as opposed to the 2 horizontal and 2 vertical image pair case, which shows erroneous results).

4 Conclusions

The goal of this paper is to present and assess several similarity measures for rigid registration of three-dimensional ultrasound volumes. We have considered resliced image pairs instead of a regular voxel grid. In general, we found that probabilistic similarity measures are potentially suitable for the registration task. Additionally we

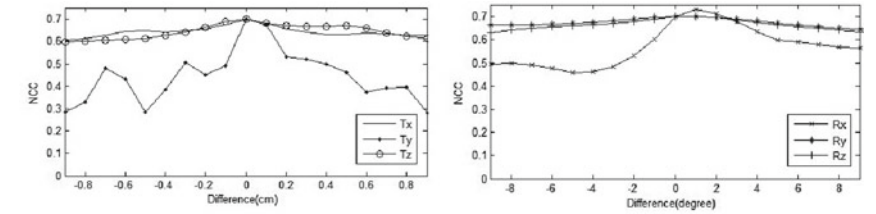

(a) Normalized Cross-correlation Coefficient

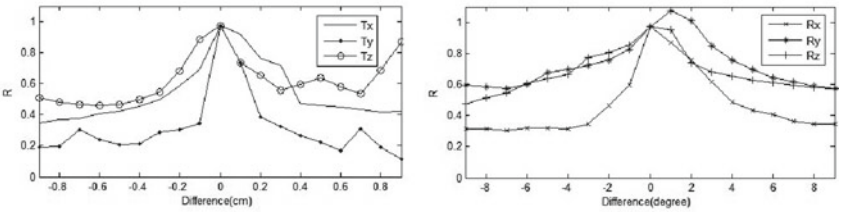

(b) χ^2-Divergence

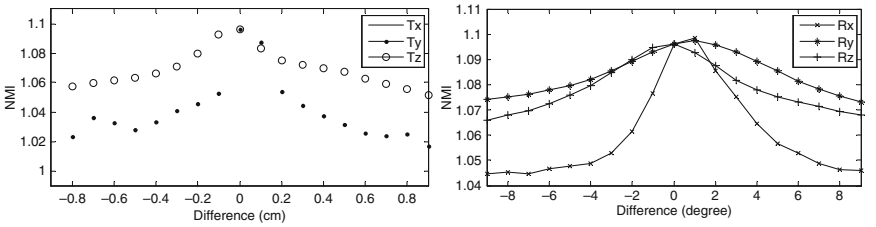

(c) Normalised Mutual Information

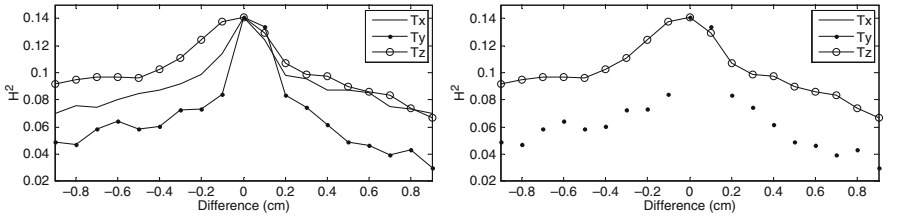

(d) Hellinger's Distance

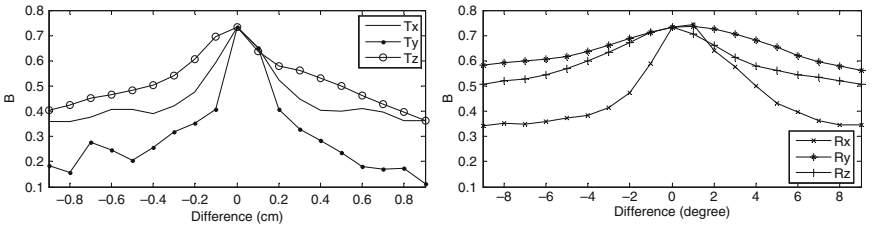

(e) Bhattacharya's Distance

Fig. 3 Some example behavior of similarity measures for the considered dataset. Tx, Ty, and Tz represent translation in x, y, and z directions and Rx, Ry, and Rz represent rotation in azimuth, elevation and roll, respectively. Both volumes are aligned at $(0, 0, 0, 0, 0, 0)^T$ by using the positions of the sensor as ground truth

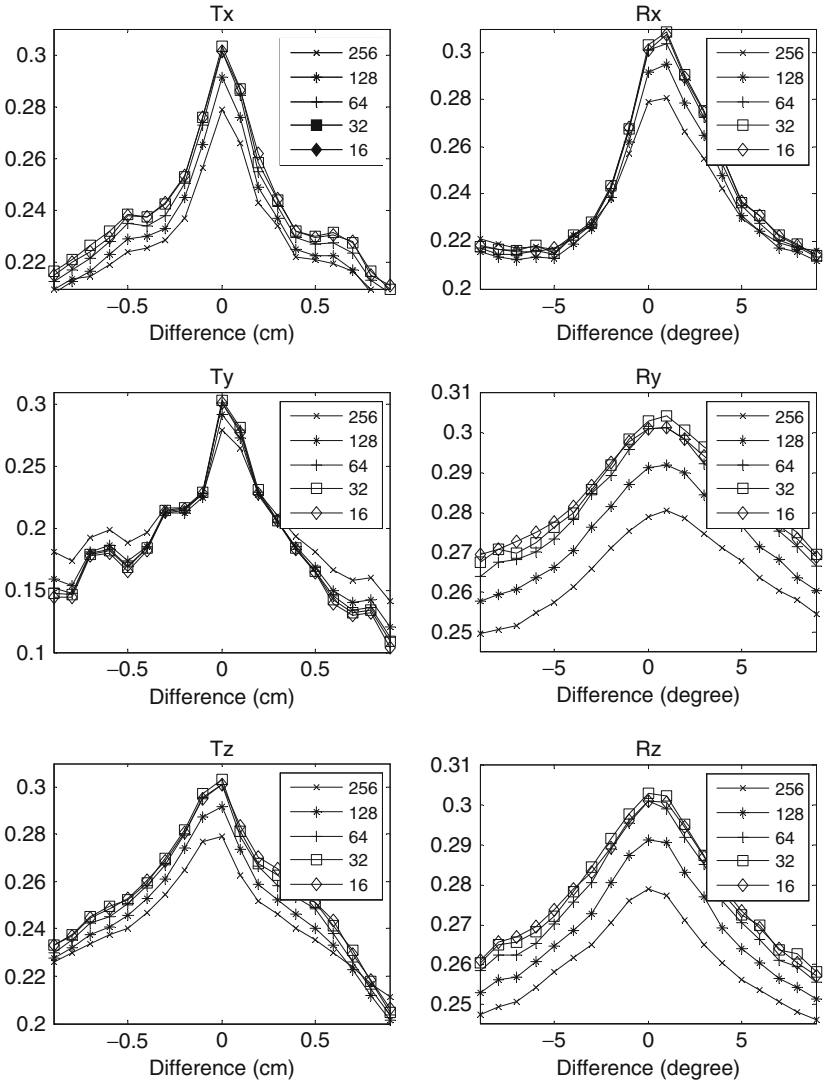

Fig. 4 Analysis of Kolmogorov's distance using 10 horizontal and 10 vertical image pairs and varying histogram bins. Tx, Ty, and Tz represent translation in x, y, and z directions, and Rx, Ry, and Rz represent rotation in azimuth, elevation and roll, respectively. Both volumes are aligned at $(0, 0, 0, 0, 0, 0)^T$ by using the positions of the sensor as ground truth

have provided an analysis of the effect of varying the number of histogram bins, and the number of image pairs. We have presented the preliminary results in this paper and in the future several criteria should be studied to compare precisely the behavior of such measures according to each step of the registration procedure including the search algorithm. Also, a comparison of similarity measures for different datasets will be beneficial.

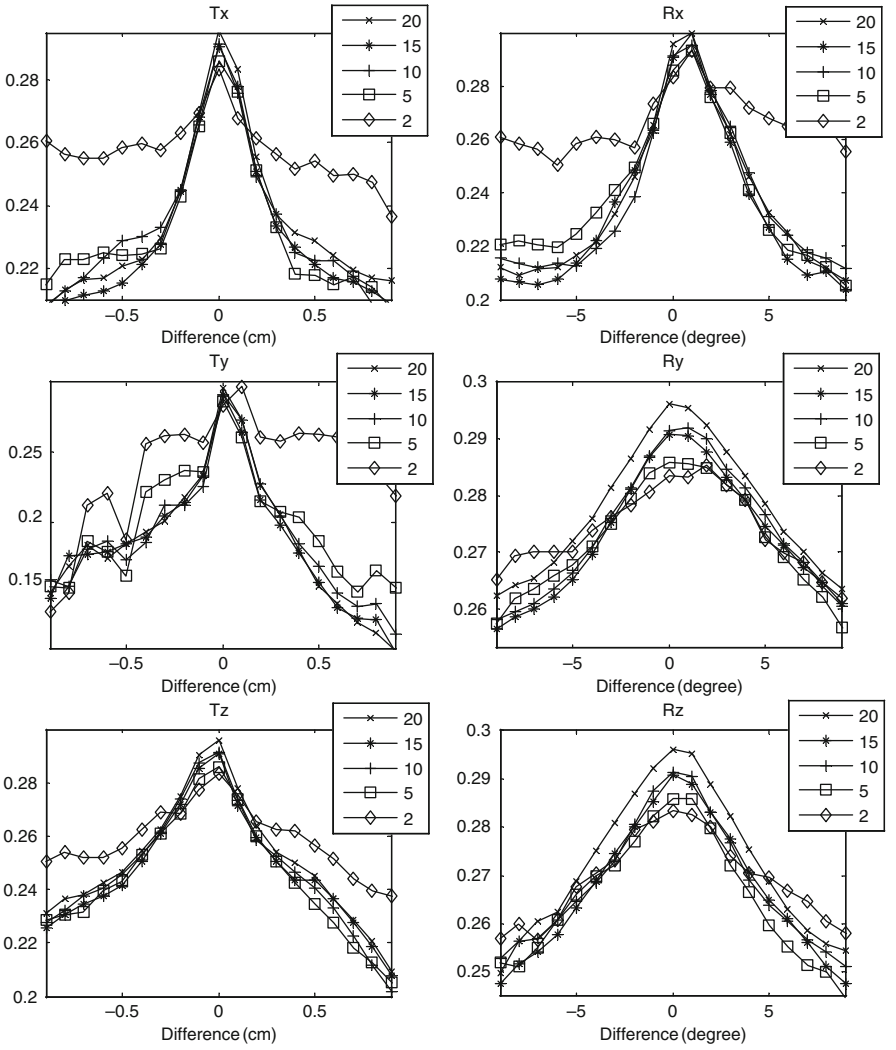

Fig. 5 Analysis of Kolmogorov's distance by varying the number of horizontal and vertical image pairs (both numbers being equal). Tx, Ty, and Tz represent translation in x, y, and z directions, and Rx, Ry, and Rz represent rotation in azimuth, elevation and roll, respectively. Both volumes are aligned at $(0, 0, 0, 0, 0, 0)^T$ by using the positions of the sensor as ground truth

Acknowledgements This work is supported by the UK Engineering and Physical Sciences Research Council (EPSRC) grant EP/F016476/1.

References

1. Pratikakis, J., Barillat, C., Hellia, P.: Robust multi-scale non-rigid registration of 3D ultrasound images. In: Scale-space and Morphology Computer Vision, vol. 2106, pp. 389–397 (2001)

2. Krücker, J.F., Meyer, C.R., LeCarpontier, J.B., Fowlkes, G.L., Carson, P.L.: 3D spatial compounding of ultrasound images using image-based nonrigid registration. Ultrasound Med. Biol. **26**(9), 1475–1488 (2000)
3. Lange, T., Eulenstein, S., Hünerbein, M., Lamecker, H., Schlag, P.M.: Augmenting intraoperative 3D ultrasound with preoperative models for navigation in liver surgery. In: Proceedings of MICCAI 2004, vol. 3217, pp. 534–541 (2004)
4. Blackall, J.M., Rueckert, D., Maurer Jr., C.R., Penney, G.P., Hill, D.L.G., Hawkes, D.J.: An image registration approach to automated calibration for freehand 3D ultrasound. In: Proceedings of MICCAI2000, vol. 1935, pp. 465–471 (2000)
5. Wachinger, C., Wein, W., Navab, N.: Registration strategies and similarity measures for three-dimensional ultrasound mosaicing. Acad. Radiol. **15**, 1404–1415 (2008)
6. Francois, R., Fablet, R., Barillot, C.: Robust statistical registration of 3D ultrasound image using texture information. In: Proceedings of the 2003 International Conference on Image Processing, vol. 1, pp. 581–584 (2003)
7. Gao, S., Xiao, Y., Hu, S.: A comparison of two similarity measures in intensity-based ultrasound image registration. In: Proceedings of the 2004 International Symposium on Circuits and Systems, vol. 4, pp. 61–64 (2004)
8. Xia, G., Brady, M., Noble, J.A., Burcher, M., English, R.: Non-rigid registration of 3-D freehand ultrasound images of the breasts. IEEE Trans. Med. Imag. **21**(4), 405–412 (2002)
9. Abel, T., Morandi, X., Comeau, R.M., Collins, D.L.: Automatic non-linear MRI-ultrasound registration for the correction of intra-operative brain deformation. In: Proceedings of MICCAI2001, vol. 2208, pp. 913–922 (2001)
10. Ionescu, G., Lavalle, S., Demongeat, J.: Automatic registration of ultrasound with CT images: Application to computer assisted prostate radio therapy and orthopedics. In: Proceedings of MICCAI99, vol. 1679, pp. 768–779 (1999)
11. Pennec, X., Cachier, P., Ayache, N.: Tracking brain deformations in time sequences of 3D US images. Pattern Recogn. Lett. **24**(4–5), 801–813 (2003)
12. Zikic, D., Wein, W., Khamene, A., Clevert, D.A., Navab, N.: Fast deformable registration of 3D-ultrasound data using a variational approach. In: Proceedings of MICCAI2006, vol. 4190, pp. 915–923 (2006)
13. Treece, G.M., Prager, R.W., Gee, A.H., Berman, L.: Correction of probe pressure artifacts in freehand 3D ultrasound. Med. Image Anal. **6**(3), 199–214 (2002)
14. Sarrut, D., Miguet, S.: Similarity measures for image registration. In: First European Workshop on Content-Based Multimedia Indexing, October 1999, Toulouse, France, pp. 263–270 (1999)

Image Quality Improvement Performance Using the Synthetic Aperture Focusing Technique Data

A Wavelet Application

P. Acevedo, A. Durán, and E. Rubio

Abstract A wavelet application to improve image quality using the Synthetic Aperture Focusing Technique (SAFT) Data is presented. This Application is based on a wavelet package analysis applied to RF signals sensed by transducers in a scanning process. SAFT is performed for each level in the wavelet package decomposition tree. For image forming, an addition and delay algorithm with focusing on pixels has been implemented, and calculations have been carried out using the Matlab toolbox. This method has been applied to image forming for a point reflector simulated using the Field II toolbox and for a phantom constructed using nine acrylic reflectors. Obtained results show that axial resolution is improved and formed images have a better signal-noise ratio.

Keywords Synthetic aperture focusing · Ultrasonic imaging · Data processing · Wavelets

1 Introduction

The quality of the image that may be obtained applying the Synthetic Aperture Focusing Technique (SAFT) in its three modes (mono-static, bi-static and multi-static holography) as well as the time reduction in image forming with the aim of implement real time systems, are the objectives of this research. SAFT allows notably reduction in the associated electronics involved in the image processing, but this also presents difficulties in relation with the quality of these images and the time required for its processing. Data acquisition in ultrasonic image systems is limited by the finite sound velocity in the exploring medium.

One of the most employed applications based on SAFT is the sum and delay method. In this application a coherent sum of the captured data in each element of the array is made. In this kind of algorithms it is usual that blurs appear in the image

P. Acevedo (✉)
Universidad Nacional Autónoma de México, DISCA-IIMAS, 01000 México
e-mail: pedro@uxdea4.iimas.unam.mx

M.P. André et al. (eds.), *Acoustical Imaging*, Acoustical Imaging 30,
DOI 10.1007/978-90-481-3255-3_37,

due to the fact that in the coherent sum to form a pixel there is no corresponding information to this point. This matter affects both the axial and lateral resolution.

In this work we present an application of the wavelet transform to improve the axial resolution in the generation of images and therefore to enlarge the signal to noise ratio. To achieve this, a multi-resolution analysis is applied to the RF signal previously obtained in the B-scan process. The application is applied to a simulated wire using the FIELD II program and to a phantom constructed using nine acrylic reflector wires. The images obtained using this application have better quality than the ones obtained with a standard application.

2 Theory

2.1 Impulse Response Model

Let us consider a synthetic aperture of N transducers. This synthetic aperture may be formed by a mono-element transducer which successively occupies the positions {x1, x2, . . . , xN} or by a transducer array whose elements are placed in the aforementioned positions.

Each element will be assumed with an arbitrary shape and it will be supposed that the image will be formed in the far field zone. Lets define $P_t(\vec{R}_i, t)$ and $P_r(\vec{R}_i, t)$ as the impulse response in transmission and reception respectively. These are referred to a point in the space whose vector from the origin will be indicated as $\vec{r}$.

The impulse response of the n$^{\text{th}}$ transducer from an echo-pulse experiment is given by the following expression:

$$P_{tr}(\vec{R}_i, t) = P_t(\vec{R}_i, t) * P_r(\vec{R}_i, t) \tag{1}$$

where

$$\vec{R} = \vec{r} - x_i\hat{\vec{i}} \tag{2}$$

We will model each transducer as a lineal electro mechanic system in which the electric impulse response in reception will be denoted as $h_{er}(t)$, the signal obtained using the n$^{\text{th}}$ transducer from the point $O(x_0, y_0, z_0)$ may be obtained using the following expression:

$$s_i(\vec{R}_i, t) = \frac{\partial v(t)}{\partial t} * h_{er}(t) * P_{tr}(\vec{R}_i, t) \tag{3}$$

If we consider that the reflection function of the medium is $f(x, z)$, integrating Equation (2) along the considered zone the signal that will receive the i$^{\text{th}}$ element from that zone is obtained.

$$s_i(t) = \frac{\partial v(t)}{\partial t} * h_{er}(t) * \int_x \int_z f(x, z) P_{tr}(\vec{R}, t) dx dz \tag{4}$$

It is assumed that the emitters are small compared to the emitted wavelength λ. Therefore, transducers may be considered as point supplies, emitting spherical waves and the synthetic aperture standard focusing technique (SAFT) based on sums and delays may be used. Under this assumption and considering the reciprocity principle the complete impulse response of the transducer may be considered as:

$$P(\vec{R}_i, t) = \frac{\delta\left(t - \frac{2|\vec{R}_i|}{c}\right)}{\left|\vec{R}_i\right|^2} \tag{5}$$

substituting Equation (5) in (4) and making equal $\bar{v}(t)$ to $\frac{\partial v(t)}{\partial t} * h_{er}(t)$ we have the following expression:

$$s_i(t) = \int_x \int_z \frac{f(x,z)\bar{v}\left(t - \frac{2|R_i|}{c}\right)}{|R_i|^2} dxdz \tag{6}$$

2.2 SAFT Algorithm

The formed image from the inspected zone is nothing more than an approximation to the reflection function which we define as $\bar{f}(x,z)$. When we reconstruct this function using the data vectors $s_i(t)$ we are including information given by $\bar{v}(t)$. One of the simplest forms to get an approximation to this function is using the sum and delay method. Each pixel of the image is formed adding the existing information about the representing point in each data vector $s_i(t)$. The coherent sum is expressed as follows:

$$\bar{f}\left(\bar{x}_j, \bar{z}_k\right) = \sum_{i=1}^{l} w_i \cdot s_i\left(t - \Delta t_{ijk}\right) \tag{7}$$

where w_i are the coefficients of a windowing function (e.g. Hamming, Hanning, Cosine, Triangle, etc.), Δt is the delay applied to the signal surrounding the sub-aperture in the present window, $\bar{f}(x,z)$ is the focused RF line in the point $\bar{x}, \bar{z}$ and the *ijk* are the sub-indices that indicate the rows and columns of the matrix of the image. l is the number of A-scan lines which provide information to the coherent sum and it depends on the aperture angle. To calculate the delay Δt we may use the following expression:

$$\Delta t_{ijk} = \frac{2}{c} \cdot \left(\bar{z}_k - \sqrt{\bar{z}_k^2 + (x_i - \bar{x}_j)^2}\right) \tag{8}$$

the number of lines l, to be considered in a window for a focus to a deepness z are calculated using the following expression:

$$l = 2 \cdot \left(\frac{Z_i \cdot \tan\left(\frac{\alpha}{2}\right)}{\Delta x} \right) \tag{9}$$

$$l = \frac{Z_i}{f/number \cdot \Delta x} \tag{10}$$

This is equivalent to the classic approximation that provides a constant *f / number* until the aperture is completely open. From this, we get the optimal *f / numbe*r for the employed aperture as follows:

$$f/number = \frac{0.5}{\tan\left(\frac{\alpha}{2}\right)} \tag{11}$$

The image forming algorithm was implemented considering a dynamic aperture, calculating the *f / number* using Equation (11) [1].

2.3 Wavelet Transform

The Continuous Wavelet Transform [2] (CWT) allows one to transform a function in the time domain into a function in the scale and space domain. This function is constructed using delays and transfers from a mother wavelet $\psi(t)$. With the aim of deleting spurious information introduced by the function $\bar{v}(t)$ in the reconstruction of the reflectivity function, we will apply the CWT to the stored data of each transducer, $s_i(t)$.

$$\hat{s}_i(a,b) = \int_t s_i(t)\psi\left(\frac{t-b}{a}\right)dt \tag{12}$$

Where a is the scale parameter and b is the position parameter. Now, substituting $s_i(t)$ (Equation 6) in Equation (12), we have:

$$\hat{s}_i(a,b) = \int_x \int_z \left[\int_t \bar{v}\left(t - \frac{2\,|R_i|}{c}\right)\psi\left(\frac{t-b}{a}\right) \right] \frac{f(x,z)}{|R_i|^2} dxdz \tag{13}$$

if a mother wavelet is selected such as in a scale $\tilde{a}$ this approximates to the function $\bar{v}(t)$

$$\psi\left(\frac{t}{\tilde{a}}\right) \sim \bar{v}(t) \tag{14}$$

this will imply that $\hat{\bar{v}}(\tilde{a},b)$ approximates to the unity when $b = \frac{2\left|\vec{Ri}\right|}{c}$.

Based on this reasoning it is possible to deduce that in $\hat{s}_i(\tilde{a},b)$ most of the data contributed by $\bar{v}(t)$ to $s_i(t)$ would have been eliminated, being kept intact the information contributed by $f(x,z)$. Therefore, to achieve a better reconstruction of $f(x,z)$ it would be necessary to find the optimal scale $\tilde{a}$, and to substitute in Equation (7) $s_i(t)$ for $\hat{s}_i(\tilde{a},b)$.

To apply the CWT might have a very high computational cost; therefore, it is a better option to work with the Stationary Wavelet Transform (SWT).

Function $s_i(t)$ is projected in each scale j to a subspace ($V_j \subset \ldots \subset V_2 \subset V_1 \subset V_0$), this projection is defined as the scalar product $c_{j,k}$ of $s_i(t)$ with the scale function $\phi(t)$ which is delayed and transferred.

In the same way the wavelet coefficients $d_{j,k}$ are obtained by means of the scalar product of the signal with the scaled and shifted mother wavelet. In the 2^jresolution, $c_{j,k}$ is the approximation coefficient and $d_{j,k}$ is the detail coefficient, these coefficients will have the same number of points that the original signal. This may be understood as a series of low-pass and high-pass filters as shown in Fig. 2. The SWT algorithm is slightly different from the DWT algorithm since it does not include the sub-sampling operation, which is the strongest side of this transform because it is time constant.

3 Data Acquisition

3.1 Simulated Database

Simulations were carried out to evaluate the performance of the imaging system as a function of the implemented algorithm. All the simulation was done with the program Field II [3, 4].

3.2 Experimental Database

Data acquisition was performed using a SEA scanning system [5] and a 3.5 MHz Krautkramer transducer, the resolution in the X axe direction was 250 μm storing 200 and 400 RF lines. Signals were sampled at 50 MHz using a digital oscilloscope connected to a PC using a GPIB port.

A phantom with 10 cylindrical acrylic bars with a 5 mm diameter was used as shown in Fig. 1. The initial storage deepness was 14.4 mm and the final storage deepness was 109 mm.

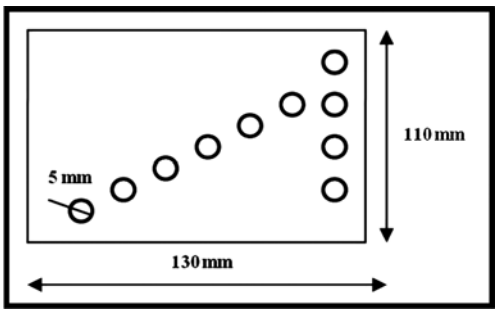

Fig. 1 Diagram of phantom with 10 cylindrical acrylic bars with a 5 mm diameter

4 Results and General Discussion

Figure 2 shows the decomposition tree in the wavelet package using a mother wavelet Daubechies 2. The letter A is the approximation coefficient while the letter D is the detail coefficient. Detail coefficients in the WP are the ones which show a quality improvement (see Fig. 2). The DDD3 element gives a significant increasing to the axial resolution. Also, it is worth to mention that lateral resolution

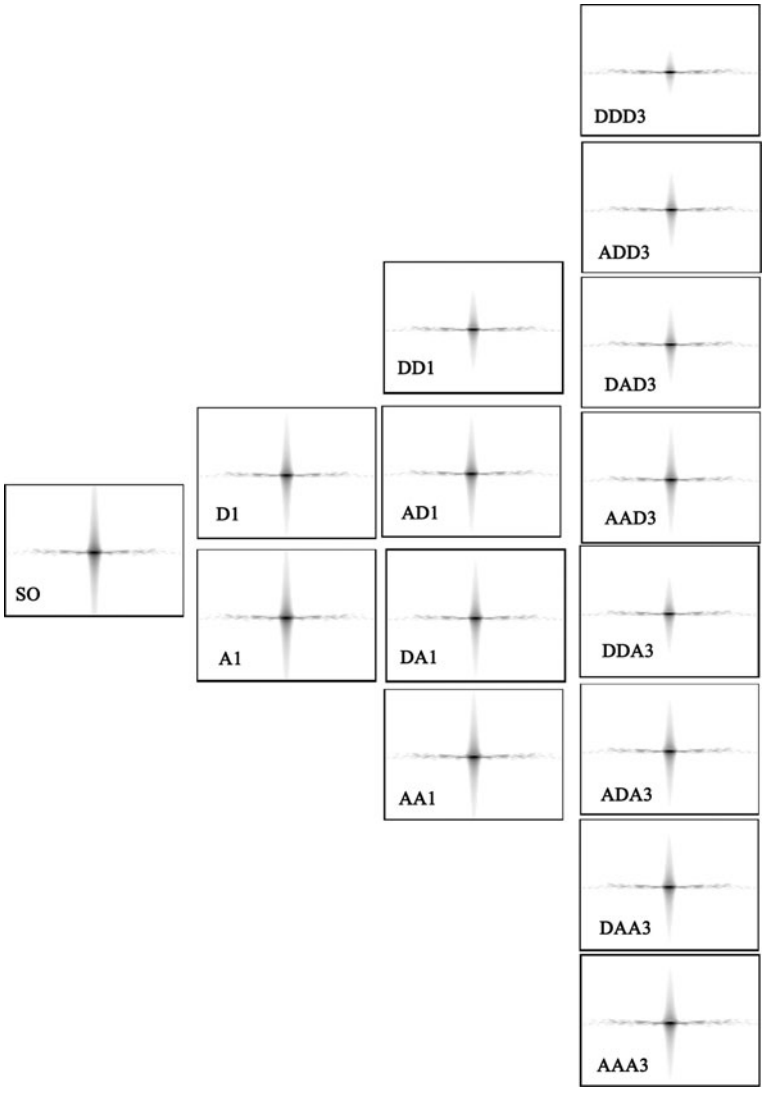

Fig. 2 Decomposition tree in the wavelet package

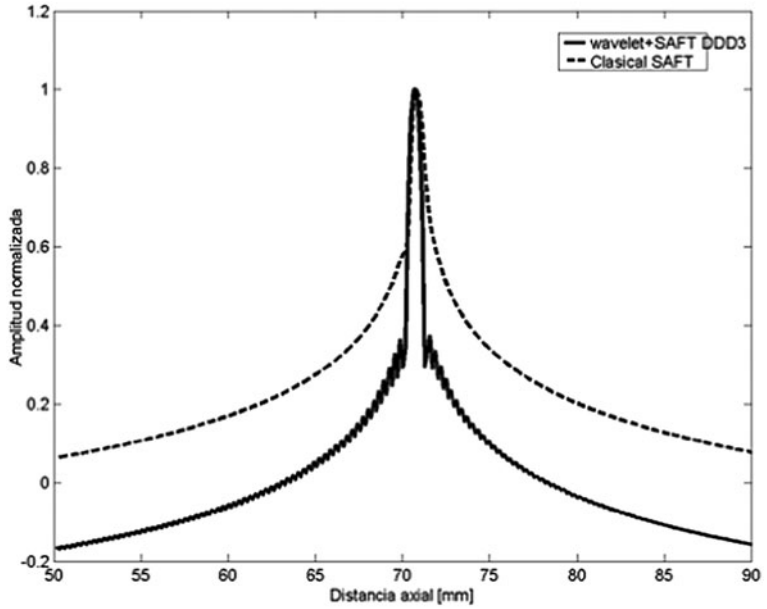

Fig. 3 Axial line spread function

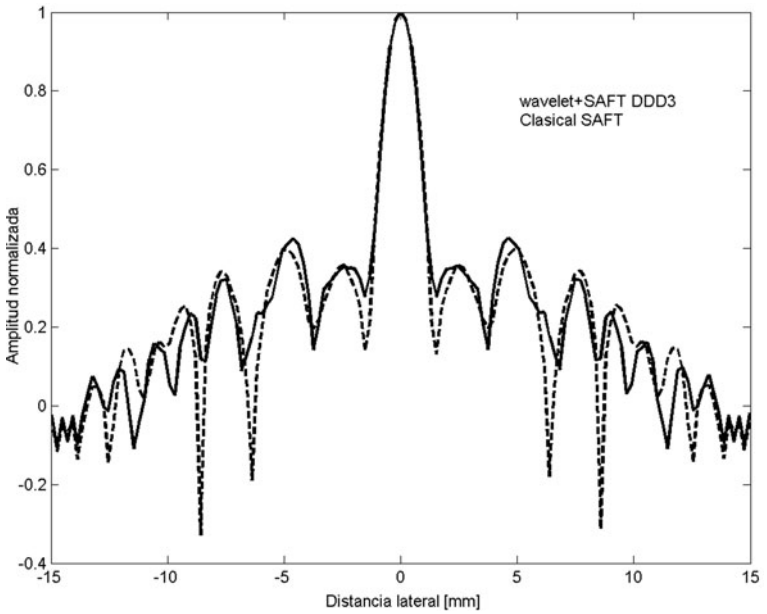

Fig. 4 Lateral line spread function

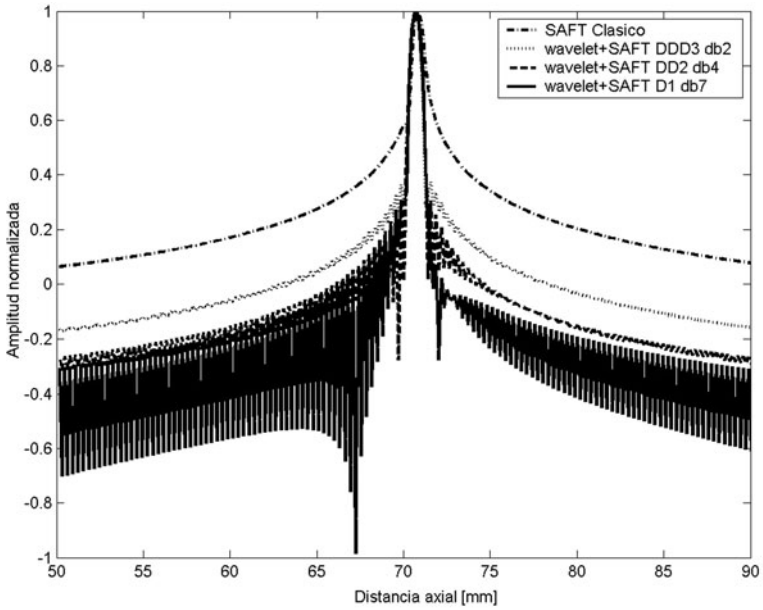

Fig. 5 Axial line spread function for DDD3

is not significantly affected during this process. These two last results are clearly seen in Figs. 3 and 4 where the axial and lateral Line Spread Functions (LSF) are respectively shown.

Figure 3 shows that the image obtained with our method has a better axial resolution, even though oscillations after the envelope process are still presented, these oscillations are not presented when the classical method is applied. Results in Fig. 4 show that the lateral representation is the same for both methods. In order to study the influence of the use of different mother wavelets the method was applied using the Daubechies 4 and Daubechies 7 wavelets, an improvement is observed in the image obtained using the Daubechies 4 wavelet in scale 2 and for the Daubechies 7 wavelet in scale 1, these results show that the process strongly depends on the selected mother wavelet. An interesting detail is the behavior of the axial LSF for each one of the studied cases. Figure 5 shows the axial LSF for the images obtained using scale DDD3 for Daubechies 2, scale DD2 for Daubechies 4 and scale D1 for Daubechies 7.

5 Conclusions

It is important in terms of application to improve the quality of the images obtained using SAFT. The application presented in this work fulfils this objective. First, we applied this method to de data obtained from a point element. Then, we applied this method to different mother waves in order to study its performance. Results show

that the axial resolution has been improved and the resulting formed images have a better signal to noise ratio.

Acknowledgements The authors acknowledge the support of DGAPA-UNAM (PAPIIT IN-109207).

References

1. Frazier, H., O'Brien, W.D.: Synthetic aperture techniques with a virtual source element. IEEE Trans. Ultrason. Ferroelect. Freq. Contr. **45**(1), 196–207 (1998)
2. Walker, J.S.: A primer on Wavelets and their scientific application, University of Wisconsin-Eua Claire, CHAPMAN & HALL/CRC (1999)
3. Jensen, J.A., Svendsen, N.B.: Calculation of pressure fields from arbitrarily shaped, apodized, and excited ultrasound transducer. IEEE Trans. Ultrason. Ferroelect. Freq. Contr. **39**, 262–267 (1992)
4. Jensen, J.A., Svendsen, N.B.: Field: A program for simulating ultrasound systems. Med. Biol. Eng. Comp., 10th Nordic-Baltic Conference on Biomedical Imaging, vol. 4, Supplement1, Part 1: 351-353 (1996b)
5. Onda Corporation. Available: http://www.ondacorp.com/index1.html

Expectation Maximization for Joint Deconvolution and Statistics Estimation

M. Alessandrini, A. Palladini, L. De Marchi, and N. Speciale

Abstract Biomedical ultrasound image quality is limited due to the blurring of tissue reflectivity introduced by the transducer Point Spread Function (PSF). Deconvolution techniques can be used to obtain the pure tissue response, otherwise called reflectivity function. Typically deconvolution methods are developed in the only purpose of image visual quality improvement. In this work we present an Expectation Maximization (EM) framework for US images deconvolution in which local statistical description of the tissue reflectivity is restored as well, so that features extracted from the deconvolved frame can theoretically be used for classification purposes.

Keywords Deconvolution · Expectation maximization · Generalized gaussian distribution

1 Introduction

Ultrasounds are widely used in medicine to obtain images representing tissue's acoustical inhomogeneities; acoustical short duration RF pulses are sent towards the region of interest and the echo signal is detected.

If weak scattering assumption is made, like is reasonable for soft tissues, first order Born approximation [1] can be used and the acquisition process can be written in terms of a linear convolution between the tissue's reflectivity and the transducer's PSF. Using the matrix vector notation, commonly adopted in image restoration literature, the following holds:

$$\mathbf{y} = \mathbf{H}\mathbf{x} + \mathbf{n} \tag{1}$$

where $\mathbf{y}$ and $\mathbf{x}$ the RF image and the tissue's response respectively, $\mathbf{H}$ the convolutional matrix representing the blur due to the PSF and $\mathbf{n}$ the measurement noise, assumed white Gaussian. Deconvolution is intended to produce an estimate of the reflectivity $\mathbf{x}$ given the data $\mathbf{y}$.

Deconvolution task can be handled using estimation theory: in this framework data are seen are realizations of statistical processes with a known parametric

M. Alessandrini (✉)
ARCES-DEIS, University of Bologna, 40136 Bologna, Italy

M.P. André et al. (eds.), *Acoustical Imaging*, Acoustical Imaging 30,
DOI 10.1007/978-90-481-3255-3_38,

distribution. Two common estimate paradigms are Maximum Likelihood (ML) and Maximum A Posteriori (MAP) [2]. If the noise **n** is white Gaussian then the ML estimate of **x,** which corresponds to value maximizing the Log-Likelihood function LL(**x**) = log(p(**y**|**x**)), is obtained with the linear filtering of **y** with the pseudo-inverse of **H**, i.e.,

$$\hat{\mathrm{x}}_{\mathrm{ML}} = \max_{\mathbf{x}}\{\log p(\mathbf{y}|\mathbf{x})\} = (\mathbf{H}^{\mathbf{T}}\mathbf{H})^{-1}\mathbf{H}^{\mathbf{T}}\mathbf{y} \tag{2}$$

As well known this solution is useless because of noise amplification due to the ill-conditioning of **H**. To overcome this problem further information must be introduced as a regularizing term; this is done in MAP framework by considering a guess of the prior distribution p(**x**):

$$\hat{\mathrm{x}}_{\mathrm{MAP}} = \max_{\mathbf{x}}\{\log p(\mathbf{x}|\mathbf{y})\} = \min_{\mathbf{x}}\{||\mathbf{y} - \mathbf{H}\mathbf{x}||_2^2 - 2\sigma_n^2 \log p(\mathbf{x})\} \tag{3}$$

where σ_n is the noise standard deviation and the first term in the functional, referred as the Log-Posterior function LP(**x**) = log(p(**x**|**y**)), is the square of the Euclidean distance between the observation **y** and the signal **x** projected in the space of the observations.

Gaussian model, i.e., $\mathbf{x} \sim \mathcal{N}(\mathbf{x}|\mu,\Sigma)$, is widely used to simulate tissue's behavior [3–4] and leads to the well known Wiener filter. Iterative Wiener-like solutions have been proposed to account for joint parameters estimate [5–6] and echogenicity macrostructure [7]. Gaussian is a suitable model for diffuse scattering; when coherent scattering phenomena can't be neglected Wiener filtering causes over-smoothing and loss of details. For this reason sparser priors have been proposed, such as the Laplacian distribution [8]. Under the Laplacian assumption the MAP estimate translates into an l-1 minimization problem, which must be solved iteratively and so it overcomes the smoothing effect of the Wiener filter at the expense of a higher computational cost.

The sparsity of the prior, e.g. Gaussian or Laplacian, is often a priori set with the only purpose of an image visual quality improvement, as a consequence the solution is inevitably biased towards the statistical description adopted, which can be considerably different from that of the underlying process, i.e., the tissue. This is an important limitation when features extracted from the deconvolved frame are used for classification purposes. In this work we develop a technique which tries to overcome this limitation. In the following sections the model adopted for the tissue and the deconvolution algorithm are presented. In the end results obtained on synthetic data are shown and comparison is made with the standard Wiener filter and Laplacian prior.

2 Tissue Model

As shown by Berbard [9] a zero mean Generalized Gaussian Distribution (GGD) is used to fit local RF data histograms. A GG zero mean random variable x has a pdf

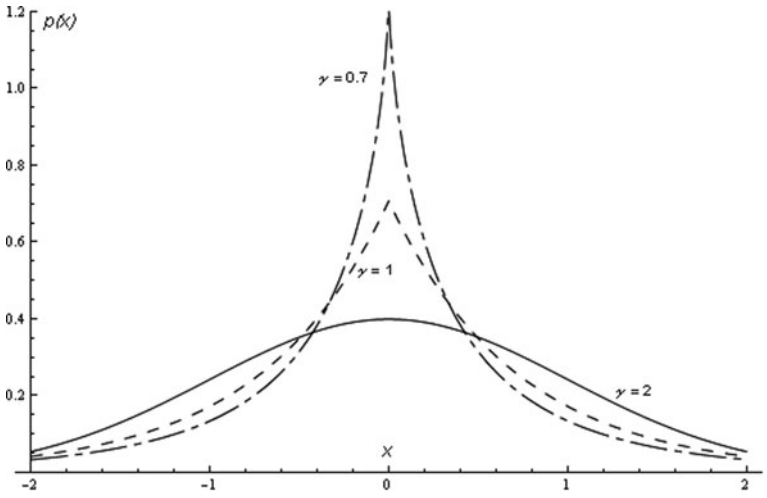

Fig. 1 Pdf of a Generalized Gaussian Distribution for different values of shape parameter

$$p(x|\gamma,\sigma) = a(\gamma,\sigma)\cdot\exp\left\{-\left|\frac{x}{b(\gamma,\sigma)}\right|^{\gamma}\right\} \tag{4}$$

where γ is the shape parameter and σ the variance. Functions a(γ,σ) and b(γ,σ) are the normalizing term and a scaling function. The shape parameter sets the tails of the probability distribution function (pdf) seen in Fig. 1, i.e. the sparsity of the realization: γ decreases as sparsity increases.

We chose to adopt the same model for the reflectivity function, i.e. we assume linear filtering not to modify the qualitative distribution of the filtered data, a part of decreasing its sparseness [10]. Moreover this choice has a physical justification since GGD can correctly model tissues with isolated reflectors (sparse reflectivity), as well as homogeneous regions (low sparsity): that is to say that the local value of the shape parameter brings important information on the tissue structure and our interest is to retrieve this information within the deconvolution framework.

We assume reflectivity samples $\mathbf{x}$ to be GG i.i.d. variables, with parameters distributed piecewise constantly within the imaged area; so the log-posterior ($\mathrm{LP}(\mathbf{x}) = \mathrm{p}(\mathbf{x}|\mathbf{y})$), a part of an additive constant and a change of sign, can be written as:

$$LP(\mathbf{x}) = \|\mathbf{y}-\mathbf{H}\mathbf{x}\|_2^2 + 2\sigma_n^2\cdot\sum_{i=1}^{K}\left\{\sum_{j=1}^{N_i}\left(\frac{|x_i^{(j)}|}{b_i}\right)^{\gamma_i} - N_i\cdot\log a_i\right\} \tag{5}$$

where K the number of regions and N_i the number of pixels within *i-th* region. The subscript i represent dependence on the region while superscript j counts pixels inside *i-th* region. Abbreviations a_i and b_i have been used for $a(\gamma_i,\sigma_i)$ and $b(\gamma_i,\sigma_i)$.

In our work we adopt an EM algorithm [11] to resolve the MAP problem, and jointly estimate parameters γ and σ within in each region, as described in the following section.

3 The Algorithm

Expectation Maximization is a well known framework to iteratively solve ML and MAP problems when they're not solvable analytically, like it is in the large majority of cases. Iterations consist of two steps, i.e., E-step and M-step, and ensure the Log-Likelihood or the Log-Posterior to monotonically decrease towards a local maximum. For further detail we address the reader to Blimes [12].

We follow Bioucas-Dias [13] to perform MAP estimation of $\mathbf{x}$ in an EM framework. The two steps of the algorithm are resumed in Table 1, where $\mathbf{D_k}$ is a diagonal matrix with entries:

$$d_i^{(j)} = \lambda_i \gamma_i / \left| x_i^{(j)} \right|^{2-\gamma_i}, \quad \lambda_i = b_i^{-\gamma_i} \tag{6}$$

and samples $x_i^{(j)}$ have to be intended as their estimate at step k. We note here that in the original work stationary data are assumed, therefore parameters are globally defined and subscript i is omitted.

In the proposed approach, as already mentioned, we are interested in both deconvolution and parameters estimation. Theoretically this task could be accomplished in the EM scheme as well: the M-step would modify with the joint maximization of the Q function with respect to both signal $\mathbf{x}$ and parameters.

Unfortunately this is not possible when GGD data are considered because in that case the Q function would require an additional term, related to parameters, which doesn't have a closed form expression [13]. Therefore, as suggested by Figueiredo [14], we adopt an approximate solution, which consists in updating parameters at regular intervals with their ML estimate [15] on the partial solution of the EM algorithm. In practice the following line is added to the M-step:

$$\hat{\boldsymbol{\theta}}_{k+1}^{(i)} = \max_{\boldsymbol{\theta}} p(\hat{\mathbf{x}}_{k+1}^{(i)} | \boldsymbol{\theta}), \quad i = 1, \ldots, K \tag{7}$$

where $\boldsymbol{\theta}^{(i)}$ is the parameters vector (γ_i, σ_i) estimated on the pixels inside i^{th} region $\mathbf{x}^{(i)}$ at iteration $k+1$. The estimated parameters are then used for computing $\mathbf{D}_{k+1}$.

Table 1 EM algorithm for GGD data

E-step:	$Q(\mathbf{x}, \hat{\mathbf{x}}_k) = \|\mathbf{y} - \mathbf{H}\mathbf{x}\|_2^2 + \sigma_n^2 \cdot \mathbf{x}^T \mathbf{D}_k \mathbf{x}$
M-step:	$\hat{\mathbf{x}}_{k+1} = \max_{\mathbf{x}} Q(\mathbf{x}, \hat{\mathbf{x}}_k) = (\sigma_n^2 \mathbf{D}_k + \mathbf{H}^\mathbf{T}\mathbf{H})^{-1} \mathbf{H}^T \mathbf{y}$

It must be noted that, being p(**y**|**x**) and p(**y**) independent on **θ**, it is:

$$\frac{\partial p(\mathbf{x}|\boldsymbol{\theta})}{\partial \boldsymbol{\theta}} = \frac{\partial p(\mathbf{x}|\mathbf{y}, \boldsymbol{\theta})}{\partial \boldsymbol{\theta}} \tag{8}$$

and so ML parameters estimate still guarantees the LP to increase, while convergence, since the algorithm is no more an EM, is no longer ensured. Nevertheless convergence has been observed in all our experimental results.

4 Experimental Results

We tested our algorithm on simulated data. A synthetic reflectivity is generated, consisting of hyper-echoic regions with a GG statistic located within a Gaussian background. The reflectivity is blurred with the PSF obtained with a homomorphic technique [3] from real RF data and then deconvolution is performed, for different values of SNR, with the standard Wiener filter and l-1 norm constraint, and with the proposed approach.

Convergence is assumed when the relative error on the Log-Posterior function falls below a prescribed threshold ε:

$$\frac{L(\hat{\mathbf{x}}^{(k)}) - L(\hat{\mathbf{x}}^{(k-1)})}{L(\hat{\mathbf{x}}^{(k-1)})} < \varepsilon \tag{9}$$

In these simulations $\varepsilon = 10^{-10}$ is used. Parameters are updated every 10 iterations. In Fig. 2 the synthetic reflectivity with the corresponding RF signal are represented.

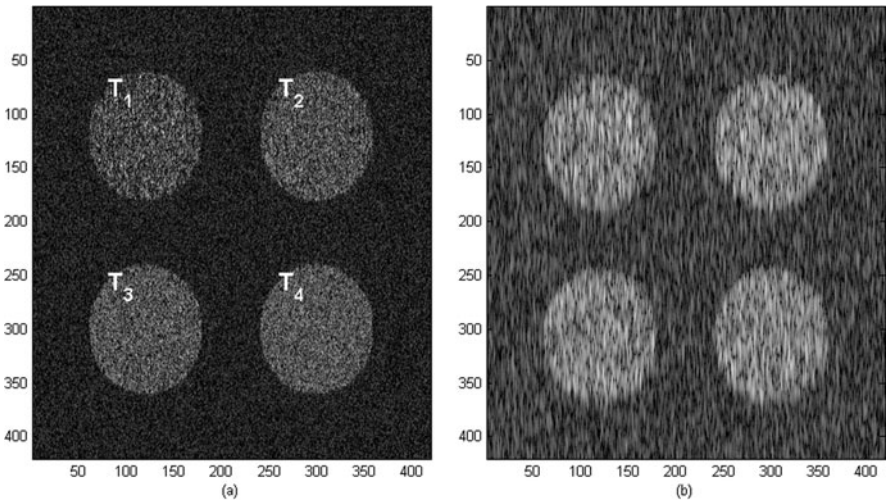

Fig. 2 (**a**) Synthetic reflectivity map. Each target has a GG statistic and the shape parameter is (from left to right) 0.6, 0.9, 1.2 and 1.5 respectively. (**b**) Synthetic RF data

Table 2 Shape parameter value within each target. Estimate is made on the reflectivity map (True), the RF signal (RF) and on the frames restored with Wiener, Laplacian prior and the proposed method (EM-GGD). The mean value over 10 trials is reported

	True	RF	Wiener	Laplacian	EM-GGD
SNR = 20 dB					
Target 1	0.6	1.46	0.87	0.72	0.72
Target 2	0.9	1.73	1.08	0.88	0.92
Target 3	1.2	1.76	1.34	1.12	1.18
Target 4	1.5	1.70	1.65	1.22	1.52
SNR = 15 dB					
	True	RF	Wiener	Laplacian	EM-GGD
Target 1	0.6	1.49	1.04	0.63	0.78
Target 2	0.9	1.72	1.30	0.73	0.98
Target 3	1.2	1.81	1.51	0.82	1.17
Target 4	1.5	1.79	1.71	0.87	1.39
SNR = 10 dB					
	True	RF	Wiener	Laplacian	EM-GGD
Target 1	0.6	1.51	1.24	0.61	0.75
Target 2	0.9	1.71	1.50	0.65	0.89
Target 3	1.2	1.82	1.63	0.67	0.99
Target 4	1.5	1.78	1.85	0.71	1.24
SNR = 5 dB					
	True	RF	Wiener	Laplacian	EM-GGD
Target 1	0.6	1.53	1.38	0.62	0.84
Target 2	0.9	1.73	1.53	0.67	0.98
Target 3	1.2	1.74	1.75	0.66	1.26
Target 4	1.5	1.84	1.83	0.69	1.34

The shape parameter is estimated within each target on the restored frames and results are reported in Table 2. Here we underline that the proposed results are obtained assuming a priori knowledge of targets location; when dealing with real data a segmentation process is mandatory as a pre-processing step.

Since the regularization weight grows with the inverse of the SNR, then for high SNR all three algorithms work properly and give results consistent with the synthetic reflectivity statistics, in this case Wiener filter has to be preferred for computational reasons, whereas, as SNR decreases, while our method, thanks to parameters adaptivity, is still seen to retrieve the local statistics with a good accuracy (see Table 2), standard methods solutions are biased towards the prior assumed for the signal. In particular Wiener filter tends to *Gaussianize* processed data, so producing sequences with a shape parameter higher than the true one, on the contrary the effect of the Laplacian prior is an excessive sparsification of the signal.

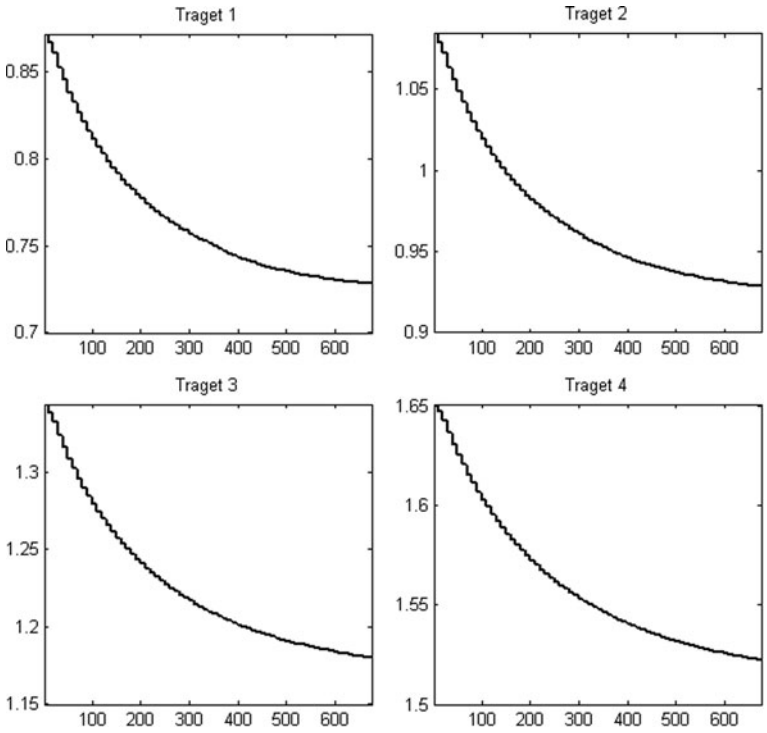

Fig. 3 Evolution of the shape parameter estimate as algorithm reaches convergence. Iterations in abscissa

In Fig. 3 it is shown how the estimate of the shape parameter within each target evolves as the algorithm reaches convergence while Fig. 4 shows the processed frames.

5 Conclusions

A novel EM algorithm for MAP ultrasound images deconvolution has been presented. Signal sparsity is estimated within the deconvolution framework and it is not a priori set, like it is in the standard methods proposed in literature. This is made possible by assuming a Generalized Gaussian model for the tissue and including parameters update within the restoration process. Results on synthetic data show how the proposed approach retrieves the local signal statistics with a good accuracy, while standard methods solutions are biased towards the prior assumed for the signal. Since the focus is on the deconvolution algorithm, in this work we have supposed to dispose of a perfect segmentation of the image; when dealing with real

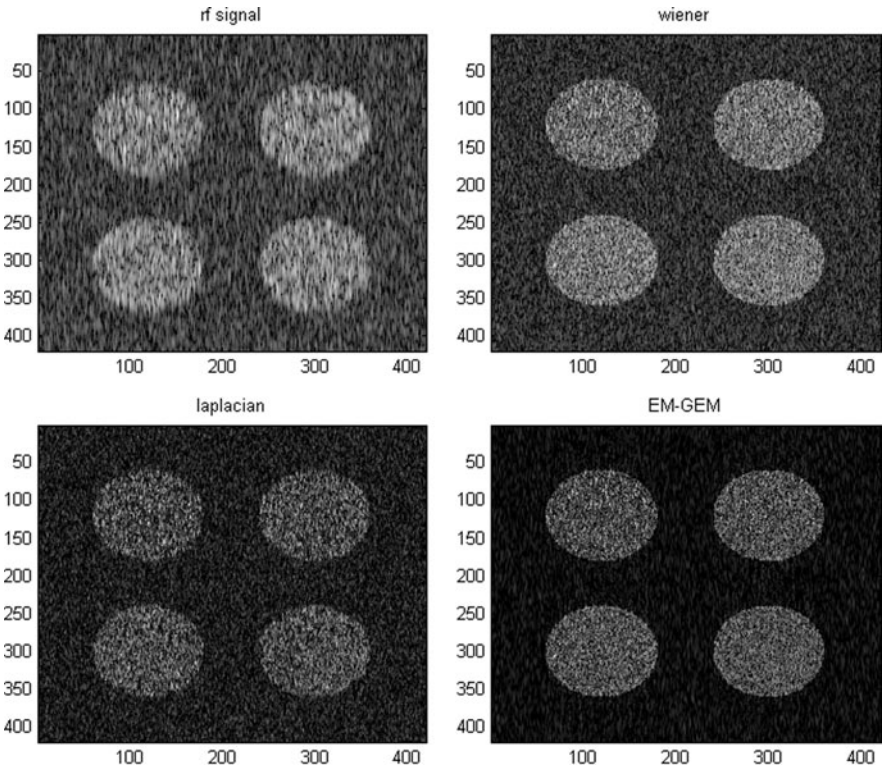

Fig. 4 Frame processed with different deconvolution algorithms

data a segmentation step must be introduced. Further investigation on segmentation modality is required and the possibility of updating regions definition with a segmentation step within the EM algorithm could be investigated.

References

1. Jensen, J.A.: A model for the propagation and scattering of ultrasound in tissue. J. Acoust. Soc. Am. **89**(1), 182–190 (1991)
2. Kay, S.M.: Fundamentals of Statistical Signal Processing: Estimation Theory. Prentice- Hall Signal Processing Series (1993)
3. Taxt, T., Strand, J.: Two-dimensional noise-robust blind deconvolution of ultrasound images. IEEE Trans. Ultrason. Ferroelect. Freq. Contr. **48**(4), 861–866 (2001)
4. Michailovich, O.V., Adam, D.: Robust estimation of ultrasound pulses using outlier-resistant de-noising. IEEE Trans. Med. Imag. **22**(3), 368–381 (2003)
5. Katsaggelos, A.K.: Digital Image Restoration. Springer Series in Information Sciences, pp. 143–176 (1991)
6. Jirik, R., Taxt, T.: Two-dimensional blind bayesian deconvolution of medical ultrasound images. IEEE Trans. Ultrason. Ferroelect. Freq. Contr. **55**(10), 2140–2153 (2008)

7. Ng, J., Prager, R., Kingsbury, N., Treece, G., Gee, A.: Wavelet restoration of medical pulse-echo ultrasound images in an EM framework. IEEE Trans. Ultrason. Ferroelect. Freq. Contr. **54**(3), 550–568 (2007)
8. Michailovich, O.V., Adam, D.: A novel approach to 2-D blind deconvolution problem in medical ultrasound. IEEE Trans. Med. Imag. **24**(1), 86–104 (2005)
9. Bernard, O., Touil, B., D'Hooge, J., Friboulet, D.: Statistical modeling of the radio-frequency signal for partially- and fully-developed speckle based on a generalized gaussian model with application to echocardiography. IEEE Trans. Ultrason. Ferroelect. Freq. Contr. **54**(10), 2189–2194 (2007)
10. Donoho, D.: On minimum entropy deconvolution. In: Findley, D.F. (ed.) Applied Time Series Analysis II, pp. 565–608. Academic Press, New York (1981)
11. Dempster, A.P., Laird, N.M., Rubin, D.B.: Maximum likelihood from incomplete data via EM algorithm. J. Roy. Stat. Soc. B **39**(1), 1–38 (1997)
12. Blimes, J.A.: A Gentle Tutorial on the EM algorithm and its applications to parameter estimation for Gaussian Mixtures and Hidden Markov Models. http://crow.ee.washington.edu/people/bulyko/papers/em.pdf
13. Bioucas-Dias, J.M.: Bayesian wavelet-based image deconvolution: A GEM algorithm exploiting a class of heavy-tailed priors. IEEE Trans. Image Process. **15**(4), 937–951 (2006)
14. Figueiredo, M.A., Nowak, R.D.: An EM algorithm for wavelet-based image restoration. IEEE Trans. Image Process. **12**(8), 906–916 (2003)
15. Varanasi, M.K., Aazhang, B.: Parametric generalized Gaussian density estimation. J. Acoust. Soc. Am. **86**(4), 1404–1415 (1989)

Particle Swarm Optimization for In Vivo 3D Ultrasound Volume Registration

U.Z. Ijaz, R.W. Prager, A.H. Gee, and G.M. Treece

Abstract As three-dimensional (3D) ultrasound is becoming more and more popular, there has been increased interest in using a position sensor to track the trajectory of the 3D ultrasound probe during the scan. One application is the improvement of image quality by fusion of multiple scans from different orientations. With a position sensor mounted on the probe, the clinicians face additional difficulties, for example, maintaining a line-of-sight between the sensor and the reference point. Therefore, the objective of this paper is to register the volumes using an automatic image-based registration technique. In this paper, we employ the particle swarm optimization (PSO) technique to calculate the six rigid-body transformation parameters (three for translation and three for rotation) between successive volumes of 3D ultrasound data. We obtain vertical and horizontal slices through the acquired volumes and then use an intensity-based similarity measure as a fitness function for each particle. We considered various settings in the PSO to find a set of parameters to give the best convergence. We found the visually acceptable registration when the initial orientations of the particles were confined to within a few degrees of the orientations obtained from position sensor.

Keywords Image registration · 3D ultrasound · Particle swarm optimizer

1 Introduction

The PSO is a population based stochastic optimization technique in which the system is initialized with a population of random solutions and then searches for optima by updating generations of solutions. Each particle keeps track of its coordinate in the problem space and also keeps track of the best solution in the population. In the literature, it has been successfully used on ultrasound data for classification [1], segmentation [2] and image registration [3].

The work of Wachowiak [3] considers registration of only single slice biomedical images to 3D volumes (stored in voxel arrays). The PSO algorithm is modified with evolutionary strategies and genetic algorithm operators and three PSO variants out of a set of eight were shown to perform reasonably well. Since at the same time, the

U.Z. Ijaz (✉)
Department of Engineering, University of Cambridge, CB2 1PZ Cambridge, UK
e-mail: uzi20@eng.cam.ac.uk

M.P. André et al. (eds.), *Acoustical Imaging*, Acoustical Imaging 30,
DOI 10.1007/978-90-481-3255-3_39,

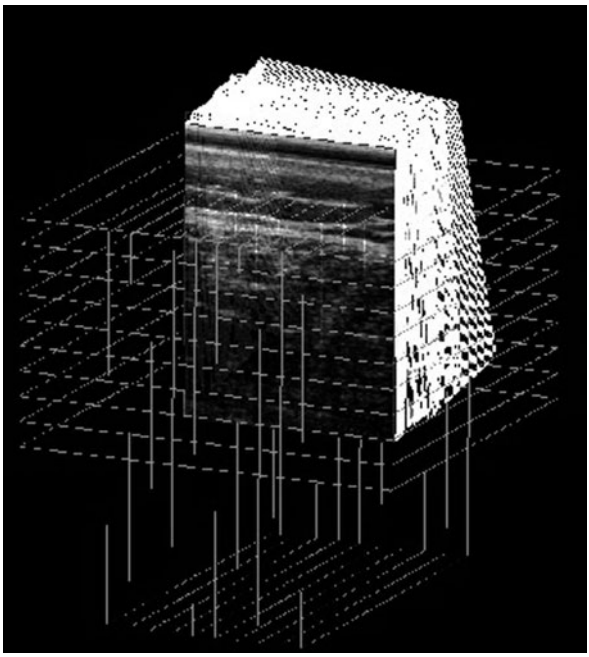

Fig. 1 Horizontal and vertical image pair boundaries are shown for two overlapping volumes obtained using a mechanically-swept 3D US probe. The probe is positioned at the top and the direction of insonification is downwards. The dimensions of the image slices are 470 × 470 pixels, whereas the dimensions of the B-scans are 266 × 353 pixels. The scale is 0.01 cm/pixel

convergence analysis and parameter selection of PSO was made available by Trelea [4], our focus in this paper is to use optimum parameters in a light-weight PSO without introducing unnecessary complexities. Our focus is particularly on improving the robustness and accuracy of the PSO while increasing the convergence rate. Rather than considering a voxel representation of the ultrasound volumes, we generate resliced image pairs (Fig. 1) from the volumes and use a similarity measure on these 2D images to calculate the fitness function for the PSO. We use Kolmogorov's distance [5] as a similarity measure. Additionally, we apply a Gaussian smoothing filter before calculating the similarity measure. Our approach is described in the following section.

2 Particle Swarm Optimization

The PSO algorithm [6] is described as

$$\mathbf{v}_{k+1} = a\mathbf{v}_k + b_1\mathbf{r}_1 \otimes (\mathbf{p}_1 - \mathbf{x}_k) + b_2\mathbf{r}_2 \otimes (\mathbf{p}_2 - \mathbf{x}_k) \tag{1}$$

$$\mathbf{x}_{k+1} = c\mathbf{x}_k + d\mathbf{v}_{k+1} \tag{2}$$

The symbol $\otimes$ denotes element-by-element vector multiplication. Equation (1) is used to calculate the velocity $\mathbf{v}_{k+1}$ of the particle $\mathbf{x}_k$ according to its current position

from its own best experience $\mathbf{p}_1$ and the group's best experience $\mathbf{p}_2$. b_1 and b_2 represent the strength of attraction towards the particle's own best experience and the group's best experience, respectively. The momentum factor a is used to control the influence of the previous history of velocities on the current velocity. The particle moves toward a new position according to Equation (2) affected by the coefficients c and d. Here, $\mathbf{x}_k$ represents the six rigid-body transformation parameters (i.e., three for translation and three for rotation) for the source volume. The random numbers $\mathbf{r}_1$ and $\mathbf{r}_2$ are introduced for good state space exploration. They are usually selected in the range [0, 1].

Trelea [4] performed the theoretical analysis of PSO, by considering the deterministic version in one-dimension. It was obtained by setting the random numbers to their expected values, i.e. $r_1 = r_2 = \frac{1}{2}$. Also, Equation (1) is simplified by considering $b = \frac{b_1+b_2}{2}$, and $p = \frac{b_1}{b_1+b_2}p_1 + \frac{b_2}{b_1+b_2}p_2$. The newly introduced coefficient b represents the average of the personal and social attraction coefficients b_1 and b_2. The attraction point p is the weighted average of p_1 and p_2. The PSO algorithm can then be written in compact form as:

$$\mathbf{y}_{k+1} = \mathbf{A}\mathbf{y}_k + \mathbf{B}p \tag{3}$$

with

$$\mathbf{y}_k = \begin{bmatrix} x_k \\ v_k \end{bmatrix},\ \mathbf{A} = \begin{bmatrix} 1-b & a \\ -b & a \end{bmatrix},\ \mathbf{B} = \begin{bmatrix} b \\ b \end{bmatrix} \tag{4}$$

By considering $c = d = 1$, it was found that the PSO is convergent if the following set of conditions is satisfied:

$$a < 1,\ b > 0,\ 2a - b + 2 > 0 \tag{5}$$

This convergent domain in the (a, b) plane is a triangle and for any initial position and velocity, the particle will converge to its equilibrium if and only if the algorithm parameters are selected inside the triangle. In that case both eigenvalues of matrix $\mathbf{A}$ will have magnitude less than 1. In the case when the eigenvalues of the matrix $\mathbf{A}$ are complex, the particle exhibits harmonic oscillations around the equilibrium point, which is equivalent to

$$a^2 + b^2 - 2ab - 2a - 2b + 1 < 0 \tag{6}$$

The particle may also exhibit zigzagging behavior around the equilibrium point when at least one of the eigenvalues of $\mathbf{A}$, whether real or complex, has a negative real part. This is equivalent to

$$a < 0 \text{ or } a - b + 1 < 0 \tag{7}$$

The PSO algorithm is initialized with random position estimates of the source volume while keeping the target volume stationary. At each iteration, the similarity

Table 1 Parameters used in the PSO for 3D ultrasound volume registration

Method	a	B
Trelea parameters set 1	0.6	0.7
Trelea parameters set 2	0.727	1.494
Harmonic oscillations with slow convergence	0.9	0.1
Harmonic oscillations with quick convergence	0.7	0.3
Harmonic oscillations with zigzagging	0.9	3.0
Nonoscillatory convergence	0.1	0.1
Symmetric zigzagging	0.1	2.1
Asymmetric zigzagging	−0.7	0.5

measure is used to update the best position $\mathbf{p}_1$ of each particle if it scores higher than the similarity measure for the previous best position. Similarly, at every iteration, the globally best position in the whole swarm $\mathbf{p}_2$ is also saved. While using the PSO algorithm for registration of US volumes, one has to be careful in choosing the PSO parameters so that a balance between the exploitation and exploration abilities of the particle is maintained. For this reason, we have considered different parameter settings in the PSO as shown in Table 1. Based on an empirical study performed by Trelea [4] for different cost functionals, it was found that the Trelea parameter sets 1 and 2 perform best.

3 Results

Ultrasound data was recorded with a GE RSP6-12 mechanically swept 3D probe interfaced to a Dynamic Imaging Diasus ultrasound machine. The depth setting was 3 cm with a single focus at 1.5 cm. Analogue RF echo signals were digitized after receive focusing and time-gain compensation, but before log-compression and envelope detection, using a Gage Compuscope CS14200 14-bit digitizer (http://www.gage-applied.com). The RF data was then converted to B-scan images using Stradwin software (http://mi.eng.cam.ac.uk/~rwp/stradwin/).

For each recorded dataset, two volumes were acquired with the probe held stationary during each sweep and repositioned by hand in between with some amount of overlap between the two volumes. Each B-scan's position and orientation was recorded using a Northern Digital Polaris optical tracking system (http://www.ndigital.com), with spatial and temporal calibration performed according to the techniques in Treece [7]. Each acquired volume consisted of 50 frames of data swept over 10 degrees. A total of 10 *in vivo* datasets were acquired consisting of 4 scans of the neck, 3 scans of the abdomen and 3 scans of calf muscles, respectively.

We tested different parameter settings for the PSO using Kolmogorov's distance. We used Calf3 to compare the performance of the PSO with different parameters. The PSO was initialized randomly near the position sensor solution. The PSO was run 5 times for each parameter set shown in Table 1 and the data was recorded. The mean and coefficient of variability of the globally best position in the whole swarm

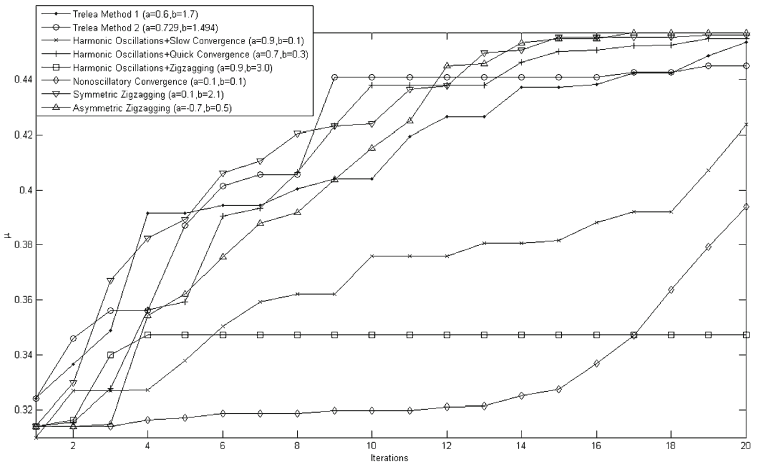

(a) Mean of the globally best position in the whole swarm

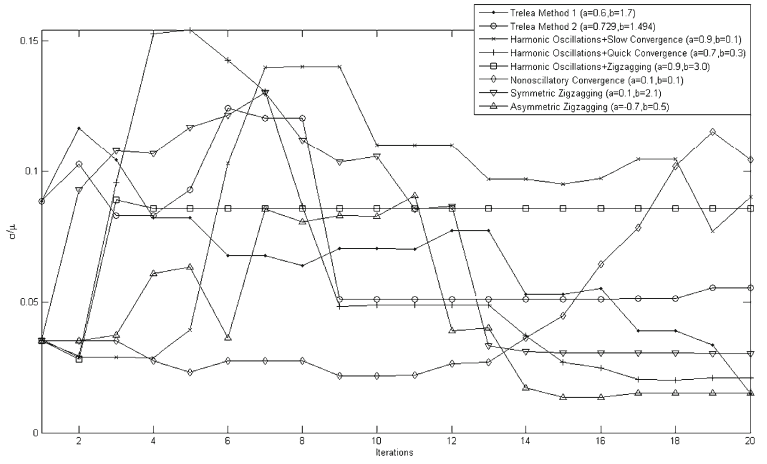

(b) Coefficient of variability of the globally best position in the whole swarm

Fig. 2 Statistical analysis of PSO for Calf3 using Kolmogorov's distance, 128 histogram bin, 10 vertical and 10 horizontal image pairs, 15 × 15 Gaussian smoothing with a standard deviation of 1 pixel, 20 iterations, and 30 particles. For each parameter setting, PSO was run 5 times

are shown in Fig. 2. The coefficient of variability is a normalized measure of dispersion of a probability distribution defined as the ratio of the standard deviation to the mean. Distributions with coefficient of variability less than 1 are considered low-variance. It can be seen that the PSO converges much faster with Trelea parameter set 2. It can also be seen that the behavior of the PSO with Trelea parameter set 2 is reasonably predictable as the coefficient of variability is less than 0.1 in later iterations. We then used PSO with Trelea parameter set 2 on different datasets. The translation parameters were initialized randomly between –1.5 and 1.5 cm from the zero offset (with centers aligned). For orientation parameters, we tried various

initialization ranges starting from values within 1 degree of the known orientation (obtained from the position sensor) and increasing to 2 degrees. While almost every attempt to register each dataset with 1-degree initialization range was successful, it was only possible to register each dataset with 2-degree initialization range after several attempts. The automatic registration results for the whole dataset are shown in Figs. 3, 4 and 5. The beneficial effect of compounding can be seen in Fig. 6 where the boundary of the artery is well-defined. It should be noted that the algorithm also achieved the visually acceptable registration with an overlap as little as 46% (Neck4 dataset) which in the previous study [3] was almost impossible.

For datasets with very little rotation between the volumes (for example Neck1 and Neck4 datasets), we therefore expect our PSO approach to be successful. However, while 1.5 cm translation may be an acceptable limit in clinical practice, the 1–2 degree limitation on rotation is more restrictive. This may require further research into alternative methods to determine the orientation or investigation of other optimization strategies. The overall registration time for the PSO depends on several factors including the number of particles, their initializations, the number of

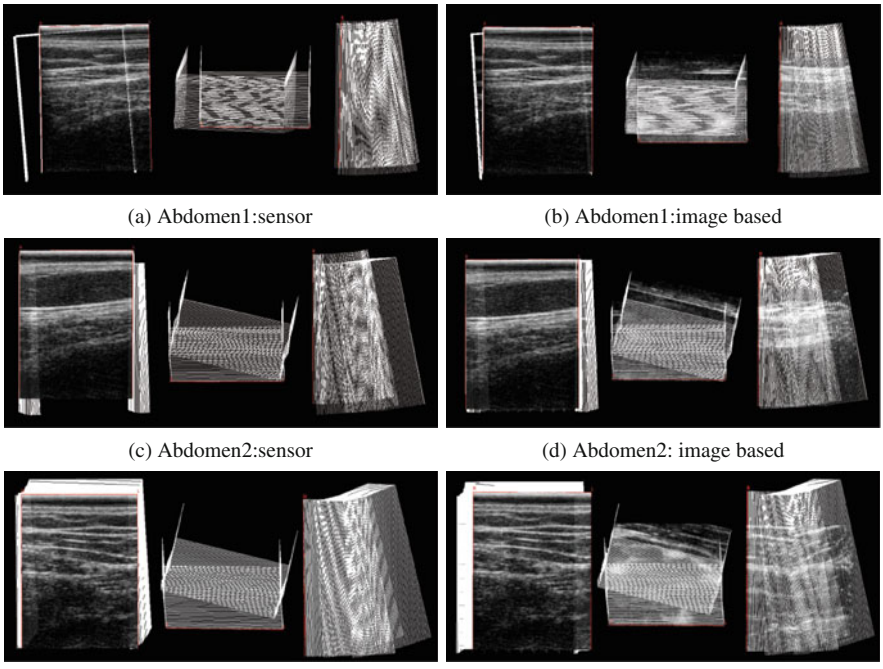

(a) Abdomen1:sensor (b) Abdomen1:image based

(c) Abdomen2:sensor (d) Abdomen2: image based

(e) Abdomen3:sensor (f) Abdomen3:image based

Fig. 3 Automatic registration results for Abdomen datasets using PSO with Kolmogorov's distance, Trelea parameter set 2, 32 histogram bins, 10 vertical and 10 horizontal image pairs, 15×15 Gaussian smoothing filter with a standard deviation of 1 pixel

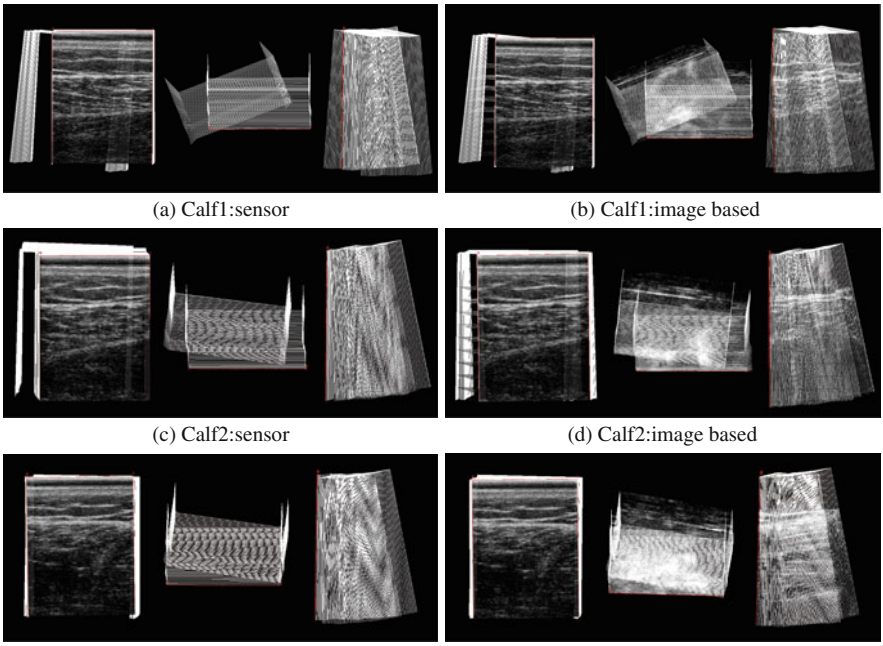

(a) Calf1:sensor (b) Calf1:image based

(c) Calf2:sensor (d) Calf2:image based

(e) Calf3:sensor (f) Calf3:image based

Fig. 4 Automatic registration results for Calf datasets using PSO with the same parameters as used in Fig. 3

image pairs, and whether we apply the smoothing filter. As a result, it is not possible to specify an overall time for the algorithm to run. However, depending on the configuration, we were able to register the datasets in 11–17 min.

4 Conclusions

The goal of this study was to assess several parameters in the particle swarm optimization to register 3D ultrasound volumes obtained from a mechanically-swept probe. By employing Trelea parameter set 2 and Kolmogorov's distance in the particle swarm optimization, we were able to find visually acceptable registration results for all the *in vivo* datasets even when they had very little overlap. The limitation of this approach is that the convergence of the algorithm depends on the initial orientation information.

Acknowledgements This work is supported by the UK Engineering and Physical Sciences Research Council (EPSRC) grant EP/F016476/1.

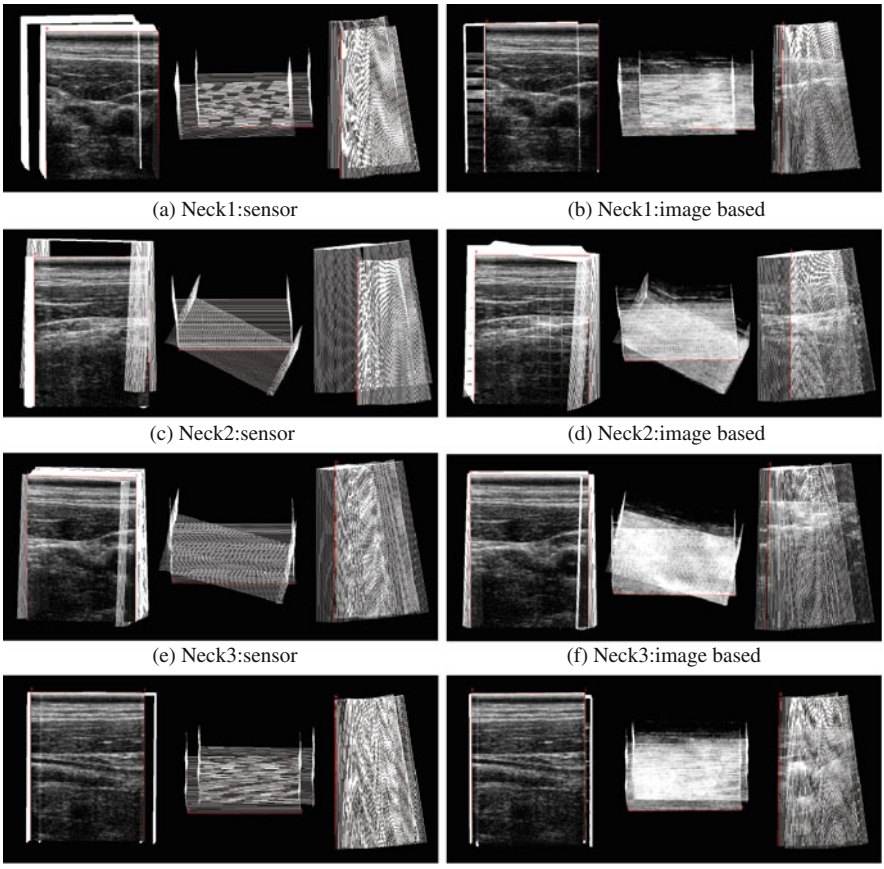

(a) Neck1:sensor (b) Neck1:image based

(c) Neck2:sensor (d) Neck2:image based

(e) Neck3:sensor (f) Neck3:image based

(g) Neck4:sensor (h) Neck4:image based

Fig. 5 Automatic registration results for Neck datasets using PSO with the same parameters as used in Fig. 3

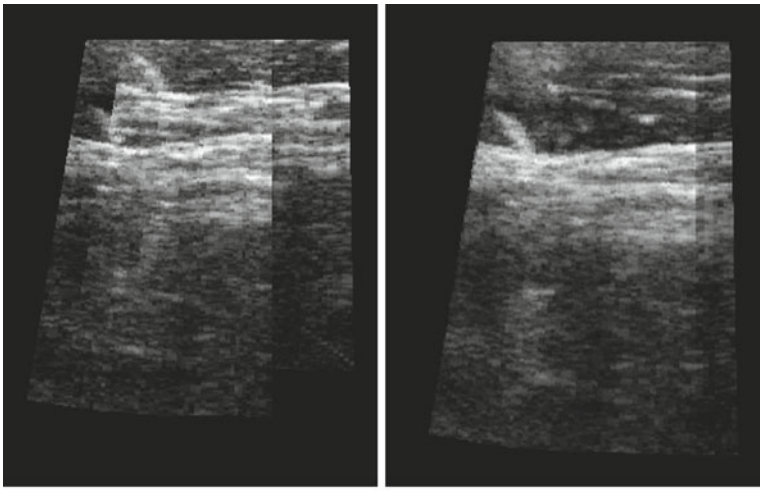

(a) Neck2:sensor (b) Neck2:image based

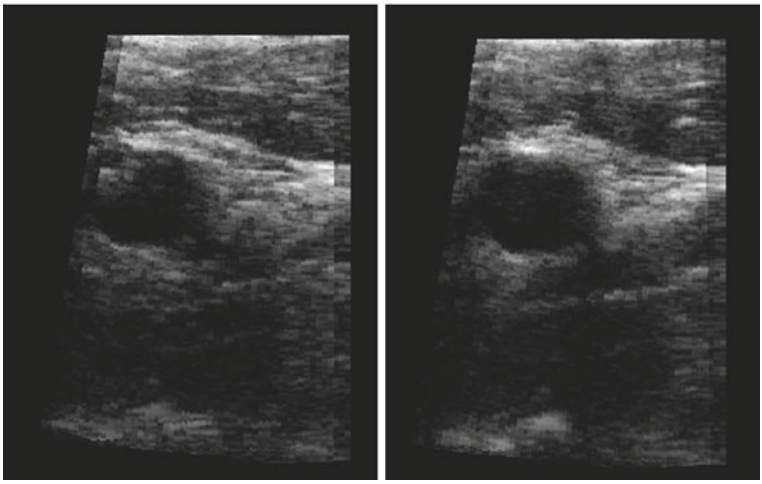

(c) Neck3:sensor (d) Neck3:image based

Fig. 6 Automatic registration results displaying the fifth vertical slice for both sensor-based and PSO based aligned data

References

1. Chang, C.–Y., Lai, C.–T., Chen, S.–J.: Applying the particle swarm optimization and Boltzmann function for feature selection and classification of lymph node in ultrasound images. In: Proceedings of the 2008 Eighth International Conference on Intelligent System Design and Applications, pp. 55–60 (2008)
2. Guo, Y., Cheng, H.D., Tian, J., Zhang, Y.: A novel approach to breast ultrasound image segmentation based on the characteristics of breast tissue and particle swarm optimization. In: Proceedings of the 11th Joint Conference on Information Science (2008)

3. Wachowiak, M.P., Smolíková, R., Zheng, Y., Zurada, J.M., Elmaghraby, A.S.: An approach to multimodal biomedical image registration utilizing particle swarm optimization. IEEE Trans. Evol. Comput. **8**(3), 289–301 (2004)
4. Trelea, I.C.: The particle swarm optimization algorithm: convergence analysis and parameter selection. Information Process. Lett. **85**, 317–325 (2003)
5. Zhang, Z.: Estimating mutual information via Kolmogorov distance. IEEE Trans. Inform. Theor. **53**(9), 3280–3282 (2007)
6. Kennedy, J., Eberhart, R.C.: Particle swarm optimization. In: Proceedings of IEEE International Conference on Neural Networks, pp. 1942–1948 (1995)
7. Treece, G.M., Prager, R.W., Gee, A.H., Berman, L.: Correction of probe pressure artifacts in freehand 3D ultrasound. Medical Image Analysis **6**(3), 199–214 (2002)

Gauge Theory Formulation of Acoustical Imaging

W.S. Gan

Abstract There are many similarities between electromagnetic waves and sound waves. Maxwell's equation is the oldest gauge theory. Three main aspects of gauge theory are considered: (1) symmetries, (2) gauge invariance, (3) covariant form of the wave equation. Two of my discoveries mentioned in my earlier papers are revisited here: (1) symmetries of velocity field and stress field in the acoustic equations of motion, (2) a new stress field equation. Higher order Christoffel equation and higher order stress field equation are derived. The latter will form the basis of a new form of imaging the nonlinear elasticity imaging. The advantages of the application of gauge theory to acoustical imaging are mentioned.

Keywords Lagrangian · Symmetries · Gauge invariance · Stress field · Elasticity · Action principle · Stiffness · Vector potential · Covariant form · Wave equation

1 Introduction

Gauge theory is a very sophisticated theory that can be applied to both the classical and quantum regimes of physics. The oldest and first gauge theory is Maxwell's equations. In recent years, gauge theory has been successfully applied to the standard model of particle physics, grand unification of forces of nature, spontaneous broken symmetry in superconductivity, etc. There are many similarities between acoustic waves and electromagnetic waves; therefore, gauge field theory may be a more accurate way to address problems of nonlinear acoustical imaging in view of the complexity of the problem. In this paper we focus especially on elasticity imaging. Gauge theory is used here to find the root of elasticity and to develop a new form of imaging, the nonlinear elasticity imaging, which is harmonic imaging but extracting the elastic properties of the sound wave.

W.S. Gan (✉)
Acoustical Technologies Singapore Pte Ltd, 637722 Singapore
e-mail: wsgan@acousticaltechnologies.com

M.P. André et al. (eds.), *Acoustical Imaging*, Acoustical Imaging 30,
DOI 10.1007/978-90-481-3255-3_40,

2 Derivation of Acoustic Equations of Motion Using Lagrangian Mechanics

In order to apply gauge fields, the Lagrangian of the world must be invariant under local gauge invariant. For the acoustic field, which fills the space, the action is the space-time integral of the Lagrangian density which must be Lorentz invariant and gauge invariant.

The fundamental object in the acoustic field is the gauge field $\vec{A}$. The action principle is used here. The complete world action is

$$S = \int L dx \tag{1}$$

where L = Lagrangian density,

$$= \frac{1}{2}\rho_0 u^2 - \rho_0 W \tag{2}$$

where W = specific strain energy of the elastic body per unit mass, ρ_0 constant density in the reference (unstressed configuration), u=particle velocity.

The equation of motion is

$$\rho_0 \frac{\partial^2 u}{\partial t^2} = \nabla_a \vec{T} \tag{3}$$

where u=displacement, $\vec{T}$=stress tensor that can be obtained from the Lagrangian equation for L with [1]

$$\vec{T} = \rho_0 \frac{\partial W}{\partial \vec{F}} \tag{4}$$

in which $\vec{F}$=deformation gradient tensor defined as

$$\vec{F} = \frac{\partial x}{\partial a} \tag{5}$$

where x=current coordinate of a particle and is displaced from its original or natural position $\vec{a}$ by the displacement

$$\vec{u} = \vec{x} - \vec{a} \tag{6}$$

and $\vec{u}$ =material coordinate.

Equation (2) is applicable to both the linear and nonlinear cases.

3 Analogies Between Acoustic Waves and Electromagnetic Waves

There are many analogies between acoustic waves and electromagnetic waves. A well-known characteristic is that of diffraction in which Huygens principle is used for diffraction of both acoustic waves and electromagnetic waves. As a result, both

the Kirchhoff diffraction formula and Helmholtz wave equation can be applied to sound waves and electromagnetic waves. Maxwell's equations are the oldest gauge theory. Presentation of the acoustic field equation in a form analogous to Maxwell's equations simplifies the task of transferring to acoustics the analytical methodology and techniques that have been applied to problems of this kind in electromagnetism. The strongest analogy with the electromagnetic equations is obtained by taking $\vec{T}$, the stress field as equivalent to $\vec{E}$ the magnetic field and $\vec{V}$ the velocity field as equivalent to $\vec{H}$ the magnetic field.

4 Principle of Acoustical Imaging

The most fundamental problem in acoustical imaging is the propagation of sound waves in solids. This will be concerned with the diffraction, scattering and transmission of sound waves in solids and the recording of sound waves after its emergence from the solids. This will carry information on the interior of the solids and will constitute the first part of the acoustical imaging system known as the forward process if one is to use the diffraction tomography imaging methodology. The second part of the imaging system will be the reconstruction to obtain image from the information recorded during the forward process. Usually rigorous diffraction theory for the interaction of ultrasound with solids results in nonlinear partial differential equations. In this paper we reformulate the theory of acoustical imaging using gauge theory, which will address large amplitude sound waves and uses the vector potential that is the gauge field to investigate the root of elasticity.

For the forward problem, we will use the higher order stress field equation given in Equation (4) as a starting point and this will be the basis of the new field of nonlinear elasticity imaging.

5 Gauge Principle and Symmetries

The gauge principle requires a physical system under investigation to have symmetry, i.e., a gauge invariance, an invariance with respect to a certain group of transformation. For acoustics we first study gauge symmetry of propagating fields with respect to translational transformations. The formulations started from a Galilean-invariant Lagrangian of a system of point masses that is known to have global gauge symmetries with respect to both translational and rotation [2]. It was then extended to a continuous material characterized with elastic energy. In addition to the global symmetry, local gauge invariance of a Lagrangian is required for such a continuous field. Thus, the convective derivative of continuum mechanics, (i.e., the Lagrangian derivative) is identified as a covariant derivative that is a building block in the framework of gauge theory. Based on this, the appropriate Lagrangian is derived for the propagation of the sound wave and the equation of motion is derived from the action principle. In acoustics the mass density can be regarded as a gauge field and it is analogous to the charge density of electromagnetic theory.

The particles are driven in motion by gauge potentials defined conjugatively with the fields. The equation of continuity is given as constraint for the variation and can be derived from the action principle.

For a continuous distribution of mass, using the action principle the action Λ is given by

$$\Lambda = \int L(x, v) d^3x \tag{7}$$

where L(x, v) =Lagrangian density where x = $X_a^k(t)$ and $v = V^k = \partial_t X_a^k(t)$ (k=1, 2, 3).

For global gauge invariance,

$$\delta A = \int \delta L(x, v) d^3x \tag{8}$$

In the local gauge invariance or local transformation, the variation field depends on the time t and space point x and the variation $\delta A = \int \delta L d^3x$ does not vanish in general.

According to gauge principle, the non-vanishing of δA means that a new field G must be taken into account in order to achieve local gauge invariance of the Lagrangian A. To that end, we will have to replace the partial time derivative ∂t by a covariance derivative D_t where the derivative D_t is defined by

$$D_t := \partial t + G \tag{9}$$

As long as the field $x = X_a^k(t)$ and $v = \partial_t x_a^k = X_a^k$ satisfy the Euler Lagrange equation, one can construct a conserved quantity T defined by

$$T = x_t^k \left(\frac{\partial L}{\partial x_t^k} \right) - L \tag{10}$$

The quantity T is equivalent to the component T_o^o of the energy-momentum tensor, i.e., the energy density. In sound propagation in solids, the symmetries to be investigated are translation symmetry and rotation symmetry.

6 Discoveries of Symmetries in Acoustic Equations of Motion and a New Stress Field Equation

Gauge theory involves invariance or symmetries and symmetries could lead to simplification of complexity of the problem and in obtaining the solutions [3].

The Newtonian mechanics gives rise to the following linear acoustic equation of motion for the case of small amplitudes of sound wave:

$$\nabla \cdot \vec{T} = \rho \frac{\partial^2 \vec{u}}{\partial t^2} - \vec{F} \tag{11}$$

where $\vec{T}$=stress field, $\vec{u}$ =particle displacement and $\vec{F}$=body force.

In electrodynamics, it is much simpler to eliminate unnecessary variables by manipulating the field equation in symbolic form where wave equations for the $\vec{E}$ or $\vec{H}$ fields are derived by eliminating either $\vec{E}$ or $\vec{H}$ from Maxwell's equations. In the same way, acoustic wave equation can be derived by eliminating either $\vec{T}$ or $\vec{v}$ from the acoustic field equation. Usually the stress field $\vec{T}$ is eliminated since it involves six field components rather than three. After the elimination of the $\vec{T}$ the Christoffel equation for sound propagation in solid is obtained which is in terms of $\vec{v}$ only.

Here we eliminate the velocity field $\vec{v}$. The lossless acoustic field equations are

$$\nabla \cdot \vec{T} = \rho \frac{\partial \vec{v}}{\partial t} - \vec{F} \tag{12}$$

$$\nabla_s \cdot \vec{v} = \vec{S} : \frac{\partial \vec{T}}{\partial t} \tag{13}$$

where $\vec{T}$=stress field, $\vec{S}$= stiffness, $\vec{F}$=body forces and ρ= density

In a source-free region, $\vec{F}$=0. From (13) taking only the x direction of propagation:

$$\frac{\partial v}{\partial x} = \vec{S} : \frac{\partial \vec{T}}{\partial t} \tag{14}$$

Differentiating (14) with respect to t:

$$\frac{\partial^2 v}{\partial t \partial x} = \vec{S} : \frac{\partial^2 \vec{T}}{\partial t^2} \tag{15}$$

Differentiating (12) with respect to x:

$$\frac{\partial}{\partial x}\left(\nabla \cdot \vec{T}\right) = \rho \frac{\partial^2 \vec{v}}{\partial x \partial t} \tag{16}$$

Since $\dfrac{\partial^2 \vec{v}}{\partial x \partial t} = \dfrac{\partial^2 \vec{v}}{\partial t \partial x}$, we have

$$\rho \vec{S} := \frac{\partial^2 \vec{T}}{\partial t^2} = \frac{\partial}{\partial x}\left(\nabla \cdot \vec{T}\right) \tag{17}$$

If we consider the simplified situation that a compression stress T, applied along the x-axis and inside an isotropic medium then

$$\rho \vec{S} : \frac{\partial^2 \vec{T}}{\partial t^2} = \frac{\partial^2 \vec{T}}{\partial x^2} \tag{18}$$

Thus we obtain a homogeneous wave equation in the stress field $\vec{T}$. Now the Christoffel equation can be written as

$$\rho \frac{\partial^2 \vec{v}}{\partial t^2} = \nabla \cdot c : \nabla_s \vec{v} \tag{19}$$

Since $\frac{1}{c} = S$ where c=compliance, we have

$$\rho \vec{S} : \frac{\partial^2 \vec{v}}{\partial t^2} = \frac{\partial^2 \vec{v}}{\partial x^2} \tag{20}$$

where only the x component of the velocity field $\vec{v}$ is taken. So we find that Equations (17) and (20) represent a set of homogenous wave equations symmetrical in $\vec{T}$ and $\vec{v}$ respectively. This set of symmetrical equation can be similarly extended to the y direction and z direction.

The stress field equation will have tremendous potential in application. For instance it forms the basis of stress imaging, a form of elasticity imaging. The properties of symmetries in acoustic field equation can have application in obtaining accurate analytical solution for complex wave equations as it can reduce the degree of complexity.

7 Derivation of the Higher Order Christoffel Equation and Higher Order Stress Field Equation

These are for the case of large amplitude sound waves. The higher order acoustic equation of motion has been obtained by Thurston and Shapiro [4] as

$$\rho \ddot{u} = \frac{\partial^2 u}{\partial x^2} \left[M_2 + M_3 \frac{\partial u}{\partial x} + M_4 \left(\frac{\partial u}{\partial x} \right)^2 + \ldots \right] \tag{21}$$

where M_2=linear combination of second-order elastic coefficients, M_3=linear combination of second and third-order coefficients, M_4= linear combination of second, third, fourth-order coefficients.

First order equation of motion gives

$$\nabla \cdot \vec{T} = -\rho \omega^2 \vec{u} \tag{22}$$

Therefore

$$u = -\frac{1}{\rho \omega^2} \frac{\partial \vec{T}}{\partial x} \tag{23}$$

Substitution of Equation (24) into Equation (22) and with simplification we obtain the higher order acoustic stress field equation:

$$\rho \frac{\partial^2 T}{\partial t^2} = \frac{\partial^2 T}{\partial x^2} \left[M_2 + M_3 \left(-\frac{1}{\rho \omega^2} \right) \frac{\partial^2 T}{\partial x^2} + M_4 \left(-\frac{1}{\rho \omega^2} \right)^2 \left(\frac{\partial^2 T}{\partial x^2} \right)^2 + \ldots \right] \tag{24}$$

Using the symmetries properties of $\vec{T}$ and $\vec{v}$ in the acoustic field equations, we obtain the higher order Christoffel equation as

$$\rho\frac{\partial^2 v}{\partial t^2} = \frac{\partial^2 v}{\partial x^2}\left[M_2 + M_3\left(-\frac{1}{\rho\omega^2}\right)\frac{\partial^2 v}{\partial x^2} + M_4\left(-\frac{1}{\rho\omega^2}\right)^2\left(\frac{\partial^2 v}{\partial x^2}\right)^2 + \ldots\right] \quad (25)$$

The higher order stress field equation will form the basis of a new form of acoustical imaging, the nonlinear elasticity imaging.

8 Advantages of the Application of Gauge Theory to Acoustical Imaging

The gauge theory helps us to find the root of elasticity. Elasticity is expressed in terms of stress and strains. Strain is the effect of stress and hence stress field is the key parameter. In gauge theory, we introduce vector potential, the most important gauge field. We can express stress field in terms of the vector potential as

$$\vec{T} = -\nabla\phi - \frac{\partial\vec{A}}{\partial t} \quad (26)$$

where ϕ =scalar potential.

For nonlinear stress field, a quadratic term in $\vec{A}$ will be added onto the above equation. The study of the root of elasticity, the solution of the nonlinear stress equation and nonlinear elasticity imaging will be the topics of the next generation nonlinear acoustics.

Another advantage of the application of gauge theory to acoustics will be the differentiation of strong and weak acoustic signals in terms of acoustic field strength and not in terms of sound wave amplitude. Thus we redefine nonlinear acoustics as study of sound wave with strong field strength.

The third advantage of the application of gauge theory to acoustics is the representation of the acoustic equation of motion in covariant form or the 4 vector form. This is the ultimate form of the acoustic wave equation in terms of the acoustic field strength.

$$F^{\mu\nu} = \partial^\mu A^\nu - \partial^\nu A^\mu \quad (27)$$

This will enable the inclusion of special relativity or Lorentz transformation. The fourth advantage is that gauge theory can address the body force term in the acoustic equation of motion. The body force will include the gravitational force. With action principle one can address the interaction of field and material.

References

1. Landau, L.D., Lifshitz, E.M.: Theory of elasticity, 3rd edn. Pergamon Press, Oxford (1986)
2. Landau, L.D., Lifshitz, E.M.: Mechanics, 3rd edn. Pergamon Press, Oxford (1976)
3. Gan, W.S.: Proceedings of 15th International Congress On Sound and Vibration, 6-10 July 2008, Daejeon, Korea (2008)
4. Thurston, R.N., Shapiro, M.J.: J. Acoust. Soc. Am. **41**, 1112 (1967)

High Resolution Pulse Compression Imaging Using Super Resolution FM-Chirp Correlation Method (SCM)

M. Fujiwara, K. Okubo, and N. Tagawa

Abstract This study addresses the issue of the super-resolution pulse compression technique (PCT) for ultrasound imaging. Time resolution of multiple ultrasonic echoes using the FM-Chirp PCT is limited by the bandwidth of the sweep-frequency. That is, the resolution depends on the sharpness of auto-correlation function. We propose the Super resolution FM-Chirp correlation Method (SCM) and evaluate its performance. This method is based on the multiple signal classification (MUSIC) algorithm. Our simulations were made for the model assuming multiple signals reflected from some scatterers. We confirmed that SCM detects time delay of complicated reflected signals successfully with high resolution.

Keywords FM-chirp · Pulse compression · Multiple signal classification (MUSIC) algorithm · Super resolution profile

1 Introduction

In recent years, there has been growing demand for ultrasound imaging in clinical diagnosis. Ultrasound diagnosis requires images with high resolution and high SN ratio. For this purpose, narrow and high-power pulses must be transmitted. However, transmission has restrictions on power consumption in a living body. Therefore, the pulse-compression technique (PCT) [1, 2] has been introduced. In the meantime, the resolution of the PCT is not sufficient, when multiple scatterers are in close formation. The resolution depends on the sharpness of auto-correlation function of transmitted signal. Therefore, for the frequency modulation (FM)-Chirp PCT, time resolution of echoes is limited by the band width of the sweep-frequency.

In this paper, in order to improve the resolution performance, we propose the Super resolution FM-Chirp correlation Method (SCM). The SCM is based on the multiple signal classification (MUSIC) algorithm [3, 4]. The outline of SCM is as follows. The FM-chirp signal with a certain center frequency is transmitted several times and the echo signals are received respectively. The same process is repeated with a slight variation of the center frequency. Analytic signals are obtained from the compressed echo signals by applying an orthogonal detector. Subsequently, the

M. Fujiwara (✉)
Faculty of System Design, Tokyo Metropolitan University, 191-0065 Tokyo, Japan

M.P. André et al. (eds.), *Acoustical Imaging*, Acoustical Imaging 30,
DOI 10.1007/978-90-481-3255-3_41,

covariance matrix of the above analytic signals, which is averaged with respect to the center frequency, is calculated using the analytic signals. By solving the general Eigenvalue problem defined by the covariance matrix calculated above and the matrix calculated using the envelope of the auto-correlation function of the transmitted signal, we can get the resulted signals with higher resolution than the original compressed echo signals.

Another Super resolution Pulse-compression Method (SPM) [5, 6] has been proposed in order to analyze the multipath structure of the radio wave propagation. The SPM uses pseudo noise (PN) sequence (M- sequence) for the transmitted signal. The PCT with FM-chirp signal, however, could be more convenient for the ultrasonic measurement.

Simulations were conducted using FM-up-chirp signals having a bandwidth of 2 MHz, a center frequency of 10 MHz, a pulse width of 1.75 μs. The SCM was applied to model signals assuming multiple scatterers. We confirmed that the SCM can generate the sufficiently high resolution signal through the simulation.

2 SCM Algorithm

We review how SCM employs the MUSIC to improve the resolution. If a signal $u(t)$ is transmitted, we receive multiple echo signals $y(t)$ from scatterers. $y(t)$ is expressed in terms of the convolution of the transmitted signal and the impulse response $h(t)$. Assuming that received echo signal is composed of multiple echo signals from unknown D scatterers with different delay times, an impulse response $h(t)$ given by

$$h(t) = \sum_{i=l}^{D} h_i \delta(t - \tau_i), \tag{1}$$

where $\{hi\}$ is a set of complex amplitudes, $\{\tau i\}$ is a set of propagation delays that we want to estimate. $\delta(\bullet)$ is the Dirac delta function.

Considering multipath propagation, the correlator output $z(\zeta)$ is the superposition of scaled copies of the chirp signal's auto-correlation. As a result, it is difficult to separate echoes having small delay between each other. Assuming the transmission of a chirp signal (linear FM) $s(t)$, the cross-correlation of echo with $s(t)$ is

$$v(\zeta) = \sum_{i=l}^{D} h_i r(\zeta - \tau_i) + \eta(\zeta). \tag{2}$$

where $r(\zeta)$ is the autocorrelation function of the chirp signal, and $\eta(\zeta)$ is the cross-correlation of the chirp signal and the noise process $n(\zeta)$. Here, we assume that $n(\zeta)$ is generated by Gaussian white noise process with variance equal to σ^2.

The received signal is described in the base-band by

$$z(\zeta) = \sum_{i=l}^{D} h_i e^{-j\omega_0 \tau_i} r(\zeta - \tau_i) + \mu(\zeta). \tag{3}$$

Next, we define a delay profile vector $z(\zeta) = [z(\zeta_1)z(\zeta_2)\cdots z(\zeta_M)]^T$. With the steering vector, $r(\tau) = [r(\zeta_1 - \tau)r(\zeta_2 - \tau)\cdots r(\zeta_M - \tau)]^T$, $z(\zeta)$ may be expressed as

$$z = \sum_{i=l}^{D} h_i e^{-j\omega_0\tau_i}\mathbf{r}(\tau_i) + \boldsymbol{\mu}. \tag{4}$$

The steering vector $\mathbf{r}(\tau)$ may be calculated for any, since the auto-correlation function $r(\cdot)$ is known.

In terms of the array manifold matrix $\boldsymbol{\Gamma} = [r(\tau_1)r(\tau_2)\cdots r(\tau_D)]$ and the gain vector $\mathbf{g} = [h_1 e^{j\omega_0\tau_1} h_2 e^{j\omega_0\tau_2}\cdots h_D e^{j\omega_0\tau_{D1}}]^T$, the delay profile vector takes the form

$$\mathbf{z} = \boldsymbol{\Gamma}\mathbf{g} + \boldsymbol{\mu}, \tag{5}$$

The covariance matrix $R = E\{zz^H\}$ can also be written as

$$R = \sum_{i,j} E\{h_i h_j^*\}e^{j\omega_0(\tau_j - \tau_i)}r(\tau_i)r(\tau_j)^H + E\{vv^H\}. \tag{6}$$

The following form of $\mathbf{R}$ will be useful:

$$\mathbf{R} = \boldsymbol{\Gamma}\mathbf{G}\boldsymbol{\Gamma}^H + \mathbf{R}_n, \tag{7}$$

where $\mathbf{G}$ is the covariance matrix $\mathbf{G} = E\{gg^H\}$. The noise correlation matrix $\mathbf{R}_n$ could be expressed as $\mathbf{R}n = E\{\mu\mu^H\} = \sigma^2\mathbf{R}_0$, where $\mathbf{R}_0$ is a Hermitian matrix. The SCM relies on a generalized Eigen-decomposition of the following form

$$\mathbf{R}\mathbf{e}_i = \lambda_i\mathbf{R}_0\mathbf{e}_i; \quad i = 1, 2, \cdots, M. \tag{8}$$

We must consider the validity of the following assumptions: the number of samples at the correlator output is greater than the number of paths (i.e., $M>D$) and the columns of $\boldsymbol{\Gamma}$ are linearly independent.

In order to estimate the delay, we use a measure of orthogonality of the steering vectors to $\{e_i\}_{i=D+1}^{M}$. Accordingly, a super-resolution profile S(τ) based on MUSIC algorithm may be defined as

$$S(\tau) = \frac{r(\tau)^H R_0^{-1} r(\tau)}{\sum_{i=D+1}^{M} \left|r(\tau)^H e_i\right|^2}, \tag{9}$$

where $r(\tau)^H R_0^{-1} r(\tau)$ is the normalizing factor, which is particular to the present method.

In experimental applications of the SCM, the minimum description length criterion is used to estimate D. Accurate second-moment estimates of the delay profile vector have been achieved by repeating the transmission of $S(\tau)$ to obtain N snapshots of the delay profile vector $\mathbf{z}$. Under these conditions, the covariance matrix can be estimated as

$$\hat{R} = \frac{1}{N}\sum_{j=1}^{N} z(j)z(j)^H. \tag{10}$$

In those equation, $z(j)$ is obtained by the jth snapshot.

Moreover, we must discuss the extensions to frequency smoothing. If the rank of matrix $\mathbf{R} - \mathbf{R}_n = \mathbf{\Gamma G \Gamma}$ reduces to unity due to the coherence, the SCM would not be able to separate correctly a noise subspace and a signal subspace. This work adopts the linear frequency smoothing to increase the rank of this matrix. We are showing the dependence on the transmission center frequency

$$R(\omega_k) = \sum_{i,j} E\{h_i h_j^*\} e^{j\omega_k(\tau_j - \tau_i)} r(\tau_i) r(\tau_j)^H + E\{v_k {v_k}^H\}. \tag{11}$$

In order to make $\mathbf{\Gamma G \Gamma}^H$ full rank, one may use a linear center frequency smoothing and transmit the FM chirp signal $s(t)$ with a certain bandwidth. We might then estimate covariance matrices and compute the average

$$\bar{R} = \frac{1}{K}\sum_{k=-K/2}^{K/2} \hat{R}(\omega_k), \tag{12}$$

where $\hat{R}(\omega_k)$ is the covariance matrix estimated with the snapshots at center frequency ω_k, and $\bar{\mathbf{R}}$ is the K-step frequency smoothed estimated covariance matrix. The carrier center frequencies set is given by $\{\omega_k = \omega_0 + k\Delta\omega \in \omega_0 - (K/2)\ \Delta\omega; \ldots; \omega_0; \omega_0 + \Delta\omega; \ldots; \omega_0 + (K/2)\Delta\omega;\}$.

3 Simulation Results and Discussions

For the one scatterer model, the computer simulation on resolution improvement by the super-resolution technique proposed in this paper was carried out. The broken line and the dotted line of Fig. 1 indicate the PCT results of the transmitted chirp signals with 2 MHz (from 9 to 11 MHz) and 4 MHz (from 8 to 12 MHz) bandwidth respectively, where the Hamming window is used in the time region. In Fig. 1, exact position of an echo signal is on 3.62 μs and σ is assumed 1% of the transmitted signal amplitude. The solid line shows the result of the high resolution estimation by the super-resolution profile $S(\tau)$. Here, we assume that the sweep frequency band is limited from 8 to 12 MHz and the sampling frequency is 100 MHz. We set 2 MHz bandwidth of each chirp signal and $\Delta\omega = 40$ kHz in the linear frequency smoothing of the transmitted signal shown in Fig. 2. That is, $\bar{R}$ of Equation (12) is calculated by averaging 49 data with $N = 10$ snapshots. Figure 1 illustrates that the proposed technique successfully give high resolution rather than the conventional PCT method. The half-value width of $S(\tau)$ becomes much narrower.

Next, the model of two scatterers is considered. The simulation result in this model is shown in Fig. 3. We assume that the amplitudes of two echo signals are

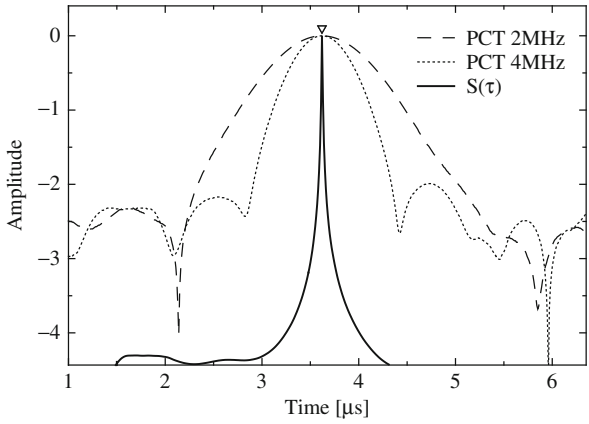

Fig. 1 S(τ) estimation for one scatterer model

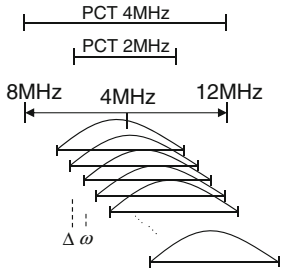

Fig. 2 Schematic diagram of linear frequency smoothing

identical. Delay time difference $\Delta\tau$ of two echo signals is set as follows: (a) $\Delta\tau =$ 300 ns, (b) $\Delta\tau = 200$ ns, (c) $\Delta\tau = 110$ ns and (d) $\Delta\tau = 100$ ns. The vertical axis of Fig. 3 is normalized by the maximum value of each signal. The solid line represents $S(\tau)$, and the broken line and the dotted line indicate the PCT results of 2 and 4 MHz bandwidth, respectively. Other conditions are identical to those of Fig. 1. $S(\tau)$ can successfully separate two echo signals in Fig. 3a, b. However, it can't sufficiently classify the signals in Fig. 3c, d. On the other hand, the PCT results can't separate the signals in all cases. Here, in the case of Fig. 3d, $\Delta\tau =$ 100 ns is corresponding to 10 sampling points. This seems to be because the phase information obtained by the smoothing was not sufficient.

Finally, consider the six scatterers model. Figure 4 shows the comparison between two conventional PCT results and Super-resolution profile. The exact positions of an echo signals are $\tau 1 = 3.62$ μs, $\tau 2 = 4.3$ μs, $\tau 3 = 4.54$ μs, $\tau 4 = 5.12$ μs, $\tau 5 = 5.74$ μs and $\tau 6 = 6.8$ μs. The relative amplitude values are –4.44 dB, –1.94 dB, –4.44 dB, –4.44 dB, –7.96 dB and –7.96 dB, respectively. Other conditions are identical to those of Figs. 1 and 3.

Figure 4 indicates that we can make the estimation of the position successfully using $S(\tau)$, where PCT results estimate spurious peaks. However, the estimation of the amplitude value is not sufficient. In this estimation, snapshot number and the

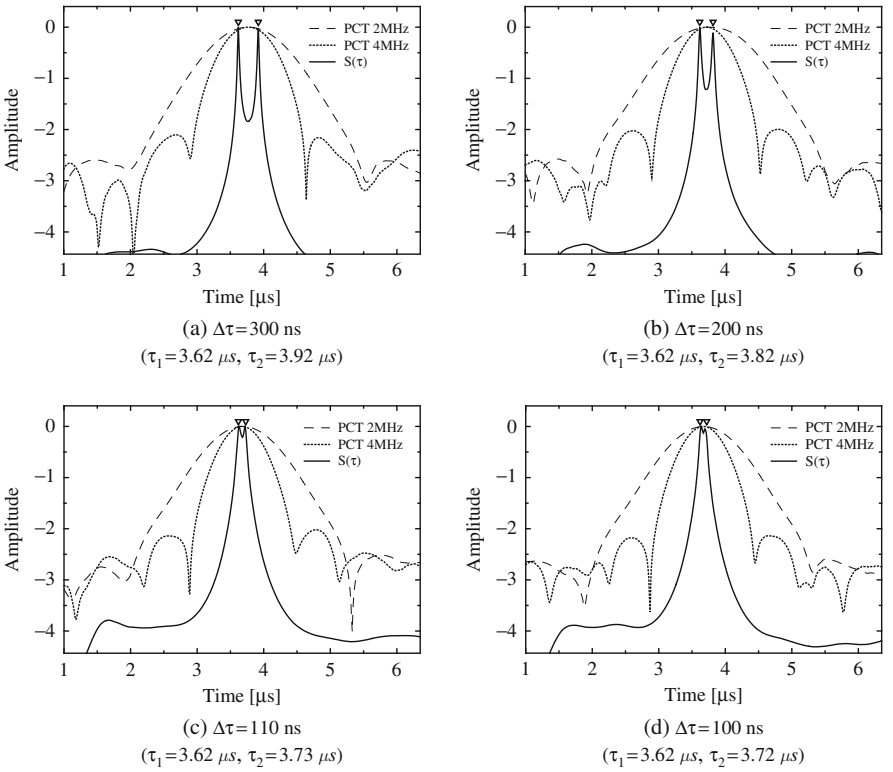

(a) $\Delta\tau$=300 ns (τ_1=3.62 μs, τ_2=3.92 μs)

(b) $\Delta\tau$=200 ns (τ_1=3.62 μs, τ_2=3.82 μs)

(c) $\Delta\tau$=110 ns (τ_1=3.62 μs, τ_2=3.73 μs)

(d) $\Delta\tau$=100 ns (τ_1=3.62 μs, τ_2=3.72 μs)

Fig. 3 The comparison of PCT and S(τ)

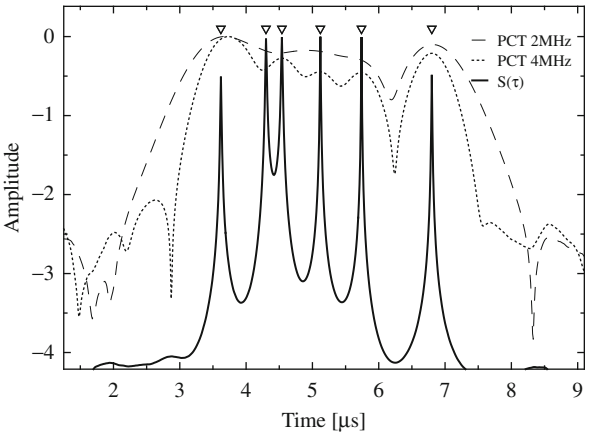

Fig. 4 The comparison of PCT and SDP in case of six scatterers

number of frequency smoothing are 10 and 49, respectively. We might require more snapshots and frequency smoothing to succeed the estimation of the amplitude.

We adopt the linear frequency smoothing in which we change the center frequency of chirp signal linearly just like step. However, we might need to apply

random frequency smoothing for more efficient estimation, in which one changes the center frequency at random in the region of the limited frequency band.

4 Conclusions

In this paper, we proposed the super resolution FM-chirp correlation method (SCM) which is based on PCT and MUSIC algorithm. We analyzed the performance of the proposed method for estimation of time delays of multiple echo signals. As a result, we clarified that super-resolution profile achieve the higher resolution estimation than conventional PCT. The peaks given by the SCM algorithm are not spurious, at the high SN ratio.

This method uses the frequency smoothing with the snapshot to obtain much phase information. This paper treats the linear frequency smoothing in which we change the center frequency of chirp signal linearly just like step. For more efficient estimation, we might need to adopt random frequency smoothing. Moreover, we may require many snapshots and frequency smoothing to succeed the estimation of the amplitude.

However, the SCM seems to give us the extremely high resolution for ultrasound imaging, rather than the PCT. In the near future, we intend to make an examination including actual vibrator system and the application to the imaging will be carried out.

References

1. Klauder, J.R., et al.: Bell Syst. Tech. J. **XXXIX**, 745–808 (1960)
2. Cox, D.: IEEE Trans. Antenn. Propag. **20**, 625–635 (1972)
3. Schmidt, R.O., et al.: IEEE Trans. Antenn. Propag. **AP-34**, 276–280 (1986)
4. Kikuma, N.: Adaptive Signal Processing with Array. Antenna (in Japanese). Science and Technology Publishing Company, Tokyo (1998)
5. Manabe, T., et al.: IEEE Trans. Acoust. Propag. **40**, 500–509 (1992)
6. Bouchereau, F., Brady, D., Lanzl, C.: IEEE Trans. Signal Process. **49**, 938–949 (2001)

Medical Ultrasound Image Deconvolution

Sensitivity to Speed of Sound and Capability of Speed Estimation

H.-C. Shin, R.W. Prager, H. Gomersall, N. Kingsbury, G.M. Treece, and A.H. Gee

Abstract In medical pulse-echo ultrasound imaging, a constant sound speed of 1,540 m/s in soft tissues is assumed. When the actual speed is different the mismatch can lead to image distortions. Even if the assumed speed is correct, ultrasound images can be difficult to interpret due to image blurring and the presence of speckle. However, this can be improved by non-blind deconvolution if the point-spread function (PSF) is known. In clinical applications a sufficiently accurate estimate of the PSF is difficult to obtain because of the unknown properties (including speed of sound) of soft tissues. In this paper, we address two topics: first, we explore the sensitivity of our deconvolution algorithm to variations in the speed of sound in the tissue; second, we extend our deconvolution algorithm to enable it to adapt to (and estimate) an unknown sound speed. In the first topic, the results reveal that the deconvolution output is sufficiently sensitive to the accuracy of the sound speed that the speed itself can be estimated using deconvolution. However, qualitative assessment suggests that we may not need the exact speed of sound for successful deconvolution so long as the assumed speed does not deviate significantly from the true value. In the second topic, the goal is gradually to adapt the assumed sound speed to improve the deconvolution and eventually estimate the true sound speed. We tested our algorithm with *in vitro* phantoms where the estimation error was found to be $+0.01 \pm 0.60\%$ (mean $\pm$ standard deviation). In addition to the speed estimation itself, our method has also proved capable of producing better restoration of the ultrasound images than deconvolution by an assumed speed of 1,540 m/s when this assumption is significantly in error.

Keywords Medical ultrasound image · Non-blind deconvolution · Point-spread function · Complex wavelet transform · Speed of sound · Sound speed estimation

1 Introduction

Ultrasound scanners are widely used in medical imaging applications, but they produce images which are often hard to interpret due to blurring and the presence

H.-C. Shin (✉)
Department of Engineering, University of Cambridge, CB2 1PZ Cambridge, UK
e-mail: hs338@eng.cam.ac.uk

M.P. André et al. (eds.), *Acoustical Imaging*, Acoustical Imaging 30,
DOI 10.1007/978-90-481-3255-3_42,

of speckle. In this regard, there has been considerable research in the restoration of ultrasound images. Recently we proposed a novel non-blind deconvolution algorithm which is capable of taking into account the structure of ultrasound speckle [1, 2]. However, the algorithm requires prior knowledge of the point-spread function (PSF). There is always uncertainty in an *in vivo* PSF because of variability in the overlying tissue. Variability in the speed of sound is the main concern in this paper. The first part of the paper is devoted to establishing the sensitivity of the deconvolution algorithm to variations in the sound speed.

In the second part of the paper, we apply our findings from the sensitivity analysis to the estimation of the average sound speed in homogenous tissue. Robinson et al. [3] carried out an extensive review of pulse-echo sound-speed estimation techniques. Most of the reviewed methods were designed to involve several apertures of ultrasound transducers: one for transmission and the rest for reception. A precise geometric relation needs to be established between transducers and scanned regions of interest. In some methods, a pair of crystal elements in a single linear array can replace a pair of transducer apertures. They may however suffer a low signal-to-noise ratio. However, there were a couple of methods which worked using a single transducer aperture, but they required the acquisition of multiple scans. In this paper, we propose a speed estimation method based on ultrasound data collected by a single scan using a single transducer array without the special equipment that other estimation methods usually involve. This is made possible using a deconvolution framework. Aside from estimating the value of the average speed, we also put an equal emphasis on the concurrent correction of the sound speed in the restored ultrasound images.

2 Deconvolution Algorithm

2.1 Ultrasound Image Formation

Linearity is generally assumed in pulse-echo medical ultrasound imaging, therefore the ultrasound image formation process can be mathematically described in the vector-matrix notation ($\mathbf{y} = \mathbf{H}\mathbf{x} + \mathbf{n}$). Here, a complex random variable $\mathbf{x}$ is the reflectivity function; $\mathbf{y}$ is the complex analytic baseband counterpart of the measured ultrasound image. Potential measurement errors are taken into account as complex additive white Gaussian noise ($\mathbf{n}$). $\mathbf{H}$ is a block diagonal matrix along the lateral and elevational dimensions. Each block matrix maps from the axial depth dimension to the time domain at a given lateral and elevational position. Our deconvolution algorithm is capable of dealing with the blurring operator ($\mathbf{H}$) as spatially shift dependent in the axial direction and shift invariant along the lateral and elevational dimensions. The complete details of the formulation can be found in our previous publication [2].

2.2 Deconvolution Under an EM Framework

The goal of the deconvolution algorithm is to estimate the reflectivity function ($\mathbf{x}$) from a noisy and blurred image ($\mathbf{y}$). Our algorithm operates in a Bayesian context.

The de-blurring procedure tends to be ill-posed, so we incorporate regularization in a maximum *a posteriori* framework (MAP) with a prior on the reflectivity function ($\mathbf{x}$). With a Gaussian prior, the problem involves Wiener deconvolution. Instead of using a prior for the entire tissue, we model the tissue reflectivity as the product ($\mathbf{x} = \mathbf{S}\mathbf{w}$) of microscopically randomized fluctuations ($\mathbf{w}$) and a macroscopically smooth echogenicity map ($\mathbf{S}$). We adopt an alternating strategy: we estimate $\mathbf{x}$ through Wiener deconvolution when $\mathbf{S}$ is known; we estimate $\mathbf{S}$ by removing the multiplicative noise $\mathbf{w}$ when $\mathbf{x}$ is known. This iterative solution is conducted in an expectation-maximization (EM) framework. For de-noising, we adopt a complex wavelet transform (DT-CWT) based algorithm to separate $\mathbf{x}$ into its $\mathbf{S}$ and $\mathbf{w}$ components. The complete details of the deconvolution algorithm in an EM framework can be found in our previous publication.

2.3 Estimation of the PSF

To estimate the PSF for our non-blind algorithm, we use the Field II simulation program [4]. We calculate the PSF according to what would happen in a largely homogeneous medium: the delay profiles for the transmit and receive apertures are fixed assuming the speed of sound is 1,540 m/s, while the actual speed of sound in the hypothetical medium can be varied to have any speed.

2.4 Reference Deconvolution

A two-dimensional simulated phantom was created with five cysts whose geometry is shown in Fig. 1. This five-cyst image corresponds to an echogenicity map ($\mathbf{S}$) characterized by macroscopically smooth features. The reflectivity within each scatterer type is then randomized by incorporating a Gaussian distribution which represents microscopic fluctuations ($\mathbf{w}$). The reference reflectivity function ($\mathbf{x}$) is shown in Fig. 1a.

We carry out blurring by calculating a forward convolution of the image in Fig. 1a with the PSF evaluated by Field II. Then, zero-mean white Gaussian noise ($\mathbf{n}$) is

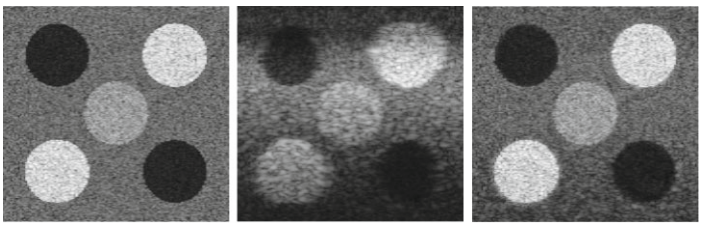

Fig. 1 Reference images for the simulation with the sound speed of 1,540 m/s. (**a**) reflectivity function, (**b**) blurred image with additive white Gaussian noise of SNR = 40 dB, (**c**) reference deconvolution. The dynamic range of the logarithmically compressed images is 60 dB

added to the simulated ultrasound image which is shown in Fig. 1b. The lateral focus of the ultrasound image is at the centre of the middle cyst.

Finally, the reference blurred and noisy image is restored using our deconvolution algorithm. The same PSF used for the blurring was used in the deconvolution. The result is shown in Fig. 1c.

3 Sensitivity to Speed of Sound

3.1 Quantification Metrics for PSF Sensitivity

The performance of the deconvolution algorithm may be quantified by using the improvement in the signal-to-noise ratio (ISNR). This is defined as:

$$\text{linear ISNR} = 20 \log_{10} \frac{\|\mathbf{y} - \mathbf{x}\|}{\|\hat{\mathbf{x}} - \mathbf{x}\|} \tag{1}$$

where $\mathbf{x}$ is the true reflectivity function as shown in Fig. 1a, $\mathbf{y}$ is the blurred baseband image from the ultrasonic transducer, as shown in Fig. 1b, and $\hat{\mathbf{x}}$ is an estimate of the reflectivity function obtained from the deconvolution process as shown in Fig. 1c. Here we mean "linear" in the sense that the arguments of the final logarithm are linear.

We have discovered that the linear ISNR is not adequate to assess *perceptual* differences between cases with different speeds of sound. The drawback of the linear ISNR is mainly because discrepancies in dark cysts are not weighted as much as those in bright cysts. Hence, a modified metric is required to weight the errors in dark cysts as much as those in bright cysts. Therefore, we have replaced linear arguments with logarithmic ones:

$$\log \text{ ISNR} = 20 \log_{10} \frac{\|\log|\mathbf{y}| - \log|\mathbf{x}|\|}{\|\log|\hat{\mathbf{x}}| - \log|\mathbf{x}|\|} \tag{2}$$

3.2 Simulation of Sound Speed Variation

There is considerable uncertainty in the speed of sound when scanning *in vivo*, both in terms of the absolute speed and its homogeneity. We investigate, however, the sensitivity only under the assumption of a homogeneous medium. The speed of sound is varied uniformly throughout the tissue away from the reference 1,540 m/s, while holding all the other PSF parameters constant.

Figure 2 shows the effect of the sound speed variation. The panel (a) illustrates quantitative metrics. The panels (b) and (c) show examples of restored images. The image (b), having the speed variation of –30 m/s, was chosen so that it looks perceptually similar to the reference deconvolution in Fig. 1c, and therefore its result may still be considered useful when the true solution is not known *a priori*. The image (c) is a case of an extreme speed error of –200 m/s.

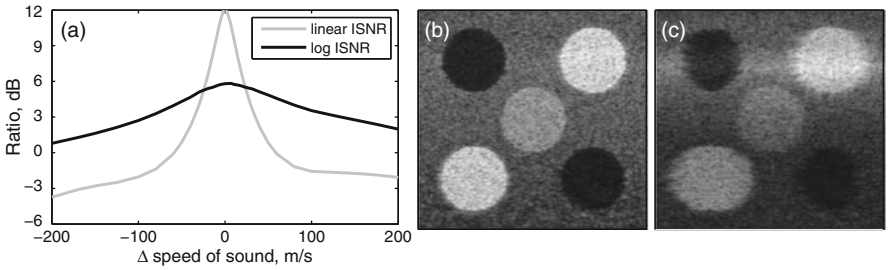

Fig. 2 Effect of the uniform variation in the sound speed in simulated soft tissue: ISNR measures and examples of restored images. The reference speed is 1,540 m/s. (**b**) Δ speed = –30 m/s; (**c**) Δ speed = –200 m/s

The linear and log ISNR values at the reference speed of 1,540 m/s are +12.04 and +5.81 dB, respectively. Those in image (b) are +4.02 and +5.10 dB, respectively, and in image (c) –3.74 and +0.79 dB. It is observed that log ISNRs are better suited to represent human perception than linear ISNRs.

The findings in this section emphasize that there is some tolerance to error in sound speed when the restoration is evaluated through human vision. Therefore we may not need the exact sound speed for the deconvolution. On the other hand, we learned that the results can always be differentiated when they are evaluated through metrics.

The complete analysis of sensitivity to other PSF parameters can be found in our previous publication [5].

4 Capability of Speed Estimation

4.1 Correlation Metric

The overall strategy of our speed estimation method is to run multiple deconvolutions using PSFs with different speeds and to pick the speed which produces the best restoration. Therefore, a metric capable of determining the best outcome is as crucial as the non-blind deconvolution algorithm itself. To this effect, the autocorrelation is calculated along the lateral line at each axial depth and then a summation is made of the magnitude of all the coefficients of the correlation. To produce a single-valued representation, another summation was taken of this value for all axial depths.

4.2 Method

We adopted an optimization procedure to find the correct speed of sound, using Newton's method for optimization. First, we start with three initial PSFs defined by three different speeds of sound. A single iteration of our EM deconvolution

algorithm is carried out with these three PSFs. The correlation metrics of the three deconvolutions are calculated, and a one-dimensional quadratic equation is formulated based on the three pairs of sound speeds and corresponding correlation metrics: $f(x) = Ax^2 + Bx + C$, where x is the speed of sound, $f(x)$ the correlation metric, and A, B, C coefficients. Then, the next search speed is determined from the first and second derivatives of $f(x)$:

$$x_{i+1} = x_i - \alpha \frac{f'(x_i)}{f''(x_i)} \tag{3}$$

Here, x_{i+1} is the new estimate, x_i the speed having the lowest correlation among three guesses at the i-th EM iteration, and α the step size ($0 < \alpha \leq 1$). Among the three guesses at each EM iteration, we discard the speed with the highest correlation measure, and then move on to the next iteration step of the EM deconvolution algorithm with three speeds: two being retained from the previous iteration step and the third being the new estimate (x_{i+1}). This procedure is repeated for a fixed number of EM iterations or until a termination criterion is met. One essential aspect is that the EM stage of the newly-found speed should be updated to the same level as the other two speeds. This update routine makes the algorithm slower in each successive iteration.

4.3 In vitro *Phantom*

We produced ultrasound tissue-mimicking phantoms locally by mixing agar powder, scatterers and water. Their speeds of sound are not known *a priori,* and hence they were measured independently using a time-of-flight method. Wires were stretched inside the phantom. An A-line with the least blurring of the target wires was chosen. Then, its envelope was detected with the Hilbert transform and the peaks from the wires were selected as known reference locations. The travelling time was worked out from the number of samples between wire peaks. The sound speed between the wires is then easily estimated.

Different ultrasound data sets were acquired using our iterative deconvolution method for in-house phantoms with various lateral focal depths and different wire alignments. The overall estimation error is +0.01 ± 0.60% (mean ± standard deviation) when the time-of-flight based estimation is taken as a reference. Anderson and Trahey quoted errors of –0.05 ± 0.44% and –0.18 ± 0.52% for phantoms composed of sponge and agar-graphite, respectively (see Table 1 in their publication) [6], by using a method based on the one-way geometric delay pattern on individual elements of a transducer array.

In Fig. 3, we provide a further enhanced image after restoration with an optimum speed of sound. Panel (a) is the original ultrasound image acquired by an ultrasound system whose beamforming delay is set to the sound speed of 1,540 m/s. Panel (b) is the restoration using the correct speed of sound (1,455.89 m/s) estimated by our algorithm. Panel (c) is the restored image using a PSF based on a sound speed of

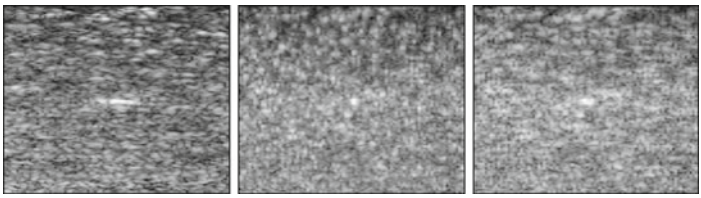

Fig. 3 Ultrasound images of an *in vitro* in-house phantom: (**a**) original ultrasound image, (**b**) deconvolution by an optimum speed of 1,455.89 m/s, (**c**) deconvolution by a nominal speed of 1,540 m/s. The dynamic range of the logarithmically compressed images is 60 dB. Note the change in the size of the wire image in the centre of each B-scan

1,540 m/s. It is observed that the deconvolution image based on the correct speed of sound has the best quality; the wire at the centre is restored to its original circular shape, and speckle in the surrounding area is of finer resolution than in the other two cases.

5 Conclusions

We studied the sensitivity of our deconvolution algorithm to variations in sound speed. We found that deconvolutions based on PSFs derived from slightly incorrect sound speeds gave visually acceptable results. However we also found that the errors in these images could be detected using numerical metrics.

Using a correlation metric, we have developed an iterative algorithm based on deconvolution capable of estimating the average speed of ultrasound in homogeneous tissues. The estimation error of our approach for *in vitro* in-house phantoms was found to be $+0.01 \pm 0.60\%$ (mean $\pm$ standard deviation) based on the speeds measured independently by the time-of-flight method.

In addition to the speed estimation itself, our algorithm has also simultaneously produced a better restoration of the ultrasound images than deconvolution by an assumed speed of 1,540 m/s, when this assumption is incorrect.

Acknowledgements This work is supported by the UK Engineering and Physical Sciences Research Council (EPSRC) grant EP/E007112/1.

References

1. Ng, J., Prager, R., Kingsbury, N., Treece, G., Gee, A.: Modeling ultrasound imaging as a linear shift-variant system. IEEE Trans. Ultrason. Ferroelect. Freq. Contr. **53**(3), 549–563 (2006)
2. Ng, J., Prager, R., Kingsbury, N., Treece, G., Gee, A.: Wavelet restoration of medical pulse-echo ultrasound images in an EM framework. IEEE Trans. Ultrason. Ferroelect. Freq. Contr. **54**(3), 550–568 (2007)
3. Robinson, D.E., Ophir, J., Wilson, L.S., Chen, C.F.: Pulse-echo ultrasound speed measurements: Progress and prospects. Ultrasound Med. Biol. **17**(6), 633–646 (1991)

4. Jensen, J.: Field: A program for simulating ultrasound systems. Med. Biol. Eng. Comput. Paper presented at the 10th Nordic-Baltic Conference on Biomedical Imaging, vol. 34, pp. 351–353 (1996)
5. Shin, H.-C., Prager, R., Ng, J., Gomersall, H., Kingsbury, N., Treece, G., Gee, A.: Sensitivity to point-spread function parameters in medical ultrasound image deconvolution. Ultrasonics **49**(3), 344–357 (2008)
6. Anderson, M.E., McKeag, M.S., Trahey, G.E.: The impact of sound speed errors on medical ultrasound imaging. J. Acoust. Soc. Am. **107**(6), 3540–3548 (2000)

Numerical and Physical Modeling of Tomography Process Based on Third-Order Nonlinear Acoustical Effects

V.A. Burov, A.A. Shmelev, and O.D. Rumyantseva

Abstract The possibility of using the nonlinear effect of the third-order combination wave generation is analyzed for medical diagnostic goals. This effect makes it possible to implement the tomography of a spatial distribution of acoustical nonlinear parameters. The contributions by both purely third-order nonlinear scattering and twofold second-order nonlinear scattering are estimated. These two parallel developing competitive processes create two similar effects, which, however, can be separated. The two-dimensional experimental scheme, which contains just three transmitters with broadband modulation of two primary waves and one receiver, is proposed. The model numerical and physical experiment results are presented.

Keywords Medical tomography · Nonlinear parameters

1 Introduction

Nonlinear parameters of medium have an important diagnostic meaning in medicine. A relative variation of nonlinear parameter values in diseased tissues as compared to healthy ones exceeds significantly linear characteristics variation of the same tissues. This fact emphasizes the nonlinear parameter diagnostic importance. The effect of sound-by-sound scattering [1] is the generation of combination waves by the interaction of two primary acoustic waves in a nonlinear medium. The possibility of using this effect for tomography has been shown References [1–3].

Third-order nonlinear scattering effects and their diagnostic validity have been investigated less thoroughly than the second-order effects. However there is interest in these processes [4, 5]. In the present paper, the nonlinear interaction of three primary waves and the third-order nonlinear scattering process are considered. As it has been shown in Reference [6] the given information from experiments due to this method makes it possible to reconstruct both a spatial distribution of the second-order nonlinear parameter and spatial distribution of a new value, the third-order nonlinear parameter $\varepsilon_3(\mathbf{r})$. Possibilities of using this effect for medical tomography require detailed analysis of the nonlinear interaction processes.

V.A. Burov (✉)
Department of Acoustics, Faculty of Physics, Moscow State University,
119991 Moscow, Russia
e-mail: burov@phys.msu.ru

M.P. André et al. (eds.), *Acoustical Imaging*, Acoustical Imaging 30,
DOI 10.1007/978-90-481-3255-3_43,

2 The Generation of Third-Order Combination Waves

Equations describing sound waves in a scalar medium include the equation of motion, the continuity equation and the state equation:

$$\rho\left[\frac{\partial \mathbf{v}}{\partial t}+(\mathbf{v}\nabla)\mathbf{v}\right]=-\nabla P+\mathbf{\Phi}_0,\ \frac{\partial \rho}{\partial t}+\mathrm{div}(\rho\mathbf{v})=0, P=P(\rho) \tag{1}$$

Here $\mathbf{\Phi}_0$ is the volume density of primary-waves sources, $P(\mathbf{r},t)$ is the total pressure, $\rho(\mathbf{r},t)$ is the density of medium, $\mathbf{v}(\mathbf{r},t)$ is the vibration velocity of medium particles. Presentation of the pressure $P(\mathbf{r},t)\equiv P_0+p(\mathbf{r},t)$ and the density $\rho(\mathbf{r},t)\equiv\rho_0+\rho'(\mathbf{r},t)$ in the form of a deviation from equilibrium values P_0 and ρ_0 makes it possible to consider the second-order and third-order nonlinear effects with respect to perturbations p, ρ', $\mathbf{v}$ ($\mathbf{v}=0$ if wave is absent). Within this approximation and under the assumption that $\rho_0\equiv \mathrm{const_r}$, the state equation has the following form:

$$\begin{aligned}P(\rho)=P_0+\left(\partial P\big/\partial\rho\right)_{\rho=\rho_0}\rho'+\frac{1}{2}\left(\partial^2 P\Big/\partial\rho^2\right)_{\rho=\rho_0}(\rho')^2+\\ +\frac{1}{6}\left(\partial^3 P\Big/\partial\rho^3\right)_{\rho=\rho_0}(\rho')^3+\ldots\end{aligned} \tag{2}$$

The Equation (2) contains characteristic parameters: $c^2(\mathbf{r})=\left(\partial P\big/\partial\rho\right)_{\rho=\rho_0}$ is the squared velocity of sound; $\varepsilon_2(\mathbf{r})=1+B\big/(2A)$ is the second-order acoustical nonlinear parameter of medium; here $A=\left(\rho_0\big/P_0\right)c^2(\mathbf{r})$, $B=\left(\rho_0^2\big/P_0\right)\left(\partial^2P\big/\partial\rho^2\right)_{\rho=\rho_0}$. By analogy, the third-order nonlinear parameter of medium can be introduced: $\varepsilon_3(\mathbf{r})=C\big/(6A)$, where $C=\left(\rho_0^3\big/P_0\right)\left(\partial^3P\big/\partial\rho^3\right)_{\rho=\rho_0}$. The wave equation for the acoustical pressure $p(\mathbf{r},t)=P(\mathbf{r},t)-P_0$ is the result of the Equations (1–2): [6]

$$\Delta p-\frac{1}{c^2(\mathbf{r})}\frac{\partial^2 p}{\partial t^2}=F_0-Q_2+Q_3. \tag{3}$$

The secondary sources $(-Q_2)$ and Q_3 generate scattered fields due to the second- and third-order nonlinear interactions, respectively. The sources, which generate scattered fields observed beyond an interaction region of primary waves, are described by the following formulas:

$$Q_2=\frac{\varepsilon_2(\mathbf{r})}{\rho_0\,c^4(\mathbf{r})}\frac{\partial^2p^2}{\partial t^2};\ Q_3=Q_3^{\mathrm{phys}}+Q_3^{\mathrm{geom}}; \tag{4}$$

$$\begin{aligned}Q_3^{\mathrm{phys}}&=\frac{\varepsilon_3'(\mathbf{r})}{\rho_0^2\,c^6(\mathbf{r})}\frac{\partial^2p^3}{\partial t^2}+\frac{2\,(\varepsilon_2(\mathbf{r})-1)}{\rho_0^2c^6(\mathbf{r})}\left(\frac{\partial\,p}{\partial t}\right)\left(\frac{\partial\,p^2}{\partial t}\right),\\ \varepsilon_3'(\mathbf{r})&\equiv 2\,(\varepsilon_2(\mathbf{r})-1)^{\,2}-\varepsilon_3(\mathbf{r}),\\ Q_3^{\mathrm{geom}}&=\frac{\rho'}{\rho_0^2c^4(\mathbf{r})}\left(\frac{\partial p}{\partial t}\right)^2-\frac{1}{2}\rho'\Delta(\mathbf{v}^2)-\rho'\mathbf{v}\,(\Delta\mathbf{v})-\\ &\quad-\mathbf{v}\left[(\mathbf{v}\nabla)(\nabla\rho')\right]-2(\nabla\rho')\,[(\mathbf{v}\nabla)\mathbf{v}]\,.\end{aligned} \tag{5}$$

By physical implication, Q_3 are divided into Q_3^{phys} and Q_3^{geom}, which are called "physical" and "purely geometric" sources, respectively. The sources Q_3^{phys} are related to the presence of the nonlinear parameters ε_2 and ε_3 in the state equation. These sources appear only in nonlinear medium. The sources Q_3^{geom} are related to the equations of motion and continuity and are independent of internal physical processes in the medium. They appear even in case of the wave interaction in linear medium.

As it follows from the relations in Equation (5), the information given from the third-order nonlinear tomography is related to reconstruction of spatial distributions of both the second- and third-order nonlinear parameters. For more detailed analyses of informational opportunities of third-order nonlinear tomography, it is convenient to consider monochromatic primary wave components. The pressure field of the primary and scattered waves at the corresponding frequencies ω_j can be represented as $p_j(\mathbf{r},t) = \left[p_j(\mathbf{r})\exp(-i\omega_j t) + p_j^*(\mathbf{r})\exp(i\omega_j t)\right]\Big/2$. Then the wave Equation (3) for the total field $p(\mathbf{r},t) = \sum_j p_j(\mathbf{r},t)$, which is the sum of the fields of the primary waves, their second and third harmonics, and the second- and third-order combination waves, decomposes into a system of equations for complex amplitudes $p_j(\mathbf{r})$. The second-order case has been considered in Reference [1]. Due to the third-order approximation, it is sufficient to consider the sources Q_3 within the approximation of the given field $p(\mathbf{r},t) \approx p_1(\mathbf{r},t) + p_2(\mathbf{r},t) + p_3(\mathbf{r},t)$, which is the sum of the primary waves p_1, p_2, p_3 with wave vectors $\mathbf{k}_1, \mathbf{k}_2, \mathbf{k}_3$. Finally, the relations (Equations 3 and 4) yield the equations for complex amplitudes $p_{\pm\pm}(\mathbf{r})$ at frequencies $\Omega_{\pm\pm} = \omega_1 \pm \omega_2 \pm \omega_3$: [6]

$$\left[\Delta + \frac{\Omega_{\pm\pm}^2}{c^2}\right]\frac{p_{\pm\pm}(\mathbf{r})}{2} = \left[A_{\pm\pm}^{\text{phys}1}(\mathbf{r}) + A_{\pm\pm}^{\text{phys}\,2}(\mathbf{r}) + A_{\pm\pm}^{\text{geom}}(\mathbf{r})\right]\times \times \frac{p_1(\mathbf{r})p_2^{(*)}(\mathbf{r})p_3^{(*)}(\mathbf{r})}{2^3}; \tag{6}$$

$$A_{\pm\pm}^{\text{phys}\,1}(\mathbf{r}) = -\frac{1}{\rho_0^2 c^6}6\Omega_{\pm\pm}^2\varepsilon_3'(\mathbf{r}); A_{\pm\pm}^{\text{phys}\,2}(\mathbf{r}) = -\frac{2}{\rho_0^2 c^6}\,(\varepsilon_2(\mathbf{r}) - 1)\times \times\,[\,\omega_1(\pm\omega_2 \pm \omega_3) \pm \omega_2(\pm\omega_3 + \omega_1) \pm \omega_3(\omega_1 \pm \omega_2)\,]\,; \tag{7}$$

the coefficient $A_{\pm\pm}^{\text{geom}}$, corresponding to the purely geometric sources, is not shown because of the estimations given below in Section 4. In the expression (Equation 7) the sign $\pm$ before frequencies is the same as for the combination frequency $\Omega_{\pm\pm} = \omega_1 \pm \omega_2 \pm \omega_3$. The conjugation sign in the combination p_1, $p_2^{(*)}$, $p_3^{(*)}$ is in parentheses because it corresponds only to the case of sign "–" for the corresponding frequency. The sources $\sim A_{\pm\pm}^{\text{phys}1}$ have a purely physical origin. The sources $\sim A_{\pm\pm}^{\text{phys}\,2}$ appear because of two effects: geometric nonlinearity and medium nonlinearity, i.e., they are "geometric-physical".

Solution of the Equation (6) within the far-field approximation is:

$$\frac{1}{2}p_{\pm\pm}(\mathbf{y}) = \frac{p_{01}\,p_{02}^{(*)}\,p_{03}^{(*)}}{2^3}G_{\pm\pm}(\mathbf{y},0)\tilde{A}_{\pm\pm}(\mathbf{K}_{\pm\pm}), \qquad \mathbf{K}_{\pm\pm} = \mathbf{k}_{\pm\pm} - (\mathbf{k}_1 \pm \mathbf{k}_2 \pm \mathbf{k}_3). \tag{8}$$

Here $\tilde{A}_{\pm\pm}(\mathbf{K}_{\pm\pm})$ is Fourier transform of the function of complicated frequency-dependent third-order nonlinear scatterer.

$A_{\pm\pm}(\mathbf{r}) \equiv A^{\text{phys1}}_{\pm\pm}(\mathbf{r}) + A^{\text{phys2}}_{\pm\pm}(\mathbf{r}) + A^{\text{geom}}_{\pm\pm}(\mathbf{r})$; the vector $\mathbf{y}$ defines an observation point, which is the centre of plane receiver; $G_{\pm\pm}(\mathbf{y}, \mathbf{r})$ is the monochromatic Green's function (for the frequency $\Omega_{\pm\pm}$) of homogeneous infinite background medium with the sound velocity $c = c_0$; $\mathbf{k}_{\pm\pm} \equiv \left(\Omega_{\pm\pm}/c_0\right)\left(\mathbf{y}/|\,\mathbf{y}|\right)$ is the wave vector of the scattered wave at the corresponding frequency $\Omega_{\pm\pm}$; $\mathbf{K}_{\pm\pm}$ is the vector of the corresponding spatial frequency. Thereby, the third-order combination wave pressure is dependent on primary wave amplitudes and spatial spectrum $\tilde{A}_{\pm\pm}(\mathbf{K}_{\pm\pm})$ of the nonlinear scatterer.

3 Acoustical Tomography Model

Figure 1 shows a nonlinear tomography model scheme. Three planar transmitters (two broadband and one monochromatic) and a planar broadband receiver are located on an aperture circle. The object under investigation is located inside the intersection area of near zones of all four transducers. Independent phase-coded $(0, \pi)$ signals are applied to the broadband transmitters 1 and 2. The third transmitter emits a monochromatic wave. The receiver records the total field, which is the result of multiple linear and nonlinear wave scattering.

In the model numerical and physical experiments described below, the following frequencies and spectrum bands of the primary and received waves were used. The signals with the same carrier frequency $f_1^0 = f_2^0 = 2$ MHz and the band $f_1 = f_2 \in [1.7 \div 2.3]$ MHz were applied to the broadband transmitters 1 and 2.

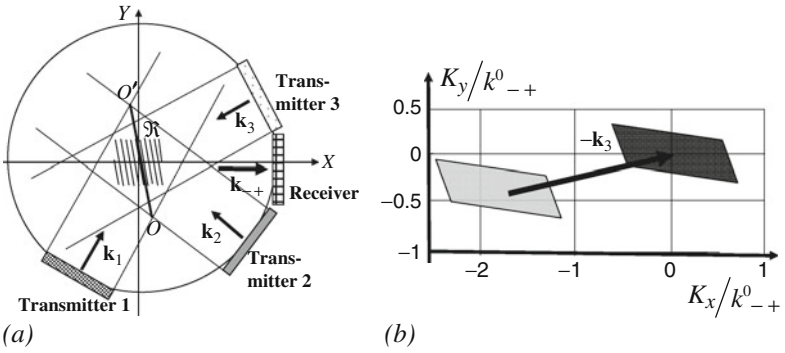

Fig. 1 (**a**) Model experiment scheme; (**b**) Shift of the localization region of the spatial spectrum of a third-order nonlinear scatterer (*darker region*), reconstructed by the combination frequencies $\Omega_{-+} = \omega_1 - \omega_2 + \omega_3$ (k^0_{-+} and λ^0_{-+} are the corresponding mean wave number and wave length), with respect to the similar region for a second-order scatterer (*lighter region*), reconstructed by the frequencies $\Omega_{-} = \omega_1 - \omega_2$. Directions of vectors of the primary waves and the reception direction are the same in both cases

The monochromatic transmitter 3 emitted at the frequency $f_3^0 = 1.3$ MHz. The third-order combination signal at difference-sum frequency $\Omega_{-+} = \omega_1 - \omega_2 + \omega_3$ was received in the band $f_{-+} \in [1.0 \div 1.6]$ MHz with the carrier frequency $f_{-+}^0 = 1.3$ MHz.

The set of wave vectors of the primary waves is: $\mathbf{k}_1 \in (\mathbf{k}_1^0 \pm \Delta\mathbf{k}_1)$, $\mathbf{k}_2 \in (\mathbf{k}_2^0 \pm \Delta\mathbf{k}_2)$, $\mathbf{k}_3 \equiv \mathbf{k}_3^0$. The additives $\Delta\mathbf{k}_1$ and $\Delta\mathbf{k}_2$ are determined by the radiation band and are co-directional with vectors $\mathbf{k}_1^0$ and $\mathbf{k}_2^0$. It is important for experimental data to have information about the zero component of the spatial spectrum $\mathbf{K}_{-+} = 0$, which corresponds to the constant component of the scatterer function. Therefore the angles between acoustical axis of the receiver and acoustical axes of the three transmitters were chosen to be $\alpha_1 = -116°$, $\alpha_2 = -38°$, $\alpha_3 = 27°$ (Fig. 1a). The direction of the received wave vector $\mathbf{k}_{-+}$ was characterized by the angle 0. The reconstructed region $\mathbf{K}_{-+}$ of spatial spectrum is shown in Fig. 1b as the dark tetragonal area; $k_{-+}^0 = (\omega_1^0 - \omega_2^0 + \omega_3^0)/c_0$ is the wave number at the combination carrier frequency. For comparison, the light area of spatial components $\mathbf{K}_- = \mathbf{k}_- - (\mathbf{k}_1 - \mathbf{k}_2)$ reconstructed due to the second-order tomography is shown in the same figure ($\mathbf{k}_-$ is the wave vector of the received wave) – more details are given in Reference [2]. The presence of the third wave shifts the available spatial frequency region by the vector $-\mathbf{k}_3$ (in case of $\mathbf{K}_{-+}$) and makes it possible to flexibly change the reconstruction region of the spatial spectrum $\tilde{A}_{-+}(\mathbf{K}_{-+})$ with the same mutual location of the receiver and two broadband transmitters.

The reconstructed nonlinear scatterer $A_3(\mathbf{r})$ is described by the set of the functions $A_{\pm\pm}^{\text{phys}1}(\mathbf{r}) + A_{\pm\pm}^{\text{phys}\,2}(\mathbf{r}) + A_{\pm\pm}^{\text{geom}}(\mathbf{r})$ (the right part of the Equation 6) generalized to the case of broadband signals. The procedure of reconstruction is analogous to the second-order tomography [2, 3] and it is based on the matched filtering of the recorded scattered signal $p(\mathbf{y}, t)$. The comparison signal (i.e. reference response) $p_\delta(\mathbf{y}|\mathbf{r}; t)$ for a point of space $\mathbf{r}$ is a predicted combination signal in the considered frequency band, which is generated by the test nonlinear scatterer $A_\delta(\mathbf{r}') \sim \delta(\mathbf{r}' - \mathbf{r})$ (normalization factor is omitted) and is registered by the same receiver. Estimation $\hat{A}_3(\mathbf{r})$ of the scatterer $A_3(\mathbf{r})$ is:

$$\hat{A}_3(\mathbf{r}) = \frac{\int p_\delta^*(\mathbf{y}|\mathbf{r}; t) p(\mathbf{y}, t) dt}{\int p_\delta^*(\mathbf{y}|\mathbf{r}; t) p_\delta(\mathbf{y}|\mathbf{r}; t) dt}. \tag{9}$$

As in the second-order tomography [2], for medium with homogeneous linear parameters, the line of intersection of two interacting plane coded wave fronts is bisector of the angle between the vectors $\mathbf{k}_1$ and $\mathbf{k}_2$. This line corresponds to constant value of mutual phase shift of these waves. Nonlinear scatterers, being located along the fixed line which is parallel to the bisector OO' (Fig. 1), generate the combination waves with the same code due to coding the two (of three) interactive waves. Each of these lines has the individual code of the generated combination signal. In Fig. 1 the identical code lines are shown as skew strips inside the scattering region $\Re$. Presence of the monochromatic wave shifts the center frequency of the combination signal without changing the code character and the signal arrival time. This

circumstance allows the formation of one test response for all points **r**, belonging to the identical code line, which significantly simplifies the reconstruction process.

Two dimensional reconstructed image is defined by two spatial coordinates of radius-vector **r**. This image is explicitly described by scattering data, which are also defined by two parameters, i.e., arrival time for points belongs to the identical code line and the individual code of this line. Such a correspondence of the dimension of the image space and the data space makes it possible to reconstruct the nonlinear parameter spatial distribution sought for.

4 Comparison of the Secondary Sources' Amplitudes and Combination Signal Levels

To determine the practical possibility of third-order nonlinear effects observation, it is necessary to compare levels of desired and interfering signals. Estimations of character values of the physical sources (Equations 5 or 7), which are the most informative for the third-order nonlinear tomography diagnostic tasks, have been made for the scatterers with nonlinear characteristics similar to water. For these estimations, the equation of state in the Theta form was used: $P = P_* \left(\rho/\rho_0\right)^{\Gamma}$, where P_* is the internal pressure of liquid, Γ is the constant (for the given liquid). For water $P_* \approx 3 \times 10^8$ Pa, $\Gamma \approx 7$, then $\varepsilon_2 \approx 4$, $\varepsilon_3 \approx 5$, $\varepsilon_3' \approx 13$.

The estimations have shown that a nonlinear source, being concentrated in a resolution element with the volume $\Delta V \cong (1 \times 1 \times 10)\ \text{mm}^3 = 10^{-8}\ \text{m}^3$ (10 mm in vertical direction is the thickness of two-dimensional layer analyzed in tomography), generates the acoustic fields $p_{-+}^{\text{phys}\,1} \cong 2 \times 10^{-4}$ Pa, $p_{-+}^{\text{phys}\,2} \cong 10^{-4}$ Pa, $p_{-+}^{\text{geom}} \cong 3 \times 10^{-5}$ Pa at distance $\cong 0.1$ m from the source. It can be seen that p_{-+}^{geom} is one order less than $p_{-+}^{\text{phys}} = p_{-+}^{\text{phys}\,1} + p_{-+}^{\text{phys}\,2}$. It makes it possible to neglect the geometric sources at the first stage of reconstruction process and to simplify the process of estimation of tomography results. The amplitudes of pressure of the physical sources $p_{-+}^{\text{phys}\,1}$ and $p_{-+}^{\text{phys}\,2}$ are of the same order, however they could be separated by different frequency dependence of their spectral components. Thus, individual information about $\varepsilon_2(\mathbf{r})$ and $\varepsilon_3(\mathbf{r})$ can be derived.

There is the problem of separating the purely third-order nonlinear interaction effect and the competitive effect of the twofold second-order nonlinear scattering. These effects generate the combination signal at the same frequency $\Omega_{-+} = \omega_1 - \omega_2 + \omega_3$ and with the same code. However, the influence of the twofold scattered wave has proved to be negligible [6].

5 Numerical Modeling

In numerical simulation of the reconstruction process, only the main physical sources $Q_3^{\text{phys}1} = \left(\varepsilon_3'(\mathbf{r})/(\rho_0^2 c^6)\right)\left(\partial^2 p^3/\partial t^2\right)$ of the third-order scattered fields were considered, The task was to reconstruct distribution $\varepsilon_3'(\mathbf{r})$. The medium was

Fig. 2 Model illustration of reconstruction processes. (**a**) Initial distribution of nonlinear parameter value; reconstruction result by the scheme using (**b**) second-order and (**c**) third-order nonlinear effects

supposed to be with homogeneous linear parameters. The estimation $\hat{A}_3(\mathbf{r}) = \hat{\varepsilon}'_3(\mathbf{r})$ was obtained by Equation (9).

In model experiments, as well as in physical experiments described below with natural objects, the tomography scheme (Fig. 1) and the operating frequencies described in paragraphs 3 and 4 were used. The test response $p_\delta(\mathbf{y}|\mathbf{r}_0; t)$ in Equation (9) was formed for the frequencies Ω_{-+}. The spatial sample was $\approx \lambda^0_{-+}/5$ along the identical code lines and $\lambda^0_{-+}/4$ along the orthogonal direction; $\lambda^0_{-+} \approx 1.1$ mm is the wave length at the carrier frequency Ω_{-+}.

As an example, the reconstruction of Cyrillic letters "МГУ" (Fig. 2a) was considered. The distance between regularly located point-like scatterers forming the image was $\lambda^0_{-+}/5$. The background value of ε'_3 was supposed to be zero; the nonlinear parameter was $\varepsilon'_3 = -6$ for the letter "М", $\varepsilon'_3 = 6$ for "Г", $\varepsilon'_3 = 2.9$ for "У". The letter height and the width of the whole inscription were $14\,\lambda^0_{-+}$ and $40\,\lambda^0_{-+}$, respectively. The record time was 0.3 s. To reconstruct the area of the spatial spectrum $\tilde{\varepsilon}_2(\mathbf{K})$ in the vicinity of zero is impossible in the second-order nonlinear tomography. Therefore, the reconstructed image has only the object's contour, the origin values $\varepsilon_2(\mathbf{r})$ not being reconstructed [2]. At the same time, the full image (including the constant component) of the third-order nonlinear parameter $\varepsilon'_3(\mathbf{r})$ distribution is reconstructed with help of the third-order tomography (Fig. 2c).

The model with the single Cyrillic letter "У" ($\varepsilon'_3 = 8$ inside it) was considered against a homogeneous nonzero background $\varepsilon'_3 = 2$ (Fig. 3a). In the third-order nonlinear tomography the complete values ε'_3 are reconstructed correctly for both the letter and the background (Fig. 3b). The nonlinear parameter distribution is reconstructed inside the hexagonal area, which is the interaction region of the three primary waves.

6 Physical Experiment

The tomography experiment was made in a round cuvette with the diameter of 35 sm and the height of 12 sm. The cuvette was filled with water; the walls and bottom were covered by absorbing rubber. Three planar transmitters and one receiver were located in the aperture circle with the radius of 13 sm, corresponding to the scheme

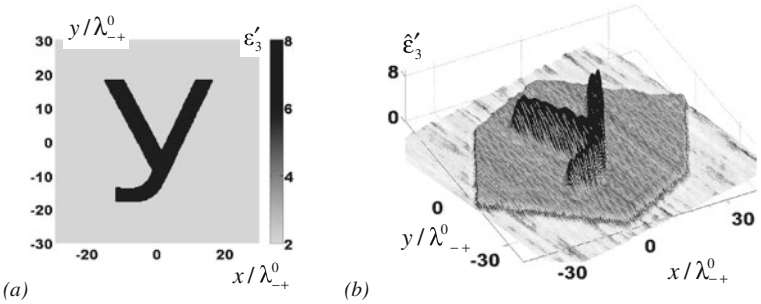

Fig. 3 Model illustration of reconstruction processes for nonlinear parameter against nonzero background. (**a**) Initial distribution of nonlinear parameter value; (**b**) axonometric view of the reconstruction result

in Fig. 1. There is the principle difficulty of realization: power of the received third-order combination signals is two orders weaker than the power of the second-order nonlinear signals. This circumstance applies more rigorous requirements to all characteristics of the used tomography scheme.

Woolen thread with the diameter of $\approx$ 1.5 mm was chosen as the first model scatterer. The thread has revealed high nonlinear characteristics in the second-order nonlinear tomography experiments [3]. Presence of this nonlinearity is caused by air bubbles in wool; the bubbles are contrast agents with very high second-order nonlinearity value. The considered tomography scheme reconstructs the distribution of the parameter $\varepsilon'_3(\mathbf{r}) \equiv 2\,(\varepsilon_2(\mathbf{r}) - 1)^2 - \varepsilon_3(\mathbf{r})$ depending quadratically on the second-order nonlinear parameter ε_2. The record time was $\approx$ 0.11 s. Figure 4a shows the normalized reconstruction result $|\hat{\varepsilon}'_3(\mathbf{r})|/\max_{\mathbf{r}}|\hat{\varepsilon}'_3(\mathbf{r})|$ of the distribution $\varepsilon'_3(\mathbf{r})$. The maximum which is distinctly seen in the middle of the reconstructed image indicates the thread location.

Together with the main considered nonlinear effect of interaction of three waves inside the region under study, primary waves are exposed to the linear scattering by medium inhomogeneities of the sound velocity and absorption. In this case the linearly scattered waves interact collinearly with each other during the whole path towards the receiver. Finally, the third-order combination waves are generated. They make a certain contribution to the informational signal because of accumulation along the path and create the competitive effect. To estimate this effect contribution, the following experiment was made. A thin metal wire was located in the center of the cuvette instead of the woolen thread. The sharp boundary of the wire reflected the primary waves. This experiment and the reconstruction result have shown the presence of the competitive effect; however it has a negligibly small contribution to the informational signal.

At the present time, the first experiments proving the possibility of nonlinear characteristic reconstruction for natural biological tissues due to the third-order effect have been made. Firstly, pork fat was used having [5] $B/A \approx 10$ and $C/A \approx 100$, whence $\varepsilon_2 \approx 6$, $\varepsilon_3 \approx 17$, $\varepsilon'_3 \approx 40$. A thin long fat strip with a thickness of 3 mm and a width of 20 mm was suspended in the center of the cuvette and

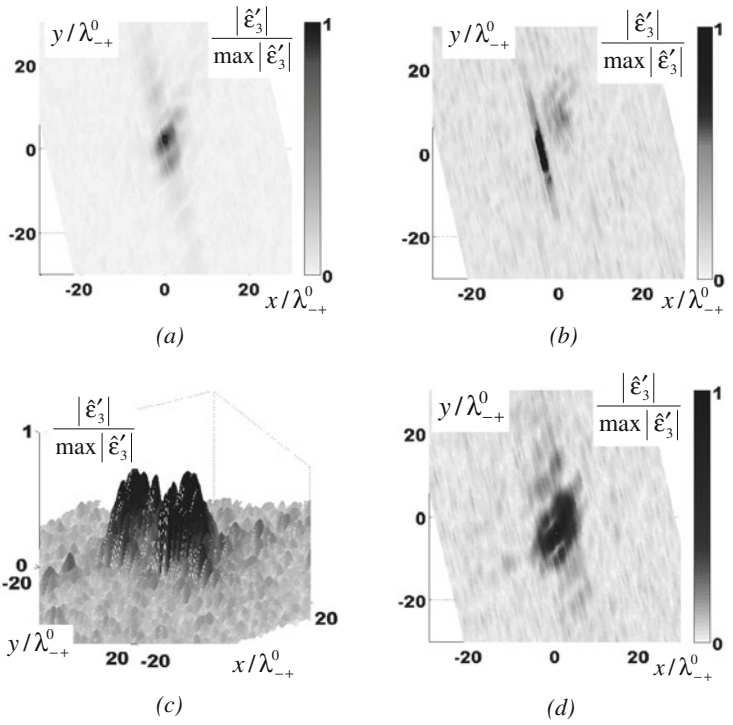

Fig. 4 Reconstruction result of natural nonlinear scatterers using third-order tomography scheme (look at Fig. 1): (**a**) woolen thread; (**b**) thin pork fat strip oriented along the identical code line; (**c**) fat column with cross-section size of (20 × 20) mm^2 (axonometric view); (**d**) human's finger

was orientated along the identical code line. Record time was ≈ 0.22 s. This strip projection on the tomography plane is clearly reconstructed in Fig. 4b. As another object, the fat column with a cross-section size of (20 × 20) mm^2 was used. Its cross-section is reproduced by the axonometric view in Fig. 4c (record time was ≈ 0.22 s). The reconstructed cross-section of a human index finger, being dipped in water perpendicularly to the tomography plane, is shown in Fig. 4d (recording time was ≈ 0.11 s).

7 Conclusion

The obtained estimation of the signal levels and the conducted first physical experiments proved the possibility of using the third-order combination waves in real tomography schemes. The main advantage of the suggested diagnostic scheme is the possibility of completely reconstructing the spatial distribution of the medium characteristics by just three transmitters and one receiver. At the same time, the same result by the second-order tomography requires about 20 ÷ 30 transducers [2]. The

suggested method using the nonlinear effects can be applied to reconstruction of a blood flow map and complete vector of blood flow velocity [7].

Acknowledgements This study was supported by the President of the Russian Federation, grant number NSh-2906.2008.2, and by the Russian Foundation for Basic Research, project no. 07-02-00239.

References

1. Burov, V.A., Gurinovich, I., Rudenko, O.V., Tagunov, E. Ya.: Nonlinear acoustical tomography in inhomogeneous media. In: Tortoli, P., Masotti, L. (eds.) Acoustical Imaging, vol. 22, pp. 125–130. Plenum Press, New York (1996)
2. Burov, V.A., Evtukhov. S.N., Tkacheva, A.M., Rumyantseva, O.D.: Acoustic tomography of the nonlinear parameter by a small number of doppler frequency. Acoust. Phys. **52**(6), 655–669 (2006)
3. Bereza, S.A., Burov, V.A., Evtukhov, S.N.: Model experiments on acoustic tomography of the nonlinear parameter. Acoust. Phys. **54**(4), 449–459 (2008)
4. Hu, X., Mao, F., Gong, X., Zhang, D.: Theoretical calculation and experimental study on the third-order nonlinearity parameter for organic liquids and biological fluids. J. Acoust. Soc. Am. **113**(3), 1743–17489 (2003)
5. Gong, X., Liu, X., Zhang, D.: In: Enflo, B.O., Hedberg, C.M., Kari, L. (eds.) 18th International Symposium on Nonlinear Acoustics, American Institute of Physics, Melville, New York, pp. 444–447 (2008).
6 Burov, V.A., Shmelev, A.A., Rumyantseva, O.D.: Tomography of the spatial distribution of a scatterer in third-order nonlinear processes. Bull. Russ. Acad. Sci.: Phys. **72**(1), 82–88 (2008)
7. Burov, V.A., Evtukhov, S.N., Rumyantseva, O.D.: Reconstruction of the blood flow pattern by tomography of the acoustic nonlinear parameter: Computer simulation and physical experiment. Acoust. Phys. **54**(5), 615–625 (2008)

Epilogue

Professor Glen Wade

H. Lee

Professor Glen Wade passed away in June, 2009. He left peacefully in his sleep. He was 88.

Glen Wade was born in Ogden, Utah, in 1921. His father was Chief Justice of the State of Utah. Glen was going to follow in his father's footsteps for a career in law. But because he had always enjoyed mathematics and physics, he instead went on to study engineering in the University of Utah.

Then Pearl Harbor happened. He applied for officers training and was sent to the University of Notre Dame. In a few months he graduated and commissioned as an Ensign. After that he was assigned as an electronics officer to go to Bowdoin College in Brunswick, Maine, to continue in electronics training. While in Brunswick, he married LaRee Bailey.

After the war, he returned to the University of Utah in 1946 and spent two years to complete a bachelor's degree and one more year for a master's degree in electrical engineering. Subsequently, he moved to the Naval Research Laboratory, where he worked on high-frequency and traveling-wave tubes.

After working at the Naval Research Laboratory, he went to Stanford for the PhD degree and was appointed Associate Professor after graduation. He left Stanford in 1960 to work at Raytheon as Director of Engineering. In 1963, he accepted an offer to join Cornell as Director of School of Electrical Engineering and holder of the J. Preston Levis Chair. He joined UC Santa Barbara in 1966, where he remained until his retirement in 1991. He continued to engage in teaching and research during his retirement (Fig. 1).

Dr. Wade was active in professional societies. He chaired the 4th the International Symposium of Acoustical Imaging in 1972, and co-chaired the 18th meeting in 1989, serving as Editor and Co-Editor for the corresponding Proceedings. He served as the Editor of IEEE Transactions on Electron Devices, Editor of the IEEE Journal

H. Lee (✉)
Department of Electrical and Computer Engineering, Center for Advanced Surgical and Interventional Technology (CASIT), University of California, Santa Barbara, CA 93106, USA
e-mail: hualee@ece.ucsb.edu

M.P. André et al. (eds.), *Acoustical Imaging*, Acoustical Imaging 30,
DOI 10.1007/978-90-481-3255-3,

Fig. 1 Wade's research group in 1977. Left to right: Larry Schlussler (PhD, 1978), Greg Lockwood (Computer Laboratory Manger), Scott Elliott (PhD, 1979), Behzad Noorbehesht (PhD, 1980), Nie-But Tse (PhD, 1979), Hua Lee (PhD, 1980), Ibraham Klugeer (MS, 1978), Agustine Coello-Vera (PhD, 1978), Dr. Joseph Eisner, Professor Glen Wade, and Dr. Gail Flesher

of Quantum Electronics, and Chief Editor of the IEEE Proceedings. He was elected IEEE Fellow in 1962, received the IEEE Centennial Medal in 1984 and the Third Millennium Medal in 2000. Prof. Wade was also an extraordinary teacher. He received the UCSB Academic Senate Distinguished Teaching Award in 1977.

Glen's wife LaRee also passed away in July 2009, one month after his passing. They were married for 65 years and had four daughters, Kathy, RaLee, Mary Sue, and Lisa.

Glen was a genuinely kind person and truly wonderful teacher. He is greatly missed.

Author Index

Subject Index